Steam-Solvent Coinjection for Bitumen Recovery under Reservoir Heterogeneity with Consideration of Water Solubility in Oil

by

Arun Venkat Venkatramani

A thesis submitted in partial fulfillment of the requirements for the degree of

Doctor of Philosophy

in

Petroleum Engineering

Department of Civil and Environmental Engineering
University of Alberta

Abstract

The main objective of this research is to determine if expanding solvent-steam assisted gravity drainage (ES-SAGD), wherein a small quantity of a condensable solvent is coinjected with steam, can be a better alternative to SAGD in highly heterogeneous formations. Specifically, three previously unanswered questions are addressed.

Firstly, the effect of dissolution of water in the oleic phase (x_{wL}) on the relative performance of ES-SAGD to SAGD in a synthetic homogeneous bitumen reservoir is examined. Experimental data show that x_{wL} can be significant at elevated temperatures, and the dilution of bitumen by water can lower the viscosity of the oleic phase. However, x_{wL} is disregarded in conventional reservoir simulation practice. Using phase behavior models that were carefully created on the basis of experimental data, the benefit of solvent coinjection relative to steam-only injection in terms of bitumen production is shown to be overestimated by nearly 10% at 35 bars when x_{wL} is disregarded. This mainly comes from the underestimation of the performance of SAGD.

Secondly, an investigation is conducted on the effects of reservoir heterogeneity on the relative performance of ES-SAGD to SAGD in terms of the steam-oil-ratio (SOR) as a function of cumulative bitumen production. x_{wL} is considered in these evaluations to ensure reliable assessment of the benefit of solvent coinjection.

Using one hundred stochastically-generated realizations of heterogeneous reservoirs comprising of clean sand and mudstone, ES-SAGD is shown to be less sensitive to reservoir heterogeneity than SAGD, and the reduction in SOR due to coinjection for a given cumulative bitumen production is demonstrated to be higher under heterogeneity. This is due to the

combination of enhanced mixing between solvent and bitumen under heterogeneity, and the interplay between solvent-bitumen mixing and temperature distribution within the reservoir.

Lastly, conditions for flow in heterogeneous reservoirs conducive to significant reduction in the cumulative SOR due to coinjection of solvent are identified in conjunction with an analytical theory for SAGD. Results show that (i) the SOR reduction by steam-solvent coinjection is positively correlated with the increase in SAGD's SOR due to heterogeneity, (ii) a larger amount of bitumen tends to be diluted in those reservoirs for which SAGD exhibits slow production of bitumen, and (iii) the dilution of bitumen by solvent under steam-solvent coinjection becomes more pronounced where flow barriers restrict the local flow of bitumen in SAGD at elevated temperatures. Accumulation of solvent in such heated slow-flow regions can facilitate a substantial increase in the flow rate of bitumen through the simultaneous reduction of the oleic-phase viscosity and improvement of the oleic-phase relative permeability by enhancement of the oleic-phase saturation. The interplay between dilution of bitumen by solvent and temperature can further facilitate the reduction of the cumulative SOR by mitigating thermal losses.

Acknowledgements

I express my deepest gratitude to my advisor, Dr. Ryosuke Okuno (currently with University of Texas at Austin), for his guidance, patience and support throughout my study at the University of Alberta. I am very appreciative of his efforts to teach me the importance of having a strong work ethic, thinking critically, and communicating effectively.

I am grateful to my co-advisor, Dr. Juliana Leung, at University of Alberta for her assistance with the geostatistical modeling conducted in this research, and her advice pertaining to the enhancement of the practical significance of this research. I am also thankful to the chairperson of my supervisory committee, Dr. Hassan Dehghanpour, members of my doctoral candidacy examination committee, Drs. Clayton Deutsch and Janet Elliott, and the members of my dissertation committee, Dr. Huazhou Li, Dr. Richard Chalaturnyk, and Dr. Mingzhe Dong (University of Calgary) for their insightful questions and suggestions on further improvement with regard to the communication of this research. I thank Ms. Arlene Figley for facilitating the arrangement of my candidacy and final exams, and for patiently answering all my questions regarding the procedural aspects of the PhD program.

I gratefully acknowledge financial supports from Japan Petroleum Exploration Company Ltd. (JAPEX), Japan Canada Oil Sands Ltd. (JACOS), and Shell enhanced learning fund (SELF, Shell Canada) without which I could not have completed this research. Further, I thank my colleagues, Dr. Ashutosh Kumar (Indian School of Mines) for his assistance with the characterization of bitumen used in this project, and Kai Sheng (University of Texas at Austin) for his participation in technical discussions.

I am indebted to my teachers, Drs. Subhash Mahajan (University of California at Davis), Patrick Phelan, Kaushal Rege, and David Nielsen from Arizona State University, and Dr. Madhusree Kundu (National Institute of Technology, Rourkela), for encouraging me to pursue a PhD. Without their support, I could not have made it to the University of Alberta. Finally, I cannot thank my family enough for everything they have done for me.

Table of Contents

Chapter 1. Introduction

The economic potential of the Alberta oil sands is immense in view of its reserves of bitumen, which exceeds 1.6 trillion barrels (Ranger and Gingras, 2003). Economically viable production of bitumen at the commercial scale, however, is still a significant engineering challenge primarily due to three aspects: (i) the location of the majority of bitumen reserves at depths unviable for mining, rendering the flow of bitumen in-situ necessary; (ii) the very low mobility of bitumen at initial reservoir conditions due to its high viscosity; and (iii) the presence of reservoir heterogeneities, which can adversely affect the hydraulic path available for fluid flow towards production wells.

Successful recovery of bitumen over the long term inevitably requires the mobilization of bitumen in-situ through the reduction of its viscosity using an external agent. Steam-assisted gravity drainage (SAGD) is currently the most widely used in-situ technique for the recovery of bitumen.

In SAGD, steam of high quality is injected into the reservoir using a horizontal well. The injected steam propagates into the reservoir forming a steam chamber. The vapor phase condenses at the chamber edge, which in turn is accompanied by the transfer of both its sensible and latent heat to the surroundings. A fraction of the thermal energy released by steam is absorbed by bitumen situated beyond the chamber edge, resulting in the reduction of its viscosity and enhancement of its mobility. The mobilized bitumen and condensate drain under the influence of gravity into another horizontal well located around 5 m below and parallel to the injection well, resulting in the expansion of the steam chamber.

The suitability of SAGD for bitumen recovery in thick and relatively homogeneous reservoirs with high bitumen saturations can be attributed to five factors: (i) the high temperature-sensitivity of the viscosity of bitumen; (ii) the substantial enthalpy of water available to heat bitumen in the range of operating pressures used in SAGD; (iii) enhanced access to the reservoir due to the use of long horizontal wells; (iv) utilization of the naturally occurring phenomenon of gravity for the drainage of heated bitumen towards production wells; and (v) the obtainability of high fluid mobilities within inter-well regions having favorable permeability distributions due to the availability of heated flow paths, derived from the use of closely-spaced horizontal wells.

A widely-used parameter to quantify the performance of steam injection processes is the cumulative steam-oil-ratio (SOR), defined as the ratio of the cumulative steam injected (cold

water equivalent) to the cumulative bitumen produced. For a given volume of steam injected, the SOR exhibits an inverse relationship to the drainage rate of the oleic phase.

For a reservoir capped by a low-permeability barrier, the efficiency with which thermal energy is used to mobilize bitumen within the reservoir diminishes as the rate of conductive heat loss to the over- and underburden increases. This increases the amount of steam required to meet a specified cumulative bitumen production, which leads to a higher cumulative SOR. For a given overburden and underburden thermal conductivity, conductive heat transfer to these regions depends on the associated temperature gradients, which in turn is dictated by the operating-chamber temperatures, and exposed contact area for heat transfer.

The average cumulative SOR in efficient field-scale SAGD projects is between 2.0 and 5.0, depending on the reservoir and fluid properties (Butler, 2001). In highly heterogeneous reservoirs (e.g., within the middle McMurray member), the average SORs are expected to be even higher due to the adverse effects of reservoir heterogeneities on hydraulic paths for fluid flow. A highly heterogeneous reservoir is one in which both the global proportion and spatial correlation of non-net facies (i.e., facies with inferior petrophysical characteristics) is significant. Prior studies of SAGD in heterogeneous reservoirs indicate that the extent to which the SOR is increased under heterogeneity is sensitive to length scales of heterogeneities, and their proximity to the well-pair (Yang and Butler, 1992; Law et al., 2003; Chen et al., 2008; Yazdi and Jensen, 2014; Wang and Leung, 2015). The main heterogeneity considered in these studies is mudstone (shale) in the form of laterally extensive barriers.

Reduction of the cumulative SOR is a salient engineering problem from both environmental and economic standpoints, with its economic importance enhanced under low oil prices. The most effective method for lowering the SOR at a given operating pressure is by simultaneously lowering operating-chamber temperatures, and accelerating drainage of the oleic phase near the chamber edge.

Expanding solvent-SAGD (ES-SAGD), wherein a small quantity of a light condensable solvent is coinjected with steam, is a widely-investigated alternative to SAGD. This is because it retains many of the advantages of SAGD, and can potentially lower the cumulative SOR by the simultaneous reduction of operating-chamber temperatures, and enhancement of bitumen production rate due to the dilution of bitumen by solvent (Nasr et al., 2003; Li et al., 2011ab; Jha et al., 2013; Keshavarz et al., 2014, 2015; Khaledi et al., 2015).

The occurrence of lower temperatures along and near the chamber edge under steam-solvent coinjection is attributed to three aspects: (i) the chamber edge, in general, represents the transition from the coexistence of the oleic, vapor and aqueous phases to that of the oleic and aqueous phases (Keshavarz et al., 2014); (ii) both mixtures of water and bitumen, and water and solvents can exhibit three-phase (oleic, vapor, and aqueous) behavior (Amani et al., 2013ab; Brunner, 1990; Brunner et al., 2006); and (iii) the oleic-vapor-aqueous to oleic-aqueous phase transition temperatures of mixtures of water and light solvents (e.g. normal hexane) can be significantly lower than the saturation temperature of water and solvent at a given pressure (Brunner, 1990). Reduction of chamber-edge temperatures in ES-SAGD is a function of the overall composition near the chamber edge, which can be controlled by varying the injection concentration of solvent.

At the pore scale, dilution of bitumen by the dissolution of solvent in the oleic phase (x_{sL}) occurs due to molecular diffusion and is facilitated by mechanical dispersion, both being temperature-dependent phenomena. The expectation that an optimal solvent volatility exists for successful implementation of ES-SAGD under a given set of operating conditions is plausible due to the interplay between temperature and dilution capability of the solvent near the chamber edge. This interplay is the result of two aspects: (i) increasing oleic-vapor-aqueous to oleic-aqueous transition temperatures for mixtures of water and solvent at a given pressure (Brunner, 1990) as solvents become heavier; and (ii) diminishing dilution capability of solvents as they become less volatile. Prior studies conducted on ES-SAGD conducted for single component n-alkane solvents indicate normal hexane (n-C_6) to be suited for Athabasca-bitumen recovery (Mohebati et al., 2012; Keshavarz et al., 2015; Ji et al., 2015).

Detailed understanding of the influence of reservoir heterogeneities on oil recovery mechanisms in ES-SAGD is necessary if its implementation is considered as a measure to lower the hurdle for development of more heterogeneous reservoirs, for which conventional SAGD is expected to be inefficient. Practical importance of such knowledge is informed by a couple of aspects, and their effects on the cumulative SOR.

Firstly, mixing between oil and solvent is expected to be improved under high permeability heterogeneity due to more tortuous hydraulic paths for fluid flow, as indicated by prior studies on miscible displacements (Adepoju et al., 2013, 2015; Connolly and Johns, 2016). Secondly,

improved mixing between solvent and bitumen may influence operating-chamber temperatures by affecting the vaporization of solvent from the oleic phase when it interacts with steam.

However, mechanistic investigations of ES-SAGD in the presence of reservoir heterogeneity are rather scarce. Research by Li et al. (2011b) is the only published mechanistic study of ES-SAGD in heterogeneous reservoirs. For synthetic reservoir models containing a single deterministically placed shale barrier at different locations, the authors showed that the recovery of oil and the accompanying SOR can be improved by coinjecting solvent with steam.

The primary limitation of the study by Li et al. (2011b) is related to the authors' choice of reservoir models. In these models, the global proportion of non-net facies (shale) and the transition from net (bitumen-rich clean sands) to non-net facies was not reasonably reflected even qualitatively. Mechanistic studies on the relative performance of ES-SAGD to SAGD under heterogeneity requires the use of several stochastically generated realizations consisting of multiple flow barriers of varying length scales and proximities to the well-pair. This requirement stems from two facets: (i) existence of numerous equiprobable spatial configurations that honor a given set of conditioning data, which arises from the inevitable sparseness of well-derived (hard) data relative to the areal extents of reservoir leases due to economic constraints (Pyrcz and Deutsch, 2014); (ii) the potential enhancement of solvent-bitumen mixing under high permeability heterogeneity (Adepoju et al., 2013, 2015; Connolly and Johns, 2016).

A secondary limitation of the research by Li et al. (2011b) is the ambiguity regarding the consideration of the dissolution of water in the oleic phase (x_{wL}) in their simulations. Experimental investigations on the phase behavior of water-containing mixtures of hydrocarbons including reservoir oils indicate that water can act as a diluting agent for heavy oil and bitumen. The data indicate three aspects.

Firstly, the solubility of water in the oleic phase (x_{wL}) can be significant at elevated temperatures (Griswold and Kasch, 1942; Reamer et al., 1944; Kobayashi and Katz, 1953; Skripka, 1979; Tsonopoulos and Wilson, 1983; Heidman et al., 1985; Glandt and Chapman, 1995; Economou et al., 1997; Shinta and Firoozabadi, 1997; Tsonopoulos, 1999; Maczynski et al., 2005; Shaw et al., 2005; Shaw et al., 2006a, b; Amani et al., 2013a, b). For example, Amani et al. (2013b) measured that x_{wL} was 54 mol% at 550 K for a mixture of water and an Athabasca bitumen.

Secondly, the affinity of water to hydrocarbons is higher for aromatics and naphthenes in comparison with paraffins (Griswold and Kasch, 1942; Tsonopoulos and Wilson, 1983; Heidman et al., 1985; Economou et al., 1997; Tsonopoulos, 1999). Thirdly, the dissolution of water in the oleic phase results in the reduction of its viscosity (Glandt and Chapman, 1995). A more detailed review of the phase behavior of water/hydrocarbon mixtures can be found in **Appendix A**.

Based on the above, it is apparent that water can form both emulsions and solutions with hydrocarbon mixtures (e.g., reservoir oils and bitumens). In the most generally terminology, both emulsions and solutions are dispersions. However, the distinction between the two stems from the size of the particles of the dispersed phase. Water-in-oil emulsions are colloids wherein clusters of water exceeding 1 nm are dispersed in oil; that is, these clusters are much larger than the size of water molecules. In contrast, when water dissolves in oil, the size of the dispersed particles in the oleic phase are comparable to that of water molecules.

Experimental measurements of Glandt and Chapman (1995) on the viscosity of the mixtures of water and hydrocarbons indicate that the viscosity of a water-in-oil emulsion can exceed that of the oil. In comparison, the dissolution of water in oil can lower its viscosity. To investigate whether water can dissolve in heavy oils and bitumen, the authors conducted two sets of viscosity measurements.

In the first set of experiments, the authors measured the viscosity of water-free samples of three heavy oils (Coalinga, Huntington Beach, and Cat Canyon) and a bitumen (Peace River) over the range of 434-558 K. In the second set of experiments, the authors measured the oleic-phase viscosities of mixtures of water and the aforementioned samples over the same interval in temperature at pressures near the pertinent saturation pressure of water (i.e., near the oleic-aqueous phase boundary). The measured oleic-phase viscosities were systematically lower for the second set of experiments relative to the first.

To conduct the first set of experiments, the authors devised a method to remove the connate water which is emulsified in these oil samples. Specifically, the hydrocarbon samples containing emulsified water were vacuum-dried until the water content was measured to be less than 0.02 wt%. Further, a cold trap with dry ice and methanol was utilized to separate the volatile components (including water) from the heavier oil fractions. The condensed fluids from the trap were then centrifuged to separate the light ends from water. The heavier oil fractions were

filtered to remove fine particles. The light ends were subsequently mixed with the heavier oil fractions, following which viscosity measurements were conducted.

SAGD is the benchmark against which ES-SAGD is evaluated as an alternative. Due to the differences in the recovery mechanisms underlying SAGD and ES-SAGD, the relative performance of ES-SAGD to SAGD may be affected by how x_{wL} affects each of these processes. However, the significance of x_{wL} in the context of bitumen recovery using SAGD and ES-SAGD is a hitherto unanswered question in the literature.

The existence of this gap is likely an outcome of the underlying uncertainties in fluid models used in reservoir simulation. The uncertainties are the result of both paucity of available experimental data for fluid properties, and shortcomings of existing frameworks to model them (Venkatramani and Okuno, 2015).

Recently, Venkatramani and Okuno (2015) presented a new framework to reliably model the multiphase compositional behavior of water-containing mixtures of reservoir oils by use of the Peng-Robinson equation of state (PR EOS) with van der Waals' mixing rules (Peng and Robinson, 1976; Robinson and Peng, 1978). The framework of Venkatramani and Okuno (2015) is particularly suited for application in reservoir engineering studies for a few reasons.

Firstly, it does not require any change in the widely-used formulation based on the traditional PR EOS with van der Waals' mixing rules. Secondly, the framework has been developed based on experimental evidence. Experimental measurements indicate that three-phase curves of water/n-alkane binaries exhibit an asymptotic limit near the vapor pressure curve of water, and that water exhibits greater affinity towards aromatics and naphthenes compared to n-alkanes. No explicit assumptions regarding the configuration of intermolecular networks have been made. This is in contrast to some recent modeling approaches such as those of Oliveira et al. (2007) and Zirrahi et al. (2015), who used complex semi-empirical fluid models. Experimental evidence on the nature of intermolecular interactions in the oleic phase for water/hydrocarbon mixtures at elevated temperatures has not been published. Thirdly, the framework offers flexibility in terms of its ability to handle the multiphase compositional behavior of different types of water/hydrocarbon systems, such as water/n-alkane mixtures and water-containing reservoir oils, which also contain aromatics and naphthenes.

The compositions of the non-aqueous phases (i.e. vapor and oleic) are accurately predicted using the framework developed by Venkatramani and Okuno (2015). A shortcoming of this

method, however, is that the concentration of hydrocarbons in the aqueous phase (x_{hcW}) is underestimated by several orders of magnitude. This underprediction is of little significance in reservoir studies focusing on mechanisms in bitumen recovery in view of the low solubility of bitumen and hydrocarbon solvents in the aqueous phase (< 0.01 mol%) even at elevated temperatures.

In this research, with the aid of numerical simulations, three previously unanswered questions of engineering significance are addressed: (i) if the consideration of x_{wL} is necessary for reliable comparison of ES-SAGD to SAGD (Chapter 2); (ii) if ES-SAGD can be a better alternative to SAGD in highly heterogeneous bitumen reservoirs in terms of the SOR as a function of cumulative bitumen production (which directly correlates with the volume of the steam chamber) [Chapter 3]; and (iii) the flow characteristics in heterogeneous reservoirs conducive to significant reduction in the cumulative SOR (Chapter 4). The practical significance of the third question mainly stems from the higher cost of solvent relative to the price of bitumen. This question is addressed using numerical simulations are in conjunction with an analytical theory for SAGD.

This research has three main hypotheses, the validity of which will be examined in Chapters 2 through 4:

- The consideration of x_{wL} is likely necessary to ensure reliable assessment of the relative performance of ES-SAGD to SAGD. The dissolution of water in the oleic phase could potentially enhance the cumulative bitumen production for both SAGD and ES-SAGD due to the lower viscosity of water relative to that of bitumen. However, the improvement in bitumen production in SAGD may be higher compared to that under ES-SAGD due to higher operating-chamber temperatures.

- ES-SAGD could potentially enhance the production of bitumen while lowering the cumulative SOR even under reservoir heterogeneity as the mechanisms by which performance is improved under homogeneity are expected to occur under heterogeneity as well. However, for a given cumulative bitumen production, the reduction in SOR because of coinjection of solvent may be higher under heterogeneity due to the possibility of enhanced mixing between solvent and bitumen, which could facilitate greater reduction in conductive heat losses to the overburden through the obtainment of lower operating-chamber temperatures.

- Reservoirs for which SAGD is adversely affected due to heterogeneity may yield greater reduction in SOR due to coinjection of solvent. The retention of solvent in-situ for a given cumulative bitumen production is expected to be higher under heterogeneity; this in turn increases the volume of solvent available for contact with bitumen and also the time for solvent-bitumen contact. Dilution of bitumen by solvent could potentially be more pronounced in heated regions of the reservoir where the local flow of bitumen is restricted by permeability barriers.

Chapter 5 presents a summary of salient findings of this research, and a proposal for future investigations.

Chapter 2. Compositional Mechanisms in SAGD and ES-SAGD with Consideration of Water Solubility in Oil

List of Tables

List of Figures

Nomenclature

Roman Symbols

L oleic phase

P pressure

q weighting factor for oleic-phase viscosity

Q cumulative bitumen production

R ratio of bitumen price to solvent cost

T temperature

V vapor phase

$\underline{V}$ molar volume

W aqueous phase

x mole fraction

Greek Symbols

α coefficient in Equation 2.6

λ scaling factor for BIP

μ viscosity

ω acentric factor

Subscripts

C_D dead bitumen

hc hydrocarbon

L oleic phase

s solvent

w water

W aqueous phase

Abbreviations

BHP	bottomhole pressure
BIP	binary interaction parameter
C	critical constant
CC	constant concentration
CN	carbon number
CP	constant pressure
CWE	cold water equivalent
EOS	equation of state
ES	expanding solvent
MW	molecular weight
PR	Peng and Robinson
SAGD	steam assisted gravity drainage
VC	time-variant concentration
VP	time-variant pressure

The main objective of this chapter is to examine if and how the dissolution of water in the oleic phase affects the relative performance of ES-SAGD to SAGD in the context of the recovery of an Athabasca bitumen. The solvents under consideration for ES-SAGD are single component normal alkanes with carbon numbers from three (i.e., propane) to ten (i.e., normal decane). A secondary objective is to examine if x_{wL} can be used to improve the operating strategy in each of these processes.

Experimental data on the phase behavior of water-bitumen and water-solvent mixtures in conjunction the current literature on the mechanisms in SAGD and ES-SAGD lead to the following hypotheses. Firstly, the dissolution of water in the oleic phase may enhance the cumulative bitumen production for both SAGD and ES-SAGD due to the lower viscosity of water relative to bitumen; however, the extent of improvement is expected to be higher for SAGD compared to ES-SAGD due to higher operating-chamber temperatures.

Secondly, both the operating pressure and choice of mixing model for the oleic-phase viscosity may influence the extent to which the cumulative bitumen production may be increased when x_{wL} is considered. An increase in operating pressure is expected to lead to higher temperatures along and near the chamber edge, which in turn could facilitate dissolution of water in the oleic phase. The choice of mixing model for the oleic-phase viscosity affects the margin by which the viscosity is reduced due to x_{wL} for a given temperature, pressure and oleic-phase composition.

Thirdly, if x_{wL} enhances bitumen production, then it could be leveraged to enhance the short-term production performance of SAGD and n-C_6 SAGD using a time-variant operating pressure strategy, wherein the operation is carried out initially at an elevated pressure, and subsequently, reduced to a smaller value.

Section 2.1 presents a mechanistic examination of SAGD and ES-SAGD including the effect of x_{wL} on bitumen recovery. In Section 2.2, the results of the investigation conducted in Section 2.1 will be used to develop an application strategy for ES-SAGD for efficient recovery of bitumen through the utilization of x_{wL} as an additional compositional mechanism.

2.1. Mechanistic Study of SAGD and ES-SAGD with Consideration of x_{wL}

This section consists of three subsections. Sections 2.1.1 and 2.1.2 present the specifications of the reservoir model and the fluid model used in numerical simulations, respectively. Section 2.1.3 gives an analysis of the numerical simulations.

2.1.1. Reservoir model

Reservoir flow simulations are performed using the STARS simulator of Computer Modelling Group (CMG, 2011). The reservoir models considered are homogeneous. The initial reservoir temperature and pressure are 286.15 K, and 15 bars, respectively. The initial saturation of water in the reservoir is 0.25, with the remainder being "live" Athabasca bitumen. Live bitumen considered in this research is a mixture of 1 mol% methane (C_1) and 99 mol% dead Athabasca bitumen; this corresponds to a gas-to-oil-ratio (GOR) of 0.44 m^3/m^3. The residual saturation of oil is assumed to be 0.13. The relative permeability model used is independent of temperature. Heat losses to over and underburden are considered in the simulations. However, other effects, such as dispersion, the effect of interfacial tension on phase compositions and pressures, and asphaltene precipitation, have not been considered.

The production well is located 3 m above the base of the model, and the injection well is located 4 m above the producer. The temperature of the injected stream is equivalent to the saturation temperature of water at the operating pressure. The quality of steam used is 90%. The production well is subject to the minimum bottom-hole pressure (BHP) constraint of 15 bars, which is the initial reservoir pressure. The reservoir is subject to an initial heating period of 6 months using steam during which there is no production.

Only a half of the steam chamber is simulated in this section. The reservoir model in these cases is of dimensions 70 m × 37.5 m × 20 m in the x, y, and z directions, respectively; the scale of this model is identical to that used by Keshavarz et al. (2014). The original bitumen in place at stock tank conditions is 11591 m^3. This model is discretized into 70 × 1 × 20 grid blocks in the x, y, and z directions, respectively; the y-coordinate in this model represents the direction along the length of the well-pair. The injection and production wells are situated in the left boundary of the reservoir model. The production well is subject to the maximum liquid flow rate constraint of 200 m^3/day at surface conditions and a maximum steam flow rate of 1 m^3/day. A summary of the reservoir model is presented in **Table 2.1**.

2.1.2. Fluid model

This section presents details of the compositional model using the PR EOS, oleic-phase viscosity model, and oleic-phase density model used for the numerical simulations. To determine the significance of water dissolution on bitumen recovery, two cases are defined: the base case, in

which x_{wL} is neglected, and the water-dissolution case, in which x_{wL} is considered. For both cases, the dissolution of hydrocarbons in the aqueous phase (x_{hcW}) is disregarded. This assumption is considered reasonable in view of low values for x_{hcW} (< 1 mol%) indicated by experimental measurements (e.g., Heidemann, 1974).

The molecular weight of the Athabasca bitumen used is 530.00 g/mol. The dead bitumen has been characterized as a single pseudo component (C_D) using the characterization method of Kumar and Okuno (2015).

In this work, simulations for SAGD use three components: water, C_1 and C_D. Those for ES-SAGD use four components: water, C_1, C_D, and a solvent component. The solvents used for ES-SAGD in this study are n-alkanes; the lightest and heaviest n-alkanes under consideration are propane (C_3) and n-decane (n-C_{10}), respectively. Component-specific critical constants (T_C, P_C) and acentric factor (ω) are presented in **Table B-1** of Appendix B.

The compositional behavior of water/solvent/Athabasca-bitumen mixtures is modeled using the PR EOS with the van der Waals mixing rules. The binary interaction parameter (BIP) for C_D with n-alkanes has been obtained from Kumar (2016).

The BIP for water with n-alkanes is calculated using the correlation developed by Venkatramani and Okuno (2015) based on the measured three-phase curves (oleic-vapor-aqueous) of water/n-alkane binaries by Brunner (1990). The correlation is given as

$$\text{BIP} = c_1[1 + \exp(c_2 - c_3 \text{MW})]^{-1/c_4}, \quad (2.1)$$

where $c_1 = 0.24200$, $c_2 = 65.90912$, $c_3 = 0.18959$, and $c_4 = -56.81257$.

The BIP for water with C_D is expected to be lower than that for an n-alkane with a similar molecular weight, because Athabasca bitumen contains aromatics and the affinity of water towards aromatics is greater than that for n-alkanes (Tsonopoulos, 1983; Heidman et al., 1985; Economou et al., 1997; Tsonopoulos, 1999). As described in Venkatramani and Okuno (2015), the BIP for water/C_D is estimated by reducing the BIP calculated from Equation 2.1 using a scaling factor (λ) of less than unity. The optimum value of λ has been determined to be 0.70 by matching the x_{wL} data measured for Athabasca bitumen by Amani et al. (2013ab). The resulting BIP for water with C_D is 0.169. **Table B-2** gives the matrix of the pair-specific BIPs. **Table B-3** shows good agreement between the measured x_{wL} for water/Athabasca bitumen mixtures (Amani

et al., 2013a, b) and the predicted x_{wL} with the PR EOS using 0.169 for the BIP for water with C_D.

The phase behavior is reflected in the simulations with STARS, in terms of component K values, defined as the ratio of concentration in one phase to another, tabulated as functions of temperature and pressure. The K values used in the simulations with STARS are independent of composition.

For the base case, K values of water corresponding to vapor-aqueous equilibrium are calculated using Raoult's law. K values for hydrocarbon components are calculated by use of the PR EOS for a fixed overall composition. For SAGD, the fixed overall composition is 100 mol% live bitumen; for ES-SAGD, the fixed overall composition is 20 mol% solvent and 80 mol% live bitumen.

For the water-dissolution case, K values of all components corresponding to oleic-vapor-aqueous equilibrium are generated by use of the PR EOS for the fixed overall composition of 90 mol% water and 10 mol% hydrocarbon. For ES-SAGD, the overall distribution of hydrocarbons is set to 2 mol% solvent and 8 mol% live bitumen. This overall composition is representative of conditions near the chamber edge.

To facilitate application in STARS, the oleic-phase viscosity (μ_L) is modeled as

$$\ln \mu_L = \sum_{i=1}^{N_C} q_i \, x_{iL} \ln \mu_{iL} \tag{2.2}$$

subject to

$$\sum_{i=1}^{N_C} q_i x_{iL} = 1, \tag{2.3}$$

where μ_{iL} and x_{iL} are the viscosity and mole fraction of the i^{th} component in the oleic phase, respectively. q_i is the weighting factor for the i^{th} component, and can be a function of the oleic-phase composition. C_D is set as the key component in this research; the weighting factors for all non-key components are set identical to each other. Equation 2.2 reduces to the conventional logarithmic mixing model when q_{CD} is set to unity. Composition-dependent functional forms have been developed for q_{CD} on the basis of experimental data for the oleic-phase viscosity [Glandt and Chapman (1995) for SAGD; Kumar (2016) and Nourozieh et al. (2013, 2015a, b) for ES-SAGD]. The composition-dependent function was developed for q_{CD} for SAGD as follows:

$$q_{C_D} = a x_{c_D L}^{\,6} + b x_{c_D L}^{\,5} + c x_{c_D L}^{\,4} + d x_{c_D L}^{\,3} + e x_{c_D L}^{\,2} + f x_{c_D L} + g \tag{2.4}$$

subject to $0 < x_{CDL} < 1$, where a = -33.95059, b = 142.19326, c = -242.14374, d = 212.01349; e = -97.35521, f = 19.05086, g = 1.19182. Note that the oleic phase consists of the water, methane, and C_D components for SAGD. In the water/C_D binary limit in composition space, use of Equation 2.4 in Equation 2.2 for SAGD renders the calculated oleic-phase viscosity to be approximately equal to that obtained from the linear mixing rule:

$$\mu_L = \sum_{i=1}^{N_C} x_{iL}\mu_{iL}. \tag{2.5}$$

The linear mixing rule for the oleic-phase viscosity was recommended by Glandt and Chapman (1995) for water-containing oil and bitumen.

For ES-SAGD, the oleic phase consists of the water, methane, solvent, and C_D components. The following equation is used for q_{CD}:

$$q_{C_D} = 1 + \alpha(CN)\left\{\frac{(1-x_{c_DL})\left(1-(1-x_{c_DL})^8\right)}{x_{c_DL}}\right\}, \tag{2.6}$$

where "α" is a parameter specific to the n-alkane solvent under consideration. The optimum α-values exhibit a monotonically decreasing trend with respect to the n-alkane CN, and the transition towards the logarithmic mixing rule is observed as the n-alkane CN increases. The values for the α-parameter used in the simulations are 0.5498 for C_3, 0.4273 for n-C_4, 0.3562 for n-C_5, 0.3050 for n-C_6, 0.2219 for n-C_7, 0.1464 for n-C_8, 0.0709 for n-C_9, 0.0 for n-C_{10}. The development of the oleic-phase viscosity model is described in **Appendix C**. The choice of mathematical formulation for q_{CD} dictates the type of mixing rule. From a quantitative standpoint, there is considerable uncertainty in the viscosity models used in this work, and it arises from the scarcity of reliable experimental data for the oleic-phase viscosity; a more detailed discussion of this uncertainty is presented in Section 2.1.3 and Appendix C.

The volumetric behavior of the oleic phase is modeled by a mixing rule that is linear in terms of component-specific molar volumes,

$$\underline{V}_L = \sum_{i=1}^{N_C} x_{iL}\underline{V}_{iL}, \tag{2.7}$$

where $\underline{V}_L$ is the molar volume of the oleic phase, and $\underline{V}_{iL}$ is the molar volume of the i^{th} component in the oleic phase. A discussion on the applicability of the linear mixing rule for the oleic-phase molar volume is given in **Appendix D**.

2.1.3. Analysis of simulation results

This subsection comprises two parts. In the first, the effects of x_{wL} on SAGD and ES-SAGD are investigated. A sensitivity analysis is subsequently conducted to examine the influence of choice of mixing model for the oleic-phase viscosity, operating pressure, and injection concentration of solvent on the extent to which x_{wL} affects bitumen production.

2.1.3a. Effect of x_{wL} on SAGD and ES-SAGD

The operating pressure is set to 35 bars unless stated otherwise. For the simulations for ES-SAGD, the concentration of the solvent in the injection stream is set to 2 mol%, unless otherwise stated.

The consideration of x_{wL} results in improved bitumen production for both SAGD and ES-SAGD. The mechanism for the improvement in bitumen production is the enhancement of the oleic-phase mobility due to x_{wL}. Following the stabilization of the chamber edge temperature, which is approximately 365 days from the commencement of the operation, the average improvement in cumulative production due to x_{wL} is higher for SAGD than for ES-SAGD. **Figure 2.1** presents the cumulative bitumen production histories for the base and water-dissolution cases for SAGD and n-C_6 SAGD. For the water-dissolution case, the steam chamber reaches the outer boundary of the reservoir model at 1004 days and 670 days from the commencement of operation for SAGD and n-C_6 SAGD processes, respectively. Figure 2.1b presents the improvement in cumulative bitumen production due to the consideration of x_{wL} for SAGD and n-C_6 SAGD. When the steam chamber reaches the outer boundary, the improvement in bitumen production due to x_{wL} is 7.66% for SAGD and 4.08% for n-C_6 SAGD. At earlier times, this difference can be even higher than 15% (Figure 2.1b).

The basis for the aforementioned observation can be understood with the aid of temperature and oleic-phase composition profiles. For each process and both the base and water-dissolution cases, **Figures 2.2 and 2.3** respectively present the profiles for temperature and oleic-phase composition for the 12th row from the top of the reservoir model at 578 days. For a given operating pressure, the effect of x_{wL} on bitumen production is observed to be greater for SAGD due to greater dissolution of water in the oleic phase near the chamber edge. This occurs due to two reasons. Firstly, the temperatures at and in the vicinity of the chamber edge are higher for SAGD than for n-C_6 SAGD. Secondly, the aromaticity of the oleic phase is greater for SAGD in

comparison with n-C_6 SAGD. The aromaticity of the oleic phase is lowered for n-C_6 SAGD due to dissolution of the n-alkane solvent in the oleic phase.

For steam-only injection, Luo and Barrufet (2005) have reported an improvement of up to 7% in oil production when x_{wL} is considered. The simulations performed by Luo and Barrufet were for steam flooding and cyclic steam stimulation. The linear mixing model was used to calculate the oleic-phase viscosity. The maximum temperature in their cases was 505.37 K, which is comparable to the saturation temperature of water at 35 bars (515.72 K); i.e., the injection temperature for the simulations in this section. Despite the greater aromaticity of the bitumen, Figure 2.1b indicates that the observed improvement in cumulative bitumen production due to x_{wL} for SAGD is only slightly higher than the upper bound for the improvement in oil production due to x_{wL} observed by Luo and Barrufet. It is not clear in their paper how accurately x_{wL} was modeled in their simulations.

The magnitude of improvement in the bitumen production rate due to consideration of x_{wL} is affected by the volatility of the solvent under consideration. This is apparent from **Figure 2.4**, which presents the variation of the yearly average bitumen production rate with respect to the carbon number (CN) of the solvent at two different times in the production phase (1.50 and 3.85 years). The average bitumen production rate is calculated based on the cumulative bitumen production history.

The significance of x_{wL} on bitumen production rate is observed to be higher for heavier solvents (e.g., CNs eight through ten). This is mainly due to the combination of higher values for x_{wL} and lower values for the solvent concentration in the oleic phase (x_{sL}) near the chamber edge, and diminished capacity of solvent to dilute bitumen compared to water. Consideration of x_{wL} results in lower values for x_{sL} near the chamber edge (see Figure 2.3b). The extent of decrease in x_{sL} due to x_{wL} is a function of temperature. Heavier solvents yield greater values for the chamber-edge temperature and hence, higher temperatures near the chamber edge. This in turn results in higher values for x_{wL} and lower values for x_{sL} near the chamber edge. N-alkanes lighter than n-C_9 are less viscous than water; the viscosity of n-C_8 is comparable to that of water at elevated temperatures.

Mechanistic understanding of the effect of x_{wL} on the steam-oil-ratio (SOR) is essential as the SOR is an important metric to evaluate the economic feasibility of steam injection processes. For a specified injection strategy, lower values for the cumulative SOR are obtained by

increasing bitumen production while lowering heat losses to the formation. When x_{wL} is accounted for, the temperature distribution along and beyond the chamber edge is not significantly altered, as seen in Figure 2.2. Hence, its influence on heat losses to the formation is small. Therefore, the extent to which x_{wL} affects the cumulative SOR is limited to its effect on cumulative bitumen production. As cumulative bitumen production is enhanced due to x_{wL}, the resulting cumulative SOR is lower when x_{wL} is considered. **Figure 2.5** compares the cumulative SOR histories for the base and water-dissolution cases for SAGD and n-C_6 SAGD. The extent to which the cumulative SOR is reduced for SAGD is higher. This is because the improvement in cumulative bitumen production due to x_{wL} is greater for SAGD in comparison with ES-SAGD (see Figure 2.1).

The simulations indicate that the optimal solvent volatility for the ES-SAGD studied here is between five and seven in terms of the n-alkane carbon number (CN). The consideration of x_{wL} apparently does not affect this conclusion on the basis of the cases tested here.

The drainage rate of bitumen at and beyond the chamber edge is strongly dependent on the temperature distribution along and beyond it. For a given process, away from the ceiling of the steam chamber, the temperatures along the chamber edge are in the neighborhood of the three-phase temperature of the water/solvent binary corresponding to the operating pressure. This indicates that the temperature distribution near the chamber edge is largely governed by water/solvent phase behavior. Experimental measurements conducted on the phase behavior of water/n-alkane mixtures show that the three-phase temperature corresponding to the transition from oleic-vapor-aqueous to oleic-aqueous equilibrium increases with decreasing volatility of the solvent for specified pertinent pressure of the system (Brunner, 1990).

Average bitumen production rates increase monotonically with decreasing solvent volatility early in the production phase as seen in Figure 2.4a. This is mainly due to higher temperatures near the chamber edge, which results in improved viscosity reduction of the oleic phase and consequently, enhanced oleic-phase mobility.

Later in the production phase (around 3.85 years), a break over point for the average bitumen production rate in terms of the solvent volatility is observed to occur in the neighborhood of more volatile solvents (i.e. for CN < 8). This is apparent in Figure 2.4b, which presents the variation in average bitumen production rate with respect to solvent volatility at 3.85 years from the commencement of production. At this time, the average bitumen production rates for CNs

five, six, and seven respectively are 2442.70, 2453.50, and 2445.30 m^3/yr for the base case, and 2482.60, 2486.60, and 2483.20 m^3/yr for the water-dissolution case. Occurrence of this break over point is the result of a balance between temperature and dilution capability of the solvent (Keshavarz et al., 2015). The break over point occurs near the CN-value of six regardless of whether x_{wL} is considered in Figure 2.4b.

SAGD serves as the basis upon which the performance of ES-SAGD is evaluated. The simulations conducted thus far show that, with the exception of C_3, the coinjection of solvent with steam yields greater bitumen production compared to steam-only injection. However, the effect of coinjection of solvent with steam is overestimated when x_{wL} is disregarded. This is because the extent to which x_{wL} improves bitumen production in SAGD is greater than that corresponding to ES-SAGD. **Figure 2.6** compares the histories of the deviation in cumulative bitumen production for n-C_6 SAGD relative to SAGD for both the base and water-dissolution cases. For n-C_6 SAGD, the chamber reaches the outer boundary of the reservoir model at 670 days when x_{wL} is considered. At this time, the improvement in cumulative bitumen production due to solvent coinjection for the base and water-dissolution cases are 84.76% and 77.51%, respectively; this represents an overestimation by 7.25%. Figure 2.6 suggests that evaluation of production performance of ES-SAGD relative to SAGD be conducted with consideration of x_{wL}; the importance of its consideration becomes even more important for evaluations performed at higher operating pressures.

2.1.3b. Sensitivity analysis

For a given operating pressure, the magnitude of the simulated improvement in bitumen production due to x_{wL} can also be affected by the choice of the mixing model used for the oleic-phase viscosity. **Figure 2.7** compares the cumulative bitumen production histories for the base and water-dissolution cases for the SAGD process for the linear and logarithmic mixing models for the oleic-phase viscosity. As mentioned previously, q_{CD} is assigned the value of unity for the logarithmic mixing rule. The linear mixing rule is given in Equation 2.5, and can be approximated by using Equation 2.4 for q_{CD}. For the 12^{th} row from top of the reservoir model, at 578 days from the commencement of the operation, **Figure 2.8a** compares the predicted oleic-phase viscosities using the two mixing models, while **Figure 2.8b** presents the pertinent distributions for x_{wL} in the vicinity of the chamber edge.

When x_{wL} is considered, use of the logarithmic mixing rule for the oleic-phase viscosity results in considerably higher improvement in cumulative bitumen production compared to the linear mixing rule (Figure 2.7)**.** The main reason for the difference given in Figure 2.7 is that, for a specified temperature and oleic-phase composition, the predicted oleic-phase viscosity using the logarithmic mixing rule is considerably lower than that calculated using the linear mixing rule (Figure 2.8a). This is because the weighting factor for water (q_w) for a given oleic-phase composition is lower than unity in the linear mixing model (see Equations 2.2 and 2.3); hence, the contribution of water towards the lowering of the oleic-phase viscosity is diminished under the linear mixing rule. The discrepancy in the simulated x_{wL} profiles for the two mixing models is small as demonstrated in Figure 2.8b**.**

In the current viscosity modeling framework, the functional form used for q_{CD} determines the type of mixing model (also see Appendix C). The reliability of the viscosity model is limited by the availability and accuracy of experimental oleic-phase viscosity data as the choice of the mathematical formulation for q_{CD} is informed based on experimental data. This currently is a significant limitation in view of the reliance on numerical simulations for the design and optimization of SAGD and ES-SAGD, the scarcity of reliable experimental data for the oleic-phase viscosity (as described in Appendix C), and the considerable impact that the choice of mixing model for the oleic-phase viscosity can have on bitumen recovery predictions.

The choice of the operating pressure also affects the extent to which x_{wL} enhances bitumen production. **Figure 2.9** demonstrates this for the SAGD process. Higher operating pressures result in higher temperatures at and beyond the chamber edge, which results in higher values for the x_{wL}, thereby enhancing its contribution towards diluting the oleic phase.

For the ES-SAGD process, the choice of the injection concentration can also affect the magnitude of improvement in bitumen production due to x_{wL} for specified operating pressure. **Figure 2.10** compares the cumulative bitumen production histories for n-C_6 SAGD corresponding to injection concentrations of 2 mol% and 10 mol%. The steam chamber reaches the right boundary of the reservoir model at 670 days for the 2 mol% case, and 639 days for the 10 mol% case. The improvement in bitumen production due to x_{wL} is observed to be lower at higher injection concentrations especially at early times in the production phase following the stabilization of the chamber edge temperature.

The effect of high injection concentrations of solvent on temperature distribution ahead of the chamber edge is small. Thus, the discrepancy in the distribution of x_{wL} ahead of the chamber edge is observed to be small. However, the accumulation of the solvent near the chamber edge is enhanced at higher injection concentrations, which can result in greater solvent dissolution in the oleic phase. This in turn diminishes the extent to which water dilutes bitumen.

The most important conclusion presented in Section 2.1.3 is that the benefit of solvent coinjection in terms of bitumen production can be overestimated when x_{wL} is disregarded. This conclusion is not significantly affected over a moderate increase in the GOR from 0.44 to 5 m^3/m^3, small to moderate perturbations (2 – 6%) in the oleic-phase density in the solvent/bitumen edge in composition space, and an increase in the dimensionality of the simulations from two to three dimensions.

2.2. Injection Strategy for ES-SAGD with Consideration of x_{wL}

The previous section presented a few important results pertaining to the ES-SAGD processes with single component n-alkane solvents on the basis of reservoir simulations. Firstly, ES-SAGD with single component n-alkane solvents with CNs four and higher yielded higher production rates in comparison with SAGD. Secondly, x_{wL} enhanced bitumen production. Thirdly, the magnitude of improvement in bitumen production due to x_{wL} was higher for SAGD relative to ES-SAGD for a specified operating pressure, and increased as the operating pressure was increased for a given process. In this section, a new injection strategy for the ES-SAGD process with n-hexane as the solvent is tested to see if it utilizes x_{wL} to improve bitumen production.

The simulation case studies considered henceforth account for the lateral expansion of the steam chamber on both sides of the well pair. The reservoir is of dimensions 142 m × 500 m × 20 m. The model has been discretized into 71 × 1 × 20 grid blocks in the x, y and, z directions, respectively. As before, the y-coordinate in this model represents the direction along the length of the well-pair. The scale of the model is increased to obtain slightly better representation of cumulative bitumen production histories at the well-pair scale used in field scenarios. The original bitumen in place at stock tank conditions in these simulation case studies is 313520 m^3. The injection and production wells are situated in the 36^{th} grid block relative to the left boundary of the model. The production well is subject to a maximum liquid production rate of 1400

m^3/day at surface conditions, which is close to values observed in some field cases. Further, production is carried out under steam-trap control with a minimum subcool of 10°C.

All simulation case studies presented in this section account for x_{wL} to ensure reliable evaluation of ES-SAGD relative to SAGD. Three injection strategies are considered for ES-SAGD.

In the first strategy, the injection concentration of the solvent and operating pressure are set to 2 mol% and 35 bars, respectively, over the entire course of the production phase. This is labeled as "CC-CP", where "CC" and "CP" stand for constant concentration and constant pressure, respectively.

The second injection strategy employs a time-variant injection concentration scheme with the operating pressure held constant. This strategy is labeled as VC-CP, where “VC” denotes variable injection concentration. Its consideration is informed by the observations of Keshavarz et al. (2015). They demonstrated that the injection of solvent at high concentrations early in the production phase expedites the accumulation of the solvent near the chamber edge. This facilitates the enhancement of the production rate of bitumen because of the increased utilization of the dilution capability of solvent. The injection concentration is gradually reduced with time so as to mitigate solvent retention in the reservoir.

The third injection strategy, which is tested with consideration of x_{wL} for the first time, employs a time-variant operating pressure scheme alongside a time-variant injection concentration scheme. This injection strategy is labeled as VC-VP, where “VP” stands for variable pressure.

The consideration of VC-VP is based upon the results presented in the previous section. That is, for both the CC-CP and VC-CP strategies, x_{wL} serves as the main mechanism for the dilution of the oleic phase prior to significant accumulation of the solvent near the chamber edge. As seen in Section 2.1.3b, the extent to which x_{wL} dilutes the oleic phase is enhanced with an increase in operating pressure as it results in higher operating temperatures. Hence, the operation of ES-SAGD at elevated pressures early in the production stage is one way to improve the production performance of the VC-CP strategy. This VC-VP strategy is consistent with common practice in SAGD operations, in which operating pressure is higher for the initial stage of production than for the later stages (Jiang et al., 2009).

The performance of ES-SAGD using each of the injection strategies is also compared with that of SAGD employing two different injection strategies – "CP", wherein the injection pressure is held constant at 35 bars; and "VP", in which a time-variant injection pressure scheme is used.

Figure 2.11 presents the cumulative bitumen production histories for SAGD and ES-SAGD for each injection strategy. The time-variant injection concentration scheme employed for the VC-CP and VC-VP cases shown in Figure 2.11 is presented in **Table 2.2**. As for the time-variant operating pressure scheme for SAGD (VP) and n-C_6 SAGD (VC-VP), the operation is carried out at 70 bars for the first two months in the production phase, during which the vertical and lateral expansion of the steam chamber occur simultaneously. After the two months, when the chamber reaches the top of the reservoir model and the lateral expansion of the steam chamber takes precedence, the operating pressure is reduced to 35 bars. For n-C_6 SAGD, the steam chamber reaches the outer boundaries of the reservoir model at around 912 days from the commencement of the operation (approximately 24 months into the production phase) for all three injection strategies. For the time-variant injection concentration strategies, the switch to steam-only injection is made once the steam chamber reaches the outer boundaries of the reservoir model (see Table 2.2).

Figure 2.11a indicates that for each process, the implementation of a time-variant operating pressure scheme (VC-VP for n-C_6 SAGD, VP for SAGD) yields the highest cumulative bitumen production over the majority of the duration of the production phase until the chamber reaches the outer boundary of the model. Figure 2.11b shows that the VC-VP strategy can yield 1000 m^3 more production than the VC-CP strategy over the short term. For SAGD, the corresponding improvement can be in excess of 3000 m^3 due to higher chamber-edge temperatures, as demonstrated in the previous section (see Figure 2.2).

The pertinent steam requirement and solvent accumulation histories for the different injection strategies are presented in **Figure 2.12**. Figure 2.12a shows that, for a given process, the consumption of steam (cold water equivalent) for a given bitumen production can also be lowered when the time-variant operating pressure scheme is used. For n-C_6 SAGD, the in-situ retention of solvent at later times is considerably lower for both VC-CP and VC-VP strategies than that for the CC-CP case, as seen in Figure 2.12b. VC-VP is also advantageous to expedite the solvent accumulation in the initial stage of production (see the rapid increase in solvent accumulation right after the beginning of production in Figure 2.12b). This is because the

solvent injected tends to be accumulated in the vapor phase, instead of condensing into the oleic phase, at initially higher temperatures with VC-VP. For n-C_6 SAGD, the combination of greater bitumen production, slightly lower steam consumption, and comparable solvent accumulation over the majority of the solvent coinjection period render the VC-VP strategy to be superior to the VC-CP strategy, and hence the best of the three tested strategies in terms of production performance.

Figure 2.13 compares the cumulative bitumen production histories and accompanying SOR for SAGD under the VP strategy and n-C_6 SAGD under the VC-VP strategy over a substantially longer period of time (≈ 13 years). The histories for the CP strategies are not shown in Figure 2.13 because for a given process, the ultimate recovery of bitumen of bitumen is practically identical under both operating pressure strategies.

Figure 2.13a shows that the coinjection of solvent can enhance the ultimate recovery of bitumen compared to steam-only injection; this occurs mainly due to the improvement of the local displacement efficiency of bitumen within the steam chamber. The improvement in local displacement efficiency of bitumen is illustrated using temperature, composition and saturation maps for a fixed cumulative bitumen production (i.e. fixed swept area by the steam chamber in these 2-D cases). **Figure 2.14** presents the maps for temperature and concentration of water in the vapor phase (x_{wV}) for the cumulative bitumen production of 240000 m^3; **Figure 2.15** presents the corresponding oleic-phase saturation maps. The dilution of bitumen by solvent increases the volatility of the oleic phase. Within the steam chamber, continuous injection of steam can vaporize the solvent dissolved in the oleic phase, leading to its accumulation in the vapor phase. The evaporated solvent accumulates in the cooler regions of the steam chamber, where partial condensation of water present in the vapor phase occurs due to lower temperatures. Hence, the accumulation of the solvent in the vapor phase is accompanied by the reduction in x_{wV} (see Figure 2.14d). The saturation of the vapor phase increases due to the evaporation of the solvent. This in turn can reduce the oleic-phase saturation to values lower than the residual oleic-phase saturation (0.13) used to define the relative permeability of the oleic phase, thereby resulting in improved local displacement efficiency of bitumen inside the steam chamber (see Figure 2.15b).

Figure 2.13b indicates that the cumulative SOR for n-C_6 SAGD can be lower than that for SAGD even at times significantly beyond that at which the switch to steam-only injection is performed. This is the result of the combination of improved recovery of bitumen, and lower

heat loss to the overburden and underburden, which is mainly due to lower operating temperatures. For both the VC-CP and VC-VP strategies, nearly 94% of the injected solvent is recovered over a production period spanning 13 years.

2.3. Conclusions

This chapter presented a detailed mechanistic study of SAGD and ES-SAGD with consideration of x_{wL} using numerical simulations. Different injection strategies were tested to examine the effect of x_{wL} on the performance of SAGD and ES-SAGD with n-alkane solvents. The phase behavior model used in the simulations was carefully created on the basis of experimental studies presented in the literature. On the basis of limited experimental data, the viscosity of the oleic phase was modeled such that the dissolution of water in bitumen would lower its viscosity. The extent to which the oleic-phase viscosity is reduced due to x_{wL} directly correlates with its magnitude, which in turn increases with temperature. Conclusions are as follows:

- Bitumen production was simulated to be improved with consideration of x_{wL} for SAGD and ES-SAGD. For a given operating pressure, the improvement in bitumen production due to x_{wL} was higher for SAGD than for ES-SAGD. This is because SAGD, in general, yields higher chamber-edge temperatures than ES-SAGD for a given operating pressure. Hence, reliable evaluation of the benefit of solvent coinjection relative to steam-only injection requires the consideration of x_{wL}; this becomes more important at higher operating pressures as the temperatures along and beyond the chamber edge increase with pressure.

- The magnitude of improvement in bitumen production due to x_{wL} is sensitive to the mixing model used for the oleic-phase viscosity. This sensitivity arises mainly due to the effect of the choice of mixing model on the component-specific weighting factors (q_i). The choice of viscosity model need not significantly alter the distribution of the oleic-phase composition along and beyond the chamber edge. The viscosity model used in this research properly reflects the qualitative difference between the bitumen/water and bitumen/solvent systems that has been reported in the literature. However, it is important to obtain more experimental data for viscosities of bitumen/solvent/water mixtures over the entire range of temperatures encountered in SAGD in order to mitigate the uncertainty in the predicted oleic-phase viscosity from a quantitative standpoint. This

would facilitate better understanding of compositional mechanisms in SAGD and ES-SAGD.

- x_{wL} affected the cumulative SOR mainly through the production rate in the simulation cases studied with the STARS simulator. The temperature along and beyond the chamber edge was not significantly affected by x_{wL}.
- The optimal solvent volatility for steam/solvent coinjection for specified operating conditions was not altered when x_{wL} was accounted for in the simulation cases in this research.
- Bitumen recovery rate in SAGD can be enhanced by employing a time-variant operating pressure strategy (VP). The bitumen production rate in ES-SAGD can be enhanced by employing a time-variant injection concentration and pressure strategy (VC-VP). In SAGD, the VP strategy facilitates increased leveraging of the bitumen dilution by water. In ES-SAGD, the VC-VP strategy additionally expedites solvent accumulation near the chamber edge, although the long-term effect on bitumen production may be small.

Table 2.1. Summary of the reservoir model used for the SAGD and ES-SAGD simulation case studies

Property	Value
Porosity	33%
Horizontal permeability	4000 mD
Vertical permeability	3000 mD
Initial reservoir pressure at the depth of 500 m	15 bars
Initial reservoir temperature	286.15 K
Initial oil saturation	0.75
Initial water saturation	0.25
Three-phase relative permeability model (CMG, 2011)	Linear interpolation
Formation compressibility	1.8E-05 1/kPa
Rock heat capacity (Keshavarz et al., 2014)	2600 kJ/m^3-^{o}C
Rock thermal conductivity (Keshavarz et al., 2014)	660 kJ/m-day-^{o}C
Over/underburden heat capacity (Keshavarz et al., 2014)	2600 kJ/m^3-^{o}C
Over/underburden thermal conductivity (Keshavarz et al., 2014)	660 kJ/m-day^{o}C
Bitumen thermal conductivity	11.5 kJ/m-day-^{o}C
Gas thermal conductivity	2.89 kJ/m-day-^{o}C
Producer bottom-hole pressure (minimum)	15 bars
Steam quality	0.9

Table 2.2. Time-variant injection concentration strategy. The reservoir is subject to an initial heating period of 182 days (approximately 6 months) with steam-only injection and no production.

Time from start of production, months	Time including heating period, days	Solvent concentration, mol%
0 – 2	182 – 244	10
2 – 10	244-486	5
10 – 18	486-731	2
18 – 24	731-912	1
> 24	> 912	0

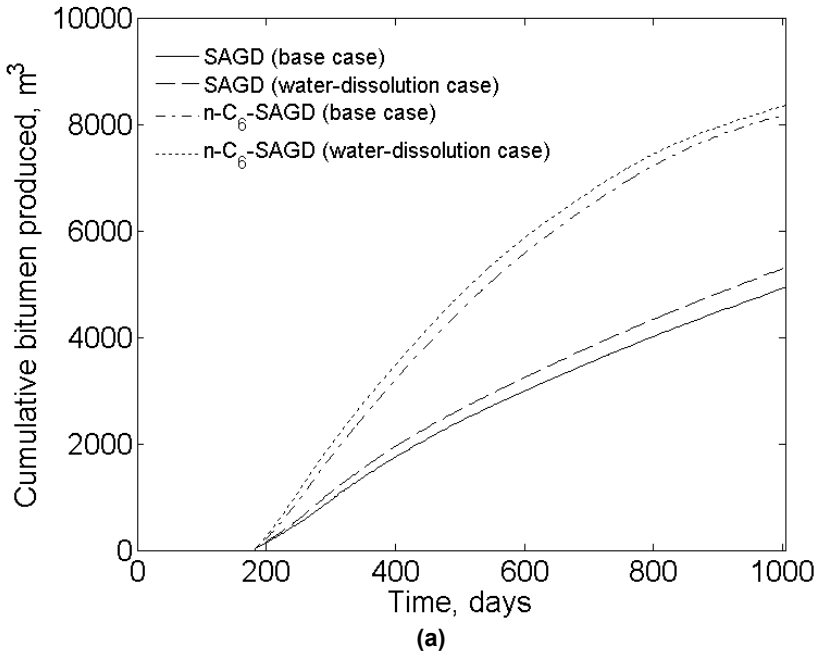

Figure 2.1. Effect of x_{wL} on cumulative bitumen production (Q) for SAGD and n-C_6 SAGD; (a) cumulative bitumen production histories; (b) Improvement in cumulative bitumen production due to x_{wL}. For the water-dissolution case, the steam chamber reaches the outer boundary of the reservoir model at 1004 days for SAGD and 670 days for n-C_6 SAGD. The original bitumen in place at stock tank conditions is 11591 m^3. The linear mixing rule (Equation 2.5) is used to the model the oleic-phase viscosity in SAGD. While the consideration of x_{wL} results in increased estimates for bitumen recovery in both SAGD and n-C_6 SAGD, the extent to which x_{wL} improves bitumen production in SAGD is greater than that for n-C_6 SAGD. This occurs due to greater operating temperatures for SAGD compared to n-C_6 SAGD which results in greater x_{wL} (also see Figures 2.2 and 2.3).

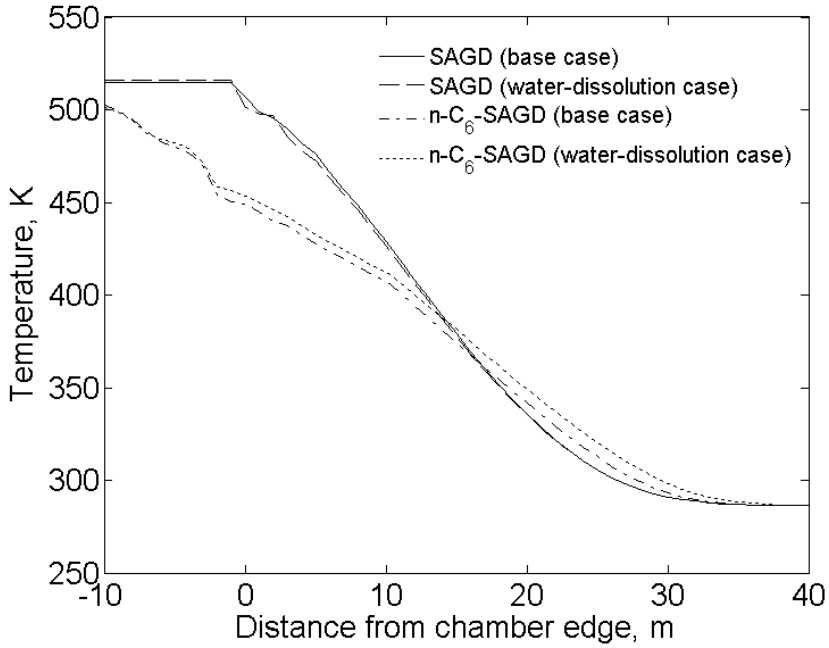

Figure 2.2. Temperature profiles for the 12th row (grid layer) from the top of the reservoir model at 578 days from the commencement of the operation for the base and water-dissolution cases.

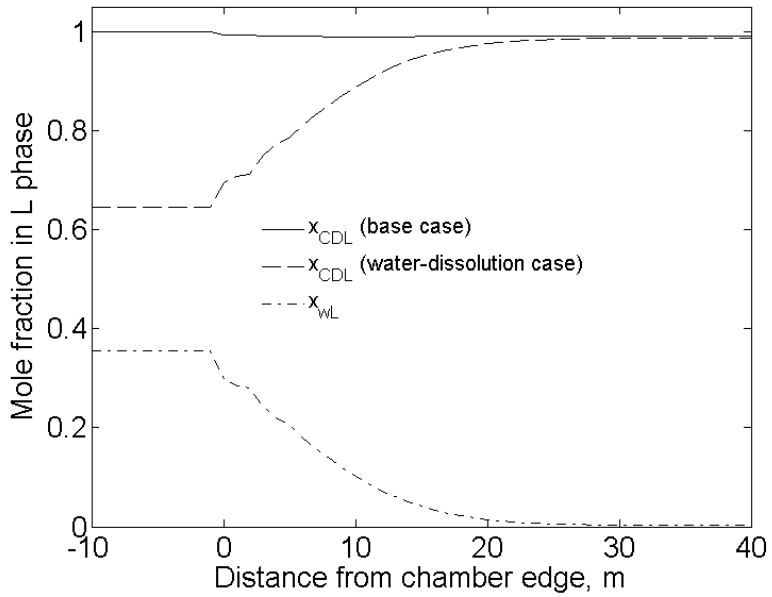

(a)

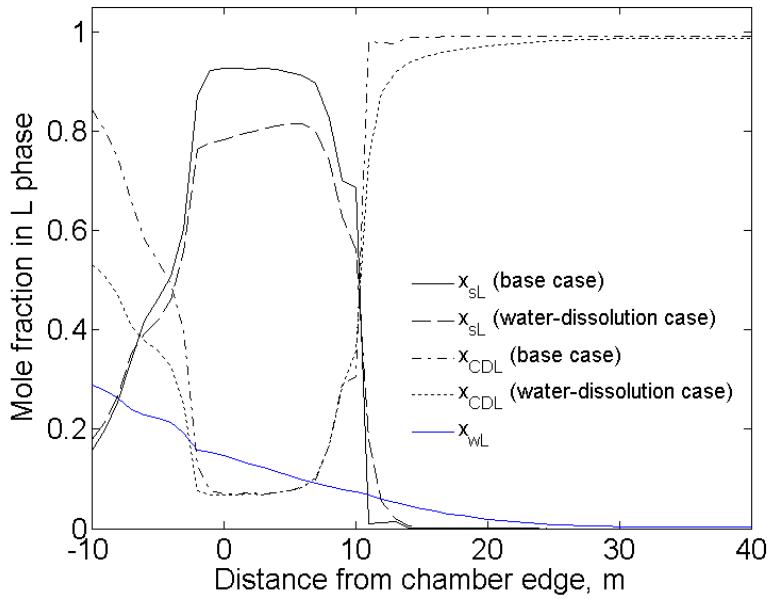

(b)

Figure 2.3. Oleic-phase composition profiles for the 12th row from the top of the reservoir model at 578 days from the commencement of the operation for the base and water-dissolution cases; (a) SAGD; (b) n-C_6 SAGD. When x_{wL} is disregarded in SAGD, x_{CDL} beyond the chamber edge is practically constant at nearly 99 mol%, the initial value used for x_{CDL} in the simulation cases. When x_{wL} is considered in SAGD, x_{CDL} monotonically increases towards 99 mol% with distance from the chamber edge due to the monotonic decrease of x_{wL} with distance. When solvent is coinjected (figure b), a solvent-rich bank liquid bank is formed immediately beyond the chamber edge, within which the concentration of the solvent in the oleic phase (x_{SL}) can be substantially greater than x_{CDL}. Consideration of x_{wL} in ES-SAGD results in the lowering of x_{sL}, without significant change in x_{CDL}. The extent to which x_{wL} enhances bitumen production in ES-SAGD for a given solvent depends on the extent to which x_{sL} is lowered due to this mechanism, and the viscosity of the solvent relative to water over the range of temperatures occurring within the solvent-rich bank.

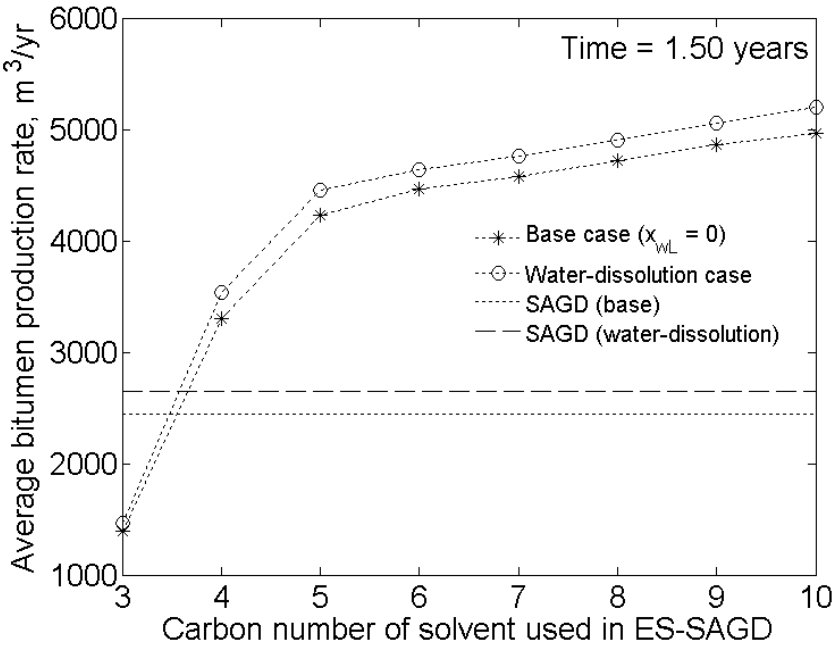

(a)

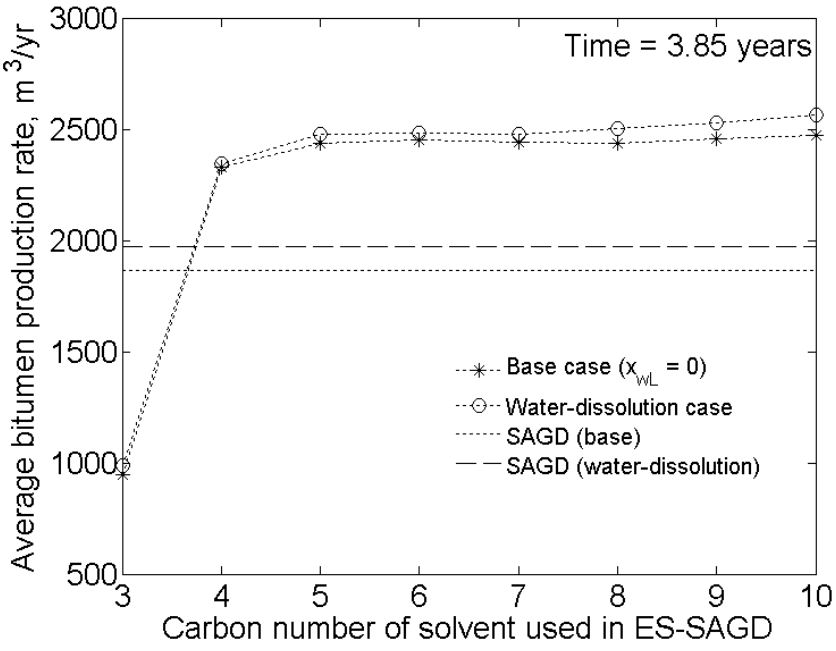

(b)

Figure 2.4. Average yearly bitumen production rate for SAGD and ES-SAGD based on cumulative bitumen production at different stages in the production phase; (a) 1.50 years; (b) 3.85 years. In (b), the average bitumen production rate for n-C_6 is greater than those corresponding to n-C_5 and n-C_7 for both the base and water-dissolution cases, indicating the occurrence of a breakover point in bitumen production rate with respect to the volatility of the solvent. The linearly increasing region for carbon numbers eight through ten for each case is likely the result of uncertainties in the mixing model used for the oleic-phase viscosity.

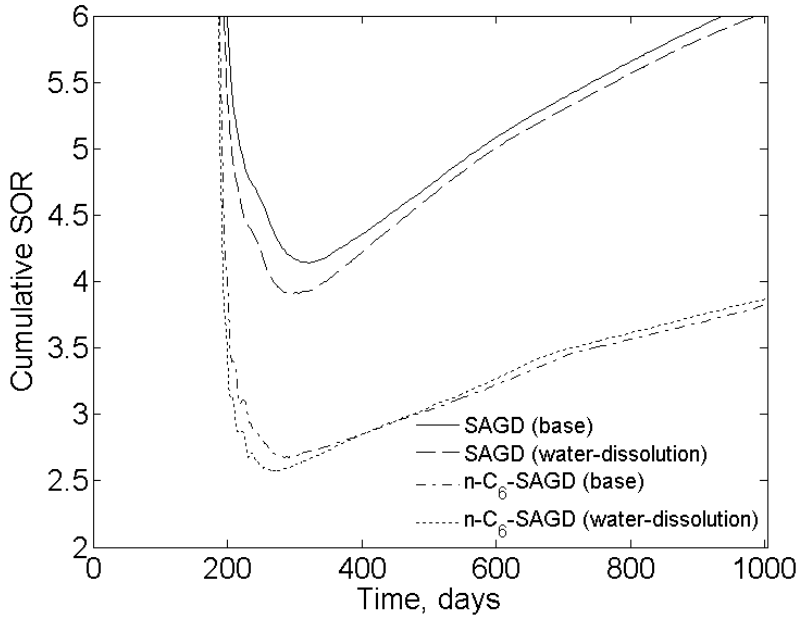

Figure 2.5. Effect of x_{wL} on cumulative SOR for SAGD and n-C_6 SAGD at 35 bars. The improvement in the cumulative SOR due to the consideration of x_{wL} mainly comes from the effect of x_{wL} on cumulative bitumen production. The temperature distribution along and beyond the chamber edge is not significantly affected by accounting for x_{wL}.

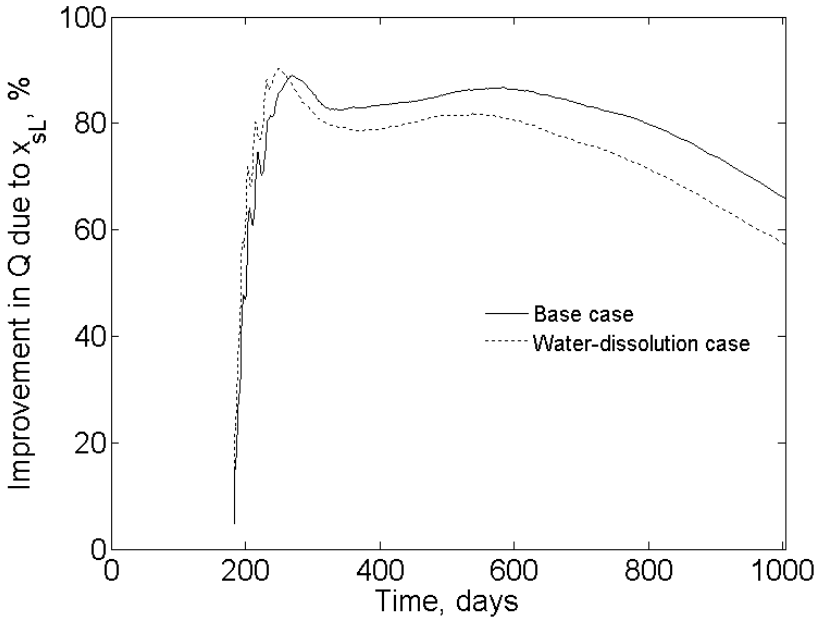

Figure 2.6. Relative deviation of n-C_6 SAGD to SAGD in cumulative production of bitumen (Q). Following the stabilization of the chamber edge temperature, the relative performance of n-C_6 SAGD to SAGD is overestimated when x_{wL} is not considered. For n-C_6 SAGD, the chamber reaches the outer boundary of the reservoir model for the water-dissolution case at 670 days from the commencement of the operation. At this time, the improvement in bitumen production due to solvent injection is overestimated by 7.25% (absolute deviation).

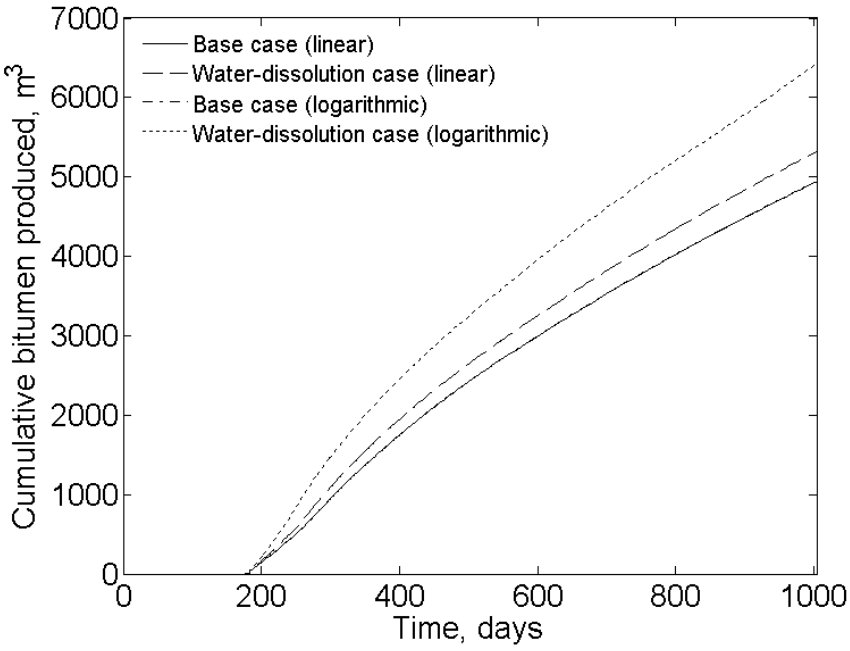

(a)

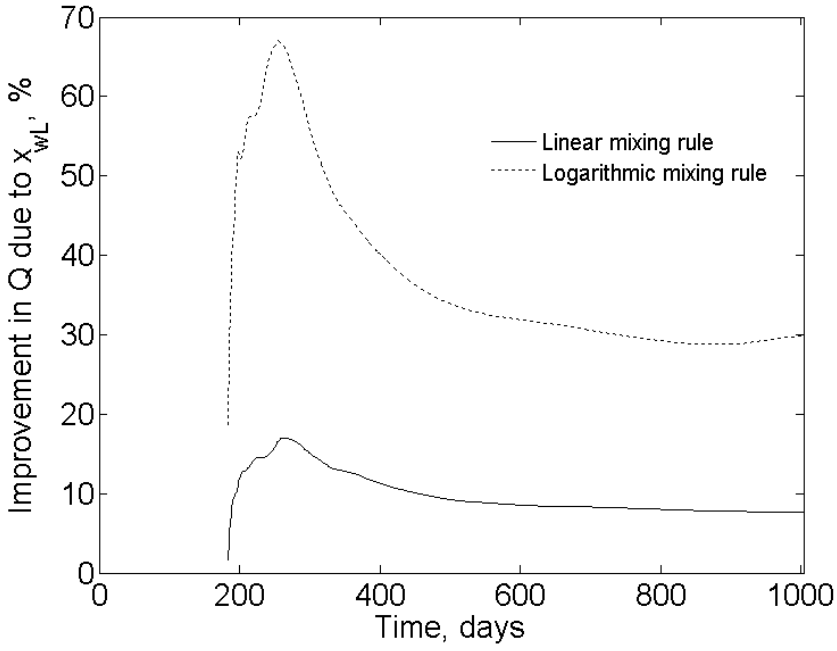

(b)

Figure 2.7. Effect of the choice of the mixing rule used for the oleic-phase viscosity on SAGD simulation considering x_{wL}; (a) cumulative bitumen production histories; (b) improvement in cumulative bitumen production (Q) due to consideration of x_{wL}.

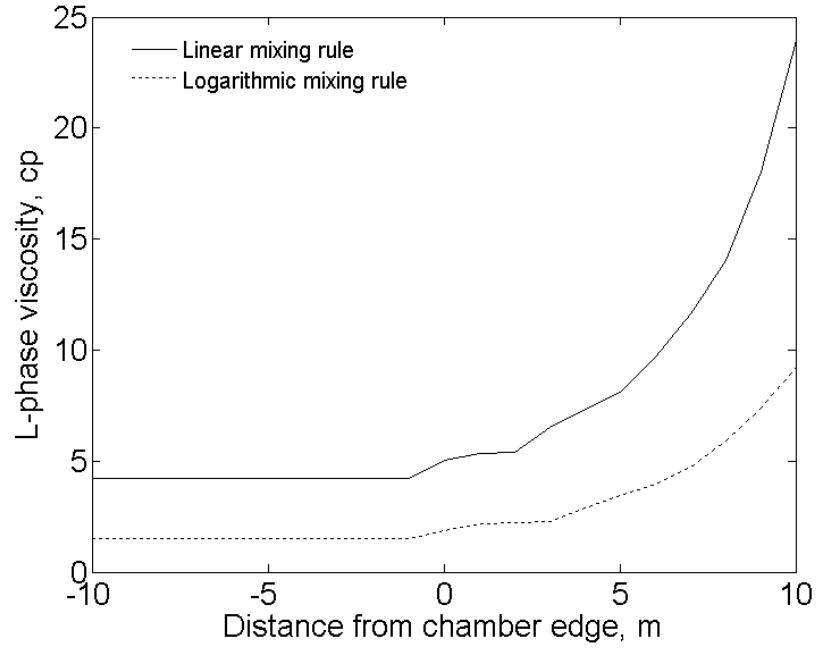

(a)

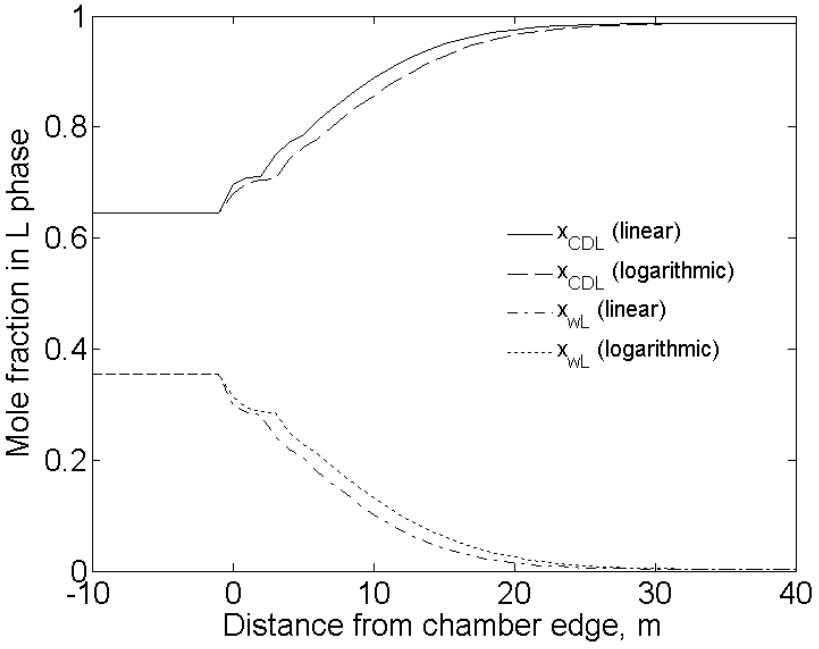

(b)

Figure 2.8. Effect of oleic-phase viscosity mixing model on property profiles for the water-dissolution case for the 12th row from the top at 578 days from the commencement of the SAGD operation; (a) oleic-phase viscosity profiles; (b) oleic-phase composition profiles. From (b), it is apparent that the choice of mixing model need not significantly alter the distribution of the oleic-phase composition at and beyond the chamber edge. That is, the extent to which the oleic-phase viscosity is reduced due to a given diluent may be restricted only to the effect the choice of mixing model has on the weighting factors (q_i) of the components (see Equation 2.2).

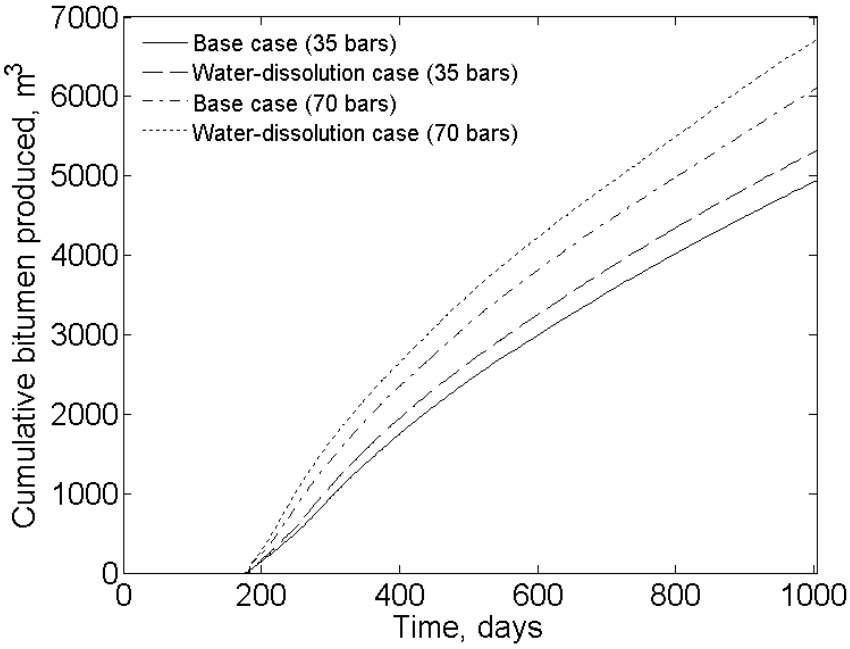

(a)

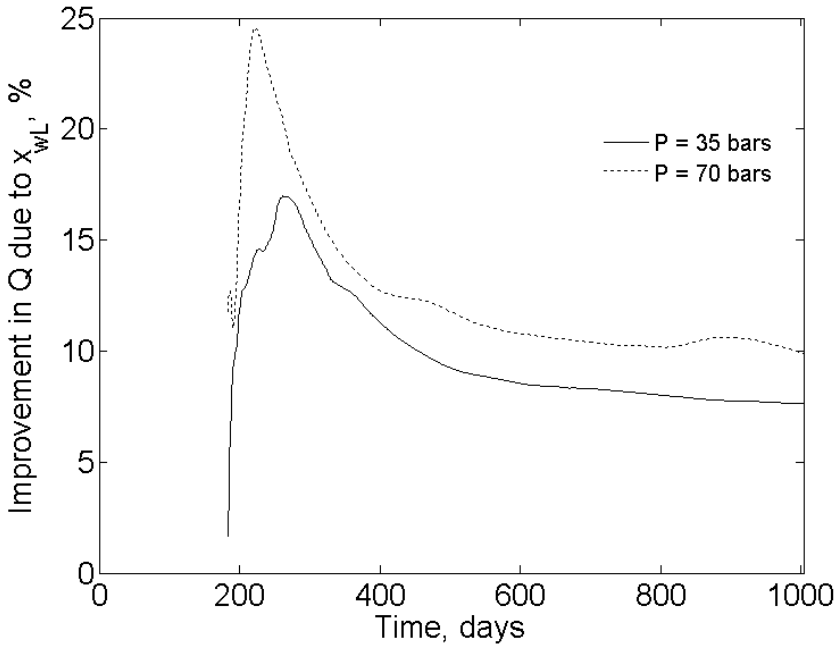

(b)

Figure 2.9. Effect of operating pressure on magnitude of improvement in cumulative bitumen production due to x_{wL} in SAGD; (a) cumulative bitumen production histories; (b) magnitude of improvement in cumulative bitumen production due to consideration of x_{wL}. Operating-chamber temperatures increase as the operating pressure increases; this enhances x_{wL} and therefore, the extent to which bitumen production is enhanced due to x_{wL}.

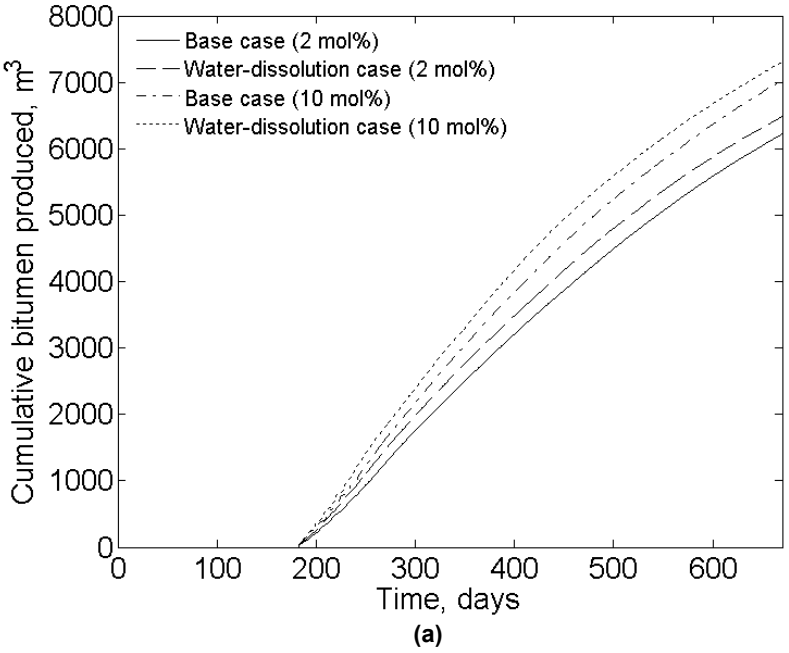

(a)

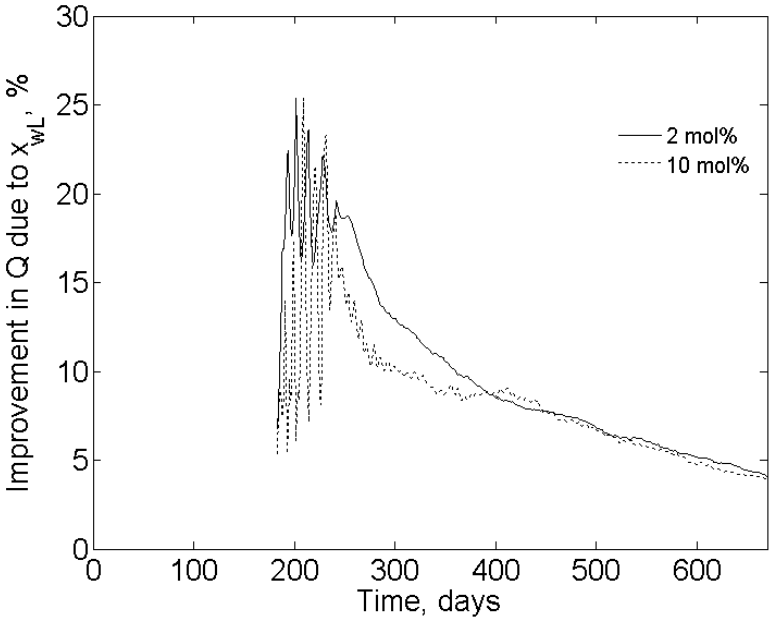

(b)

Figure 2.10. Effect of injection concentration on the magnitude of improvement in cumulative bitumen production due to x_{wL} in n-C_6 SAGD; (a) 2 mol%; (b) 10 mol%. For the water-dissolution case, the chamber reaches the outer boundary of the reservoir model at 670 days for the 2 mol% case, and 639 days for the 10 mol% case. The extent to which x_{wL} enhances bitumen production reduces as the injection concentration of the solvent increases due to the combined effects of greater dissolution of solvent in the oleic phase within the solvent-rich liquid bank near the chamber edge, and occurrence of higher temperatures within the solvent-rich bank. The oleic phase in the high-temperature region within the solvent-rich liquid bank beyond the chamber edge (where x_{wL} is significant) becomes richer in solvent as the injection concentration of solvent increases. This in turn diminishes the contribution of the dilution effect brought forth by water towards the drainage rate of bitumen.

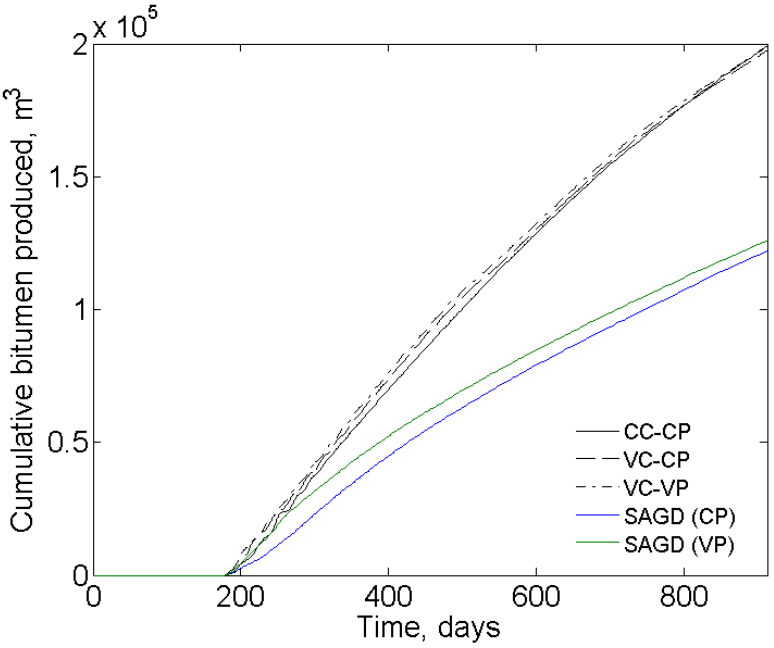

(a)

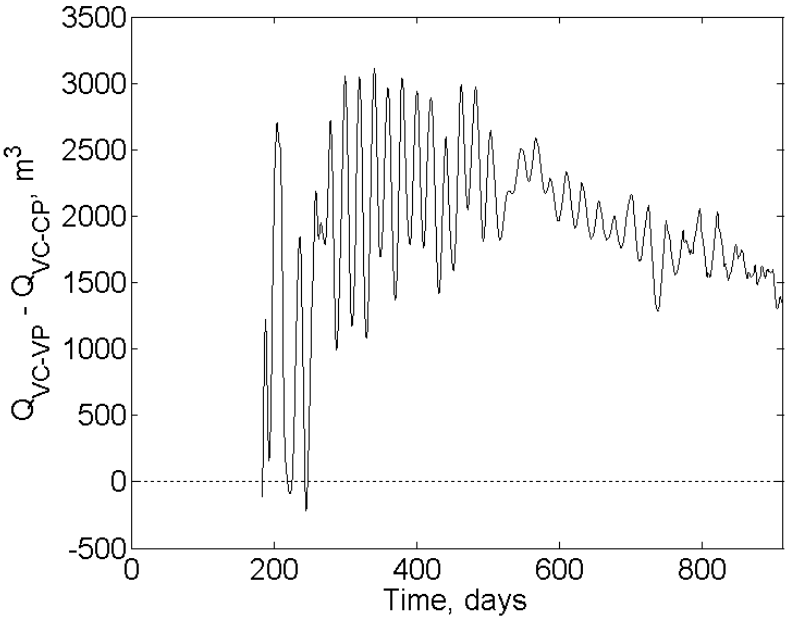

(b)

Figure 2.11. Bitumen production performance for SAGD and n-C_6 SAGD for the water-dissolution case for different operating scenarios; (a) Cumulative bitumen production histories; (b) Difference between the cumulative bitumen production for VC-VP and VC-CP in ES-SAGD with n-C_6 as the solvent. The variation in the injection concentration with respect to time for the VC cases is presented in Table 2.2. In the VP strategy for both SAGD and n-C_6 SAGD, the operation is carried out at 70 bars during the first two months of the production phase, and is subsequently reduced to 35 bars. The OBIP at stock tank conditions is 313520 m^3. The linear mixing model (Equation 2.5) is used to predict the oleic-phase viscosity in SAGD. In Figure 2.11b, the cumulative bitumen production for the VC-CP strategy ($Q_{VC\text{-}CP}$) corresponding to each time has been subtracted from the corresponding cumulative bitumen production for the VC-VP strategy ($Q_{VC\text{-}VP}$).

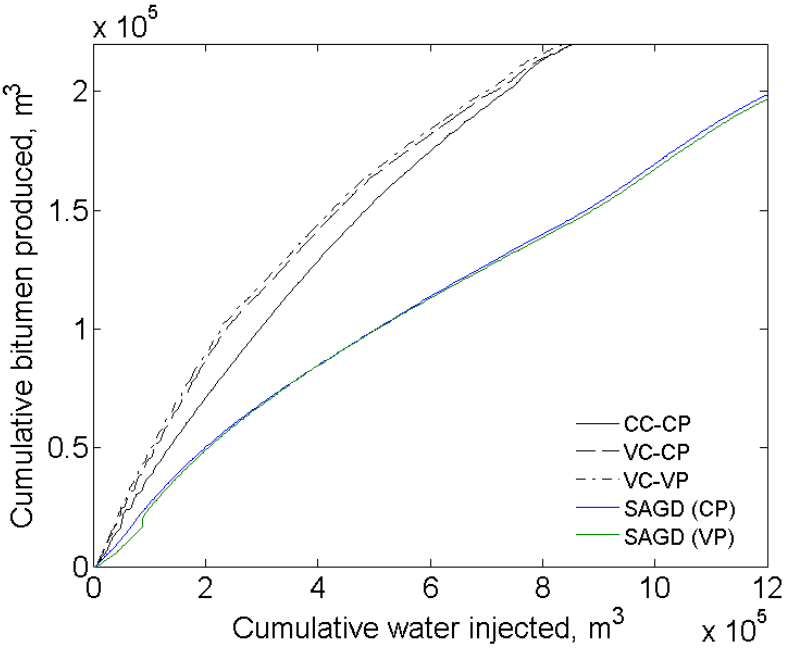

(a)

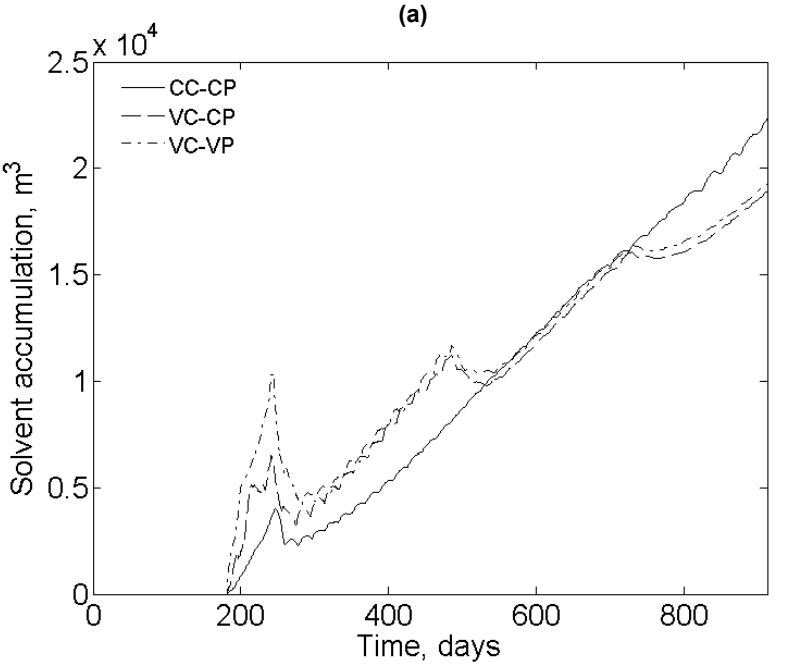

(b)

Figure 2.12. Steam requirement for SAGD and n-C_6 SAGD, and solvent accumulation n-C_6 SAGD for the water-dissolution case for different operating scenarios: (a) steam requirement; (b) solvent accumulation. As before, in the VP strategy for both SAGD and n-C_6 SAGD, the operation is carried out at 70 bars during the first two months of the production phase, and is subsequently reduced to 35 bars. In (b), there are three apparent spikes: one near 244 days, the second near 486 days, and the third near 730 days. The first spike corresponds to the transition in the dominant mode of steam chamber expansion from vertical to lateral, which occurs due to the reaching of the steam chamber to the top of the reservoir model. The remaining two spikes occur due to a change in the injection concentration of the solvent, from 5 to 2 mol% at 486 days, and 2 to 1 mol% at 731 days (also see Table 2.2).

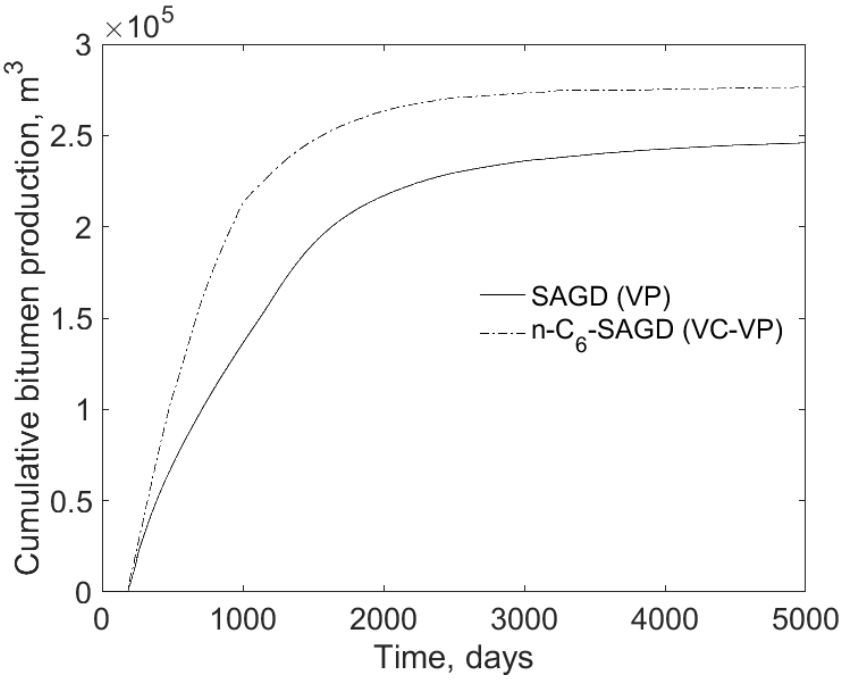

(a)

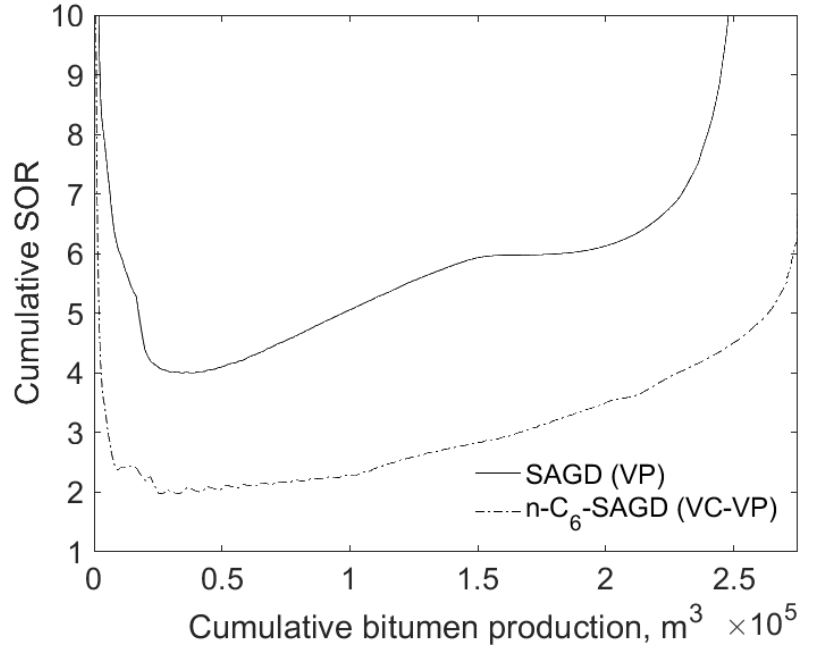

(b)

Figure 2.13. Cumulative bitumen production history, and cumulative SOR for SAGD under the VP strategy and n-C_6 SAGD under the VC-VP strategy over the long term; (a) cumulative bitumen production; (b) cumulative SOR.

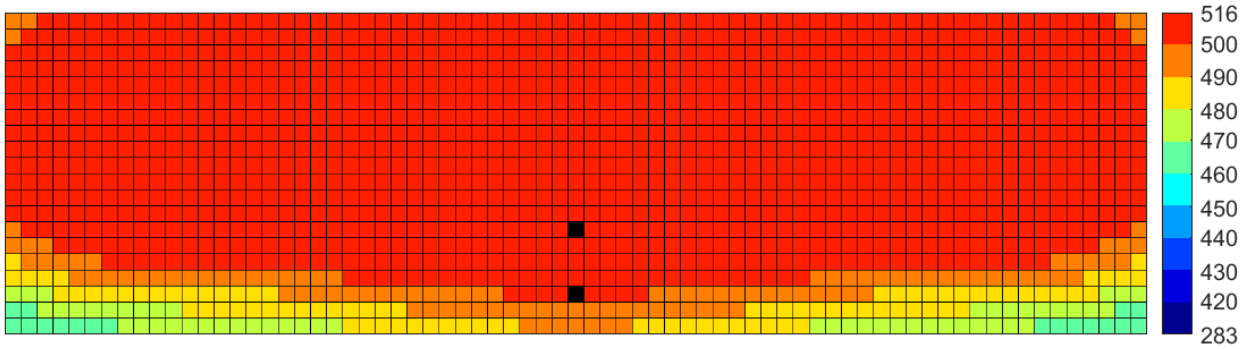
516
500
490
480
470
460
450
440
430
420
283

(a)

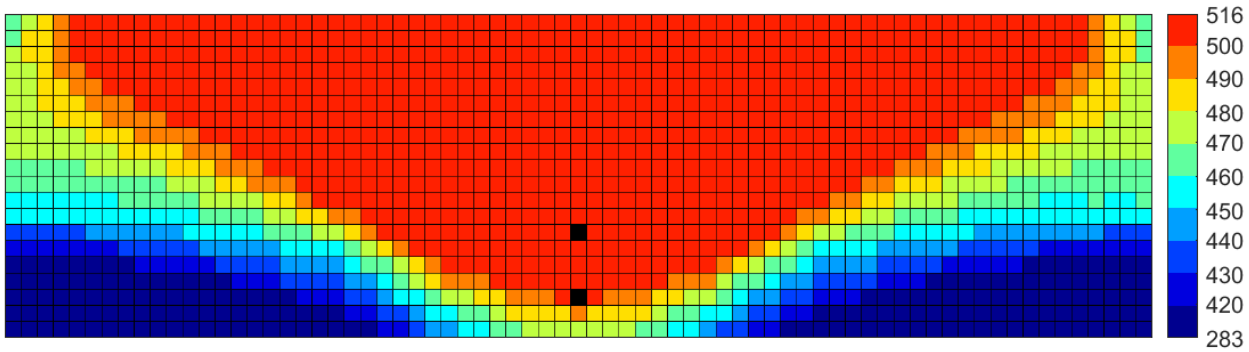
516
500
490
480
470
460
450
440
430
420
283

(b)

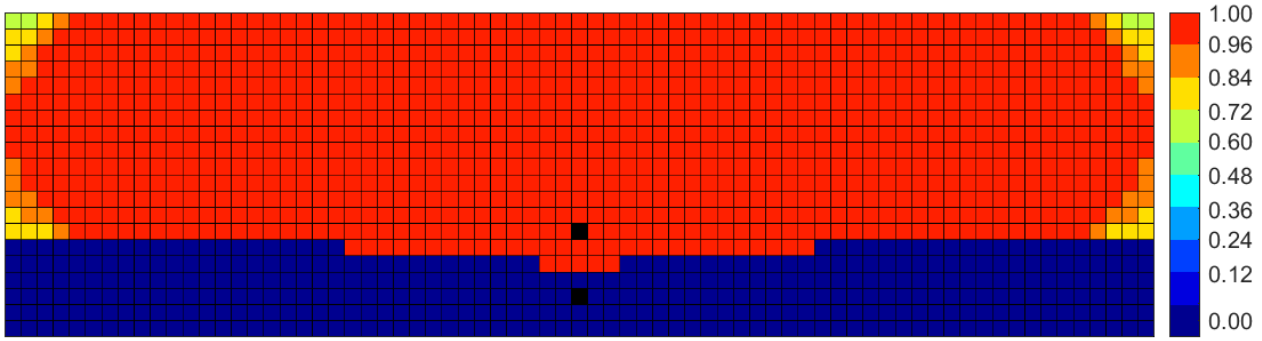
1.00
0.96
0.84
0.72
0.60
0.48
0.36
0.24
0.12
0.00

(c)

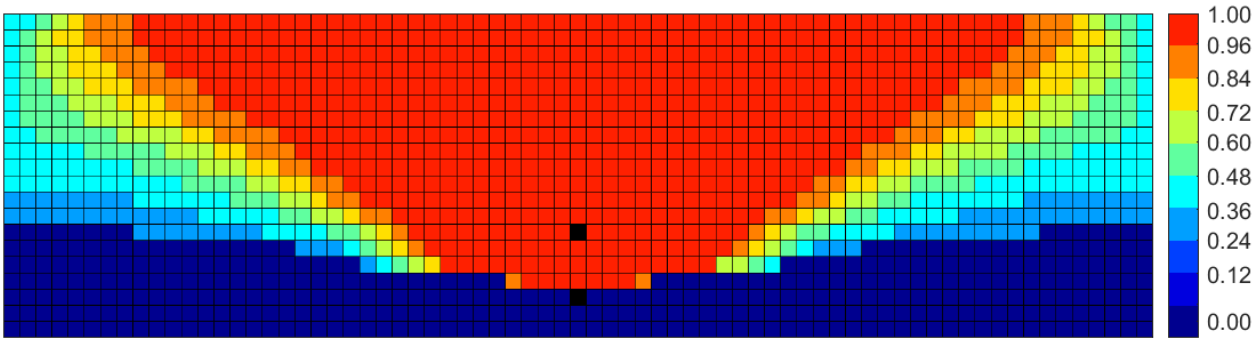

(d)

Figure 2.14. Maps for temperature (in Kelvin) and mole fraction of water in the vapor phase (x_{wv}) for SAGD and n-C_6 SAGD corresponding to the value of 240000 m^3 for the cumulative bitumen production; (a) temperature map for SAGD; (b) temperature map for n-C_6 SAGD; (c) x_{wv} map for SAGD; (d) x_{wv} map for n-C_6 SAGD. Grid blocks containing the wells are shown in black. The steam chamber in both SAGD and ES-SAGD have reached the outer boundary of the reservoir model in these maps. The coinjection of solvent results in lower temperatures near the periphery of the steam chamber (no-flow boundaries in this example). The injected solvent accumulates in the vapor phase in the cooler parts of the steam chamber due to the partial condensation of water present in the vapor phase; the partial condensation of water within the chamber results in the decrease of x_{wv}.

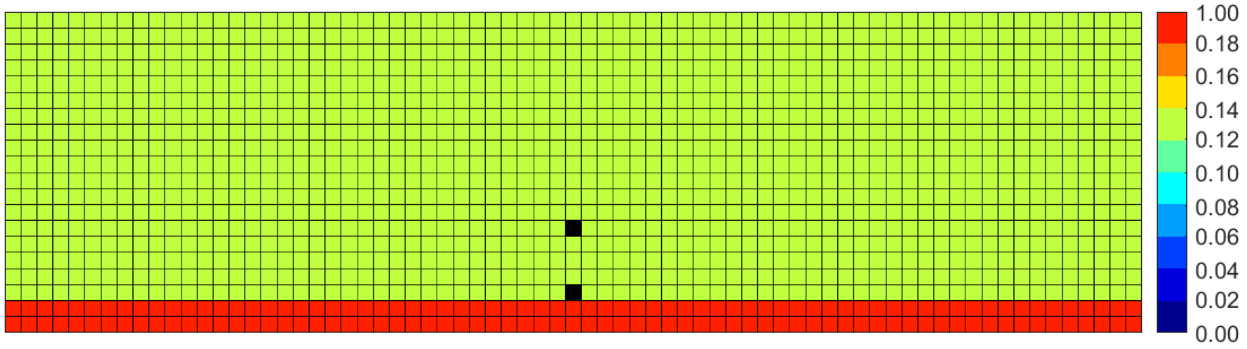

(a)

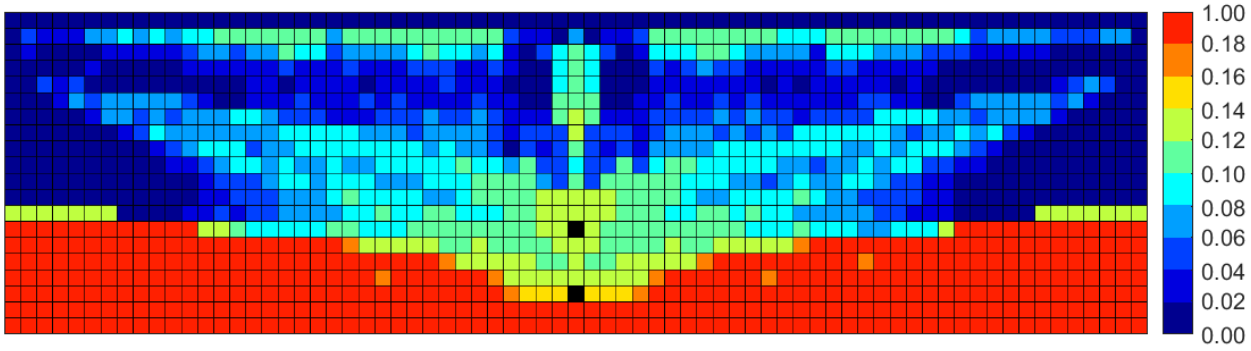

(b)

Figure 2.15. Oleic-phase saturation maps for SAGD and n-C_6 SAGD corresponding to the value of 240000 m^3 for the cumulative bitumen production; (a) SAGD; (b) n-C_6 SAGD. Grid blocks containing the wells are shown in black. The accumulation of solvent in the vapor phase is accompanied by the decrease in the oleic-phase saturation. The value of the oleic-phase saturation can be lower than the residual oleic-phase saturation (0.13) used to define the relative permeability curve for the oleic phase. Due to this mechanism, the local displacement efficiency of bitumen can be higher for n-C_6 SAGD compared to SAGD, and can contribute to the enhancement of the ultimate recovery of bitumen. The lowest value of the oleic-phase saturation observed within the steam chamber is 7×10^{-8}.

Chapter 3. Steam-Oil Ratio in SAGD and ES-SAGD under Reservoir Heterogeneity

List of Tables

List of Figures

Nomenclature

Roman Symbols

d	dispersivity
L	oleic phase
n	number of moles
N	number of grid blocks in Equation 3.1
P	pressure
PV	pore volume
S	saturation
T	temperature
t	time

V vapor phase

V volume

W aqueous phase

x mole fraction

Greek Symbols

λ scaling factor for BIP

$\underline{\rho}$ molar density

ω acentric factor

Subscripts

C_D dead bitumen

l longitudinal direction

L oleic phase

s solvent

T transverse direction

V vapor phase

w water

Abbreviations

BHP bottom-hole pressure

BIP binary interaction parameter

C critical constant

CWE cold water equivalent

EOS equation of state

ES expanding solvent

hom homogeneous case

het heterogeneous case

MW molecular weight

PR Peng and Robinson

SAGD steam assisted gravity drainage

SIS sequential indicator simulation

SOR steam-oil-ratio

VC time-variant concentration

VP time-variant injection pressure

The main objective of this chapter is to quantitatively determine if ES-SAGD can be a better alternative to SAGD in highly heterogeneous bitumen reservoirs in terms of the cumulative SOR as a function of cumulative bitumen production. The heterogeneity under consideration is mudstone. To this end, numerical simulations for SAGD and ES-SAGD with normal hexane as solvent (n-C_6 SAGD) are conducted for numerous geostatistical realizations of heterogeneous Athabasca-bitumen reservoirs.

Normal hexane (i.e., n-C_6) was chosen as solvent in view of three aspects: (i) the use of a single-component solvent reduces computational time for simulations; (ii) the availability of sufficient experimental data for the characterization of the compositional behavior of mixtures of water/bitumen/solvent required for simulations; (iii) the prior observation (see Chapter 2) that the optimal solvent volatility for ES-SAGD with normal alkane solvents is between carbon numbers five and seven. The suitability of n-C_6 as a solvent is also supported by a few prior studies (Mohebati et al., 2012; Keshavarz et al., 2015; Ji et al., 2015).

On the basis of the existing literature, the following are hypothesized. Firstly, the coinjection of solvent with steam could potentially enhance the production of bitumen while lowering the cumulative SOR even under reservoir heterogeneity. This is because the mechanisms by which production is enhanced under homogeneity (i.e., x_{sL} and lower operating chamber temperatures) are expected to prevail under heterogeneity as well.

Secondly, the margin by which the SOR is reduced due to coinjection of solvent may be higher under heterogeneity for a given cumulative bitumen production due to lower operating-chamber temperatures stemming from the potential for enhanced mixing between solvent and bitumen under tortuous hydraulic paths. Tortuous hydraulic paths for flow under heterogeneity may facilitate contact between solvent and bitumen leading to higher x_{sL}. Increased volatility of the oleic phase due to higher x_{sL} under heterogeneity could then facilitate vaporization of solvent upon subsequent contact with steam leading to greater accumulation of solvent near the chamber edge, resulting in lower operating-chamber temperatures. So, the reduction in conductive heat losses to the overburden due to coinjection could be higher under heterogeneity.

Section 3.1 presents the basic conditions used in numerical simulations. The validity of the aforementioned hypotheses is examined in Section 3.2. Section 3.3 presents the conclusions drawn from the simulation case studies.

3.1. Basic Conditions for Simulations

3.1.1. Reservoir model

Two-dimensional numerical flow simulations are performed using the STARS simulator of Computer Modelling Group (CMG, 2011). Two kinds of reservoirs are studied: a homogeneous reservoir consisting entirely of clean sand; and a heterogeneous reservoir consisting of two rock types, clean sand and mudstone (mainly comprising of clay), with mudstone being the heterogeneity (i.e., non-net facies). Heterogeneous realizations are generated by use of unconditional sequential indicator simulation (SIS) with the SGeMS simulator (Remy, 2005) developed at Stanford University.

Heterogeneous reservoirs simulated using SIS can be characterized in terms of a set of indices: (i) number of facies; (ii) global proportions of facies associations (which influences stationary variance); (iii) azimuth of facies-specific indicator variograms and range parameters along the azimuth of the indicator variogram (which influence the spatial correlation and orientation of geo bodies).

The initial reservoir temperature and pressure are assumed to be 286.15 K and 15 bars, respectively. Bitumen considered in this research is "live", comprising of a mixture of 10.22 mol% methane (C_1) and 89.78 mol% dead Athabasca bitumen. The corresponding gas-to-oil-ratio (GOR) is 5.0 m^3/m^3.

The reservoir model used is of dimensions 141 m × 500 m × 20 m in the x, y, and z directions, respectively, in which the y-direction represents the length along the well-pair. The model is discretized into 141 × 1 × 40 grid blocks in the x, y, and z directions, respectively. That is, each grid block is 1 m × 0.5 m in the x-z plane. In 2-D flow simulations in heterogeneous reservoirs, grid blocks of dimensions 1 m × 1 m in the x-z plane are conventionally used (Deutsch, 2010; Wang and Leung, 2015). In this paper, discretization along the z-direction is made finer to further reduce numerical dispersion. The lateral, top and bottom boundaries of the reservoir model are impermeable to fluid flow.

Both the injection and production wells are situated in the 71st grid column from the left boundary of the reservoir model. The injection and production wells are respectively located in the 28th and 36th grid layers from the top of the reservoir model.

The temperature of the injected stream is equivalent to the saturation temperature of water at the operating pressure, 35 bars. The quality of steam used is 90%. The production well is

subject to the minimum bottom-hole pressure (BHP) constraint of 15 bars, which is the initial reservoir pressure, maximum liquid flow rate constraint of 1400 m^3/day at surface conditions, and steam trap control with a minimum subcool of 10 K. For both the homogeneous and heterogeneous models, the reservoir is subject to an initial heating period of approximately 6 months using steam for each process, following which production is commenced.

Conductive heat losses to the over and underburden are considered in the simulations; the thermal conductivities of the overburden and underburden are set to 660 kJ/m-day-^{o}C. Capillary pressures and asphaltene precipitation are not considered.

The modeling of phase-specific relative permeabilities in this paper is based on Keshavarz et al. (2014). Relative permeabilities of the oleic, vapor, and aqueous phases are specified on the basis of two sets of two-phase relative permeability curves, one for the simultaneous flow of the oleic and aqueous phases, and the other for the flow of the vapor and liquid phases. These curves are assumed to be independent of temperature and facies type, and generated using Corey's model with a fixed exponent of 2.0 for each phase. The linear interpolation model (Baker, 1988) is used to specify the relative permeability of the oleic phase in the three-phase region. The residual saturation of oil is assumed to be 0.13 for the definition of the oleic-aqueous relative permeability curves; the irreducible water saturation is assumed to be equal to the initial water saturation of the clean sand facies. The critical liquid saturation used for the specification of the vapor-liquid relative permeability curve is 0.38. For the oleic-aqueous relative permeability curves, the end-point relative permeabilities of the oleic and aqueous phases are set to 1.0 and 0.3, respectively. The values of 0.3 and 1.0 are used for the end-point relative permeabilities of the vapor and liquid phases for the vapor-liquid relative permeability curves. A summary of the reservoir model is presented in **Table 3.1**.

3.1.2. Fluid model

The molecular weight of the dead Athabasca bitumen used in this research is 530.00 g/mol. The dead bitumen has been characterized as a single pseudocomponent ("dead bitumen" component, or C_D) using the Peng-Robinson (PR) EOS (Peng and Robinson, 1976; Robinson and Peng, 1978) with the characterization method of Kumar and Okuno (2015). The critical temperature, pressure and acentric factor of C_D are 847.17 K, 10.64 bars and 1.0406, respectively.

Simulations for SAGD use three components: water, C_1 and C_D. Those for ES-SAGD use four components: water, C_1, C_D, and normal hexane (n-C_6).

Compositional behavior of water/solvent/Athabasca-bitumen mixtures is modeled using the PR EOS with van der Waals' mixing rules. The binary interaction parameter (BIP) for C_D with n-C_6 is 0.088, and has been obtained from Kumar (2016).

As with Chapter 2, the BIPs for water with n-alkanes is calculated using the correlation developed by Venkatramani and Okuno (2015), which is based on the three-phase curves (oleic-vapor-aqueous) of water/n-alkane binaries measured by Brunner (1990). This correlation was given in Equation 2.1 (reproduced here)

$$\text{BIP} = c_1[1 + \exp(c_2 - c_3 \text{MW})]^{-1/c_4}, \quad (2.1)$$

where $c_1 = 0.24200$, $c_2 = 65.90912$, $c_3 = 0.18959$, and $c_4 = -56.81257$.

The BIP for water with C_D is estimated to 0.169. It was obtained by reducing the BIP calculated from Equation 2.1 using a scaling factor (λ) of 0.70, and which in turn was determined by matching the x_{wL} data measured for Athabasca bitumen by Amani et al. (2013ab)

The phase behavior is reflected in the simulations in terms of component K values, defined as the ratio of concentration in one phase to another, tabulated as functions of temperature and pressure. The K values used in the simulations with STARS are independent of composition. K values of all components corresponding to oleic-vapor-aqueous equilibrium are generated by use of the PR EOS for the fixed overall composition of 90 mol% water and 10 mol% hydrocarbons. For ES-SAGD, the overall distribution of hydrocarbons is set to 2 mol% solvent and 8 mol% live bitumen. This overall composition is considered to be representative of conditions near the chamber edge.

3.2. Simulation Case Studies

Prior simulation studies on the basis of homogeneous reservoir models presented that oil drainage along the edge of a steam chamber in successful ES-SAGD is faster, and takes place at lower temperatures than that in SAGD (Jha et al., 2013; Keshavarz et al., 2014, 2015; Khaledi et al., 2015). Consequently, an ES-SAGD chamber tends to be exposed to the overlying formation rocks with a smaller area and for a shorter period for a given production volume of bitumen. Therefore, such successful ES-SAGD is expected to result in a lower SOR than conventional SAGD for a given set of reservoir and operating conditions. This section begins by reviewing

the difference between SAGD and ES-SAGD with a homogeneous reservoir model in terms of SOR and chamber geometry, which forms the basis for further comparisons under heterogeneity.

Figures 3.1 and 3.2 compare SAGD (Figure 3.1) and n-C_6 SAGD (Figure 3.2) at 35 bars in terms of chamber shape for a given cumulative bitumen production in a homogeneous reservoir. The values assigned to the porosity, horizontal permeability, vertical permeability, and initial oil saturation for the clean sand are 0.33, 6000 mD, 4000 mD, and 0.75, respectively. Other model parameters are given in Table 3.1. Figure 3.1 shows the simulated temperature and vapor-phase saturation maps for SAGD at 456 days, at which the cumulative bitumen production is 77487 m^3. The cumulative SOR for this cumulative bitumen production is calculated to be 4.02.

Figure 3.2 shows the simulated temperature and vapor-phase saturation maps for n-C_6 SAGD at 365 days from the start of the operation. The injection concentration of solvent has been set to 2 mol% for this simulation. The cumulative bitumen production at this time is 76617 m^3, and the accompanying SOR is 2.27. That is, the cumulative SOR in n-C_6 SAGD is simulated to be lower than that in SAGD by 1.75 for almost the same bitumen production volume. Figure 3.2a shows that the temperature in the interior of the steam chamber is comparable to the saturation temperature of water at 35 bars (515.72 K). However, temperatures along and near the chamber edge are lower.

Table 3.2 presents analytical estimates for the oleic-vapor-aqueous to oleic-aqueous transition temperatures corresponding to the simulated pressure and overall compositions of grid blocks along the chamber-edge. Chamber-edge grid blocks at each grid layer are identified on the basis of the simulated vapor-phase saturation map (Figure 3.2b). The accumulation of methane has an impact on chamber-edge temperature near the top of the reservoir model, and accumulation of n-C_6 contributes to the reduction in chamber-edge temperature away from the reservoir top.

Despite lower chamber-edge temperatures, n-C_6 SAGD yields a higher drainage rate of bitumen along the sides of the steam chamber through the enhancement of the oleic-phase mobility because of $x_{sL.}$ This results in a lower cumulative SOR, and alters the geometry of the steam chamber by making it less laterally extensive near the top for this case. Figures 3.1 and 3.2 are given to qualitatively explain the major difference between SAGD and ES-SAGD that is often discussed in the literature on the basis of the particular set of conditions used.

However, it is uncertain how the above-mentioned aspects of ES-SAGD are affected by reservoir heterogeneity. The main question to be addressed in this section is whether the

advantage of ES-SAGD over SAGD in terms of SOR is expected to be more significant under heterogeneity. This question is of primary importance because reservoir heterogeneity largely determines the geometry of a steam chamber, which in turn affects the exposure of heated zones to the overlying formation rocks.

In the subsequent subsections, simulations for SAGD and n-C_6 SAGD are conducted for the operating pressure of 35 bars and injection concentration of 2 mol% for the solvent. Two case studies (Sections 3.2.1 and 3.2.2), each comprising of 50 stochastically generated heterogeneous realizations using SIS in addition to the homogeneous reservoir model, have been defined based on the orientation of simulated mudstone barriers relative to the top and basal planes of the reservoir model, and petrophysical properties assigned to the net and non-net facies. Section 3.2.3 presents a sensitivity analysis in terms of transverse dispersivity, which primarily affects the distribution of solvent ahead of the edge of a steam chamber.

For each case study, the performance of each process and reservoir is analyzed on the basis of the cumulative SOR (CWE) as a function of cumulative bitumen production. This allows us to compare different cases on the basis of the steam usage for a given amount of bitumen production. In this paper, 2-D maps for different parameters are shown for selected amounts of cumulative bitumen production, which are indicated as fractions of the simulated cumulative bitumen production in SAGD for the homogeneous model when the lateral boundaries begin to affect the propagation of the steam chamber $\left(V_{SAGD}^{hom}\right)$.

3.2.1. Case study 1: horizontal mudstone barriers

In this case study, the orientation of the simulated mudstone barriers relative to the top and basal planes of the reservoir is predominantly horizontal. **Table 3.3** summarizes the pertinent parameters used to generate the realizations using SIS. The values assigned to the porosity, horizontal permeability, vertical permeability, and initial oil saturation for the clean sand are 0.33, 6000 mD, 4000 mD, and 0.75, respectively. The corresponding values for the mudstone facies are set to 0.02, 6000 mD and 0.04 mD, and 0.15. The reservoir models and the assignment of facies properties in this case study are consistent with the conventional approach used in reservoir engineering studies focusing on effects of mudstone barriers on SAGD performance (e.g., Chen et al., 2008; Wang and Leung, 2015). In this modeling paradigm, mud layers within

a given muddy flow simulation grid block are assumed to be thin such that their influence on the hydraulic conductivity of the grid block is restricted only to its vertical component (i.e., k_z).

The simulated value of V_{SAGD}^{hom} in this case study is approximately 196190 m^3; the corresponding recovery factor is 64%. **Tables 3.4 and 3.5** compare the cumulative SOR for SAGD and n-C_6 SAGD across different realizations for the cumulative bitumen productions of 49048 m^3 ($0.25V_{SAGD}^{hom}$) and 98095 m^3 ($0.50V_{SAGD}^{hom}$), respectively. The realizations in these tables are labeled using numerical indices; the homogeneous case has been assigned the index of zero. Note that these cumulative bitumen production targets are not met by all realizations, which leads to gaps in these tables. This is either due to the presence of mudstone distributions that severely impede the propagation of the steam chamber within the reservoir or non-convergence of numerical solution. The latter issue was observed to be prevalent with n-C_6 SAGD, and is likely due to reservoir models exhibiting extreme contrasts in permeability over short length scales. Nevertheless, the realizations depicted in Tables 3.4 and 3.5 qualitatively exhibit a wide variety of steam chamber geometry. Tables 3.4 and 3.5 show the cumulative SORs for a fixed cumulative bitumen production to be systematically lower under steam-solvent coinjection relative to steam-only injection. For each cumulative bitumen production, a paired t-test on the two sets of SORs was performed to verify that the difference in SOR between SAGD and n-C_6 SAGD for a specified cumulative bitumen production is statistically significant. As described for a specific case below, reduction of the cumulative SOR under steam-solvent coinjection is attributed to the combination of improved oleic-phase mobility due to x_{sL} and lower thermal losses to the overburden, although relative magnitudes of contribution from different factors depend on the reservoir heterogeneity under consideration.

As with the homogeneous case, the coinjection of solvent can facilitate the lowering of conductive heat losses to the overburden in heterogeneous reservoirs by the reduction of operating chamber temperatures and exposed area for heat transfer. This is illustrated in **Figure 3.3**, which presents the simulated vapor-phase saturation and temperature maps for SAGD and n-C_6 SAGD for realization 23 for the cumulative bitumen production of approximately 98095 m^3. The diminished lateral span of the steam chamber near the top for n-C_6 SAGD comes from the reduction of the oleic-vapor-aqueous to oleic-aqueous transition temperature at the chamber edge due to the accumulation of n-C_6. For this realization, **Figures 3.4 and 3.5** respectively give the

maps for the cumulative SOR (CWE) as a function of cumulative bitumen production, and cumulative heat losses as a function of time and cumulative bitumen production for each process.

The extent to which each process is detrimentally affected by heterogeneity is quantified in terms of the resulting increase in cumulative SOR for a given cumulative bitumen production. That is, the metric, $(\mathrm{SOR_{het}} - \mathrm{SOR_{hom}})$, is evaluated for each process and realization as a function of cumulative bitumen production. The terms, $\mathrm{SOR_{het}}$ and $\mathrm{SOR_{hom}}$, represent the cumulative SORs for a given heterogeneous realization and homogenous reservoir, respectively. The adverse effect of reservoir heterogeneity on a given process diminishes with decreasing values of this metric. Tables 3.4 and 3.5 also present the values of $(\mathrm{SOR_{het}} - \mathrm{SOR_{hom}})$ for SAGD and n-C_6 SAGD across different realizations for the cumulative bitumen productions of 49048 and 98095 m^3, respectively. For the cumulative bitumen production of 49048 m^3, SAGD yields an average value of 3.61 for $(\mathrm{SOR_{het}} - \mathrm{SOR_{hom}})$, while n-$C_6$ SAGD yields the value of 2.37 for the same; the corresponding variances are 4.99 and 1.92. For the cumulative bitumen production of 98095 m^3, pertinent means are 3.11 and 1.94, and the respective variances are 1.23 and 0.51. Hence, n-C_6 SAGD, on average, is adversely affected by heterogeneity to a lesser extent compared to SAGD for these simple cases. A paired t-test was conducted for the two sets of values for $(\mathrm{SOR_{het}} - \mathrm{SOR_{hom}})$ for each cumulative bitumen production to ensure that the aforementioned conclusion is statistically valid.

The reduction in cumulative SOR due to coinjection for a given realization is calculated as $(\mathrm{SOR_{SAGD}} - \mathrm{SOR_{ES-SAGD}})$ as a function of cumulative bitumen production; the terms $\mathrm{SOR_{SAGD}}$ and $\mathrm{SOR_{ES\text{-}SAGD}}$ respectively represent cumulative SORs for SAGD and ES-SAGD for a given cumulative bitumen production. Tables 3.4 and 3.5 also present the variation of this metric across different realizations for the cumulative bitumen productions of 49048 and 98095 m^3, respectively.

For the heterogeneous cases, the average value of $(\mathrm{SOR_{SAGD}} - \mathrm{SOR_{ES-SAGD}})$ is 2.51 for the cumulative bitumen productions of 49048 m^3, and 2.75 for the cumulative bitumen production of 98095 m^3; the corresponding values for the homogeneous case (realization 0) are 1.27 and 1.58. That is, on average, the reduction in cumulative SOR due to coinjection of solvent is simulated to be greater for the heterogeneous cases compared to the homogeneous case (realization 0). This is because the reduction in cumulative SOR due to the accelerated lateral expansion of the steam

chamber is offset to a lesser extent by thermal losses to the overburden due to a smaller exposed area under reservoir heterogeneity (see Figure 3.3, as an example).

In heterogeneous reservoirs, the extent to which the solvent dissolves in the oleic phase is expected to be higher than that under homogeneity. This is because more-tortuous hydraulic paths in a heterogeneous reservoir not only facilitates the mixing of solvent with mobile bitumen (i.e., dispersive flux in the transverse direction along the edge of a steam chamber), but also increases the retention time for the injected solvent in the reservoir. That is, the ratio of dispersive flux in the transverse direction to convective flux in the longitudinal direction along the chamber edge tends to be increased under heterogeneity. This can be viewed to be analogous to the well-known situation of gas injection in which the mixing of gas components with bypassed oil in a heterogeneous reservoir is enhanced when Damköhler number is increased in convection-dispersion-capacitance behavior of oil displacement by gas (Coats and Smith 1964, Dai and Orr 1987, Zhang and Okuno 2015). The questions to be answered below are whether and to what extent x_{sL} is enhanced under heterogeneity.

Table 3.6 presents the ratio of the accumulated solvent volume to the cumulative bitumen production (i.e., solvent retention ratio) for the homogeneous and heterogeneous models in the current case study for the cumulative bitumen production of 98095 m^3 ($0.50V_{SAGD}^{hom}$). The retention ratio is calculated using the simulated cumulative bitumen production, solvent injection and production histories at stock-tank conditions. Table 3.6 indicates that the retained volume of solvent for a given cumulative bitumen production increases under heterogeneity. Details of the simulation have indicated that the increase in solvent accumulation is sensitive to the spatial distribution of mudstone barriers.

Maps for x_{sL} for a given cumulative bitumen production show that x_{sL} is enhanced under heterogeneity. However, simulations for some realizations exhibit that the liquid solvent accumulates in regions with low oleic-phase mobility, or above laterally-extensive mudstone bodies located near the well-pair. For example, let us consider realization 23 in this case study (see Figure 3.3). **Figure 3.6a** presents the simulated x_{sL} distribution map for the cumulative bitumen production of approximately 98095 m^3 for this realization, and **Figure 3.7a** presents the corresponding map for the homogeneous case. The areal span of regions of elevated x_{sL} (> 80 mol%), indicated in purple and pink in this illustration, is greater for the heterogeneous cases compared to that observed for the homogeneous case depicted in Figure 3.7a. As presented in

the maps for the oleic-phase mole fraction (β_L) **(Figure 3.6b)** and the product of β_L and x_{sL} **(Figure 3.6c),** however, the relative mobility of the oleic phase within the clean sand grid blocks whose x_{sL} values are elevated can be quite low. Even when the oleic-phase saturation in these grid blocks is high enough for the oleic-phase to be mobile (e.g., near the top of the model in **Figure 3.6d**), such regions are often situated above laterally-extensive mudstone barriers, which impede the drainage of the oleic phase towards the production well. Discrepancies in the distribution of x_{sL} between the homogeneous and heterogeneous cases are interdependent with the differences in the corresponding temperature distributions. This is apparent from comparison of the temperature map given in **Figure 3.7b** for the homogeneous case and Figure 3.3d for realization 23 for the cumulative bitumen production of approximately 98095 m^3. Note, however, that the accumulation of liquid solvent in slow-flow (stagnant) regions is simulated only on the basis of two-dimensional simulations in this research. More thorough investigation into the possibility of in-situ retention of liquid solvent in slow-flow regions should be made with three-dimensional flow simulations.

To recap on the main point from this case study, the advantage of n-C_6 SAGD over SAGD in terms of SOR was simulated to be more significant under heterogeneity with horizontal mudstone bodies. The mechanisms exemplified for a homogeneous reservoir in Figures 3.1 and 3.2 were enhanced mainly because of a larger amount of solvent residing in the oleic phase under heterogeneity. The distribution of temperature and the dissolution of solvent in the oleic phase near the chamber edge are connected phenomena through the interplay between phase behavior and flow under heterogeneity. At a given time and location within the reservoir, temperature dictates the extent to which the solvent dissolves in the oleic phase near the chamber edge. x_{sL} near the chamber edge determines the volatility of the oleic phase and hence, influences the extent to which the solvent is vaporized upon subsequent contact with steam; this affects the extent to which the solvent accumulates near the chamber edge, and consequently, the temperature distribution along it. The temperature distribution near the chamber edge in turn influences the geometry of a steam chamber and the cumulative SOR. These arguments reinforce the importance of mixing between bitumen and solvent near the chamber edge, and its understanding for effective implementation of ES-SAGD under heterogeneity.

3.2.2. Case study 2: inclined mudstone barriers

In this section, the applicability of the conclusions regarding the relative performance of n-C_6 SAGD to SAGD obtained using the reservoir models in Section 3.2.1 is examined for those more representative of the middle McMurray member. **Appendix E** presents a brief overview of the geological architecture of the McMurray formation, and justification of our reservoir modeling methodology on the basis of: (i) an interpretation of the geology of the middle McMurray member; and (ii) the challenges associated with the use of previously developed geostatistical modeling paradigms for the middle McMurray member in K-value-based flow simulations for ES-SAGD.

As with Section 3.2.1, the relative performance of ES-SAGD to SAGD is evaluated by use of a two-facies reservoir model comprising of clean sand and mudstone with unconditional SIS in this section. The reservoir gridding is identical to that described in Section 3.1.1. The dimensions of the grid cells used for geostatistical modeling are identical to that used in flow simulation; that is, neither upscaling nor grid refinement is performed. The assignment of petrophysical properties of clean sand and mudstone are informed by experimental data reported by Musial et al. (2013). The porosity, horizontal and vertical permeabilities, and bitumen saturation of the clean sand facies has been set to 36%, 6100 mD and 3500 mD, and 85%, respectively. The corresponding values for mudstone facies are 5%, 1 mD and 0.1 mD, and 15%. So, a major distinction between the heterogeneous models used in this case study and those used previously is the spatial discontinuity of the horizontal component of the absolute permeability (i.e., k_x). The values for the reservoir properties assigned to the non-net facies in these simulations are identical to those reported by Musial et al. (2013) for clay plugs, which exhibit the poorest petrophysical characteristics among the five facies associations studied by the authors. This facilitates the obtainment of conservative estimates for the production performance of SAGD and n-C_6 SAGD.

Table 3.7 presents values for input parameters for SIS in this case study. The input parameters for SIS are chosen such that the resulting realizations exhibit the following characteristics. Firstly, the predicted distributions of mudstone should, on average, appear inclined relative to the base and top planes of the reservoir model; this is because inclined heterolithic strata represent the main form of mudbed heterogeneity within tidally influenced point bars. For a given set of range parameters for the indicator variogram model of the

mudstone facies, this requirement can be met by changing the azimuths of both the indicator variogram model, and the orientation of the search ellipse for indicator kriging to reflect the desired inclination of the simulated mudstone barriers. The azimuth for the 2D geostatistical simulations conducted here is given by 90° minus the desired inclination angle, which in this case study is 12°. Secondly, the three commonly occurring forms of inclined mudstone barriers should be predicted, as described in Appendix A.

As with the first simulation case study, the extent to which reservoir heterogeneity detrimentally affects the cumulative SOR for a given cumulative bitumen production for the current case study is lower for n-C_6 SAGD compared to SAGD. Similarly, the advantage of ES-SAGD in terms of its ability to lower the consumption of steam to meet a given cumulative bitumen production is more pronounced when mudstone barriers spatially conform to moderately impede the vertical propagation of the steam chamber.

The value of V_{SAGD}^{hom} is 218795 m^3 for the current case study. **Table 3.8** captures the variation in the cumulative SOR across different realizations for the cumulative bitumen production of 54699 m^3 ($0.25V_{SAGD}^{hom}$); **Table 3.9** presents the same for the cumulative bitumen production of 98458 m^3 ($0.45V_{SAGD}^{hom}$). These tables also present pertinent values for the reduction in cumulative SOR due to coinjection of solvent for the aforementioned cumulative bitumen productions.

The combination of improved drainage rate due to x_{sL}, and lower heat losses to the overburden due to lower temperatures and exposed area of transfer results in lower cumulative SORs in steam-solvent coinjection compared to steam-only injection for the current case study. This is shown in **Figures 3.8 and 3.9**, which respectively present the vapor-phase saturation and temperature maps for realization 17 for the cumulative bitumen production of approximately 98458 m^3. **Figures 3.10 and 3.11** respectively give the variation in cumulative SOR as a function of cumulative bitumen production, and the heat loss maps for this particular realization.

Further, it is also observed that the retention of the solvent in the reservoir for a given cumulative bitumen production is higher for the heterogeneous reservoirs considered in this case study relative to the homogeneous case. **Table 3.10** presents the solvent retention ratios for different realizations for the cumulative bitumen production of 98458 m^3. The advantage of n-C_6 SAGD over SAGD that is simulated to be enhanced under heterogeneity can be explained by the larger amount of solvent being used for a given bitumen production under heterogeneity than

homogeneity. However, the excess retention of solvent is not necessarily desirable considering that a fraction of the solvent is unrecoverable.

Figure 3.12 presents maps for x_{sL}, oleic-phase saturation, mole fraction of the oleic phase (β_L), and the product of β_L and x_{sL} for the clean sand grid blocks in realization 17 of this case study for the cumulative bitumen production of approximately 98458 m^3. The x_{sL} maps for realization 23 from the previous case study (Figure 6) and realization 17 from this case study (Figure 12a) indicate that under certain reservoir architectures, domains within the immobile regions inside the steam chamber where significant solvent-bitumen mixing occurs can be situated near the top of the reservoir model.

An approach to reducing solvent accumulation within the reservoir over a long term is to adopt a time-variant injection concentration strategy (VC) using a condensable solvent, wherein the injection concentration of the solvent is gradually reduced and culminates in steam-only injection (Keshavarz et al., 2015). In heterogeneous reservoirs, the optimal sequence of injection concentrations under the VC strategy is expected to be sensitive to the spatial distribution of mudstone barriers. Although the development of such strategies is beyond the scope of this paper, **Appendix F** presents how excessive accumulation of solvent later in the production phase can be mitigated by use of the VC strategy for realization 17 of this case study.

A major distinction between the two case studies in terms of the observed geometry of the steam chamber is that the steam chambers for several realizations in the current case study exhibit preferential growth towards the top of the reservoir model along the direction of inclination of the mudstone barriers (see Figure 3.8). This can render the steam chamber to grow asymmetrically relative to the grid column containing the well-pair near the top of the model for a significant duration of the production phase. A consequence of this difference in chamber growth is that the average SOR in SAGD for a given cumulative bitumen production is greater in reservoirs with inclined mudstone bodies later in the production phase. The average reduction in the cumulative SOR due to coinjection for a given cumulative bitumen production is also observed to be higher even for lower cumulative bitumen productions. For instance, for the cumulative bitumen production of 54699 m^3 (i.e., $0.25V_{SAGD}^{hom}$ for the second case study), the average SORs for SAGD and ES-SAGD are 7.08 and 4.57 in the first case study, and 6.98 and 4.27 in the second case study. The pertinent values for the cumulative bitumen production of 76578 m^3 ($0.35V_{SAGD}^{hom}$) are 7.35 and 4.59 in the first case study, and 7.83 and 4.62 in the second

case study. The corresponding values for the cumulative bitumen production of 109398 m^3 ($0.50V_{SAGD}^{hom}$) in the first and second case studies are 7.28 and 4.38, and 8.18 and 4.59, respectively.

The current and previous simulation case studies demonstrated that the reduction in SOR due to coinjection of solvent can be greater under heterogeneity than that under homogeneity regardless of the inclination of mudstone barriers. The improvement in SOR reduction under heterogeneity was shown to be a consequence of enhanced solvent/bitumen mixing and its interplay with temperature. This conclusion was confirmed with the reservoir gridding eight times finer than the current case. The motivation for use of gridding that is finer than that utilized thus far was to further mitigate numerical dispersion, which can behave like hydrodynamic dispersion. A detailed discussion of numerical dispersion in the context of the simulations conducted in this chapter, and specifics pertaining to the aforementioned sensitivity study is presented in **Appendix G**. The levels of numerical dispersivities were analyzed in this appendix by following the research of Garmeh and Johns (2010), and Adepoju et al. (2015) along with dynamic simulation conditions (e.g., flow velocities and time-step sizes) for the homogeneous case and one heterogeneous realization. It was confirmed that the numerical dispersion is approximately 50% of the largest grid-block dimension, which is 0.5 m in the current reservoir model.

Quantitative investigation into the mixing in ES-SAGD would require three-dimensional flow simulation with realistic heterogeneity with proper modeling of hydrodynamic dispersion, and is beyond the scope of the current research. Nevertheless, section 3.3 will give a qualitative study of the sensitivity of 2-D ES-SAGD simulations to dispersivity. **Appendix H** presents that the aforementioned results are likely preserved in heterogeneous reservoirs by using a simple 3-D heterogeneous reservoir model.

3.2.3. Case study 3: effect of transverse dispersion on production performance in ES- SAGD

This subsection gives a qualitative analysis of the impact of solvent/bitumen mixing on the performance of ES-SAGD under heterogeneity. This case study was motivated by the substantial effect of heterogeneity on the amount of solvent mixed with bitumen in ES-SAGD, as presented in the previous subsections (also see Tables 3.6 and 3.10).

Flow velocities in the vicinity of a chamber edge in the current simulation cases are on the order of several to ten cm per day. At these velocities, numerical dispersion controls components' mixing; that is, small Fickian diffusion coefficients for solvent in bitumen [e.g., 4.32×10^{-5} m^2/day for n-C_6 in bitumen (Ji et al. 2015)] has no practical significance in the current simulations.

Experimental measurements of hydrodynamic dispersion coefficients for mixtures of solvent and bitumen under gravity drainage have not been published, to the best of our knowledge. Hydrodynamic dispersivity depends at least on average particle size, local heterogeneity, and flow distance (Lake and Hirasaki 1981; Gelhar et al. 1992; Adepoju et al. 2013). Longitudinal dispersivities were reported to range from 10^{-4} m at lab scale to 100 m at field scale (Gelhar et al. 1992; Adepoju et al. 2015). Data for transverse dispersivities are much scarcer. However, common ratios of longitudinal to transverse dispersitivies are 3 to 30 in the literature (Gelhar et al. 1992; Grane and Gardner 1961). A ratio of 3 was also measured by Alkindi et al. (2011) in their dispersion experiment using ethanol and glycerol, mimicking solvent dispersion in heavy oil. Then, transverse dispersivities may be estimated to range up to a few meters for typical flow distances along the edge of a steam chamber in SAGD. Therefore, the numerical dispersivity estimated for the current simulation model, 0.5 m, is unlikely beyond the expected range of transverse dispersivity at SAGD's field scale. Since, the level of dispersivity in ES-SAGD in Athabasca oil sands is an open question, until the issue is resolved, sensitivity analysis by perturbation of hydrodynamic dispersivity in numerical simulation can provide qualitative knowledge of how such mixing can affect ES-SAGD.

An additional note regarding the STARS simulator for this analysis is that a priori specification of a dominant flow direction is necessary, and the specified longitudinal and transverse directions must be aligned with the coordinate axes used to define the grid blocks. This means that the z-coordinate represents the longitudinal direction, while the x-coordinate represents the transverse direction for the reservoir models used in this research. Furthermore, dispersivities are sensitive to the frequency with which changes in flow direction occur. As no two stochastically generated heterogeneous realizations have identical spatial distributions of flow barriers, changes in dominant flow directions are different for different realizations.

Figure 3.13a compares the simulated cumulative bitumen production histories for the homogeneous model under different non-zero input values for transverse dispersivity (d_T) with

respect to the base case, for which d_T is set to zero; **Figure 3.13b** presents the pertinent variations in cumulative SOR with respect to cumulative bitumen production. The lowest non-zero value for d_T used in this sensitivity analysis is 2×10^{-5} m, which was used for the mixing between normal hexane and Athabasca bitumen by Gates and Chakrabarty (2008) and Ji et al. (2015). They obtained this value by use of the semi-empirical correlation developed by Perkins and Johnston (1963) based on laboratory-scale measurements. However, the d_T value of 2×10^{-5} m did not give meaningful differences in simulation results in comparison with zero d_T; hence, the results are not shown in Figure 3.13. The largest value for d_T used in this analysis is 5 m, which is expected to bracket the range of reasonable values for d_T as mentioned above. Figure 3.13 indicates that cumulative bitumen production is increased by transverse dispersion. The reduced span of the cumulative bitumen production histories at elevated values of d_T in Figure 3.13 is due to convergence issues.

The basis for improved production performance under elevated values of d_T is attributed to the combination of two aspects: (i) enhanced drainage rate of the oleic phase along and beyond the chamber edge; and (ii) increased local displacement efficiency of the oleic phase inside the steam chamber. Transverse dispersion enhances both the areal span of the solvent-rich bank beyond the chamber edge and the extent to which the solvent mixes with bitumen (i.e., greater x_{sL}) within this bank, which results in higher drainage rates. This is apparent from **Figures 3.14ab**, which present maps for x_{sL} for the cumulative bitumen production of approximately 175036 m^3 ($0.80V_{SAGD}^{hom}$) under the d_T values of 0 and 5 m. In these figures, grid blocks along the chamber edge in each grid layer are delineated in brown to facilitate comparison between the two cases.

The local displacement efficiency of bitumen inside the steam chamber in ES-SAGD, regardless of whether transverse dispersivity is considered, can be greater than that in SAGD (Jha et al., 2013; Keshavarz et al., 2014). This is evident from the observation of grid blocks whose oleic-phase saturation is lower than the residual oleic-phase saturation (0.13 in this work) used to specify the two-phase oleic-aqueous relative permeability curves. **Figures 3.14cd** demonstrate this for the homogeneous model under the values of 0 and 5 m for d_T. The underlying reason for this observation is x_{sL}.

The oleic phase near the chamber edge under coinjection is more volatile because of x_{sL}. As steam continues to propagate within the reservoir, it vaporizes a fraction of the solvent dissolved

within the oleic phase. The evaporated solvent creates cooler parts of the steam chamber where partial condensation of water occurs. This in turn can lower the oleic-phase inside the steam chamber to values below the residual saturation used to specify the relative permeability curves.

The occurrence of a more volatile oleic phase over a larger reservoir volume beyond the chamber edge due to transverse dispersion increases the prevalence of the distillation mechanism described above with time, and consequently, the local displacement efficiency inside the steam chamber is enhanced. This is supported by **Figures 3.15ab**, which present the x_{sV} maps for the cumulative bitumen production of approximately 175036 m^3 under the two d_T values, and **Figure 3.15c**, which presents the amount of solvent retained in the reservoir within the vapor and oleic phases as a function of cumulative bitumen production. The calculations in Figure 15c were performed using the equation,

$$n_{sj}(t) = \sum_{i=1}^{N} \left(PV \times S_j \times \underline{\rho}_j \times x_{sj} \right)_i, \tag{3.1}$$

where n_{sj} is the moles of the solvent residing in the j^{th} phase within the reservoir, and t is the time under consideration; PV is the pore volume of the i^{th} grid block; S_j, and $\underline{\rho}_V$, respectively, are the saturation and molar density of the j^{th} phase, while x_{sj} is the concentration of solvent in the j^{th} phase, all for the i^{th} grid block. There are 5640 grid blocks in total within each reservoir model used in this chapter (i.e., N = 5640).

Increased accumulation of the solvent near the chamber edge (see Figure 3.15) lowers the oleic-vapor-aqueous to oleic-aqueous transition temperatures, thereby altering the geometry of the steam chamber; this is apparent from the temperature maps given in **Figure 3.16**. The occurrence of lower temperatures near the top of the model (see Figure 3.16b) in turn reduces conductive heat losses to the overburden, facilitating the obtainment of lower SORs.

For several heterogeneous realizations in the second case study, **Tables 3.11 and 3.12** compare the performance of n-C_6 SAGD under the d_T value of 2 m with respect to the base case for the cumulative bitumen productions of 54699 m^3 ($0.25V_{SAGD}^{hom}$) and 98458 m^3 ($0.45V_{SAGD}^{hom}$). These tables demonstrate that both the bitumen production rate and cumulative SOR are improved at higher values of d_T even in the presence of reservoir heterogeneity. The basis underlying the improved production performance in the homogeneous model also occurs in the heterogeneous models. Under heterogeneity, however, the improvement in performance may mainly stem from the increased drainage rate of the oleic phase near the well-pair, and to a lesser

extent from higher local displacement efficiency of the oleic phase inside the steam chamber. The diminished contribution of the latter effect is likely due to the resistance offered by the mudstone barriers to the vertical propagation of the vapor phase. This is illustrated in **Figures 3.17 through 3.19** for realization 37. Figures 3.17 and 3.18 present the vapor-phase saturation, x_{sV}, oleic-phase saturation and x_{sL} maps for the cumulative bitumen production of approximately $0.25V_{SAGD}^{hom}$ for the d_T values of 0 and 2 m, respectively. Figure 3.19 presents the in-situ distribution of the solvent in the vapor and oleic phases as a function of time and cumulative bitumen production. The pertinent cumulative bitumen production histories and SORs for the two cases are furnished in **Figure 3.20**.

Figure 3.19 demonstrates that the extent to which the solvent accumulates in the vapor phase under the d_T of 2 m is comparable to that for the base case; consequently, the prevalence of the distillation mechanism, and the resulting oleic-phase displacement efficiency inside the steam chamber does not differ between the two cases by a significant margin. In contrast, the difference between the two cases in terms of the accumulation of the solvent in the oleic phase is more significant, which in turn increases the corresponding differences in the oleic-phase mobility. Comparison of Figures 3.17d and 3.18d (see the bottom left part) indicates that x_{sL} near the production well is increased under the d_T of 2 m, which in turn enhances the mobility of the oleic phase in this region.

3.3. Conclusions

This chapter presented a mechanistic investigation of SAGD and n-C_6 SAGD in highly heterogeneous reservoirs. The relative performance of n-C_6 SAGD to SAGD under stochastically generated heterogeneity was evaluated in terms of cumulative SOR as a function of cumulative bitumen production. The effect of reservoir heterogeneity on cumulative SOR was elucidated in terms of the interplay among temperature, chamber geometry, and solvent-bitumen mixing near the chamber edge. Conclusions are as follows:

1. Simulation results for heterogeneous reservoir models with horizontal and inclined mudstone bodies showed that SOR of n-C_6 SAGD was less sensitive to heterogeneity than that of SAGD. Also, the reduction in SOR by use of solvent was simulated to be more pronounced under reservoir heterogeneity than in a homogeneous reservoir model. The observed advantage of n-C_6 SAGD over SAGD is because of the dilution of bitumen by solvent (i.e., x_{sL}) and lower chamber-edge temperatures. The lowering of operating chamber-edge

temperatures alters the geometry of the steam chamber such that the exposed area for conductive heat losses to the overlying formation rocks is reduced. Steam-solvent coinjection can significantly reduce the consumption of steam to meet a specified cumulative bitumen production when mudstone barriers are spatially distributed to moderately impede fluid propagation.

2. A larger amount of solvent tends to reside in the oleic phase in heterogeneous cases than in the homogeneous case for a given cumulative bitumen production. The areal span of regions within which x_{sL} exceeds 80 mol% was considerably larger in the presence of mudstone bodies, regardless of the orientation of the mudstone barriers. Reservoir heterogeneity tends to increase the relative magnitude of the dispersive flux in the transverse direction to the convective flux in the longitudinal direction along the edge of a steam chamber in ES-SAGD.

3. The simulation case studies considered in this research show that the average reduction in cumulative SOR due to the coinjection of solvent can be higher in the presence of inclined mudstone bodies relative to that under predominantly horizontal mudstone bodies. For instance, at the operating pressure of 35 bars and solvent injection concentration of 2 mol%, the average cumulative SORs for SAGD and ES-SAGD for the cumulative bitumen production of 109398 m^3 respectively are 7.28 and 4.38 for heterogeneous models with horizontal barriers, and 8.18 and 4.59 for those with inclined barriers.

4. Solvent-bitumen mixing is enhanced under heterogeneity. However, it was observed for some realizations that liquid solvent mixed with bitumen is accumulated in slow-flow (stagnant) regions; i.e., regions of low oleic-phase mobilities and/or regions above laterally-extensive mudstone barriers. The retention of solvent in-situ in the long term could be reduced by use of a time-variant injection concentration of strategy (VC) as presented in Appendix F for realization 17 from the second case study. However, the injection sequence must be designed to ensure that the increase in cumulative SOR following the switch to steam-only injection does not outweigh the benefit of lowering solvent accumulation. The optimal injection sequence will be different for different realizations.

5. Sensitivity analysis in terms of transverse dispersivity in range of 0.5 – 5 m showed that transverse dispersion tends to improve cumulative bitumen production and SOR in ES-SAGD in both homogeneous and heterogeneous reservoirs. More mixing of solvent with bitumen near the edge of a steam chamber results in higher oil-drainage rates and higher efficiency of oil distillation inside the steam chamber. Enhanced mixing between solvent and bitumen can also influence the geometry of the steam chamber by altering the temperature distribution near the chamber edge through its effect on the accumulation of the solvent in vapor phase, thereby mitigating heat losses to the overburden. This influence was simulated to be more pronounced in homogeneous reservoirs, wherein the resistance to vertical propagation of the vapor phase is lower than that exhibited by heterogeneous reservoirs.

6. Sensitivity analysis conducted for realization 16 from the second case study showed that reduction in SOR due to coinjection of solvent is more pronounced under heterogeneity than that under homogeneity even when (i) the grid block size in 2-D simulations is reduced in order to decrease numerical dispersion (Appendix G), and (ii) spatial variation of facies is considered in all three dimensions [i.e., 3-D heterogeneity (Appendix H)]. However, the margin of SOR reduction is lower under both scenarios. In the first scenario, the diminished level of SOR reduction for the fine-scale simulations compared to the coarse-scale simulations is attributed to the combination of higher temperature and lower levels of temperature and concentration dispersion. For the second scenario, the availability of additional hydraulic paths for flow along the direction of well-pair reduces the retention of solvent in-situ and extent of mixing between solvent and bitumen, thereby lowering the margin of SOR reduction due to steam-solvent coinjection.

Table 3.1. Summary of the reservoir model used in simulation case studies

Property	Value
Initial reservoir pressure at the depth of 280 m	15 bars
Initial reservoir temperature	286.15 K
Three-phase relative permeability model (CMG, 2011)	Linear interpolation
Formation compressibility	1.8E-05 1/kPa
Rock heat capacity (Keshavarz et al., 2014)	2600 kJ/m^3 ^{o}C
Rock thermal conductivity (Keshavarz et al., 2014)	660 kJ/m day ^{o}C
Over/underburden heat capacity (Keshavarz et al., 2014)	2600 kJ/m^3 ^{o}C
Over/underburden thermal conductivity (Keshavarz et al., 2014)	660 kJ/m day ^{o}C
Bitumen thermal conductivity	11.5 kJ/m day ^{o}C
Gas thermal conductivity	2.89 kJ/m day ^{o}C
Producer bottom-hole pressure (minimum)	15 bars
Steam quality	0.9

Table 3.2. Analytically estimated oleic-vapor-aqueous to oleic-aqueous transition temperature ($T_{3\varphi}$) using flash calculations in n-C_6 SAGD from Figure 3.2. z_i represents the overall mole fraction of the i^{th} component in a chamber-edge grid block located in a specified grid layer from the top of the model; P represents the grid block pressure. Grid blocks along the chamber edge are identified on the basis of the simulated vapor-phase saturation map. Temperatures along the chamber-edge are also very sensitive to the overall mole fraction of methane (C_1); C_1 tends to accumulate near the top of the reservoir model. The eighth column presents the analytical estimate of the phase-transition temperature within a chamber-edge grid block when the overall composition is normalized after neglecting the presence of C_1. The ninth column presents the difference between the two estimates for $T_{3\varphi}$.

Grid layer from top of model	z_{C1}, mol%	z_{C6}, mol%	z_{CD}, mol%	z_w, mol%	P, bars	$T_{3\varphi}$, K	$T_{3\varphi}$, K (without C_1)	$\Delta T_{3\varphi}$, K
1	1.9415	0.1075	8.8163	89.1347	34.68	303.00	515.00	212.00
2	1.8539	0.4598	8.6933	88.9930	34.68	314.00	512.00	198.00
3	1.7091	0.0683	8.8611	89.3615	34.69	322.00	514.25	192.25
4	1.6824	0.0467	8.8751	89.3958	34.70	325.00	514.25	189.25
5	2.1944	16.5461	3.3617	77.8978	34.71	418.00	476.00	58.00
6	1.8579	7.9512	6.6064	83.5844	34.75	396.00	485.00	89.00
7	1.5210	1.4973	8.5556	88.4261	34.79	369.00	507.00	138.00
8	1.4563	0.1633	8.9337	89.4468	34.79	358.00	513.75	155.75
9	1.2145	0.0156	9.0098	89.7601	34.79	405.00	514.55	109.55
10	1.0320	0.0032	9.0377	89.9271	34.78	440.00	514.60	74.60
11	0.9866	0.0017	9.0364	89.9753	34.77	447.00	514.60	67.60
12	0.9829	0.0013	9.0287	89.9870	34.77	447.00	514.60	67.60

13	0.9852	0.0012	9.0231	89.9906	34.78	447.00	514.60	67.60
14	0.9882	0.0013	9.0207	89.9898	34.78	446.00	514.60	68.60
15	1.3857	11.7017	1.0975	85.8151	34.75	423.00	475.00	52.00
16	0.8509	1.7591	5.9557	91.4343	34.79	425.00	502.00	77.00
17	0.8069	9.7422	0.7158	88.7351	34.75	443.00	474.00	31.00
18	0.7557	9.2874	0.9725	88.9844	34.76	444.00	475.00	31.00
19	0.8546	11.0159	1.0501	87.0795	34.75	446.00	475.00	29.00
20	0.7236	11.2886	0.9398	87.0481	34.77	452.00	475.00	23.00
21	0.7143	12.3100	1.0853	85.8904	34.78	455.00	475.00	20.00
22	0.6039	13.0000	1.3061	85.0900	34.79	459.00	475.00	16.00
23	0.4916	12.6068	1.6201	85.2815	34.80	462.00	475.00	13.00
24	0.3623	11.6884	1.8751	86.0742	34.81	466.00	476.00	10.00
25	0.2652	10.8395	2.0480	86.8473	34.82	468.00	476.00	8.00
26	0.1802	9.9731	2.1805	87.6662	34.83	471.00	476.00	5.00
27	0.0978	8.7038	2.3920	88.8065	34.85	473.00	477.00	4.00
28	0.1468	8.8432	2.5242	88.4859	34.88	472.00	477.00	5.00
29	0.0628	6.6407	2.9201	90.3764	34.90	476.00	479.00	3.00
30	0.0750	6.7824	3.0205	90.1222	34.93	476.00	479.00	3.00
31	0.0199	3.5293	3.3330	93.1178	34.95	485.00	487.00	2.00

Table 3.3. Input parameters for sequential indicator simulation for simple heterogeneous reservoir models comprising of clean sand and mudstone for the first case study in Section 3.2 (see Section 3.2.1). The spherical model is used for the indicator variogram for the mudstone facies.

Property	Value
Global proportion of clean sand	0.75
Global proportion of mudstone	0.25
Nugget effect for indicator variogram model	0.10
Azimuth for variogram model	90°
Horizontal range parameter, m	25.0
Vertical range parameter, m	1.0

Table 3.4. Cumulative SOR for SAGD and n-C_6 SAGD for the cumulative bitumen production of 49048 m^3 for realizations in the first case study (case study 3.2.1). The homogeneous reservoir model is denoted as realization 0. The average increase in SOR due to heterogeneity ($\Delta_{het}SOR$) for SAGD is 3.61; the corresponding value for n-C_6 SAGD is 2.37. The average reduction in SOR due to coinjection of solvent ($\Delta_{sol}SOR$) for the heterogeneous cases is 2.51.

Realization	Time, days (SAGD)	Time, days (n-C_6 SAGD)	SOR (SAGD)	SOR (n-C_6 SAGD)	$\Delta_{het}SOR$ (SAGD)	$\Delta_{het}SOR$ (n-C_6 SAGD)	$\Delta_{sol}SOR$
0	335.64	292.69	3.48	2.21	0.00	0.00	1.27
1	587.31	374.47	6.28	3.83	2.80	1.62	2.45
2	406.29	311.24	4.45	2.72	0.97	0.50	1.73
3	2456.75	1660.37	12.09	7.89	8.61	5.67	4.21
4	711.49	463.98	6.28	4.12	2.79	1.91	2.15
5	845.02	535.97	6.71	4.38	3.23	2.17	2.33
6	972.83	569.00	7.65	5.28	4.17	3.07	2.37
8	395.16	312.13	4.17	2.68	0.69	0.47	1.48
9	1426.60	1202.36	5.56	3.34	2.08	1.13	2.22
10	1229.49	1292.82	5.44	3.48	1.95	1.27	1.95
12	758.01	456.37	6.65	4.06	3.17	1.85	2.59
13	816.92	485.81	7.07	4.18	3.59	1.96	2.90
14	1073.40	577.43	7.03	4.79	3.54	2.58	2.23
15	455.63	327.95	4.42	2.91	0.94	0.70	1.51
16	1957.39	997.11	12.71	7.50	9.23	5.28	5.21
17	1504.20	907.47	9.54	6.87	6.06	4.65	2.68
18	771.01	524.90	6.38	4.13	2.90	1.92	2.25
19	3077.38	2986.34	8.50	4.37	5.02	2.16	4.13
20	916.43	607.57	7.05	5.02	3.56	2.81	2.02
21	779.47	503.36	6.62	4.43	3.13	2.21	2.19
22	1746.62	776.65	11.27	6.25	7.79	4.04	5.02
23	957.53	632.26	6.31	4.91	2.82	2.70	1.39
24	713.62	438.37	6.64	4.13	3.15	1.91	2.51
25	556.41	407.32	5.26	3.77	1.78	1.56	1.49

27	434.33	313.13	4.48	2.74	0.99	0.53	1.73
28	528.93	351.31	5.12	3.21	1.63	0.99	1.91
29	1189.98	660.44	8.91	4.98	5.43	2.77	3.93
30	607.19	443.62	5.91	4.27	2.43	2.06	1.64
31	460.66	324.35	4.97	2.94	1.48	0.73	2.02
32	665.92	426.38	6.34	4.07	2.86	1.85	2.28
33	968.80	653.16	7.55	5.67	4.06	3.45	1.88
35	452.36	351.36	4.54	3.50	1.05	1.29	1.03
36	563.17	375.76	5.26	3.63	1.78	1.41	1.63
37	2536.65	1314.84	10.05	7.27	6.57	5.06	2.78
38	506.14	390.32	4.72	3.09	1.24	0.88	1.63
39	3435.87	1334.58	12.40	7.39	8.91	5.17	5.01
40	423.88	315.80	4.30	2.76	0.82	0.55	1.54
41	1493.59	1484.47	5.85	3.91	2.37	1.70	1.94
42	938.25	576.35	7.34	5.27	3.86	3.06	2.07
43	1632.89	1703.93	8.57	5.17	5.08	2.96	3.39
44	922.14	546.72	7.55	5.31	4.06	3.09	2.24
45	1882.66	2186.61	6.72	4.06	3.24	1.85	2.66
47	2499.51	1090.16	10.68	6.77	7.20	4.55	3.91
48	805.83	465.73	8.04	4.74	4.56	2.53	3.30
49	587.77	392.15	5.91	4.08	2.43	1.87	1.83
50	1485.66	866.68	9.88	6.48	6.40	4.27	3.40

Table 3.5. Cumulative SOR for SAGD and n-C_6 SAGD for the cumulative bitumen production of 98095 m^3 for realizations in the first case study (case study 3.2.1). The homogeneous reservoir model is denoted as realization 0. The average increase in SOR due to heterogeneity ($\Delta_{het}SOR$) for SAGD is 3.11; the corresponding value for n-C_6 SAGD is 1.94. The average reduction in SOR due to coinjection of solvent ($\Delta_{sol}SOR$) for the heterogeneous cases is 2.75.

Realization	Time, days (SAGD)	Time, days (n-C_6 SAGD)	SOR (SAGD)	SOR (n-C_6 SAGD)	$\Delta_{het}SOR$ (SAGD)	$\Delta_{het}SOR$ (n-C_6 SAGD)	$\Delta_{sol}SOR$
0	526.68	425.06	3.92	2.34	0.00	0.00	1.58
2	788.33	483.24	5.39	3.11	1.47	0.77	2.28
4	1632.45	794.23	7.49	4.32	3.57	1.97	3.18
5	1444.91	846.16	6.87	4.68	2.95	2.34	2.19
6	1768.28	865.30	7.84	4.82	3.92	2.47	3.02
8	1064.01	581.24	6.09	3.72	2.17	1.38	2.37
9	1937.70	1424.33	6.04	3.61	2.12	1.27	2.43
10	1734.44	1493.89	6.02	3.44	2.10	1.10	2.57
12	1678.14	774.70	7.63	4.11	3.71	1.77	3.52
13	1745.29	786.39	8.06	4.06	4.14	1.72	4.00
14	1772.76	838.46	7.19	4.44	3.26	2.10	2.74
15	1174.30	598.35	6.27	3.91	2.35	1.57	2.35
17	2430.06	1426.48	8.42	6.25	4.50	3.91	2.16
18	1557.55	782.38	7.43	3.99	3.51	1.65	3.44
20	1371.69	793.54	6.72	4.22	2.80	1.88	2.50
21	1528.50	763.71	7.36	4.23	3.44	1.89	3.13
23	3526.86	1300.45	9.77	5.62	5.85	3.28	4.15
25	1533.90	685.37	8.20	4.54	4.28	2.20	3.66
27	977.87	505.88	5.95	3.29	2.03	0.95	2.66
28	1456.76	686.52	6.92	4.32	3.00	1.98	2.60
30	1608.53	797.56	8.11	4.94	4.19	2.59	3.17
31	1026.15	565.03	6.07	3.90	2.15	1.55	2.18
32	1441.23	697.33	7.64	4.59	3.72	2.25	3.05
35	1239.99	703.34	6.62	4.65	2.70	2.30	1.97
36	1065.39	564.65	6.06	3.73	2.14	1.38	2.34
38	843.83	552.38	5.08	3.14	1.16	0.79	1.94
40	1105.25	591.25	6.35	3.82	2.43	1.48	2.53
41	1859.34	1695.61	5.82	3.94	1.90	1.60	1.89
42	1781.57	875.91	7.28	4.27	3.36	1.92	3.02
43	2563.51	2039.50	8.74	5.20	4.82	2.85	3.54
45	2106.50	2390.88	5.32	4.03	1.40	1.68	1.29
49	1300.40	691.17	7.38	4.47	3.46	2.13	2.91
50	2184.12	1146.28	8.83	5.73	4.91	3.39	3.10

Table 3.6. Solvent retention ratios for the homogeneous and heterogeneous models in the first case study (horizontal mudstone barriers) for the cumulative bitumen production of 98095 m^3 ($0.50V_{SAGD}^{hom}$). These ratios are calculated on the basis of the simulated cumulative bitumen production, solvent injection and production histories at stock-tank conditions.

Realization	Time, days	Accumulated solvent volume, m^3	Solvent retention ratio
0 (homogeneous)	425.06	7125.10	0.07
2	483.24	14417.25	0.15
3	1932.19	11629.75	0.12
4	794.23	18727.17	0.19
5	846.16	12749.83	0.13
6	865.30	15019.29	0.15
8	581.24	13149.04	0.13
9	1424.33	13798.34	0.14
10	1493.89	13170.84	0.13
12	774.70	29721.11	0.30
13	786.39	27764.81	0.28
14	838.46	22725.20	0.23
15	598.35	10879.02	0.11
16	1651.02	30133.92	0.31
17	1426.48	29718.04	0.30
18	782.38	23640.68	0.24
19	3411.86	28892.36	0.29
20	793.54	14920.84	0.15
21	763.71	20016.15	0.20
23	1300.45	29880.59	0.30
25	685.37	14939.90	0.15
27	505.88	14187.38	0.14
28	686.52	16226.81	0.17
30	797.56	14254.97	0.15
31	565.03	9011.96	0.09
32	697.33	15576.50	0.16
34	1622.19	14001.65	0.14
35	703.34	13394.94	0.14
36	564.65	11335.42	0.12
37	1917.13	12706.92	0.13
38	552.38	13112.65	0.13
40	591.25	16418.41	0.17
41	1695.61	11725.57	0.12
42	875.91	18797.29	0.19
43	2039.50	27323.69	0.28
45	2390.88	12939.54	0.13

47	1967.40	46006.40	0.47
49	691.17	22802.83	0.23
50	1146.28	18096.80	0.18

Table 3.7. Input parameters for sequential indicator simulation for simple heterogeneous reservoir models comprising of clean sand and mudstone for the second case study (inclined mudstone barriers) in Section 3.2 (see Section 3.2.2). The spherical model is used for the indicator variogram for the mudstone facies.

Property	Value
Global proportion of clean sand	0.75
Global proportion of mudstone	0.25
Nugget effect for indicator variogram model	0
Azimuth for variogram model	78°
Horizontal range parameter, m	12.0
Vertical range parameter, m	1.0

Table 3.8. Cumulative SOR for SAGD and n-C_6 SAGD for the cumulative bitumen production of 54699 m^3 for realizations in the second case study (see Section 3.2.2). The homogeneous reservoir model is denoted as realization 0. The average increase in SOR due to heterogeneity ($\Delta_{het}SOR$) for SAGD is 3.90; the corresponding value for n-C_6 SAGD is 2.27. The average reduction in SOR due to coinjection of solvent ($\Delta_{sol}SOR$) for the heterogeneous cases is 2.71.

Realization	Time, days (SAGD)	Time, days (n-C_6 SAGD)	SOR (SAGD)	SOR (n-C_6 SAGD)	$\Delta_{het}SOR$ (SAGD)	$\Delta_{het}SOR$ (n-C_6 SAGD)	$\Delta_{sol}SOR$
0	342.72	295.91	3.08	2.00	0.00	0.00	1.08
4	1238.31	598.17	7.13	3.94	4.05	1.94	3.19
6	733.95	481.50	5.22	3.56	2.14	1.56	1.66
7	778.54	501.29	6.11	4.11	3.03	2.11	2.00
12	1145.16	615.01	7.19	4.04	4.11	2.04	3.15
13	1055.56	567.87	6.55	3.64	3.46	1.64	2.90
14	1679.46	1504.71	7.51	5.19	4.43	3.20	2.32
15	562.39	372.45	4.73	2.99	1.65	0.99	1.74
16	2230.84	1080.11	12.54	7.61	9.45	5.61	4.93
17	946.46	509.93	6.82	3.63	3.74	1.64	3.19
18	930.28	541.44	6.58	4.05	3.50	2.05	2.53
20	925.78	556.06	6.30	3.95	3.22	1.95	2.35
21	648.45	405.52	4.94	3.09	1.86	1.09	1.85
23	1627.46	669.96	9.33	4.69	6.24	2.69	4.64
26	944.46	550.78	6.53	4.03	3.45	2.03	2.50

31	979.04	572.08	6.29	4.20	3.20	2.20	2.09
32	724.64	435.96	5.63	3.40	2.55	1.41	2.23
33	984.92	530.81	6.02	3.75	2.93	1.75	2.27
35	706.17	441.40	5.28	3.41	2.20	1.41	1.87
36	1557.68	811.94	8.90	5.21	5.82	3.21	3.70
37	1880.82	988.69	10.74	7.35	7.66	5.35	3.39
44	690.75	430.81	5.30	3.43	2.22	1.43	1.87
48	1337.70	702.79	7.62	4.33	4.53	2.34	3.28
49	956.29	509.77	6.59	3.68	3.51	1.68	2.91
50	1203.40	698.37	7.65	5.11	4.57	3.11	2.54

Table 3.9. Cumulative SOR for SAGD and n-C_6 SAGD for the cumulative bitumen production of 98458 m^3 for realizations in the second case study (Section 3.2.2). The homogeneous reservoir model is denoted as realization 0. The average increase in SOR due to heterogeneity ($\Delta_{het}SOR$) for SAGD is 4.87; the corresponding value for n-C_6 SAGD is 2.50. The average reduction in SOR due to coinjection of solvent ($\Delta_{sol}SOR$) for the heterogeneous cases is 3.86.

Realization	Time, days (SAGD)	Time, days (n-C_6 SAGD)	SOR (SAGD)	SOR (n-C_6 SAGD)	$\Delta_{het}SOR$ (SAGD)	$\Delta_{het}SOR$ (n-C_6 SAGD)	$\Delta_{sol}SOR$
0	499.20	398.01	3.51	2.02	0.00	0.00	1.49
6	1433.49	740.78	6.13	3.58	2.62	1.56	2.55
7	2511.51	951.98	9.32	5.23	5.81	3.21	4.09
15	1349.45	661.62	6.32	3.91	2.81	1.90	2.41
17	3555.48	1085.64	10.60	4.70	7.09	2.68	5.90
18	1952.58	905.72	7.49	4.61	3.98	2.59	2.88
20	3010.76	1034.51	10.17	4.84	6.66	2.83	5.33
21	2541.77	835.31	8.80	4.13	5.29	2.11	4.67
33	2180.70	889.11	7.52	4.43	4.01	2.41	3.09
35	1591.08	836.55	6.78	4.33	3.27	2.32	2.44
44	2224.59	838.70	8.50	4.40	4.99	2.38	4.10
50	2975.84	1241.10	10.56	5.56	7.05	3.54	5.00

Table 3.10. Solvent retention ratios for the homogeneous and heterogeneous models in the second case study (inclined mudstone barriers) for the cumulative bitumen production of 98458 m^3 ($0.45V_{SAGD}^{hom}$). The solvent retention ratio is defined as the ratio of the accumulated solvent volume to the cumulative volume of bitumen produced. These ratios are calculated on the basis of the simulated cumulative bitumen production, solvent injection and production histories at stock tank conditions.

Realization	Time, days	Accumulated solvent volume, m^3	Solvent retention ratio
0 (homogeneous)	398.01	7229.17	0.07
4	1245.40	27844.34	0.28
6	740.78	19983.71	0.20
7	951.98	13252.27	0.13
15	661.62	16603.76	0.17
17	1085.64	24077.02	0.24
18	905.72	15432.47	0.16
20	1034.51	19625.11	0.20
21	835.31	17903.96	0.18
33	889.11	10693.03	0.11
35	836.55	14475.66	0.15
36	1706.74	17094.11	0.17
44	838.70	18114.18	0.18
50	1241.10	18259.89	0.19

Table 3.11. Effect of transverse dispersivtiy (d_T) on the production performance of n-C_6 SAGD for the heterogeneous models considered in the second case study (inclined mudstone barriers) for the cumulative bitumen production of 54699 m^3 ($0.25V_{SAGD}^{hom}$).

Realization	Time, days (d_T = 0 m)	Time, days (d_T = 2 m)	SOR (d_T = 0 m)	SOR (d_T = 2 m)	Δt, days	ΔSOR
4	598.17	578.75	3.94	3.68	19.42	0.25
6	481.50	454.04	3.56	3.40	27.45	0.16
12	615.00	586.71	4.04	3.79	28.30	0.25
13	567.87	548.59	3.64	3.49	19.28	0.15
15	372.45	349.33	2.99	2.74	23.12	0.25
18	541.43	510.56	4.05	3.57	30.87	0.48
20	556.06	520.36	3.95	3.74	35.70	0.21
21	405.52	378.42	3.09	2.89	27.10	0.20
31	572.08	511.69	4.20	3.85	60.39	0.35
35	441.40	400.40	3.41	3.09	41.00	0.32
36	811.94	715.91	5.21	4.35	96.03	0.85
37	988.67	735.70	7.35	5.37	252.98	1.98
44	430.81	353.79	3.43	2.75	77.02	0.68

48	702.79	667.49	4.33	4.14	35.30	0.20
49	509.77	481.34	3.68	3.57	28.43	0.11
50	698.37	649.23	5.11	4.67	49.14	0.44

Table 3.12. Effect of transverse dispersivity on the production performance of n-C_6 SAGD for the cumulative bitumen production of 98458 m^3 ($0.45V_{SAGD}^{hom}$) for the heterogeneous models considered in the second case study (inclined mudstone barriers).

Realization	Time, days (d_T = 0 m)	Time, days (d_T = 2 m)	SOR (d_T = 0 m)	SOR (d_T = 2 m)	Δt, days	ΔSOR
6	740.78	732.78	3.58	3.57	8.00	0.01
15	661.62	582.83	3.91	3.62	78.79	0.29
18	905.72	819.69	4.61	4.02	86.04	0.59
21	835.30	648.14	4.13	3.40	187.16	0.73
35	836.55	705.10	4.33	3.65	131.44	0.68

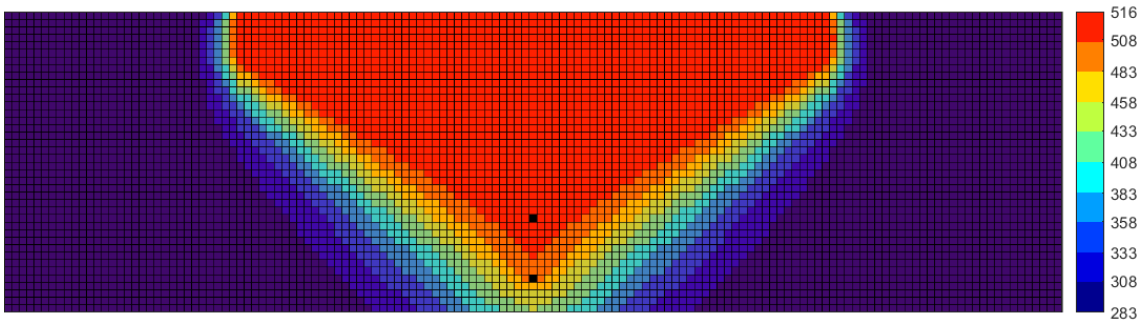

(a)

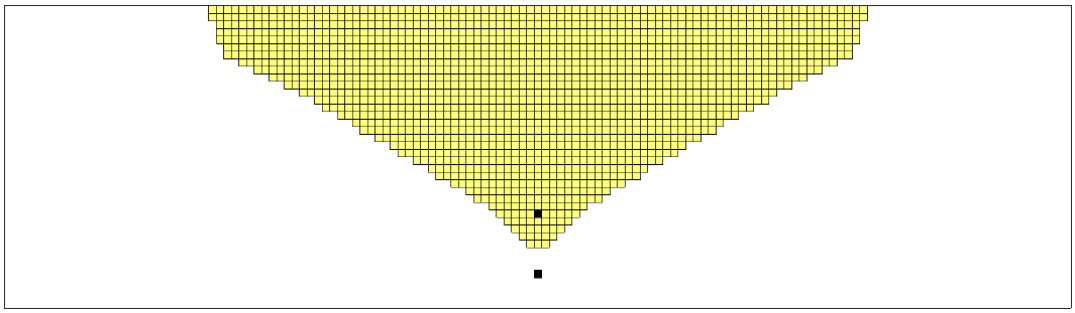

(b)

Figure 3.1. (a) Temperature (in Kelvin) and (b) vapor-phase saturation (S_V) maps corresponding to the cumulative bitumen production of 77487 m^3 for SAGD at 35 bars. In (b), S_V in grid blocks shown in yellow is greater than 5%. Injector and producer grid blocks are indicated in black. This cumulative bitumen production is met at 456 days.

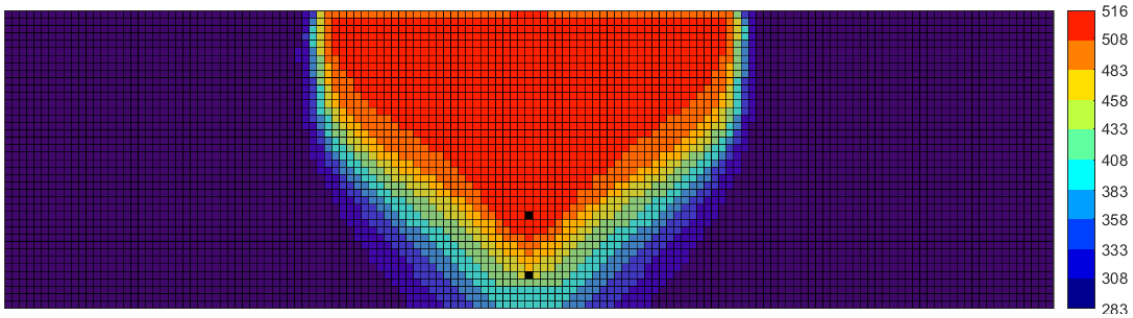

(a)

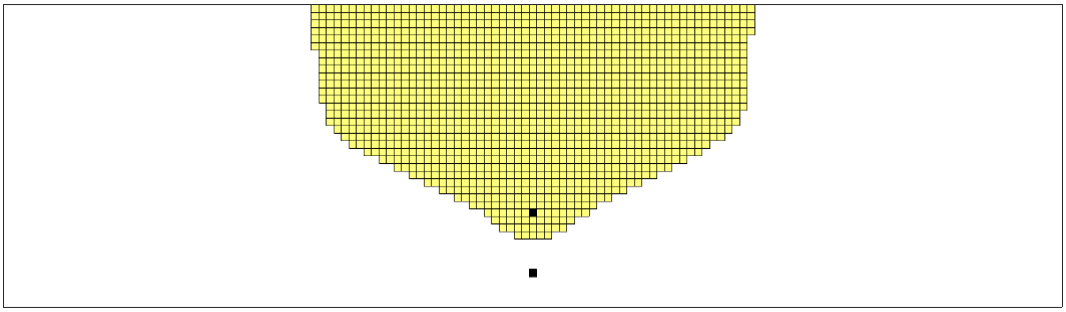

(b)

Figure 3.2. (a) Temperature (in Kelvin) and (b) vapor-phase saturation maps corresponding to the cumulative bitumen production of 76617 m^3 for n-C_6 SAGD at 35 bars and injection concentration of 2 mol%. In (b), the vapor-phase saturation (S_V) in grid blocks shown in yellow is greater than 5%. Injector and producer grid blocks are indicated in black. This cumulative bitumen production is met at 365 days from the start of the operation.

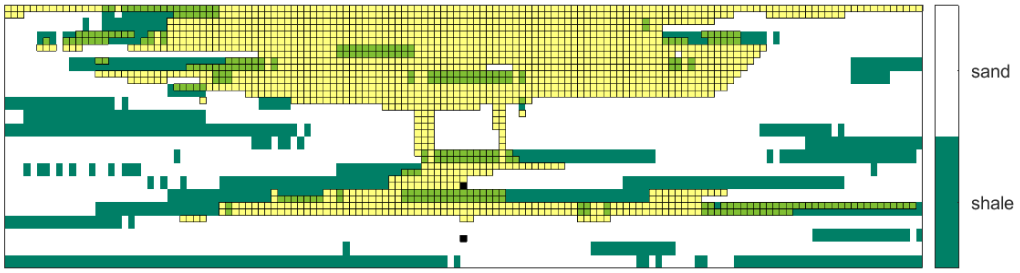

(a)

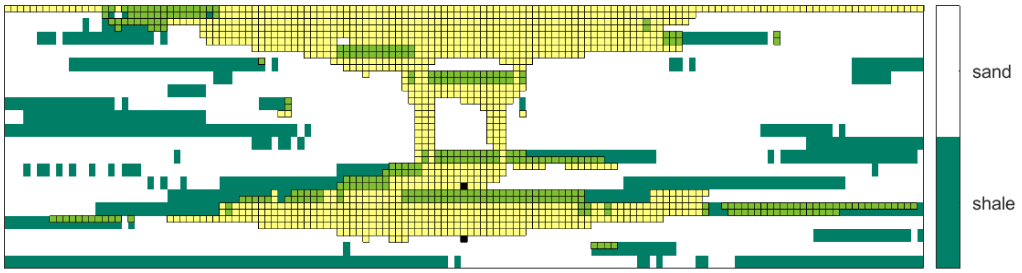

(b)

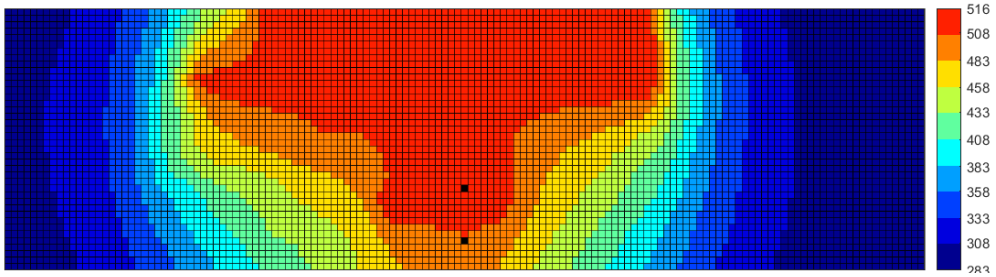

(c)

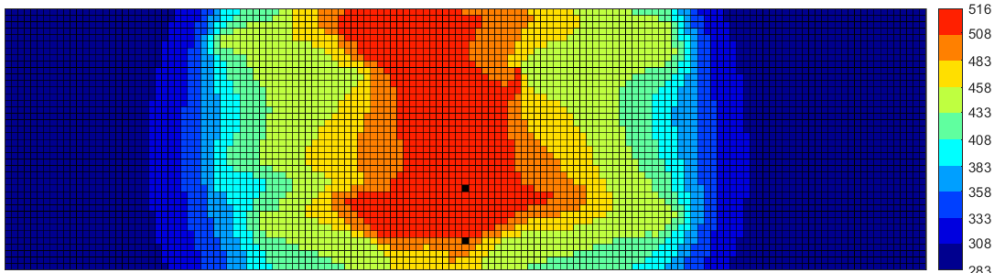

(d)

Figure 3.3. Vapor-phase saturation (S_v) and temperature (in Kelvin) maps for SAGD and n-C_6 SAGD realization 23 for the cumulative bitumen production of approximately 98095 m^3 ($0.50V_{SAGD}^{hom}$); (a) S_v map for SAGD; (b) S_v map for n-C_6 SAGD; (c) temperature map for SAGD; (d) temperature map for n-C_6 SAGD. In part (a), the grid blocks in yellow correspond to S_v-values greater than 5%. Injector and producer grid blocks are indicated in black. Near the well-pair, the chamber for ES-SAGD has a larger area compared to SAGD while the opposite is true towards the top of the model. The aforementioned cumulative bitumen production is reached at 3527 days for SAGD and at 1300 days for n-C_6 SAGD; this includes the initial heating period of 183 days (also see Table 3.6).

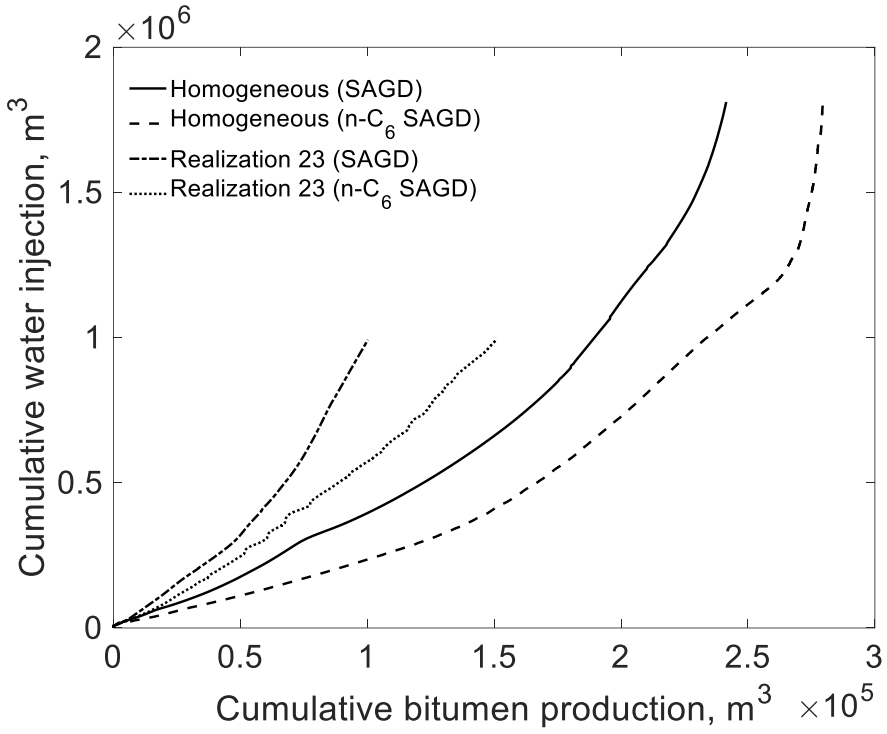

Figure 3.4. Cumulative SOR (CWE) as a function of cumulative bitumen production in SAGD and n-C_6 SAGD for the homogeneous reservoir model and realization 23 in the first case study (Section 3.2.1).

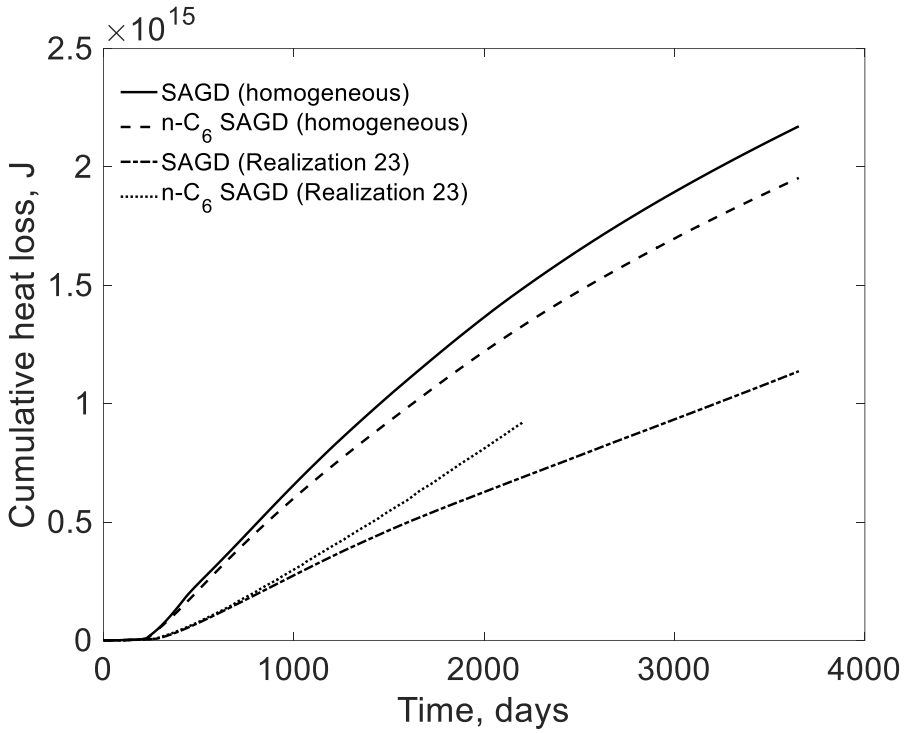

(a)

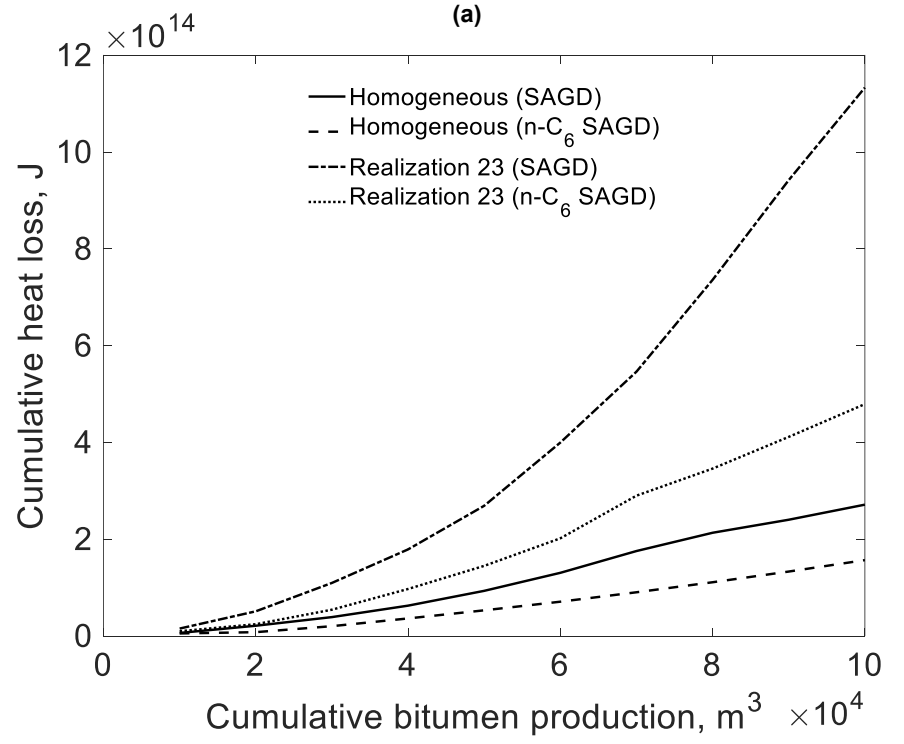

(b)

Figure 3.5. Cumulative heat loss as a function of time and cumulative bitumen production in SAGD and n-C_6 SAGD for the homogeneous reservoir model and realization 23 in the first case study (Section 3.2.1); (a) cumulative heat loss history; (b) cumulative heat loss as a function of cumulative bitumen production.

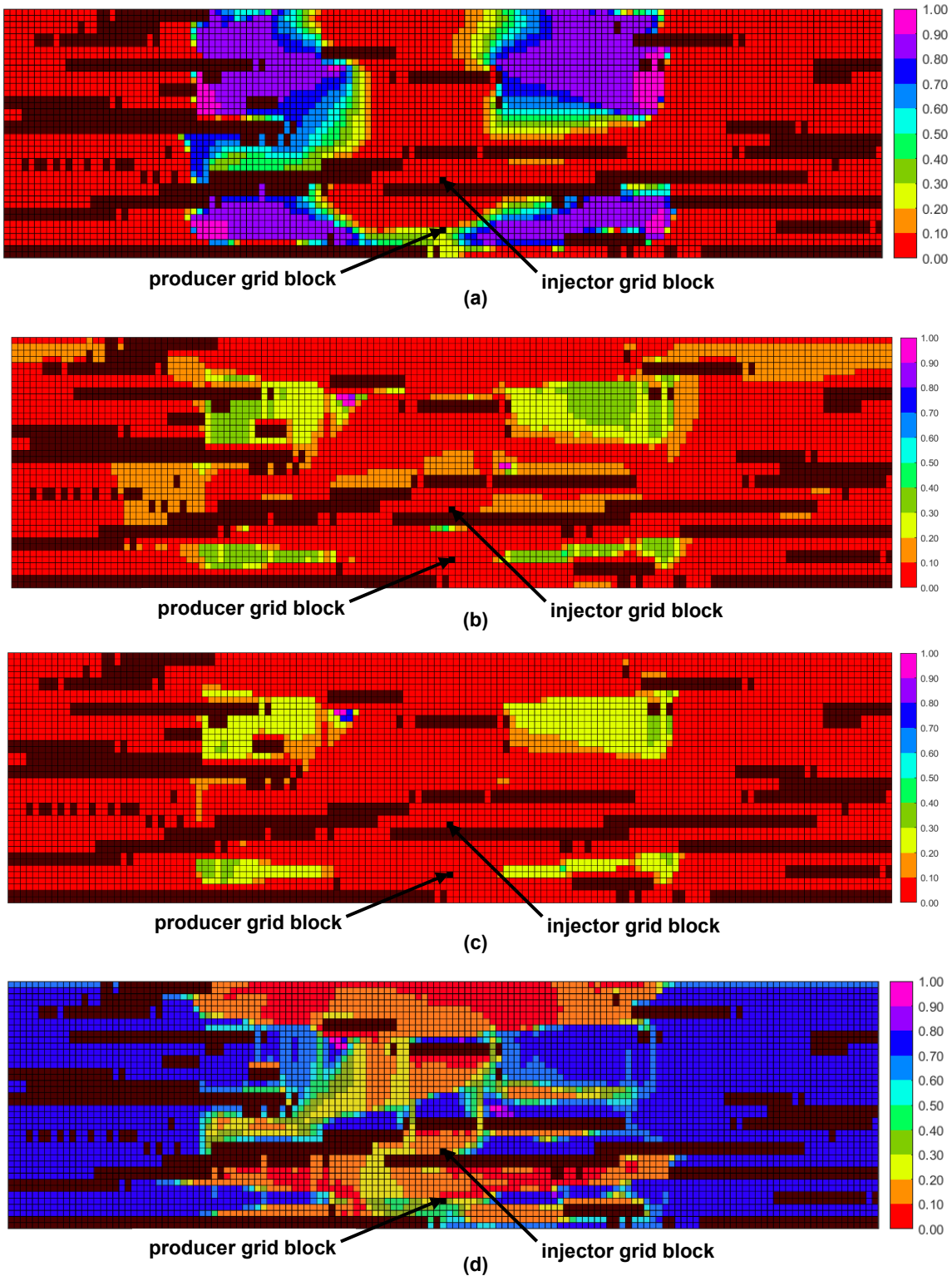

Figure 3.6. Property maps for clean sand grid blocks in n-C_6 SAGD for realization 23 from the first case study for the cumulative bitumen production of approximately 98095 m^3 ($0.50V_{SAGD}^{hom}$); (a) x_{sL} map; (b) β_L map; (c) $\beta_L x_{sL}$ map; (d) S_L map. Mudstone barriers are indicated in the background. This cumulative bitumen production is met at 1300 days from the start of the operation.

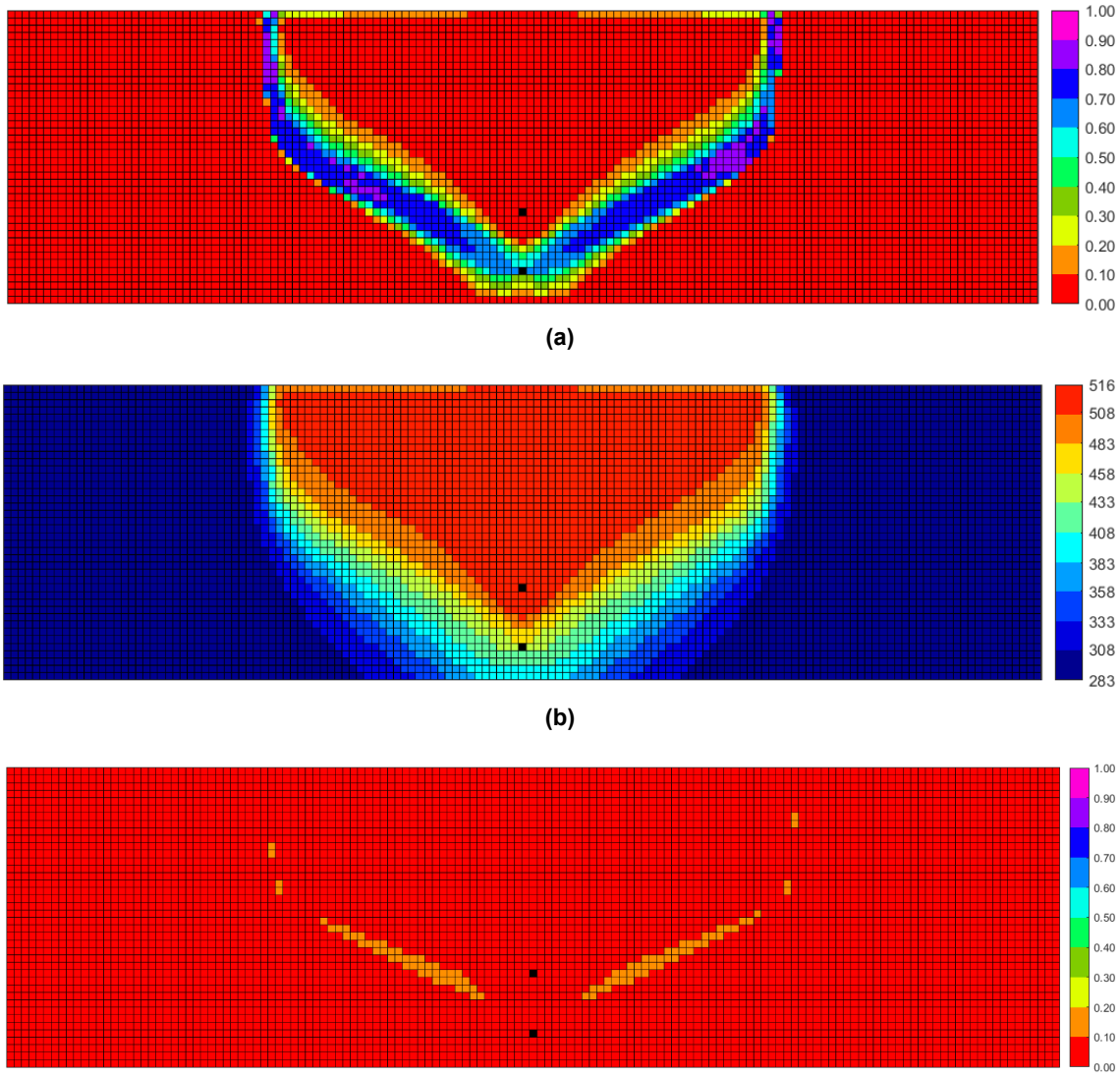

Figure 3.7. x_{sL}, temperature and $\beta_L x_{sL}$ maps in n-C_6 SAGD for the homogeneous model in the first case study for the cumulative bitumen production of approximately 98095 m^3 ($0.50V_{SAGD}^{hom}$); (a) x_{sL} map; (b) temperature map; (c) $\beta_L x_{sL}$ map. The injector and producer grid blocks are indicated in black. This cumulative bitumen production is met at 425 days from the start of the operation.

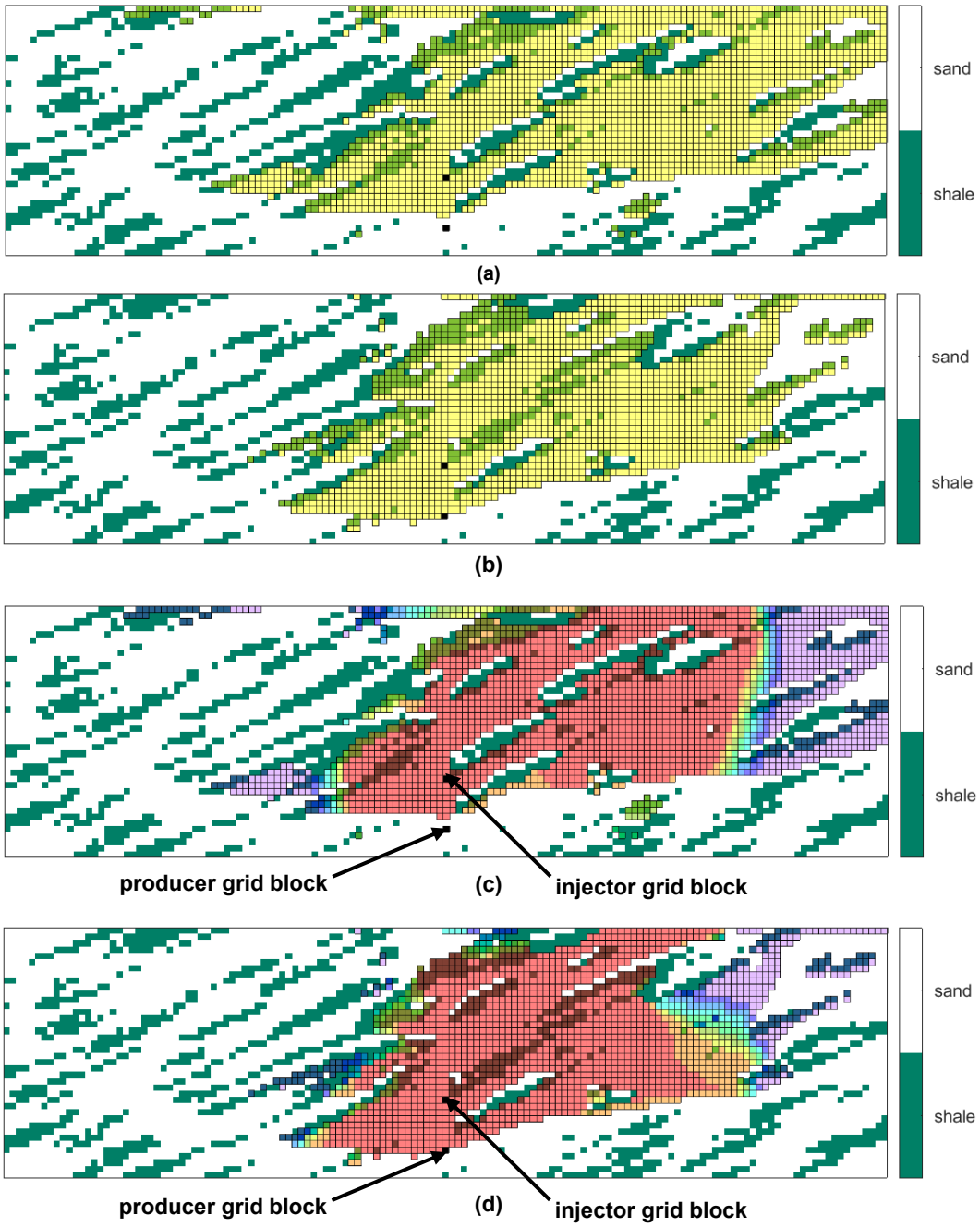

Figure 3.8. Steam chambers for SAGD and n-C_6 SAGD for realization 17 in the second case study for the cumulative bitumen production of approximately 98458 m^3 ($0.45V_{SAGD}^{hom}$); (a) S_V map for SAGD; (b) S_V saturation map for n-C_6 SAGD; (c) map for concentration of methane in the vapor phase (x_{C1V}) for SAGD; (d) x_{C1V} map for n-C_6 SAGD. In parts (a) and (b), the grid blocks shown in yellow correspond to saturations greater than 5%. Maps for x_{C1V} have been provided to delineate the steam chamber. The high temperatures within the steam chamber results in the vaporization of methane dissolved in bitumen; the liberated methane then accumulates in the cooler parts of the reservoir, which leads to low values for x_{C1V} inside the steam chamber. In parts (c) and (d), the value of x_{C1V} in grid blocks shown in pink is lower than 5 mol%. This cumulative bitumen production is met at 3555 days for SAGD and 1086 days for n-C_6 SAGD.

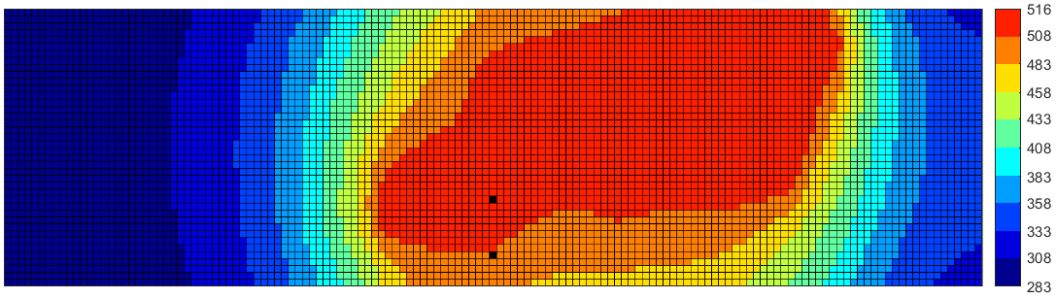

(a)

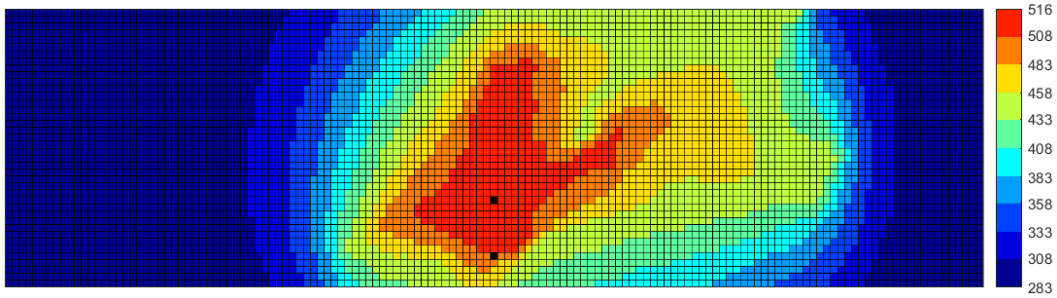

(b)

Figure 3.9. Maps for temperature (in Kelvin) for SAGD and n-C_6 SAGD for realization 17 for the cumulative bitumen production of approximately 98458 m^3 ($0.45V_{SAGD}^{hom}$) for the second case study; (a) SAGD; (b) n-C_6 SAGD. The injector and producer grid blocks are indicated in black. This cumulative bitumen production is met at 3555 days for SAGD and 1086 days for n-C_6 SAGD.

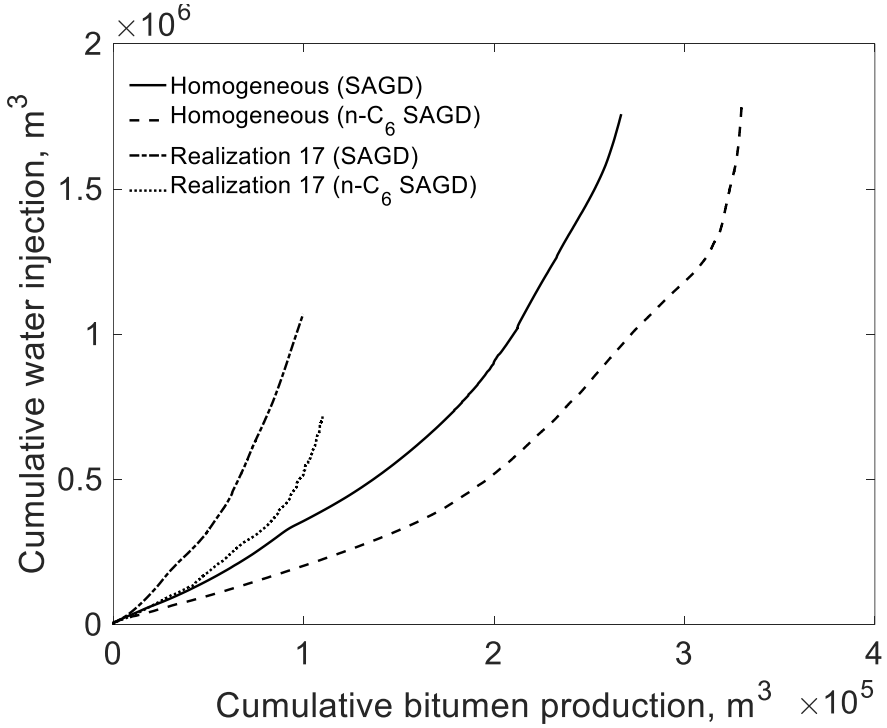

Figure 3.10. Cumulative SOR (CWE) as a function of cumulative bitumen production in SAGD and n-C_6 SAGD for the homogeneous reservoir model and realization 17 in the second case study (Section 3.2.2).

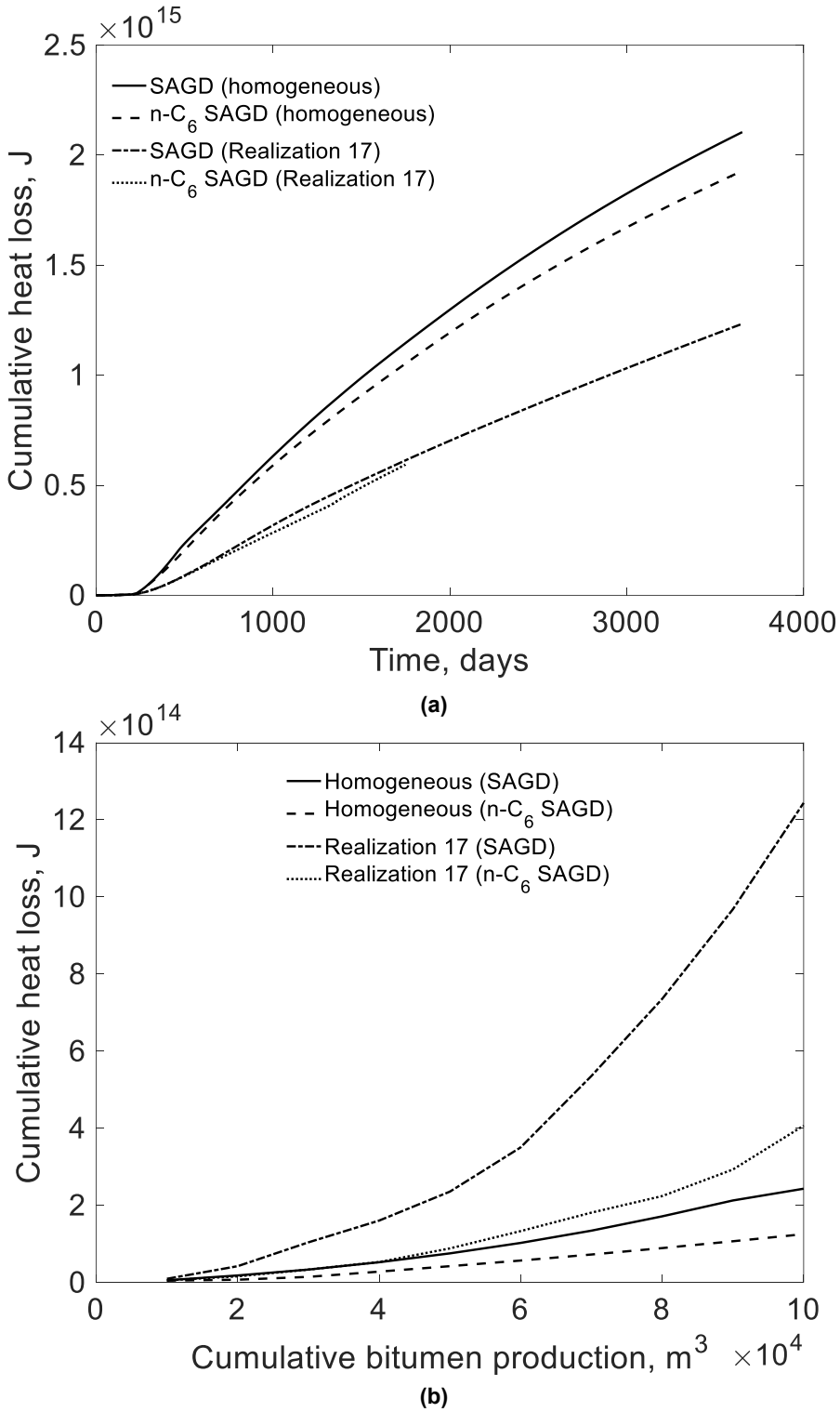

Figure 3.11. Cumulative heat loss as a function of time and cumulative bitumen production in SAGD and n-C_6 SAGD for the homogeneous reservoir model and realization 17 in the second case study (Section 3.2.2); (a) cumulative heat loss history; (ii) cumulative heat loss as a function of cumulative bitumen production.

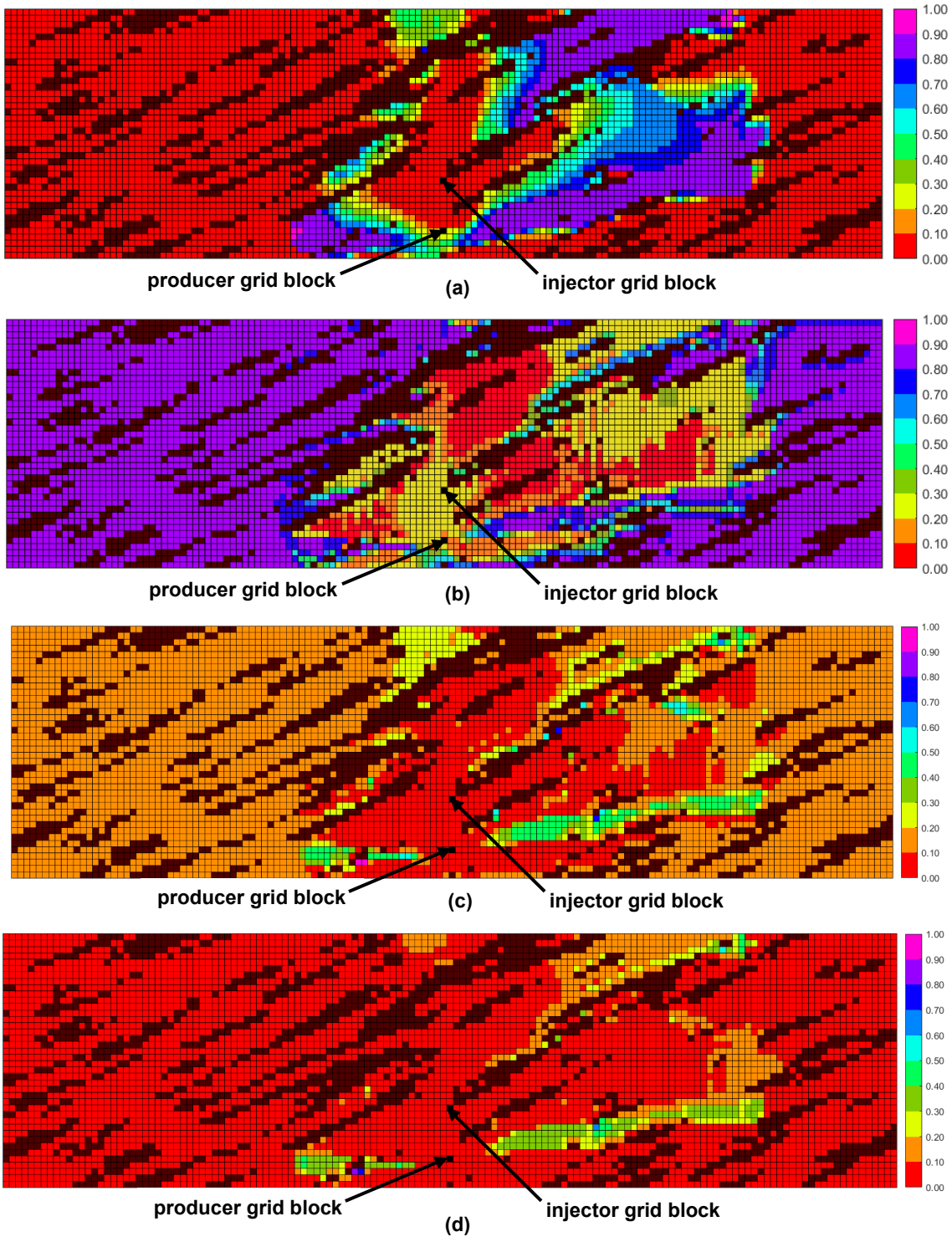

Figure 3.12. Property maps for clean sand grid blocks in n-C_6 SAGD for realization 17 from the second case study for the cumulative bitumen production of 98458 m^3 ($0.45V_{SAGD}^{hom}$); (a) x_{sL} map; (b) S_L map; (c) β_L map; (d) $\beta_L x_{sL}$ map. Mudstone barriers are indicated in the background. This cumulative bitumen production is met at 1086 days.

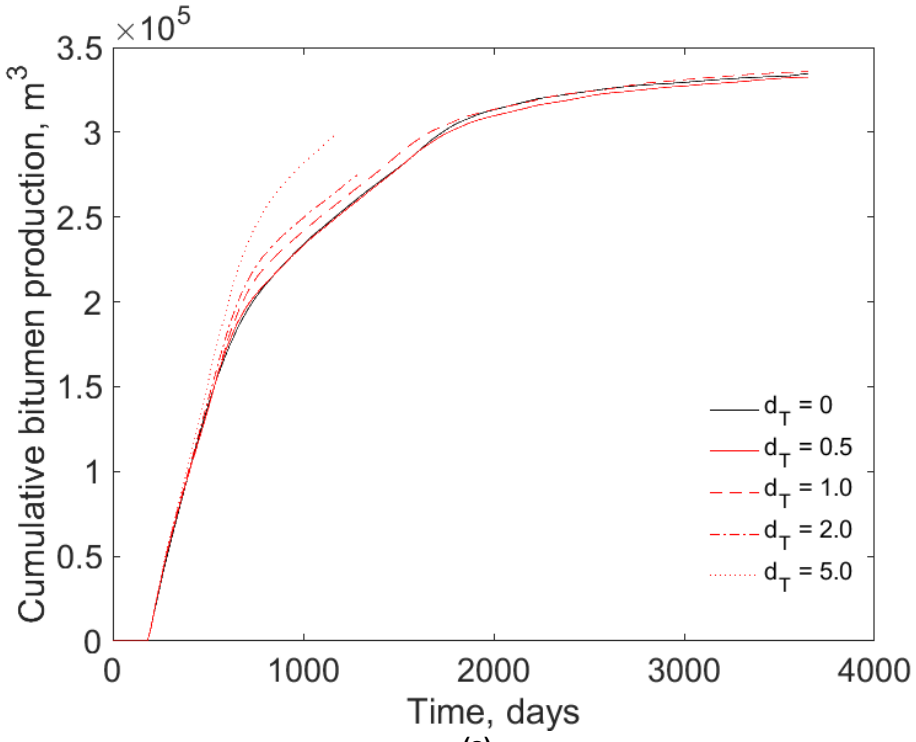

(a)

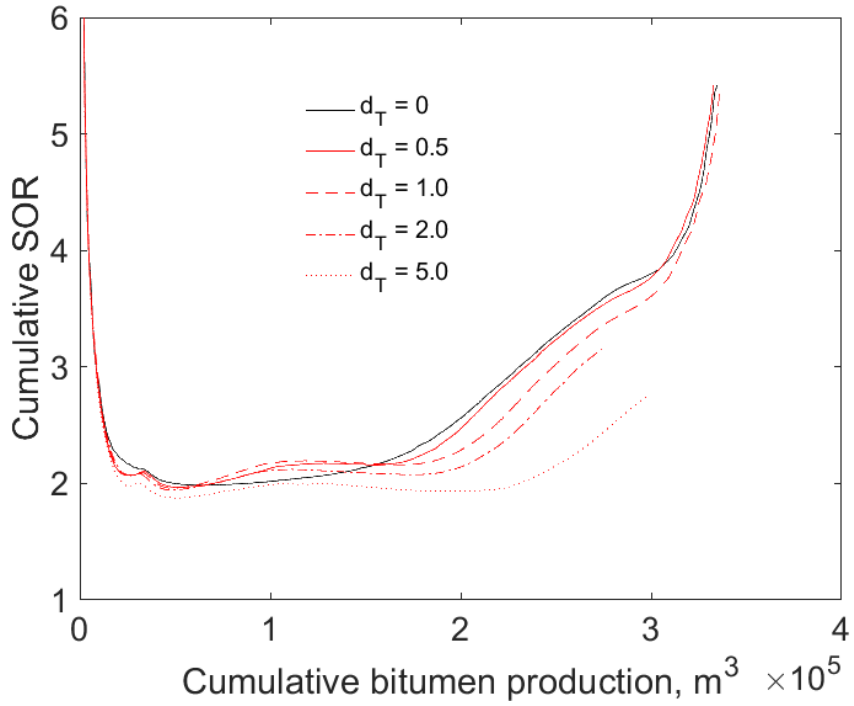

(b)

Figure 3.13. Cumulative bitumen production history and cumulative SOR as a function of cumulative bitumen production for n-C_6 SAGD for the homogeneous reservoir model under different values of transverse dispersivities [d_T (in meters)]; (a) cumulative bitumen production histories; (b) cumulative SOR as a function of cumulative bitumen production.

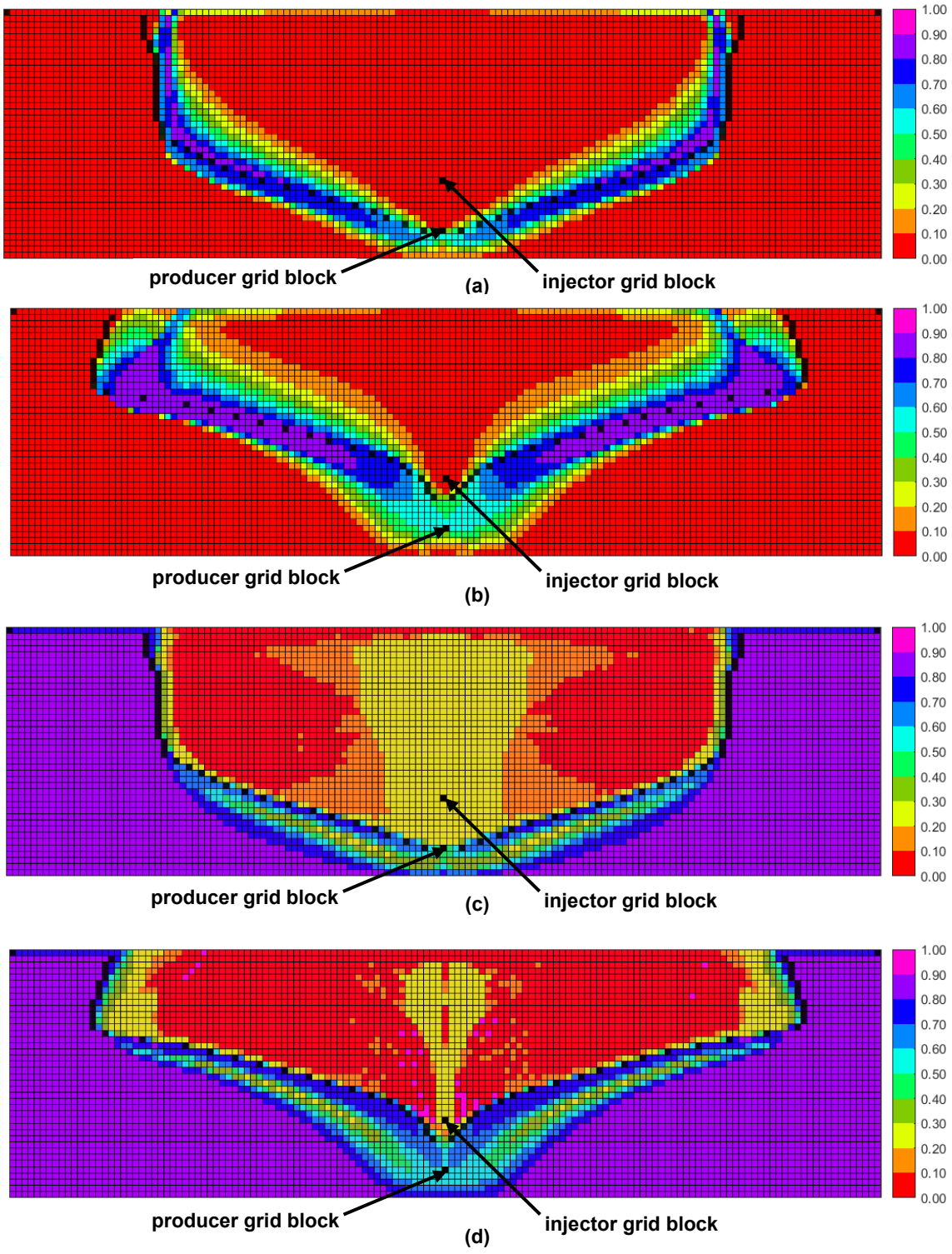

Figure 3.14. Maps for x_{sL} and oleic-phase saturation (S_L) for the cumulative bitumen production of 175036 m^3 ($0.80V_{SAGD}^{hom}$) for the homogeneous model in the second case study under the d_T values of 0 and 5 m; (a) x_{sL} map for d_T = 0 m; (b) x_{sL} map for d_T = 5 m; (c) S_L map for d_T = 0 m; (d) S_L map for d_T = 5 m. Grid blocks at the chamber edge in each grid layer are indicated in brown. This cumulative bitumen production is met at 616 days for d_T = 0 m and at 549 days for d_T = 5 m.

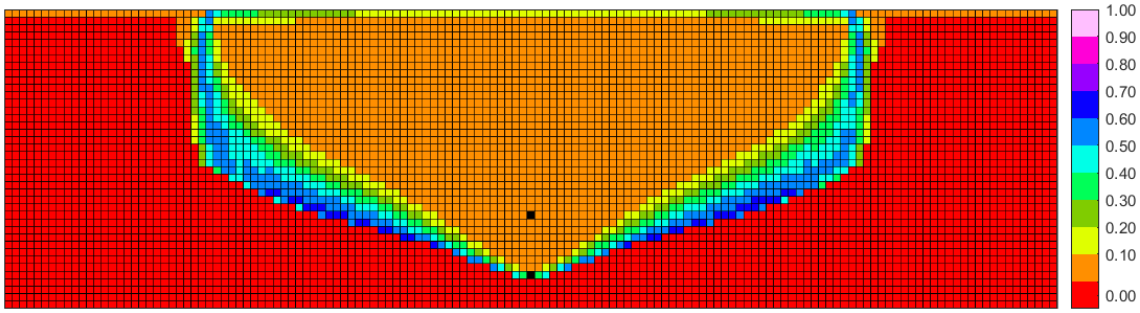
1.00
0.90
0.80
0.70
0.60
0.50
0.40
0.30
0.20
0.10
0.00

(a)

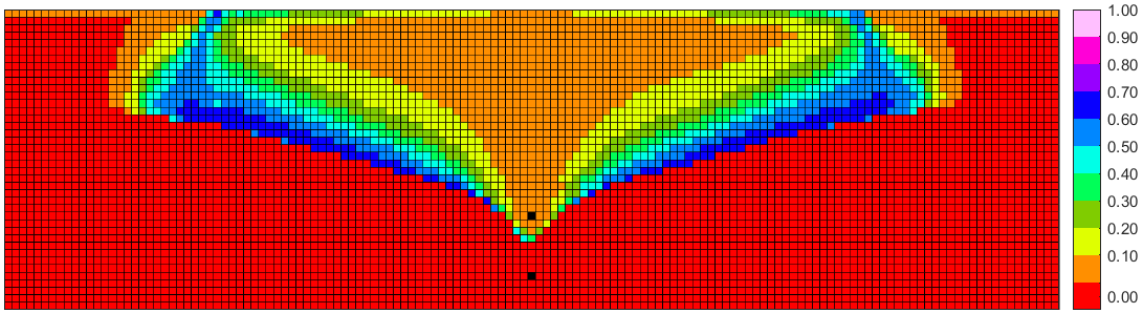
1.00
0.90
0.80
0.70
0.60
0.50
0.40
0.30
0.20
0.10
0.00

(b)

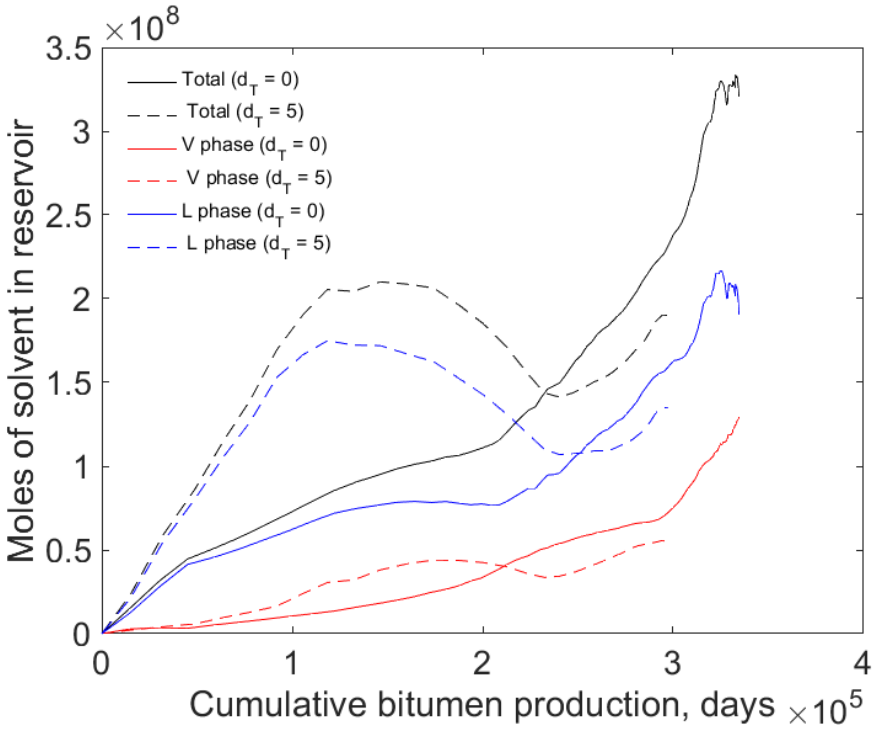

(c)

Figure 3.15. Map for x_{sv} for the cumulative bitumen production of approximately 175036 m^3 (0.80V_{SAGD}^{hom}), and retention of solvent in-situ in vapor and oleic phases as a function of cumulative bitumen production for the homogeneous model in the second case study; (a) x_{sv} map under d_T = 0 m; (a) x_{sv} map under d_T = 5 m; (c) solvent retention curves. In parts (a) and (b), the injector and producer grid blocks are indicated in black. The calculations in part (c) were performed using the equation, $n_{sj}(t) = \sum_{i=1}^{N} \left(PV \times S_j \times \underline{\rho}_j \times x_{sj} \right)_i$, where n_{sj} is the moles of the solvent residing in the jth phase within the reservoir, and t is the time under consideration; PV is the pore volume of the ith grid block; S_j, and $\underline{\rho}_V$, respectively, are the saturation and molar density of the jth phase, while x_{sj} is the concentration of solvent in the jth phase, all for the ith grid block. There are 5640 grid blocks in total within each reservoir model used in this work (i.e., N = 5640). The aforementioned cumulative bitumen production is met at 616 days for d_T = 0 m and at 549 days for d_T = 5 m.

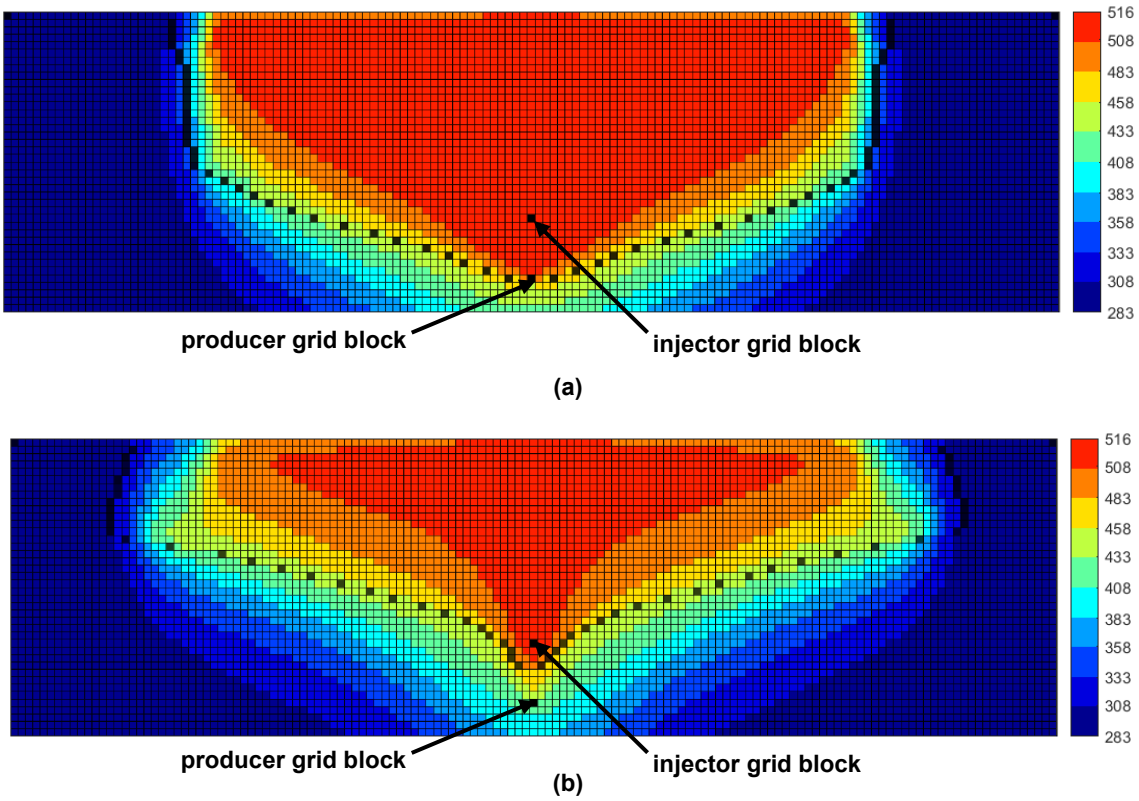

Figure 3.16. Temperature maps for the cumulative bitumen production of approximately 175036 m^3 ($0.80V_{SAGD}^{hom}$) for the homogeneous model in the second case study under different d_T values; (a) d_T = 0 m; (b) d_T = 5 m. Grid blocks at the chamber edge in each grid layer are indicated in brown.

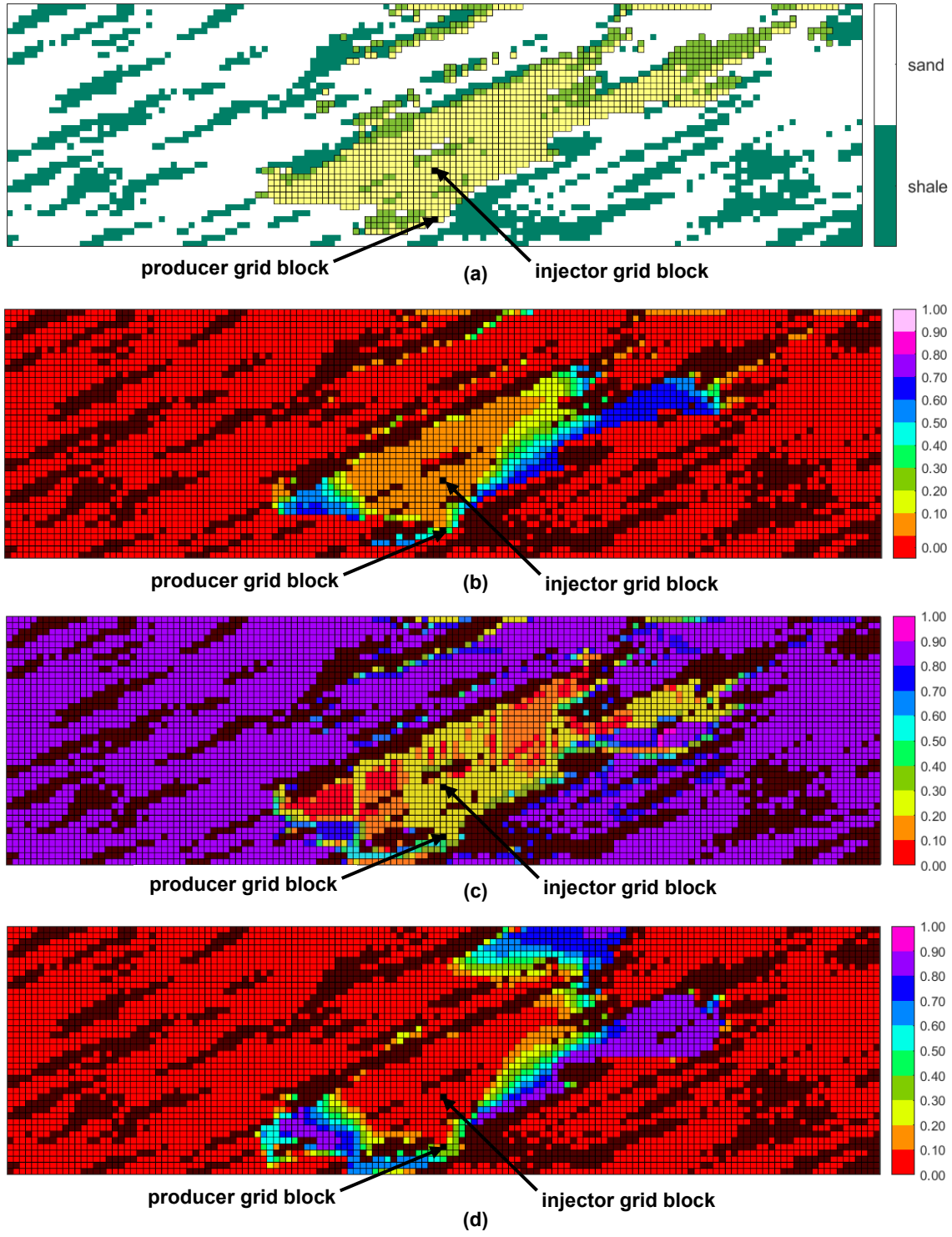

Figure 3.17. Vapor-phase saturation (S_V), x_{sV}, oleic-phase saturation (S_L), and x_{sL} maps for the clean sand grid blocks in realization 37 for the cumulative bitumen production of approximately 54699 m^3 ($0.25V_{SAGD}^{hom}$), and d_T value of 0 m; (a) S_V map; (b) x_{sV} map; (c) S_L map; (d) x_{sL} map. The mudstone bodies are shown in the background in each of these maps. The value of d_T is set to zero in this case. This cumulative bitumen production is met at 989 days.

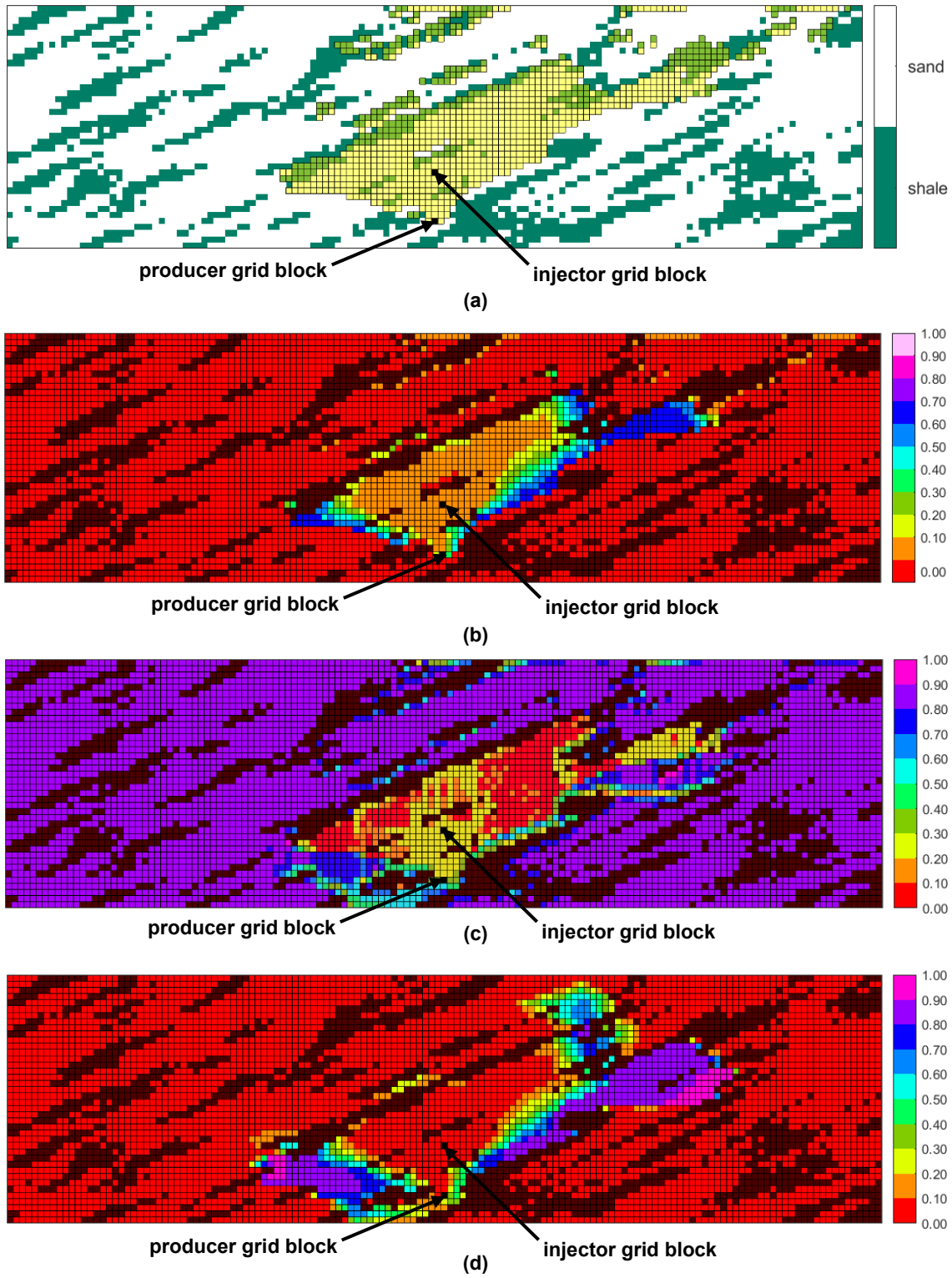

Figure 3.18. Vapor-phase saturation (S_V), x_{sV}, oleic-phase saturation (S_L), and x_{sL} maps for the clean sand grid blocks in realization 37 for the cumulative bitumen production of approximately 54699 m^3 ($0.25V_{SAGD}^{hom}$), and d_T value of 2 m; (a) S_V map; (b) x_{sV} map; (c) S_L map; (d) x_{sL} map. This cumulative bitumen production is met at 736 days.

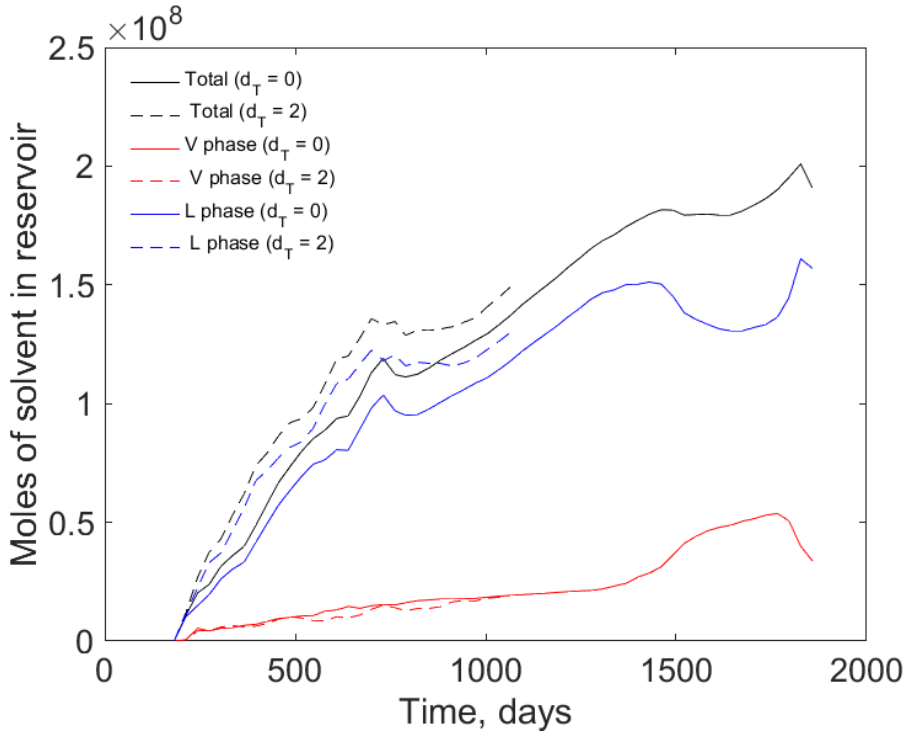

(a)

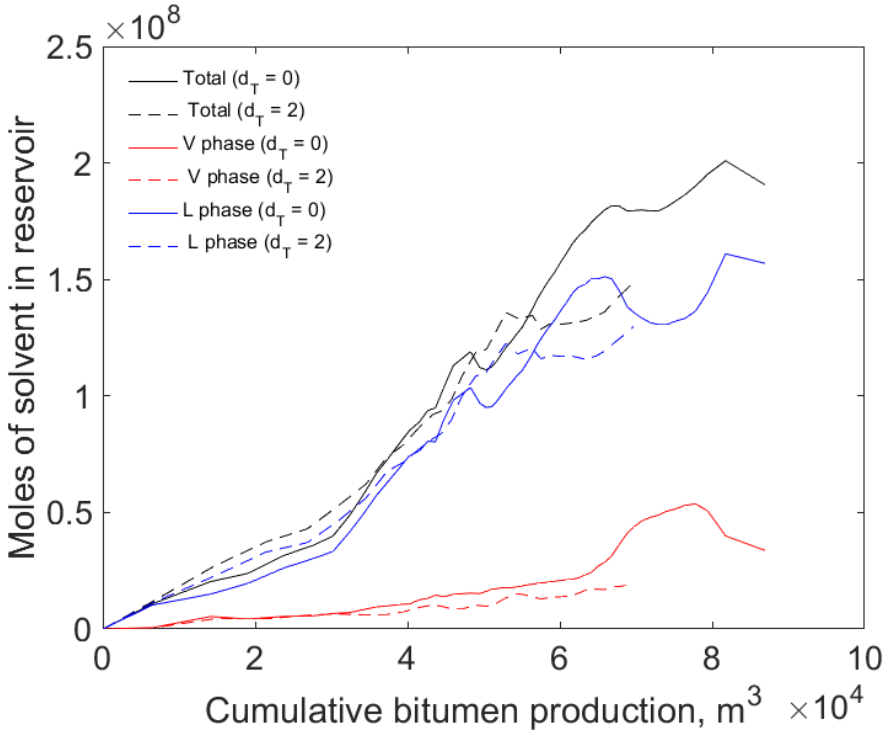

(b)

Figure 3.19. Effect of transverse dispersion of distribution of solvent in-situ in the vapor and oleic phases for realization 37.

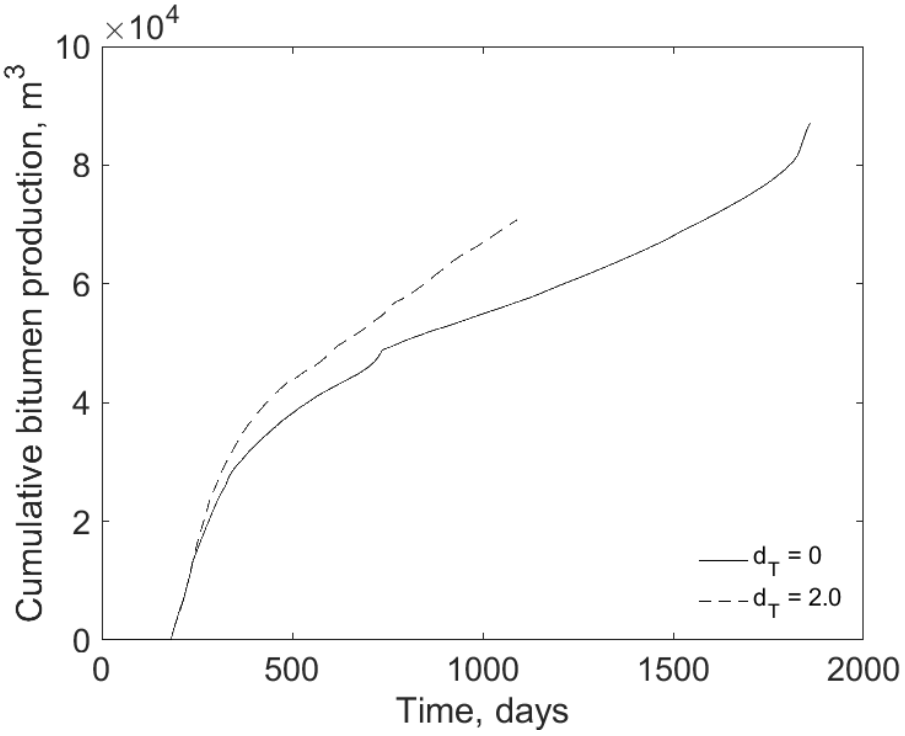

(a)

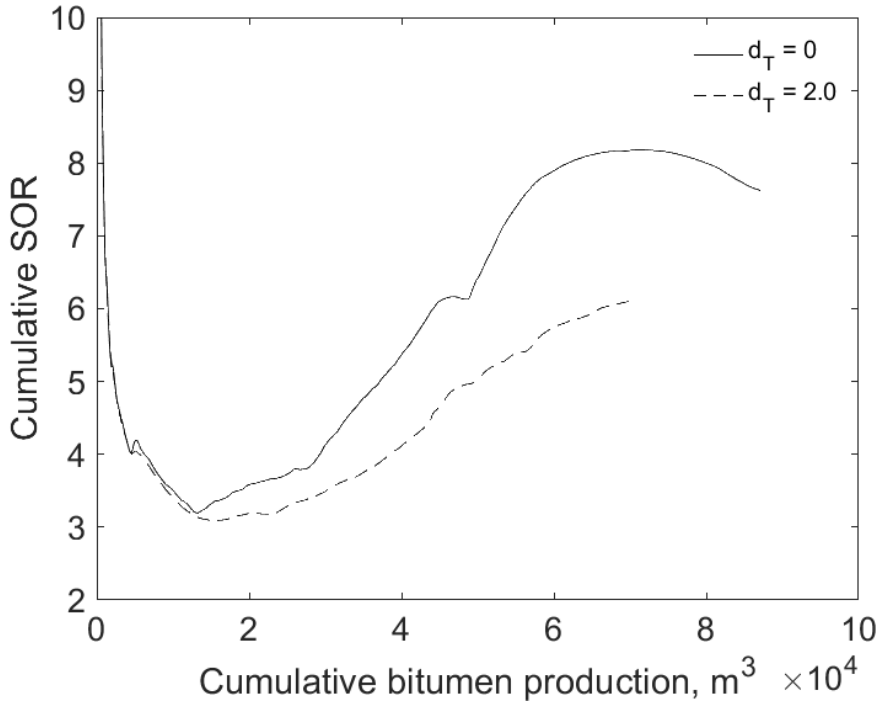

(b)

Figure 3.20. Effect of transverse dispersion on cumulative bitumen production and SOR for realization 37.

Chapter 4. Characterization of Reservoir Heterogeneity in SAGD and ES-SAGD: Under What Type of Heterogeneity is ES-SAGD More Likely to Lower SOR?

List of Tables

List of Figures

Nomenclature

Roman Symbols

I	term related to relative effects of heat transfer to fluid flow in Equation 4.3
g	acceleration due to gravity
k	absolute permeability
q	volumetric flow rate
Q	cumulative bitumen production
U	velocity
z	vertical distance
T	temperature

Greek Symbols

τ	dimensionless parameter in Equation 4.6
θ	angle subtended by chamber edge
ξ	distance

Subscripts

edge	chamber edge
s	solvent
o	oil
D	dimensionless

Abbreviations

BHP	bottom-hole pressure
BIP	binary interaction parameter
CWE	cold water equivalent
ES	expanding solvent
SAGD	steam assisted gravity drainage
hom	homogeneous case
het	heterogeneous case
SIS	sequential indicator simulation
SOR	steam-oil-ratio

With the aid of numerical simulations conducted for one hundred geostatistical realizations for SAGD and n-C_6 SAGD, Chapter 3 demonstrated that (i) the SOR for ES-SAGD is less sensitive to heterogeneity compared to that for SAGD; and (ii) the reduction in SOR by steam-solvent coinjection is enhanced under heterogeneity. These observations were attributed to enhanced mixing between solvent and bitumen under heterogeneity, and the interplay between solvent-bitumen mixing and temperature distribution within the reservoir.

While Chapter 3 presented useful insights on the relative performance of ES-SAGD to SAGD under heterogeneity, it did not elucidate how heterogeneous reservoirs may be identified in terms of their suitability for the application of ES-SAGD. This is an important engineering question in view of the greater cost of solvent relative to the price of bitumen. The main objective of this chapter is to numerically investigate the flow characteristics of heterogeneous reservoirs for which solvent coinjection is more likely to lower SOR of SAGD, and the basis underlying the effectiveness of solvent in such cases. The reservoir model and the petrophysical attributes used in this chapter are identical to that from the second case study of Chapter 3. The operating pressure and injection concentration of solvent for the numerical simulations are set to 35 bars and 2 mol%, respectively.

Section 4.1 presents an analysis of SAGD and n-C_6 SAGD on the basis of analytical equations for oleic-phase flow along the edge of a steam chamber. The analytical model developed by Shi and Okuno (2017) [see **Appendix I**] developed for single-phase incompressible flow in a homogeneous-isotropic reservoir is extended for the discussion of simulation results. Section 4.2 summarizes the main conclusions of this chapter.

4.1. Characterization of heterogeneity for ES-SAGD

This section presents that the SOR reduction by steam-solvent coinjection is significantly correlated with the SOR increase due to heterogeneity under SAGD on the basis of numerical simulations for fifty realizations of a heterogeneous reservoir. The results are then explained in terms of flow characteristics ahead of the edge of a steam chamber by use of analytical equations for SAGD.

4.1.1. Results of SAGD and n-C_6 SAGD simulations under homogeneity and heterogeneity

Figure 4.1 presents the variation of the simulated increase in SAGD's SOR due to heterogeneity with respect to the SOR reduction by steam-solvent coinjection across different realizations for the cumulative bitumen production of 42290 m^3; **Table 4.1** presents the pertinent Spearman rank

correlation coefficients and p-values for several cumulative bitumen productions. Statistically, the SOR reduction by steam-solvent coinjection is positively correlated with the increase in SAGD's SOR due to heterogeneity. The confidence interval used for the calculation of the correlation coefficients is 0.05. Note that the number of realizations that meet a given cumulative bitumen production decreases as the cumulative bitumen production increases. This is because low-permeabilities near the well-pair in some cases result in substantially slow expansion of a steam chamber and/or because of numerical convergence issues. The latter is prevalent with simulations for ES-SAGD for heterogeneous cases.

The increase in SAGD's SOR due to heterogeneity is a consequence of restricted bitumen flow. Tortuous hydraulic paths for gravity drainage tend to increase the time for a unit amount of bitumen to be produced, which increases the amount of heat conduction to over and underburden. **Figure 4.2** presents the variation of the increase in SAGD's SOR due to heterogeneity with the simulated production rate of bitumen across different realizations for the cumulative bitumen production of 42290 m^3; **Table 4.2** presents the pertinent statistics for several different cumulative bitumen productions.

As demonstrated in Chapter 3, for a specified cumulative bitumen production, a larger amount of solvent dissolves in the oleic phase under heterogeneity. For example, **Figure 4.3** compares the simulated distribution of the solvent mole fraction in the oleic phase (x_{sL}) within clean sand grid blocks for the homogeneous case and realizations 15 and 17 for the cumulative bitumen production of approximately 86124 m^3. At this cumulative bitumen production, the SOR reduction by steam-solvent coinjection is simulated to be 1.48 for the homogeneous-anisotropic case, 2.34 for realization 15, and 5.03 for realization 17. Specifically, Figures 4.3a through c indicate that the areal span of high solvent concentration regions (i.e., $x_{sL} > 80$ mol% under the current operating conditions) is significantly greater under heterogeneity. **Table 4.3** presents Spearman's rank correlation coefficients between the increase in SAGD's SOR due to heterogeneity and the number of grid blocks within the mobile zone (where oleic-phase flow rate is at least 0.05 m^3/day) with x_{sL} greater than 80 mol% across different realizations as a function of cumulative bitumen production. Table 4.3 shows that the SOR reduction by steam-solvent coinjection tends to be enhanced if a larger amount of solvent is used for diluting bitumen.

For a given steam-chamber volume (or cumulative bitumen production), the contribution of improved bitumen dilution under heterogeneity to the production rate of bitumen can be

statistically demonstrated by examining the variation of the term, Δt_D, with respect the reduction in SOR due to coinjection of solvent across different realizations. Δt_D is defined as

$$\Delta t_D(Q) = \frac{t^{het}_{SAGD}(Q) - t^{het}_{ES-SAGD}(Q)}{t^{hom}_{SAGD}(Q) - t^{hom}_{ES-SAGD}(Q)}, \quad (4.1)$$

where $t(Q)$ is the time taken for a given process and reservoir type (i.e., homogeneous/heterogeneous) to meet a specified cumulative bitumen production, Q. Δt_D is the normalized margin by which the time taken to meet a given cumulative bitumen production is reduced by steam-solvent coinjection for a specified reservoir. A higher value of Δt_D is indicative of increased acceleration of the production rate of bitumen relative to SAGD for the realization under consideration. The positive correlation observed in **Figure 4.4** indicates that the margin by which coinjection of solvent enhances the bitumen production rate also increases as the extent to which heterogeneity adversely affects the performance of SAGD increases. This figure has been created for the cumulative bitumen production of 42290 m^3. The Spearman rank correlation coefficient for this case is 0.9054 with a p-value close to zero.

The observation of simulation results from a statistical standpoint (Tables 4.1 through 4.3 and Figures 4.1 through 4.4) indicates that a larger amount of bitumen tends to be diluted by solvent in those reservoirs for which SAGD exhibits slow production of bitumen. For such cases, ES-SAGD is more likely to lower SOR of SAGD. The central hypothesis from the above observation is that there is a certain type of flow characteristics in SAGD for heterogeneous reservoirs that makes efficient use of solvent. In what follows, the observed results will be analyzed by use of a SAGD analytical model that clarifies influential factors for bitumen drainage rate along the edge of a steam chamber.

4.1.2. Theory

This section reviews the classical equations for bitumen drainage beyond the edge of a SAGD steam chamber at elevation z measured from the production well. Darcy's law applied to oleic-phase flow along the edge of a steam chamber is

$$U_o(z) = -k_o g \sin\theta / \nu_o, \quad (4.2)$$

where U_o is the oleic-phase velocity measured in the direction from the reservoir bottom to the top, k_o is oleic-phase permeability, g is the gravity constant, θ is the flow angle measured from the horizontal line, and ν_o is oleic-phase kinematic viscosity. Integrating U_o for a cross-section perpendicular to the edge of a steam chamber, oleic-phase flow rate at elevation z is

$$q_o(z) = \int_o^{\xi_L} U_o \Delta y d\xi = -\int_0^{\xi_L} (k_o g \sin\theta/\nu_o)\Delta y d\xi = -kg\sin\theta\,\Delta y I_o, \quad (4.3)$$

where "I_o" is defined as

$$I_o(z) = \int_0^{\xi_L} \frac{k_{ro}}{\nu_o} d\xi. \quad (4.4)$$

In Equations 4.3 and 4.4, Δy is the length of the horizontal section for bitumen production, ξ is the distance from the edge of a steam chamber measured in the perpendicular direction, and ξ_L is where U_o diminishes. k is permeability, and k_{ro} is oleic-phase relative permeability.

As done in previous SAGD models, 1-D steady-state heat conduction through a moving boundary (Carslaw and Jaeger, 1959) is used for transformation from ξ to temperature. That is, temperature distribution, $T(\xi)$, along the cross-section originated at elevation z for $\xi = 0$ is

$$T(\xi, z) = T_R + [T_e - T_R]\exp[-\xi U/\alpha], \quad (4.5)$$

where T_R is the initial reservoir temperature, T_e is the local chamber-edge temperature at elevation z, U is local chamber-edge advancing velocity measured at z in the horizontal direction, and α is thermal diffusivity of the reservoir.

Use of Equation 4.5 with Equation 4.4 enables to express I_o in terms of temperature (instead of ξ), and gives the following dimensionless variable:

$$\tau(z) = uI_o = \int_{T_L}^{T_e} \alpha k_{ro}/[\nu_o(T - T_R)]\, dT. \quad (4.6)$$

With Equation 4.6, Equation 4.3 is simplified as

$$uq_o + kg\tau\Delta y\sin\theta = 0 \quad (4.7)$$

for the cross-section perpendicular to the edge of a steam chamber at elevation z. Note again that u, q_o, and τ are all specified for elevation z measured from the production well. It is easy to show that bitumen production rate (i.e., $-q_o$ evaluated at $z = 0$ denoted as $q_{oil-prod}$) is proportional to $\tau^{0.5}$ by combining Equation 4.7 with local and global material balance equations for a given chamber geometry (Okuno, 2015; Shi and Okuno, 2017); for example, the chamber geometries of Butler et al. (1981) and Reis (1992). For a linear interface (i.e., chamber edge), this reads as (Shi and Okuno, 2017),

$$q_{oil-prod} = \sqrt{kg\varphi H\Delta S_o(\Delta y)^2}\sqrt{\frac{\tau}{2z_D(1-z_D^2)}}, \quad (4.8)$$

where H is the vertical distance between the producer and the top of the reservoir, ΔS_o is the difference between the initial and residual saturations of the oleic phase, z_D is the elevation relative to the production well normalized by H, and φ is the porosity.

The observation in the previous section implied that steam-solvent coinjection may counter the negative impact of heterogeneity on bitumen flow in SAGD, $q_o = -kg\tau\Delta y \sin\theta/U$. Detailed analysis of individual simulation cases for different realizations have indicated that there are at least two main factors that can lower q_o under heterogeneity. Firstly, fluid flow becomes more tortuous under heterogeneity, which tends to reduce the effective reservoir conductivity for gravity drainage in SAGD. Secondly, a larger amount of water (steam condensate) tends to accumulate in a heterogeneous reservoir. As an example, **Figure 4.5** shows the historical variation of the accumulated water in the reservoir for the homogeneous case and realization 17. Presence of a larger amount of water tends to lower the relative permeability to the oleic phase, k_{ro}, which reduces q_o through τ. Furthermore, if the increased accumulation of water occurs near the edge of a steam chamber, where steam condenses, the oleic-phase flow occurs at lower temperatures further away from the chamber edge. This would adversely affect q_o through the oleic-phase viscosity.

The combination of these two facets results in the reduction of τ through the reduction of both the chamber-edge advancing velocity (u) and the term I_o defined in Equation 4.4. **Figure 4.6** illustrates this for the cumulative bitumen production of 42290 m^3. This figure visualizes relationships between the simulated production rate of bitumen and τ, τ and U, and U and I_o across different realizations. These calculations are based on the assumption that any homogeneous-anisotropic and heterogeneous reservoir has a homogeneous-isotropic equivalent, and are performed for the z_D value of 0.5; the procedure for these calculations can be found in **Appendix J**. For a homogeneous-isotropic reservoir, Shi and Okuno (2017) demonstrated that the deviation between the simulated temperature profile along an axis transverse to the chamber edge and that calculated analytically by assuming 1-D steady state conductive heat transfer transverse is smallest midway between the producer and the top of the reservoir model (i.e., $z_D = 0.5$).

The most obvious contribution of solvent to enhancement of q_o is made through reduction of the oleic-phase kinematic viscosity, ν_o, as part of the integrand for τ. In **Figure 4.7,** the integrand of Equation 6 with $k_{ro} = 1.0$ is plotted with respect to temperature at different dilution levels by n-C_6 for the bitumen studied. The contribution of solvent to increasing the area under the curve is calculated to be more significant at higher temperature because $1/\nu_o$ rapidly increases with increasing temperature, as is the case for bitumen. It might be somewhat counter-intuitive

that the bitumen dilution can be fairly effective in enhancing the transport of the oleic phase that is already mobile at high temperature. The next section will show that steam-solvent coinjection makes it possible to recover a certain amount of bitumen that would stay for a long time in a slow-flow region under heterogeneity in SAGD.

Another potential contribution of coinjected solvent to enhancement of q_o can be made through increasing oleic-phase saturation, which in turn increases k_{ro}. Solvent makes part of the oleic phase upon condensation, which certainly counter the adverse effect of the increased water (steam condensate) amount on q_o under heterogeneity (Figure 4.5).

4.1.3. Discussion and analysis

The aforementioned facets are illustrated by use of the simulated property maps for realization 17 for the cumulative bitumen production of approximately 31218 m^3. Property maps for other realizations are given in **Appendix K**. For this realization and cumulative bitumen production, the bitumen production rate simulated for SAGD is 71.60 m^3/day with the cumulative SOR of 6.20. When solvent is coinjected with steam for this realization, the SOR is simulated to be 3.42. That is, the SOR reduction is as much as 2.78 for this case.

For the SAGD process, **Figure 4.8** presents the simulated distribution of five different properties for realization 17 (the cumulative bitumen production is approximately 31218 m^3). Figure 4.8a presents the vapor-phase saturation map simulated. In this map, clean-sand grid blocks across which a substantial change in vapor-phase saturation occurs are indicated in brown, and are designated as chamber-edge grid blocks. Figure 4.8b presents the temperature distribution in clean sand grid blocks. Figure 4.8c presents the distribution of molar flow rate of the bitumen component. Figures 4.8de respectively give the distribution of the oleic- and aqueous-phase saturations within the clean-sand grid blocks.

Figure 4.8c in conjunction with Figures 4.8b shows that the local flow of bitumen near the chamber edge in SAGD can be limited even though the oleic phase is heated to the saturation temperature of water (515.72 K at 35 bars). That is, the thermal energy may not be enough to efficiently mobilize bitumen in slow-flow hydraulic paths; that is, the conductivity to flow in such slow-flow paths should be enhanced by dilution to compete with higher-conductivity paths in SAGD under heterogeneity.

For realization 17, this is prominent in the highlighted region in Figure 4.8a, where condensation of the vapor phase occurs near a large mudstone barrier. Limited bitumen flow is

primarily because the mudstone barrier hinders the efficient transport of heated bitumen. The thickness of heated bitumen potentially available for flow can also be reduced due to lower oleic-phase saturations, especially when the volume of water retained in-situ is higher than that under homogeneity (Figure 4.8e). For this cumulative bitumen production, the accumulation of water for the homogeneous case and realization 17 are approximately 11609 and 15108 m^3, respectively (see Figure 4.5). Within the encircled region in Figure 4.8a, the saturation of the aqueous phase adjacent to the chamber edge is in excess of 80%, which is detrimental to bitumen flow due to reduced oleic-phase relative permeability.

Figure 4.9 presents the vapor-phase saturation, temperature, mole fraction of solvent in the oleic phase (x_{sL}), molar flow rate of bitumen, and oleic-phase saturation maps for realization 17 for n-C_6 SAGD (the cumulative bitumen production is approximately 31218 m^3). Figure 4.9d indicates that the dilution of bitumen by solvent is pronounced in the heated slow-flow regions under SAGD (Figure 4.8). These maps also illustrate that the molar flow rate of bitumen is enhanced through simultaneous improvements in viscosity-reduction, and oleic-phase saturations where considerable dilution of bitumen by solvent occurs (compare Figures 4.8e and 4.9e).

Improved reduction in the SOR due to coinjection of solvent under heterogeneity as a result of enhanced dilution is attributed to both the enhancement of the flow rate of bitumen, and reduction of thermal losses to the overburden relative to steam-only injection. Chapter 3 demonstrated that the dilution of bitumen by solvent can lower temperatures within the reservoir by rendering the oleic phase more volatile, which facilitates the vaporization of solvent upon subsequent contact with steam. Accumulation of the solvent in the vapor phase near the chamber edge can in turn reduce the temperature at which transition from oleic-aqueous-vapor to oleic-aqueous coexistence occurs at the chamber edge.

Figure 4.10 presents the distribution of the concentration of solvent in the vapor phase (x_{sV}) for the cumulative bitumen productions of approximately 31218 m^3, and 86124 m^3 for realization 17; **Figure 4.11** presents the pertinent distribution of temperature for SAGD and n-C_6 SAGD for the cumulative bitumen production of approximately 86124 m^3. Unlike the homogeneous case, steam-rich regions wherein temperatures are comparable to the saturation temperature of water at the operating pressure need not reach the top of the formation when solvent is coinjected with steam under heterogeneity (see Figures 4.8b, 4.9b and 4.11ab). Further, the margin by which the SOR is reduced due to coinjection of solvent for realization 17 is greater for the cumulative

bitumen of 86124 m^3 than that for 31218 m^3 because of greater accumulation of solvent in-situ (see Figures 4.3c, 4.9d, and 4.10ab). The retention of solvent for realization 17 estimated on the basis of the simulated solvent-injection and production histories at stock-tank conditions are 9893 m^3 for the cumulative bitumen production of 31218 m^3, and 22644 m^3 at 86124 m^3.

The results and discussion presented thus far indicate that the use of solvent in steam-solvent coinjection tends to be more effective in reducing SOR under heterogeneity, but this likely requires a larger amount of solvent retention. As the cost of solvent is higher than the price of bitumen, its retrieval is a priority towards later stages of production. Maximization of solvent-retrieval under heterogeneity inevitably requires the development of an optimal application strategy in terms of the concentration of solvent in the injection stream in conjunction with detailed cost-to-benefit analysis for 3-D simulations (also see Keshavarz et al., 2015, Chapter 2, and Appendices F and H). Optimal conditions for the application of steam-solvent coinjection are expected to vary across different groups of realizations due to the underlying differences in bitumen-production rates. Detailed development of such strategies is beyond the scope of the current research.

4.2. Conclusions

This chapter presented a study of the flow characteristics of heterogeneous bitumen reservoirs that make it more likely for steam-solvent coinjection to lower SAGD's SOR. SAGD and coinjection of steam and n-C_6 were compared mainly in terms of SOR for fifty realizations of a heterogeneous reservoir. Mechanistic explanation of the results was based on analytical equations for bitumen flow beyond the edge of a SAGD steam chamber, which clarified how steam-solvent coinjection can contribute to enhancement of bitumen flow under heterogeneity. The conclusions of this chapter are as follows:

1. Simulation results statistically showed that SOR reduction by steam-solvent coinjection is expected to be more significant if SAGD's SOR is more significantly increased by the presence of permeability barriers. For such cases, enhancement of bitumen flow is crucial for lowering SOR, and is possible with steam-solvent coinjection. For the heterogeneous reservoir models under consideration at the operating pressure of 35 bars, and 2 mol% for the injection concentration of solvent, the margin by which the SOR is reduced as a result of coinjection of n-C_6 is at least 2.0 when the average increase in SAGD's SOR due to heterogeneity is 2.45.

2. A larger amount of solvent tends to accumulate if SAGD in the reservoir results in higher SOR in the presence of permeability barriers. Such accumulation of solvent was particularly observed in slow-flow regions near permeability barriers, where steam-only injection did not make bitumen mobility sufficiently high for efficient transport of the bitumen to fast-flow regions.

3. Analysis of SAGD equations for bitumen flow indicates that the enhancement of bitumen flow by dilution is more pronounced at higher temperature. This comes mainly from the rapid reduction of the bitumen kinematic viscosity with increasing temperature as indicated in Figure 4.7. Solvent accumulation also counters the adverse effect of the increased water accumulation in heterogeneous cases by increasing the oleic-phase saturation, therefore, relative permeability. Enhanced dilution of bitumen by solvent under heterogeneity reduces the SOR both through the improvement of molar flow rate of bitumen and reduction of thermal losses to the overburden.

Table 4.1. Spearman's rank correlation coefficient (ρ) between the increase in SAGD's SOR due to heterogeneity for a given cumulative bitumen production and the corresponding SOR reduction by steam-solvent coinjection across different realizations. For a given cumulative bitumen production, the last column in this table presents the threshold value for the increase in SAGD's SOR due to heterogeneity beyond which the SOR reduction by steam-solvent coinjection becomes greater than 2.0.

Cumulative bitumen production, m^3	ρ	p-value	Threshold
19569	0.967	0.0000E+00	2.41
31218	0.896	2.8939E-07	2.79
42290	0.871	1.4216E-06	2.53
52238	0.918	1.8035E-06	2.51
61845	0.909	1.9548E-06	2.44
70816	0.860	1.3732E-06	2.47
78357	0.906	3.5914E-06	2.58
86124	0.954	0.0000E+00	2.15
94268	0.962	0.0000E+00	2.15

Table 4.2. Spearman's rank correlation coefficient (ρ) between the increase in SAGD's SOR due to heterogeneity for a given cumulative bitumen production and the bitumen production rate in SAGD across different realizations.

Cumulative bitumen production, m^3	ρ	p-value
19569	-0.9192	2.6480E-07
31218	-0.8862	8.7688E-07
42290	-0.8600	2.2041E-06
52238	-0.8745	2.6634E-06
61845	-0.8735	2.6314E-06
70816	-0.8737	0.0000E+00
78357	-0.9386	4.5752E-06
86124	-0.9286	0.0000E+00
94268	-0.8601	5.9708E-04

Table 4.3. Spearman's rank correlation coefficient (ρ) between the increase in SAGD's SOR due to heterogeneity for a given cumulative bitumen production and the corresponding number of grid blocks in n-C_6 SAGD for which x_{sL} exceeds 80 mol%. The confidence interval used for the calculation of the correlation coefficients is 0.05. The number of realizations that meet a given cumulative bitumen production decreases as the cumulative bitumen production increases. The systematic increase in p-values with cumulative bitumen production is likely because of the smaller sample sizes used for statistical analysis.

Cumulative bitumen production, m^3	ρ	p-value
19569	0.8134	4.6645E-08
31218	0.6822	4.5824E-05
42290	0.5933	1.4009E-03
52238	0.6497	5.9041E-04
61845	0.5504	6.0397E-03
70816	0.5740	7.4573E-03
78357	0.5353	1.6386E-02
86124	0.6615	1.2187E-02
94268	0.5549	5.2532E-02

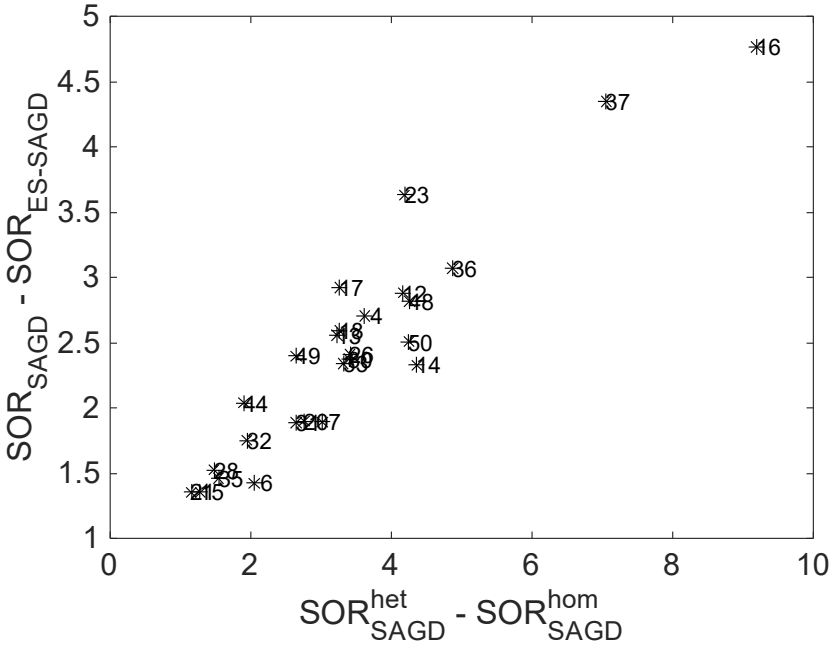

Figure 4.1. SOR reduction by steam-solvent coinjection is positively correlated with the increase in SAGD's SOR due to heterogeneity. The SOR values are calculated for different realizations for the cumulative bitumen production of 42290 m³. The pertinent values for the Spearman rank correlation coefficient and null-hypothesis probability are given in Table 4.1.

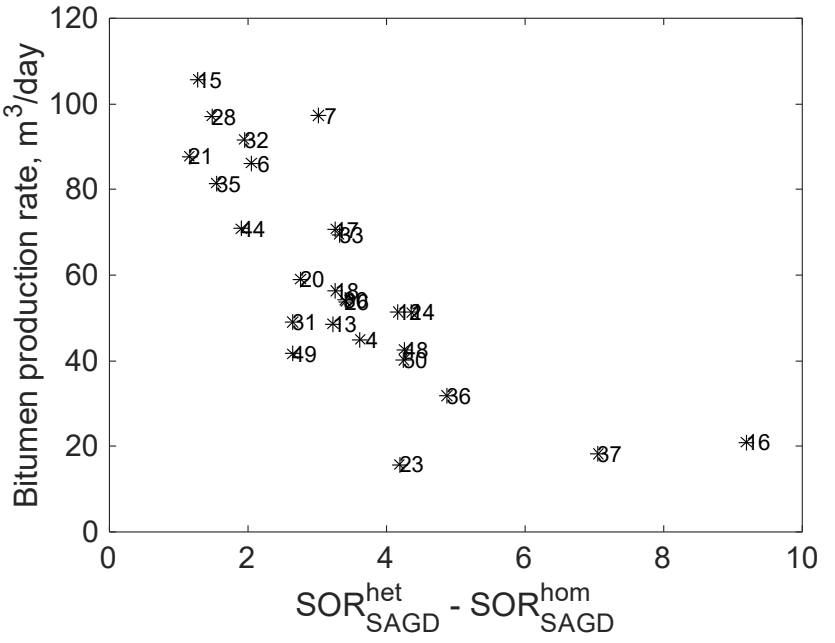

Figure 4.2. Bitumen production rate in SAGD is negatively correlated with the increase in SAGD's SOR due to heterogeneity. The SOR values are calculated for different realizations for the cumulative bitumen production of 42290 m³. The pertinent values for the Spearman rank correlation coefficient and null-hypothesis probability are given in Table 4.2.

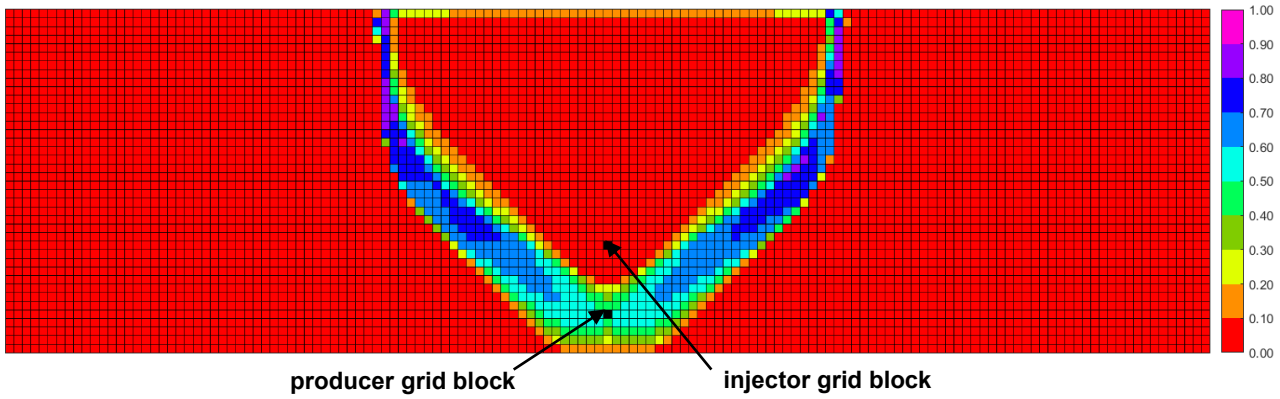

(a) Homogeneous-anisotropic case

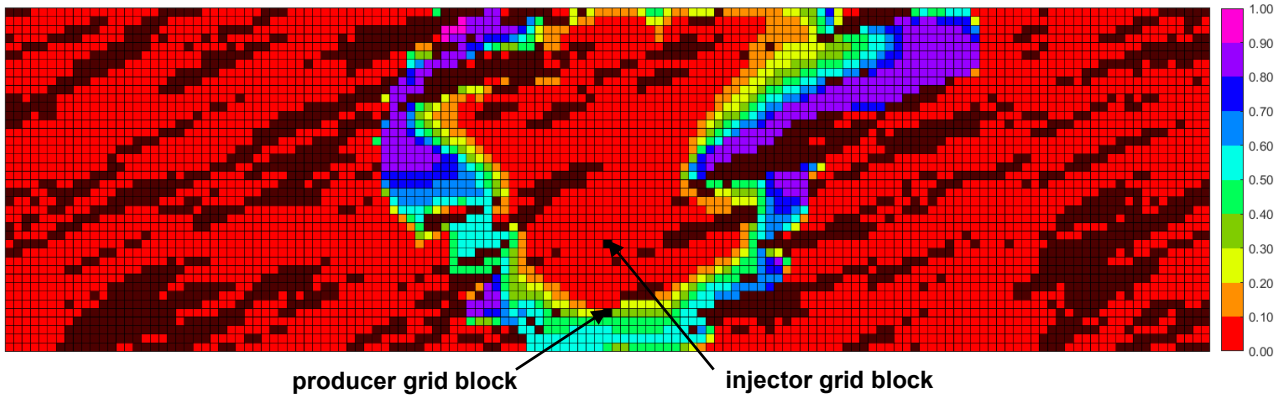

(b) Realization 15

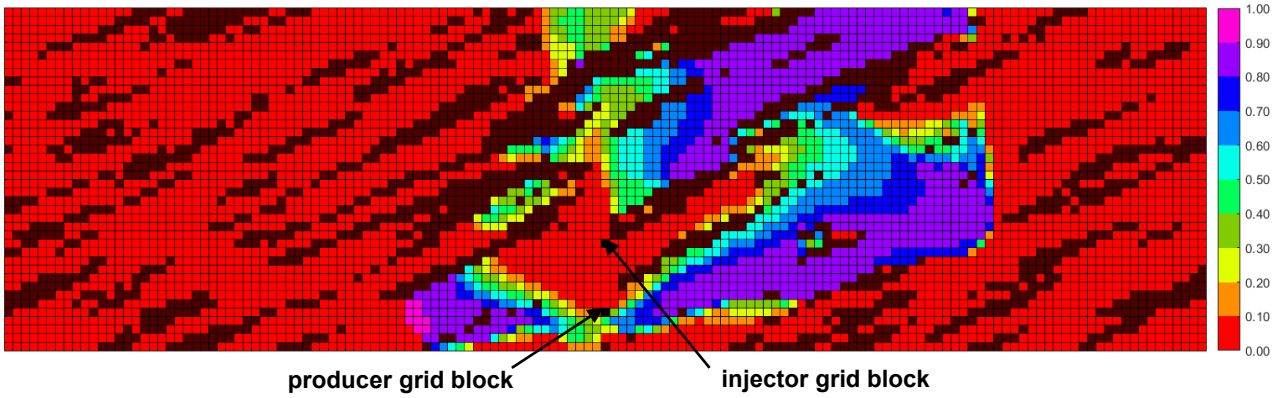

(c) Realization 17

Figure 4.3. Distribution of mole fraction of solvent in the oleic phase (x_{sL}) within clean sand grid blocks for different cases for the cumulative bitumen production of approximately 86124 m^3; (a) homogeneous-anisotropic case; (b) realization 15; (c) realization 17. For the heterogeneous realizations (i.e., parts b and c), the mudstone barriers are indicated in brown. The mole fraction of solvent in the grid blocks indicated in purple exceed 80 mol%. These maps demonstrate that the dilution of bitumen by solvent can be higher under heterogeneity for a given cumulative bitumen production.

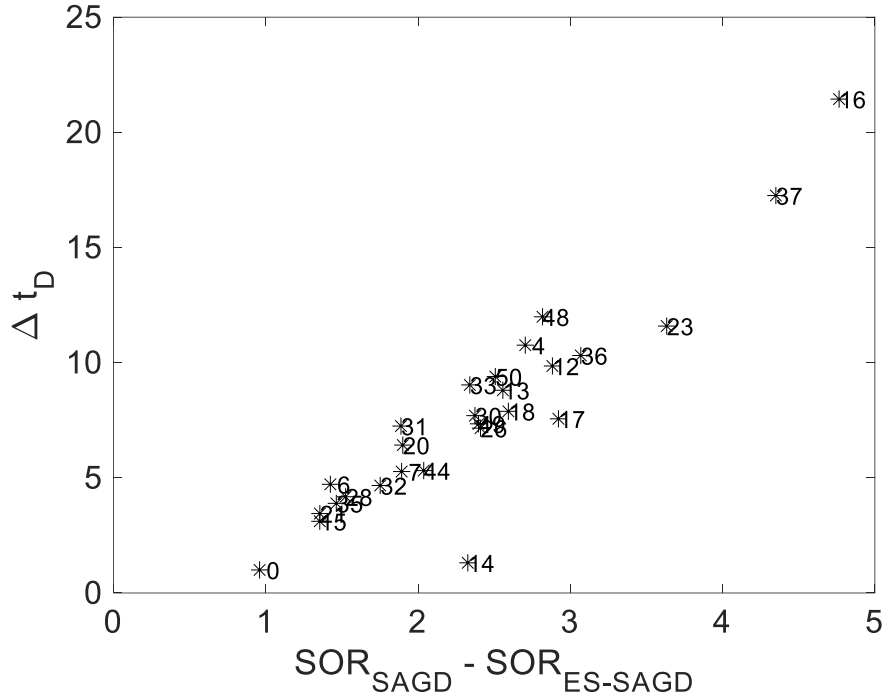

Figure 4.4. Variation of Δt_D with respect to the reduction in SOR by steam-solvent coinjection across different realizations for the cumulative bitumen production of 42290 m³. Δt_D is defined in Equation 4.1 in Section 4.1.1.

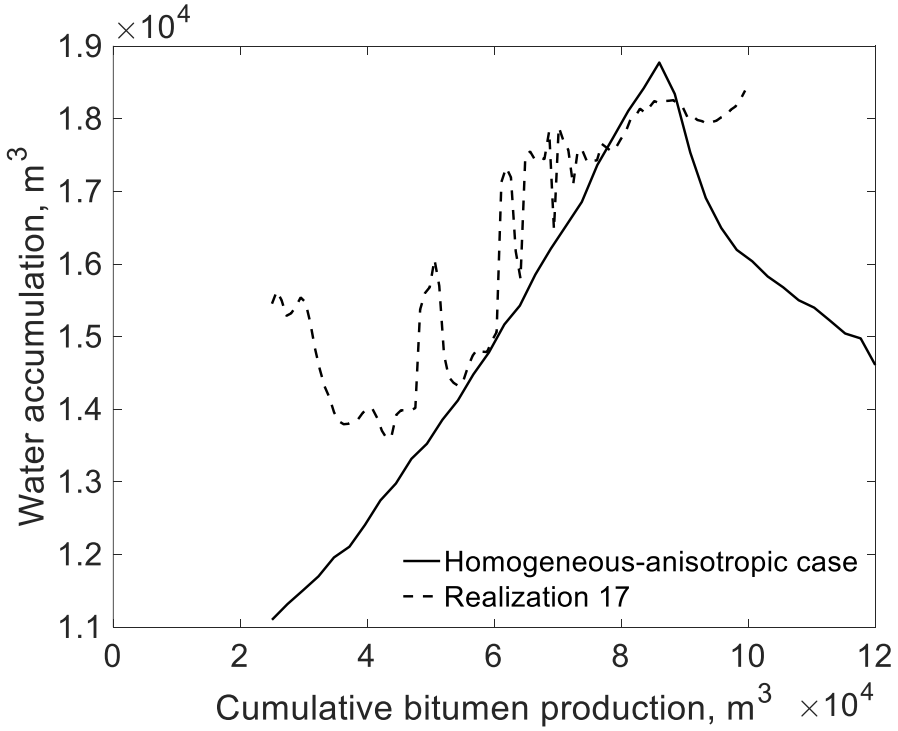

Figure 4.5. Historical variation of water accumulation for the homogeneous-anisotropic case and realization 17.

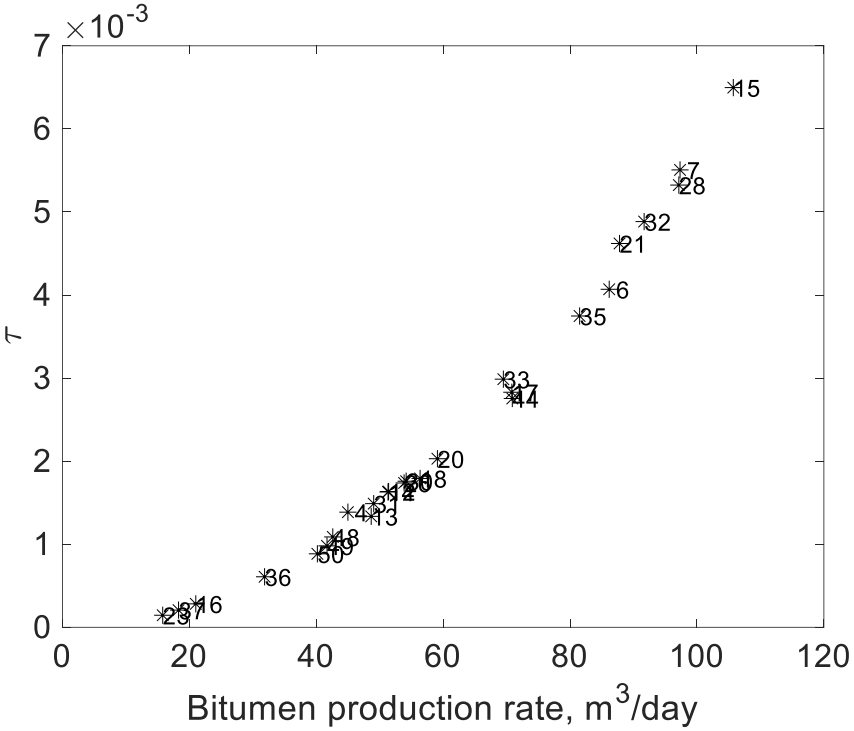
×10^-3
7
6
5
4
3
2
1
0
τ
0
20
40
60
80
100
120
Bitumen production rate, m^3/day

(a)

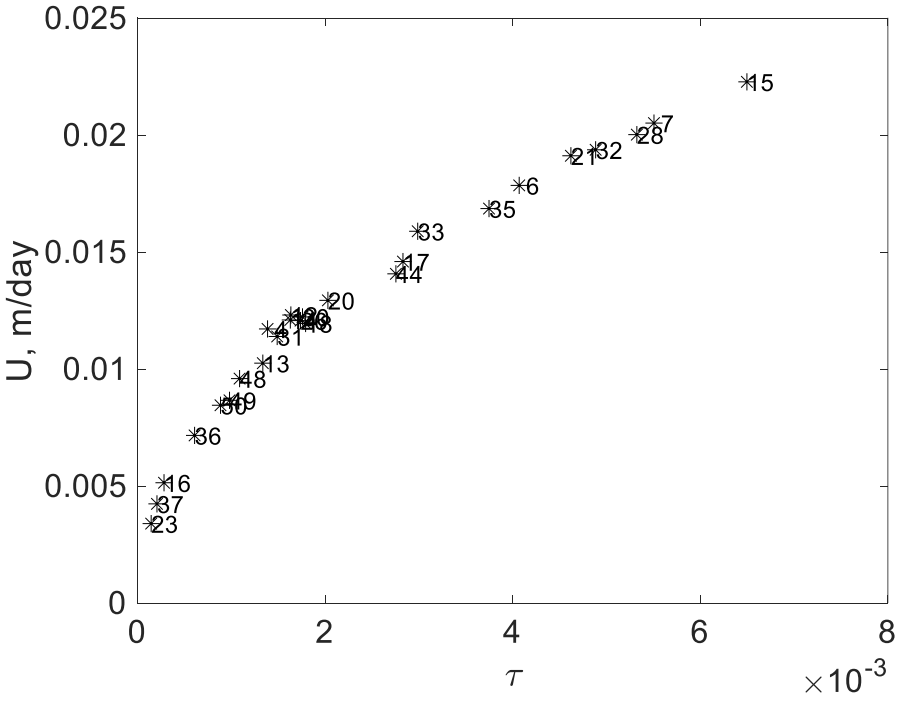
0.025
0.02
0.015
0.01
0.005
0
U, m/day
0
2
4
6
8
τ
×10^-3

(b)

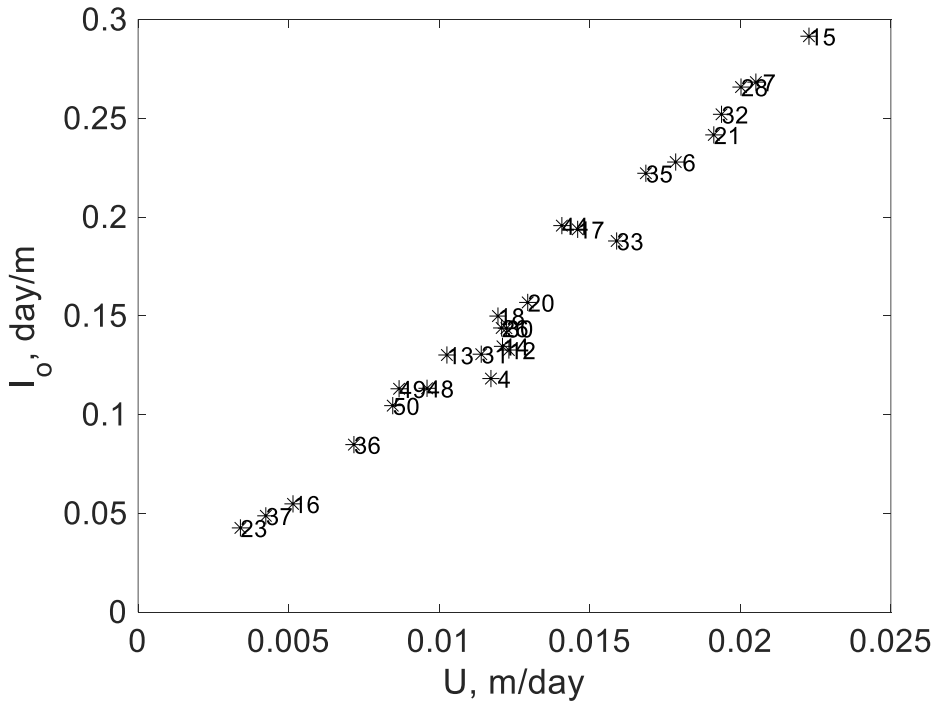

(c)

Figure 4.6. Relationships between the production rate of bitumen in SAGD, τ, U, and I_o for the cumulative bitumen production of 42290 m^3; (a) variation of production rate of bitumen with respect to τ; (b) variation of τ with U; and (c) variation of U with I_o. For this cumulative bitumen production, the values of the production rate of bitumen in SAGD, τ, U, and I_o for the homogeneous-anisotropic case are 338.92 m^3/day, 0.063, 0.064 m/day, 0.098 day/m, respectively. As the production rate of bitumen in SAGD is lower under heterogeneity, the value of τ for the homogeneous-isotropic equivalents of the heterogeneous realizations are also lower relative to the homogeneous-anisotropic reservoir model. Reduction of τ due to heterogeneity is result of lower U and I_o.

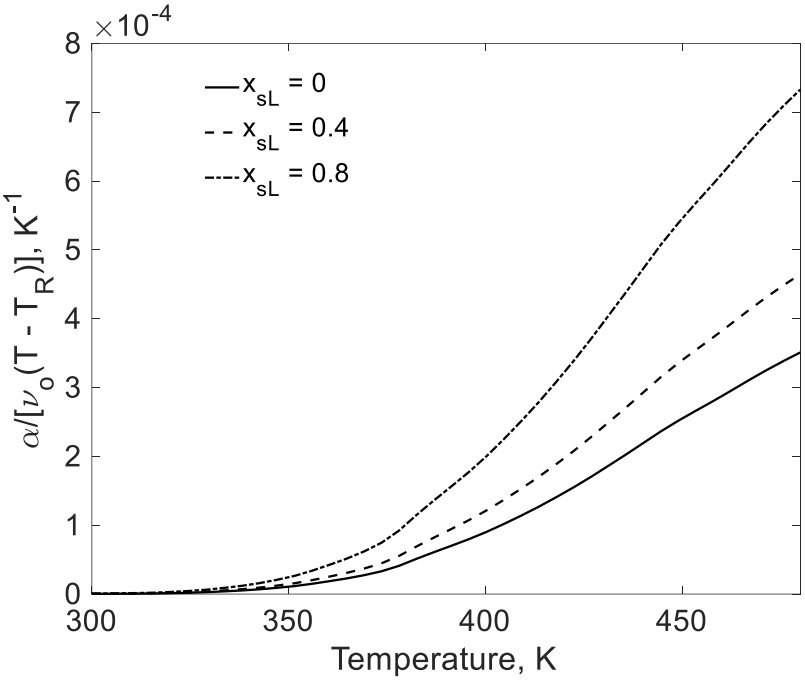

Figure 4.7. The integrand of Equation 4.6 with k_{ro} = 1.0 is plotted with respect to temperature at different dilution levels by n-C_6 for the bitumen studied. The contribution of solvent to increasing the area under the curve is calculated to be more significant at higher temperature because the oleic-phase kinematic viscosity rapidly decreases with increasing temperature, as is the case for bitumen.

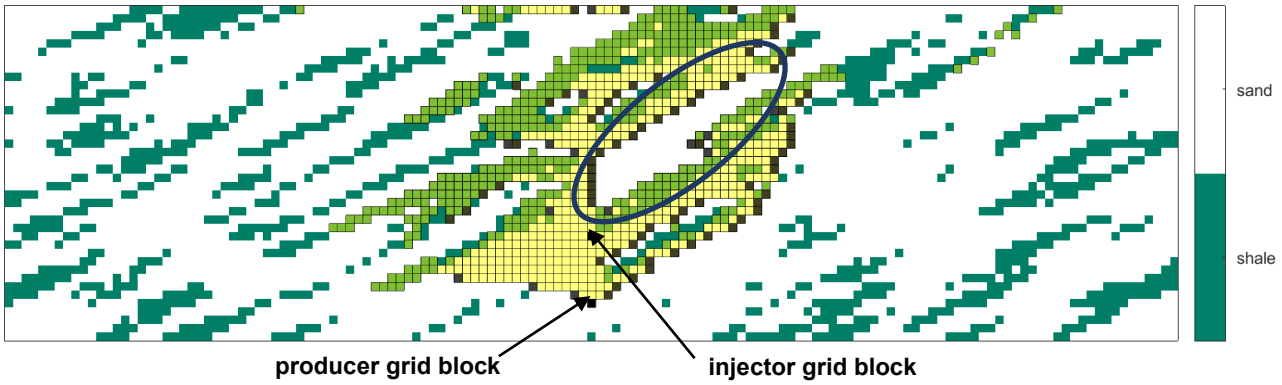

(a) Vapor-phase saturation map in SAGD for realization 17

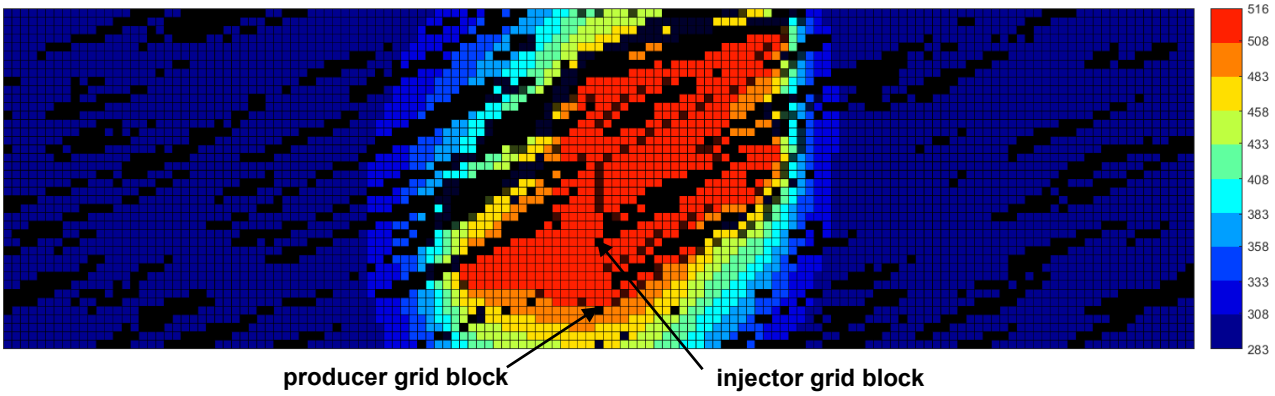

(b) Temperature distribution (in Kelvin) in clean sand grid blocks in SAGD for realization 17

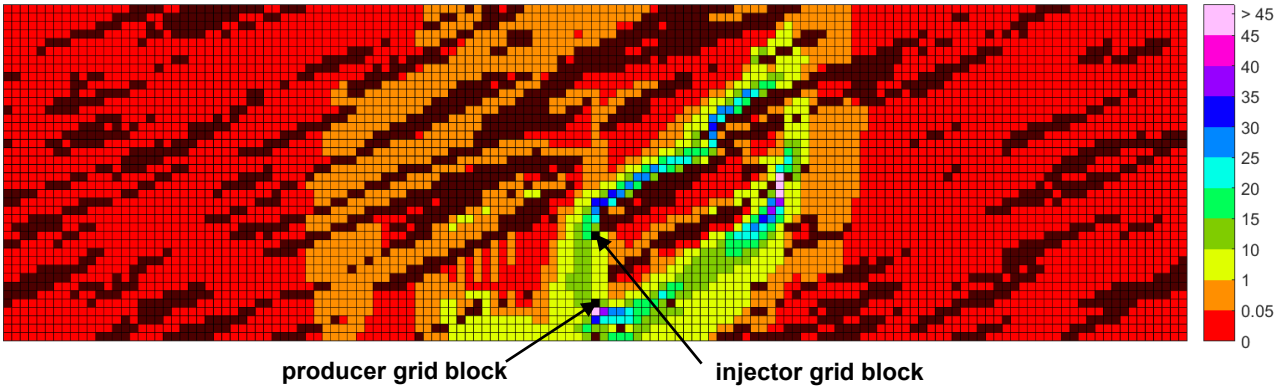

(c) Distribution of bitumen molar flow rate (kg-mole/day) in clean sand grid blocks in SAGD for realization 17

Figure 4.8. Continued below.

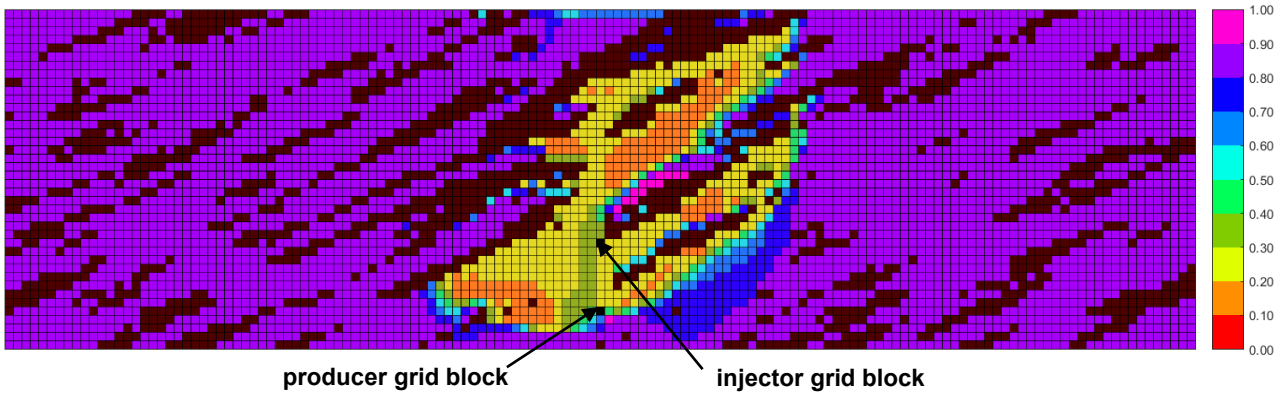

(d) Oleic-phase saturation distribution in clean sand grid blocks in SAGD for realization 17

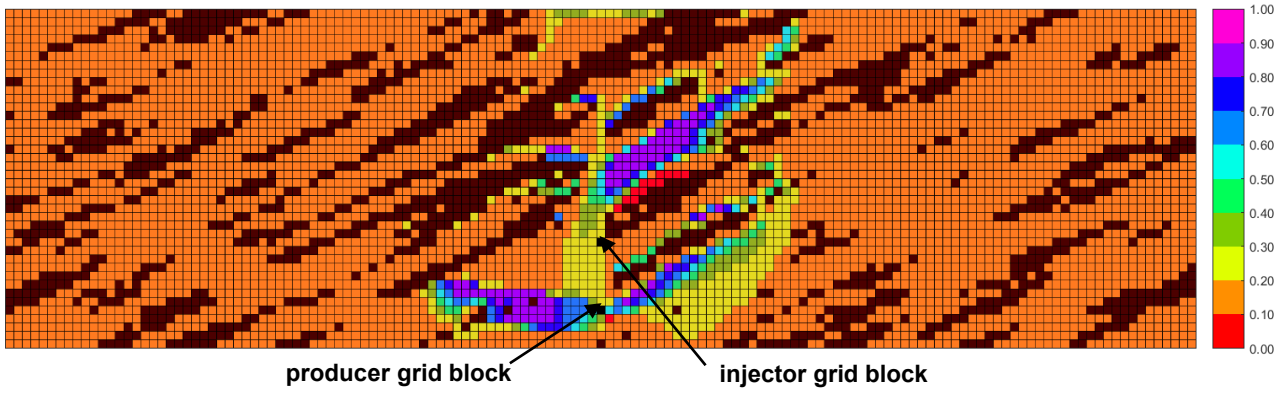

(e) Aqueous-phase saturation distribution in clean sand grid blocks in SAGD for realization 17

Figure 4.8. Simulated property maps in SAGD for realization 17 for the cumulative bitumen production of approximately 31218 m^3; (a) vapor-phase saturation; (b) temperature (in Kelvin) in clean sand grid blocks; (c) molar flow rate of bitumen (in kg-mole/day) in clean sand grid blocks; (d) oleic-phase saturation in clean sand grid blocks; (e) aqueous-phase saturation in clean sand grid blocks. In parts (a) and (b), grid blocks along the chamber edge are indicated in brown. Within the encircled region in part (a), temperature within the transition zone beyond the chamber edge is comparable to the saturation temperature of water at the operating pressure (515.72 K). Despite this, the molar flow rate of bitumen (part c) can be significantly low in this region. Relative to the homogeneous case, the thickness of heated bitumen available for flow can also be lowered when the aqueous-phase saturation [see part (e)] beyond the chamber edge is elevated, which can occur when a larger volume of water resides in-situ.

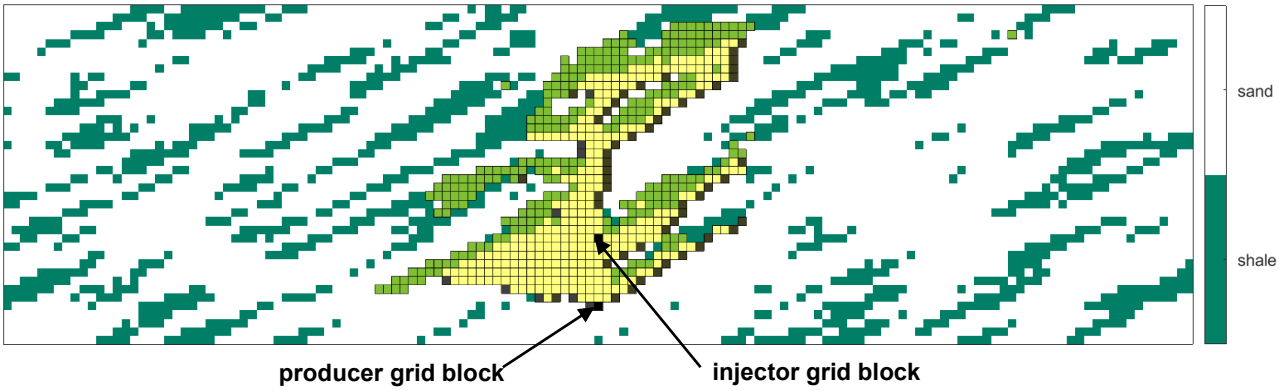

(a) Vapor-phase saturation map in n-C_6 SAGD for realization 17

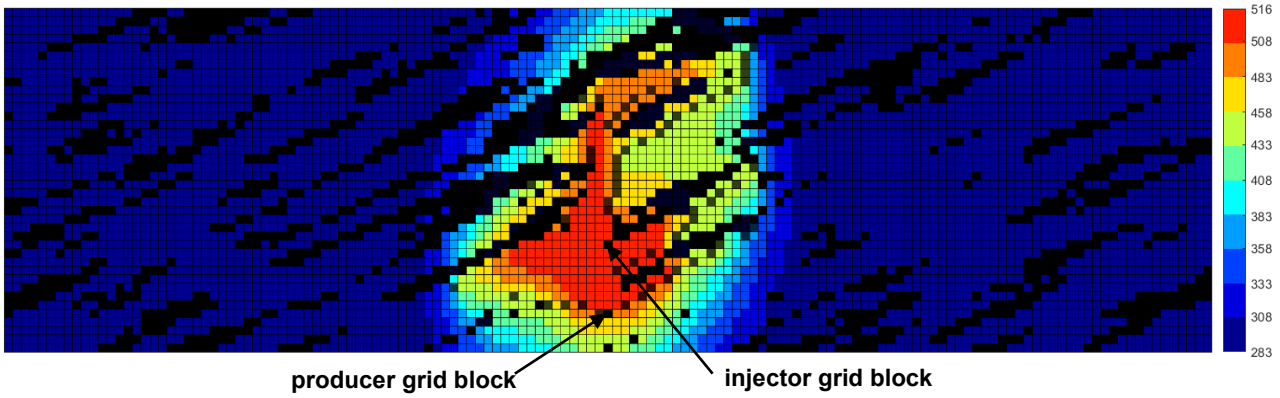

(b) Distribution of temperature (in Kelvin) in clean sand grid blocks in n-C_6 SAGD for realization 17

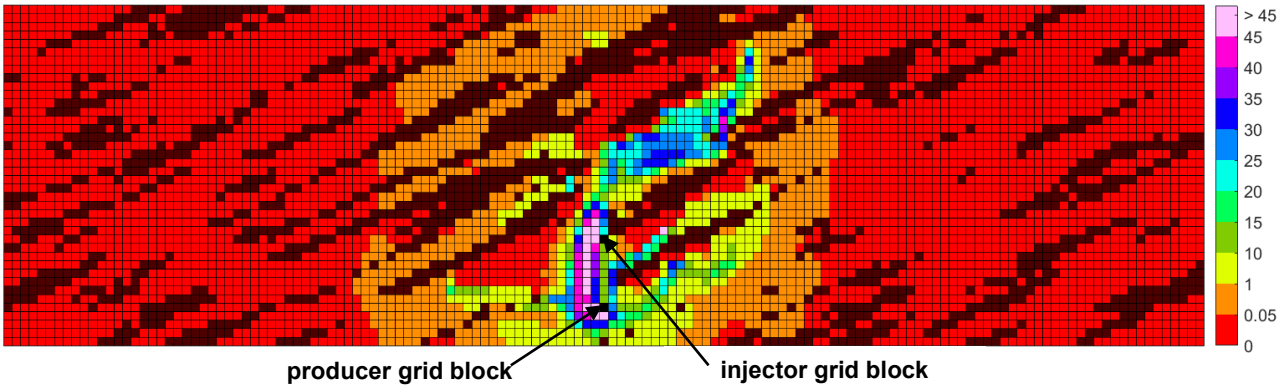

(c) Distribution of bitumen molar flow rate (kg-mole/day) in clean sand grid blocks in n-C_6 SAGD for realization 17

Figure 4.9. Continued below.

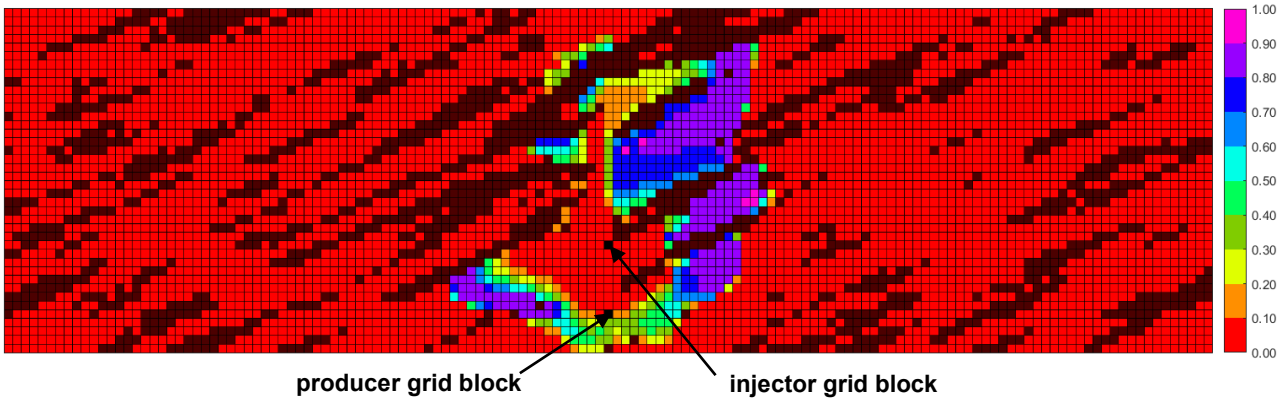

(d) Distribution of mole fraction of solvent in oleic phase (x_{sL}) in clean sand grid blocks in n-C_6 SAGD for realization 17

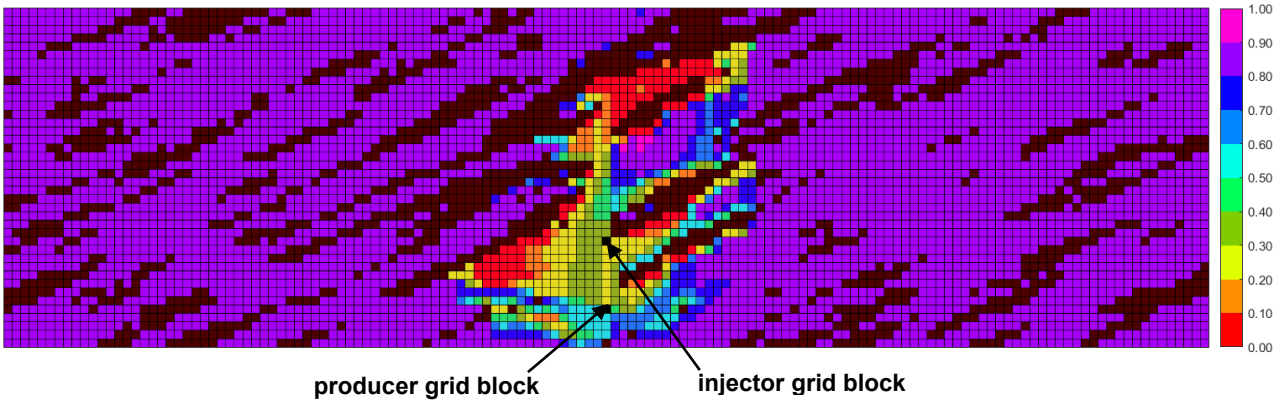

(e) Oleic-phase saturation distribution in clean sand grid blocks in n-C_6 SAGD for realization 17

Figure 4.9. Simulated property maps in n-C_6 SAGD for realization 17 case for the cumulative bitumen production of approximately 31218 m^3; (a) vapor-phase saturation; (b) temperature in clean sand grid blocks (in Kelvin); (c) molar flow rate of bitumen in clean sand grid blocks (in kg-mole/day); (d) x_{sL} in clean sand grid blocks; (e) oleic-phase saturation in clean sand grid blocks. In parts (a) and (b), grid blocks along the chamber edge are indicated in brown. Where the dilution of bitumen by solvent is significant [see part (d)], the molar flow rate of bitumen is locally enhanced [compare part (c) with Figure 4.8c] by the combination of lower oleic-phase viscosity and higher oleic-phase saturation [compare part (e) with Figure 4.8e].

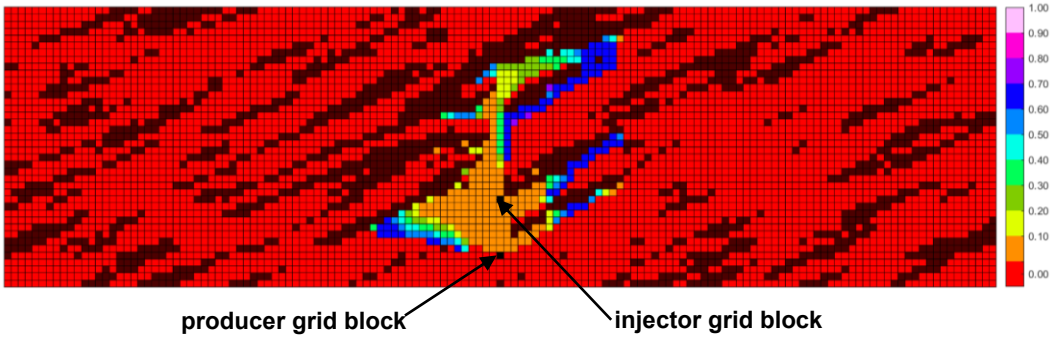

(a) Distribution of x_{sv} within clean sand grid blocks for the cumulative bitumen production of approximately 31218 m^3

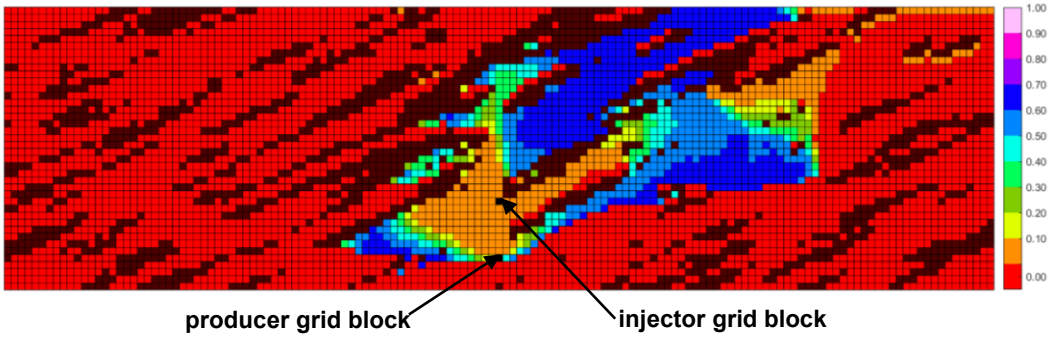

(b) Distribution of x_{sv} within clean sand grid blocks for the cumulative bitumen production of approximately 86124 m^3

Figure 4.10. Distribution of mole fraction of solvent in the vapor phase (x_{sv}) in clean sand grid blocks for realization 17 as a function of cumulative bitumen production (Q); (a) Q = 31218 m^3; (b) Q = 86124 m^3. Accumulation of the solvent in the vapor phase near the chamber edge reduces the temperature at which the vapor phase condenses [also see Figures 4.9b and 4.11ab]. Reduction in thermal losses to the overburden due to coinjection of solvent relative to steam-only injection is greater under heterogeneity compared to that under homogeneity due to lower operating-chamber temperatures.

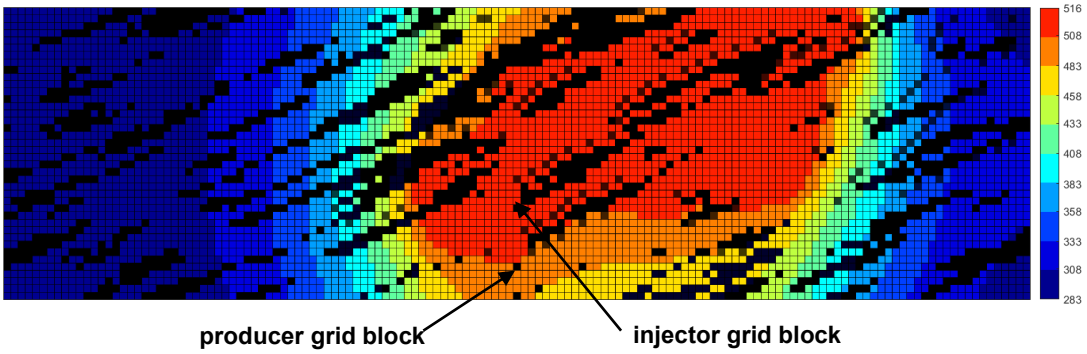

(a) Distribution of temperature (in Kelvin) in clean sand grid blocks in SAGD for realization 17

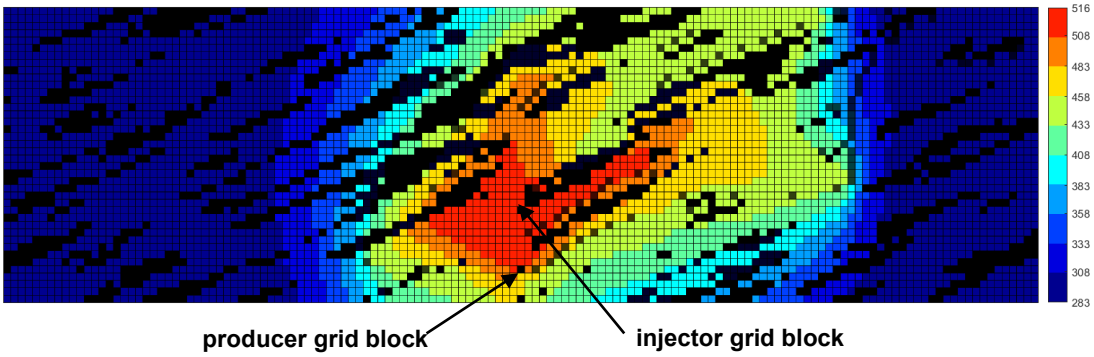

(b) Distribution of temperature (in Kelvin) in clean sand grid blocks in n-C_6 SAGD for realization 17

Figure 4.11. Distribution of temperature in clean sand grid blocks in SAGD and n-C_6 SAGD for realization 17 for the cumulative bitumen production of approximately 86124 m^3.

Chapter 5. Conclusions, Discussion and Future Work

This research attempted to address three hitherto unanswered questions of engineering significance using numerical reservoir simulation: (i) whether and how the consideration of the dissolution of water in the oleic phase (x_{wL}) could potentially enhance the recovery performance of bitumen in SAGD and ES-SAGD in a homogeneous reservoir, and its effect on the relative performance of ES-SAGD to SAGD; (ii) if ES-SAGD (i.e., n-C_6 SAGD) could potentially be a better alternative to SAGD in terms of the cumulative steam-oil ratio for a given cumulative bitumen production in simple synthetic heterogeneous reservoirs, and (iii) conditions of flow under reservoir heterogeneity conducive to significant reduction of cumulative SOR under steam-solvent coinjection with n-C_6. To our knowledge, this is the first study to address these topics in the context of bitumen recovery and stochastically distributed heterogeneity (for Chapters 3 and 4).

The objective of this chapter is three-fold: (i) summarize the key findings of this research on a chapter-basis (Section 5.1); (ii) present additional discussions on aspects that were not within the original scope of the investigations presented in Chapters 2 through 4 (Section 5.2); and (iii) identify potential directions for future research (Section 5.3).

5.1. Summary, Conclusions and Application

Chapter 1 presented the motivation for this research. SAGD is currently the most widely-used in-situ technique for the recovery of bitumen, and has several advantages over its predecessors. However, elevated steam-oil-ratios accompanying its implementation in highly heterogeneous formations is an important cause for concern. ES-SAGD is an attractive alternative to SAGD as it retains many of the advantages of SAGD, and can potentially lower the SOR through the simultaneous acceleration of oil drainage rate, and reduction of operating-chamber temperatures. However, the greater cost of solvent relative to the price of bitumen necessitates a detailed examination of the underlying mechanisms, and the influence of geological architecture on these mechanisms prior to implementation in the field.

Chapter 2 demonstrated that the dissolution of water in the oleic phase can act as a compositional mechanism in both SAGD and ES-SAGD in a homogeneous reservoir. On the basis of simulations conducted at 35 bars, it was shown that the main mechanism by which the cumulative bitumen production was enhanced in SAGD and ES-SAGD due to x_{wL} is through the

reduction of the oleic-phase viscosity; temperature profiles indicated that the distribution of temperature near the chamber edge is not significantly altered when x_{wL} is considered.

At 35 bars, the average margin by which the cumulative bitumen production is enhanced in SAGD was calculated to be close to 10%, while that for n-C_6 SAGD was estimated to be about half as much. This discrepancy is the result of higher operating-chamber temperatures in SAGD compared to n-C_6 SAGD. Since the extent to which x_{wL} improves bitumen production is greater for SAGD relative to n-C_6 SAGD due to greater operating-chamber temperatures, its consideration was deemed necessary to ensure reliable comparison between the two processes especially at elevated operating pressures.

Further, the extent to which x_{wL} enhances bitumen production was demonstrated to be sensitive to the mixing model used to predict the oleic-phase viscosity. The simulated improvement in cumulative bitumen production in SAGD due to x_{wL} was shown to increase from around 10% for the linear mixing model to around 30% under the logarithmic mixing model at the operating pressure of 35 bars. Lastly, it was demonstrated that x_{wL} could be leveraged to enhance the production rate of bitumen over the short term by initially operating the process at higher pressures.

Chapter 3 examined the effects of reservoir heterogeneity on the relative performance of n-C_6 SAGD to SAGD in terms of the cumulative SOR as a function of cumulative bitumen production in simple 2-D heterogeneous reservoirs comprising of clean sand and mudstone. For the operating pressure of 35 bars and injection concentration of 2 mol%, the SOR of ES-SAGD was shown to be less sensitive to heterogeneity compared to that of SAGD for a given cumulative bitumen production regardless of the inclination of mudstone barriers.

For these simple cases and operating conditions, the accumulation of solvent for a given cumulative bitumen production was simulated to be higher under heterogeneity compared to that under homogeneity. This in turn is accompanied by a larger areal span of regions with elevated x_{sL} (exceeding 80 mol%) for the heterogeneous cases.

Improved solvent-bitumen mixing under heterogeneity increases the extent to which the drainage rate of the oleic phase is accelerated due to n-C_6 coinjection, while the interplay between solvent-bitumen mixing and temperature facilitates greater reduction of operating-chamber temperatures. The combination of these facets result in a larger margin of SOR reduction under coinjection for the heterogeneous cases. Use of finer grid blocks (size-reduction

by a factor of 8), and consideration of spatial variation of facies along the well-pair direction (i.e., 3-D variant of realization 16 with inclined flow barriers) did not qualitatively alter this observation.

The margin of SOR reduction due to coinjection of n-C_6 was observed to be higher under inclined mudstone barriers. For instance, the average cumulative SORs for SAGD and ES-SAGD for the cumulative bitumen production of 109398 m^3 respectively are 7.28 and 4.38 for heterogeneous models with horizontal barriers, and 8.18 and 4.59 for those with inclined flow barriers. The potential effectiveness of a time-variant injection concentration strategy in terms of reduction of solvent retention over the long term was demonstrated for a single heterogeneous case (realization 17 with inclined barriers).

In Chapter 4, the stochastically-generated heterogeneous realizations with inclined mudstone barriers from Chapter 3 were characterized in terms of their potential to yield significant reduction in SOR under the coinjection of n-C_6. The injection-concentration of 2 mol% and pressure of 35 bars was used in simulations.

The reduction in SOR due to coinjection was demonstrated to exhibit a statistically significant correlation with the increase in SAGD's SOR due to heterogeneity. Over the cumulative bitumen production range of 19000 – 95000 m^3, the pertinent Spearman's rank correlation coefficients were consistently observed to be greater than 0.85 with near-zero p-values. The average reduction in cumulative SOR as a result of coinjection is at least 2.0 when the average increase in SAGD's SOR due to heterogeneity exceeds 2.45 over this range of cumulative bitumen productions at these operating conditions.

In heterogeneous reservoirs that yield high SORs for SAGD, local accumulation of solvent in the oleic phase under steam-solvent coinjection is observed to be pronounced in heated slow-flow regions within which the transport of bitumen is inefficient under steam-only injection. Occurrence of such heated slow-flow regions is attributed to (i) the restriction of local bitumen flow by permeability barriers through the increase of tortuosity of flow paths, and diminished oleic-phase relative permeability due to greater local flow of the aqueous phase near the chamber edge under heterogeneity. Elevated values for x_{sL} (greater than 70 mol%) coupled with high temperatures in such regions facilitates significant improvement of the mobility of the oleic phase through (i) considerable reduction of kinematic viscosity of the oleic phase, and (ii) improvement of oleic-phase relative permeability by enhancement of its saturation. The

interplay solvent-bitumen mixing and temperature further mitigates conductive heat losses to the overburden. These in turn improve the margin of SOR reduction.

The findings of this research could facilitate the development of application strategies for ES-SAGD under actual reservoir conditions. Presented below, is a simple workflow for practical application of ES-SAGD at the well-pair scale:

i. Rigorous geostatistical reservoir modeling on the basis of well-derived data. Typically, well-log data serve as high-resolution data for geostatistical modeling and are on the order of decimeters. The length scale of flow simulation grid blocks is in meters. So, for proper petrophysical modeling at the volume support of flow simulation grid blocks, minimodels at the volume support of the highest resolution data must be constructed, and subsequently upscaled. Dynamic (or flow-based) upscaling is a common approach; it is preferable if the upscaling approach accounts for the actual nature of flow (e.g., multiphase flow, displacement/drainage etc.) that is expected to occur within the reservoir when a specific process is implemented.

ii. P-V-T analysis and characterization of bitumen using an EOS. If the solvent to be used is also a reservoir fluid, then it too must be characterized on the basis of P-V-T experiments.

iii. Compositional modeling of water/solvent/bitumen on the basis of available experimental data. That is, BIPs for solvent/water, bitumen/water, and solvent/bitumen systems must be developed on the basis of phase equilibrium measurements.

iv. Measurement and modeling of oleic-phase viscosity at operating conditions.

v. Consideration of 100 realizations could be sufficient. Perform SAGD simulations for all realizations, and ES-SAGD simulations for a fraction of the total number of realizations (perhaps 30 realizations) for a pertinent operating pressure inferred based on the geological setting of the reservoir. Simulations should also be conducted for a hypothetical homogeneous reservoir whose petrophysical attributes is representative of the petrophysical properties of the net (or clean sand) facies of the heterogeneous reservoir model. The injection concentration of solvent can be held constant for this set of simulations (i.e., CC strategy can be used).

vi. Establishment of a correlation between the increase in SOR for SAGD due to heterogeneity and reduction in SOR due to coinjection of solvent.

vii. For a specified cumulative bitumen production target, estimate a threshold for the increase in SAGD's SOR due to heterogeneity beyond above which the reduction in SOR due to coinjection of solvent is significant (e.g., 2.0). Identify realizations for which the increase in SAGD's SOR due to heterogeneity exceeds the estimated threshold. Subsequently, group realizations in terms of the similarity of their SOR; there should be at least two realizations within each group.

viii. For at least two realizations in each group, develop a time-variant injection concentration strategy for SAGD that yields the best performance in terms of the cumulative SOR for a specified cumulative bitumen production target, and economics.

ix. Based on the results from the previous step (i.e., step viii), infer a potentially feasible application strategy for ES-SAGD in terms of the sequence of injection concentrations for the reservoir under consideration and the preferred operating pressure.

5.2. Additional Topics of Discussion

5.2.1. Effects of x_{wL} on SAGD and ES-SAGD under heterogeneity

The key conclusions of Chapter 2 are observed to be qualitatively preserved even under heterogeneity. To illustrate this, results of SAGD and n-C_6 SAGD simulations conducted for realizations 16 and 17 from the second case study of Chapter 3 [Section 3.2.2 (inclined mudstone barriers)] are presented. Realizations 16 and 17 are chosen for this sensitivity analysis as the reduction in SOR due to coinjection of solvent exceeds 2.0 under significantly large steam-chamber volumes (see Chapter 3). The linear mixing model is used to predict the oleic-phase viscosity (also see Chapter 2 and Appendix C).

Figure 5.1 presents the simulated histories for cumulative bitumen production for the base (i.e., x_{wL} = 0) and water-dissolution cases for SAGD and n-C_6 SAGD for the homogeneous reservoir and realizations 16 and 17. **Figure 5.2** presents the accompanying SOR for each case and reservoir. As with the homogeneous case, when x_{wL} is considered for the heterogeneous cases, the performance of SAGD is predicted to be improved to a greater extent than that for n-C_6 SAGD both in terms of the time taken to meet a given cumulative bitumen production, and the accompanying cumulative SOR. An interesting distinction between the homogeneous and heterogeneous cases is that the extent to which the production rate of bitumen and cumulative SOR in SAGD is improved as a result of x_{wL} could potentially be higher under heterogeneity than that under homogeneity. This is mainly because of the occurrence of high-temperature

regions with diminished local bitumen flow. As illustrated in Chapter 4, local transport of bitumen in SAGD can be significantly hindered when the vapor phase in SAGD condenses near a large flow barrier even when the local temperatures are comparable to the saturation temperature of water at the operating pressure (for example, see Figure 4.8). In such high-temperature regions, a considerable amount of water can potentially dissolve in the oleic phase. This in turn can enhance its mobility through the reduction of its viscosity thereby leading to greater production of bitumen.

5.2.2. Economic performance of the simple simulation cases in Chapter 3

In Chapter 3, the effect of heterogeneity on the relative performance of ES-SAGD to SAGD in terms of economics was not examined. Reliable economic evaluation of ES-SAGD and SAGD under heterogeneity necessitates conducting numerical simulations in 3-D geological models conditioned by primary (i.e., well-derived) and secondary (e.g., seismic) data. Further, the simulator in use must be robust enough to provide numerical convergence over the entire simulation period.

The reservoir models used in this research are synthetic, and mainly 2-D. The obtainment of numerical convergence over the entire simulation period of ten years also proved to be difficult due to the coupling of an advanced phase behavior model with a reservoir model with extreme variations in petrophysical properties (mainly absolute permeability) over short length scales. Nevertheless, a simple economic analysis in terms of the net present value (NPV) is conducted in this section for selected reservoirs from the second case study of Chapter 3 (see Chapter 3.2.2). The following cases are considered for this analysis:

1. SAGD and n-C_6 SAGD for the homogeneous reservoir model for the operating pressure of 35 bars and solvent injection-concentration of 2 mol% [i.e., constant injection-concentration strategy (CC)].
2. SAGD and n-C_6 SAGD for the 2-D heterogeneous reservoirs labelled realizations 16 and 17 for the operating pressure of 35 bars and solvent injection-concentration of 2 mol%.
3. SAGD and n-C_6 SAGD for realization 17 for the operating pressure of 35 bars, and a time-variant injection concentration (VC) strategy with the following time-sequence of injection concentrations: (i) 10 mol% for the first four months of production; (ii) 5 mol% for months four through eight; (iii) 2 mol% for months eight through twelve; (iv) steam-only injection beyond the first year of production.

4. SAGD and n-C_6 SAGD for the 3-D variant of realization 16 for the operating pressure of 35 bars and injection concentration of 2 mol%. As explained in **Appendix H**, the 3-D variant of realization 16 is generated by creating alternating sequences of homogeneous and heterogeneous x-z cross-sections along the y-coordinate (i.e., well-pair direction).

The NPV for n-C_6 SAGD can be calculated as follows (Deng, 2005),

Net Present Value (NPV) [USD] = (cumulative oil x oil price) x (1.0 - discount rate) [USD]
- capital cost of exploration
- capital cost of well pair [USD]
- water treatment equipment [USD]
- steam generator cost [USD]
- capital cost of solvent distribution [USD]
- administration and head office [USD]
- blending and transportation [USD]
- production years x well pair and field operation [USD/yr]
- production years x solvent handling [USD/yr]
- cumulative steam injection [m^3 CWE] x (generator operation [USD/m^3 CWE] + fuel cost [USD/m^3 CWE])
- cumulative water production [m^3] x treatment of production water [USD/m^3]
- (cumulative solvent injection [m^3] - cumulative solvent production [m^3]) x solvent price [USD/m^3]. (5.1)

Equation 5.1 can be used to calculate the NPV for SAGD after disregarding the capital costs associated with solvent distribution, and costs associated with solvent handling and accumulation. **Table 5.1** presents the input parameters for the NPV calculations.

Figure 5.3 captures the effect of heterogeneity (i.e., 2-D heterogeneity) on the economic performance of SAGD and n-C_6 SAGD under the CC strategy. Figures 5.3a and 5.3b respectively depict the NPV and cumulative bitumen production histories. **Figure 5.4ab** respectively visualize the effect of implementing the aforementioned VC strategy for realization 17 on the NPV and cumulative bitumen production histories of n-C_6 SAGD. **Figure 5.5ab** respectively compare the NPV and cumulative bitumen production histories of SAGD and n-C_6

SAGD under the CC strategy for the 2-D and 3-D variants of realization 16. The price of bitumen and cost of solvent used in the calculations pertaining to Figures 1 through 3 are 35 USD/bbl (CAPP, 2015) and 78 USD/bbl (Platts, 2016), respectively. **Figures 5.6 through 5.8** present the effect of a 30% reduction in solvent cost (i.e., 55 USD/bbl) on the NPV and cumulative bitumen production histories. The following can be inferred on the basis of Figures 5.3 through 5.8:

- For the homogeneous case, the coinjection of solvent under the CC strategy enhances the production rate of bitumen while lowering the SOR (Figure 5.3b). In addition to this, the economic performance of n-C_6 SAGD under the CC strategy is better than that for SAGD prior to the influence of the lateral boundaries on steam-chamber expansion (Figure 5.3a). The recovery factor of bitumen exceeds 70% by the time the lateral boundaries begin to interfere with the expansion of the n-C_6 SAGD steam chamber; so beyond this time, the coinjection of solvent with steam is not necessary.

- Coinjection of solvent under the CC strategy results in a greater reduction in SOR for the heterogeneous case than that for the homogeneous case due to improved solvent-bitumen mixing and the interplay between solvent-bitumen mixing and temperature. However, Figure 5.3a indicates that greater retention of solvent in-situ under heterogeneity can render the economic performance of n-C_6 SAGD to be inferior to that for SAGD. This suggests that the practical significance of implementing a VC strategy in steam-solvent coinjection is enhanced under heterogeneity. Figure 5.4a shows that the economic performance of n-C_6 SAGD under the VC strategy approaches closer to that of SAGD over time and could perhaps exceed it if numerical convergence could be obtained for times beyond that indicated in Figure 5.4a.

- The 2-D heterogeneity cases, wherein spatial variation of facies along the well-pair direction is ignored, represent an extreme limit in terms of economic performance. Excessive retention of solvent later in the production phase is mitigated when additional hydraulic paths for flow in the direction of the well-pair become available (i.e., under 3-D heterogeneity). This in turn facilitates the improvement of the economic performance of n-C_6 SAGD. The economic performance of n-C_6 SAGD can be comparable to that of

SAGD under 3-D heterogeneity even with the CC strategy (see Figure 5.5a). The NPV of n-C_6 SAGD in the 3-D variant of realization 16 could potentially be significantly greater than that of SAGD if the VC strategy were to be implemented.

– The relative performance of n-C_6 SAGD to SAGD in terms of economics is highly sensitive to the difference between the price of bitumen and cost of solvent (compare Figure 5.6a with 5.3a, Figure 5.7a with 5.4a, and Figure 5.8a with 5.5a).

Use of a single-component normal alkane solvent like n-C_6 in field application of ES-SAGD is unlikely in view of the significant volume of solvent required for coinjection with steam, and the high costs associated the production of n-C_6 (i.e., synthesis and purification). To lower costs, the solvent in use would most likely be a reservoir fluid (e.g., condensate or naphtha). If the cost of the solvent mixture is at least 30% of that of n-C_6, and yields a production performance that is comparable to that obtained using n-C_6, then ES-SAGD (with a suitable VC strategy) could likely be a superior alternative to SAGD in heterogeneous reservoirs both in terms of the steam-oil-ratio and economics over the long term.

5.2.3. Effects of overburden properties on simulation results for SAGD and n-C_6 SAGD

The top, bottom and lateral boundaries of the homogeneous and heterogeneous reservoir models are no-flow boundaries. However, conductive heat loss to the overburden and underburden is considered. The reservoir models in use are synthetic and have not been rigorously conditioned using measurements conducted in the McMurray formation. The thermal conductivities of the overburden and underburden were set to 660 kJ/day-^{o}C, and were obtained from published literature (Butler, 1997; Keshavarz et al., 2014).

Chapters 3 and 4 demonstrated that mixing between solvent and bitumen is improved under heterogeneity, and the interplay between solvent-bitumen mixing and temperature facilitates the obtainment of lower operating-chamber temperatures. As a result, the margin by which heat losses to the overburden are reduced due to coinjection of solvent is greater under heterogeneity. Improved reduction in SAGD's SOR due to coinjection of solvent in heterogeneous reservoirs is partially due to this mechanism.

This section demonstrates that the relative performance of n-C_6 SAGD to SAGD in terms of the cumulative SOR for a given cumulative bitumen production is sensitive to the overburden and underburden thermal conductivities. Specifically, the margin by which the cumulative SOR

is reduced as a result of coinjection decreases when the thermal conductivities of the overburden and underburden are lowered.

For the reservoir models in the second case study of Chapter 3 (Section 3.2.2), Table 3.8 (Chapter 3) presented the range of SORs in SAGD and n-C_6 SAGD for the cumulative bitumen production of 54699 m^3. The average increase in SOR due to heterogeneity was reported to be 3.90 for SAGD and 2.27 for n-C_6 SAGD. The average reduction in SOR due to coinjection of solvent for the heterogeneous cases is 2.71 and that for the homogeneous case is 1.08.

Table 5.2 presents the pertinent SORs for each process for the aforementioned cumulative bitumen production when the overburden and underburden thermal conductivities are set to 110 kJ/day-^oC (i.e., for a six-fold reduction). The average increase in SOR due to heterogeneity for this case is calculated to be 2.60 for SAGD and 1.80 for n-C_6 SAGD. The average reduction in SOR due to coinjection of solvent for the heterogeneous cases is 1.59 and that for the homogeneous case is 0.76. That is, the average reduction in SOR due to coinjection of solvent under heterogeneity is diminished by approximately 41% for this cumulative bitumen production for a six-fold reduction in overburden and underburden thermal conductivities. **Figure 5.9** visualizes the distribution of the simulated reduction in SOR due to coinjection of solvent across different realizations under the two scenarios for this cumulative bitumen production. Further, for a given realization, the extent to which the time taken to meet a given cumulative bitumen is reduced as a result of coinjection of n-C_6 is observed to be lower when the thermal conductivity is reduced as presented in **Table 5.3**.

5.2.4. Other solvents for use in ES-SAGD in heterogeneous reservoirs

Effectiveness of ES-SAGD is contingent upon three facets: (i) accumulation of solvent near the steam-chamber edge; (ii) oleic-vapor-aqueous to oleic-aqueous phase transition at the chamber edge; (iii) interplay between temperature and dilution capability of solvent. The experimental investigation of Brunner (1990) on the phase behavior of binary mixtures of water and n-alkanes clearly demonstrates that the oleic-vapor-aqueous to oleic-aqueous phase transition temperatures increase monotonically with the carbon number of the n-alkane for a given pressure. So, the operating-chamber temperatures in ES-SAGD are higher when heavier solvents are used (Keshavarz et al., 2015). However, the dilution capability of solvent diminishes as the solvent becomes heavier.

Mitigation of solvent retention later in the production phase is a priority from an economic standpoint. So, at some stage in the production phase, a switch from steam-solvent coinjection to steam-only injection is necessary to facilitate the vaporization of dissolved solvent in the oleic phase from stagnant-flow regions from the reservoir. Hence, it is preferable if the saturation temperature of the solvent is lower than the saturation temperature of water at the operating pressure. At the operating pressure of 35 bars, the saturation temperature of water is 515.72 K. The heaviest n-alkane that fulfills this criterion at 35 bars is n-C_6; it's saturation temperature is approximately 506 K at this pressure.

For a homogeneous reservoir, Chapter 2 showed that the bitumen-recovery performance of n-C_5 SAGD and n-C_6 SAGD at 35 bars are comparable, with the average yearly production rate of bitumen slightly greater under n-C_6 compared to n-C_5 earlier in the production phase. Also, the production performance of C_3-SAGD is observed to be consistently inferior to that of SAGD [see Chapter 2 and also Keshavarz et al. (2015)]. So, the only other potential alternative to n-C_6 besides n-C_5 for the recovery of bitumen using ES-SAGD with single-component n-alkane solvents at the operating pressure of 35 bars is n-C_4.

Simulations for n-C_4 SAGD were conducted at this operating pressure for realizations 16 and 17 from the second case study in Chapter 3 (Section 3.2.2). **Figure 5.10** presents the simulated cumulative bitumen production histories for SAGD, n-C_4 SAGD and n-C_6 SAGD for these realizations; **Figures 5.11 and 5.12** respectively give the cumulative SOR and solvent accumulation as a function of cumulative bitumen production. The discernment of medium and long term trends in the production performance of n-C_4 SAGD proved to be difficult due to lack of numerical convergence. As with the homogeneous case discussed in Chapter 2, Figure 5.10 indicates the production rate of bitumen in n-C_6 SAGD to be systematically greater than that in n-C_4 SAGD for these realizations until the time at which convergence could be achieved. The accompanying cumulative SOR and solvent accumulation can also be higher under n-C_4 SAGD (see Figure 5.11a and Figures 5.12ab). The rather limited snapshots presented in this section suggest n-C_6 to be a better choice for solvent compared to n-C_4 for the operating pressure of 35 bars for the simple heterogeneous reservoirs considered in this research.

5.2.5. Discussion on initial aqueous-phase mobility

In the simulations conducted thus far, the initial (or connate) saturation of the aqueous phase (S_{Wc}) was set equal to the irreducible saturation (S_{Wirr}); this renders the aqueous immobile at

initial conditions. However, prior experimental studies on the measurement of phase relative permeabilities both in fresh cores comprising of heavy oil and water and heavy-oil-water systems in physically simulated porous media have challenged this assumption (Maini and Batycky, 1985; Chan et al., 2012).

Zhou et al. (2015) measured the mobility of the aqueous phase at its connate saturation in a sand pack comprising of paraffin wax and water. At temperatures lower than 294 K (i.e., 21 ºC), the wax becomes immobile; so, at low temperatures, the wax-water system, qualitatively represents the bitumen-water system in terms of the difference in the viscosities of the wetting and non-wetting phases. In these experiments, the aqueous phase was observed to be mobile even under saturations as low as 5%. The aforementioned observations warrant the examination of whether and how the mobility of the aqueous phase at its connate saturation affects the performance of SAGD.

Osakouei and Maini (2012) conducted an experimental study on the effects of initial aqueous-phase mobility on SAGD. The recovery factor of bitumen reduced by 6.6% when the initial aqueous-phase saturation increased from 14.8 to 31.8%. The accompanying SOR increased by two-fold. The experimental study used superheated steam injected at 518 K (246 ºC) and 35.50 bars.

Alvarez et al. (2014) examined the sensitivity of the performance of SAGD to the initial aqueous-phase saturation in a homogeneous reservoir at 40 bars using numerical simulations. The irreducible aqueous-phase saturation was set to 0.13, while the maximum aqueous-phase saturation considered in the sensitivity study was 0.30. The production rate declined as the initial aqueous-phase saturation increased. Further, vertical growth of the steam chamber was accelerated under elevated values for the initial aqueous-phase saturation, which led to distinctions in the geometry of the steam chamber at a specified time in the production phase. During the spreading phase, the simulated steam chamber is wider near the top of the model when the initial aqueous-phase saturation is higher. Consequently, the exposed area of the steam-chamber for conductive heat transfer to the overburden is also increased.

Zhou et al. (2016) conducted a SAGD simulation study in a laterally unconfined homogeneous bitumen reservoir at 21 bars. The performance of SAGD was demonstrated to be adversely affected under moderate to high increments in the initial aqueous-phase saturation

relative to the irreducible aqueous-phase saturation of the medium (i.e., $S_{Wc} - S_{Wirr} \geq 0.10$); the value of 0.15 was used for the irreducible aqueous-phase saturation in their simulations.

Gradients in pressure between the steam-chamber boundary and the unswept region of the reservoir can drive lateral movement of the aqueous phase if it is mobile at initial conditions. Further, the preferential expansion of the steam chamber near the top of the model under elevated initial aqueous-phase saturations results in increased conductive heat losses to the overburden. Consequently, a larger volume of aqueous phase tends to flow near the chamber edge when the discrepancy between the initial and irreducible aqueous-phase saturation is significant. The flow of the heated aqueous phase near the chamber edge can facilitate convective heating of the bitumen. However, the thickness of heated bitumen potentially available for flow can also be reduced when a significant volume of the aqueous phase flows near the chamber edge due to the reduction of the relative permeability of the oleic phase. This in turn detrimentally affects the production rate of bitumen and the accompanying steam-oil ratio.

While the effects of initial aqueous-phase mobility on the performance of ES-SAGD have not yet been published, it is conceivable that the production rate of bitumen and cumulative SOR in steam-solvent coinjection would respectively decrease and increase when the discrepancy between the initial and irreducible aqueous-phase saturations is significant. However, the sensitivity of these attributes to the initial aqueous-phase saturation could be potentially be lower for ES-SAGD. This is because: (i) the dilution of bitumen by solvent can improve the drainage rate of the oleic phase through both the reduction of the oleic-phase viscosity, and the enhancement of the oleic-phase relative permeability, as the solvent is less dense than bitumen; and (ii) reduction in operating-chamber temperatures due to steam-solvent coinjection lowers conductive heat losses to the overburden.

Detailed examination of the effects of the initial aqueous-phase mobility on the performance of SAGD and ES-SAGD is beyond the scope of this research. Nevertheless, a simple sensitivity analysis is conducted to observe the effect of a moderate increase in the initial aqueous-phase saturation on a key conclusion of this study, that the margin by which the cumulative SOR is reduced due to coinjection of solvent for a given cumulative bitumen production can be higher under heterogeneity than that under homogeneity. To this end, simulations for SAGD and n-C_6 SAGD under the operating pressure of 35 bars for the homogeneous reservoir model and

realizations 16 and 17 are conducted for the initial and irreducible aqueous-phase saturations of 0.25 and 0.15, respectively.

Figures 5.13 and 5.14 respectively present the simulated bitumen production histories for SAGD and n-C_6 SAGD and the accompanying cumulative SOR for the homogeneous reservoir and realizations 16 and 17. Numerical convergence over the entire simulation period of ten years could not be obtained for the heterogeneous n-C_6 SAGD simulations regardless of the choice of value for the initial aqueous-phase saturation. For realization 17, the lack of numerical convergence is observed to be exacerbated with an increase in the initial aqueous-phase saturation. **Figure 5.15** presents the deviation in cumulative bitumen production relative to the case in which the aqueous phase at initial conditions is immobile as a function of time for each process and reservoir type. **Figure 5.16** presents the reduction in cumulative SOR due to coinjection of solvent as a function of cumulative bitumen production for each reservoir type and case.

Figure 5.13 indicates that the production rate of bitumen diminishes when the initial aqueous-phase saturation (0.25) moderately exceeds the irreducible aqueous-phase saturation (0.15) for both SAGD and n-C_6 SAGD leading to an increase in the accompanying cumulative SOR (see Figure 5.14). However, prior to the influence of the impermeable lateral boundaries of the reservoir on the lateral expansion of the steam chamber, the margins by which the cumulative bitumen production is reduced due to a moderate increase in the initial aqueous-phase saturation is on average lower for n-C_6 SAGD compared to that for SAGD (Figure 5.15). This is likely because the reduction in the oleic-phase permeability due to increased flow of the aqueous phase near the chamber edge is lower for n-C_6 SAGD compared to SAGD due to the dissolution of the solvent in the oleic phase under steam-solvent coinjection.

Figure 5.16 shows that the reduction in cumulative SOR due to coinjection of solvent is more pronounced under heterogeneity even the aqueous phase is mobile under initial conditions. The increase in the reduction of the cumulative SOR due to coinjection of solvent under heterogeneity could potentially be higher when the aqueous phase is initially mobile because of the greater sensitivity of SAGD's SOR to the initial aqueous-phase saturation compared to that for n-C_6 SAGD.

It is important to note that the boundaries of the reservoir model used in this sensitivity study do not permit the transport of mass. Zhou et al. (2016) indicate that the simulated effects of the

initial aqueous-phase saturation on the performance of SAGD can be sensitive to whether the reservoir is laterally confined. Detailed investigation of the sensitivity of the relative performance of ES-SAGD to SAGD to the initial aqueous-phase mobility in a laterally unconfined reservoir is potentially a topic for future study.

5.2.6. Discussion on effects of formation compressibility on ES-SAGD simulations

Detailed investigation of the effects of geomechanical phenomena on the relative performance of ES-SAGD to SAGD under homogeneity and heterogeneity are beyond the scope of the current research. Nevertheless, a simple sensitivity study on the effect of a three-fold increase in formation compressibility (from 1.8×10^{-5} 1/kPa to 5.4×10^{-5} 1/kPa) on the relative performance of n-C_6 SAGD to SAGD for the homogeneous reservoir model and realization 17 from the second case study of Chapter 3 (Section 3.2.2) is conducted. **Figure 5.17** presents the simulated cumulative bitumen production histories and accompanying cumulative SOR for each case and reservoir type. The simulated production rate of bitumen is lower when the compressibility of the formation is increased due to a reduction in porosity. The conclusion that the reduction in SOR due to coinjection of solvent can be pronounced under heterogeneity relative to that under homogeneity is still qualitatively preserved under the aforementioned perturbation in formation compressibility.

5.3. Future Work

Conducting flow simulations for SAGD and n-C_6 SAGD inevitably requires the use of several simplifying assumptions. This mainly stems from the simultaneous occurrence of multiple physical phenomena in steam-injection and steam-solvent coinjection, and the complex interplay between them. Capturing all physical phenomena at all length scales in flow simulations is rendered challenging due to the following realities:

- Paucity of reliable experimental data to model certain physical phenomena (e.g., oleic-phase viscosity, phase-specific relative permeabilities)
- Lack of availability of computationally efficient modeling frameworks to reliably predict certain physical processes (e.g., asphaltene precipitation).
- Occurrence of heterogeneities at practically all length scales, which challenges the notion of a representative elementary volume (Deutsch, 2010). Further, the non-linear increase in computational time accompanying the reduction in the size of grid blocks used in

simulations coupled with the necessity to conduct flow simulations over large reservoir volumes constrains the lower bound for the grid block size that can be used in practice. This introduces numerical dispersion in simulation results.

- Inherent shortcomings of simulation frameworks. For example, the K-value-based framework employed in STARS permits simultaneous flow of up to two liquid phases. Further, the coupling of an advanced phase behavior model with reservoir models that exhibit extreme variations in permeability over short length scales can lead to lack of numerical convergence of ES-SAGD simulations. In this case, inclusion of another physical phenomenon (e.g., asphaltene precipitation) could potentially exacerbate the issue of obtaining numerical convergence.

The majority of flow simulations conducted in this research are two-dimensional. That is, variations in petrophysical properties along the direction of the well-pair are ignored. In addition to this, the following simplifications were used:

i. The coupled mass and energy conservation equations were solved by setting temperature, pressure, phase-saturations, and phase-compositions expressed in the form of K values (tabulated as a function of temperature and pressure) as the primary variables. The oleic, vapor, and aqueous phases coexist within the steam chamber (i.e. $N_P = 3$), while the oleic and aqueous phases coexist outside of it (i.e. $N_P = 2$). The fugacity constraint is solved a priori for a single overall composition using an EOS at different temperatures and pressures. It is preferable to use total enthalpy, pressure and overall composition as primary variables in thermal compositional simulations and conduct isenthalpic flash calculations for each grid block during simulations. This approach obviates the a priori restriction of the maximum number of phases.

ii. The effect of interfacial tension was not considered in phase equilibrium equations (i.e. fluid interfaces are flat), and capillary pressures are not considered in the calculation for phase-specific flow potentials. Capillary pressure can influence phase equilibrium calculations in nanopores smaller than 200 nm (Neshat et al., 2017). Such nanopores are prevalent in shales. For shale gas condensates, the authors demonstrated that: (i) two-phase (i.e., vapor-liquid) behavior can be significantly affected under high capillary pressures; (ii) the extent of the effect depends on the relative distributions of fluid phases within the pore spaces (i.e., saturations); (iii) bubble point pressures tend to be suppressed

while dew point pressures are increased under high capillary pressures; (iv) conventional methods of phase equilibrium calculation are often not robust. The lack of consideration of capillary phenomena in phase equilibrium calculations is not expected to have a significant influence on bitumen-recovery predictions using SAGD. This is mainly because the petrophysical properties of the shaly/muddy facies associations have poor vertical permeabilities. Therefore, the contribution of these facies associations to fluid flow is expected to be negligible.

iii. The hydrodynamic dispersion tensor for water and solvent was set to be zero for the majority of the simulation cases.

iv. The heterogeneous reservoir models are synthetic. So, they were not calibrated against hard data derived from well-logs.

v. The same set of relative permeability curves was used for both homogeneous and heterogeneous reservoirs. The shape and span of relative permeability curves in saturation space are modeled to be temperature-independent. The saturation of the aqueous phase at initial conditions for all reservoirs studied in Chapters 2 through 4 was assumed to be equal to the irreducible aqueous-phase saturation for the medium; that is the aqueous phase at initial conditions is immobile.

vi. The precipitation of asphaltenes and hence, their effect on wettability of the rock was not modeled.

vii. Geomechanical effects were not adequately captured.

Listed below are potential topics for future research:

1. Rigorous development of geological models representative of the middle McMurray member that are conditioned by measured data at different length scales (well-logs to seismic) in addition to outcrop observations.
2. Development of robust numerical reservoir simulators based on the isenthalpic flash framework capable of handling extreme variations in absolute permeability over short length scales.
3. Technical evaluation of relative performance of ES-SAGD to SAGD under representative geological models using a characterized reservoir fluid as solvent with consideration of (i) geomechanical effects; (ii) initial aqueous-phase mobility; (iii) asphaltene precipitation and its effects on rock wettability; and (iv) capillary pressures.

4. Economic evaluation of ES-SAGD to SAGD under field conditions for different time-variant injection concentration strategies.

Table 5.1. Input parameters for economic analysis. With the exception of the values for the price of bitumen and cost of solvent, the values for all other parameters have been obtained from Keshavarz et al. (2015).

Property	Value	Unit
Bitumen price	35	USD/bbl
Solvent price	78	USD/bbl
Exploration	200000	USD
Well-pair completion	4800	USD/m
Steam generator	2260000	USD
Water-treatment equipment	1000000	USD
Well-pair and field operation	150000	USD/yr
Administration and head office	7.48	USD/m^3 oil
Blending and transportation	6.29	USD/m^3 oil
Steam-generator operation	2.83	USD/m^3 CWE
Fuel for steam generator	10.1	USD/m^3 CWE
Treatment of water production	1.96	USD/m^3 CWE
Solvent distribution line	100000	USD
Solvent handling	20000	USD/yr

Table 5.2. Cumulative SOR for SAGD and n-C_6 SAGD for the cumulative bitumen production of 54699 m^3 for realizations in the second case study of Chapter 3 (Section 3.2.2). The value of 110 kJ/day-^oC is used for the overburden and underburden thermal conductivities. The homogeneous reservoir model is denoted as realization 0. The average increase in SOR due to heterogeneity ($\Delta_{het}SOR$) for SAGD is 2.60; the corresponding value for n-C_6 SAGD is 1.80. The average reduction in SOR due to coinjection of solvent ($\Delta_{sol}SOR$) for the heterogeneous cases is 1.59.

Realization	Time, days (SAGD)	Time, days (n-C_6 SAGD)	SOR (SAGD)	SOR (n-C_6 SAGD)	$\Delta_{het}SOR$ (SAGD)	$\Delta_{het}SOR$ (n-C_6 SAGD)	$\Delta_{sol}SOR$
0	332.89	289.60	2.53	1.77	0.00	0.00	0.76
4	1081.37	558.95	5.19	3.24	2.66	1.46	1.96
6	661.22	458.15	4.14	3.06	1.61	1.29	1.08
7	707.90	469.74	4.76	3.49	2.22	1.71	1.27
13	932.28	531.38	4.80	3.05	2.27	1.28	1.75
14	1469.95	1175.57	5.52	4.22	2.98	2.45	1.30
15	531.95	365.89	3.74	2.67	1.20	0.89	1.07
16	2031.62	1002.71	8.25	5.97	5.71	4.19	2.28
17	969.57	495.17	5.34	3.08	2.80	1.30	2.26
18	835.25	518.52	4.96	3.50	2.43	1.73	1.46
20	833.08	527.95	4.91	3.42	2.38	1.64	1.49
21	614.76	399.16	3.99	2.76	1.46	0.99	1.23
23	1399.22	667.04	6.12	3.86	3.59	2.08	2.27
24	1631.42	867.12	6.43	4.54	3.89	2.77	1.89
26	820.06	512.57	4.72	3.27	2.19	1.50	1.45
30	1000.16	533.38	5.20	3.10	2.67	1.33	2.10
31	869.17	532.01	4.66	3.44	2.12	1.66	1.22
32	681.23	428.72	4.35	2.89	1.81	1.12	1.45
33	869.12	498.01	4.36	3.16	1.82	1.38	1.20
35	655.08	431.93	4.20	3.05	1.66	1.27	1.15
36	1421.29	753.96	6.26	4.20	3.73	2.42	2.07
37	1652.07	849.63	7.24	5.55	4.71	3.78	1.69
44	665.20	425.78	4.16	3.06	1.63	1.29	1.10
48	1203.52	647.63	5.56	3.49	3.03	1.72	2.07
49	820.31	483.41	4.67	3.05	2.14	1.28	1.62
50	1061.02	660.71	5.71	4.31	3.18	2.53	1.40

Table 5.3. Effect of overburden and underburden thermal conductivities (k_{th}) on the reduction in time taken to meet a given cumulative bitumen production in n-C_6 SAGD relative to SAGD.

Realization	Δt, days k_{th} = 660 kJ/day-°C	Δt, days k_{th} = 110 kJ/day-°C
0	46.80	43.29
4	640.13	522.42
6	252.45	203.07
7	277.25	238.15
13	487.69	400.90
14	174.74	294.38
15	189.93	166.07
16	1150.72	1028.91
17	436.53	474.40
18	388.85	316.74
20	369.72	305.12
21	242.92	215.60
23	957.50	732.18
26	393.67	307.50
31	406.96	337.17
32	288.68	252.52
33	454.11	371.11
35	264.76	223.15
36	745.73	667.33
37	892.13	802.43
44	259.94	239.42
48	634.90	555.89
49	446.51	336.91
50	505.03	400.31

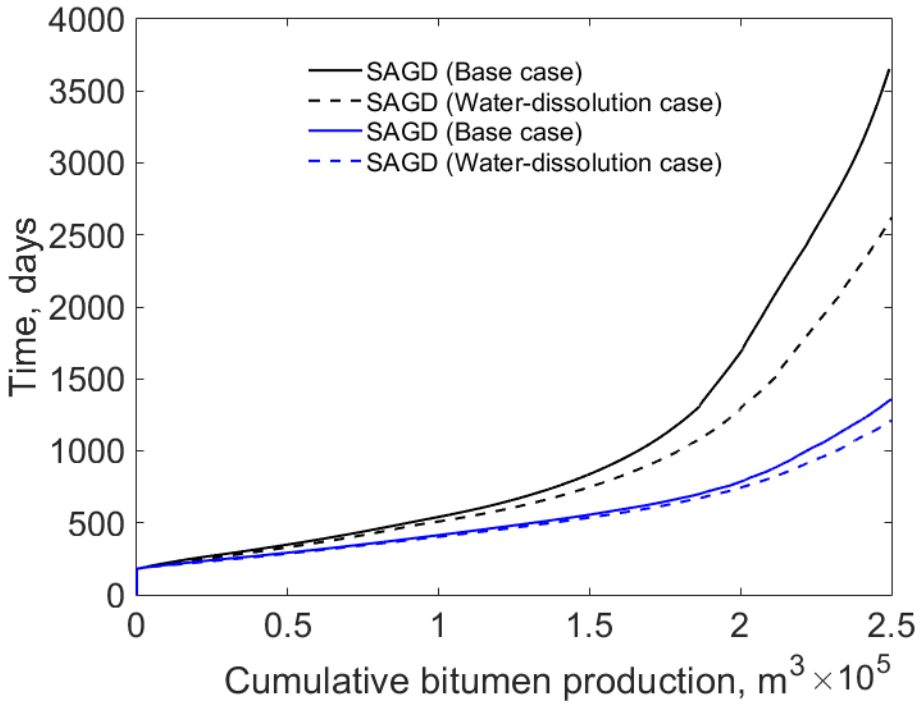
SAGD (Base case)
SAGD (Water-dissolution case)
SAGD (Base case)
SAGD (Water-dissolution case)
Time, days
Cumulative bitumen production, m3 ×105
0
500
1000
1500
2000
2500
3000
3500
4000
0
0.5
1
1.5
2
2.5

(a)

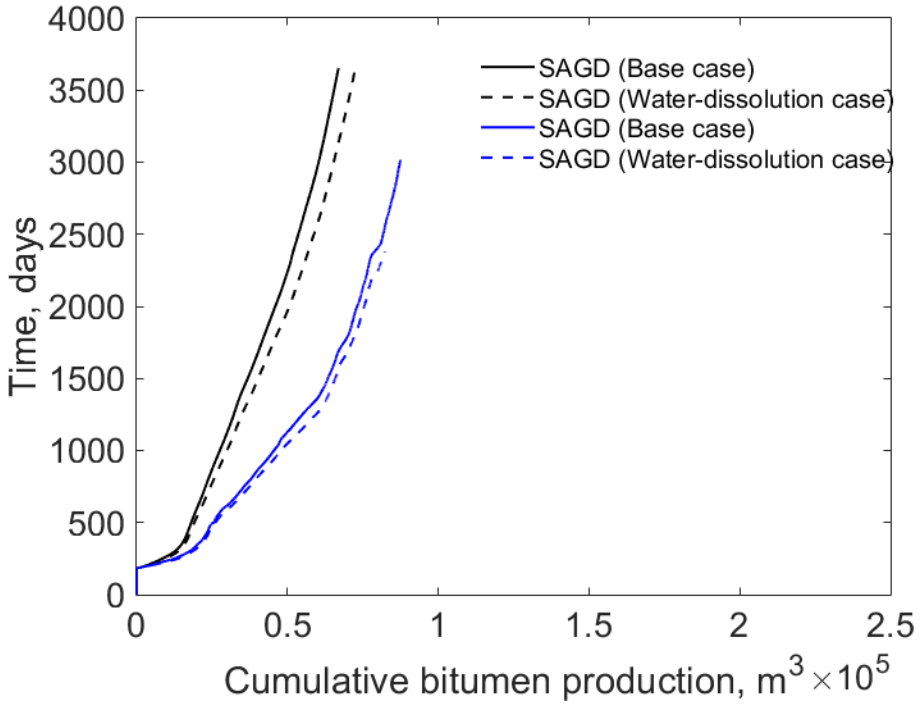
SAGD (Base case)
SAGD (Water-dissolution case)
SAGD (Base case)
SAGD (Water-dissolution case)
Time, days
Cumulative bitumen production, m3 ×105
0
500
1000
1500
2000
2500
3000
3500
4000
0
0.5
1
1.5
2
2.5

(b)

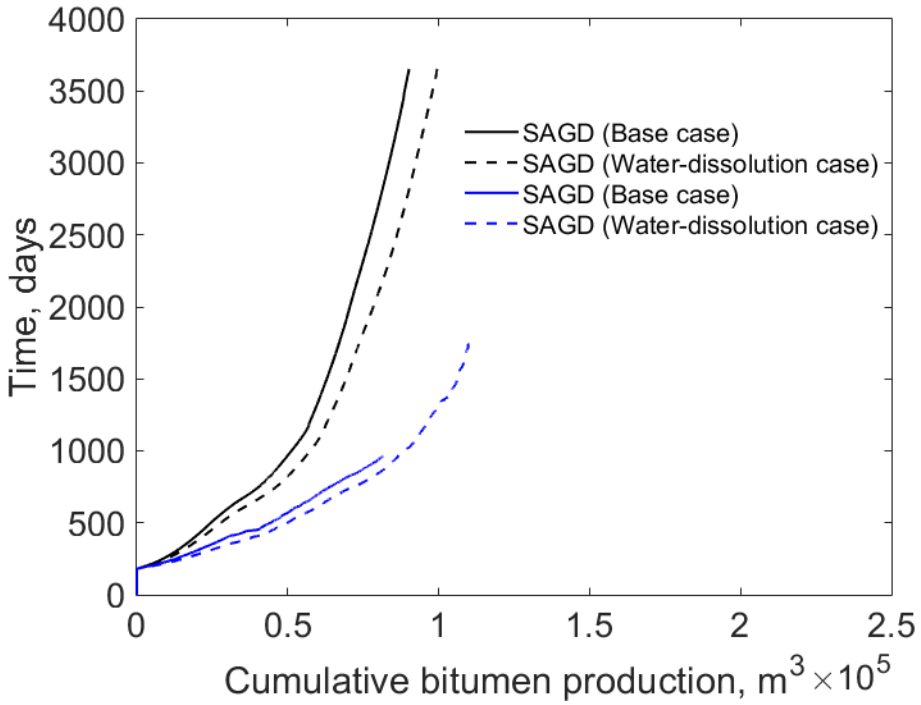

(c)

Figure 5.1. Effect of x_{wL} on cumulative bitumen production for the homogeneous reservoir and realizations 16 and 17 of the second case study in Chapter 3 (Section 3.2.2).

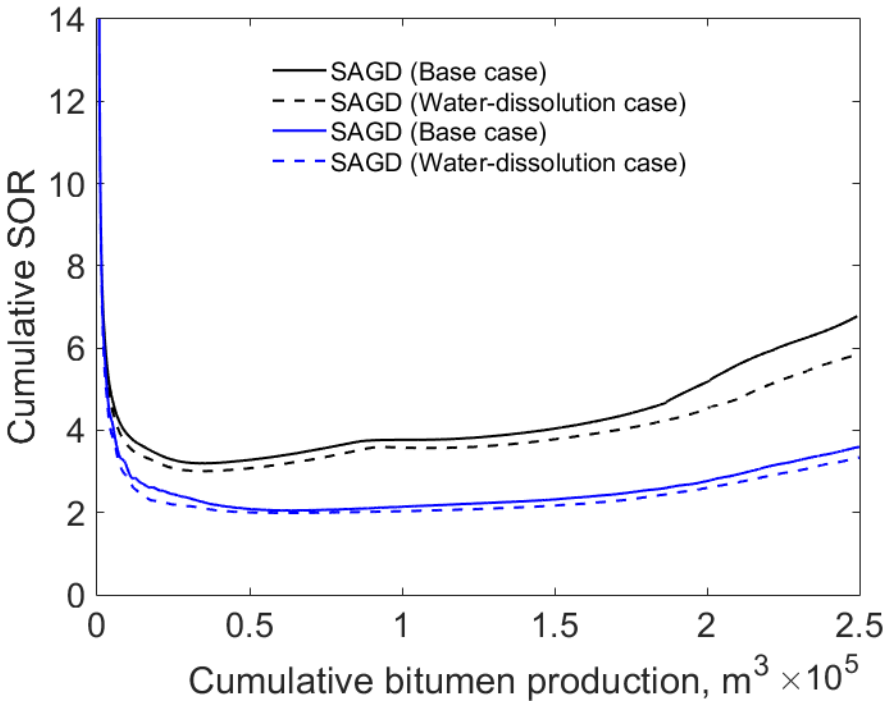
SAGD (Base case)
SAGD (Water-dissolution case)
SAGD (Base case)
SAGD (Water-dissolution case)
Cumulative SOR
Cumulative bitumen production, m3 ×105
0
2
4
6
8
10
12
14
0
0.5
1
1.5
2
2.5

(a)

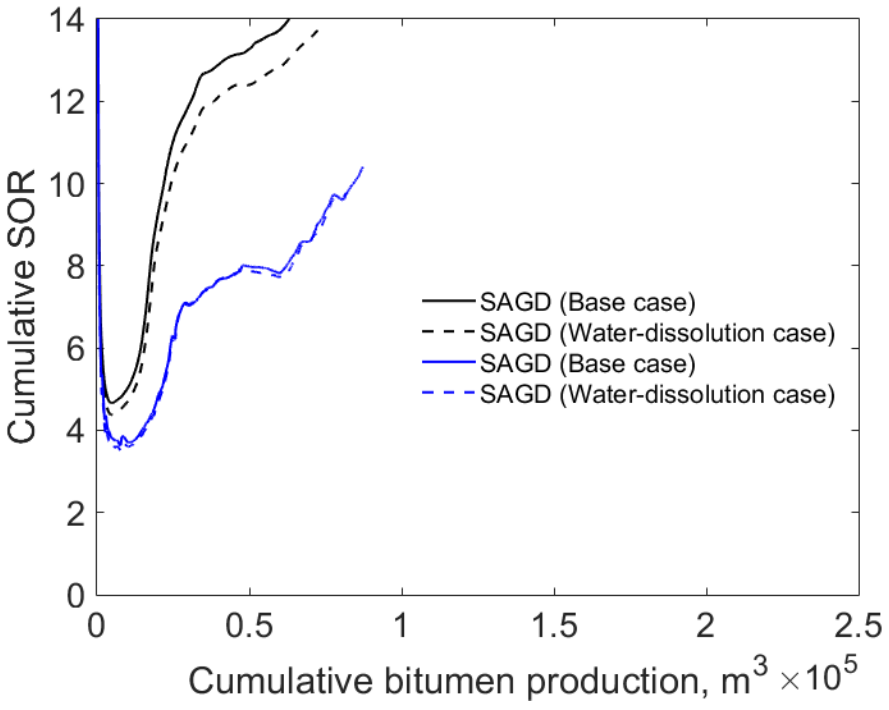
SAGD (Base case)
SAGD (Water-dissolution case)
SAGD (Base case)
SAGD (Water-dissolution case)
Cumulative SOR
Cumulative bitumen production, m3 ×105
0
2
4
6
8
10
12
14
0
0.5
1
1.5
2
2.5

(b)

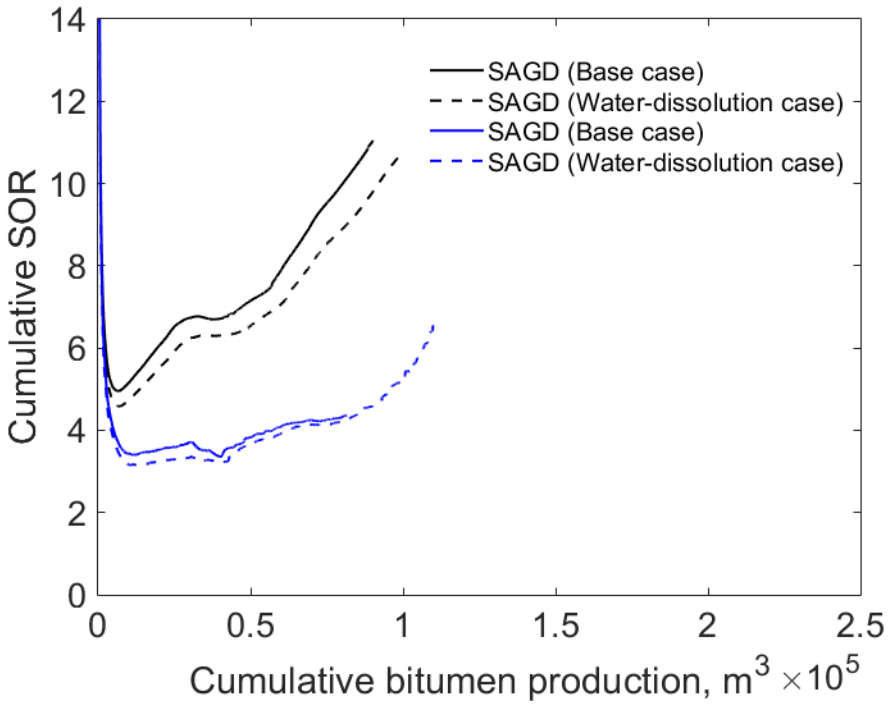

(c)

Figure 5.2. Effect of x_{wL} on cumulative SOR as a function of cumulative bitumen production for the homogeneous reservoir and realizations 16 and 17 of the second case study in Chapter 3 (Section 3.2.2).

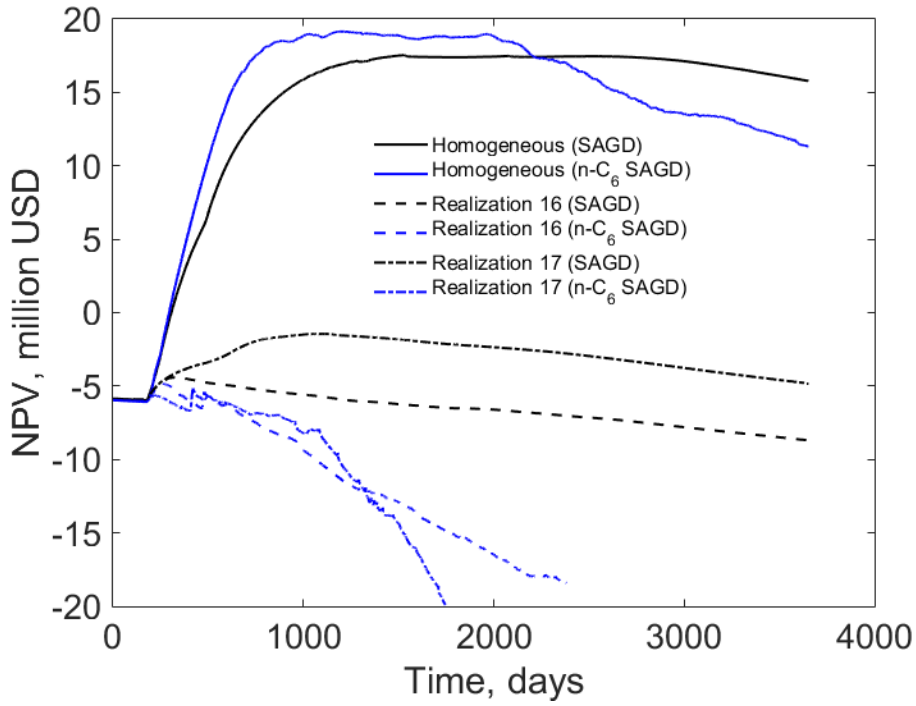

(a)

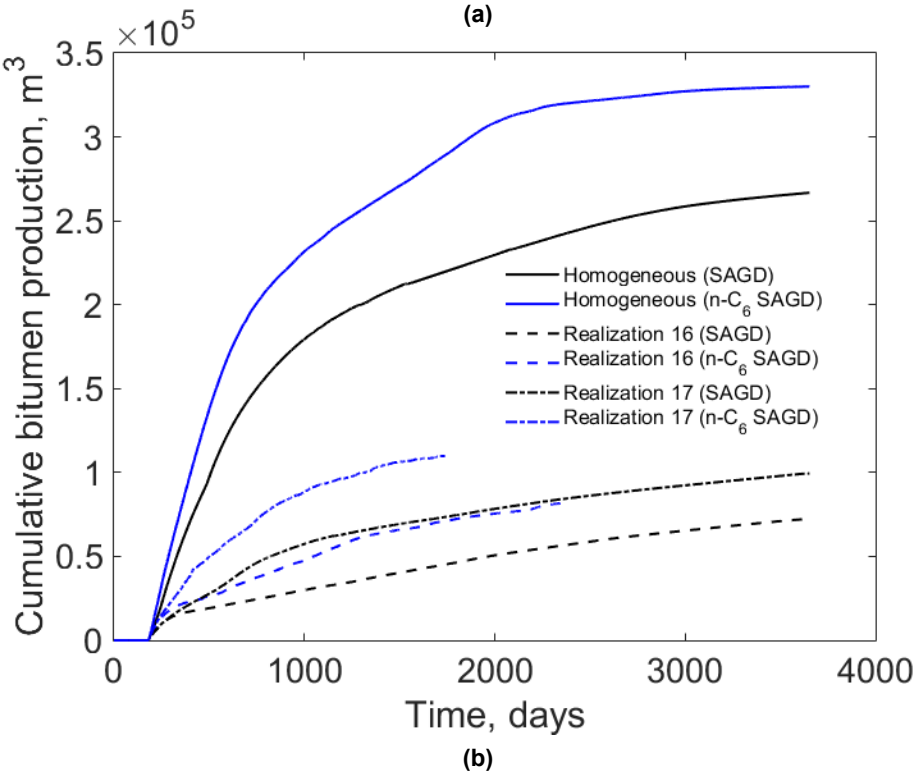

(b)

Figure 5.3. NPV and cumulative bitumen production histories for SAGD and n-C_6 SAGD for the homogeneous reservoir and realizations 16 and 17; (a) NPV histories; (b) cumulative bitumen production histories. The injection concentration of solvent in n-C_6 SAGD is set to 2 mol%. The price of bitumen and cost of solvent are set to 35 USD/bbl and 78 USD/bbl, respectively.

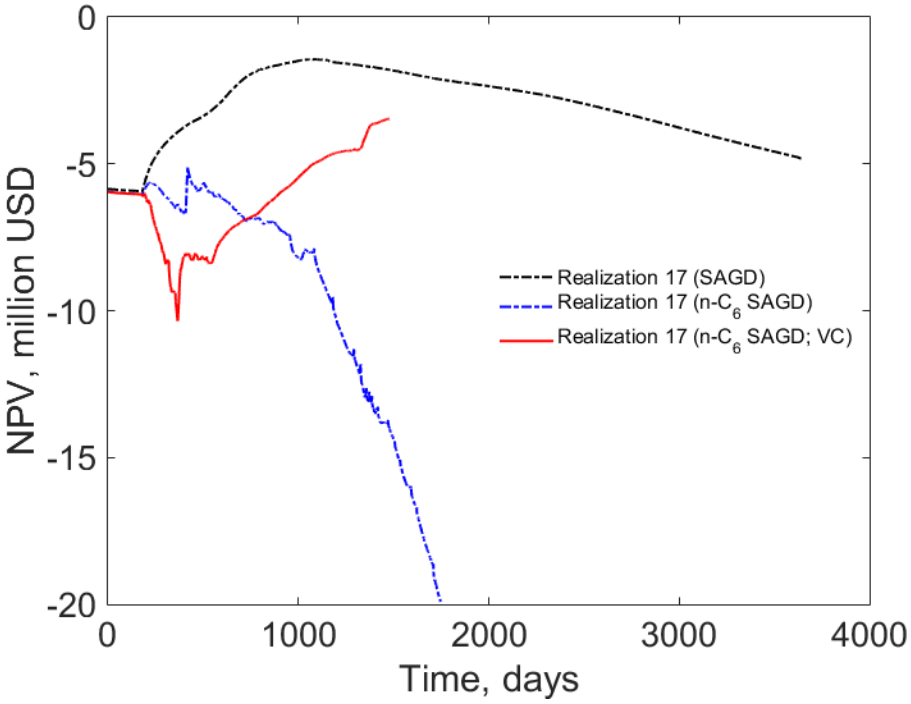

(a)

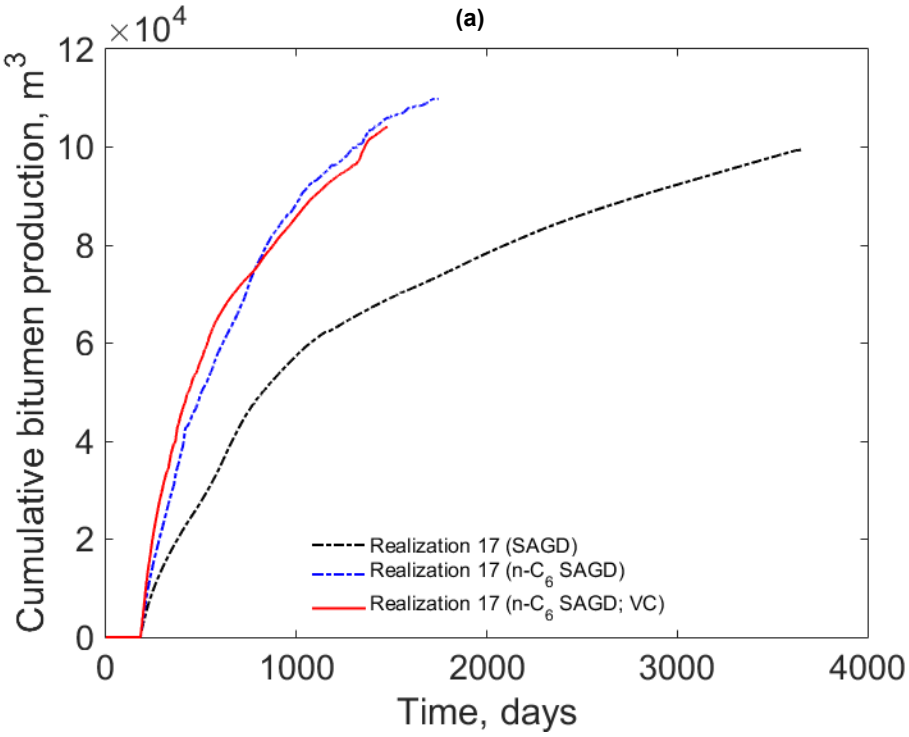

(b)

Figure 5.4. Effect of using a time-variant injection concentration (VC) strategy for realization 17 on NPV and cumulative bitumen production histories; (a) NPV histories; (b) cumulative bitumen production histories. The price of bitumen and cost of solvent are set to 35 USD/bbl and 78 USD/bbl, respectively.

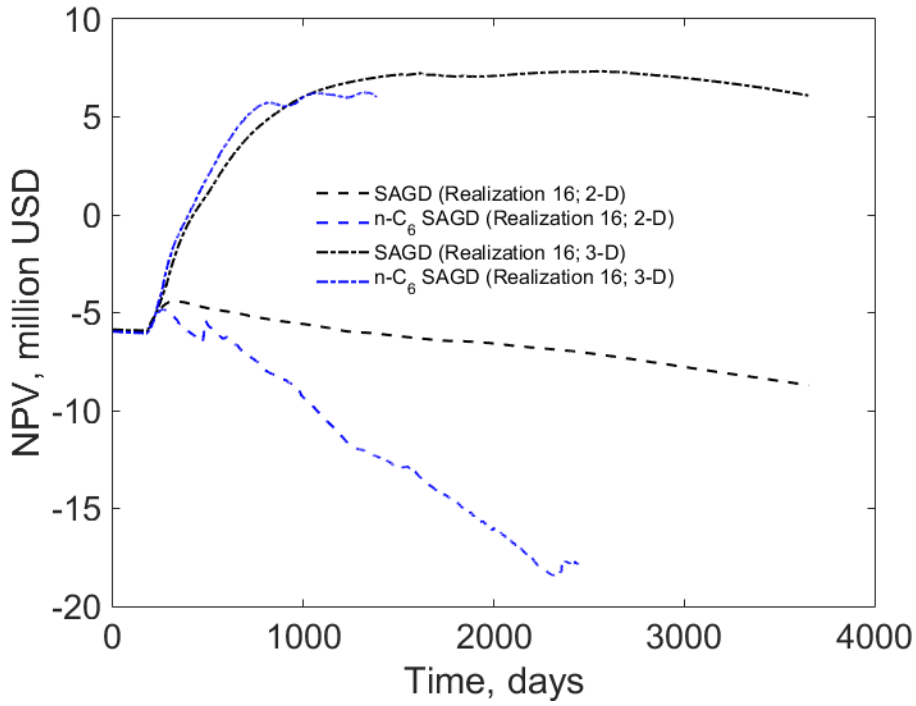

(a)

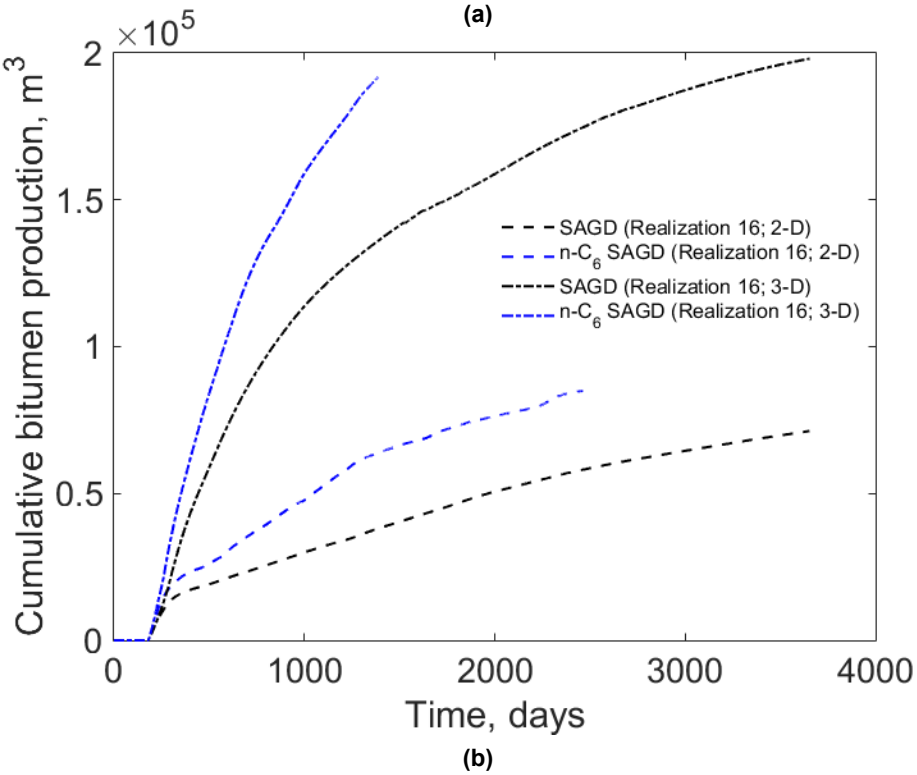

(b)

Figure 5.5. NPV and cumulative bitumen production histories for the 2-D and 3-D variants of realization 16; (a) NPV histories; (b) cumulative bitumen production histories. The price of bitumen and cost of solvent are set to 35 USD/bbl and 78 USD/bbl, respectively.

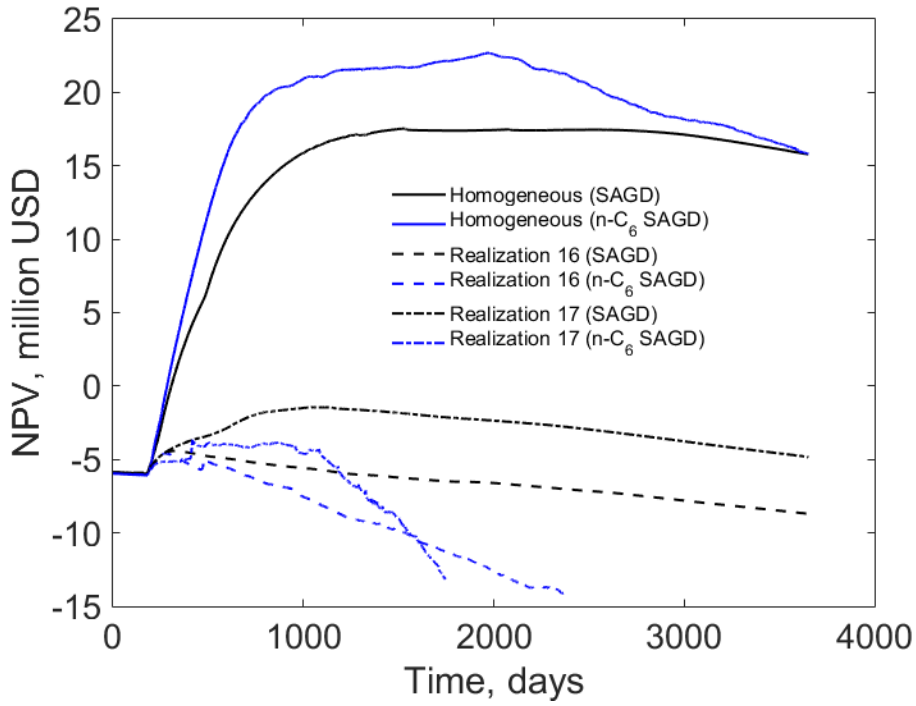

Figure 5.6. NPV histories for SAGD and n-C_6 SAGD for the homogeneous reservoir and realizations 16 and 17; The injection concentration of solvent in n-C_6 SAGD is set to 2 mol%. The price of bitumen and cost of solvent are set to 35 USD/bbl and 55 USD/bbl, respectively.

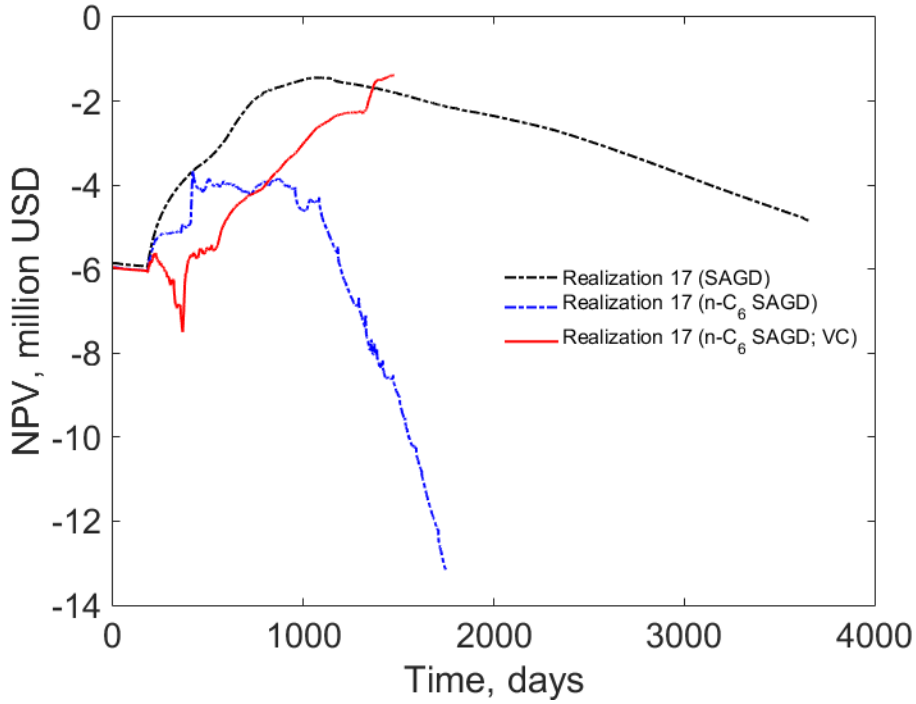

Figure 5.7. Effect of using a time-variant injection concentration (VC) strategy for realization 17 on NPV history. The price of bitumen and cost of solvent are set to 35 USD/bbl and 55 USD/bbl, respectively.

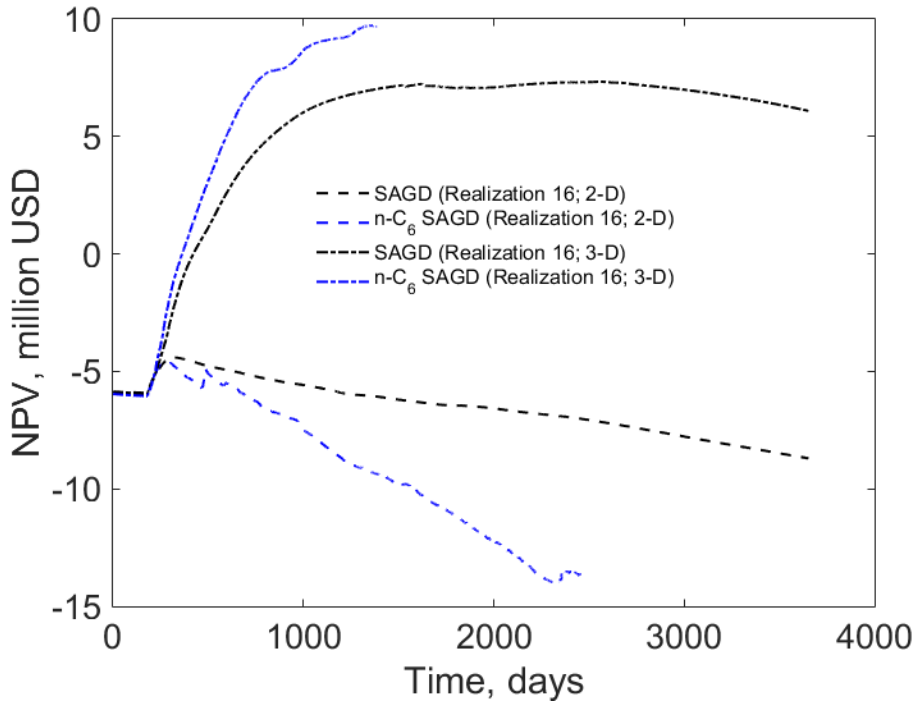

Figure 5.8. NPV histories of the 2-D and 3-D variants of realization 16. The price of bitumen and cost of solvent are set to 35 USD/bbl and 55 USD/bbl, respectively.

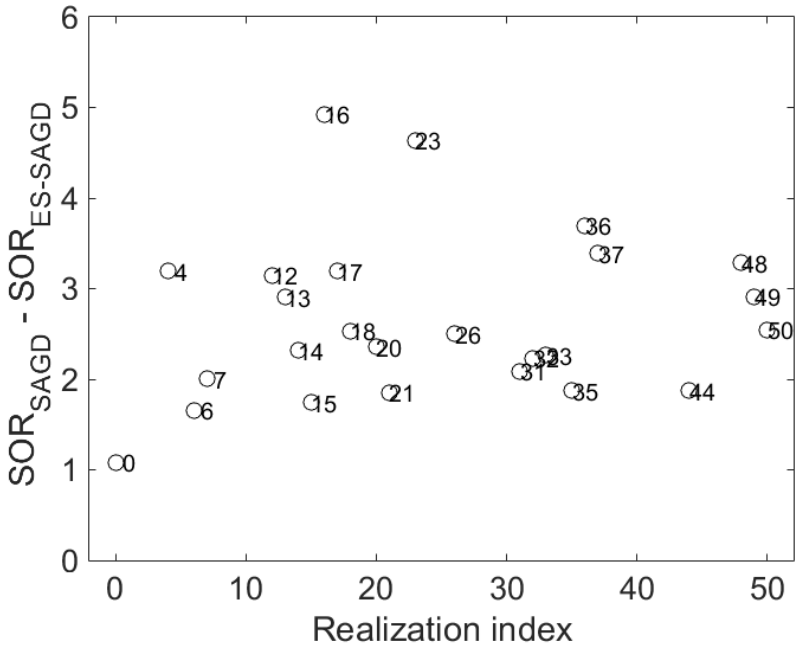

(a)

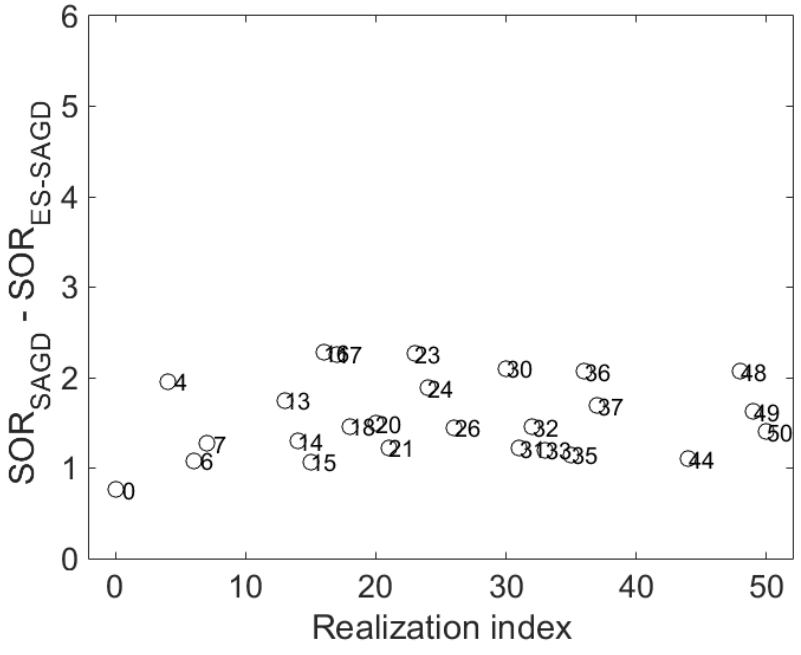

(b)

Figure 5.9. Effect of thermal conductivity of overburden and underburden (k_{th}) on the reduction in SOR due to coinjection of n-C_6 for the cumulative bitumen production of 54699 m^3; (a) k_{th} = 660 kJ/day-^oC; (b) k_{th} = 110 kJ/day-^oC. The horizontal axis represents the index assigned to each realization from set of realizations considered in Section 3.2.2 (second case study of Chapter 3). The index of 0 is assigned to the homogeneous model. The gaps in these figures are the result of either unfavorable permeability distributions or lack of numerical convergence.

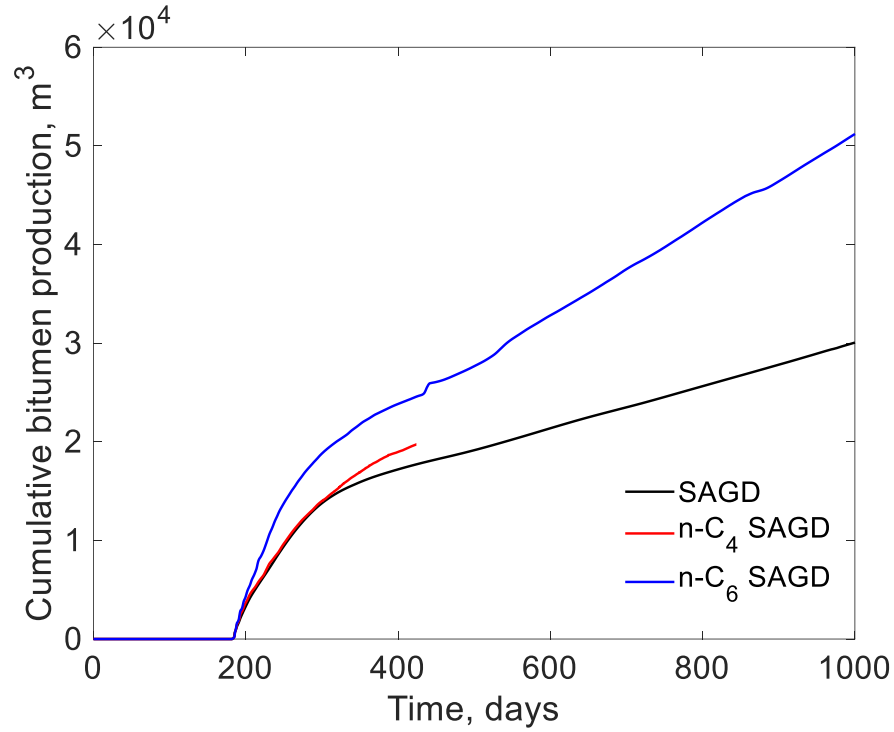

(a)

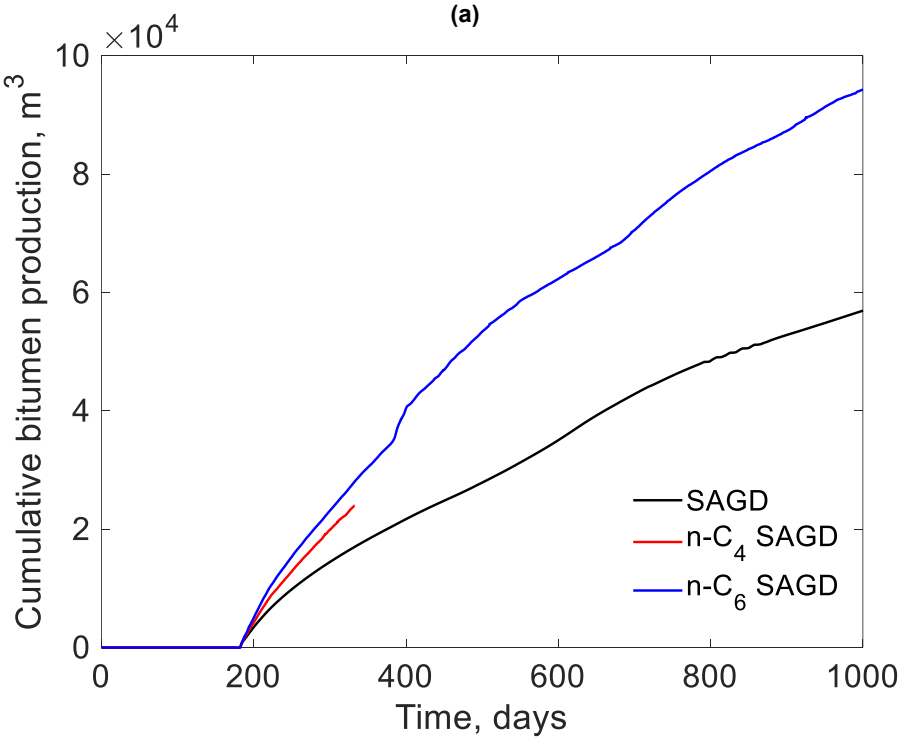

(b)

Figure 5.10. Cumulative bitumen production histories in SAGD, n-C_4-SAGD and n-C_6 SAGD for realizations 16 and 17 from the second case study in Chapter 3 (see Section 3.2.2); (a) realization 16; (b) realization 17.

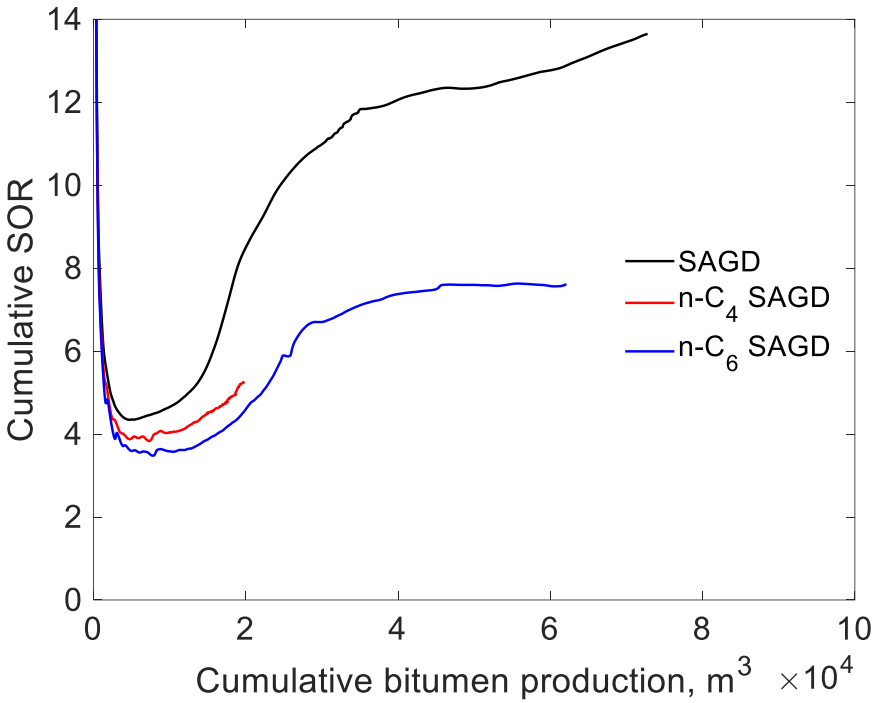

(a)

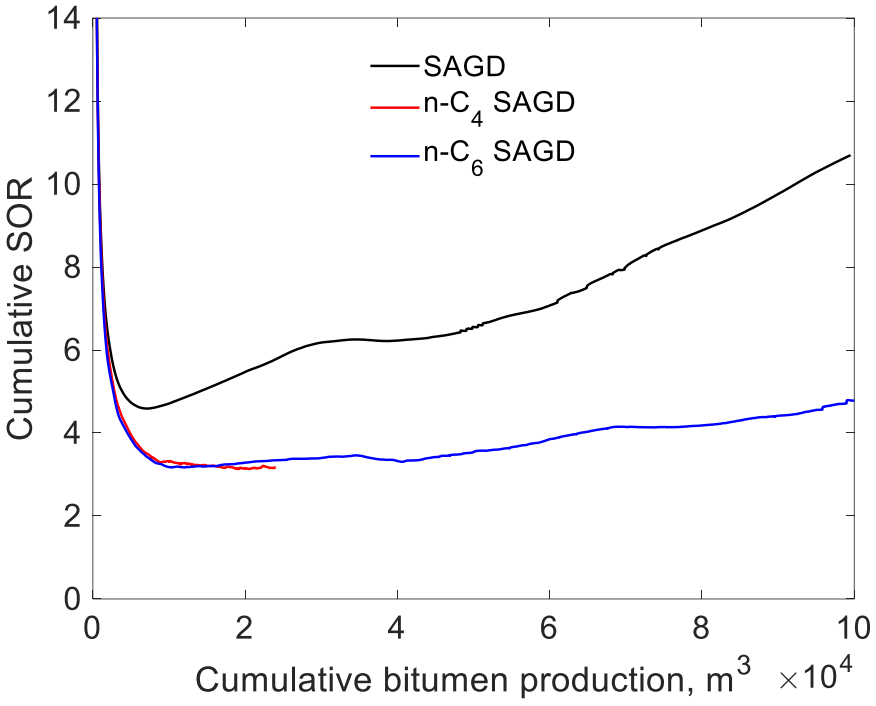

(b)

Figure 5.11. Cumulative SOR as a function of cumulative bitumen production in SAGD, n-C_4-SAGD and n-C_6 SAGD for realizations 16 and 17 from the second case study in Chapter 3 (see Section 3.2.2); (a) realization 16; (b) realization 17.

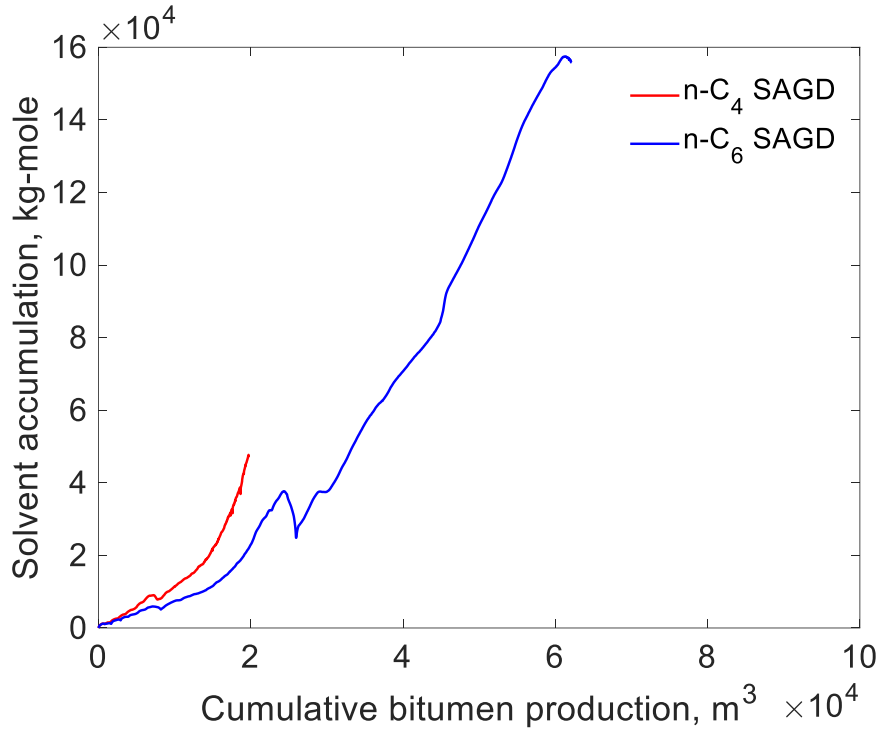

(a)

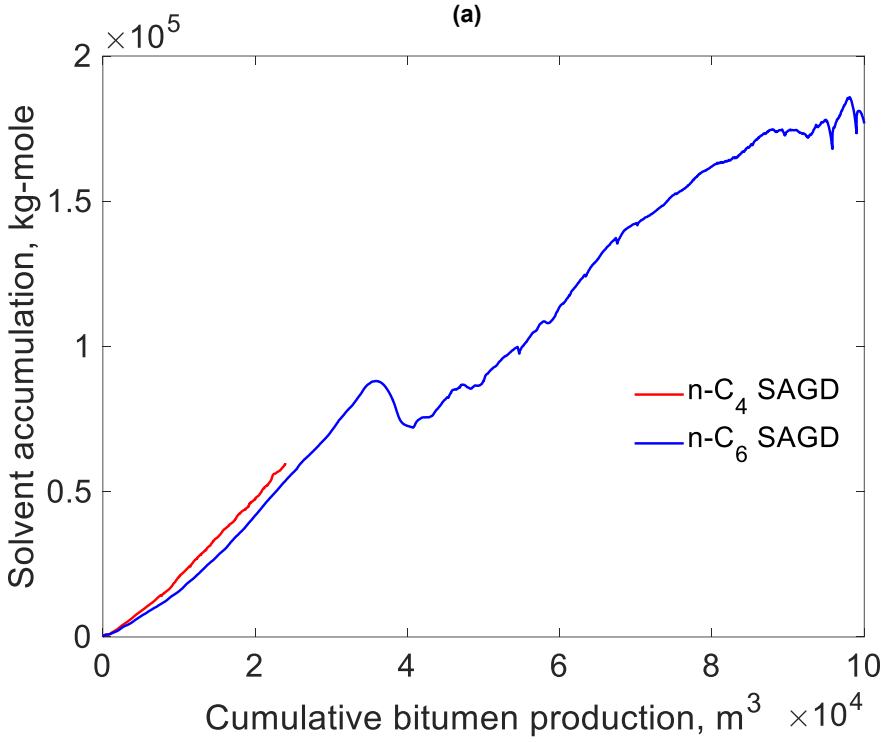

(b)

Figure 5.12. Solvent accumulation as a function of cumulative bitumen production in SAGD, n-C_4-SAGD and n-C_6 SAGD for realizations 16 and 17 from the second case study in Chapter 3 (see Section 3.2.2); (a) realization 16; (b) realization 17.

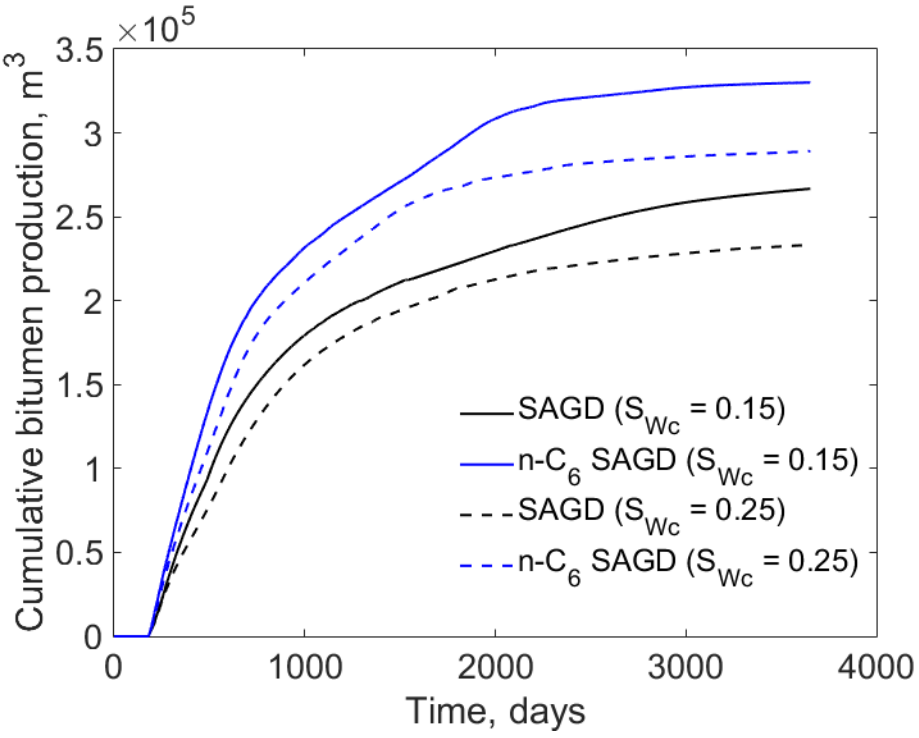
×10^5
3.5
3
2.5
2
1.5
1
0.5
0
Cumulative bitumen production, m^3
0
1000
2000
3000
4000
Time, days
SAGD (S_Wc = 0.15)
n-C_6 SAGD (S_Wc = 0.15)
SAGD (S_Wc = 0.25)
n-C_6 SAGD (S_Wc = 0.25)

(a)

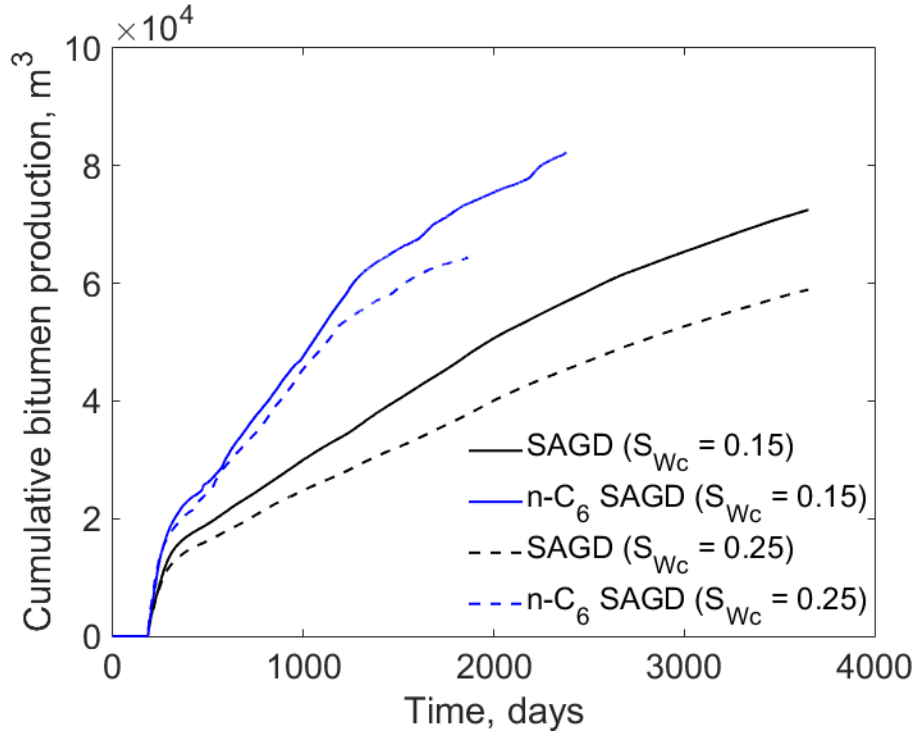
×10^4
10
8
6
4
2
0
Cumulative bitumen production, m^3
0
1000
2000
3000
4000
Time, days
SAGD (S_Wc = 0.15)
n-C_6 SAGD (S_Wc = 0.15)
SAGD (S_Wc = 0.25)
n-C_6 SAGD (S_Wc = 0.25)

(b)

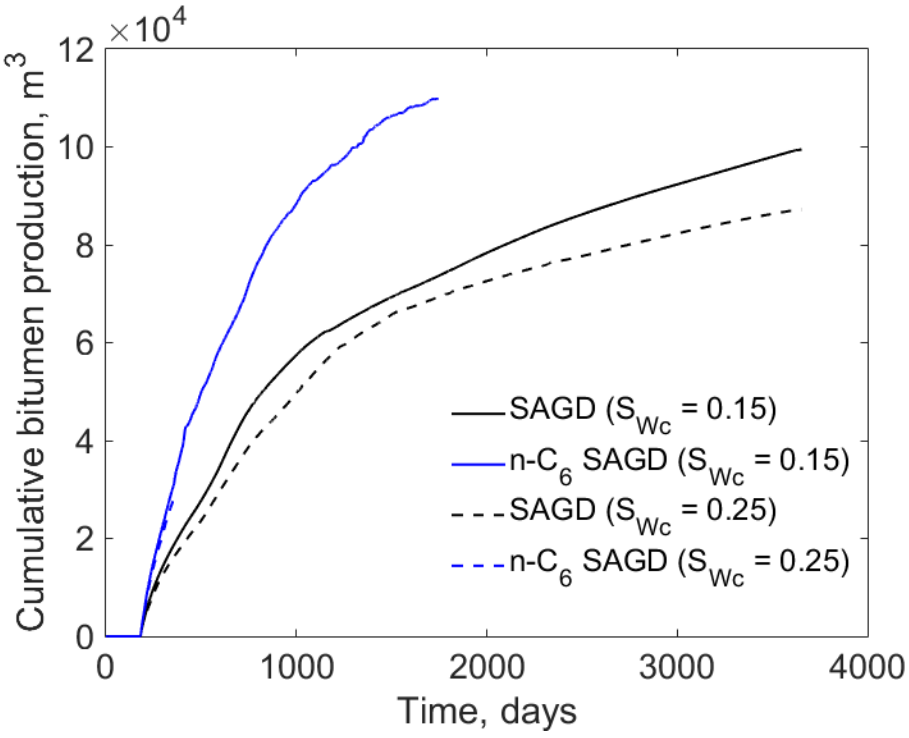

(c)

Figure 5.13. Effect of initial aqueous-phase saturation (S_{wc}) on cumulative bitumen production histories for the homogeneous reservoir model and realizations 16 and 17 in the second case study of Chapter 3 (see Section 3.2.2); (a) homogeneous case; (b) realization 16; (c) realization 17. The irreducible aqueous-phase saturation is set to 0.15.

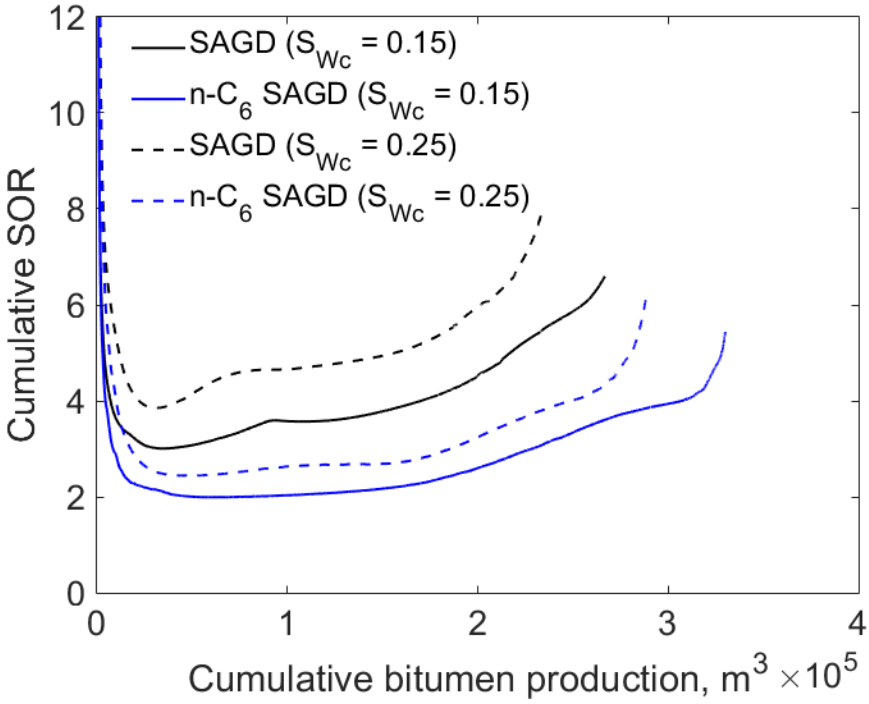
SAGD (S_{Wc} = 0.15)
n-C_6 SAGD (S_{Wc} = 0.15)
SAGD (S_{Wc} = 0.25)
n-C_6 SAGD (S_{Wc} = 0.25)
Cumulative SOR
Cumulative bitumen production, m^3 $\times 10^5$
0
2
4
6
8
10
12
0
1
2
3
4

(a)

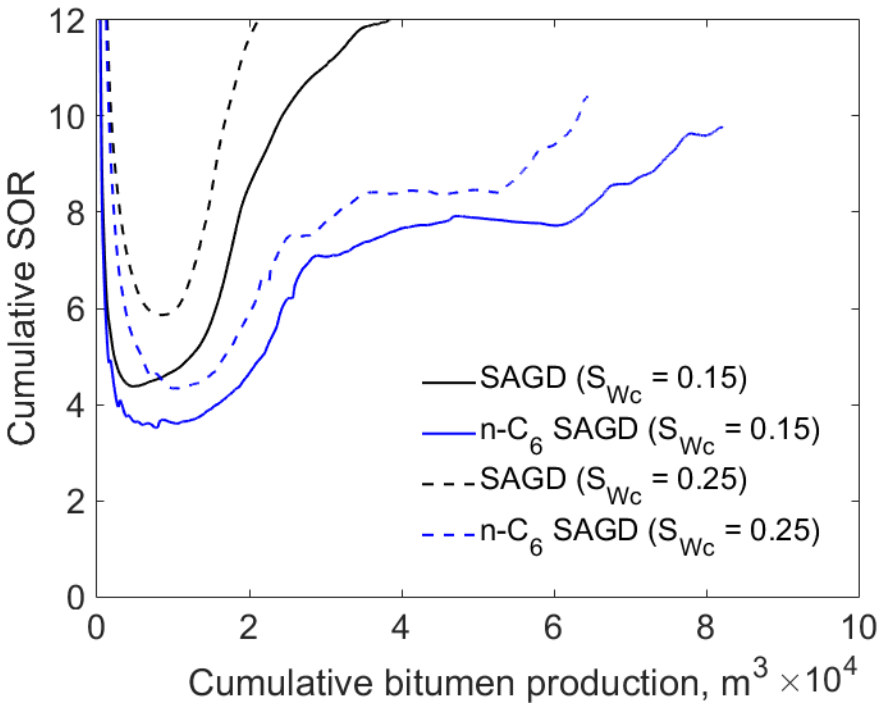
SAGD (S_{Wc} = 0.15)
n-C_6 SAGD (S_{Wc} = 0.15)
SAGD (S_{Wc} = 0.25)
n-C_6 SAGD (S_{Wc} = 0.25)
Cumulative SOR
Cumulative bitumen production, m^3 $\times 10^4$
0
2
4
6
8
10
12
0
2
4
6
8
10

(b)

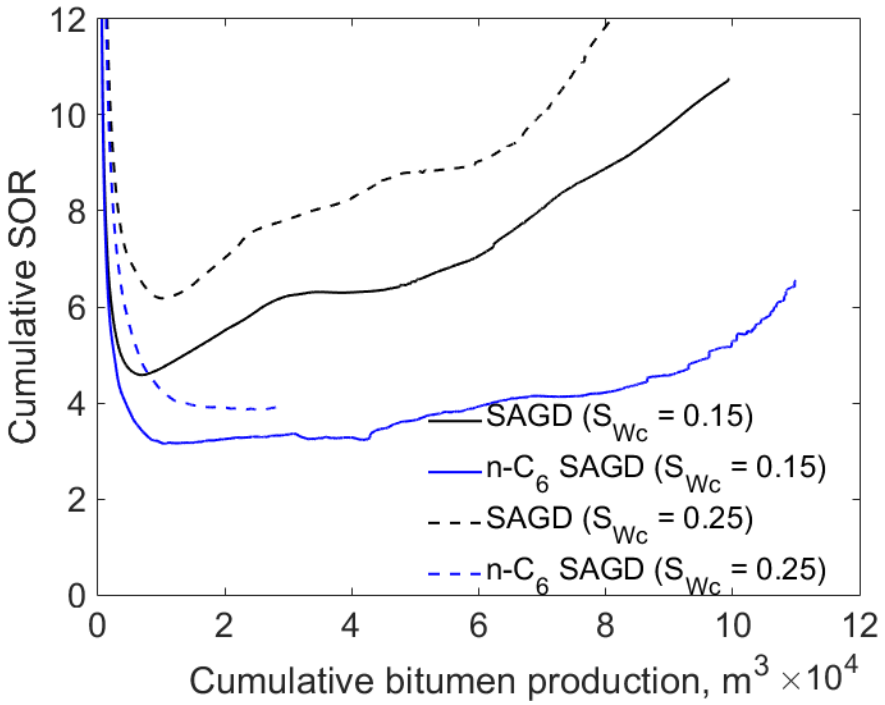

(c)

Figure 5.14. Effect of initial aqueous-phase saturation (S_{wc}) on cumulative SOR as a function of cumulative bitumen production for the homogeneous reservoir model and realizations 16 and 17 in the second case study of Chapter 3 (see Section 3.2.2); (a) homogeneous case; (b) realization 16; (c) realization 17. The irreducible aqueous-phase saturation is set to 0.15.

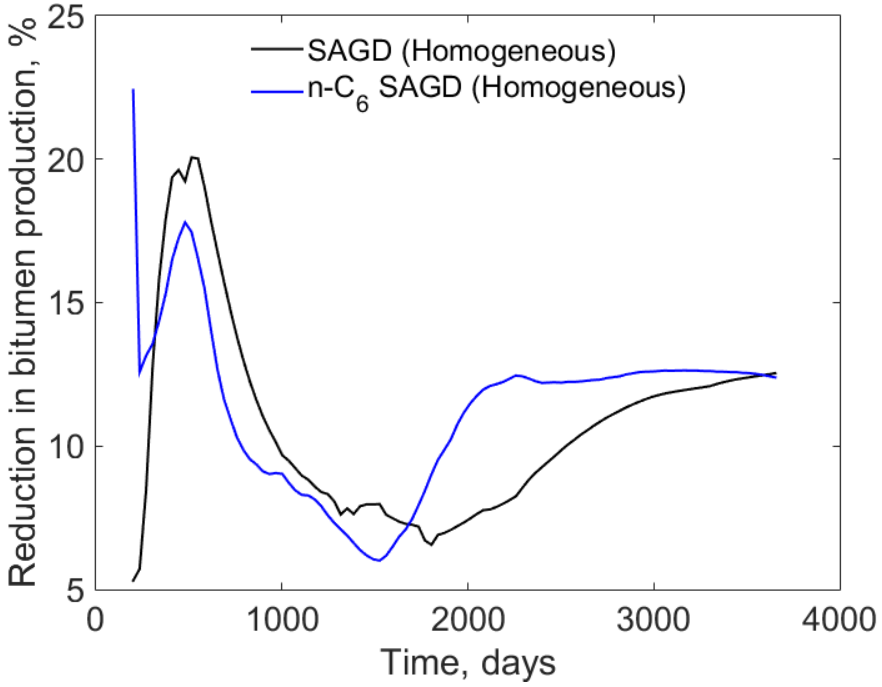
SAGD (Homogeneous)
n-C6 SAGD (Homogeneous)
Reduction in bitumen production, %
Time, days
25
20
15
10
5
0
1000
2000
3000
4000

(a)

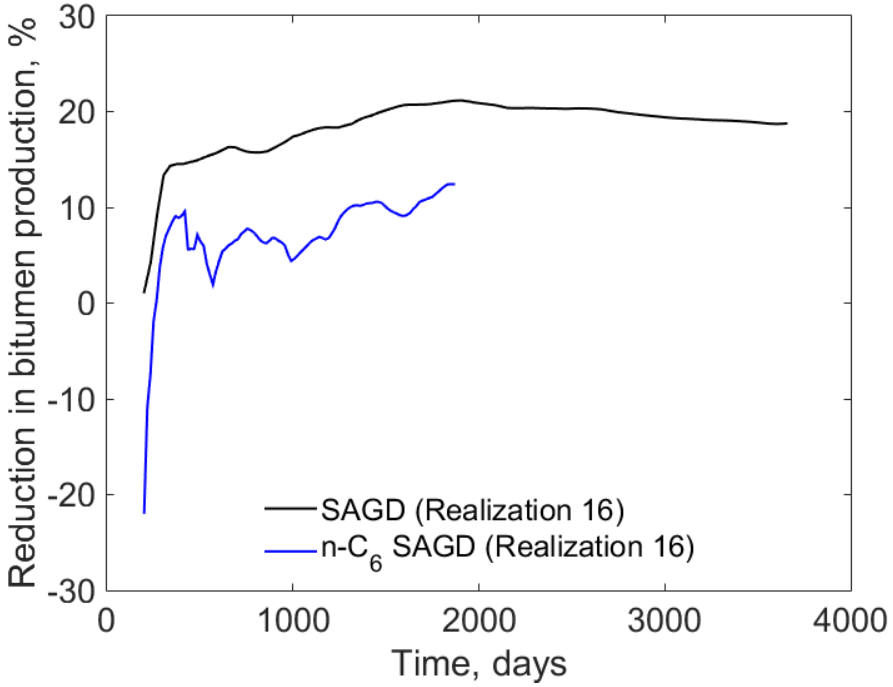
SAGD (Realization 16)
n-C6 SAGD (Realization 16)
Reduction in bitumen production, %
Time, days
30
20
10
0
-10
-20
-30
0
1000
2000
3000
4000

(b)

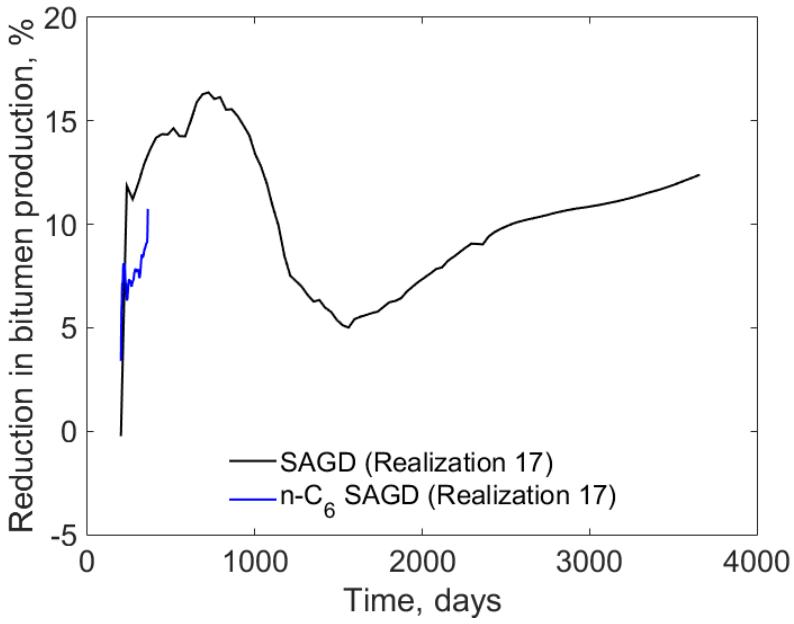

(c)

Figure 5.15. Effect of initial aqueous-phase saturation (S_{wc}) on the reduction in cumulative bitumen production for SAGD and n-C_6 SAGD for the homogeneous reservoir and realizations 16 and 17 in the second case study of Chapter 3 (see Section 3.2.2); (a) homogeneous case; (b) realization 16; (c) realization 17.

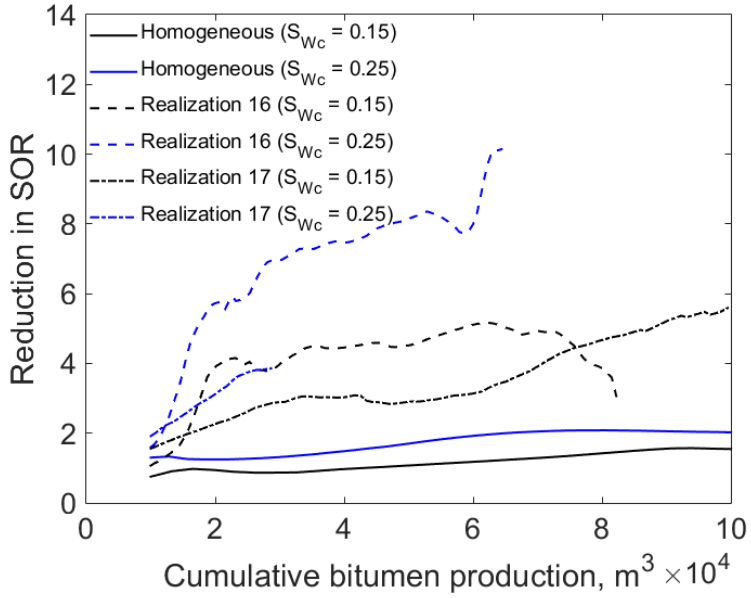

Figure 5.16. Effect of initial aqueous-phase saturation (S_{wc}) on the reduction in SOR due to coinjection of solvent as a function of cumulative bitumen production for the homogeneous reservoir and realizations 16 and 17 in the second case study of Chapter 3 (see Section 3.2.2).

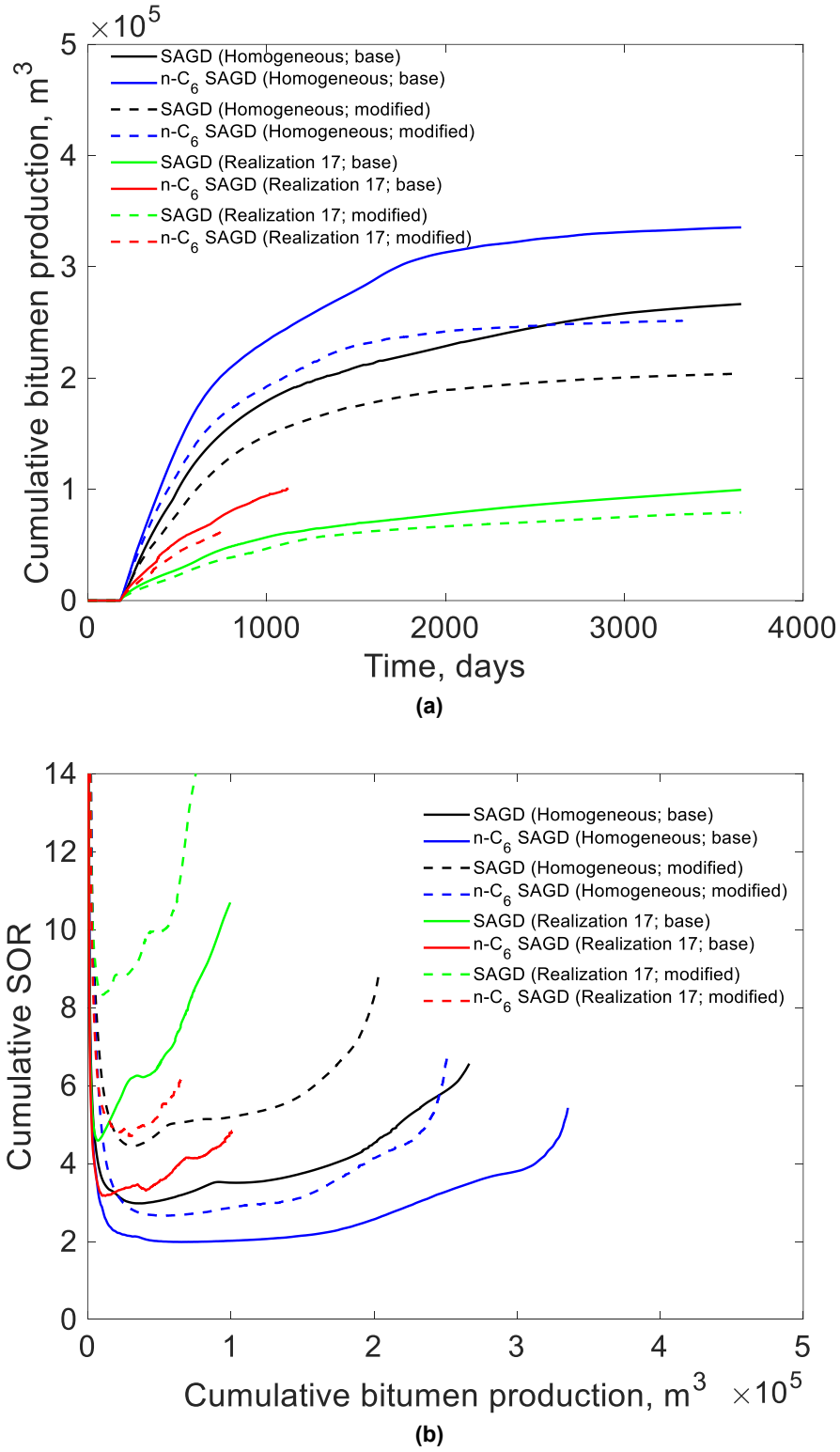

Figure 5.17. Effect of formation compressibility on the production performance of SAGD and n-C_6 SAGD for the homogeneous reservoir and realization 17 from the second case study of Chapter 3 (Section 3.2.2). The formation compressibilities for the base and modified cases are 1.8 × 10^{-5} and 5.4 × 10^{-5} 1/kPa, respectively.

Bibliography

Adepoju, O. O., Lake, L. W., and Johns, R. T., 2013. Investigation of Anisotropic mixing in miscible displacements. SPE Reservoir Evaluation & Engineering 16(01): 85-96.

Adepoju, O. O., Lake, L. W., & Johns, R. T., 2015. Anisotropic Dispersion and Upscaling for Miscible Displacement. SPE Journal 20(03): 421-432.

Alkindi, A.S., Al-Wahaibi, Y.M., and Muggeridge, A.H. 2011. Experimental and Numerical Investigations into Oil Drainage Rates During Vapor Extraction of Heavy Oils. SPE Journal 16 (02): 343-357. SPE 141053-PA.

Al-Bahlani, A., Babadagli, T. 2009. SAGD Laboratory Experimental and Numerical Simulation Studies: A Review of Current Status and Future Issues. Journal of Petroleum Science and Engineering 68: 135-150.

Amani, M.J., Gray, M.R. and Shaw, J.M. 2013a. Phase Behavior of Athabasca Bitumen Water Mixtures at High Temperature and Pressure. The Journal of Supercritical Fluids 77: 142-152.

Amani, M.J., Gray, M.R. and Shaw, J.M. 2013b. Volume of Mixing and Solubility of Water in Athabasca Bitumen at High Temperature and Pressure. Fluid Phase Equilibria 358: 203-211.

Abdulagatov, I. M. and Rasulov, S. M. 1996. Viscosity of N-Pentane, N-Heptane and Their Mixtures Within the Temperature Range from 298 K up to Critical Points at the Saturation Vapor Pressure. Berichte der Bunsengesellschaft für physikalische Chemie 100(2): 148-154.

Alvarez, J.M., Moreno, R., and Sawatzky, R.P. 2014. Can SAGD be Exported? Potential

Challenges. Presented at SPE Heavy and Extra Heavy Oil Conference, Colombia, SPE 171089-MS.

Azom, P.N., and Srinivasan, S. 2011. Modeling the Effect of Permeability Anisotropy on the Steam-Assisted Gravity Drainage (SAGD) Process. Presented at Canadian Unconventional Resources Conference SPE 149274-MS.

Baker, L.E. 1988. Three-Phase Relative Permeability Correlations. Presented at Enhanced Oil Recovery Symposium, Oklahoma, SPE 17369-MS.

Brunner, E. 1990. Fluid mixtures at high pressures IX. Phase Separation and Critical Phenomena in 23 (n-alkane + water) mixtures. The Journal of Chemical Thermodynamics 22(4): 335-353.

Brunner, E., Thies, M. C., and Schneider, G. M., 2006. Fluid Mixtures at High Pressures: Phase Behavior and Critical Phenomena for Binary Mixtures of Water with Aromatic Hydrocarbons. The Journal of Supercritical Fluids 39(2): 160-173.

Butler, R., 1997. Thermal Recovery of Oil and Bitumen. Blackbook series, GravDrain Inc., Calgary, Alberta.

Butler, R., 2001. Some Recent Developments in SAGD. Journal of Canadian Petroleum Technology 40(1): 18-22.

Butler, R.M., McNab, G.S. and Lo, H.Y. 1981. Theoretical Studies on the Gravity Drainage of Heavy Oil During In-Situ Steam Heating. The Canadian Journal of Chemical Engineering 59: 455-460.

Canadian Association of Petroleum Producers. 2015. Alberta Oil Sands Bitumen Valuation Methodology.

Chan, S., Chen, Z., and Dong, M. 2012. Experimental and Numerical Study of Initial Water Mobility in Bitumen Reservoirs and its Effect on SAGD. Journal of Petroleum Science and Engineering; 92–93: 30-39.

Chen, Z. 2007. Reservoir simulation: mathematical techniques in oil recovery (Vol. 77). Society of Industrial and Applied Mathematics.

Chen, Q., Gerritsen, M. G., and Kovscek, A. R., 2008. Effects of Reservoir Heterogeneities on the Steam-Assisted Gravity-Drainage Process. SPE Reservoir Evaluation & Engineering 11(05): 921-932.

Coats, K. H., and Smith, B. D., 1964. Dead-End Pore Volume and Dispersion in Porous Media. SPE Journal 4(01): 73-84.

Connolly, M., and Johns, R. T., 2016. Scale-Dependent Mixing for Adverse Mobility Ratio Flows in Heterogeneous Porous Media. Transport in Porous Media 113(1): 29-50.

Computer Modeling Group. 2011. STARS Version 2011 User Guide: Calgary, Alberta, Canada: CMG.

Crabtree, A., & Simon-Tov, M. 1993. Thermophysical properties of saturated light and heavy water for advanced neutron source applications (No. ORNL/TM-12322). Oak Ridge National Lab., TN (United States).

Dai, K. K., and Orr Jr, F. M., 1987. Prediction of CO2 Flood Performance: Interaction of Phase Behavior with Microscopic Pore Structure Heterogeneity. SPE Reservoir Engineering 2(04): 531-542.

Deutsch, C. V., 2010. Estimation of Vertical Permeability in the McMurray Formation. Journal of Canadian Petroleum Technology 49(12): 10-18.

Dymond, J. H. and Oye, A.H. 1994. Viscosity of Selected Liquid n-Alkanes. Journal of physical and chemical reference data 23(1): 41-53.

Dymond, J. H. and Young, K. J. 1980. Transport Properties of Nonelectrolyte Liquid Mixtures-I. Viscosity Coefficients for n-Alkane Mixtures at Saturation Pressure from 283 to 378 K. International Journal of Thermophysics 1(4): 331-344.

Economou, I., Heidman, J., Tsonopoulos, C. and Wilson, G. 1997. Mutual Solubilities of Hydrocarbons and Water: III. 1-Hexene, 1-Octene, C10- C12 Hydrocarbons. AIChE Journal 43(2): 535-546.

Gates, I. D., and Chakrabarty, N., 2008. Design of the Steam and Solvent Injection Strategy in Expanding Solvent Steam-Assisted Gravity Drainage. Journal of Canadian Petroleum Technology 47(09): 12-20.

Garmeh, G., and Johns, R.T. 2010. Upscaling of Miscible Floods in Heterogeneous Reservoirs Considering Reservoir Mixing. SPE Reservoir Evaluation & Engineering 13(05): 747-7643. SPE 124000-PA.

Gelhar, L.W., Welty, C. and Rehfeldt, K.R. 1992. A Critical Review of Data on Field-Scale Dispersion in Aquifers. Water Resources Research 28(7):1955-1974.

Glandt, C.A. and Chapman, W.G. 1995. Effect of Water Dissolution on Oil Viscosity. SPE Reservoir Engineering 10(1): 59-64.

Grane, F. 1961. Measurements of Transverse Dispersion in Granular Media. Journal of Chemical and Engineering Data 6(2): 283-287.

Griswold, J. and Kasch, J.E. 1942. Hydrocarbon-Water Solubilities at Elevated Temperatures and Pressures. Industrial and Engineering Chemistry 34(7): 804-806.

Hassanpour, M. M., Pyrcz, M. J., and Deutsch, C. V., 2013. Improved Geostatistical Models of Inclined Heterolithic Strata for McMurray Formation, Alberta, Canada. AAPG bulletin 97(7): 1209-1224.

Heidman, J.L., Tsonopoulos, C., Brady, C.J. and Wilson, G.M. 1985. High-Temperature Mutual Solubilities of Hydrocarbons and Water. Part II: Ethylbenzene, Ethylcyclohexane, and n-Octane. AIChE Journal 31(3): 376-384.

Heidemann, R.A. 1974. Three-Phase Equilibria Using Equations of State. AIChE Journal 20(5): 847-855.

Jha, R. K., Kumar, M., Benson, I., and Hanzlik, E., 2013. New Insights into Steam/Solvent-Coinjection-Process Mechanism. SPE Journal 18(05): 867-877.

Ji, D., Dong, M., and Chen, Z. 2015. Analysis of Steam–Solvent–Bitumen Phase Behavior and Solvent Mass Transfer for Improving the Performance of the ES-SAGD Process. Journal of Petroleum Science and Engineering 133: 826-837.

Jiang, Q., Thornton, B., Houston, J.R., and Spence, S. 2009. Review of Thermal Recovery Technologies for the Clearwater and Lower Grand Rapids Formations in the Cold Lake Area in Alberta. Canadian International Petroleum Conference, Calgary.

Kariznovi, M. 2013. Phase Behaviour Study and Physical Properties Measurement for Athabasca Bitumen/Solvent Systems Applicable for Thermal and Hybrid Solvent Recovery Processes. PhD Thesis. University of Calgary, Alberta. Canada.

Kariznovi, M., Nourozieh, H., and Abedi, J. 2014. Volumetric Properties of Athabasca Bitumen+ n-Hexane Mixtures. Energy & Fuels 28(12): 7418-7425.

Keshavarz, M., Okuno, R., and Babadagli, T. 2014. Efficient Oil Displacement Near the Chamber Edge in ES-SAGD. Journal of Petroleum Science and Engineering 118: 99-113.

Keshavarz, M., Okuno, R., and Babadagli, T. 2015. Optimal Application Conditions for Steam/Solvent Coinjection. SPE Reservoir Evaluation & Engineering 18(01): 20-38.

Khaledi, R., Boone, T.J., Motahhari, H.R., Subramanian, G. 2015. Optimized Solvent for Solvent Assisted-Steam Assisted Gravity Drainage (SA-SAGD) Recovery Process. Presented at SPE Heavy Oil Technical Conference SPE 174429-MS.

Kobayashi, R. and Katz, D. 1953. Vapor-Liquid Equilibria for Binary Hydrocarbon-Water Systems. Industrial and Engineering Chemistry 45(2): 440-446.

Kumar, A. 2016. Characterization of Reservoir Fluids Based on Perturbation from n-Alkanes. The University of Alberta (PhD thesis).

Kumar, A., and Okuno, R. 2015. Direct Perturbation of the Peng-Robinson Attraction and Covolume Parameters for Reservoir Fluid Characterization. Chemical Engineering Science 127: 293-309.

Kumar, D., Murugesu, M., and Srinivasan, S. 2014. Modeling Effect of Permeability Heterogeneities on SAGD Performance Using Improved Upscaling Schemes. Presented at SPE Heavy Oil Conference SPE 170115-MS.

Lake, L.W. 1989. Enhanced Oil Recovery. Prentice-Hall

Lake, L. W., and Hirasaki, G. J. 1981. Taylor's Dispersion in Stratified Porous Media. SPE Journal 21(04): 459-468.

Law, D. H. S., Nasr, T. N., and Good, W. K. (2003). Field-Scale Numerical Simulation of SAGD Process with Top-Water Thief Zone. Journal of Canadian Petroleum Technology 42(08).

Li, W., Mamora, D., and Li, Y., 2011a. Light-and Heavy-Solvent Impacts on Solvent-Aided-SAGD Process: A Low-Pressure Experimental Study. Journal of Canadian Petroleum Technology 50(04): 19-30.

Li, W., Mamora, D., Li, Y., and Qiu, F., 2011b. Numerical Investigation of Potential Injection Strategies to Reduce Shale Barrier Impacts on SAGD Process. Journal of Canadian Petroleum Technology 50(03): 57-64.

Luo, S. and Barrufet, M.A. 2005. Reservoir Simulation Study of Water-in-Oil Solubility Effect on Oil Recovery in Steam Injection Process. SPE Reservoir Evaluation and Engineering 8(6): 528-533.

Maczynski, A., Shaw, D.G., Goral, M., et al. 2005. IUPAC-NIST Solubility Data Series. 81. Hydrocarbons with Water and Seawater-Revised and Updated. Part 4. C6H14 Hydrocarbons with Water. Journal of Physical and Chemical Reference data 34(2): 709-753.

Maini B.B., Batycky J.P. 1985. Effect of Temperature on Heavy-Oil/Water Relative Permeabilities in Horizontally and Vertically Drilled Core Plugs. Journal of Petroleum Technology 37(8):1500–1510.

Mehrotra, A.K. and Svrcek, W.Y. 1986. Viscosity of Compressed Athabasca Bitumen. The Canadian Journal of Chemical Engineering 64: 844-847.

Mohebati, M. H., Maini, B. B., and Harding, T. G., 2012. Numerical-simulation investigation of the effect of heavy-oil viscosity on the performance of hydrocarbon additives in SAGD. SPE Reservoir Evaluation & Engineering 15(02): 165-181.

Musial, G., Reynaud, J. Y., Gingras, M. K., Féniès, H., Labourdette, R., and Parize, O., 2012. Subsurface and Outcrop Characterization of Large Tidally Influenced Point Bars of the Cretaceous McMurray Formation (Alberta, Canada). Sedimentary Geology 279: 156-172.

Musial, G., Labourdette, R., Franco, J., and Reynaud, J. Y. 2013. Modeling of a Tide-Influenced Point-bar Heterogeneity Distribution and Impacts on Steam-Assisted Gravity Drainage Production: Example from Steepbank River, McMurray Formation, Canada. AAPG Studies in Geology 64: 545-564.

Nasr, T. N., Law, D. H. S., Beaulieu, G., Golbeck, H., Korpany, G., and Good, W. K., 2003. SAGD Application in Gas Cap and Top Water Oil Reservoirs. Journal of Canadian Petroleum Technology, 42(01): 32-38.

Neshat, S.S., Okuno, R., and Pope, G.A. 2017. A Rigorous Solution to the Problem of Phase Behavior in Unconventional Formations with High Capillary Pressure. Presented at Annual Technical Conference and Exhibition SPE 187260-MS.

Nourozieh, H. 2013. Phase Partitioning and Thermo-physical Properties of Athabasca Bitumen/Solvent Mixtures. PhD Thesis. University of Calgary, Alberta. Canada.

Nourozieh, H., Kariznovi, M., and Abedi, J. 2015a. Viscosity Measurement and Modeling for Mixtures of Athabasca Bitumen/n-Pentane at Temperatures up to 200° C. SPE Journal 20(02): 226-238.

Nourozieh, H., Kariznovi, M., and Abedi, J. 2015b. Viscosity Measurement and Modeling for Mixtures of Athabasca Bitumen/Hexane. Journal of Petroleum Science and Engineering 129: 159-167.

Nourozieh, H., Kariznovi, M., Guan, J. G., and Abedi, J. 2013. Measurement of Thermophysical Properties and Modeling for Pseudo-binary Mixtures of n-Decane and Athabasca Bitumen. Fluid Phase Equilibria 347: 62-75.

Nourozieh, H., Kariznovi, M., and Abedi, J. 2014. Measurement and Prediction of Density for the Mixture of Athabasca Bitumen and Pentane at Temperatures up to 200° C. Energy & Fuels 28(5): 2874-2885.

Oliveira, M. B., Coutinho, J. A. P., & Queimada, A. J. (2007). Mutual solubilities of hydrocarbons and water with the CPA EoS. Fluid Phase Equilibria 258(1): 58-66.

Oskouei S.J., Maini B., Moore R.G., and Mehta S.A. 2012. Effect of Initial Water Saturation On the Thermal Efficiency of the Steam-Assisted Gravity-Drainage Process. Journal of Canadian Petroleum Technology 51(5):351–361.

Peng, D.Y. and Robinson, D.B. 1976. A New Two-Constant Equation of State. Industrial and Engineering Chemistry Fundamentals 15(1): 59-64.

Perkins, T. K., and Johnston, O. C., 1963. A Review of Diffusion and Dispersion in Porous Media. SPE Journal 3(01): 70-84.

Platts. 2015. Solventswire 38(37). McGraw Hill Financial, https://www.platts.com/IM.Platts.Content/ProductsServices/Products/solventswire.pdf, (accessed March 4, 2016).

Pyrcz, M. J., and Deutsch, C. V., 2014. Geostatistical Reservoir Modeling. Oxford University Press.

Ranger, M. J., and Gingras, M., 2010. Geology of the Athabasca oil sands: Field Guide & Overview. Canadian Society of Petroleum Geologists.

Reamer, H.H., Olds, R.H., Sage, B.H., and Lacey, W.N. 1944. Phase Equilibria in Hydrocarbon Systems. n-Butane–Water System in Three-Phase Region. Industrial and Engineering Chemistry 36(4): 381-383.

Reis, J.C. 1992. A Steam-Assisted Gravity Drainage Model for Tar Sands: Linear Geometry. *The* Journal of Canadian Petroleum Technology 31(10): 14-20.

Remy, N., 2005. S-GeMS: The Stanford Geostatistical Modeling Software: A Tool for New Algorithms Development. In Geostatistics Banff 2004 Springer Netherlands: 865-871.

Robinson, D.B and Peng, D.Y. 1978. The Characterization of the Heptanes and Heavier Fractions for the GPA Peng-Robinson Programs. Gas Processors Association Research Report RR-28.

Shaw, D.G., Maczynski, A., Goral, M., et al. 2005. IUPAC-NIST Solubility Data Series. 81. Hydrocarbons With Water and Seawater- Revised and Updated. Part 7. C8H12–C8H18 Hydrocarbons With Water. Journal of Physical and Chemical Reference Data 34(4): 2261-2298.

Shaw, D.G., Maczynski, A., Goral, M., et al. 2006a. IUPAC-NIST Solubility Data Series. 81. Hydrocarbons With Water and Seawater-Revised and Updated. Part 9. C10 Hydrocarbons with Water. Journal of Physical and Chemical Reference Data 35(1): 93-151.

Shaw, D.G., Maczynski, A., Goral, M., et al. 2006b. IUPAC-NIST Solubility Data Series. 81. Hydrocarbons With Water and Seawater-Revised and Updated. Part 11. C13–C36 Hydrocarbons with Water. Journal of Physical and Chemical Reference Data 35(2): 687-784.

Sheng, K., Okuno, R., and Wang, M. 2017. Water-Soluble Solvent as an Additive to Steam for Improved SAGD. Presented at Heavy Oil Technical Conference SPE 184983-MS.

Shi, X., and Okuno, R. 2017. Analytical Solution for Steam Assisted Gravity Drainage With Consideration of Temperature Variation along the Edge of A Steam Chamber. Fuel (*Submitted*).

Shinta, A.A. and Firoozabadi, A. 1997. Predicting Phase Behavior of Water/Reservoir-Crude Systems With the Association Concept. SPE Reservoir Engineering 12(2): 131-137.

Skripka, V.G. 1979. Solubility of Water in Normal Alkanes at Elevated Temperatures and Pressures. Chemistry and Technology of Fuels and Oils 15(2): 88-90.

Reamer, H.H., Olds, R.H., Sage, B.H., and Lacey, W.N. 1944. Phase Equilibria in Hydrocarbon Systems. n-Butane–Water System in Three-Phase Region. *Industrial and Engineering Chemistry* **36**(4): 381-383.

Thomas, R. G., Smith, D. G., Wood, J. M., Visser, J., Calverley-Range, E. A., and Koster, E. H., 1987. Inclined Heterolithic Stratification—Terminology, Description, Interpretation and Significance. Sedimentary Geology 53(1-2): 123-179.

Tsonopoulos, C. 1999. Thermodynamic Analysis of the Mutual Solubilities of Normal Alkanes and Water. Fluid Phase Equilibria 156(1): 21-33.

Tsonopoulos, C. and Wilson, G.M. 1983. High-Temperature Mutual Solubilities of Hydrocarbons and Water. Part I: Benzene, Cyclohexane and n-Hexane. AIChE Journal 29(6): 990-999.

Van Konynenburg, P.H. and Scott, R.L. 1980. Critical Lines and Phase Equilibria in Binary van der Waals Mixtures. *Philosophical Transactions of the Royal Society of London.Series A, Mathematical and Physical Sciences* **298**(1442): 495-540.

Venkatramani, A. 2014. Modeling of Water-Containing Reservoir Oil for Steam Injection Simulation. MSc Thesis. University of Alberta, Canada.

Venkatramani, A., and Okuno, R. 2015. Characterization of Water Containing Oil Using an EOS for Steam Injection Processes. Journal of Natural Gas Science and Engineering 26: 1091-1106.

Wagner, W. and Pruß, A. 2002. The IAPWS Formulation 1995 for the Thermodynamic Properties of Ordinary Water Substance for General and Scientific use. Journal of Physical and Chemical Reference Data 31(2): 387-535.

Wang, C., and Leung, J., 2015. Characterizing the Effects of Lean Zones and Shale Distribution in Steam-Assisted-Gravity-Drainage Recovery Performance. SPE Reservoir Evaluation & Engineering: 329-345.

Yang, G., and Butler, R. M., 1992. Effects of Reservoir Heterogeneities on Heavy Oil Recovery by Steam-Assisted Gravity Drainage. Journal of Canadian Petroleum Technology 31(08): 37-43.

Yazdi, M. M., and Jensen, J. L., 2014. Fast Screening of Geostatistical Realizations for SAGD Reservoir Simulation. Journal of Petroleum Science and Engineering 124: 264-274.

Younglove, B. A. and Ely, J. F. 1987. Thermophysical Properties of Fluids. II. Methane, Ethane, Propane, Isobutane, and Normal Butane. Journal of Physical and Chemical Reference Data 16(4): 577-798.

Zirrahi, M., Hassanzadeh, H., and Abedi, J. 2015. Prediction of Water Solubility in Petroleum Fractions and Heavy Crudes Using Cubic-Plus-Association Equation of State (CPA-EoS). Fuel 159: 894-899.

Zhang, B., and Okuno, R., 2015. Modeling of Capacitance Flow Behavior in EOS Compositional Simulation. Journal of Petroleum Science and Engineering 131: 96-113.

Zhou. W., Dong, M., and Chen, S. 2015. Investigation of Initial Water Mobility and its Effects on SAGD Performance in Bitumen Reservoirs and Oil Sands. Journal of Petroleum Science and Engineering 135:39–49.

Zhou. W., Chen, S., and Dong, M. 2016. Novel Insights on Initial Water Mobility: Its Effects of Steam-Assisted Gravity Drainage Performance. Fuel 174:274–286.

Appendix A. Overview of Phase Behavior of Water/Hydrocarbon Mixtures

A-1. Multiphase behavior of water/n-alkane binaries

This section gives an overview for multiphase behavior of water/n-alkane binaries. The contents of this appendix is mainly informed by a prior study by Venkatramani and Okuno (2015) [also see Venkatramani (2014)].

In the context of compositional modeling for ES-SAGD, the three-phase curves and the solubility of water in the oleic (L) phase (x_{wL}) for water/n-alkane binaries are of significance considering that the chamber-edge represents the transition from oleic-vapor-aqueous to oleic-aqueous coexistence, and that water exhibits the least affinity to n-alkanes compared to naphthenes and aromatics (Tsonopoulos and Wilson, 1983; Heidman et al., 1985). Hence, it is pertinent to begin this appendix with an overview of the phase behavior of binary mixtures of water and n-alkanes.

The multiphase behavior of water/n-alkane binaries was classified into types IIIa and IIIb by Brunner (1990) according to the classification scheme of van Konynenburg and Scott (1980). A common aspect of both types is that at a given temperature, the oleic-vapor-aqueous (L-V-W) to oleic-aqueous transition pressure is systematically higher than the saturation pressures of water and n-alkane. Or, the oleic-vapor-aqueous to oleic-aqueous transition temperature for a given pressure lies on the lower temperature side of the vapor pressure curves of water and n-alkane.

Type IIIa was observed to occur for water with n-alkanes with carbon numbers (CNs) up to 25. The relative volatility of n-alkane to water changes at CN six. So, for water/n-alkane binaries with CNs lower than six, the vapor pressure curve of the n-alkane component lies on the higher pressure side of the water vapor pressure curve. And for binaries with CNs higher than six, the relative volatilities are the other way around. The upper critical endpoint (UCEP) for a type IIIa system is where the oleic and vapor phases merge in the presence of the aqueous phase, with the oleic phase being less dense than the aqueous phase along the three-phase curve.

Brunner (1990) observed barotropic reversal between the oleic and aqueous phases along the three-phase curve for water with n-alkanes with the CN of 28 and higher; this renders the aqueous phase to be less dense than the oleic phase at the UCEP for these binaries. This is a key characteristic of type IIIb binaries, where the aqueous and vapor phases merge in the presence of

the oleic phase at the UCEP. According to Brunner (1990), the temperature at which the barotropic reversal of the two liquid phases takes place along the three-phase curve decreases with increasing CN of n-alkane.

Figure A-1 gives schematic pressure-temperature (P-T) projections for water/n-alkane binaries (Venkatramani, 2014); **Figures A-2 and A-3** give schematic pressure-composition (P-x) cross-sections for $T \leq T_{UCEP}$ (Venkatramani, 2014). **Figure A-4** gives predicted P-x cross-sections for the water/n-C_6 binary using the Peng-Robinson (PR) EOS with van der Waals' mixing rules for the temperatures of approximately 448 and 473 K; values for the EOS parameters can be found in Appendix B. The systematic investigation made by Brunner (1990) showed that the three-phase curve becomes closer to the water vapor pressure curve as n-alkane becomes heavier (see **Figure A-5**), and approaches a certain asymptotic limit near the water vapor pressure curve in P-T space.

A-2. Solubility of water in the oleic phase

Figure A-6 shows the x_{wL} values measured along three-phase curves for water with n-alkanes with CNs 3, 4, 6, 7, 8, 9, 10, 12, 16, and 20 (Reamer et al. 1944; Kobayashi and Katz 1953; Skripka 1979; Tsonopoulos and Wilson 1983; Heidman et al 1985; Economou et al. 1997; Maczynski et al. 2005; Shaw et al. 2005; Shaw et al. 2006ab). Based on Maczynski et al. (2005) and Shaw et al. (2005, 2006ab), the experimental uncertainties in the measurements were approximately ±30% relative to the reported values. Experimental data for x_{wL} along the three-phase curves have not been presented for CNs higher than 20. **Figure A-6** indicates that x_{wL} along the three-phase curve increases with temperature for a given binary. The dependency of x_{wL} on n-alkane CN for a given temperature is apparently weak except in the near-UCEP region.

At a given temperature, the value of x_{wL} is observed to be greater in aromatics (e.g., reservoir oils and bitumens) compared to that in n-alkanes. This is illustrated in **Figure A-7**, which compares the measured x_{wL} values for a couple of water/n-alkane binaries and water/Athabasca-bitumen near the three-phase region as a function of temperature.

A-3. Chamber-edge temperature in bitumen recovery using ES-SAGD

The experimental investigations of Amani et al. (2013ab) indicate that mixtures of water and Athabasca bitumen can also exhibit three-phase behavior. The authors identified the behavior to be consistent with Type IIIb following the classification scheme of van Konynenburg and Scott

(1980). **Figure A-8** presents a schematic P-T projection and P-x cross-sections for a "pseudo-binary" mixture of water and Athabasca bitumen (Amani et al., 2013a). **Figure A-9** presents a measured P-T cross-section and P-x cross-section for the same system (Amani et al., 2013ab). The measured P-T cross-sections by Amani et al. (2013ab) over a wide range of overall compositions of Athabasca-bitumen and water indicate that in the range of the operating pressures used in SAGD, the oleic-aqueous-vapor to oleic-aqueous transition temperatures occur near the saturation temperature of water. So, when solvent is coinjected with steam, the temperature at the chamber-edge is expected to be bounded between the oleic-vapor-aqueous to oleic-aqueous transition temperatures of the solvent/water and bitumen/water systems, respectively.

For example, **Figure A-10** gives the predicted tie-triangle for a ternary mixture of water/n-C_6/dead Athabasca-bitumen (C_D) at 35 bars for the overall composition of 95 mol% water + 4 mol% n-C_6 + 1 mol% C_D; the oleic-vapor-aqueous to oleic-aqueous transition temperature at these conditions is 476 K. At the same pressure, the phase transition temperature for the water/Athabasca-bitumen pseudo binary and water/solvent binary are approximately equal to 516 and 473 K, respectively. The EOS-parameters for these calculations are given in Appendix B. In steam-injection and steam-solvent coinjection, since a large quantity of water is injected into the reservoir, it is conceivable for the overall mole fraction of water near the chamber edge to be around 85 – 90 mol%. From Figure A-10, it is apparent that if the concentration of solvent in the injection stream is set to 2 mol%, the overall mole fraction of solvent near the chamber edge must be significantly greater than this value for a significant reduction in chamber-edge temperature (around 8 – 10 mol%). This is aspect is also illustrated in the early part of Section 3.2 in Chapter 3 (also see Table 3.2).

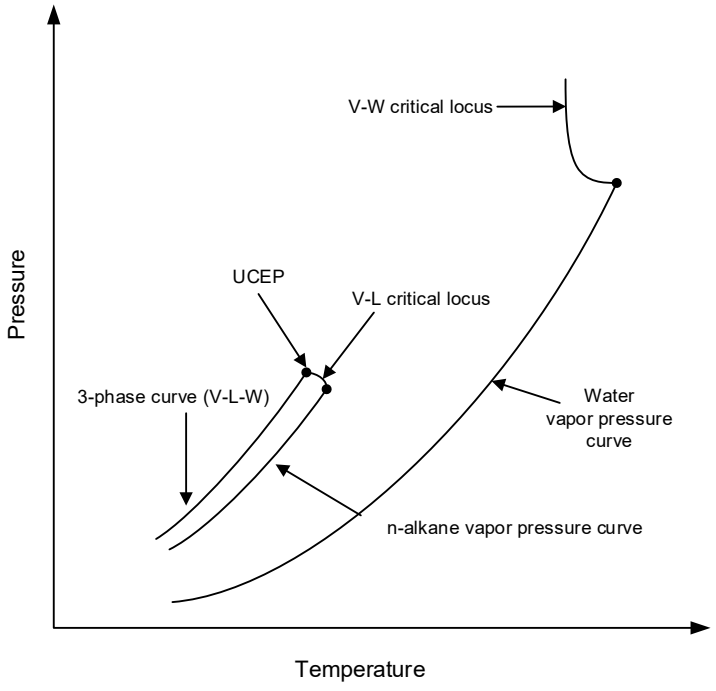
V-W critical locus
UCEP
V-L critical locus
3-phase curve (V-L-W)
Water
vapor pressure
curve
n-alkane vapor pressure curve
Pressure
Temperature

(a)

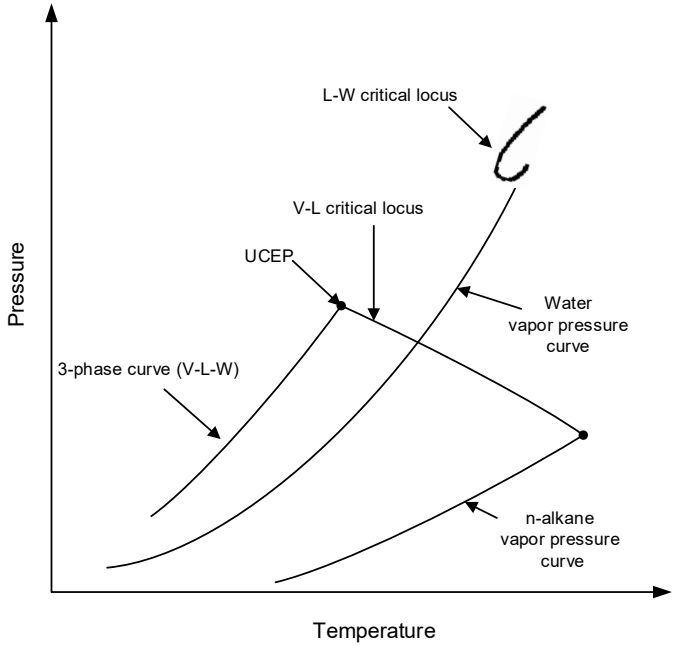
L-W critical locus
V-L critical locus
UCEP
Water
vapor pressure
curve
3-phase curve (V-L-W)
n-alkane
vapor pressure
curve
Pressure
Temperature

(b)

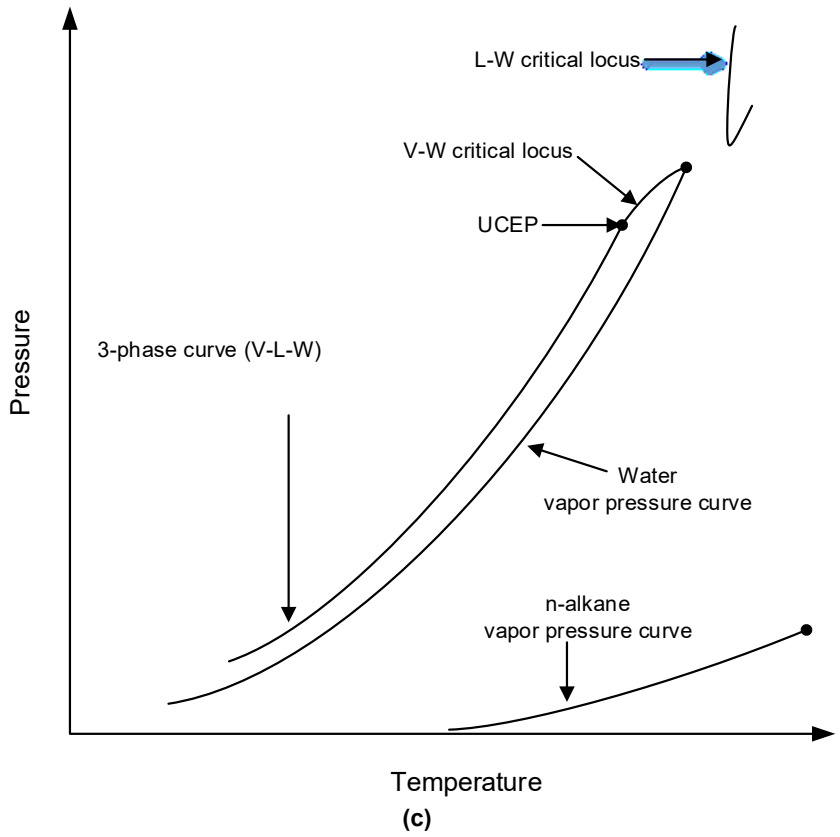

Figure A-1. Schematic P-T projections for type IIIa and IIIb water/n-alkane binaries; (a) type IIIa with n-alkane component is more volatile than water (e.g., water/n-C_4); (b) type IIIa with n-alkane component is less volatile than water (e.g., water/n-C_{12}); (c) type IIIb (e.g., water/n-C_{28}).

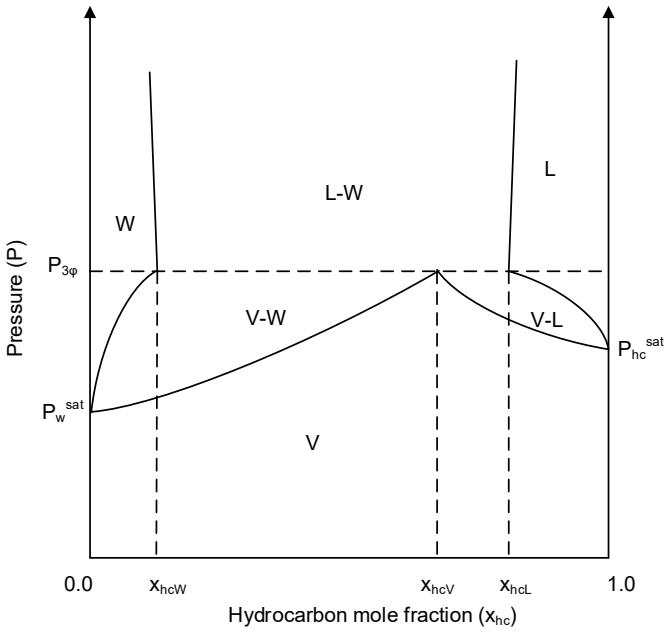

(a)

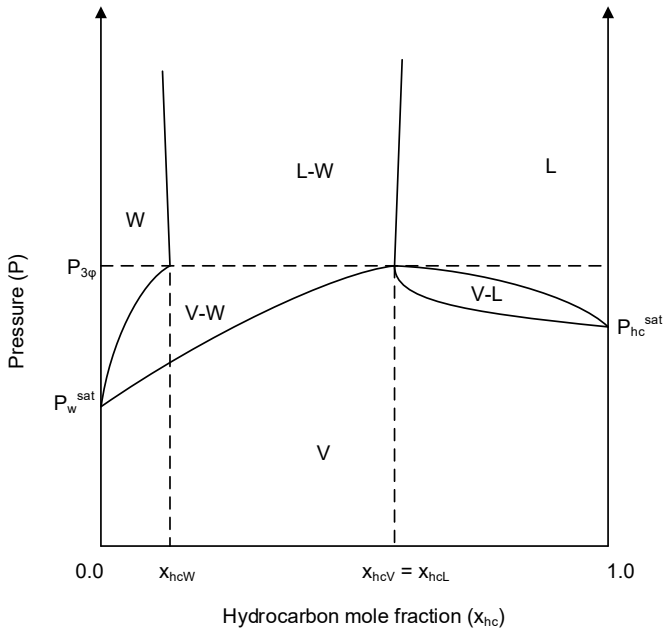

(b)

Figure A-2. Schematic P-x cross-section for a type IIIa binary in which water is less volatile than the n-alkane component; (a) $T < T_{UCEP}$ (b) $T = T_{UCEP}$.

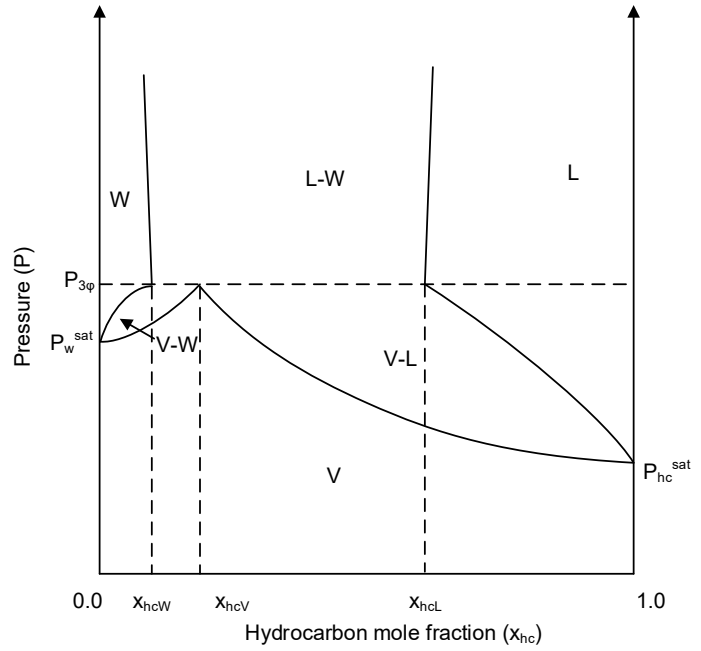

(a)

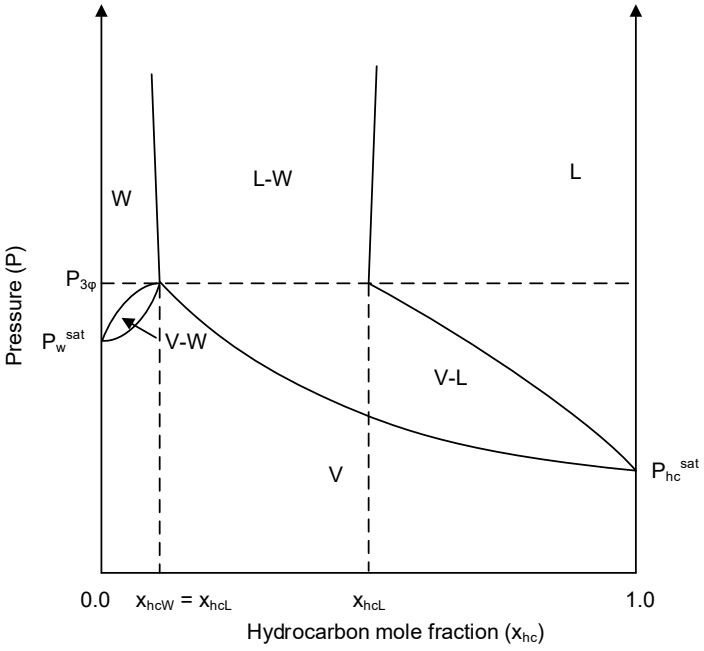

(b)

Figure A-3. Schematic for the P-x cross-section for a type IIIb binary; (a) $T < T_{UCEP}$ (b) $T = T_{UCEP}$.

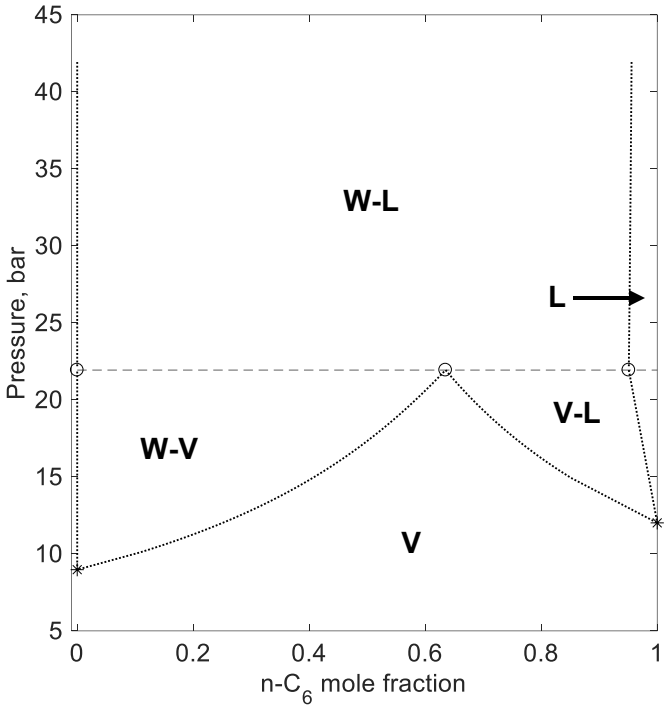

(a)

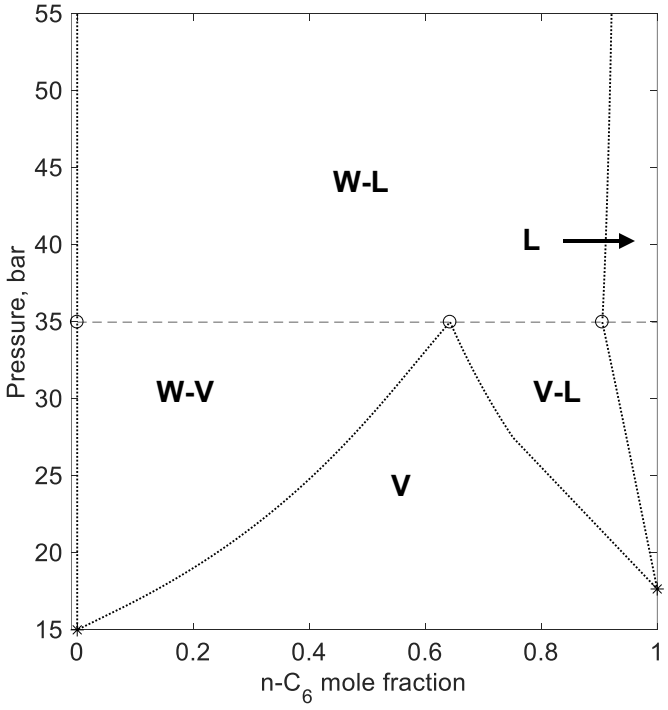

(b)

Figure A-4. Predicted P-x cross-sections for the water/n-C_6 binary using the PR EOS; (a) T = 448; (b) T = 473 K.

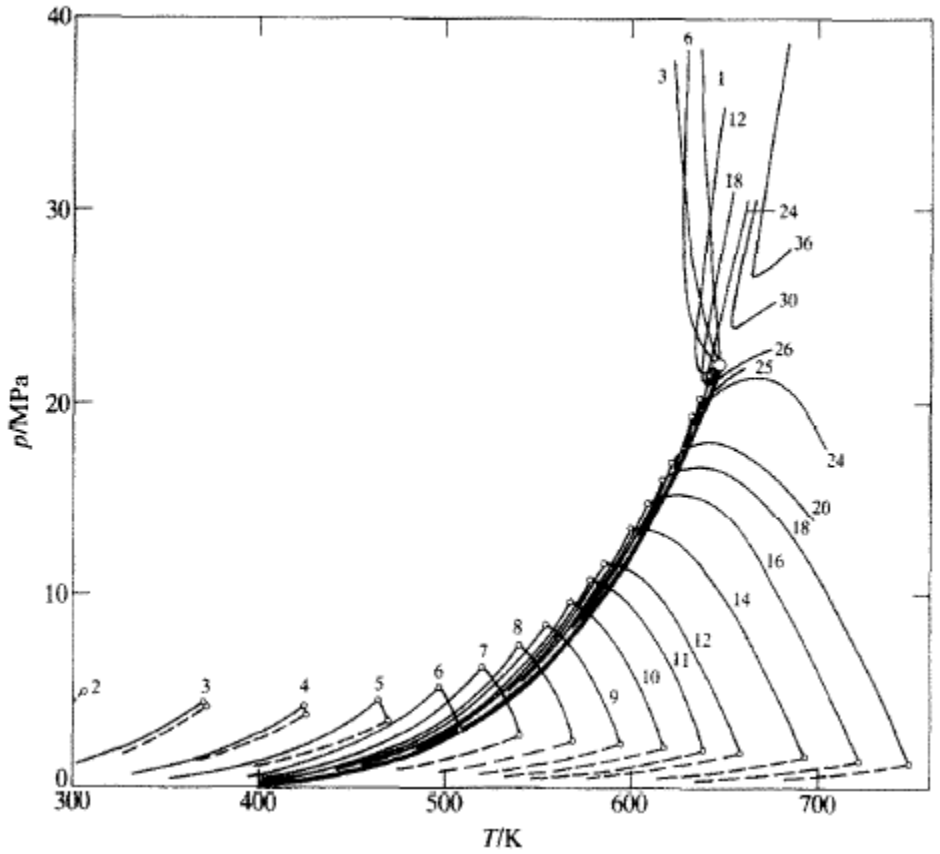

Figure A-5. Asymptotic approach of three-phase (oleic-vapor-aqueous) P-T projections of water/n-alkane binaries to a limit near the vapor pressure curve of water (taken from Brunner, 1990).

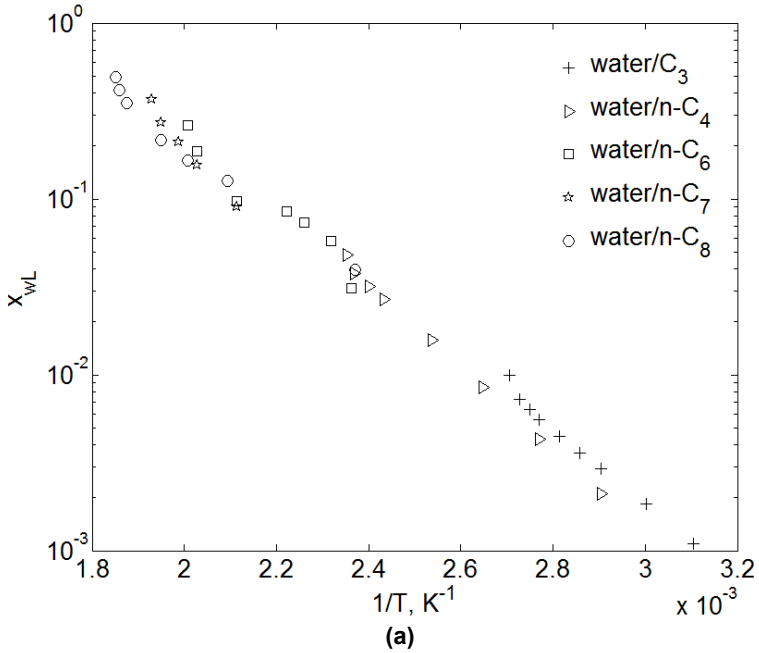

Figure A-6. x_{wL} measured along the three-phase curves for different binaries. Data sources are as follows: Kobayashi and Katz (1953) for water/C_3; Reamer et al. (1944) for water/n-C_4; Skripka (1979), Tsonopoulos and Wilson (1983), and Maczynski et al. (2005) for water/n-C_6; Skripka (1979) for water/n-C_7, and Skripka (1979), Heidman et al. (1985), Shaw et al. (2005) for water/n-C_8, Skripka (1979) for water/n-C_9, water/n-C_{12}, and water/n-C_{20}; Skripka (1979) and Shaw et al. (2006a) for water/n-C_{10}, and Skripka (1979) and Shaw et al. (2006b) for water/n-C_{16}.

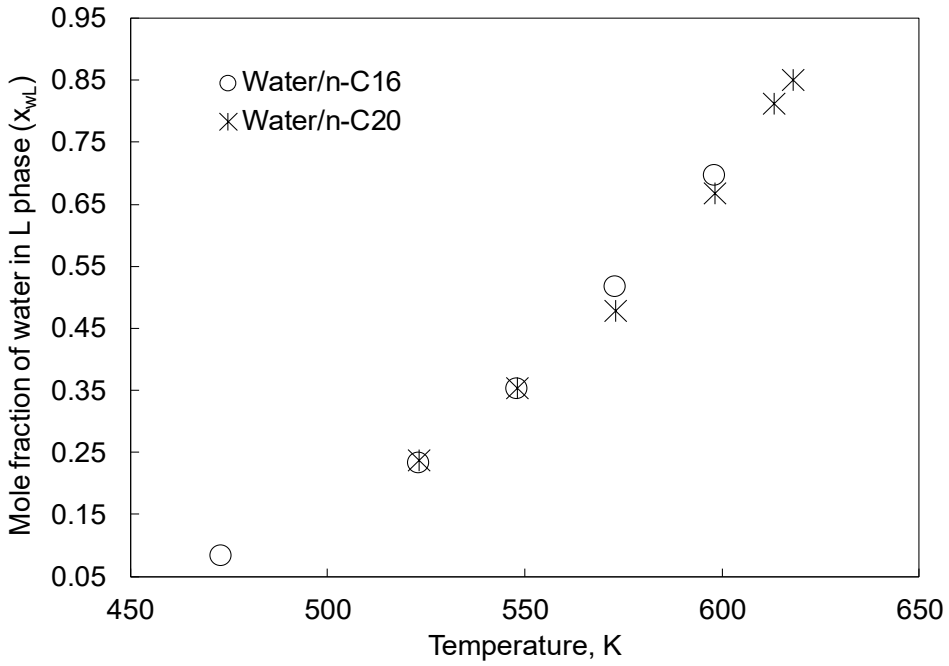

(a)

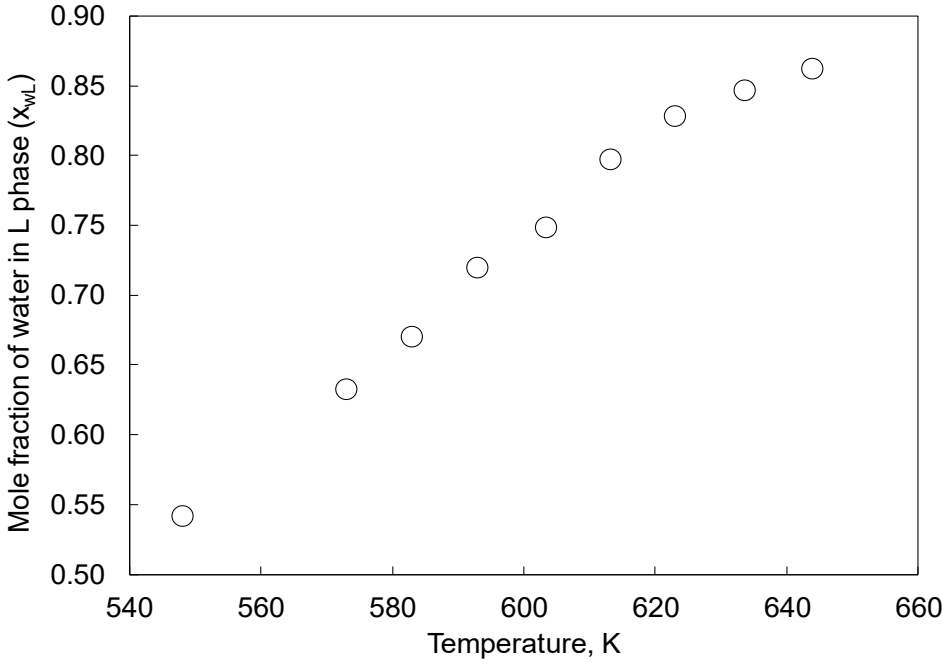

(b)

Figure A-7. Measured x_{wL} in the three-phase region for different water/hydrocarbon mixtures; (a) water/n-alkanes; (b) water/Athabasca-bitumen. Data for water/n-alkane binaries were obtained from Skripka (1979) and Shaw et al. (2006). Data for water/Athabasca-bitumen were obtained from Amani et al. (2013ab).

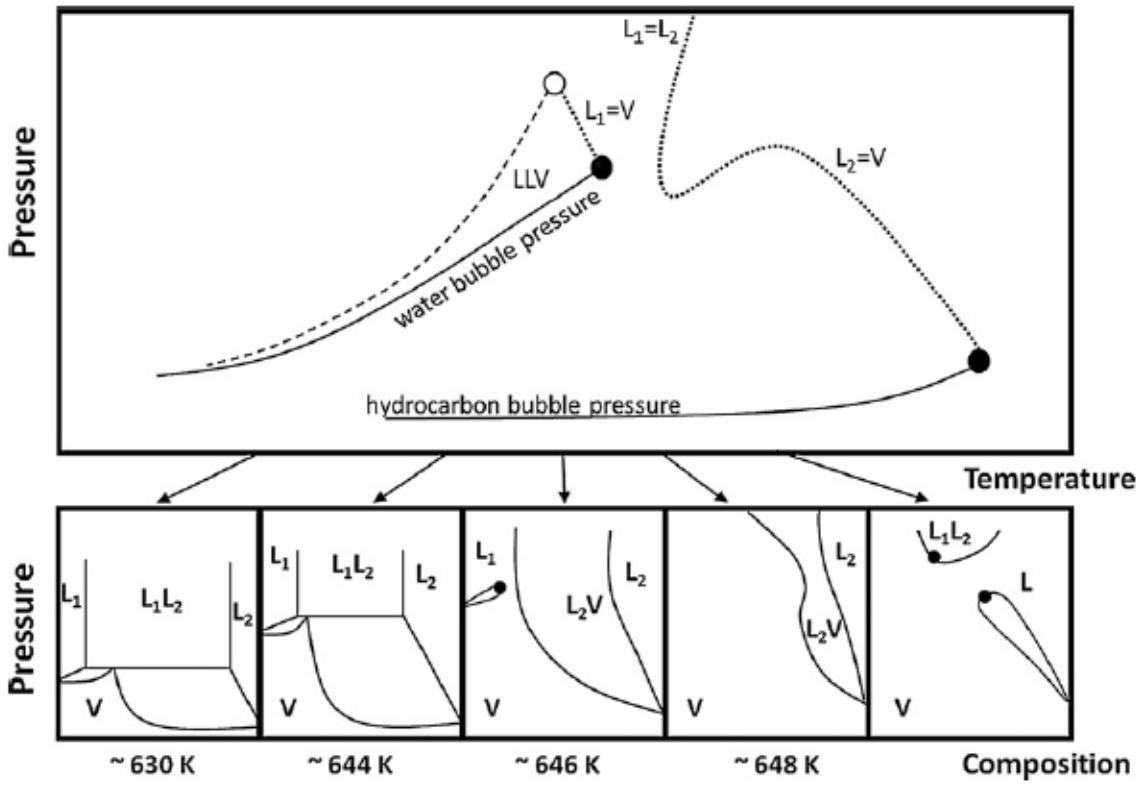

Figure A-8. Schematic P-T projection and pressure-composition cross-sections of a pseudo binary mixture of water and Athabasca bitumen (taken from Amani et al., 2013a). The aqueous and oleic phases were respectively designated as L_1 and L_2 by the authors.

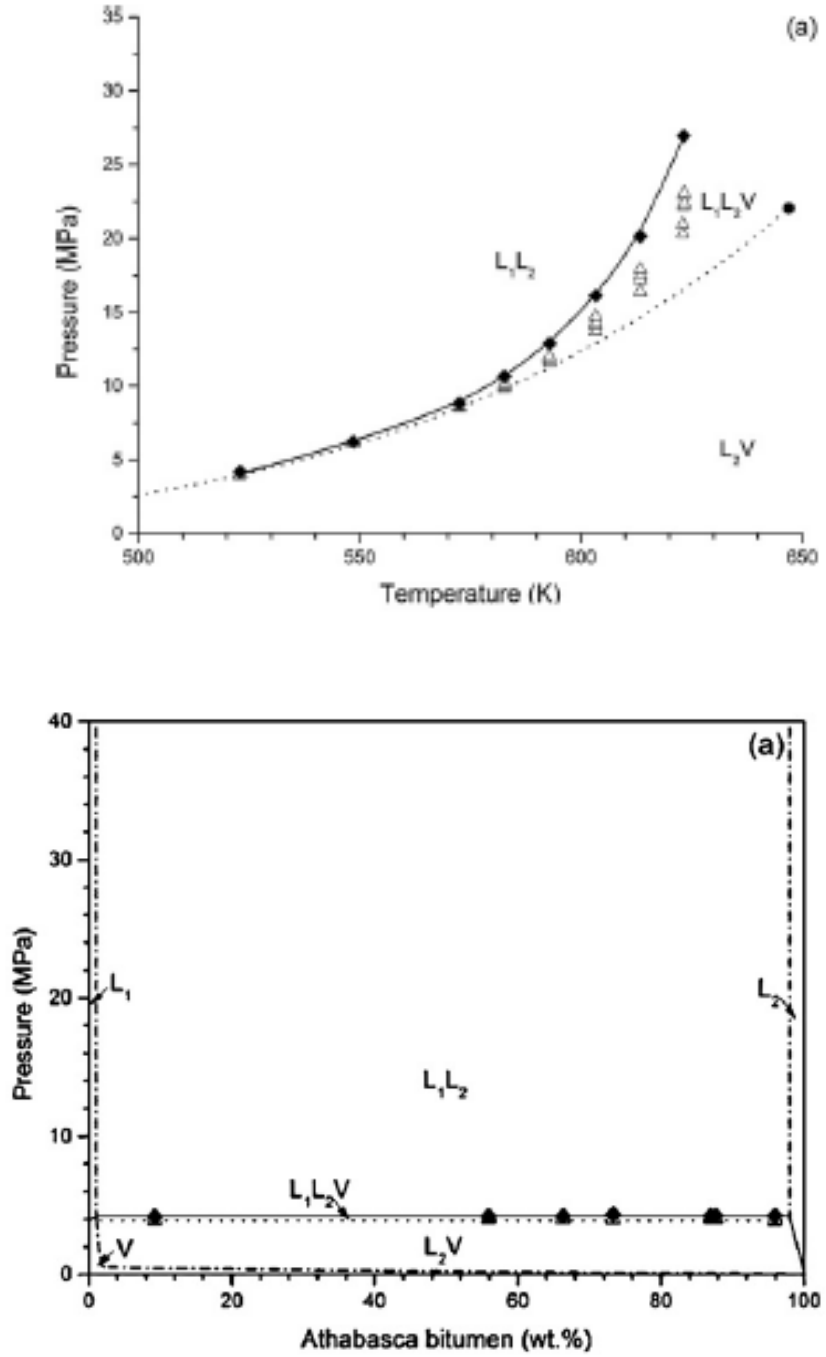

Figure A-9. Measured P-T and pressure-composition cross-sections for water/Athabasca-bitumen system (taken from Amani et al., 2013ab); (a) P-T cross-section of overall bitumen concentration of 9.2 wt%; (b) pressure-composition cross-section at 523 K.

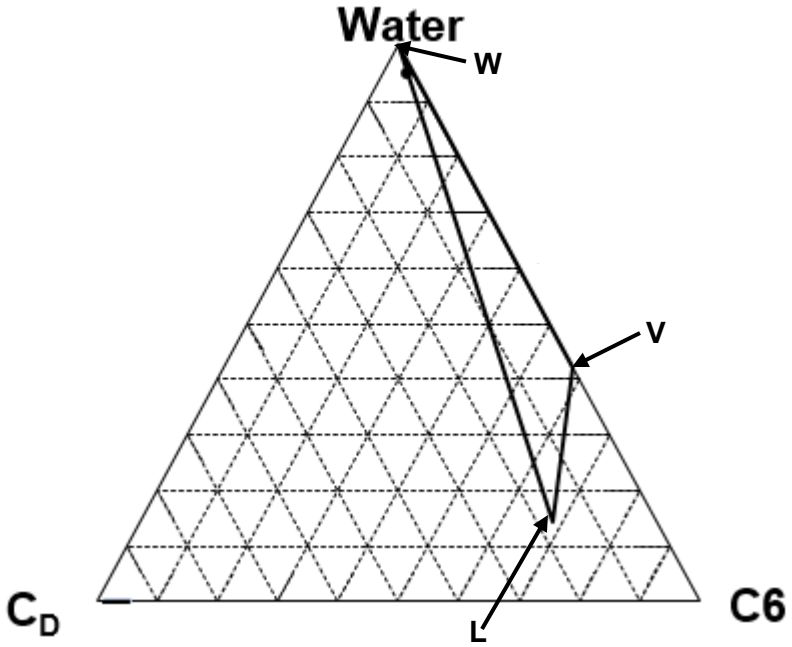

Figure A-10. Predicted three-phase (oleic-vapor-aqueous) tie-triangle using the PR EOS for water/n-C_6/Athabasca-bitumen (C_D) system for the water/n-C_6 binary using the PR EOS at 35 bars and 476 K (Sheng et al., 2017). The black dot indicates the overall composition at which the flash calculation is performed (95 mol% water + 4 mol% solvent + 1 mol% C_D).

Appendix B. EOS Model for Water/Solvent/Bitumen

Table B-1. Component-specific critical constants (T_C, P_C), acentric factor (ω) and molecular weights (MW). The values of T_C, P_C, and ω for n-alkanes were obtained from Venkatramani and Okuno (2015). Dead bitumen supplied by JACOS was characterized as a single pseudo component (C_D) by the perturbation from n-alkanes (PnA) method developed Kumar and Okuno (2015); this was conducted on the basis of phase equilibrium and density measurements made for methane-saturated bitumen. The pertinent experimental data were obtained from Kariznovi (2013) and Nourozieh (2013). A detailed description of the characterization method can be found in Kumar (2016).

Component	T_C, K	P_C, bar	ω	MW, g/mol
C_1	190.5611	45.9908	0.0157	16.0427
C_3	369.8278	42.4807	0.1543	44.0961
n-C_4	425.1222	37.9605	0.2014	58.1228
n-C_5	469.7000	33.7009	0.2511	72.1495
n-C_6	507.6000	30.2507	0.3010	86.1762
n-C_7	540.2000	27.4005	0.3505	100.2029
n-C_8	568.7000	24.9245	0.3980	114.2296
n-C_9	594.6000	22.9002	0.4459	128.2563
n-C_{10}	617.7000	21.1000	0.4898	142.2830
C_D	847.1700	10.6381	1.0406	530.0000
Water	647.0960	220.6400	0.3433	18.0100

Table B-2. BIP matrix for water/solvent/Athabasca-bitumen. Kumar (2016) presented a correlation for the BIP for Athabasca bitumen with n-alkane solvents in terms of component-specific critical volumes. It was developed on the basis of phase equilibrium measurements performed by Kariznovi (2013) and Nourozieh (2013) for C_3/bitumen and n-C_4/bitumen in the vapor-liquid and liquid-liquid regions. The BIPs for bitumen with n-alkanes heavier than n-C_4 were obtained by extrapolating the correlation of Kumar (2016). Detailed description of the characterization of the BIP for water with hydrocarbons with references to pertinent experimental data can be found in Venkatramani and Okuno (2015).

	C_1	C_3	n-C_4	n-C_5	n-C_6	n-C_7	n-C_8	n-C_9	n-C_{10}	C_D	Water
C_1	0.000	0.000	0.000	0.000	0.000	0.000	0.000	0.000	0.000	0.000	0.732
C_3	0.000	0.000	0.000	0.000	0.000	0.000	0.000	0.000	0.000	0.067	0.666
n-C_4	0.000	0.000	0.000	0.000	0.000	0.000	0.000	0.000	0.000	0.075	0.636
n-C_5	0.000	0.000	0.000	0.000	0.000	0.000	0.000	0.000	0.000	0.081	0.607
n-C_6	0.000	0.000	0.000	0.000	0.000	0.000	0.000	0.000	0.000	0.088	0.579
n-C_7	0.000	0.000	0.000	0.000	0.000	0.000	0.000	0.000	0.000	0.094	0.553
n-C_8	0.000	0.000	0.000	0.000	0.000	0.000	0.000	0.000	0.000	0.098	0.527
n-C_9	0.000	0.000	0.000	0.000	0.000	0.000	0.000	0.000	0.000	0.102	0.503
n-C_{10}	0.000	0.000	0.000	0.000	0.000	0.000	0.000	0.000	0.000	0.105	0.480
C_D	0.000	0.067	0.075	0.081	0.088	0.094	0.098	0.102	0.105	0.000	0.169
Water	0.732	0.666	0.636	0.607	0.579	0.553	0.527	0.503	0.480	0.169	0.000

Table B-3. Comparison between predicted and measured values of x_{wL} for water-containing Athabasca bitumen. The BIP for water with bitumen (0.169) has been calculated using Equation 2.1 scaled by a factor of 0.70. The properties for water and characterized dead Athabasca bitumen (C_D) are shown in Table B-1. The P-T conditions shown in this table are situated near the oleic-vapor-aqueous/oleic-aqueous boundary. The experimental data were measured for the overall composition of 81.15 mol% water and 18.85 mol% bitumen by Amani et al. (2013b). The "—" indicates a homogeneous liquid phase.

P, bars	T, K	x_{wL} (data)	x_{wL} (EOS)
60.42	548.20	0.5412	0.5064
87.18	573.10	0.6321	0.6321
100.25	583.20	0.6699	0.6877
114.50	593.10	0.7192	0.7464
131.00	603.50	0.7477	—
148.30	613.40	0.7964	—
167.20	623.20	0.8274	—
189.90	633.80	0.8462	—
216.47	644.00	0.8620	—

Appendix C. Oleic-Phase Viscosity Model for Water/Solvent/Bitumen

The viscosity of C_D at different temperatures in the vicinity of 35 bars, the operating pressure of the simulation case studies, is given in **Table C-1**. The viscosities of n-alkanes and water in the oleic phase correspond to that in the saturated liquid state. The pertinent component-specific viscosity data can be found in Dymond and Young (1980), Younglove and Ely (1987), Crabtree and Simon-Tov (1993), Dymond and Oye (1994), and Abdulagtov and Rasulov (1996). For several of the solvents considered in the study, the temperatures in the interior of the steam chamber away from the edge can be in excess of the critical temperature of the solvent. At these temperatures, the liquid phase viscosities of the solvent are obtained by extrapolation of the saturated liquid viscosity curve of the solvent.

Composition-dependent functions for q_{CD} are developed by matching experimental data; the development is restricted by data availability. However, oleic-phase viscosity data are available only for two pseudo binaries, which are water/bitumen and solvent/bitumen.

Simulations for ES-SAGD in this research use the q_{CD} functions developed by using oleic-phase viscosity measurements for the solvent/bitumen binary. Oleic-phase viscosity data for n-alkane/Athabasca-bitumen mixtures are available for n-alkanes with CNs 3, 4, 5, 6, and 10 (Kumar, 2016; Nourozieh et al., 2013; Nourozieh et al., 2015a; Nourozieh et al., 2015b).

Equation 2.6 (Chapter 2) gives the general functional form for q_{CD} developed on the basis of the experimental data where the α-parameter is specific to the n-alkane solvent under consideration. The second term on the right-hand side of Equation 2.6 may be viewed as a function that represents the departure from the logarithmic mixing rule.

The optimum α-values exhibit a monotonically decreasing trend with respect to the n-alkane CN; that is, transition towards the logarithmic mixing rule is observed as the n-alkane CN increases. The pertinent values for the α-parameter are presented in **Table C-2**. Due to the limited data availability, the a-values for n-alkanes with CNs 7 through 9 have been determined using a linear fit shown below,

$$\alpha(\mathrm{CN}) = -0.07551\mathrm{CN} + 0.75051 \qquad \text{(C-1)}$$

Equation C-1 gives the R^2 value of 0.9618 for the set of optimized values for the α-parameter with respect to the n-alkane CN. When Equation C-1 is used in the water/bitumen limit,

systematic underestimation of the oleic-phase viscosity is observed. Nevertheless, Equation C-1 is preferable for application in ES-SAGD simulations. This is because the alternative approach, which is the use of Equation 2.4, is considerably more erroneous when applied in the solvent/bitumen limit.

For SAGD simulations, a composition-dependent function for q_{CD} has been developed based on data corresponding to the water/bitumen edge in composition space. For water/Athabasca-bitumen, oleic-phase viscosity data have not been published, to the best of our knowledge. Therefore, a composition-dependent function for q_{CD} was developed using synthetic data.

The synthetic data were generated on the basis of the experimental study conducted by Glandt and Chapman (1995) on the oleic-phase viscosity of water-containing Peace River bitumen and other reservoir oils. The temperatures in these experiments lie between 434 K and 558 K. The corresponding experimental pressures are near the boundary between two and three phases where the aqueous phase (W) can exist[1]. For water-containing Peace River bitumen, Glandt and Chapman (1995) have demonstrated that the conventional logarithmic mixing rule overestimates the reduction of the oleic-phase viscosity due to x_{wL}. On the other hand, the linear mixing rule, given in Equation 2.5, was shown to satisfactorily predict the oleic-phase viscosity over the aforementioned temperature range.

Synthetic oleic-phase viscosity data for water/Athabasca-bitumen have been generated using a two-step process. For temperatures between 434 K and 558 K, and pressures slightly higher than the corresponding saturation pressure of water, the composition of the oleic phase is first determined by performing P-T flash calculations. The linear mixing rule is subsequently applied to calculate the oleic-phase viscosity. The composition-dependent function developed for q_{CD} using the synthetic data is presented in Equation 2.4. Use of Equation 2.4 results in the average relative deviation (ARD) and absolute average deviation (AAD) values of 0.17%, and 0.12 cp, respectively, with respect to the synthetic oleic-phase viscosity data generated between 434 K and 558 K.

Let us examine the importance of oleic-phase viscosity measurements for water/solvent/bitumen systems for compositions lying within the composition space formed by these components in ES-SAGD simulations. This requires analysis of the mathematical behavior of Equations 2.2 and 2.3. These equations can be rearranged in the following form,

[1] Personal communication with Professor W.G. Chapman, Rice University, Houston, Texas.

$$\ln \mu_L = \overrightarrow{\ln \mu} . \left(\overline{\overline{Q}}\, \vec{x}\right), \quad \text{(C-2)}$$

subject to

$$\left\| \overline{\overline{Q}}\, \vec{x} \right\|_1 = 1.0 \quad \text{(C-3)}$$

where $\vec{x}$ and $\overrightarrow{\ln \mu}$ are column matrices of length N_C, and $\overline{\overline{Q}}$ is a N_C-by-N_C diagonal matrix of component-specific weighting factors (q_i). Equation C-2 indicates at a given temperature, pressure and oleic-phase composition, the predicted oleic-phase viscosity is sensitive to the action of $\overline{\overline{Q}}$ on composition $\vec{x}$; Equation C-3 tells us that the action of $\overline{\overline{Q}}$ on the composition point $\vec{x}$ displaces it to another location within composition space.

Figures C-1 and C-2 present the effect of the action of $\overline{\overline{Q}}$ on lines of constant water and solvent concentration (i.e. fixed x_{wL} and x_{sL}) for SAGD and ES-SAGD. In this demonstration, Equation 2.4 is used to obtain $\overline{\overline{Q}}$ for SAGD, while Equation 2.6 with α-values obtained from Table C-2 and Equation C-1 is used to calculate $\overline{\overline{Q}}$ for ES-SAGD. As seen in these figures, departure from the logarithmic mixing rule is characterized by skewing of the composition lines towards the 100% C_D vertex in composition space. The extent of distortion is affected by the choice of mixing model (see Figure C-2). The mathematical relationship between the weighting factor and composition (i.e., $\overline{\overline{Q}}$) dictates the type of mixing model.

Away from the logarithmic limit, for a specified mixing model, the extent to which a given composition is displaced towards the 100% C_D vertex due to $\overline{\overline{Q}}$ depends on its location relative to the water/C_D and solvent/C_D edges in composition space. Along a line of constant bitumen concentration (i.e. for a composition line with fixed x_{CDL}), compositions near the water/C_D and solvent/C_D edges are skewed to a greater extent towards the 100% C_D edge (see Figure C-2). Or, the extent of distortion due to $\overline{\overline{Q}}$ for lines of constant x_{wL} and x_{sL} increases as 100% water and solvent vertices are approached.

The oleic-phase composition can be situated closer to the water/C_D edge in composition space at high temperatures. At a given pressure, higher temperatures result in higher x_{wL} and lower x_{sL}. Consequently, the oleic-phase composition is shifted closer towards the water/C_D edge in composition space. In these situations, accurate prediction for the reduction of the oleic-phase viscosity due to x_{wL} becomes important. Thus, oleic-phase viscosity measurements at the solvent/bitumen edge in composition space alone may not be adequate for the development of a

reliable viscosity model for ES-SAGD application. This inadequacy is potentially significant under higher operating pressures and when heavier solvents are used for ES-SAGD.

Table C-1. Viscosity data for dead Athabasca bitumen at different temperatures. These data have been measured near 35 bars, the operating pressure for most of the simulation case studies used in this work.

T, K	μ_{CDL}, cp	T, K	μ_{CDL}, cp
283.150	2457801.750	413.150	42.300
293.150	479830.640	423.150	31.000
303.150	114116.110	433.150	23.500
313.150	32282.500	443.150	18.300
323.150	10642.800	453.150	15.010
333.150	4072.870	463.150	12.500
343.150	1650.000	473.150	10.640
353.150	787.000	483.150	9.240
363.150	422.000	493.150	8.160
373.150	241.000	503.150	7.310
383.150	133.000	513.150	6.640
393.150	85.600	523.150	6.100
403.150	58.700		

Table C-2. Optimized values for the α-parameter for ES-SAGD cases. The error in the predicted oleic-phase viscosity in the water/bitumen limit has been evaluated against the synthetic data generated for temperatures between 464 K and 558 K. The ARD in this limit is considerably lower between 283 K and 558 K. Although the ARD for n-C_5/Athabasca-bitumen and n-C_6/Athabasca-bitumen cases seem high, the corresponding AAD values for the predicted oleic-phase viscosities are only 0.92 cp and 1.05 cp, respectively.

CN	α	Data points	Temperature, K	ARD, % (solvent/C_D)	Data sources	ARD, % (water/C_D)	AAD, cp (water/C_D)
3	0.5498	2	373.15	3.42	Kumar (2016)	18.18	1.25
4	0.4273	2	423.15	9.00	Kumar (2016)	30.24	1.96
5	0.3562	18	374.00 - 464.00	33.26	Nourozieh et al. (2015a)	36.30	2.33
6	0.3050	18	374.00 - 464.00	29.78	Nourozieh et al. (2015b)	40.29	2.58
10	0.0000	60	301.00 - 344.00	9.62	Nourozieh et al. (2013)	58.85	3.81

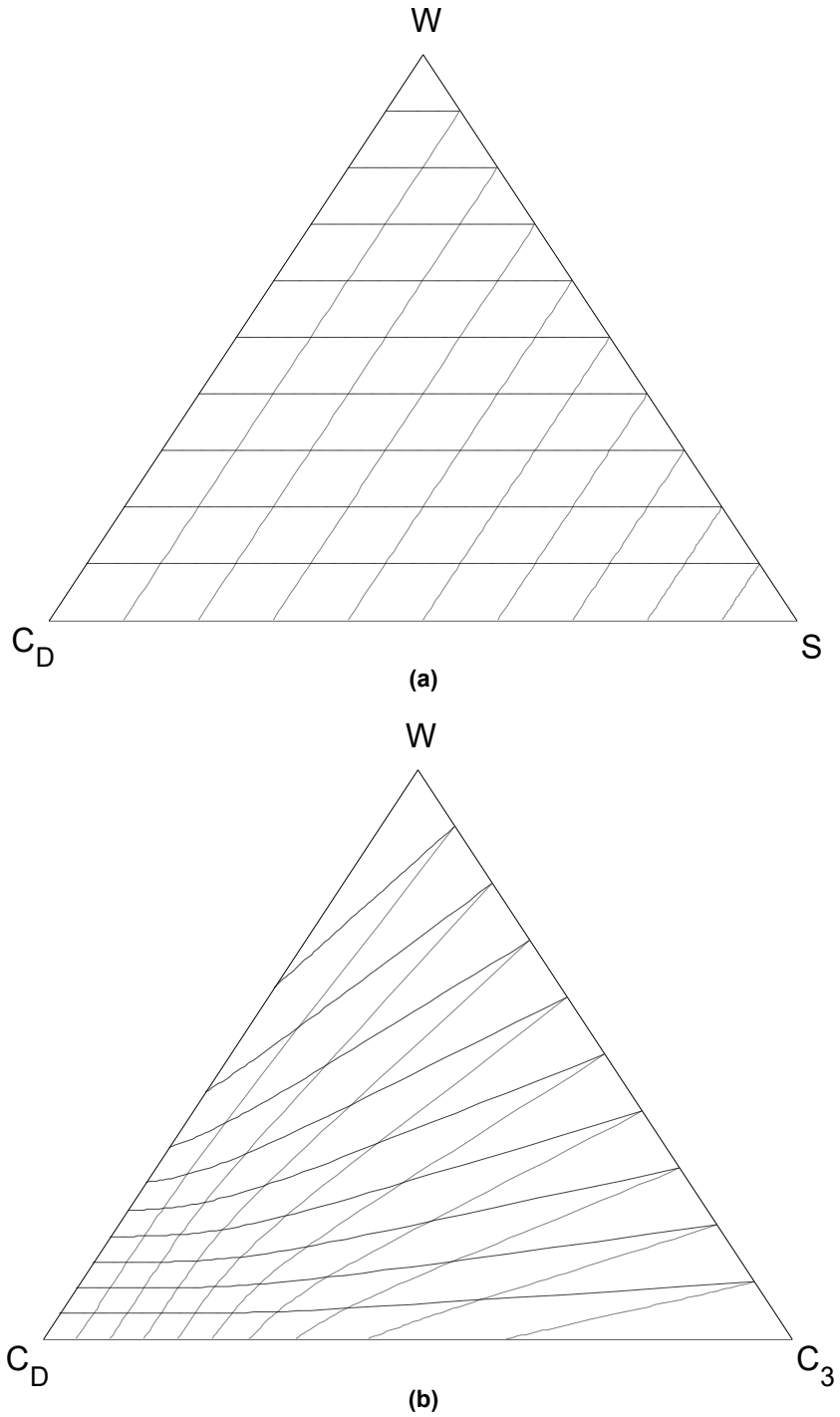

Figure C-1. Effect of the action of the Q-matrix on lines of constant water and solvent concentration for ES-SAGD; (a) α-parameter value of zero (logarithmic limit, as with water/n-C_{10}/bitumen); (b) α-parameter value of 0.3050 as with water/n-C_6/bitumen. The lines are skewed towards the 100% C_D edge in composition space due to the use of a non-zero value for the α-parameter.

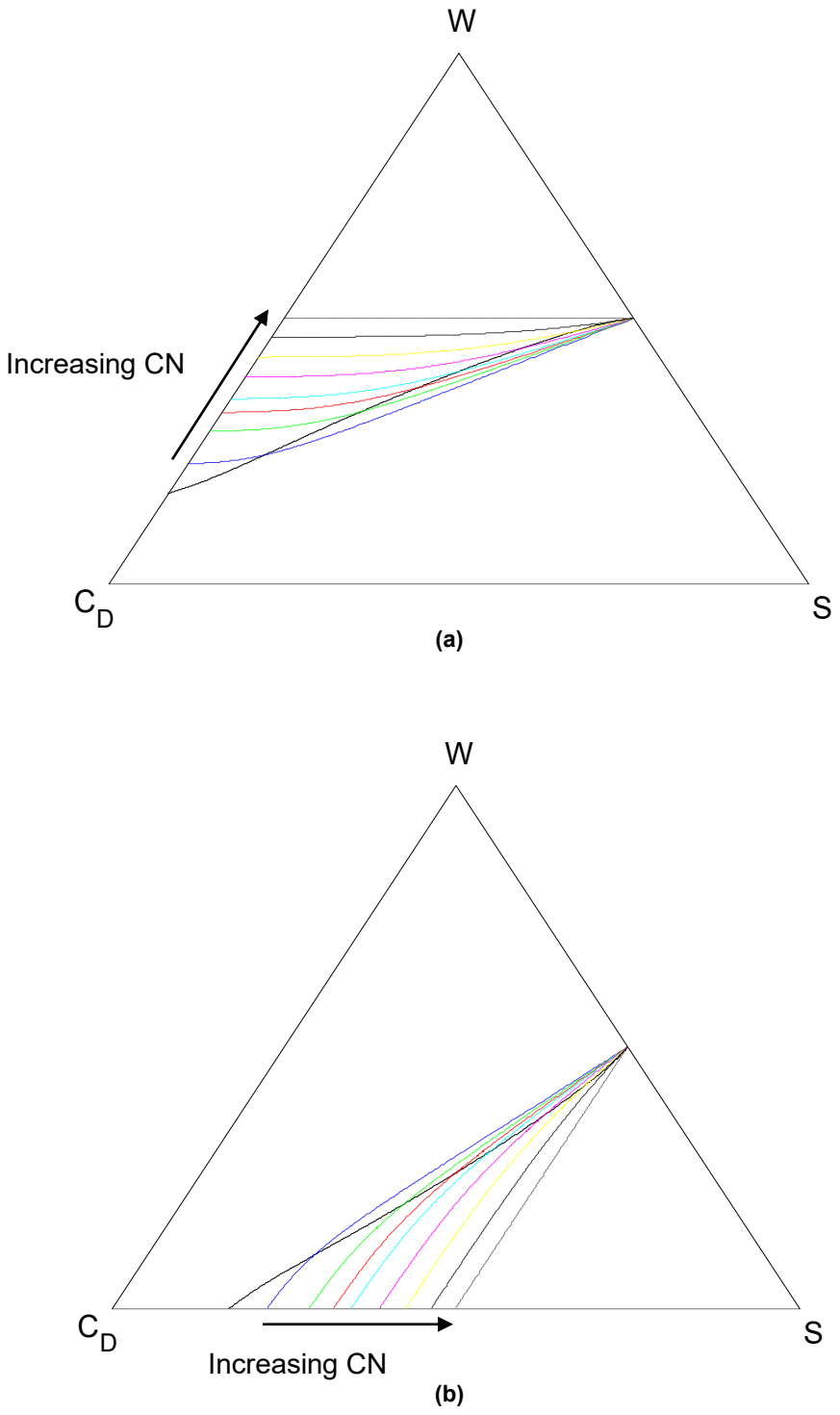

Figure C-2. Effect of the action of Q-matrices determined for SAGD and ES-SAGD on a line of constant water and solvent concentration; (a) x_{wL} = 0.5; (b) x_{sL} = 0.5. The solid black line corresponds to the SAGD case (water/C_1/bitumen). The dashed and dotted lines correspond to the ES-SAGD cases (CNs 3 through 10). For water/n-C_{10}/C_D, the action of the Q-matrix does not distort the reference line as the mixing rule is logarithmic for this system.

Appendix D. Oleic-Phase Density Model for Water/Solvent/Bitumen

The numerical simulations in this paper use the linear mixing rule for the oleic-phase molar volume (Equation 2.7). This appendix discusses the implementation of the linear mixing rule in STARS and its applicability in reservoir simulation. In terms of the mass density, Equation 2.7 can be rewritten as

$$\rho_L = MW_L\left[\sum_{i=1}^{N_c}(x_{iL}MW_i/\rho_{iL})\right]^{-1} \quad \text{(D-1)}$$

where MW_L is the molecular weight of the oleic phase, and MW_i is the molecular weight of the i^{th} component; ρ_L and ρ_{iL} are the mass density of the oleic phase, and the i^{th} component in the oleic phase, respectively.

To facilitate application in STARS (CMG, 2011), the component-specific mass densities (ρ_{iL}) in the oleic phase are correlated using the following functional form,

$$\rho_{iL} = \rho_{iref}e^{a_1(P-P_{ref})-a_2(T-T_{ref})-0.5a_3(T^2-T_{ref}{}^2)+a_4(P-P_{ref})(T-T_{ref})} \quad \text{(D-2)}$$

where T_{ref} = 288.15 K, and P_{ref} = 101.325 kPa (= 1.01325 bars). ρ_{iref} corresponds to the density of the i^{th} component at T_{ref} and P_{ref}. For the calculation of the mass density at an arbitrary P-T condition using Equation D-2, the pertinent units to be used are kPa for pressure and Kelvin for temperature. The values of a_1 through a_4 for each component are determined by optimization against measured data. For n-alkanes and bitumen these coefficients have been obtained from Kumar (2016).

The pertinent coefficients for water have been determined by optimization against the saturated liquid phase density data calculated using the experimentally determined correlation recommended by Wagner and Pruß (2002),

$$\rho_{wL} = 0.322\left(1 + b_1\vartheta^{\frac{1}{3}} + b_2\vartheta^{\frac{2}{3}} + b_3\vartheta^{\frac{5}{3}} + b_4\vartheta^{\frac{16}{3}} + b_5\vartheta^{\frac{43}{3}} + b_6\vartheta^{\frac{110}{3}}\right), \quad \text{(C-3)}$$

where $\vartheta = 1 - (T/647.096)$; b_1 = 1.99274064; b_2 = 1.099653042; b_3 = -0.510839303; b_4 = -1.75493479; b_5 = -45.5170352; and $b_6 = -6.74694450 \times 10^5$.

Between 283.15 K and 558.15 K, the ARD resulting from use of Equation D-3 is 0.16%. The values for ρ_{iref} and coefficients a_1 through a_4 for different water/solvent/Athabasca-bitumen mixtures are given in **Tables D-1 and D-2**.

For both water/Athabasca-bitumen, and solvent/Athabasca bitumen with n-alkane CNs between 5 and 10, use of linear mixing rule to predict the oleic-phase density results in a reasonably good match with respect to the measured data. The pertinent AAD and ARD values are summarized in **Table D-3**.

Table D-1. Coefficients for component-specific densities in the oleic phase to be used with Equation D-2.

Component	ρ_{ref}, kg/m^3	a_1	a_2	a_3	a_4
Water	998.5	0.00E+00	-1.67E-03	6.48E-06	0.00E+00
C_1	320.15	5.13E-06	1.32E-03	5.77E-06	4.05E-08
C_3	651.83	3.02E-06	2.12E-04	5.46E-06	1.08E-08
n-C_4	769.81	2.55E-06	5.19E-05	5.05E-06	4.56E-09
n-C_5	823.47	2.20E-06	-8.87E-05	4.77E-06	2.88E-09
n-C_6	858.69	1.88E-06	-1.21E-04	4.20E-06	2.04E-09
n-C_7	846.36	1.66E-06	-1.30E-04	3.79E-06	1.59E-09
n-C_8	859.85	1.48E-06	-1.28E-04	3.39E-06	1.23E-09
n-C_9	869.99	1.34E-06	-1.24E-04	3.09E-06	9.84E-10
n-C_{10}	869.99	1.22E-06	-1.17E-04	2.80E-06	7.75E-10

Table D-2. Coefficients for density of C_D in the oleic phase to be used with Equation D-2.

System	ρ_{ref}, kg/m^3	a_1	a_2	a_3	a_4
Water/C_3/C_D	992.64	3.88E-07	-2.23E-05	9.09E-07	3.73E-09
Water/n-C_4/C_D	992.64	3.88E-07	-2.23E-05	9.09E-07	4.28E-09
Water/n-C_5/C_D	992.64	3.85E-07	-1.95E-05	8.95E-07	4.72E-09
Water/n-C_6/C_D	992.64	3.85E-07	-1.93E-05	8.95E-07	4.80E-09
Water/n-C_7/C_D	992.64	3.85E-07	-1.95E-05	8.96E-07	4.80E-09
Water/n-C_8/C_D	992.64	3.85E-07	-1.98E-05	8.97E-07	4.79E-09
Water/n-C_9/C_D	992.64	3.86E-07	-2.01E-05	8.98E-07	4.77E-09
Water/n-C_{10}/C_D	992.64	3.86E-07	-2.03E-05	8.99E-07	4.78E-09

Table D-3. Accuracy of the linear mixing rule for prediction of the oleic-phase density of solvent/bitumen and water/bitumen mixtures. For solvent/bitumen mixtures, the validation is performed for pressures in the neighborhood of 35 bars (±5 bars), which is the operating pressure for the simulation cases. The densities of the individual components are calculated using Equation D-2 with the coefficients presented in Tables D-1 and D-2.

System	Data points	Data sources	Temperature, K	Pressure, bars	AAD, g/cc	ARD, %
n-C_5/bitumen	30	Nourozieh et al. (2014)	295 - 463	39 - 41	0.065	8.39
n-C_6/bitumen	30	Kariznovi et al. (2014)	296 - 463	39 - 41	0.066	8.23
n-C_{10}/bitumen	60	Nourozieh et al. (2013)	296 - 333	30 - 40	0.046	5.27
Water/bitumen	21	Amani et al. (2013b)	594 - 643	54 - 260	0.045	5.85

Appendix E. Basis for Modeling of Inclined Mudstone Barriers in Chapter 3

The McMurray formation is divided into three stratigraphic members based on the inferred depositional setting: (i) lower, where the environment is fluvial; (ii) middle, wherein the setting is fluvio-estuarine (tidally influenced point bars); (iii) upper, whose depositional environment is marine (Ranger and Gingras, 2003; Musial et al., 2012, 2013; Hassanpour et al., 2013). The middle member is the most economically significant of the three stratigraphic layers as it holds approximately 70% of the total bitumen reserves contained within the Athabasca deposit (Musial et al., 2013).

The middle McMurray member comprises of composite sets of inclined strata (Musial et al., 2012, 2013) stacked laterally. According to Thomas et al. (1987), a composite set of inclined strata within a point bar deposit has two main features: (i) predominantly homogeneous, inclined, and often trough-shaped cross-stratified sand stone (CSS), known as inclined stratification (IS) that occurs near the base of the point bar; (ii) inclined couplets of sandstone and mudstone, known as inclined heterolithic stratification (IHS) that overlay IS. For the middle McMurray member, the inclination can vary from nearly zero to about twelve degrees relative to the horizontal (Ranger and Gingras, 2003; Musial et al., 2012, 2013).

Outcrops along Steepbank river indicate that the IHS becomes increasingly mud-dominated towards the top of the point bar (Musial et al., 2012); muddy IHS can manifest as drapes. Thomas et al. (1987) identified three different forms of drapes in IHS deposits based on observation of several different outcrops: (i) discontinuous up-dip attached, which originate near the top of point bar and extend towards the middle of the point bar; (ii) continuous, which originate near the top and extend towards the base of the point bar, where they can interbed with the CSS; (iii) discontinuous. A single point bar can be up to 30 m thick; so, the continuous shale drapes can extend over 30 m. The thickness of the mudstone in the IHS couplets can vary from a few millimeters up to a meter (Ranger and Gingras, 2003; Hassanpour et al., 2013; Musial et al., 2013). Gradation from IS to IHS can occur both vertically and laterally (Musial et al., 2012). Transition from IS to sandy IHS, and sandy IHS to muddy IHS can be abrupt; the boundaries between the different rock types can be erosive surfaces containing mudclast breccia, which are

formed due to overbank failure. The top of the point bar has clay deposits, which likely are the result of the filling of abandoned flow channels.

The summary presented above indicates that there are at least five major associations within the middle McMurray member: (i) clean sand (CSS); (ii) slightly heterolithic sands (sandy IHS); (iii) highly heterolithic sands (muddy IHS); (iv) mud clast breccia; (v) abandoned channel fill (clay plugs). Musial et al. (2013) reported the petrophysical properties of the aforementioned facies measured from extracted core samples. The observed geological architecture of the middle member, and experimental measurements reported by Musial et al. (2013) indicate that muddy IHS represents the main reservoir heterogeneity within the middle McMurray member.

Detailed geostatistical modeling of the middle member requires the consideration of two important facets: (i) spatial prediction of all major facies associations; (ii) preservation of the overall ordering of the facies and geometries of the architectural elements. Hassanpour et al. (2013) demonstrated that grid-free object-based approaches are better suited to represent the geometry of the architectural elements observed in fluvial point bars at different length scales. Gridding of the simulated objects for other applications (e.g., flow simulations) is subsequently performed using a two-step process. The shortest bounding box having the same orientation as that of the overall grid is first identified; subsequently, the bounding box is refined locally to approximately reproduce the geometry of the simulated objects.

The coupling of an advanced phase behavior model with a reservoir model with large permeability contrasts significantly increases the computational time and causes convergence issues in ES-SAGD simulations even for the relatively coarse-scale reservoir model described in Section 3.2.1. Further local refinement would increase the computational time still, and perhaps render the obtainment of convergence even more difficult due to the use of a non-uniform spatial grid for the solution of the conservation equations. Hence, the object-based modeling approach of Hassanpour et al. (2013) is not conducive to application in this research.

Musial et al. (2013) demonstrated variogram-based techniques, which arguably are simpler than object-based methods, can qualitatively predict the geological architecture observed in the outcrops along Steepbank River. Facies-specific variograms were first inferred on the basis of outcrop observations, and well-logs. Spatial distributions of facies were then stochastically generated using truncated Gaussian simulation (TGS). Qualitative reproduction of the geostatistical simulation results of Musial et al. (2013) is difficult as the global facies

proportions, mathematical models for the facies-specific variograms, and conditioning data for kriging used by the authors are not available in the public domain, to the best of our knowledge. Alternatively, we evaluate the relative performance of ES-SAGD to SAGD using a two-facies reservoir model comprising of clean sand and mudstone with unconditional SIS in Section 3.2.2.

Appendix F. Coinjection of Solvent with Decreasing Concentration

This objective of this appendix is to demonstrate use of a time-variant injection concentration (VC) strategy can potentially lower retention of solvent in-situ later in the production phase even under heterogeneity. In this strategy, the solvent is initially injected at moderate to high concentrations (e.g., 5 – 10 mol% or 28 – 46 vol% for n-C_6 SAGD); the injection concentration of solvent is gradually reduced over time with the eventual switch to steam-only injection (also see Keshavarz et al., 2015).

The logic behind the VC approach is informed by the following aspects. Firstly, there is little value in injecting a high-cost component like solvent when a significant volume of bitumen within the reservoir has been depleted; this renders early coinjection of solvent preferable. Secondly, injecting solvent at high concentrations early in the production phase can expedite the accumulation of the solvent near the chamber edge. Thirdly, the switch to steam-only injection can facilitate recovery of solvent by facilitating its vaporization from stagnant-flow regions of the reservoir.

For realization 17 and the homogeneous reservoir model from case study 3.2.2 (Chapter 3), the performance of n-C_6 SAGD using the VC strategy is compared to that using the constant injection concentration (CC) strategy (2 mol%) in terms of the accumulated solvent volume and cumulative SOR accompanying a given cumulative bitumen production. The homogeneous reservoir model serves as a bench mark to evaluate the effectiveness of a particular injection strategy. The following sequence of injection concentrations is used for the VC strategy: (i) 10 mol% for the first four months of production (i.e., up to ≈ 120 days); (ii) 5 mol% months five through eight (≈ 121 – 240 days); (iii) 2 mol% for months nine through twelve (≈ 241 – 365 days); (iv) steam-only injection beyond the first year of production.

Figure F-1 presents the simulated histories for cumulative bitumen production, cumulative solvent injection, production and accumulation, and solvent recovery factor. The solvent recovery factor is defined as the ratio of the cumulative volume of solvent produced to that injected at stock-tank conditions. **Figure F-2** presents the cumulative SOR and solvent recovery factor as a function of cumulative bitumen production.

The default stopping time for the simulations is approximately 10 years (i.e., 3653 days). However, for the heterogeneous n-C_6 SAGD cases, numerical convergence could not be achieved over the entire period. The time at which the simulations terminate for this realization is 1120 days for the constant injection concentration case, and 1479 days for the time-variant injection concentration case; this includes the initial heating period of 183 days. The corresponding cumulative bitumen productions are 100827 and 104617 m^3; the initial bitumen in place at stock-tank conditions for this realization is approximately 291440 m^3.

The variation of the concentration of the solvent in the injection stream with time is identical for both the homogeneous reservoir model and realization 17. However, the rates at which steam and solvent are injected into reservoir at a given time differ between the homogeneous and heterogeneous cases, with the solvent injection rate being higher for realization 17. This discrepancy stems from the following aspects. Firstly, the injection well (or injector grid block) is subject to only one constraint– that the bottomhole pressure for the injection well be subject to the pressure of 35 bars. Hence, the rate at which steam and solvent is injected into the reservoir is mainly sensitive to the production rate of the oleic phase. Secondly, the production of bitumen from muddy grid blocks is negligible due to their poor petrophysical attributes. So, they mainly influence fluid flow by rendering hydraulic paths more tortuous. Because of this, the injected amount of steam (and solvent) accompanying a given cumulative bitumen production is greater under heterogeneity.

Injection of solvent at higher concentrations early in the production phase increases its accumulation in-situ regardless of whether the reservoir is homogeneous or heterogeneous, and results in greater dissolution of solvent in the oleic phase in regions both near the well-pair and those farther away. Increased accumulation of solvent near the chamber edge under the VC strategy lowers the operating chamber temperature. However, the margin of reduction in operating-chamber temperatures near the well-pair is greater under homogeneity than that under heterogeneity. Consequently, the benefit of the VC strategy in terms of the production rate of bitumen at earlier times is pronounced under heterogeneity compared to that under homogeneity. **Figures F-3 through F-6** present the simulated maps for x_{sL} and $\beta_L x_{sL}$ at 305 days from the start of the operation for the homogeneous and heterogeneous cases under the CC and VC strategies. **Figures F-7 and F-8** present the pertinent temperature maps.

For realization 17, Figures F1 and F2 show that use of the aforementioned VC strategy can significantly reduce solvent retention over the long term in addition to lowering the cumulative SOR early in the production phase through improvement of bitumen production rate. Further, the trend in the recovery factor with respect to cumulative bitumen production is also more stable under the VC strategy compared to that under the CC strategy for this realization. The reduction in solvent retention for this realization is accompanied by a moderate increase in the SOR (< 1.0). For example, for the cumulative bitumen production of 100000 m^3, the SOR for the constant and time-variant injection concentration strategies are 4.78 and 5.71, respectively; the corresponding solvent accumulation, estimated on the basis of the cumulative solvent injection and production histories at stock-tank conditions, are 23300 and 15140 m^3, respectively. That is, relative to the constant injection concentration case, the SOR for the time-variant injection concentration case is 19.5% higher, while the retained solvent volume is 35% lower.

For around the first 400 days of production, the recovery of solvent under the VC strategy is more efficient under heterogeneity compared to homogeneity. This is informed by the following: (i) it is easier to recover solvent when the steam chamber is rather small; and (ii) for a specified injection strategy, the production rate of bitumen at a given time is lower under heterogeneity, which results in a smaller steam-chamber volume compared to that under homogeneity. However, the ultimate recovery of solvent is greater for the homogeneous case under the VC strategy because the increasing tortuosity of flow paths for the heterogeneous case with continued expansion of the steam chamber lowers the solvent recovery efficiency over time. Nevertheless, the VC strategy is preferable to the CC strategy for the heterogeneous case due to the potential for substantial reduction of solvent retention over time. However, the injection sequence must be carefully designed to obtain an acceptable balance between the reduction in solvent retention and increase in cumulative SOR. The recovery efficiency of solvent is expected to vary across different realizations due to the underlying differences in hydraulic paths for flow towards the producer. Consequently, the optimal injection sequence under the VC strategy will likely be different for other realizations.

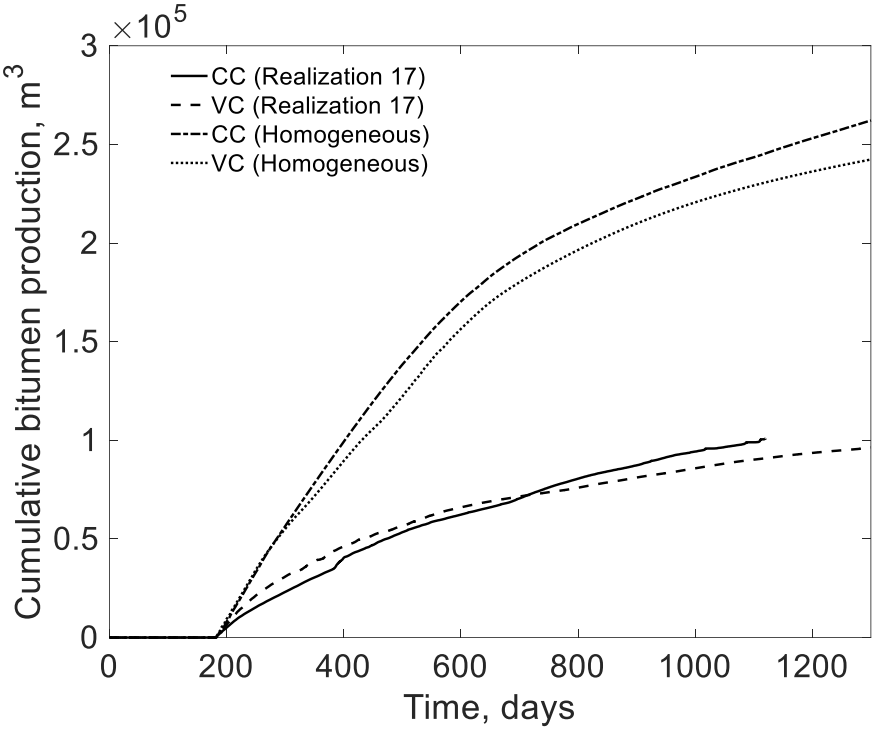
×10^5
3
2.5
2
1.5
1
0.5
0
Cumulative bitumen production, m^3
CC (Realization 17)
VC (Realization 17)
CC (Homogeneous)
VC (Homogeneous)
0
200
400
600
800
1000
1200
Time, days

(a)

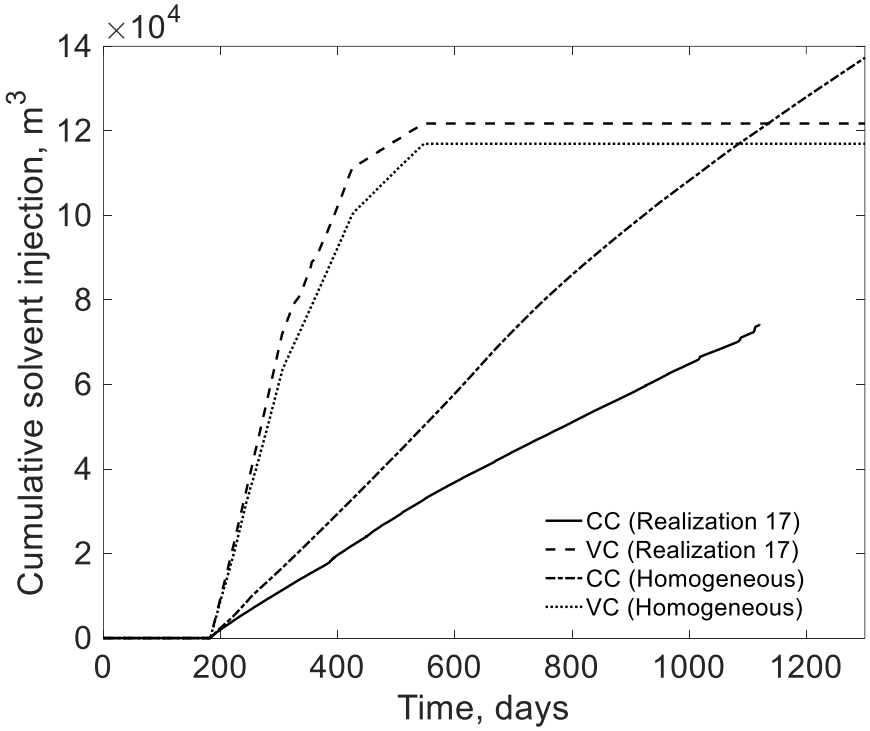
×10^4
14
12
10
8
6
4
2
0
Cumulative solvent injection, m^3
CC (Realization 17)
VC (Realization 17)
CC (Homogeneous)
VC (Homogeneous)
0
200
400
600
800
1000
1200
Time, days

(b)

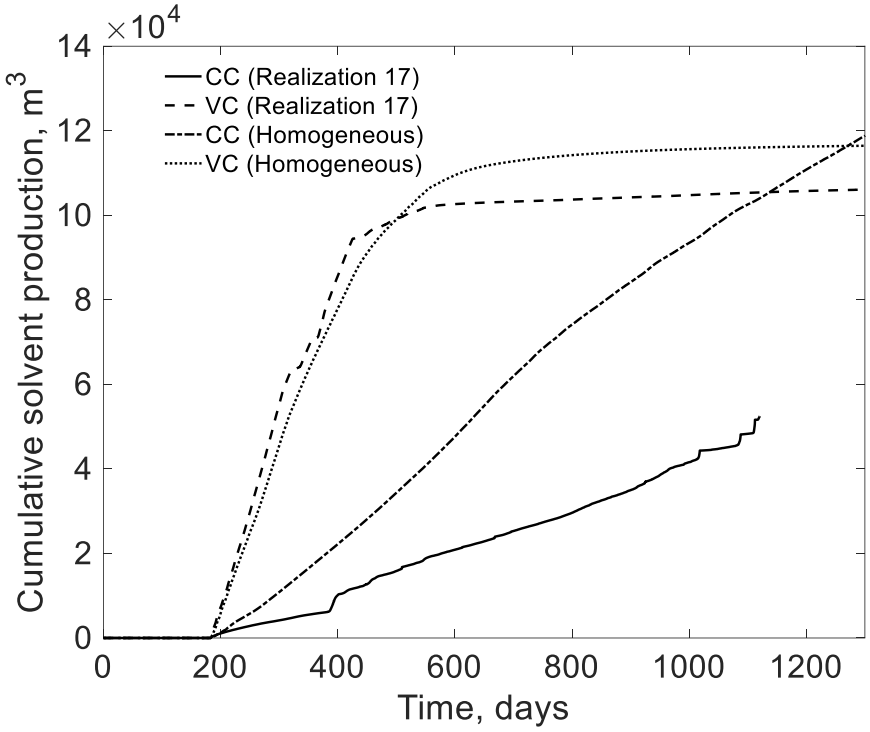
×10^4
14
12
10
8
6
4
2
0
Cumulative solvent production, m^3
CC (Realization 17)
VC (Realization 17)
CC (Homogeneous)
VC (Homogeneous)
0
200
400
600
800
1000
1200
Time, days

(c)

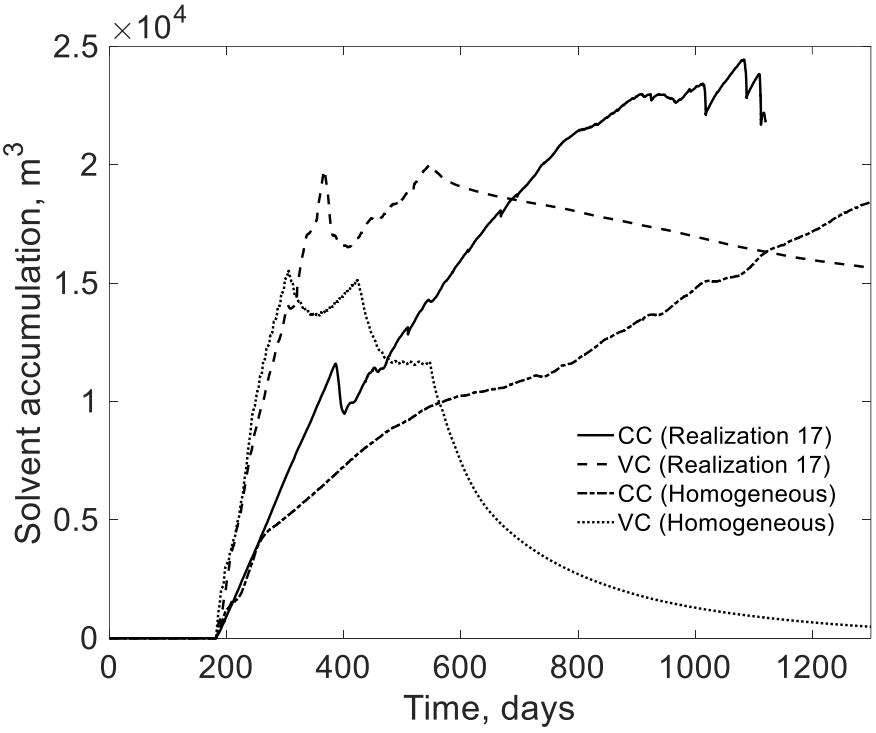
×10^4
2.5
2
1.5
1
0.5
0
Solvent accumulation, m^3
CC (Realization 17)
VC (Realization 17)
CC (Homogeneous)
VC (Homogeneous)
0
200
400
600
800
1000
1200
Time, days

(d)

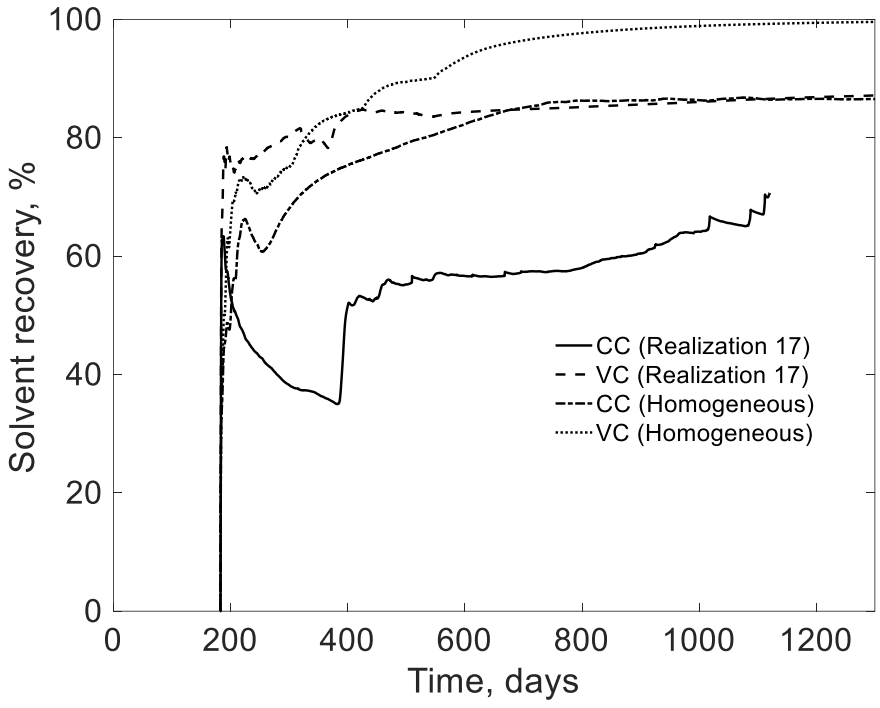

(e)

Figure F-1 Simulated property histories in n-C_6 SAGD under the CC and VC strategies for the homogeneous reservoir model and realization 17 from Section 3.2.2 (Chapter 3); (a) cumulative bitumen production; (b) cumulative solvent injection; (c) cumulative solvent production; (d) solvent accumulation; (e) solvent recovery factor.

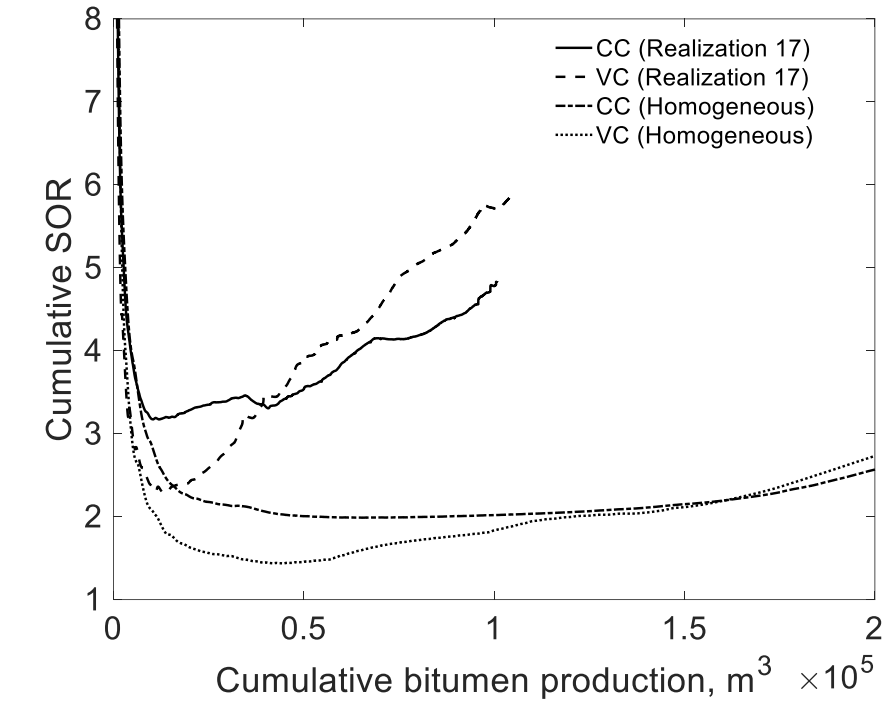

(a)

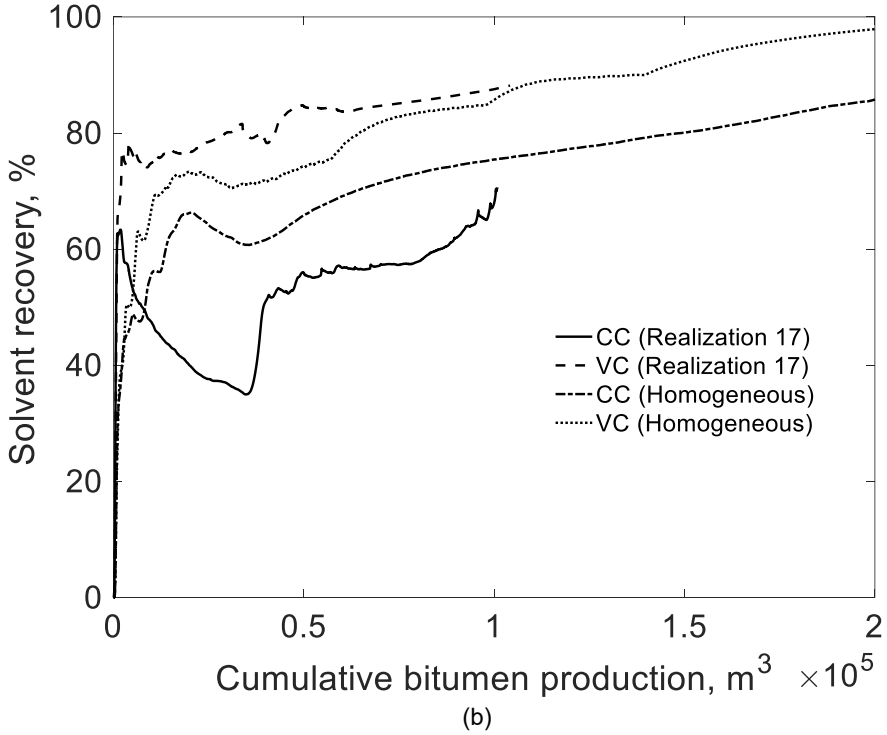

(b)

Figure F-2. Cumulative SOR and solvent recovery factor as a function of cumulative bitumen production under the CC and VC strategies; (a) cumulative SOR; (b) solvent recovery factor.

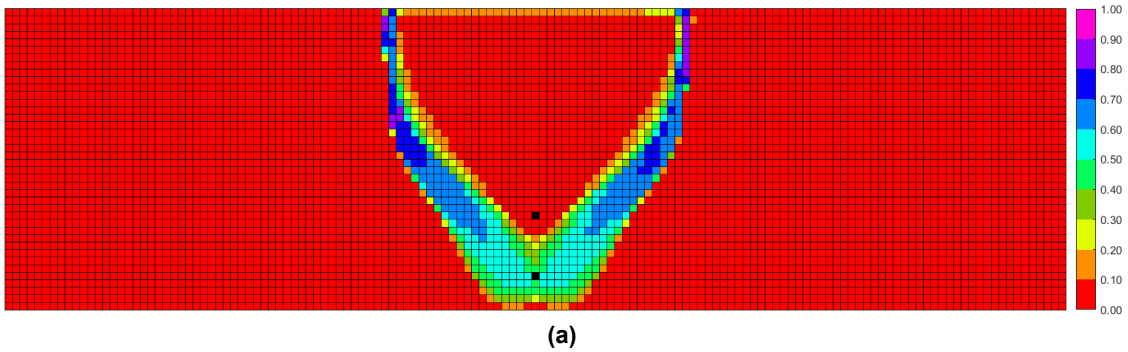

(a)

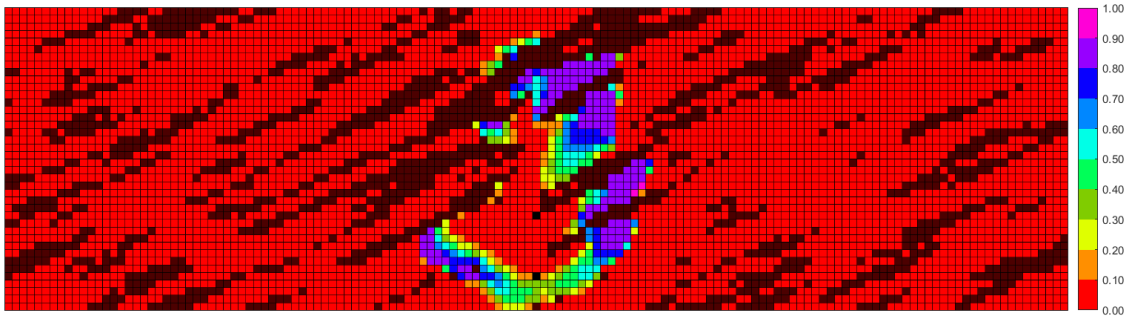

(b)

Figure F-3. Distribution of x_{sL} in clean sand grid blocks of the homogeneous reservoir model and realization 17 under the CC strategy at 305 days. Injector and producer grid blocks are indicated in black.

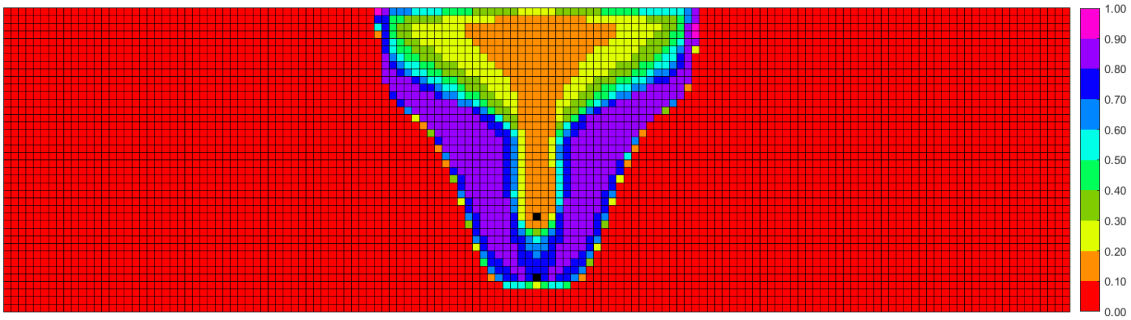

(a)

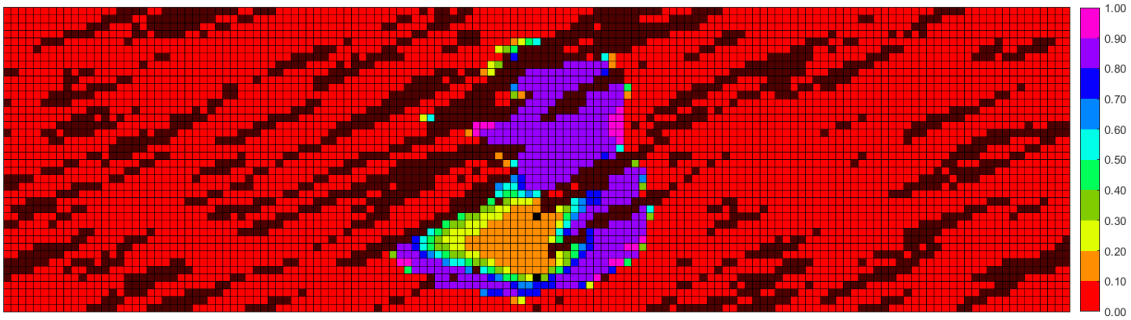

(b)

Figure F-4. Distribution of x_{sL} in clean sand grid blocks of the homogeneous reservoir model and realization 17 under the VC strategy at 305 days. Injector and producer grid blocks are indicated in black.

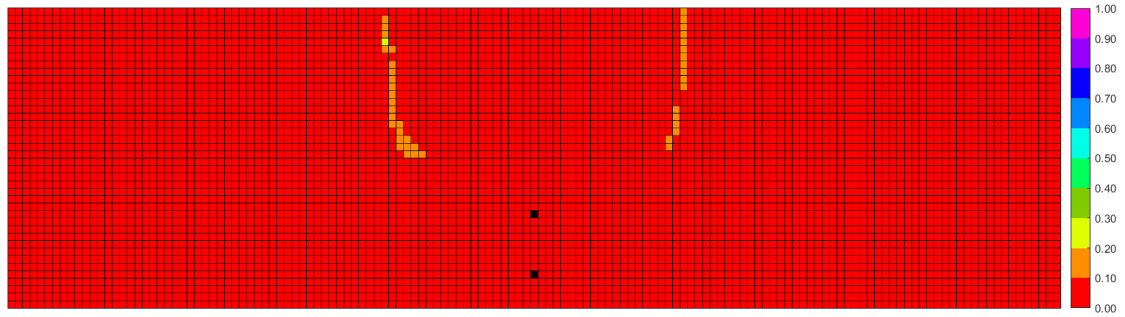

(a)

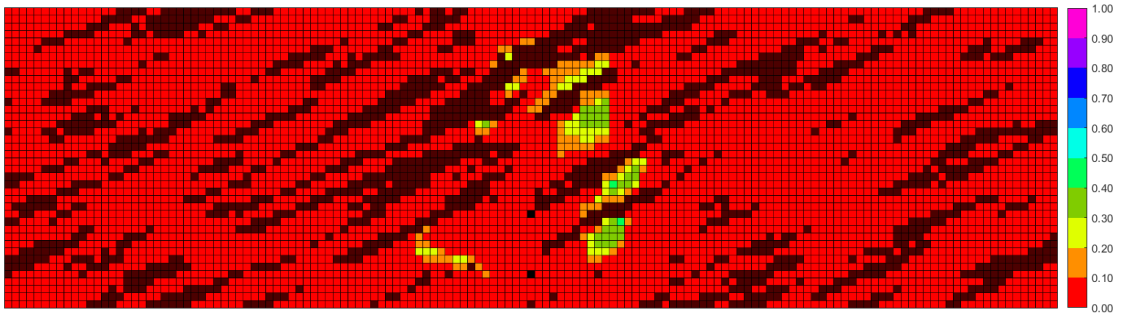

(b)

Figure F-5. Distribution of $\beta_L x_{sL}$ in clean sand grid blocks of the homogeneous reservoir model and realization 17 under the CC strategy at 305 days. Injector and producer grid blocks are indicated in black.

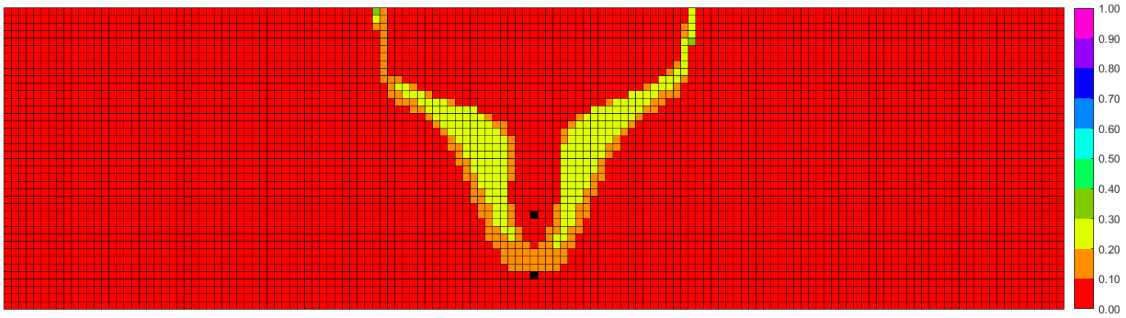

(a)

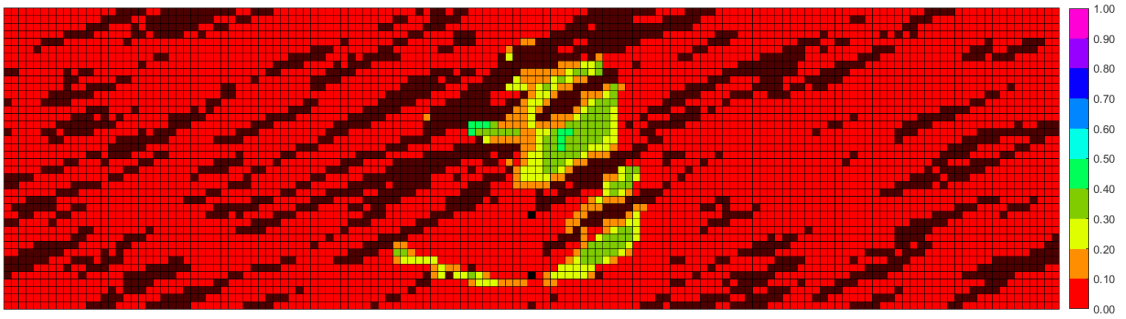

(b)

Figure F-6. Distribution of $\beta_L x_{sL}$ in clean sand grid blocks of the homogeneous reservoir model and realization 17 under the VC strategy at 305 days. Injector and producer grid blocks are indicated in black.

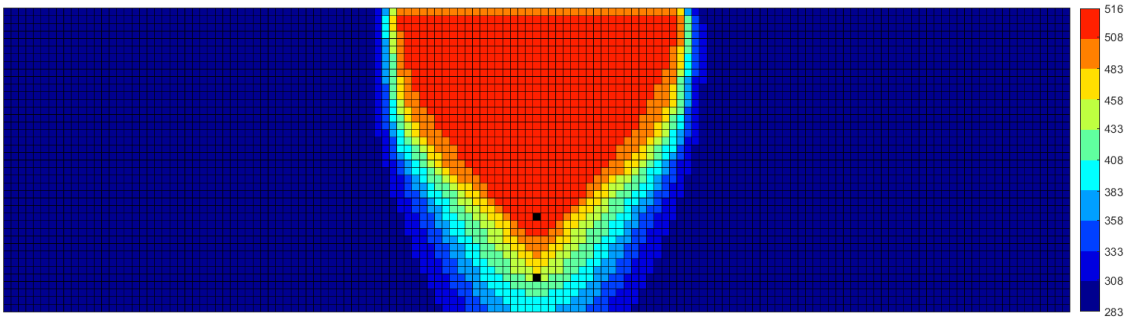

(a)

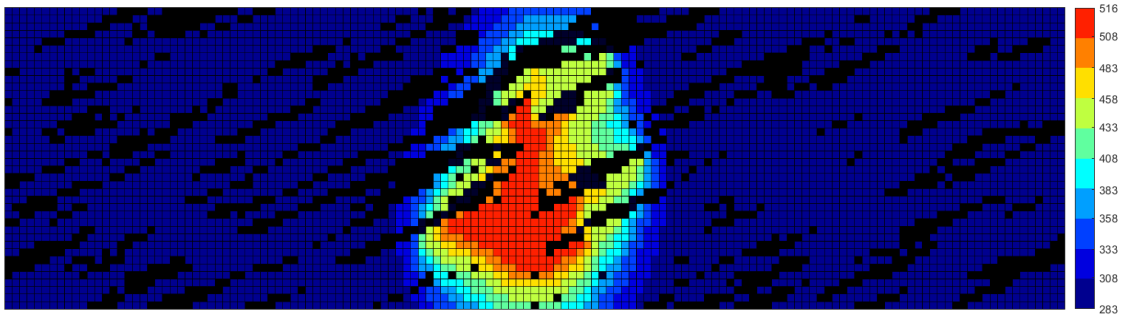

(b)

Figure F-7. Distribution of temperature (in Kelvin) in clean sand grid blocks of the homogeneous reservoir model and realization 17 under the CC strategy at 305 days. Injector and producer grid blocks are indicated in black.

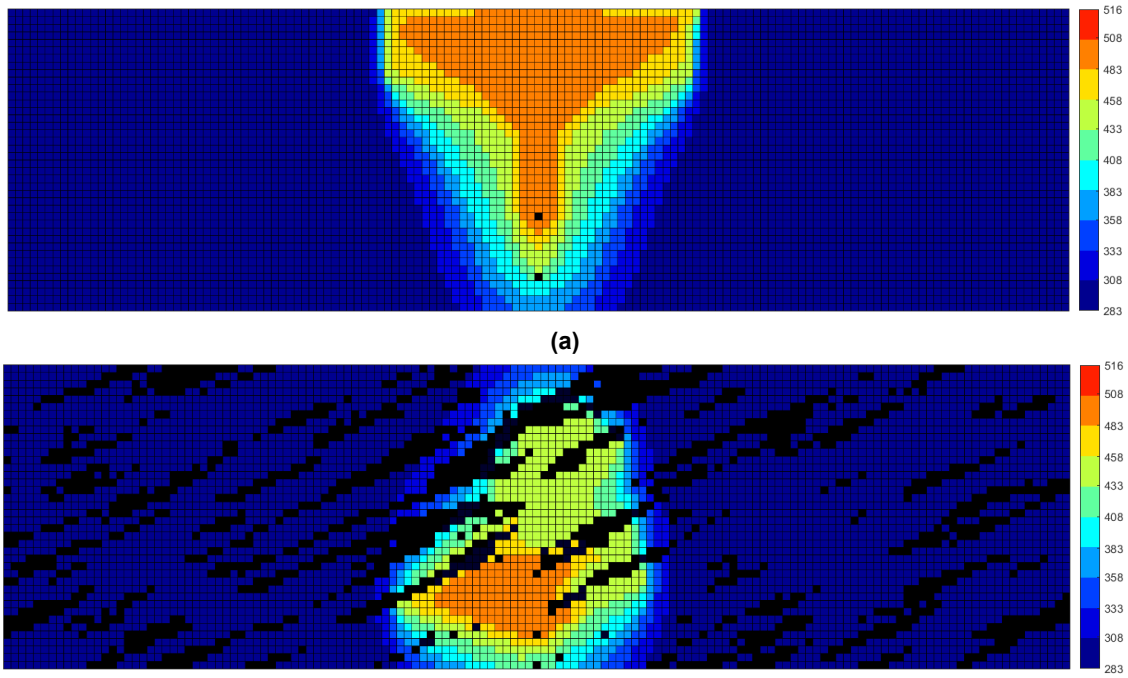

Figure F-8. Distribution of temperature (in Kelvin) in clean sand grid blocks of the homogeneous reservoir model and realization 17 under the VC strategy at 305 days. Injector and producer grid blocks are indicated in black. The mudstone barriers are also indicated in the background for the heterogeneous maps.

Appendix G. Numerical Dispersion in n-C_6 SAGD Simulations

This appendix has two objectives: (i) to demonstrate that a main conclusion of this research that the reduction in SOR due coinjection of solvent can be higher under heterogeneity is qualitatively preserved even when the numerical dispersion is lowered by grid refinement; and (ii) to quantify directional numerical dispersion coefficients and dispersivities. Section G-1 presents an overview of the mathematical framework in thermal compositional reservoir simulation with the assumption of local equilibrium. Section G-2 gives an analytical demonstration of how numerical dispersion can behave liquid hydrodynamic dispersion.

Section G-3 provides quantitative estimates for the numerical dispersion coefficients and dispersivities associated with the 2-D n-C_6 SAGD simulations conducted for the homogeneous reservoir model and realization 16 from case study 3.2.2, which will henceforth be referred to as coarse-scale simulations. Section G-4 discusses the effects of the reduction of numerical dispersion through the lowering of grid block size on the relative performance of n-C_6 SAGD to SAGD under homogeneity and heterogeneity (realization 16). The injection concentration of solvent in n-C_6 SAGD is set to 2 mol%; the operating pressure is 35 bars.

G-1. Overview of thermal compositional reservoir simulation

Recovery histories of oil and spatial distributions of properties that influence oil recovery are predicted in finite difference thermal compositional reservoir simulation by (i) discretizing the reservoir into grid blocks, and (ii) numerically solving material and energy balance equations for each grid block using a set of constraints. For non-isothermal flow of N_C components that can exist in N_P fluid phases and do not interact with the solid, there are $N_CN_P + 3N_P + 1$ variables for each grid block. The mole fractions of the N_C components in the N_P phases constitute N_CN_P variables; there are N_P variables each for phase pressures, saturations, velocities, and one for temperature.

To make the system well-posed, $N_CN_P + 3N_P + 1$ equations are needed. There are N_C material balance equations (i.e., one for each component), and one equation for energy balance. The material balance equation for the i^{th} component reads as

$$\frac{\partial}{\partial t}\left(\varphi \sum_{j=1}^{N_P} \underline{\rho}_j S_j x_{ij}\right) + \vec{\nabla}.\left(\sum_{j=1}^{N_P} \underline{\rho}_j \vec{u}_j x_{ij}\right) - \vec{\nabla}.\left(\varphi \sum_{j=1}^{N_P} S_j \overline{\overline{D}}_{ij}.\vec{\nabla}\left(\underline{\rho}_j x_{ij}\right)\right) = \underline{R}_i \;\forall\, i, \qquad \text{(G-1)}$$

where φ is the porosity of the medium, $\underline{\rho}_j$, $\vec{u}_j$ and S_j are respectively the molar density, velocity and saturation of the j^{th} phase, x_{ij} and $\bar{\bar{D}}_{ij}$ are respectively the mole fraction and hydrodynamic dispersion tensor of the i^{th} component in the j^{th} phase, and $\underline{R}_i$ is the source or sink term for the i^{th} component. The hydrodynamic dispersion tensor (Chen, 2007) is given by

$$\bar{\bar{D}}_{ij} = D_{Mij}\bar{\bar{I}} + d_{Lij}\left(\vec{u}_j \otimes \vec{u}_j \Big/ \left\|\vec{u}_j\right\|_2\right) + d_{Tij}\left(\bar{\bar{I}}\left\|\vec{u}_j\right\|_2 - \vec{u}_j \otimes \vec{u}_j \Big/ \left\|\vec{u}_j\right\|_2\right) \quad \text{(G-2)}$$

where D_{Mij}, d_{Lij}, d_{Tij} respectively are the molecular diffusivity (after accounting for tortuosity), longitudinal, and transverse dispersitivies for the i^{th} component in the j^{th} phase; $\bar{\bar{I}}$ is the unit matrix; $\otimes$ is the operator for the outer product of two vectors; $\left\|\vec{u}_j\right\|_2$ is the second norm (magnitude) of the velocity vector of the j^{th} phase. Based on Equation G-2, the hydrodynamic dispersion tensor can be split into two components: (i) molecular diffusion, which is the first term in Equation G-2; and (ii) mechanical dispersion, which is made up of the last two terms. The unit of molecular diffusivity is [length^2/time], while that for the transverse and longitudinal dispersivities is [length].

The simplified energy balance equation is given by (Lake, 1989)

$$\frac{\partial}{\partial t}\left(\underline{\rho H}\right) + \vec{\nabla}.\left(\sum_{j=1}^{N_P} \underline{\rho}_j \vec{u}_j \underline{H}_j\right) - \vec{\nabla}.\left(\bar{\bar{k}}_{th}.\vec{\nabla}T\right) = q_s - q_L \quad \text{(G-3)}$$

$$\text{with } \underline{\rho H} = \varphi \sum_{j=1}^{N_P} \underline{\rho}_j \underline{H}_j + (1-\varphi)\underline{\rho}_s \underline{H}_s \quad \text{(G-4)}$$

where T is temperature, $\underline{H}_j$ and $\underline{H}_s$ are the molar enthalpies of the j^{th} phase and rock, respectively, $\bar{\bar{k}}_{th}$ is the thermal conductivity tensor, and q_s and q_L respectively are the terms representing heat source and heat loss to the overburden and underburden. The latter is assumed to occur due to thermal conduction.

The phase velocities in reservoir simulation are modeled using Darcy's law. There are N_P equations in total and the velocity of the j^{th} phase which is written as

$$\vec{u}_j = -\left(k_{rj} \Big/ \mu_j\right)\bar{\bar{k}}.\left(\vec{\nabla}P_j + \rho_j g\vec{\nabla}z\right) \;\forall\, j, \quad \text{(G-5)}$$

where k_{rj}, μ_j, P_j, ρ_j respectively are the relative permeability, viscosity, pressure and mass density of the j^{th} phase, g is the acceleration due to gravity, z is the elevation, and $\bar{\bar{k}}$ is the permeability tensor. There are N_P phase-specific mole balance equations, which are given by

$$\sum_{i=1}^{N_C} x_{ij} = 1.0 \;\forall\, j, \quad \text{(G-6)}$$

and (N_P -1) capillary pressure equations, which read as

$$P_{cj} = P_j - P_{N_P} \forall\, j \neq N_P, \quad \text{(G-7)}$$

where P_{cj} is the capillary pressure of the j^{th} phase relative to a reference phase (say N_P), and a singular phase-saturation constraint,

$$\sum_{j=1}^{N_P} S_j = 1.0. \quad \text{(G-8)}$$

This leaves us with the specification of $N_C(N_P\text{-}1)$ equations to render the system of equations to be well-posed. These equations can be obtained by assuming local thermodynamic equilibrium within the spatial domain of each grid block, according to which the component-specific chemical potentials (μ_{ij}) or fugacities ($\hat{f}_{ij}$) are phase-invariant. That is,

$$\mu_{i1} = \mu_{i2} = \cdots = \mu_{ij} = \cdots \mu_{iN_P}, \forall\, i, \quad \text{(G-9)}$$

and

$$\hat{f}_{i1} = \hat{f}_{i2} = \cdots = \hat{f}_{ij} = \cdots \hat{f}_{iN_P}, \forall\, i \quad \text{(G-10)}$$

The assumption of local equilibrium is applied within the spatial domain of each grid block.

In actual reservoir processes, dissolution of solvent in the oleic phase is a non-equilibrium process at all length scales, and hydrodynamic dispersion drives the concentration of the solvent in the oleic phase closer to equilibrium values. However, in the conventional framework for simulations, local equilibrium is assumed to apply thermodynamic modeling of fluid properties to transient processes. Consequently, the dispersion term in Equation G-1 (i.e., the third term) only applies to length scales greater than the dimensions of the grid blocks in use, which are greater than REV scale.

G-2. Mathematical Similarity between Numerical and Hydrodynamic Dispersion

In finite difference simulations, the derivatives of various quantities are typically approximated using truncated Taylor's series. These truncation errors can introduce a numerical artifact that behaves like hydrodynamic dispersion even when the flow is assumed to be convection-dominant (i.e., when the hydrodynamic dispersion tensor in Equation G-1 is assumed to be zero). This is of significant concern in ES-SAGD simulations due to the possibility of overestimation of the lateral thickness of the solvent-diluted region of the reservoir beyond the chamber edge. Analytical demonstration of this effect is arguably easiest for single-phase, isothermal, two-dimensional flow for a two-component system in the absence of source/sink terms (Garmeh and

Johns, 2010; Adepoju et al., 2015).

The governing equation for single-phase, isothermal, compositional flow comprising of two components without source/sink terms is the commonly known convection-dispersion equation, which reads as

$$\frac{\partial}{\partial t}(\varphi c) + \vec{\nabla}.(\vec{u}c) - \vec{\nabla}.\left(\varphi\bar{\bar{D}}.\vec{\nabla}c\right) = 0, \tag{G-11}$$

where c is the molar concentration of a component of interest, and is equal to the product of the molar density of the phase in which it is dissolved and its mole fraction in that phase. If the porosity is assumed to be constant, and the flow is assumed to be convection-dominant with negligible spatial dependence of the phase velocity, then Equation G-11 can be simplified as

$$\frac{\partial c}{\partial t} + \vec{v}.\vec{\nabla}c = 0, \tag{G-12}$$

where $\vec{v} = \vec{u}/\varphi$ is the interstitial velocity.

For two-dimensional flow, with the longitudinal direction designated as "z" and transverse direction designated as "x", Equation G-12 can be expanded as

$$\frac{\partial c}{\partial t} = -\left[v_x\frac{\partial c}{\partial x} + v_z\frac{\partial c}{\partial z}\right]. \tag{G-13}$$

For a five-point grid stencil, Equation G-13 can be discretized for the grid block centered at (i,j) using a implicit scheme in time as

$$\frac{c^n_{i,j} - c^{n-1}_{i,j}}{\Delta t} = -\left[v_x\frac{c^n_{i+\frac{1}{2},j} - c^n_{i-\frac{1}{2},j}}{\Delta x} + v_z\frac{c^n_{i,j+\frac{1}{2}} - c^n_{i,j-\frac{1}{2}}}{\Delta z}\right], \tag{G-14}$$

where "n" denotes the time-step, while Δt, Δx and Δz, respectively denote sizes of steps in time, the x-and z-directions, respectively.

Finite difference reservoir simulations conventionally use a block-centered system, wherein properties of interest are calculated at the center of a grid block. Properties at the edges of a given grid block $\left(\text{e.g., } c^n_{i+\frac{1}{2},j}\right)$ are generally expressed in terms of a linear combination of values at one or more neighboring grid block centers. That is,

$$c^n_{i+\frac{1}{2},j} = \omega c^n_{i,j} + (1-\omega)c^n_{i+1,j} \tag{G-15a}$$

$$c^n_{i-\frac{1}{2},j} = \omega c^n_{i-1,j} + (1-\omega)c^n_{i,j} \tag{G-15b}$$

$$c^n_{i,j+\frac{1}{2}} = \omega c^n_{i,j} + (1-\omega)c^n_{i,j+1} \tag{G-15c}$$

$$c^n_{i,j-\frac{1}{2}} = \omega c^n_{i,j-1} + (1-\omega)c^n_{i,j}, \tag{G-15d}$$

where ω is a weighting factor. A commonly-used approach to calculate the properties at the grid block edges is the upstream weighting technique, in which the value of ω is set to unity. Based on this, Equation G-15 simplifies to

$$c^n_{i+\frac{1}{2},j} = c^n_{i,j} \tag{G-16a}$$

$$c^n_{i-\frac{1}{2},j} = c^n_{i-1,j} \tag{G-16b}$$

$$c^n_{i,j+\frac{1}{2}} = c^n_{i,j} \tag{G-16c}$$

$$c^n_{i,j-\frac{1}{2}} = c^n_{i,j-1} \tag{G-16d}$$

Using Equation G-16 in Equation G-14,

$$\frac{c^n_{i,j}-c^{n-1}_{i,j}}{\Delta t} = -\left[v_x \frac{c^n_{i,j}-c^n_{i-1,j}}{\Delta x} + v_z \frac{c^n_{i,j}-c^n_{i,j-1}}{\Delta z}\right]. \tag{G-17}$$

The truncation error (ε) is defined as

$$\varepsilon^n_{i,j} = \left|\left[\frac{\partial c}{\partial t} + v_x \frac{\partial c}{\partial x} + v_z \frac{\partial c}{\partial z}\right]_{i,j,n} - \left[\frac{c^n_{i,j}-c^{n-1}_{i,j}}{\Delta t} + v_x \frac{c^n_{i,j}-c^n_{i-1,j}}{\Delta x} + v_z \frac{c^n_{i,j}-c^n_{i,j-1}}{\Delta z}\right]\right|. \tag{G-18}$$

The term $c^{n-1}_{i,j}$ can be approximated using Taylor's series as follows,

$$c^{n-1}_{i,j} \cong c^n_{i,j} - \Delta t \frac{\partial c}{\partial t}\Big|_{i,j} + \frac{1}{2}(\Delta t)^2 \frac{\partial^2 c}{\partial t^2}\Big|_{i,j,n}. \tag{G-19}$$

The term $\frac{\partial^2 c}{\partial t^2}$ can be written using Equation C-13 as

$$\frac{\partial^2 c}{\partial t^2} = -\left[v_x \frac{\partial}{\partial x}\left(\frac{\partial c}{\partial t}\right) + v_z \frac{\partial}{\partial z}\left(\frac{\partial c}{\partial t}\right)\right] = \left[v_x \frac{\partial}{\partial x}\left\{v_x \frac{\partial c}{\partial x} + v_z \frac{\partial c}{\partial z}\right\} + v_z \frac{\partial}{\partial z}\left\{v_x \frac{\partial c}{\partial x} + v_z \frac{\partial c}{\partial z}\right\}\right], \tag{G-20}$$

which yields

$$\frac{\partial^2 c}{\partial t^2} = {v_x}^2 \frac{\partial^2 c}{\partial x^2} + {v_z}^2 \frac{\partial^2 c}{\partial z^2} + v_x v_z \frac{\partial^2 c}{\partial x\,\partial z} + v_z v_x \frac{\partial^2 c}{\partial z\,\partial x}. \tag{G-21}$$

Using Equation G-21 in Equation G-19,

$$\frac{c^n_{i,j}-c^{n-1}_{i,j}}{\Delta t} = \frac{\partial c}{\partial t}\Big|_{i,j,n} - \frac{1}{2}\Delta t\left[{v_x}^2 \frac{\partial^2 c}{\partial x^2} + {v_z}^2 \frac{\partial^2 c}{\partial z^2} + v_x v_z \frac{\partial^2 c}{\partial x\,\partial z} + v_z v_x \frac{\partial^2 c}{\partial z\,\partial x}\right]_{i,j,n}$$

$$= \frac{\partial c}{\partial t}\Big|_{i,j,n} - \vec{\nabla}.\left(\bar{\bar{D}}_1.\vec{\nabla}c\right)\Big|_{i,j,n}, \tag{G-22}$$

where $\bar{\bar{D}}_1 = \frac{1}{2}\Delta t\begin{bmatrix} {v_x}^2 & v_x v_z \\ v_z v_x & {v_z}^2 \end{bmatrix}$

Similarly, the terms $c^n_{i-1,j}$ and $c^n_{i,j-1}$ can be approximated as follows

$$c^n_{i-1,j} \cong c^n_{i,j} - \Delta x \frac{\partial c}{\partial x}\Big|_{i,j,n} + \frac{1}{2}(\Delta x)^2 \frac{\partial^2 c}{\partial x^2}\Big|_{i,j,n}, \tag{G-23}$$

$$c^n_{i,j-1} \cong c^n_{i,j} - \Delta z \frac{\partial c}{\partial z}\Big|_{i,j,n} + \frac{1}{2}(\Delta z)^2 \frac{\partial^2 c}{\partial z^2}\Big|_{i,j,n} \tag{G-24}$$

Hence,

$$v_x \frac{c^n_{i,j} - c^n_{i-1,j}}{\Delta x} + v_z \frac{c^n_{i,j} - c^n_{i,j-1}}{\Delta z} \cong v_x \frac{\partial c}{\partial x}\Big|_{i,j,n} + v_z \frac{\partial c}{\partial z}\Big|_{i,j,n} - \vec{\nabla}.\left(\bar{\bar{D}}_2.\vec{\nabla}c\right)\Big|_{i,j,n}, \tag{G-25}$$

where $\bar{\bar{D}}_2 = \frac{1}{2}\begin{bmatrix} v_x\Delta x & 0 \\ 0 & v_z\Delta z \end{bmatrix}$

Using Equations G-22 and G-25 in Equation G-18, we obtain

$$\varepsilon^n_{i,j} = \left|\left[\frac{\partial c}{\partial t} + v_x\frac{\partial c}{\partial x} + v_z\frac{\partial c}{\partial z}\right]_{i,j,n} - \left[\frac{\partial c}{\partial t} + v_x\frac{\partial c}{\partial x} + v_z\frac{\partial c}{\partial z} - \vec{\nabla}.\left(\bar{\bar{D}}_{num}.\vec{\nabla}c\right)\right]_{i,j,n}\right| = \vec{\nabla}.\left(\bar{\bar{D}}_{num}.\vec{\nabla}c\right)\Big|_{i,j,n}, \tag{G-26}$$

where $\bar{\bar{D}}_{num} = \bar{\bar{D}}_1 + \bar{\bar{D}}_2 = \frac{1}{2}\begin{bmatrix} v_x(\Delta x + v_x\Delta t) & v_xv_z\Delta t \\ v_zv_x\Delta t & v_z(\Delta z + v_z\Delta t) \end{bmatrix} = \begin{bmatrix} D^{num}_{xx} & D^{num}_{zx} \\ D^{num}_{xz} & D^{num}_{zz} \end{bmatrix}$.

$\bar{\bar{D}}_{num}$ is called the numerical dispersion tensor. The term D^{num}_{ij} in the numerical dispersion tensor is the numerical dispersion coefficient along the i^{th} direction due to flow along the j^{th} direction. Equation G-26 demonstrates that even in convection-dominated flow, truncation errors can introduce a numerical artifact that behaves like hydrodynamic dispersion. An expression for the numerical dispersivity can be derived from the numerical dispersion tensor by dividing each of its elements by the magnitude of the interstitial velocity ($\|\vec{v}\|_2$). That is,

$$\bar{\bar{d}}_{num} = \frac{1}{\|\vec{v}\|_2}\begin{bmatrix} D^{num}_{xx} & D^{num}_{zx} \\ D^{num}_{xz} & D^{num}_{zz} \end{bmatrix} = \frac{1}{2}\begin{bmatrix} \frac{1}{\|\vec{v}\|_2}v_x(\Delta x + v_x\Delta t) & \frac{1}{\|\vec{v}\|_2}v_xv_z\Delta t \\ \frac{1}{\|\vec{v}\|_2}v_zv_x\Delta t & \frac{1}{\|\vec{v}\|_2}v_z(\Delta z + v_z\Delta t) \end{bmatrix} = \begin{bmatrix} d^{num}_{xx} & d^{num}_{zx} \\ d^{num}_{xz} & d^{num}_{zz} \end{bmatrix} \tag{G-27}$$

The units of the components of $\bar{\bar{D}}_{num}$ and $\bar{\bar{d}}_{num}$ are [length^2/time] and [length], respectively. The numerical dispersion tensor is derived from the governing equations for flow on the basis of specific discretization schemes in space and time. The derivation of such expressions for thermal simulations is not easy due to the coupling of the energy balance equation with the material balance equation(s). Nevertheless, using Equations G-26 and G-27, quantitative estimates for the numerical dispersion and dispersivity matrices can be obtained.

G-3. Numerical dispersion coefficients in 2-D coarse-scale n-C_6 SAGD simulations

This section presents averaged estimates of numerical dispersion coefficients and dispersivities for the coarse-scale n-C_6 SAGD simulations for the homogeneous reservoir model and realization 16 from case study 3.2.2 for the cumulative bitumen production of approximately 55263 m^3. In the coarse-scale simulations, grid blocks of size 1 m x 0.5 m (x-z plane) are used.

Simulations in this research are fully-implicit in time, and the time-step is adjusted automatically to facilitate convergence. The smallest time-step size permissible in STARS is 10^{-8} days. For the homogeneous reservoir model and realization 16 in case study 3.2.2, **Figure G-1** presents the variation of the average time-step size with respect to cumulative bitumen production for the coarse-scale n-C_6 SAGD simulations. For both the homogeneous and heterogeneous reservoir models, Figure G-1 indicates the time-step size to fluctuate over the course of the simulations regardless of the choice of reservoir gridding. So, to estimate the numerical dispersion tensor for a specified cumulative bitumen production, it is preferable to average the time-step sizes used in the simulations up until the cumulative bitumen production is met.

Average values for the magnitude of the Darcy velocity of the oleic phase (u) and it's horizontal (u_x) and vertical (u_z) components in simulations can be obtained as follows: (i) maps for the volumetric flow rate of the oleic phase corresponding to a specified cumulative bitumen production can be retrieved from simulation results; (ii) a threshold for the oleic-phase flow rate could be specified (e.g., 1 m^3/day), and grid blocks that exceed this threshold can be identified; and (iii) the arithmetic average of the magnitude of the oleic-phase Darcy velocity and its components for the set of grid blocks identified from the previous step can be calculated. Average estimates for the interstitial velocities, v, v_x, and v_z, can subsequently be obtained by dividing u, u_x, and u_z by the porosity used for the clean sand facies, which is equal to 0.36 in case study 3.2.2.

Figures G-2 and G-3 present the pertinent simulated maps for the magnitude of the Darcy velocity of the oleic phase and its components for the homogeneous and heterogeneous cases under the coarse-scale gridding for the cumulative bitumen production of approximately 55236 m^3. **Table G-1** summarizes the numerical values for parameters necessary for the estimation of the numerical dispersion tensor. For the aforementioned cumulative bitumen production, the

numerical dispersion coefficient and numerical dispersivity matrices for the homogeneous and heterogeneous cases read as follows,

$$\bar{\bar{D}}^{hom}_{num,CS} = \begin{bmatrix} 0.1591 & 0.0098 \\ 0.0098 & 0.0594 \end{bmatrix}, \quad \text{(G-28)}$$

$$\bar{\bar{d}}^{hom}_{num,CS} = \begin{bmatrix} 0.4101 & 0.0253 \\ 0.0253 & 0.1532 \end{bmatrix}, \quad \text{(G-29)}$$

$$\bar{\bar{D}}^{het}_{num,CS} = \begin{bmatrix} 0.1627 & 0.0098 \\ 0.0098 & 0.0205 \end{bmatrix}, \quad \text{(G-30)}$$

$$\bar{\bar{d}}^{het}_{num,CS} = \begin{bmatrix} 0.5777 & 0.0348 \\ 0.0348 & 0.0727 \end{bmatrix}. \quad \text{(G-31)}$$

From Equations C-28 and C-30, it is apparent that the component with the largest value in the matrix for $\bar{\bar{D}}_{num}$ is D^{num}_{xx} for the homogeneous and heterogeneous reservoir. Consequently, d^{num}_{xx} is greater than the value of other components of $\bar{\bar{d}}_{num}$. The largest eigenvalues of $\bar{\bar{d}}_{num}$ are 0.4126 and 0.5801 for the homogeneous and heterogeneous cases, respectively. So, the numerical dispersivity is calculated to be close to 50% of the largest grid-block dimension in the x-z plane (i.e., ≈ 0.5 m).

The dispersion tensor in simulations is equal to the sum of the hydrodynamic and numerical dispersion tensors. In the coarse-scale simulations of case study 3.2.2, the hydrodynamic dispersion tensor is zero. So, in order to investigate the effects of transverse dispersion on ES-SAGD simulations, it is apparent that the input value for transverse dispersivity (d_T) should be at least comparable to or even greater than one-half of the largest grid block dimension in order to ensure that the total dispersion is not dominated by the numerical-dispersion component. The sensitivity study presented in Section 3.2.3 indicates that the effect of transverse dispersivity on cumulative bitumen production histories becomes clearer when d_T-values exceeding 2.0 m are used (i.e., twice the largest grid block dimension in the x-z plane).

G-4. Effect of Grid Block Size on Relative Performance of n-C_6 SAGD to SAGD

Numerical dispersion in finite difference simulations can be lowered by one of two ways: (i) using a higher-order scheme for the approximation of derivatives for a given reservoir gridding; or (ii) reduction of grid block size for a given grid stencil. For a given reservoir gridding,

STARS permits the use of five-point and nine-point discretization formulations to solve the conservation equations. For the commonly-used grid block size of 1 m × 1 m (e.g., Deutsch, 2010; Wang and Leung, 2015; Chen et al., 2008), the shape of the simulated steam chamber for realization 25 in Section 3.2.1 was observed to be comparable to that for the homogeneous case. That is the deviation of the chamber shape from that of an inverted triangle is not captured adequately under the nine-point stencil. So, a better approach towards the reduction of numerical dispersion is by the use of grid blocks of smaller size. To this end, the grid block size in the x-z plane is reduced to 0.25 m × 0.25 m (i.e., fine-scale simulations). This grid block size is on the same order of magnitude as well-log measurements (Pyrcz and Deutsch, 2014).

In addition to longer running times, the issue of lack of numerical convergence in n-C_6 SAGD for the heterogeneous reservoir models was observed to become more severe when smaller grid blocks are used. Due to this, the current discussion of the effect of grid block size on the relative performance of ES-SAGD to SAGD under heterogeneity is restricted to realization 16, for which the issue of lack of numerical convergence is observed to be less pronounced.

The conclusion that the reduction in SOR due to coinjection of solvent can be higher under heterogeneity compared to that under homogeneity for a specified cumulative bitumen production is preserved even when numerical dispersion is reduced through the reduction of grid block size. However, there are a couple of important distinctions between the coarse-scale and fine-scale simulations: (i) the margin of the reduction in SOR due to coinjection of solvent is predicted to be lower for the fine-scale simulations; and (ii) the accumulation of solvent for a given cumulative bitumen production is also observed to be lower. These observations are attributed to the prediction of diminished levels of temperature and concentration dispersion under finer gridding.

Use of a finer grid model can yield higher estimates for bitumen production rate in both SAGD and n-C_6 SAGD under heterogeneity. However, the observed increase is greater for SAGD compared to n-C_6 SAGD, which diminishes the reduction in SOR due to coinjection of solvent compared to a coarser grid model for a given cumulative bitumen production. **Figures G-4 and G-5** respectively give the cumulative bitumen production histories and accompanying SOR for SAGD and n-C_6 SAGD under coarse-scale and fine-scale grid models for the homogeneous and heterogeneous cases. **Figure G-6** illustrates the effect of reservoir gridding on

the simulated reduction in SOR due to coinjection of solvent the homogeneous case and realization 16.

Due to lower temperature dispersion, the number of grid blocks for which the temperature is comparable to the saturation temperature of water at the operating pressure (515.72 K at 35 bars) is predicted to be greater under finer gridding. However, the extent of this increase can be greater for SAGD compared to that under n-C_6 SAGD. These aspects are illustrated for realization 16 with the aid of simulated 2-D property maps. **Figure G-7** presents maps for temperature and oleic-phase saturation in SAGD for the fine- and coarse-scale grid models for the cumulative bitumen production of approximately 45250 m^3. For the coarse-scale grid model, this cumulative bitumen production is met at approximately 1400 days from the start of the operation under steam-only injection. **Figure G-8** presents the temperature and oleic-phase saturation maps at this time. **Figures G-9 and G-10** give the pertinent maps for temperature, oleic-phase saturation, mole fraction of solvent in the vapor (x_{sV}) and oleic (x_{sL}) phases for each grid model under n-C_6 SAGD for realization 16. **Table G-2** presents quantitative summaries for the maps given for each process.

The local displacement efficiency of the oleic phase inside the steam chamber can be higher under steam-solvent coinjection. Consequently, locally, the oleic-phase saturation in ES-SAGD can be lower than the value of the residual oil saturation used to define the oil-water relative permeability curves (0.13 in this research). For a given cumulative bitumen production, the margin by which the local displacement efficiency of the oleic phase is enhanced as a result of coinjection is not significantly altered when the gridding is made finer. The number of grid blocks for which the saturation of the oleic-phase in n-C_6 SAGD is lower than 0.13 is greater under finer gridding (after accounting for the difference in grid block size). However, the number of grid blocks under steam-only injection for which the temperature is comparable to the saturation temperature water is also increased when the gridding is made finer.

In n-C_6 SAGD, the combination of lower levels of dispersion in temperature and solvent concentration in the vapor and oleic phases under finer gridding results in the prediction of lower retention of solvent for a given cumulative bitumen production. The improvement in local displacement efficiency of the oleic phase inside the steam chamber near its edge expedites the recovery of both the dead-bitumen component and the solvent dissolved in the oleic phase.

Table G-3 presents the parameters pertinent to the estimation of the numerical dispersion coefficients and dispersivities for the fine-scale n-C_6 SAGD simulations for the homogeneous reservoir model and realization 16 for the cumulative bitumen production of approximately 55263 m^3. **Figure G-11** visualizes the variation in time-step size with respect to cumulative bitumen production. **Figures G-12 and G-13** give the simulated interstitial velocity maps for the fine-scale cases for each reservoir type. The numerical dispersion coefficient and dispersivity matrices for the aforementioned cumulative bitumen production are calculated to be

$$\bar{\bar{D}}^{hom}_{num,FS} = \begin{bmatrix} 0.0532 & 0.0044 \\ 0.0044 & 0.0330 \end{bmatrix}, \quad \text{(G-32)}$$

$$\bar{\bar{d}}^{hom}_{num,FS} = \begin{bmatrix} 0.1157 & 0.0096 \\ 0.0096 & 0.0718 \end{bmatrix}, \quad \text{(G-33)}$$

$$\bar{\bar{D}}^{het}_{num,FS} = \begin{bmatrix} 0.1399 & 0.0120 \\ 0.0120 & 0.0256 \end{bmatrix}, \quad \text{(G-34)}$$

$$\bar{\bar{d}}^{het}_{num,FS} = \begin{bmatrix} 0.1759 & 0.0151 \\ 0.0151 & 0.0322 \end{bmatrix}. \quad \text{(G-35)}$$

The largest eigenvalues of the numerical dispersivity matrices are 0.1177 for the homogeneous case and 0.1778 for realization 16. These values are comparable to 50% of the grid block dimension (i.e., ≈ 0.125 m), and are lower than those calculated for the coarse-scale simulations.

Table G-1. Summary of numerical values of parameters pertinent to the calculation of the numerical dispersion coefficients and numerical dispersivities in n-C_6 SAGD for the homogeneous reservoir model and realization 16 under coarse-scale gridding. The values furnished here are on the basis of the simulated property maps for the cumulative bitumen production of approximately 55263 m^3.

Property	Homogeneous	Realization 16
Δt	0.3228	1.0828
u_x, m/day	0.1047	0.0918
u_z, m/day	0.0754	0.0256
u, m/day	0.1396	0.1014
v_x, m/day	0.2908	0.2550
v_z, m/day	0.2094	0.0710
v, m/day	0.3878	0.2817
D_{xx}^{num}, m^2/day	0.1591	0.1627
D_{zx}^{num}, m^2/day	0.0098	0.0098
D_{zz}^{num}, m^2/day	0.0594	0.0205
d_{xx}^{num}, m	0.4101	0.5777
d_{zx}^{num}, m	0.0253	0.0348
d_{zz}^{num}, m	0.1532	0.0727

Table G-2. Number of grid blocks (N) in SAGD and n-C_6 SAGD for realization 16 that fulfill a specific constraint for the fine-scale and coarse-scale gridding schemes. The cumulative bitumen production under consideration is approximately 45250 m^3. Note that the grid for the fine-scale case is eight times finer than that for the coarse-scale case; the numerical values given in the first and third columns of this table have been reported after accounting for this difference. That is, this table presents the number of 1 m × 1 m regions in the coarse-scale and fine-scale cases that satisfies a particular constraint for each process for a specified cumulative bitumen production. The saturation temperature of water at the operating pressure of 35 bars is 515.72 K. The residual oil saturation used for the definition of oil-water relative permeability curves is 0.13. S_L stands for the oleic-phase saturation.

Constraint	N_{SAGD} (fine-scale)	N_{SAGD} (coarse-scale)	$N_{ES\text{-}SAGD}$ (fine-scale)	$N_{ES\text{-}SAGD}$ (coarse-scale)
$T \geq 510$ K	606	576	248	237
$0.12 < S_L < 0.14$	98	65	40	30
$0 < S_L \leq 0.12$	0	0	153	115

Table G-3. Summary of numerical values of parameters pertinent to the calculation of the numerical dispersion coefficients and numerical dispersivities in n-C_6 SAGD for the homogeneous reservoir model and realization 16 under fine-scale gridding. The values furnished here are on the basis of the simulated property maps for the cumulative bitumen production of approximately 55263 m^3.

Property	Homogeneous	Realization 16
Δt	0.0992	0.1826
u_x, m/day	0.1336	0.2628
u_z, m/day	0.0868	0.0651
u, m/day	0.1656	0.2864
v_x, m/day	0.3711	0.7301
v_z, m/day	0.2410	0.1807
v, m/day	0.4601	0.7954
D_{xx}^{num}, m^2/day	0.0532	0.1399
D_{zx}^{num}, m^2/day	0.0044	0.0120
D_{zz}^{num}, m^2/day	0.0330	0.0256
d_{xx}^{num}, m	0.1157	0.1759
d_{zx}^{num}, m	0.0096	0.0151
d_{zz}^{num}, m	0.0718	0.0322

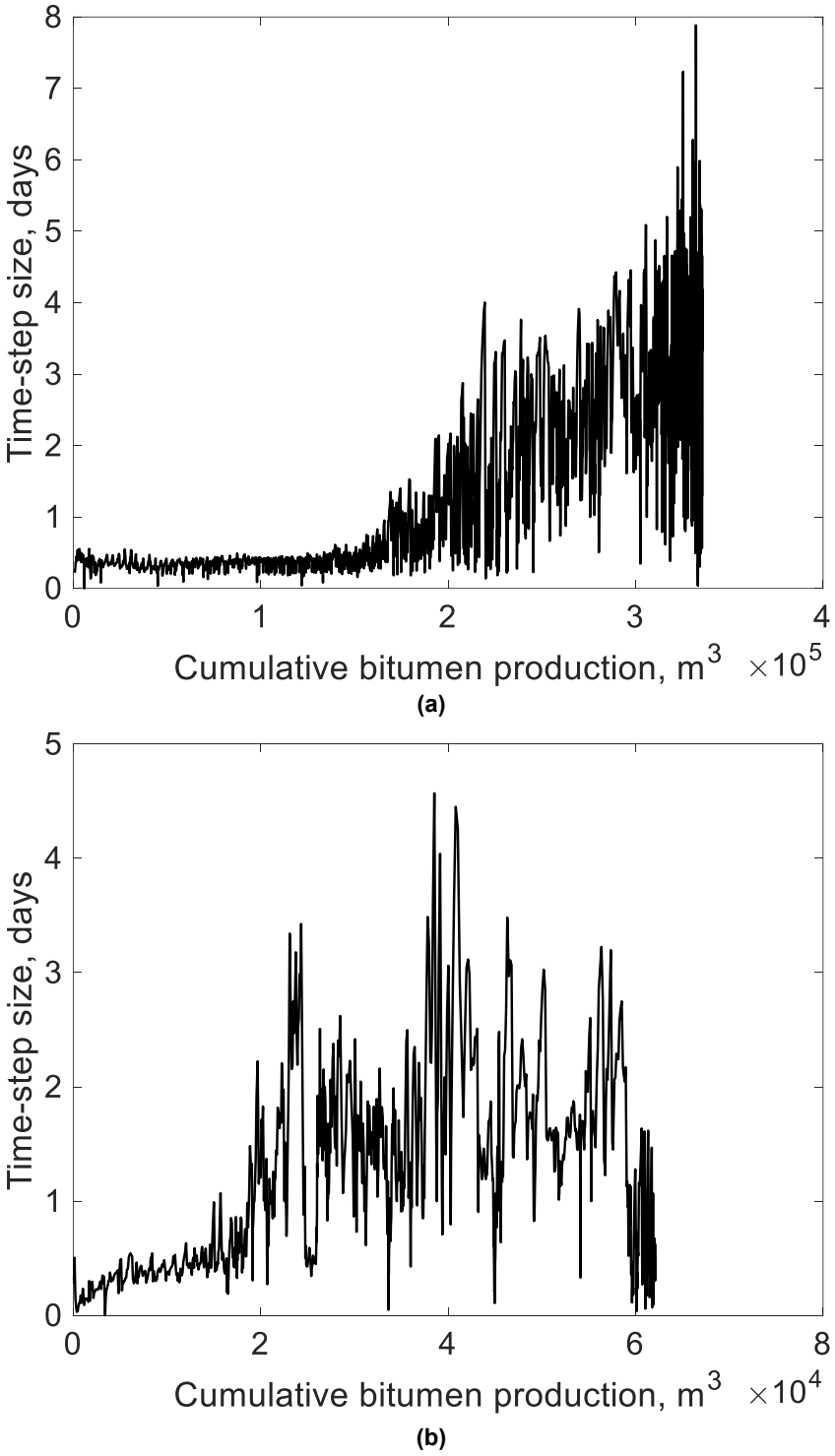

Figure G-1. Time-step size (days) used in coarse-scale n-C_6 SAGD simulations as a function of cumulative bitumen production for reservoir models in the second case study of Chapter 3 (Section 3.2.2); (a) homogeneous reservoir; (b) realization 16.

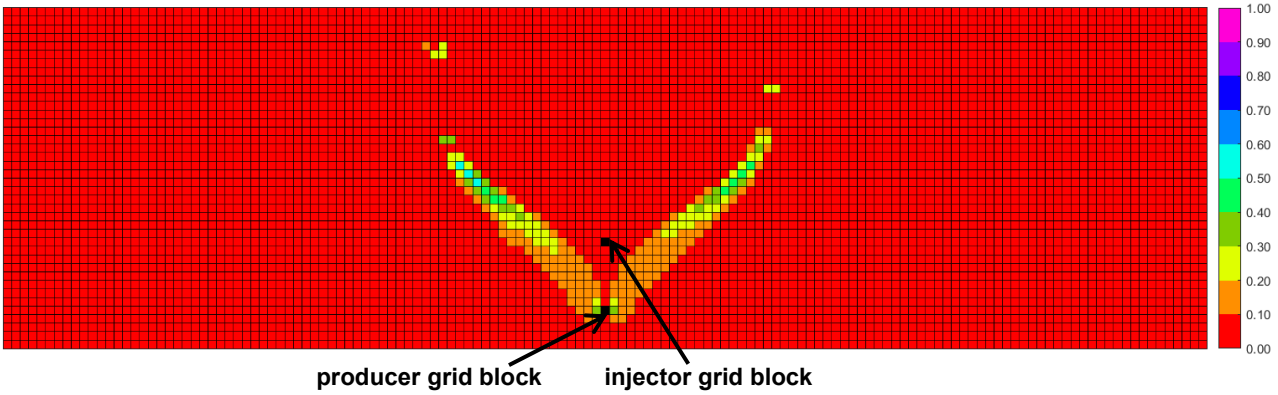

(a) Magnitude of x-directional component of Darcy velocity of the oleic phase

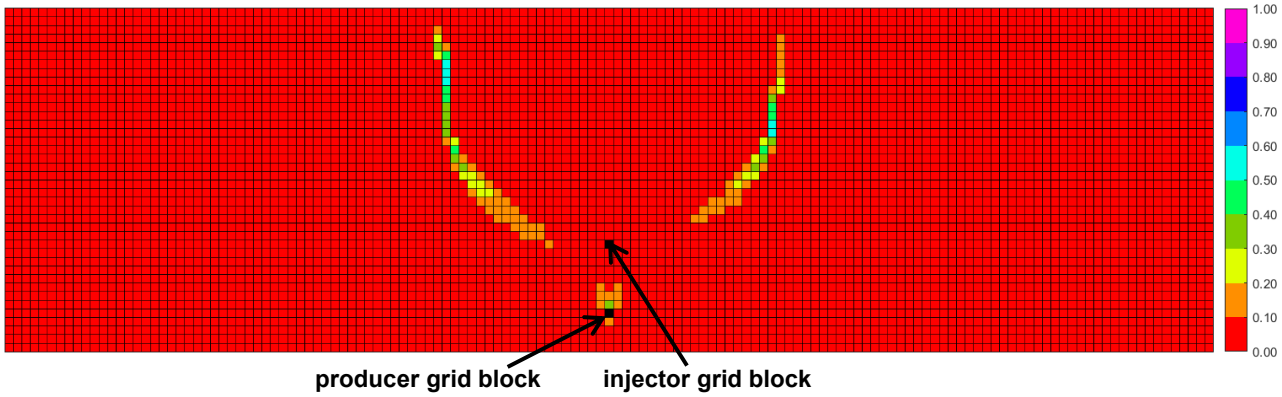

(b) Magnitude of z-directional component of Darcy velocity of the oleic phase

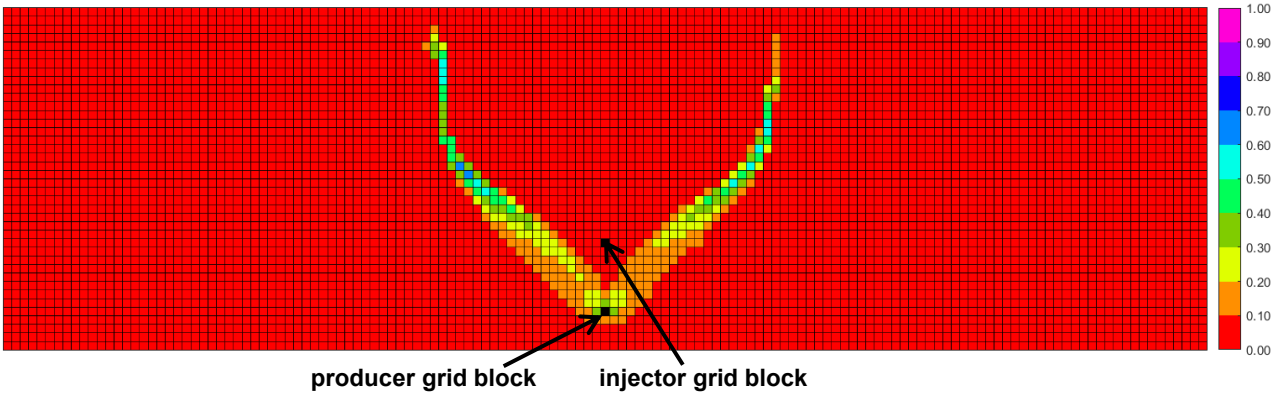

(c) Magnitude of Darcy velocity of the oleic phase

Figure G-2. Magnitude of Darcy velocity (in m/day) of the oleic phase for the homogeneous reservoir model in the second case study of Chapter 3 (Section 3.2.2) for the cumulative bitumen production of approximately 55263 m^3 under coarse-scale gridding; (a) magnitude of horizontal (x) component; (b) magnitude of vertical (z) component; (c) overall magnitude (i.e., including x-and z-components).

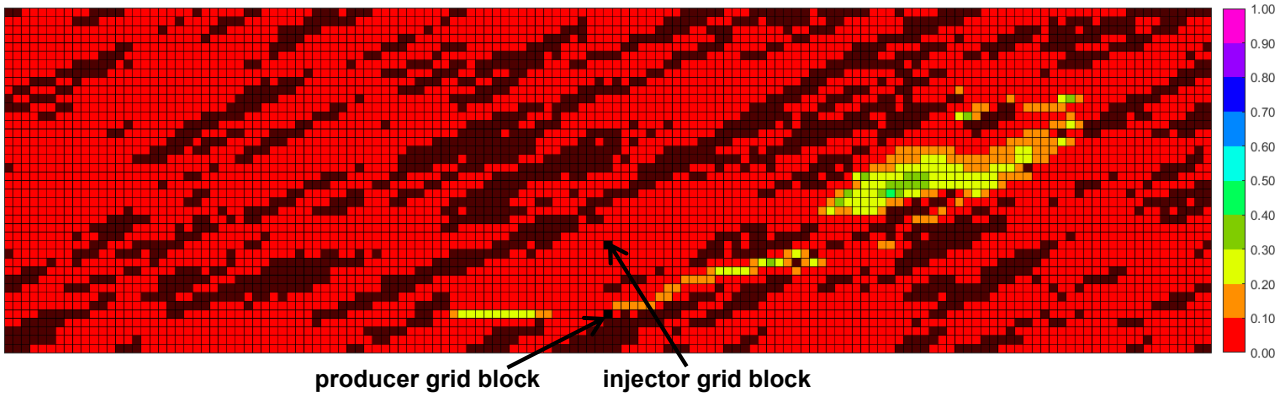

(a) Magnitude of x-directional component of Darcy velocity of the oleic phase

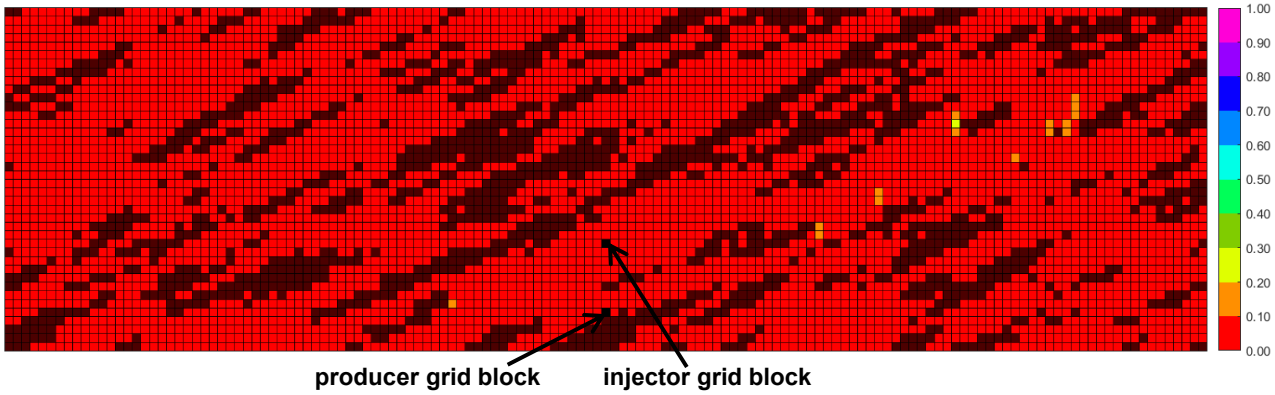

(b) Magnitude of z-directional component of Darcy velocity of the oleic phase

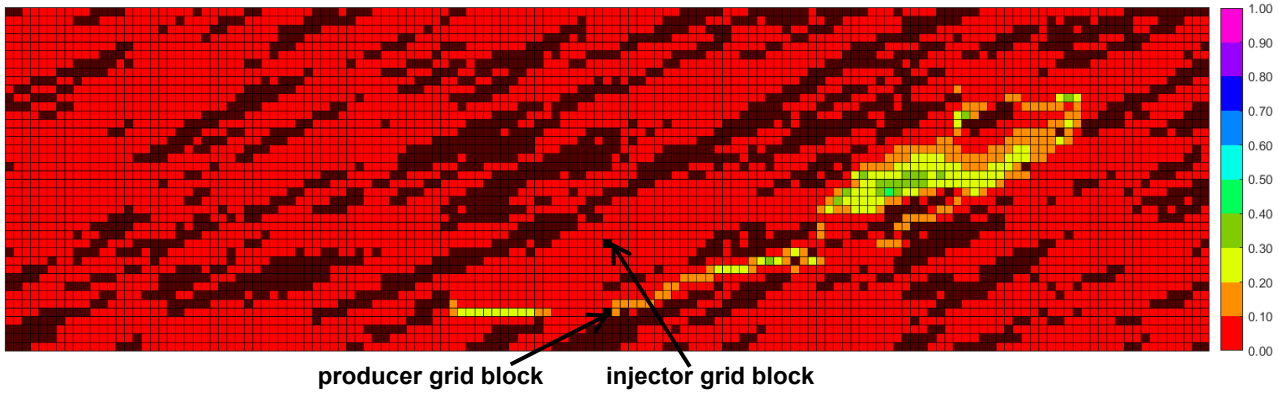

(c) Magnitude of Darcy velocity of the oleic phase

Figure G-3. Distribution of the magnitude of Darcy velocity (in m/day) of the oleic phase in clean sand grid blocks of realization 16 in the second case study of Chapter 3 (Section 3.2.2) for the cumulative bitumen production of approximately 55263 m^3; (a) magnitude of horizontal (x) component; (b) magnitude of vertical (z) component; (c) overall magnitude (i.e., including x-and z-components).

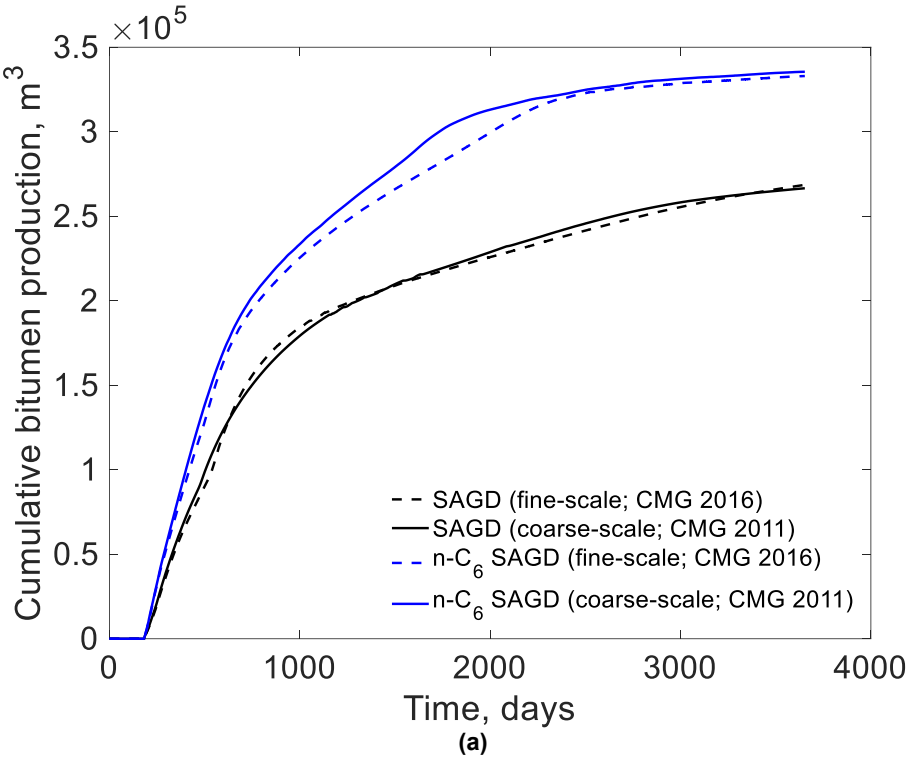

(a)

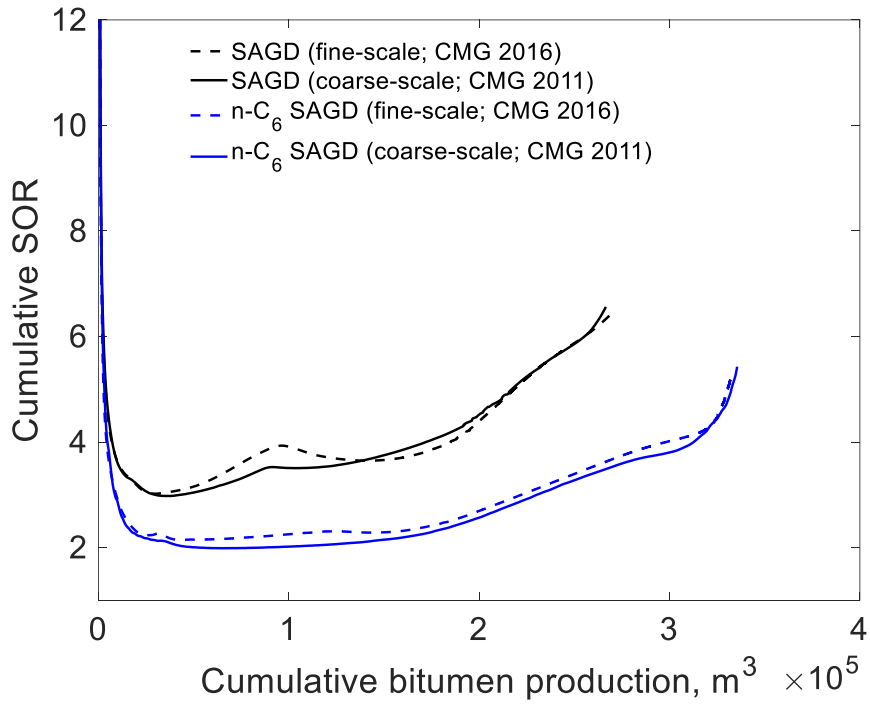

(b)

Figure G-4. Effect of grid block size on the cumulative bitumen production history and accompanying SOR for the homogeneous reservoir model in case study 3.2.2.

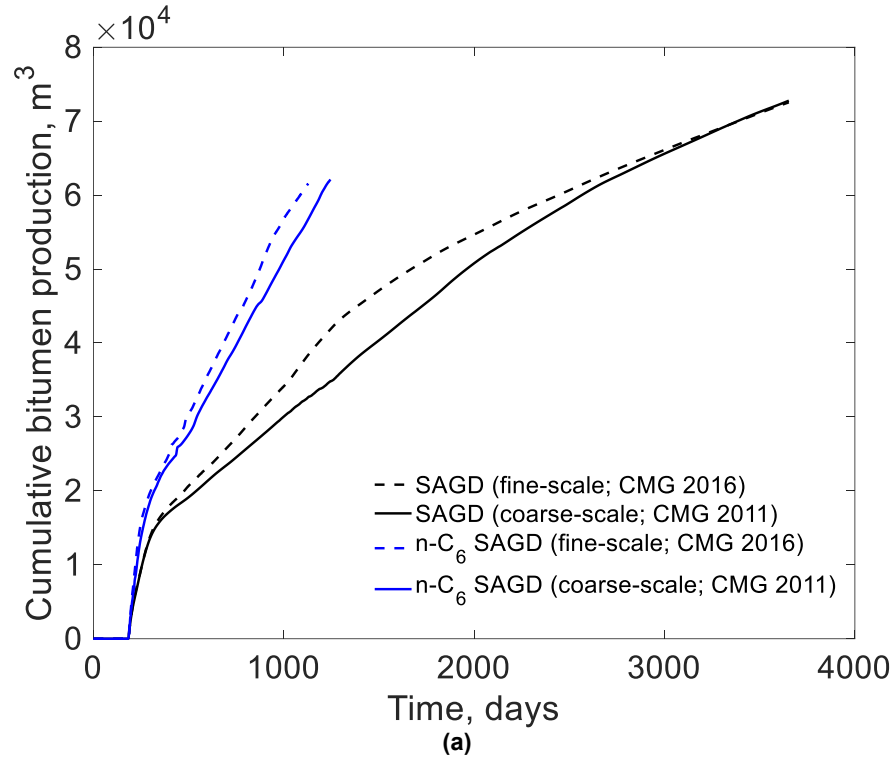

Figure G-5. Effect of grid block size on the cumulative bitumen production history and accompanying SOR for realization 16 in case study 3.2.2.

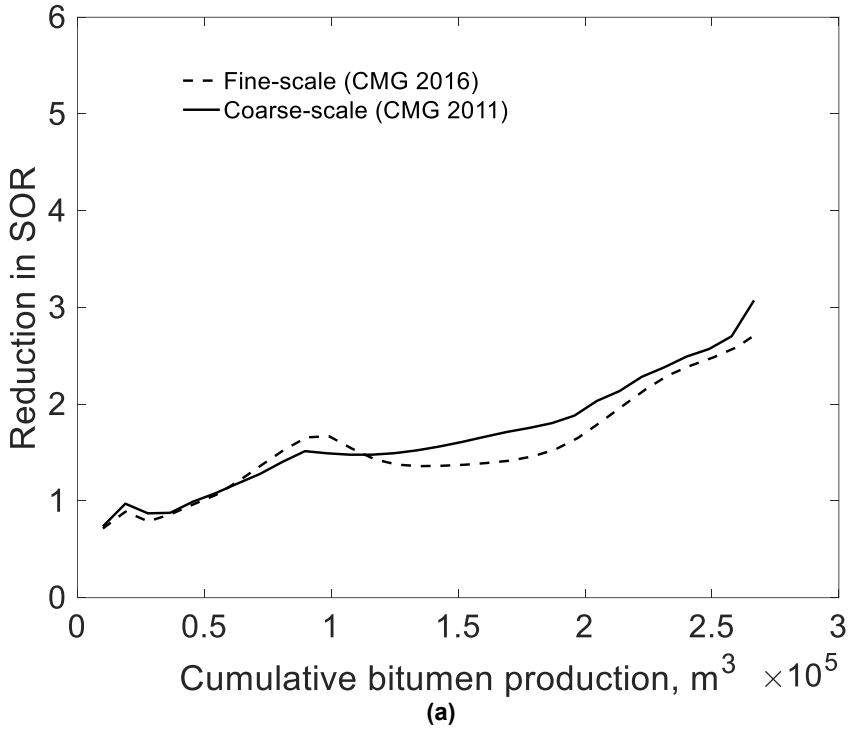

(a)

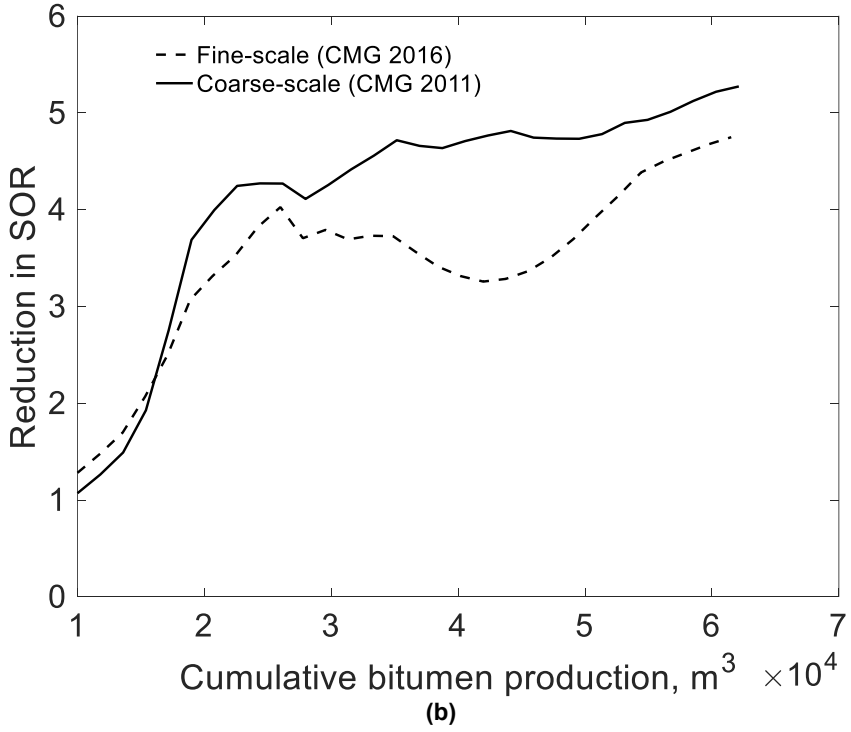

(b)

Figure G-6. Reduction in SOR due to coinjection of solvent under homogeneity and heterogeneity in case study 3.2.2; (a) homogeneous model; (b) realization 16.

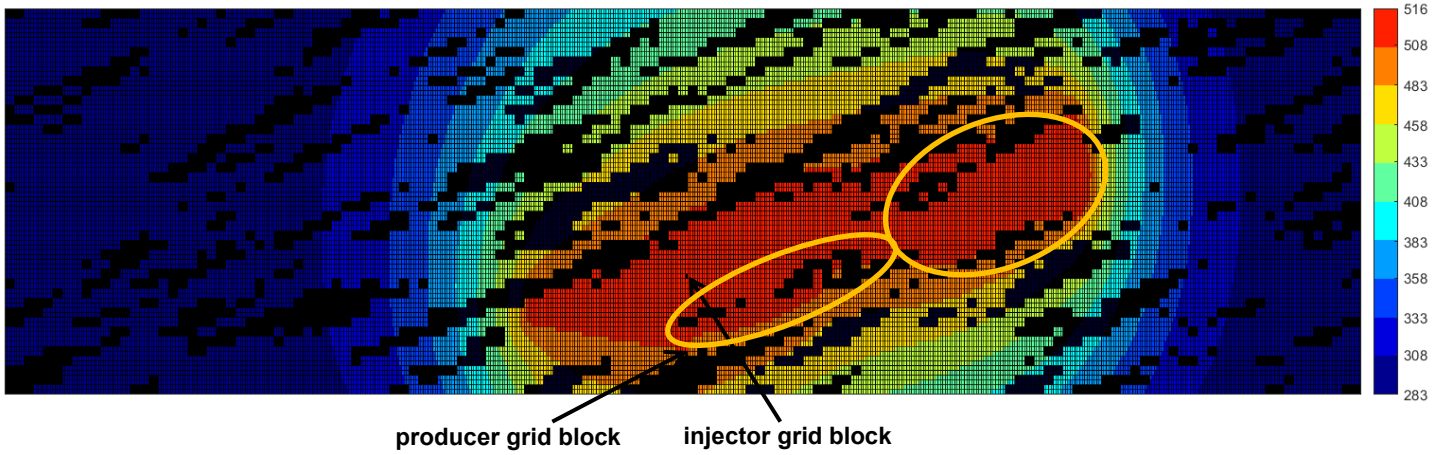

(a) Temperature map (in Kelvin) in SAGD for the fine-scale case

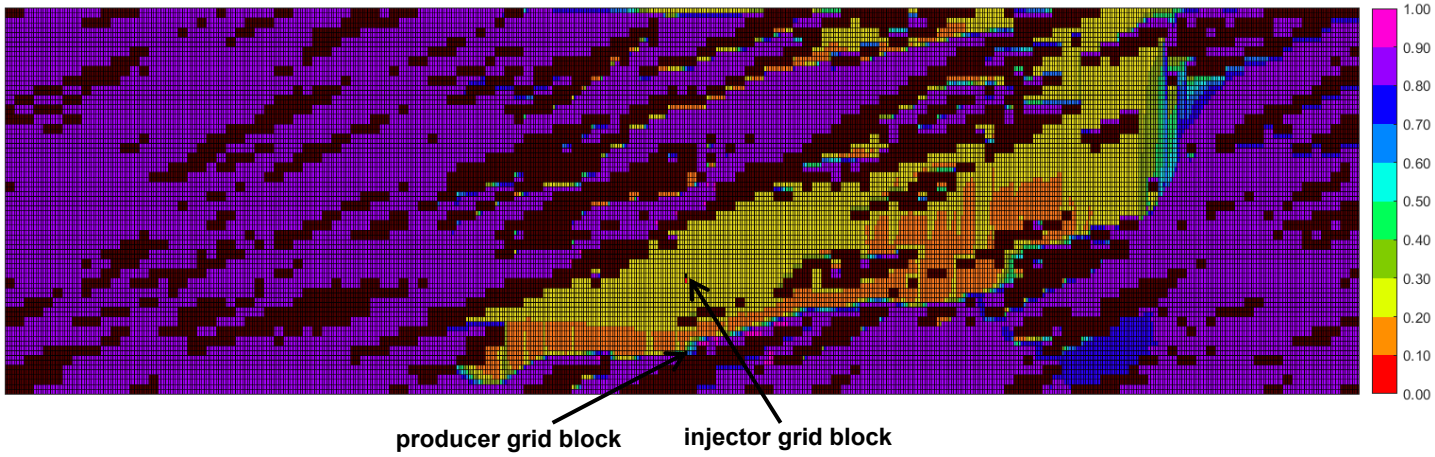

(b) Oleic-phase saturation map in SAGD for the fine-scale case

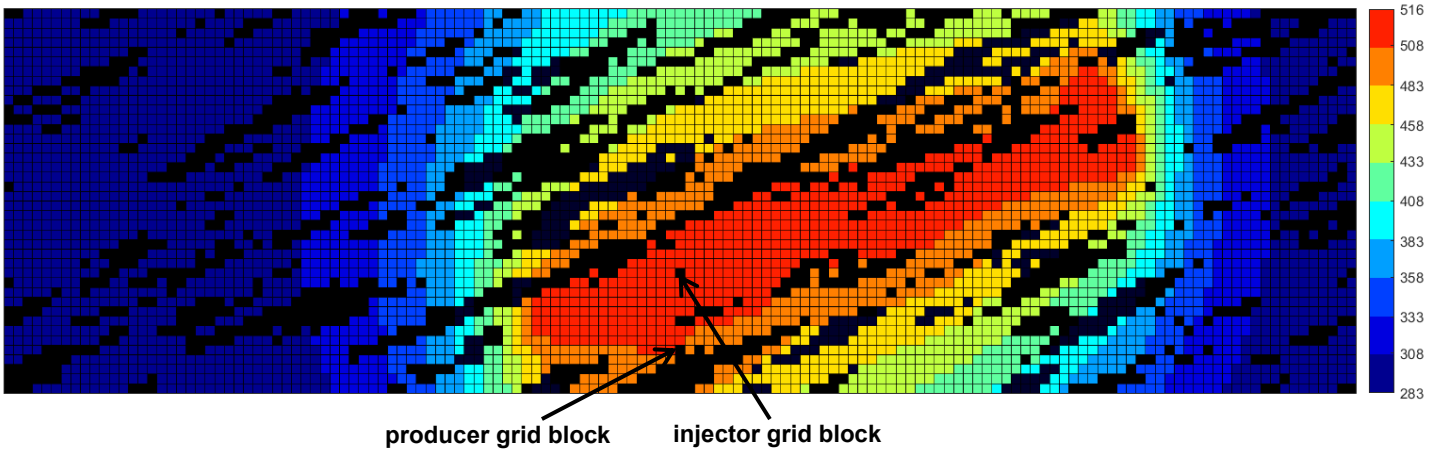

(c) Temperature map (in Kelvin) in SAGD for the coarse-scale case

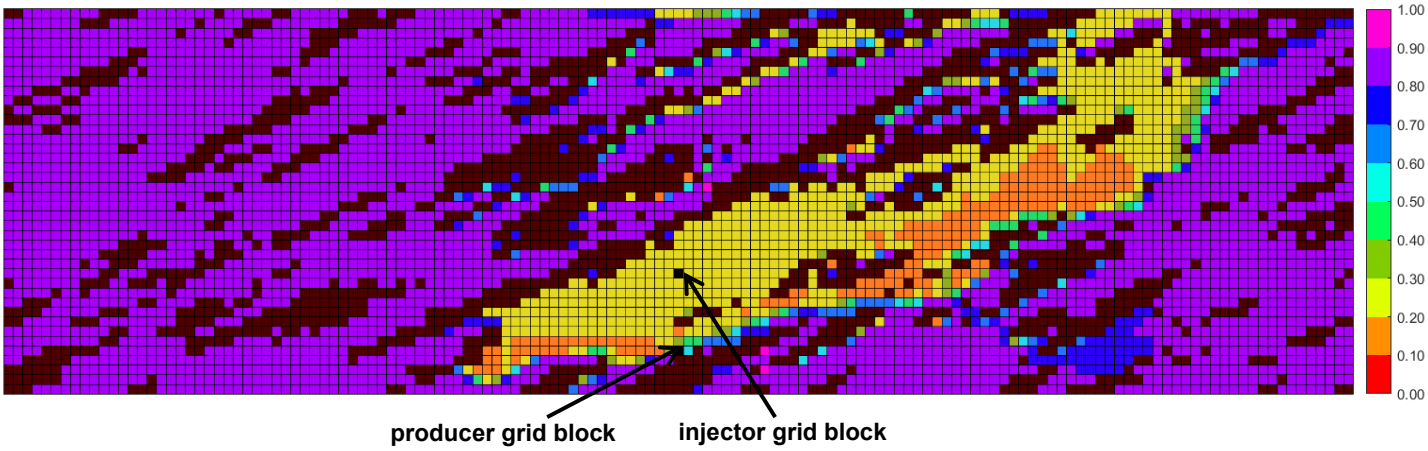

(d) Oleic-phase saturation map in SAGD for the coarse-scale case

Figure G-7. Distribution of temperature (in Kelvin) and oleic-phase saturation in clean sand grid blocks of realization 16 for SAGD for the cumulative bitumen production of approximately 45250 m^3 under fine-scale and coarse-scale gridding; (a) temperature map for the fine-scale case; (b) oleic-phase saturation map for the fine-scale case; (c) temperature map for the coarse-scale case; (d) oleic-phase saturation map for the coarse-scale case. The shape of the SAGD steam-chamber is altered when the resolution of the spatial grid is made finer, and is a consequence of the underlying discrepancies in the predicted distribution of temperature. The number of grid blocks for which the temperature is comparable to the saturation temperature of water (i.e., greater than 510 K) is 4850 for the fine-scale case, and 576 for the coarse-scale case. Accounting for the differences in gridding, this corresponds to 606 and 576 grid blocks for the fine-scale and coarse-scale cases, respectively [4850 divided by 8 is approximately 606]. This difference appears to be pronounced in the highlighted regions of the reservoir in part (a). The number of grid blocks where the oleic-phase saturation is comparable to the residual oil saturation of the medium (0.13) is greater for the fine-scale case. That is, the prediction of higher temperatures facilitates the improvement of the local displacement efficiency of the oleic phase, leading to quicker expansion of the steam chamber. For the fine-scale case, the aforementioned cumulative bitumen production is met at 1400 days from the start of the operation; for the coarse-scale case, this is met at 1739 days. Figure G-8 gives the pertinent property maps for the coarse-scale case at 1400 days from the start of the operation.

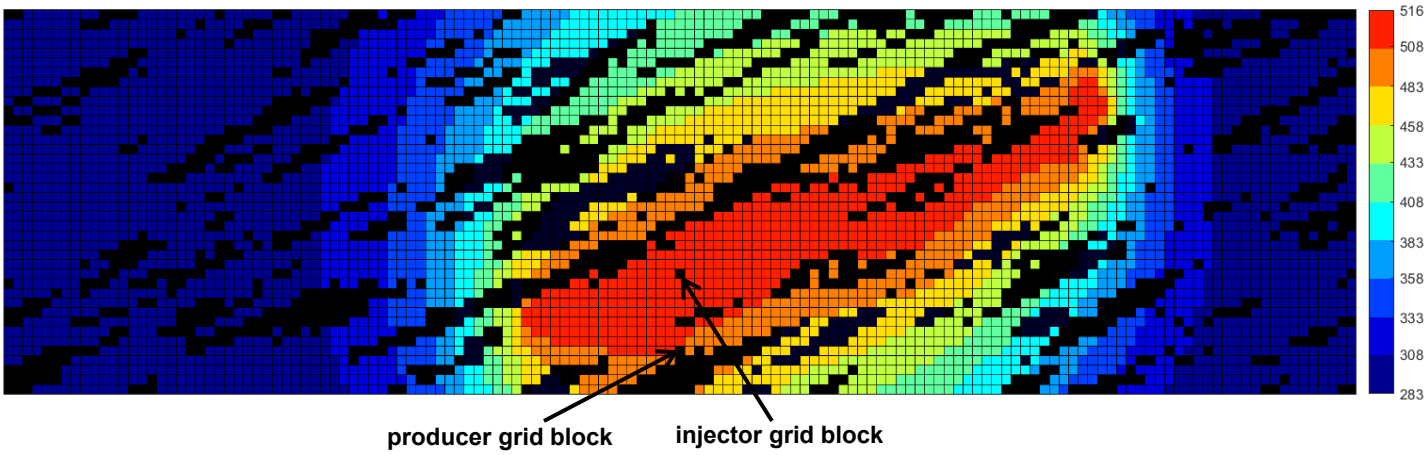

(a) Temperature map in SAGD for the coarse-scale case at 1400 days

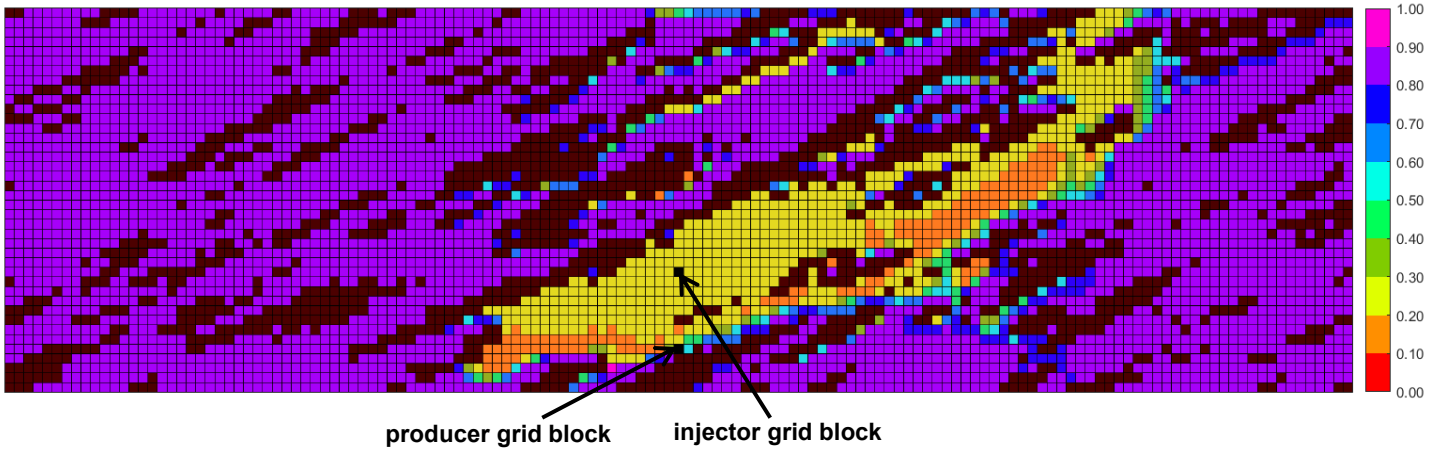

(b) Oleic-phase saturation map in SAGD for the coarse-scale case at 1400 days

Figure G-9. Distribution of temperature and oleic-phase saturation in clean sand grid blocks of realization 16 for the coarse-scale gridding at 1400 days from the start of the operation; (a) temperature map; (b) oleic-phase saturation map.

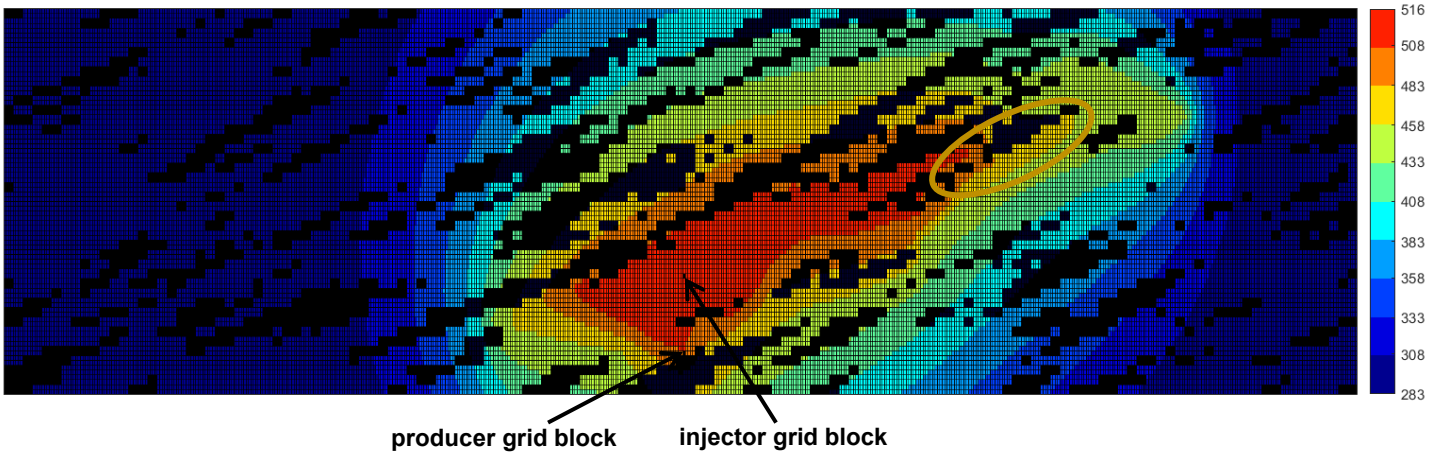

(a) Temperature map in n-C_6 SAGD for realization for the fine-scale case

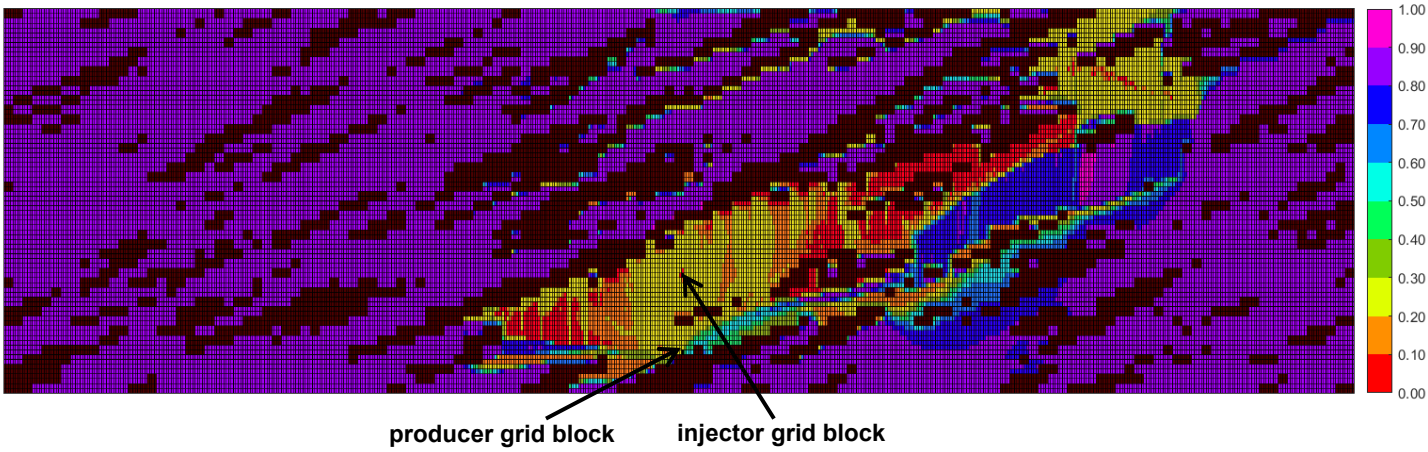

(b) Oleic-phase saturation map in n-C_6 SAGD for realization for the fine-scale case

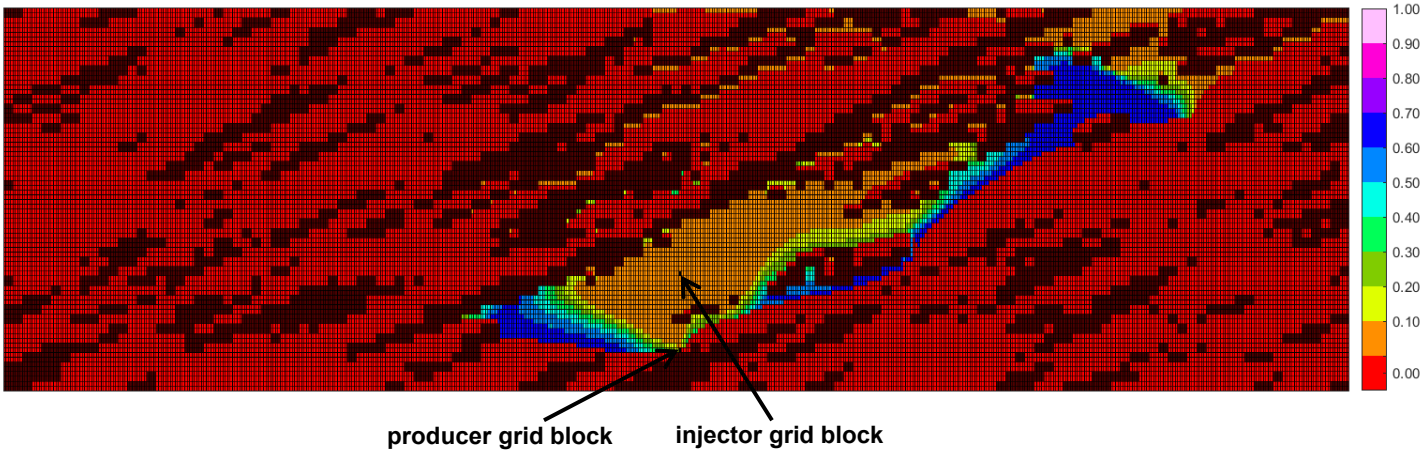

(c) x_{sV} map in n-C_6 SAGD for realization for the fine-scale case

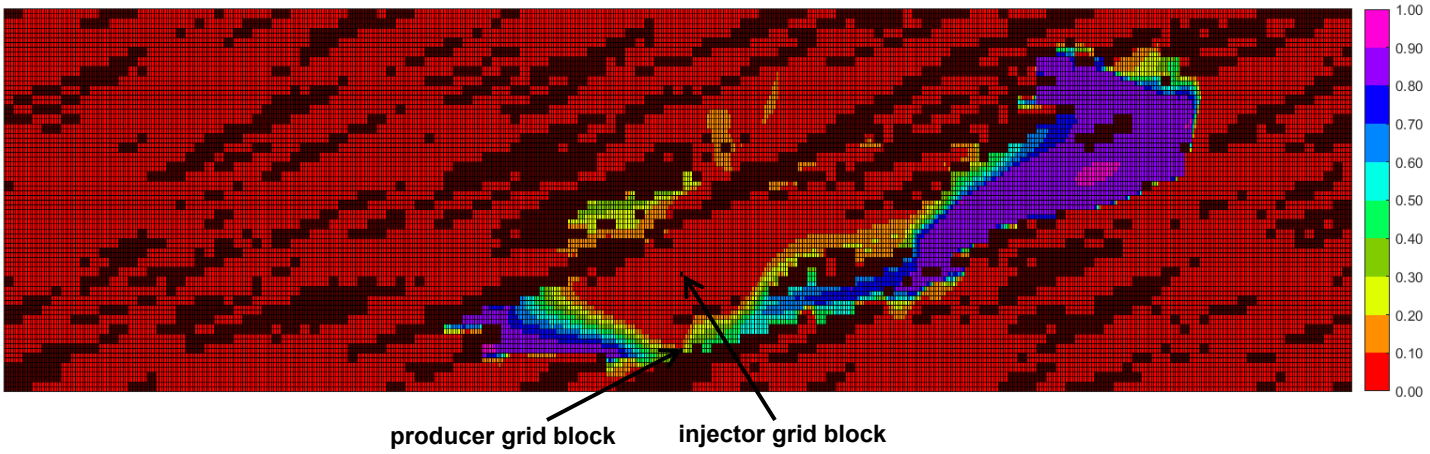

(d) x_{sL} map in n-C_6 SAGD for realization for the fine-scale case

Figure G-9. Distribution of temperature, oleic-phase saturation, mole fraction of solvent in the vapor phase (x_{sV}), and mole fraction of solvent in the oleic phase (x_{sL}) in clean sand grid blocks of realization 16 for the fine-scale case for the cumulative bitumen of approximately 52918 m^3; (a) temperature; (b) oleic-phase; (c) x_{sV}; (d) x_{sL}. The temperature in the highlighted region of part (a) is greater than that under the coarse-scale case (see Figure G-10a). This likely contributes to the increased prevalence of the distillation mechanism in this region under fine-scale gridding.

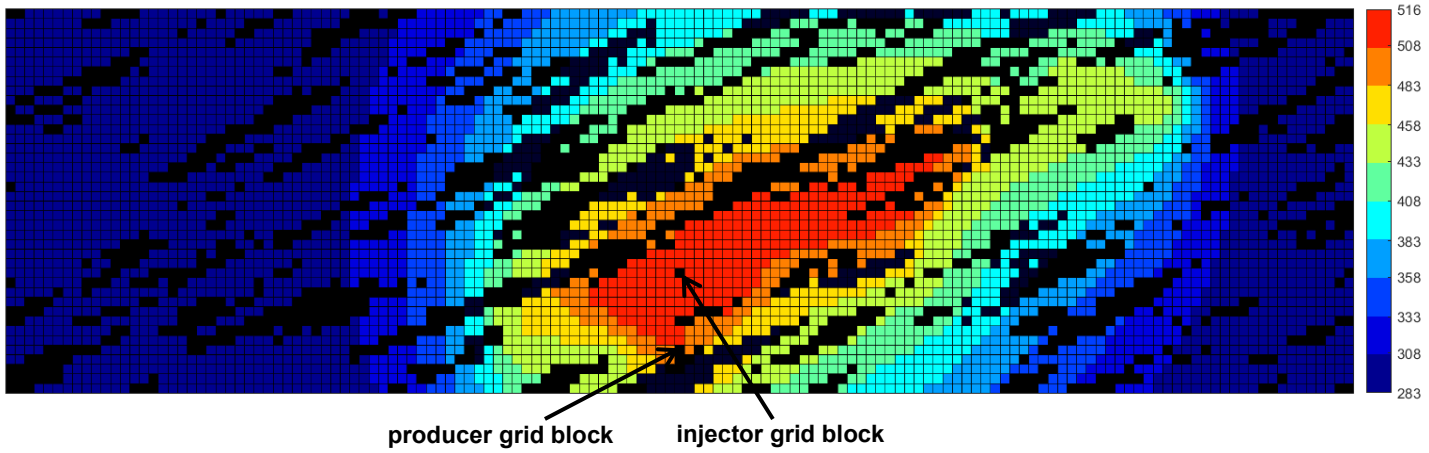

(a) Temperature map in n-C_6 SAGD for realization for the coarse-scale case

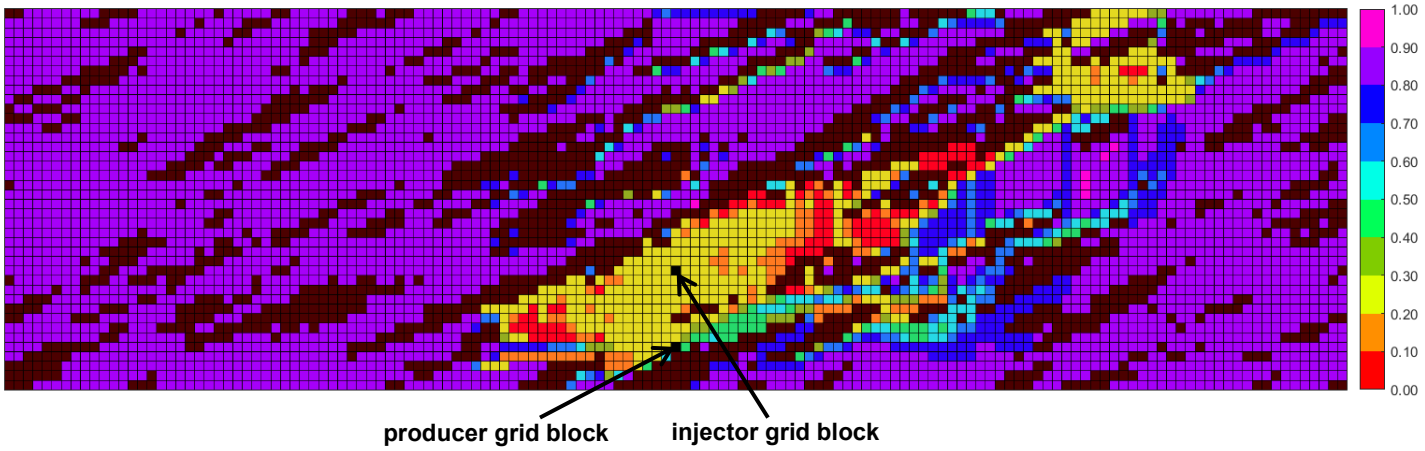

(b) Oleic-phase saturation map in n-C_6 SAGD for realization for the coarse-scale case

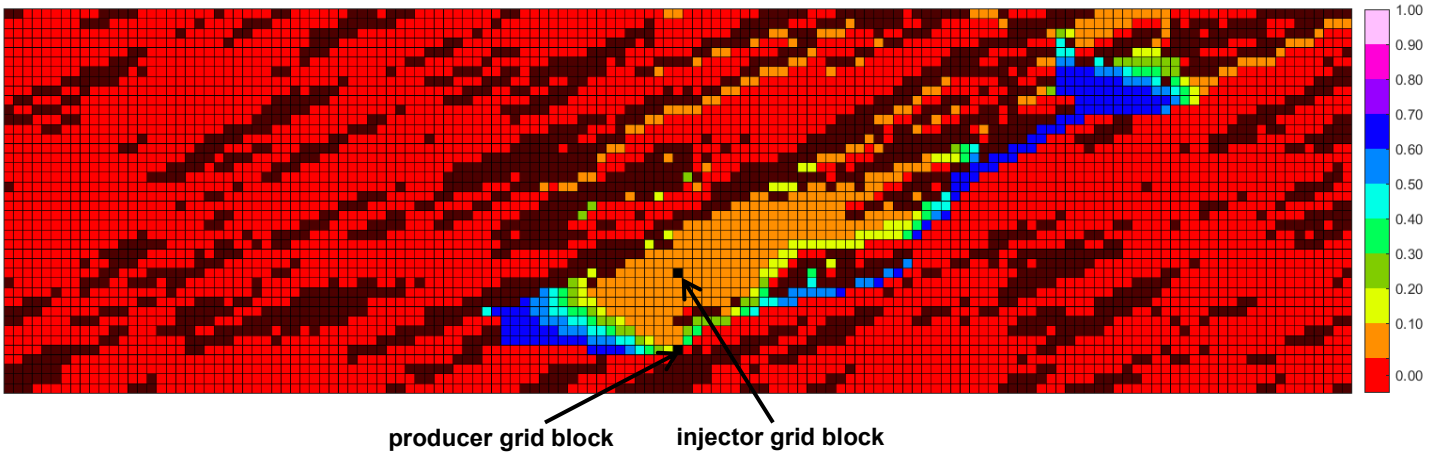

(c) x_{sv} saturation map in n-C_6 SAGD for realization for the coarse-scale case

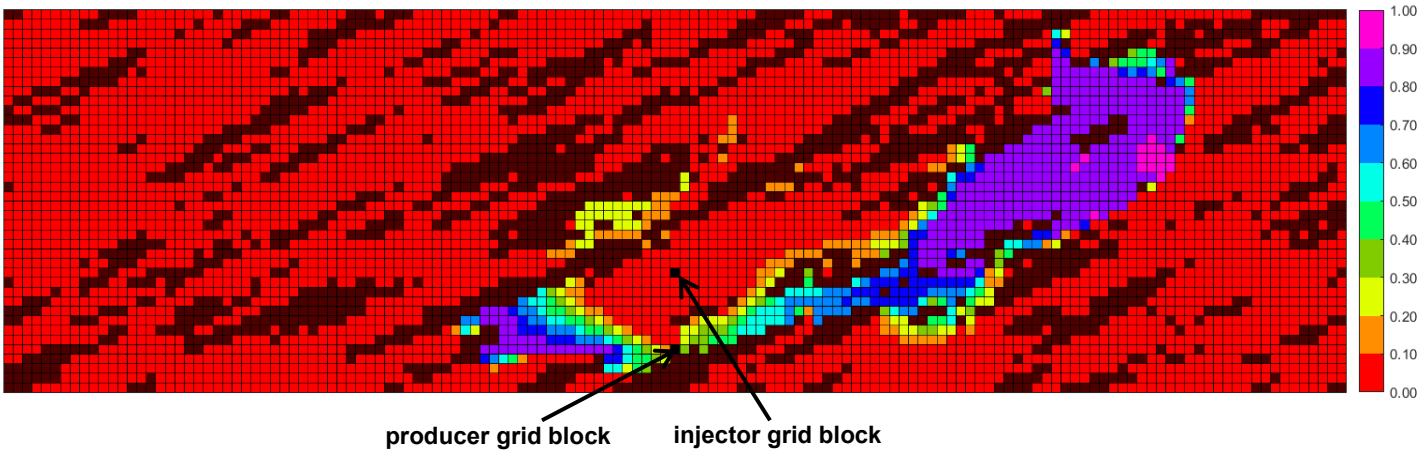

(d) x_{sL} map in n-C_6 SAGD for realization for the coarse-scale case

Figure G-10. Distribution of temperature, oleic-phase saturation, mole fraction of solvent in the vapor phase (x_{sV}), and mole fraction of solvent in the oleic phase (x_{sL}) in clean sand grid blocks of realization 16 for the coarse-scale case for the cumulative bitumen of approximately 52918 m^3; (a) temperature; (b) oleic-phase; (c) x_{sV}; (d) x_{sL}.

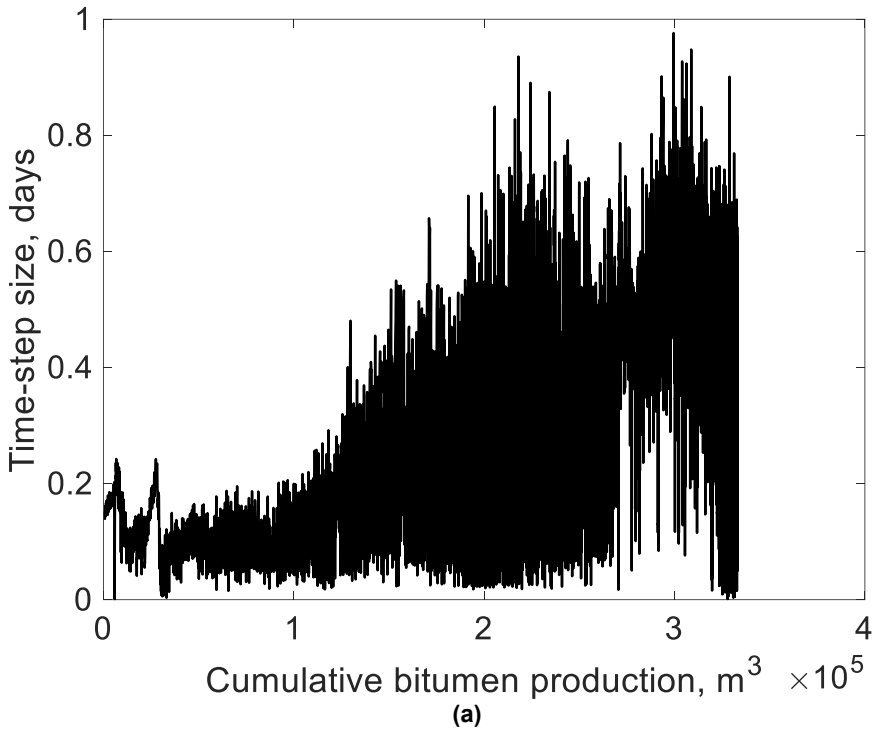

(a)

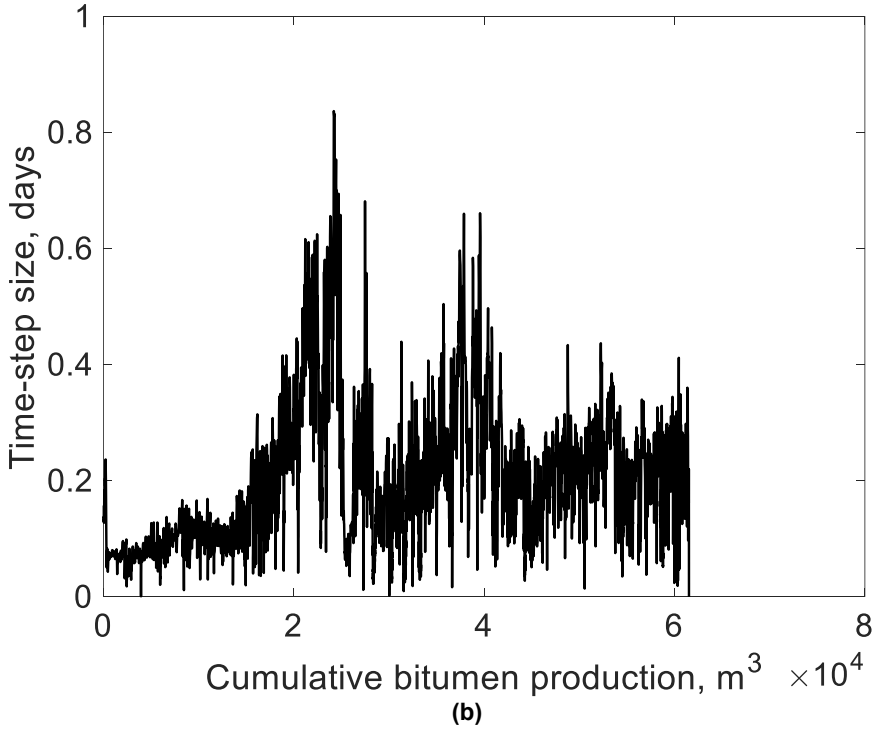

(b)

Figure G-11. Time-step size (days) used in fine-scale n-C_6 SAGD simulations as a function of cumulative bitumen production for reservoir models in the second case study of Chapter 3 (Section 3.2.2); (a) homogeneous reservoir; (b) realization 16.

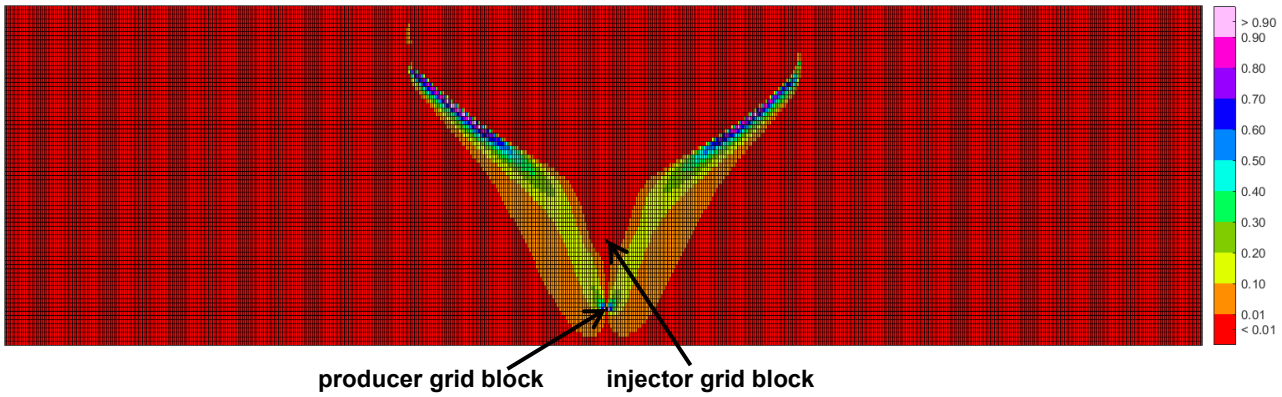

(a) Magnitude of x-directional component of Darcy velocity of the oleic phase

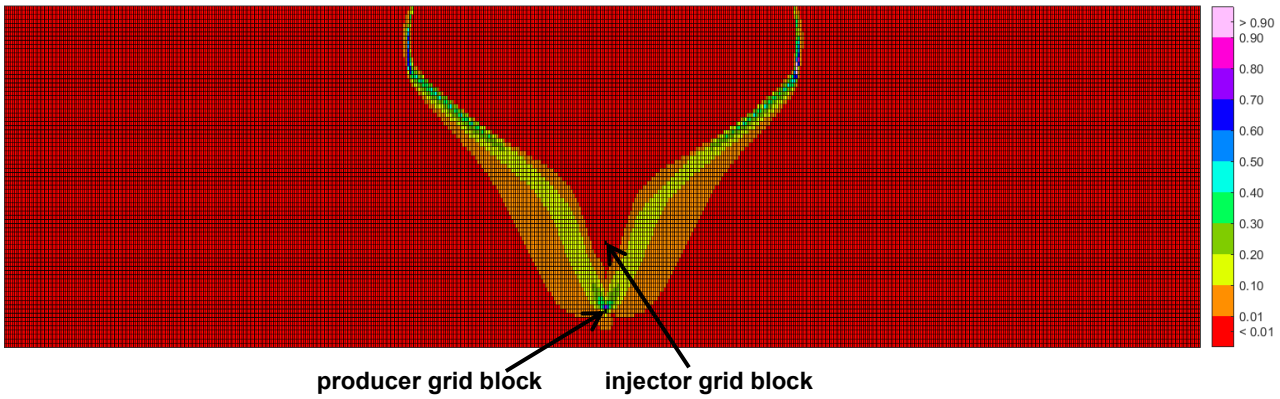

(b) Magnitude of z-directional component of Darcy velocity of the oleic phase

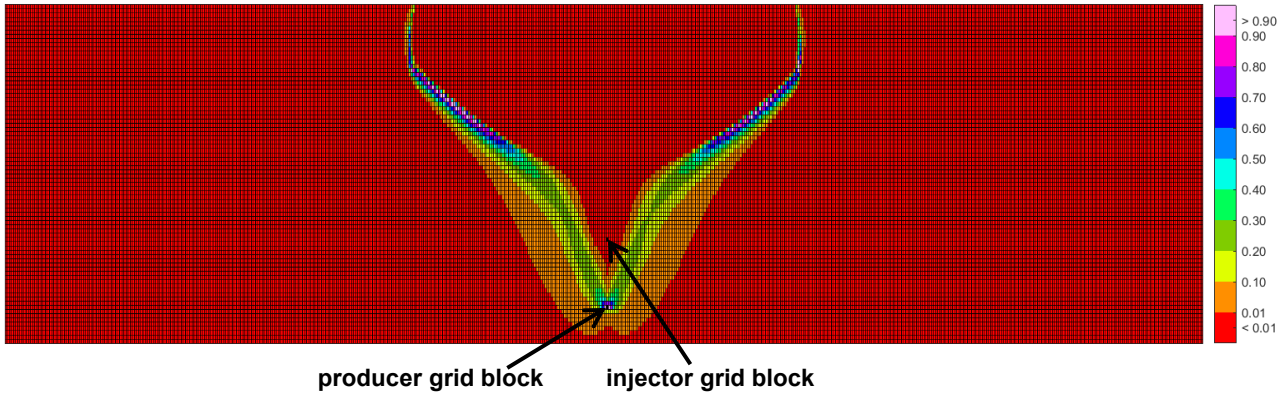

(c) Magnitude of Darcy velocity of the oleic phase

Figure G-12. Magnitude of Darcy velocity (in m/day) of the oleic phase for the homogeneous reservoir model in the second case study of Chapter 3 (Section 3.2.2) for the cumulative bitumen production of approximately 55263 m^3 under fine-scale gridding; (a) magnitude of horizontal (x) component; (b) magnitude of vertical (z) component; (c) overall magnitude (i.e., including x-and z-components).

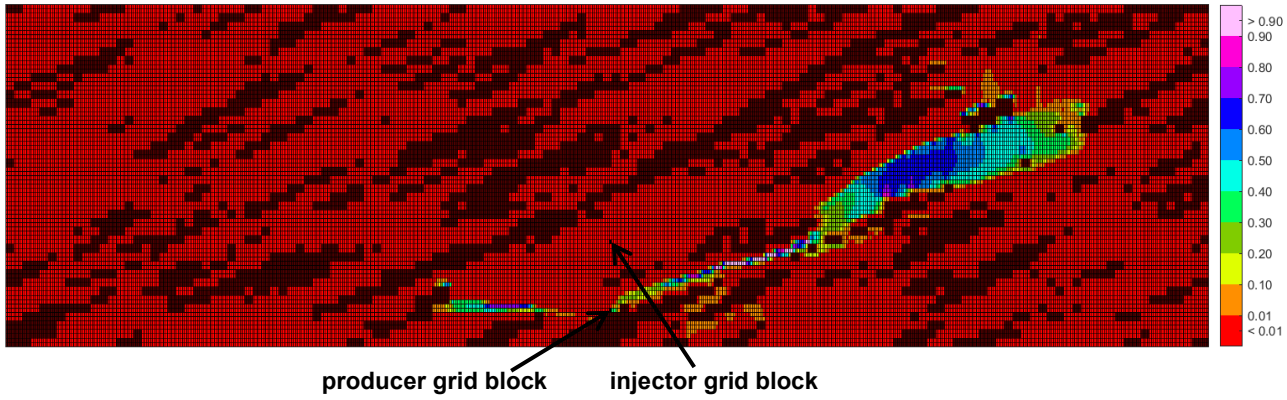

(a) Magnitude of x-directional component of Darcy velocity of the oleic phase

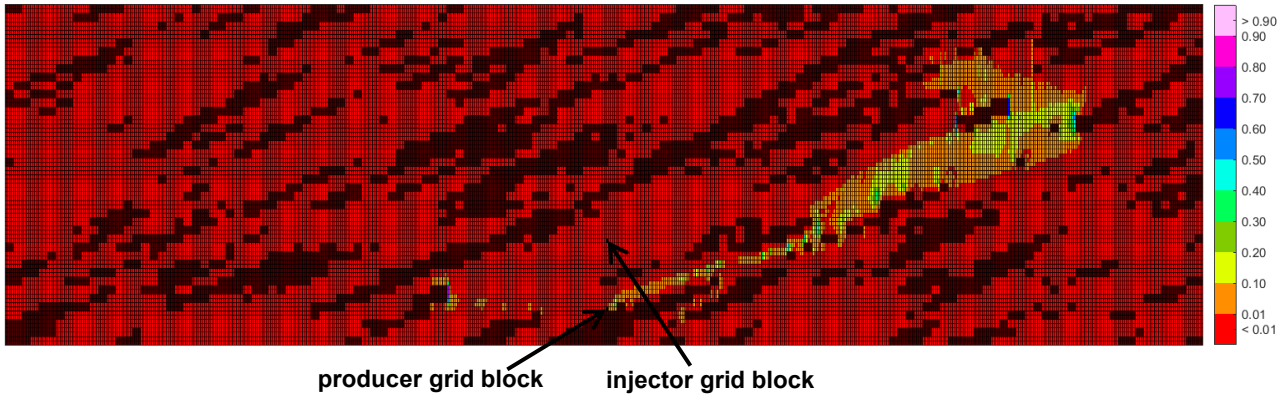

(b) Magnitude of z-directional component of Darcy velocity of the oleic phase

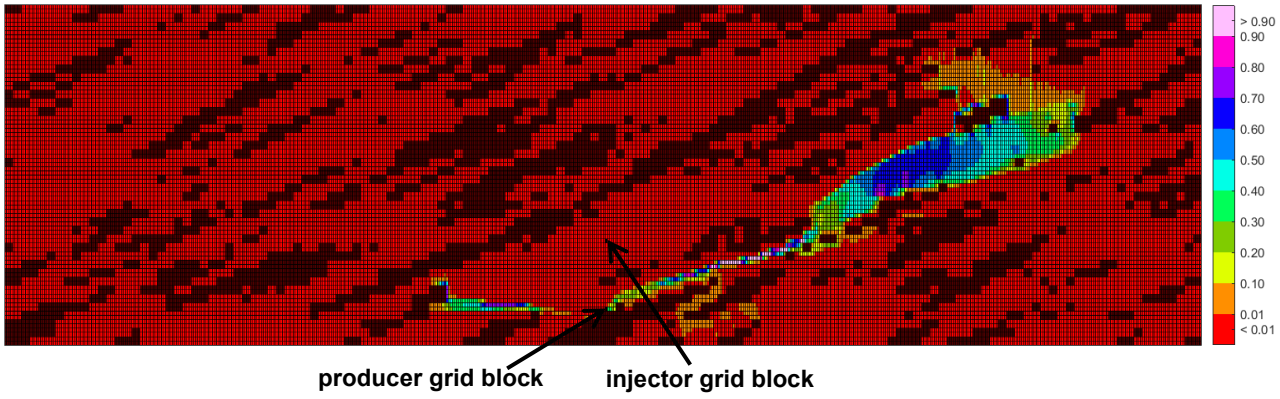

(c) Magnitude of Darcy velocity of the oleic phase

Figure G-13. Magnitude of Darcy velocity (in m/day) of the oleic phase for realization in the second case study of Chapter 3 (Section 3.2.2) for the cumulative bitumen production of approximately 55263 m^3 under fine-scale gridding; (a) magnitude of horizontal (x) component; (b) magnitude of vertical (z) component; (c) overall magnitude (i.e., including x-and z-components).

Appendix H. Relative Performance of n-C_6 SAGD to SAGD under 3-D Heterogeneity

This appendix examines the effect of considering spatial variation of facies along the y-coordinate (well-pair direction) on the relative performance of n-C_6 SAGD to SAGD. Three cases are considered in this analysis: (i) homogeneous case from case study 3.2.2; (ii) realization 16 from case study 3.2.2 for which spatial variation of facies is restricted to x-z plane; (iii) a variant of realization 16 in which spatial variation of facies along the y-direction is accounted for by creating an alternating sequence of heterogeneous and homogeneous cross-sections. The injection concentration of solvent in n-C_6 SAGD is set to 2 mol%.

Discretization of the reservoir is conducted along all three dimensions for each case. The dimensions of the reservoir (x, y, and z) are 141 m × 500 m × 20 m. The dimensions of each grid block (x, y, and z) are 1 m × 50 m × 0.5 m; there are 56400 grid blocks in total. As before, the y-coordinate represents the direction along the well-pair. The reservoir is fragmented into ten grid blocks, each of length 50 m along the y-coordinate; this is within the range of values used in flow simulations (Deutsch, 2010).

For the homogeneous model, and 2-D heterogeneous case (where variation of facies along the well-pair direction is ignored), discretization of the reservoir along the y-coordinate does not have a significant effect on the production performance of each process. This is mainly because the flux of the oleic phase along the y-coordinate (i.e., y-directional component of the oleic-phase Darcy velocity) is rather small, and the y-directional numerical dispersion coefficients are sensitive to the corresponding directional interstitial velocities (see Appendix G).

Figure H-1 presents the simulated bitumen production histories and accompanying SOR for SAGD and n-C_6 SAGD for each reservoir model. **Figure H-2** gives the reduction in cumulative SOR due to coinjection of solvent as a function of cumulative bitumen production. **Figure H-3** presents the accumulated solvent volume in-situ as a function of cumulative bitumen production, and solvent recovery factor with respect to both the cumulative bitumen production and time.

The performance curves given in Figures H-1 and H-2 for the heterogeneous reservoir model, wherein the spatial variation of facies along well-pair direction is considered (i.e., 3-D heterogeneous case), is on average bounded between those for the homogeneous case, and 2-D heterogeneous case. This is because the extent to which flow is impeded for the 3-D

heterogeneous case is lower than that for the 2-D heterogeneous due to the availability of additional hydraulic paths for flow in the direction of the well-pair (i.e., y-direction). Consequently, the production rate of bitumen is higher while the rate of accumulation of solvent is lower for the 3-D heterogeneous case compared to the 2-D heterogeneous case.

Figures H-4 and H-5 present the cross-sectional maps for the simulated vapor-phase saturation in SAGD for the cumulative bitumen production of approximately 55330 m^3 for the 2-D and 3-D heterogeneous cases. The pertinent maps for n-C_6 SAGD for the cumulative bitumen production of approximately 83932 m^3 are given in **Figures H-6 and H-7**. There are a few important distinctions between 2-D and 3-D heterogeneous cases in terms of the geometry of the steam chamber. Firstly, unlike the 2-D heterogeneous case, the shape of the steam chamber for the 3-D heterogeneous case in the x-z plane is not self-similar across all cross-sections along the y-coordinate. Secondly, expansion of the steam chamber predominantly occurs in cross-sections along the y-direction (i.e., x-z slices) that are homogeneous. In the homogeneous x-z cross-sectional planes, the shape of the steam chamber resembles that of an inverted triangle. Further, the width (i.e., horizontal span) of the steam chamber in the x-z cross-section that is homogeneous within the 3-D heterogeneous case is greater than that of the homogeneous case (where all cross-sections along the y-direction are homogeneous). This is because for the 3-D heterogeneous case, the combined thickness of all the homogeneous cross-sections along the y-direction is only half of that for the homogeneous case. **Figures H-8 and H-9** present the cross-sectional maps for the vapor-phase saturation in SAGD and n-C_6 SAGD for the homogeneous case for the cumulative bitumen productions of 55330 and 83932 m^3, respectively.

The conclusion that the reduction in cumulative SOR due to coinjection of solvent for a given cumulative bitumen production can be greater under heterogeneity compared to that under homogeneity is qualitatively preserved even for the 3-D heterogeneous case. However, the margin of improvement in the reduction in cumulative SOR due to coinjection of solvent is lower for the 3-D case compared to that for the 2-D heterogeneous case. This is due to the availability of additional hydraulic paths for fluid flow along the well-pair direction in the 3-D heterogeneous case, which lowers the extent to which the solvent accumulates within the reservoir, and dilutes bitumen compared to that for the 2-D heterogeneous case for a given cumulative bitumen production. **Figures H-10 and H-11** respectively present the simulated cross-sectional maps for x_{sL} (mole fraction of solvent in oleic phase) in n-C_6 SAGD for the 2-D

and 3-D heterogeneous cases for the cumulative bitumen production of approximately 83932 m^3; **Figures H-12 and H-13** present the pertinent cross-sectional maps for $\beta_L x_{sL}$, where β_L is the mole fraction of the oleic phase.

Figure H-14 presents the simulated x_{sL} and $\beta_L x_{sL}$ maps for the homogeneous case for the cumulative bitumen production of approximately 83932 m^3. For a given cumulative bitumen production, the thickness of the solvent-rich liquid bank beyond the chamber-edge even in the homogeneous cross-sections along the y-coordinate of the 3-D heterogeneous case is observed to be greater than that for the homogeneous case (compare Figures H-11b and H-14a, and Figures H-13b and H-14b). So, there are two factors that contribute to the observation that the reduction in the SOR due to coinjection of solvent is greater for the 3-D heterogeneous case compared to the homogeneous case. Firstly, a thicker solvent-rich liquid bank beyond the chamber edge for the 3-D heterogeneous case enhances the extent to which the drainage rate of the oleic phase is increased relative to steam-only injection. Secondly, the interplay between x_{sL} and temperature improves the margin by which heat losses from the formation are reduced due to coinjection of solvent for the 3-D heterogeneous case. **Figure H-15** presents the cumulative heat loss from the reservoir by conductive heat transfer as a function of cumulative bitumen production for SAGD and n-C_6 SAGD for the homogeneous and 3-D heterogeneous cases.

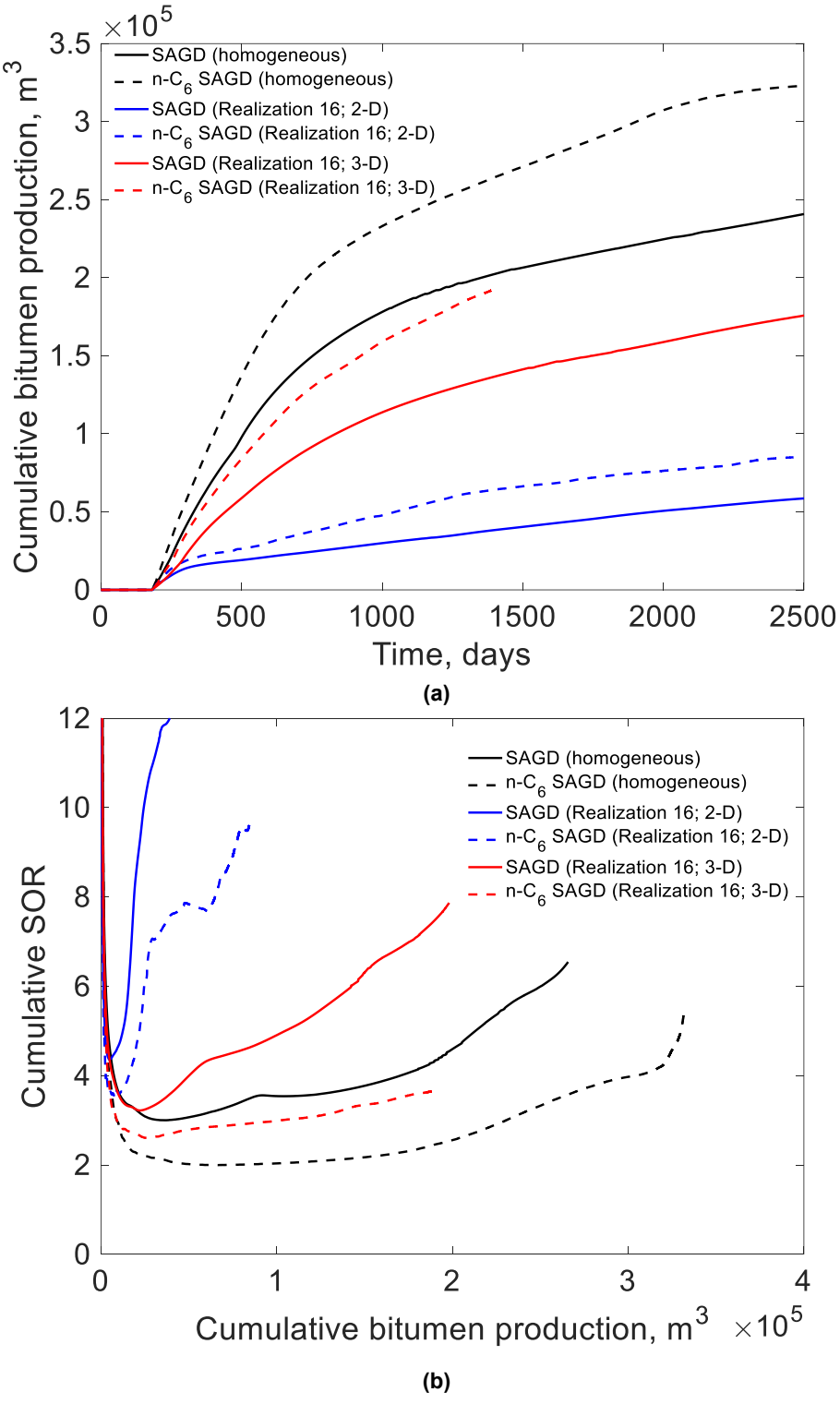

Figure H-1. Cumulative bitumen production histories and accompanying SOR for SAGD and n-C_6 SAGD for the homogeneous and heterogeneous reservoirs; (a) cumulative bitumen production histories; (b) cumulative SOR as a function of cumulative bitumen production.

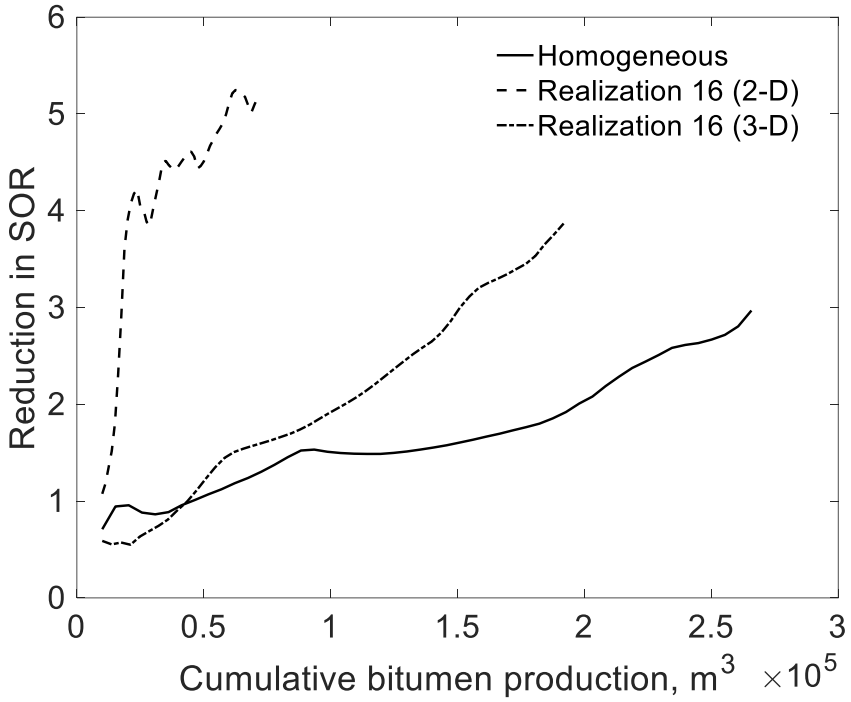

Figure H-2. Reduction in cumulative SOR due to coinjection of solvent as a function of cumulative bitumen production.

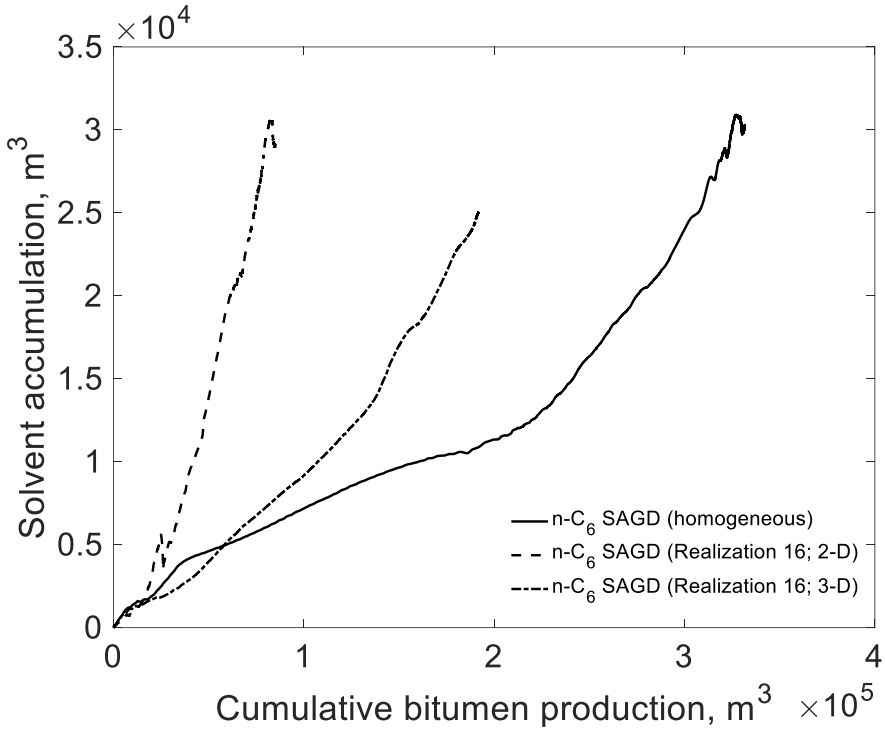
×10^4
3.5
3
2.5
2
1.5
1
0.5
0
Solvent accumulation, m^3
0
1
2
3
4
Cumulative bitumen production, m^3
×10^5
n-C6 SAGD (homogeneous)
n-C6 SAGD (Realization 16; 2-D)
n-C6 SAGD (Realization 16; 3-D)

(a)

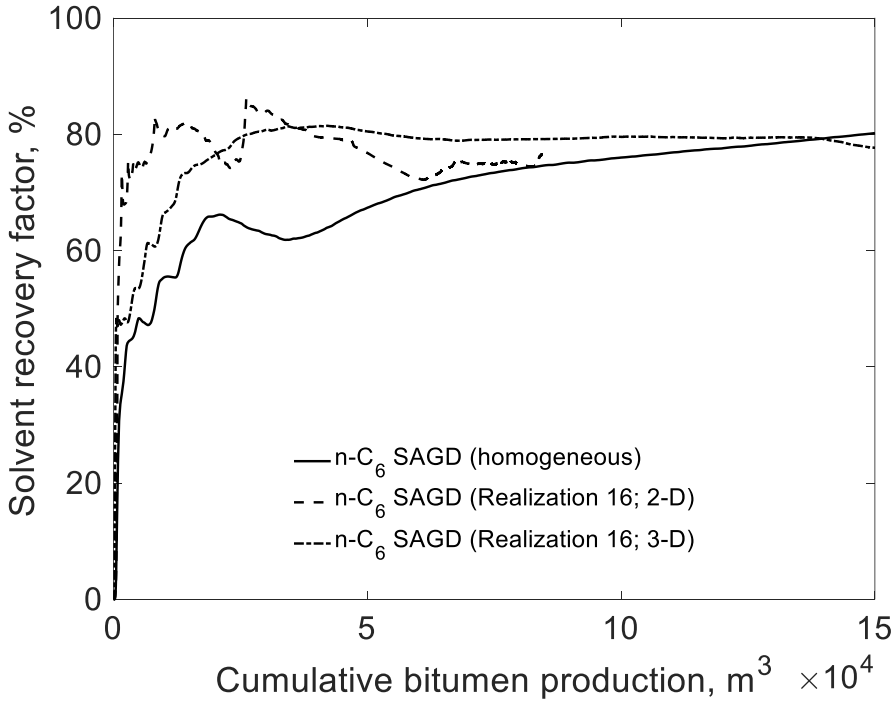
100
80
60
40
20
0
Solvent recovery factor, %
0
5
10
15
Cumulative bitumen production, m^3
×10^4
n-C6 SAGD (homogeneous)
n-C6 SAGD (Realization 16; 2-D)
n-C6 SAGD (Realization 16; 3-D)

(b)

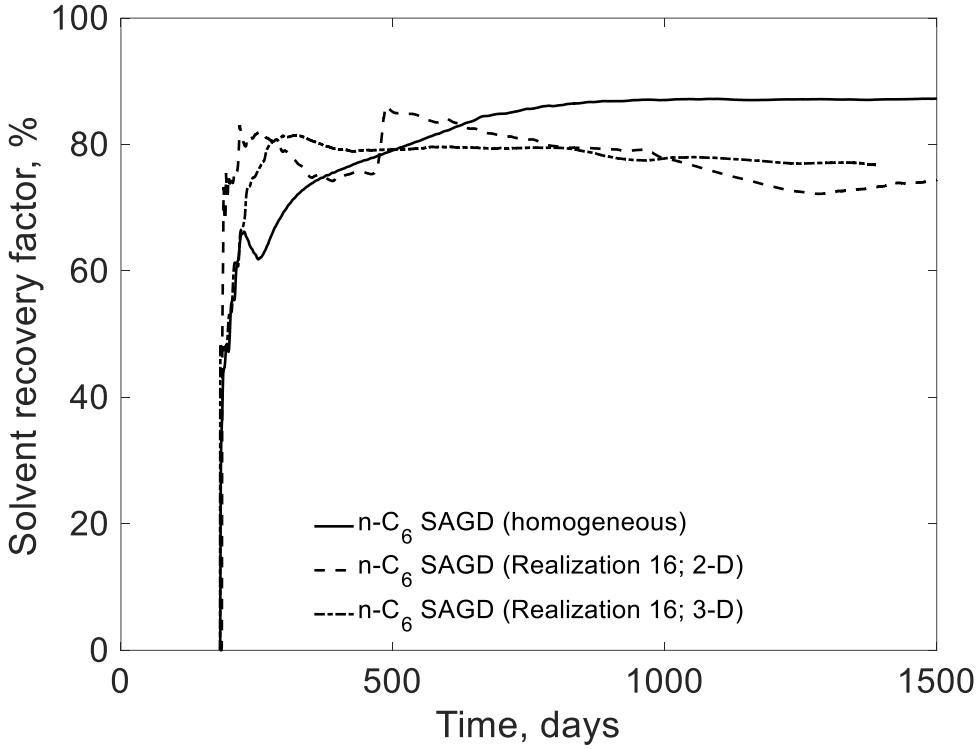

(c)

Figure H-3. Solvent accumulation and solvent recovery factor as a function of cumulative bitumen production, and solvent recovery factor history in n-C_6 SAGD for the homogeneous and heterogeneous cases. Solvent accumulation is calculated on the basis of the solvent injection and production histories at stock-tank conditions. Solvent recovery factor is defined as the ratio of the cumulative solvent production to the cumulative solvent injection at stock-tank conditions.

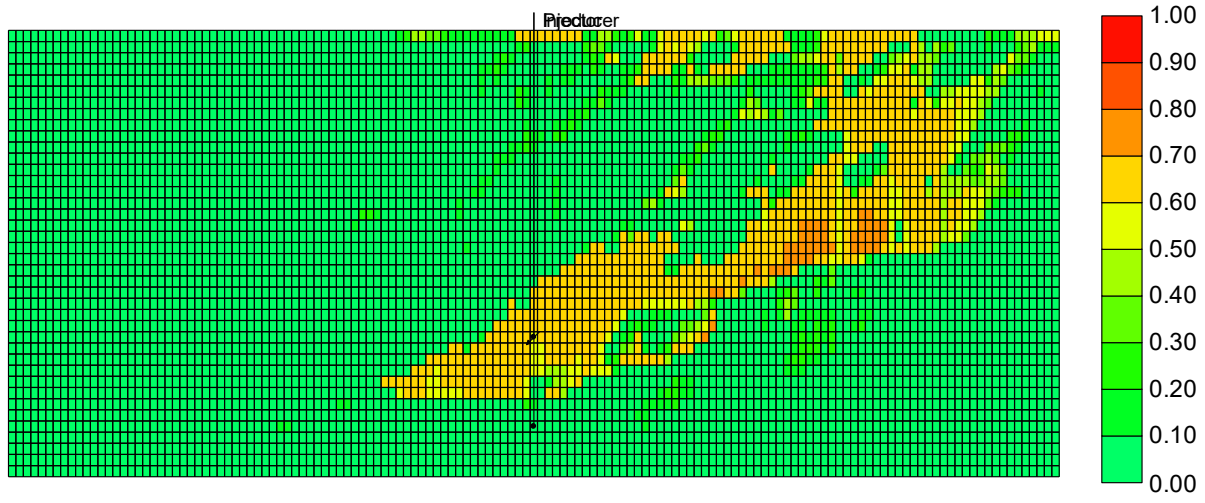

(a) x-z cross-sectional map for vapor-phase saturation at y = 1

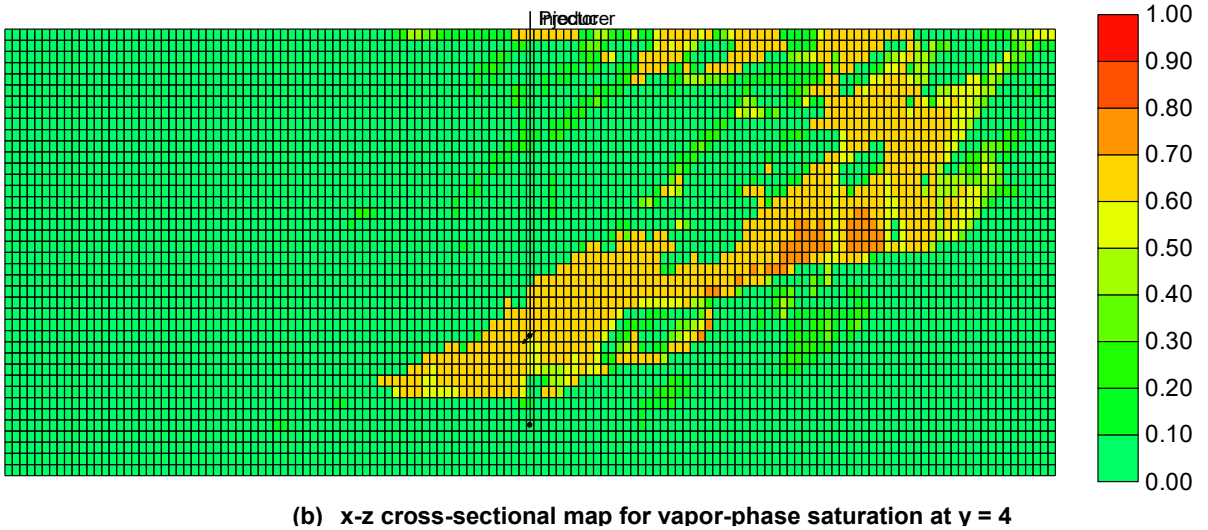

(b) x-z cross-sectional map for vapor-phase saturation at y = 4

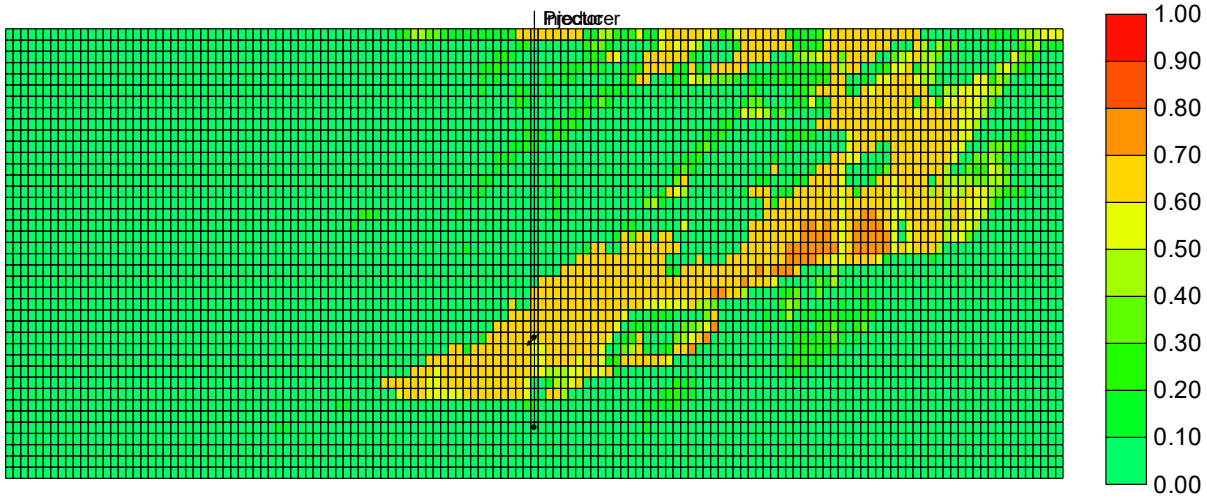

(c) x-z cross-sectional map for vapor-phase saturation at y = 7

Figure H-4. Simulated x-z cross-sectional maps for vapor-phase saturation in SAGD for the 2-D heterogeneous case for the cumulative bitumen production of approximately 55330 m^3. There are ten x-z cross-sections along the y-coordinate; y = j corresponds to the j^{th} cross-section.

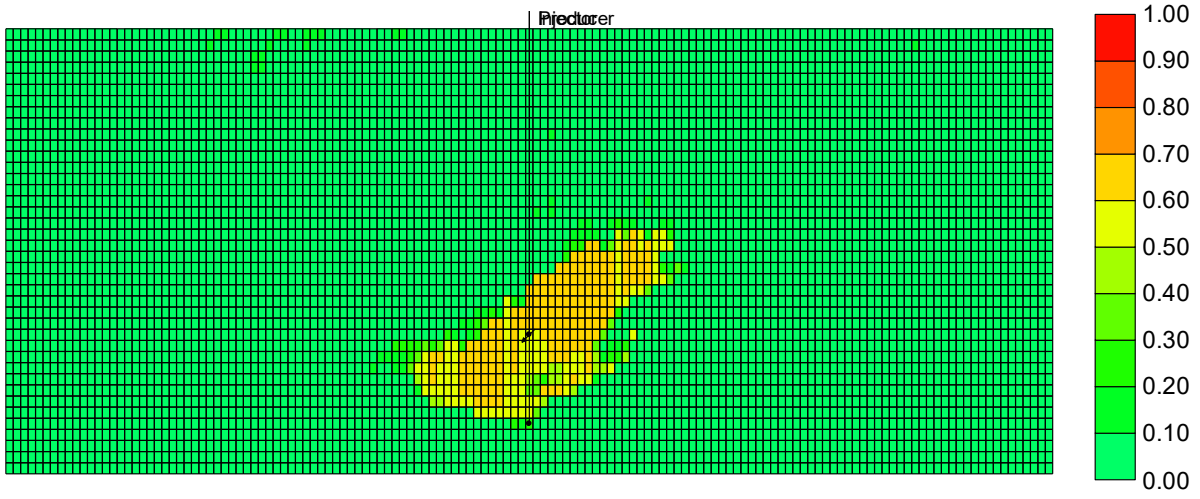

(a) x-z cross-sectional map for vapor-phase saturation at y = 1

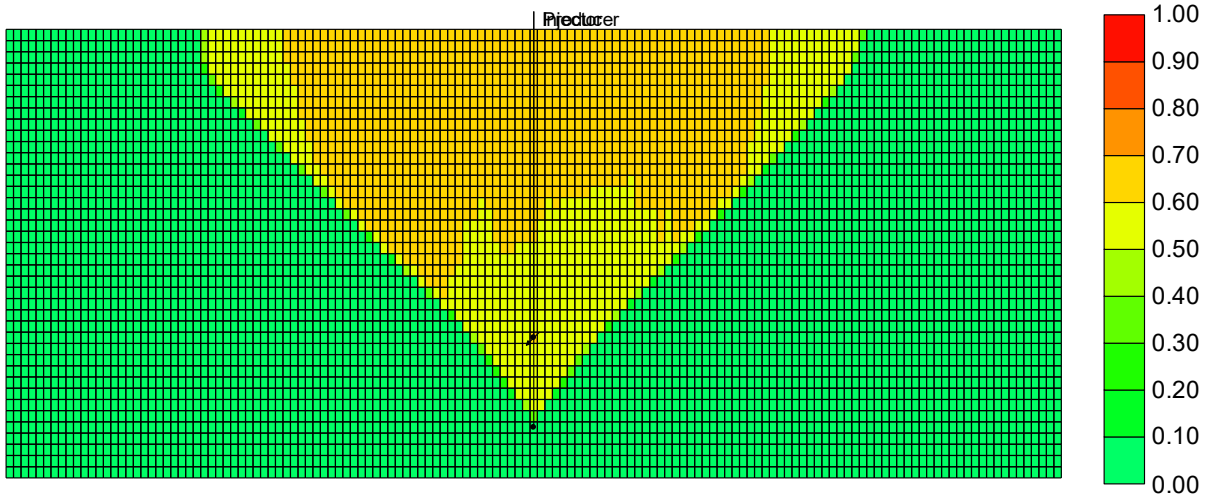

(b) x-z cross-sectional map for vapor-phase saturation at y = 4

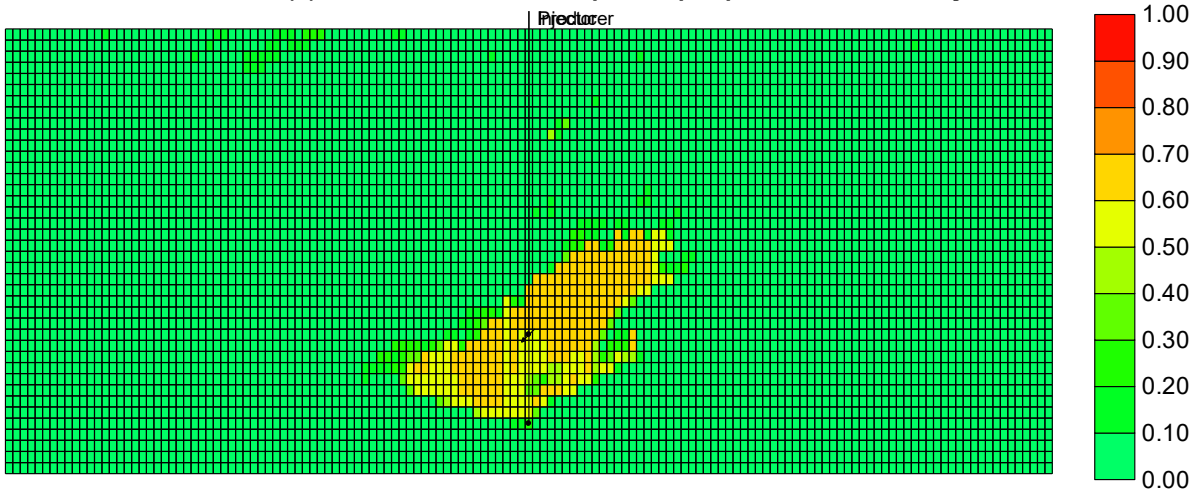

(c) x-z cross-sectional map for vapor-phase saturation at y = 7

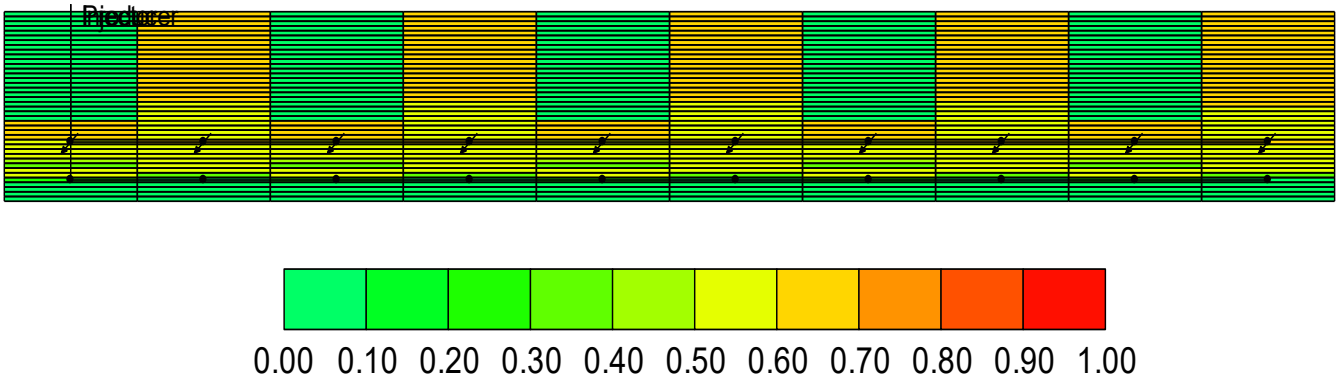

(d) y-z cross-sectional map for vapor-phase saturation at x = 71

Figure H-5. Simulated x-z and y-z cross-sectional maps for vapor-phase saturation in SAGD for the 3-D heterogeneous case for the cumulative bitumen production of approximately 55330 m^3. There are ten x-z cross-sections along the y-coordinate; y = j corresponds to the j^{th} cross-section. There are 141 y-z cross-sections along the x-coordinate; x = k corresponds to the k^{th} cross-section. The well-pairs are located at the 71^{st} cross-section in the x-coordinate (i.e., 71^{st} grid column in the x-z plane).

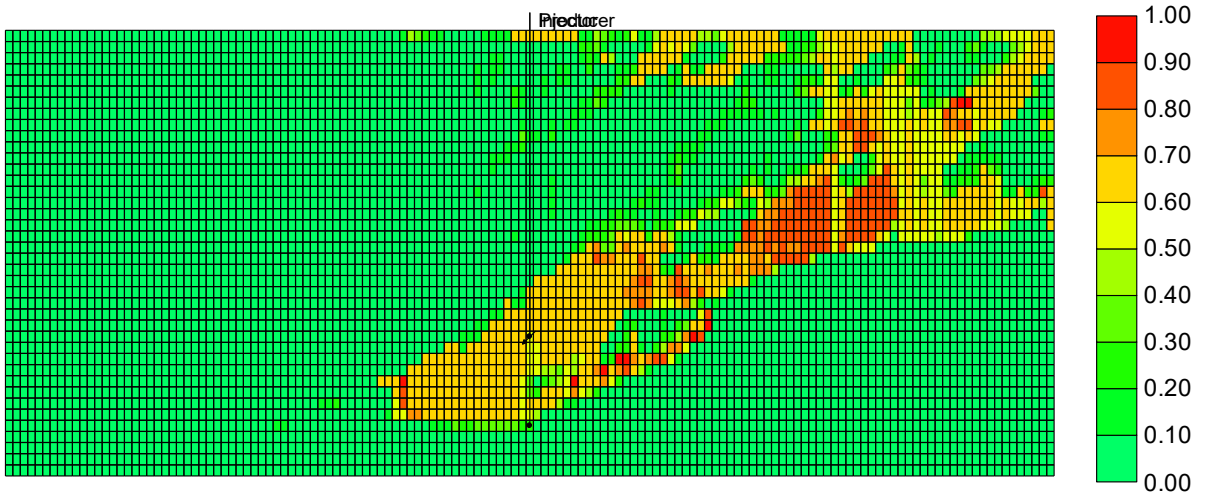

(a) x-z cross-sectional map for vapor-phase saturation at y = 1

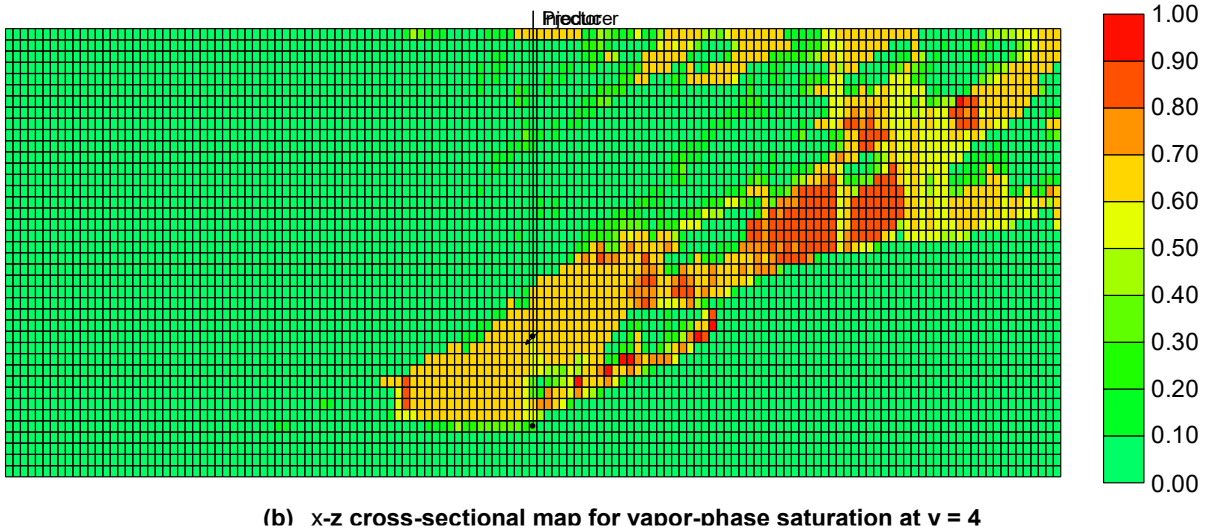

(b) x-z cross-sectional map for vapor-phase saturation at y = 4

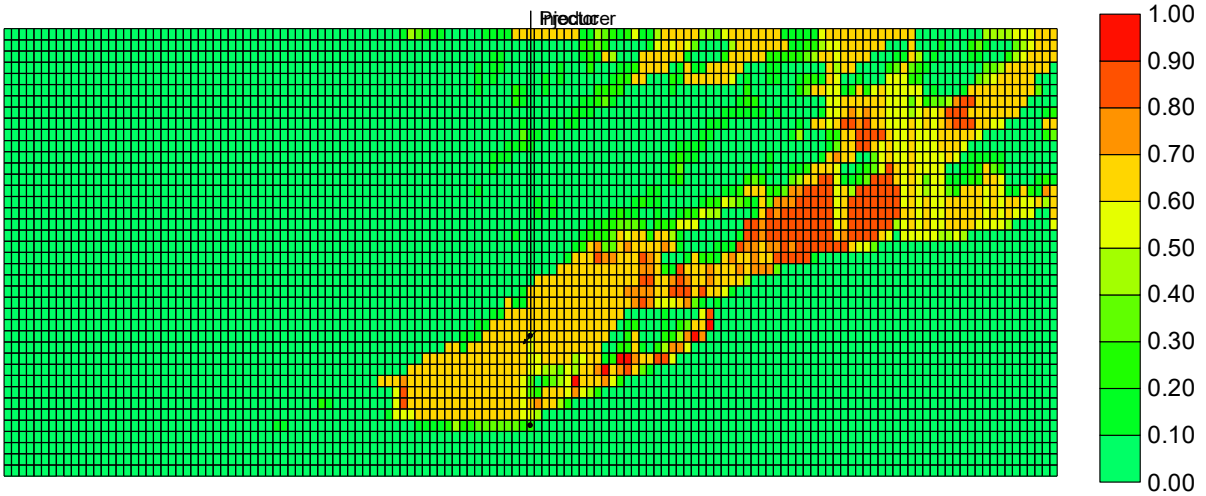

(c) x-z cross-sectional map for vapor-phase saturation at y = 7

Figure H-6. Simulated x-z cross-sectional maps for vapor-phase saturation in n-C_6 SAGD for the 2-D heterogeneous case for the cumulative bitumen production of approximately 83932 m^3. cross-sections along the y-coordinate; y = j corresponds to the j^{th} cross-section.

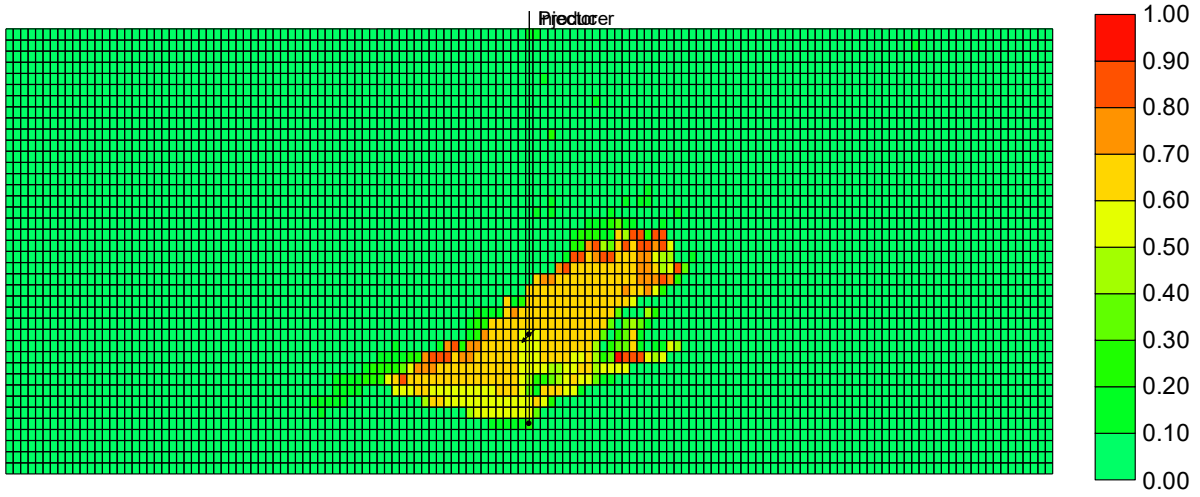

(a) x-z cross-sectional map for vapor-phase saturation at y = 1

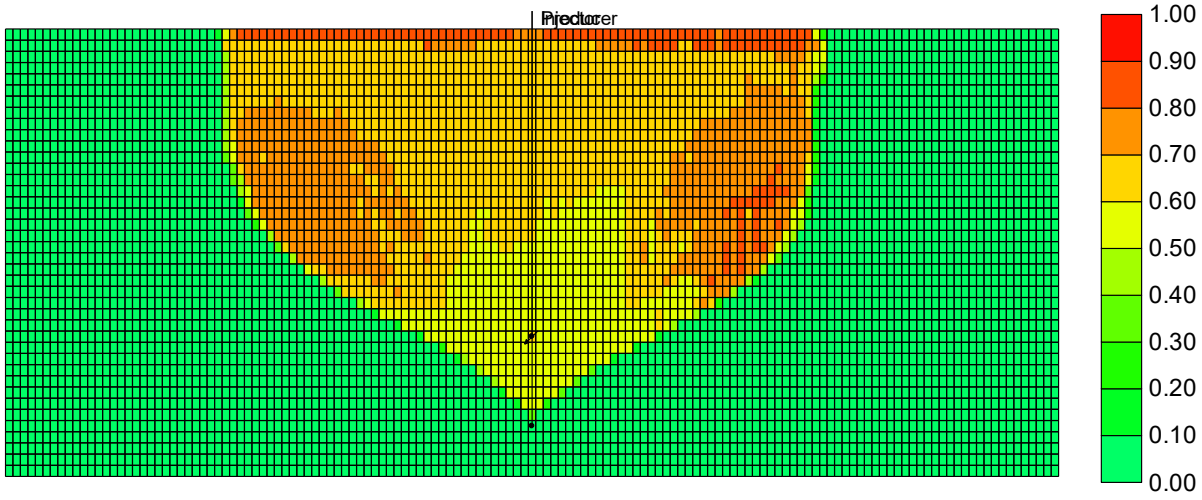

(b) x-z cross-sectional map for vapor-phase saturation at y = 4

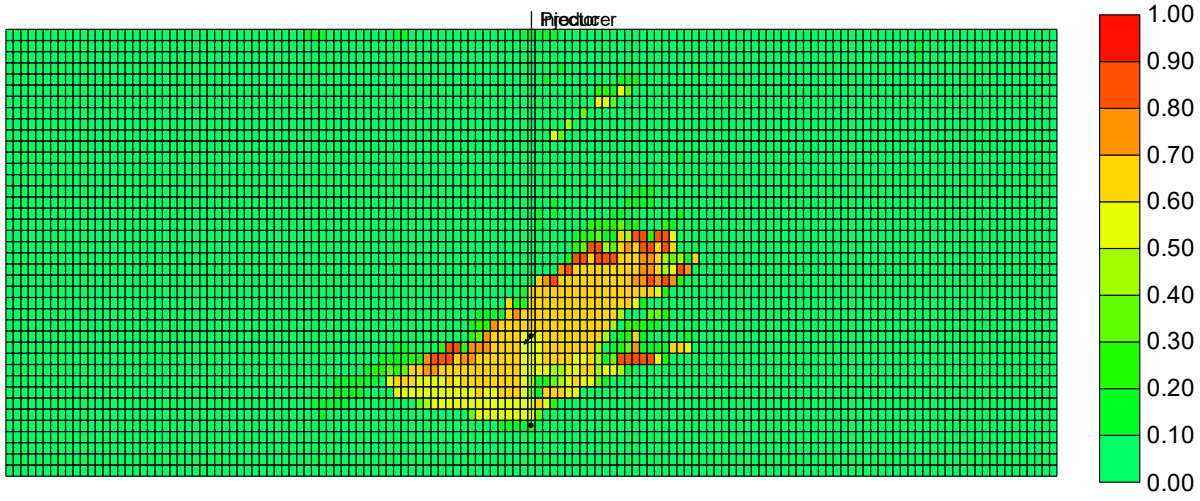

(c) x-z cross-sectional map for vapor-phase saturation at y = 1

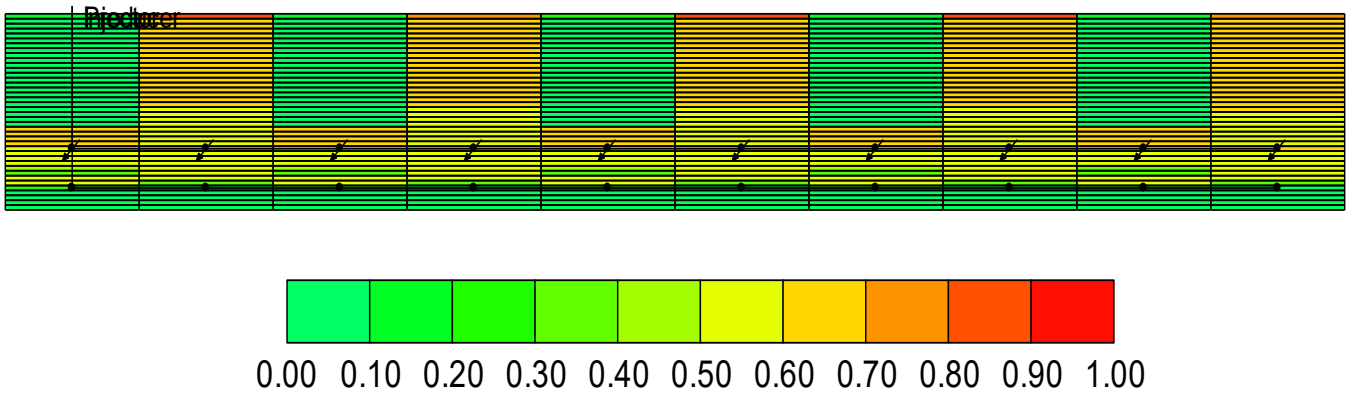

(d) y-z cross-sectional map for vapor-phase saturation at x = 71.

Figure H-7. Simulated x-z and y-z cross-sectional maps for vapor-phase saturation in n-C_6 SAGD for the 3-D heterogeneous case for the cumulative bitumen production of approximately 83932 m^3. There are ten x-z cross-sections along the y-coordinate; y = j corresponds to the j^{th} cross-section. There are 141 y-z cross-sections along the x-coordinate; x = k corresponds to the k^{th} cross-section. The well-pairs are located at the 71^{st} cross-section in the x-coordinate (i.e., 71^{st} grid column in the x-z plane).

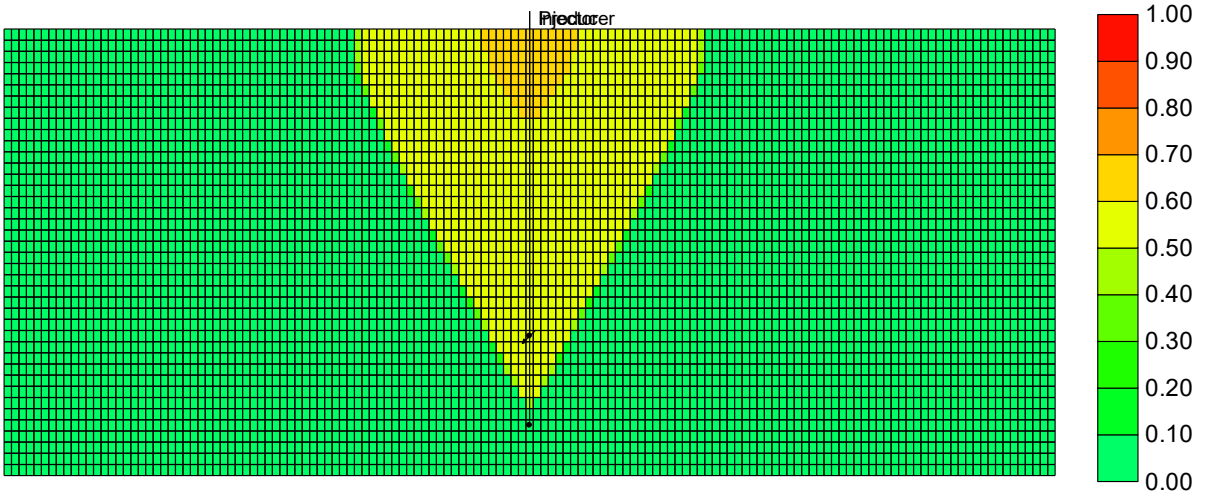

Figure H-8. Simulated x-z cross-sectional map for vapor-phase saturation in SAGD for the homogeneous case (3-D discretized) for the cumulative bitumen production of approximately 53330 m^3.

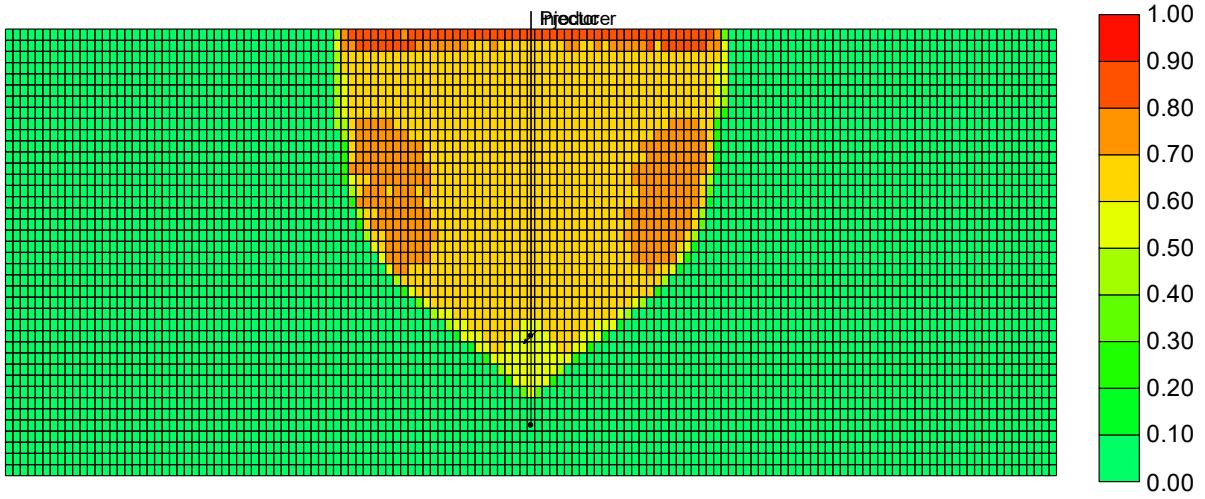

Figure H-9. Simulated x-z cross-sectional map for vapor-phase saturation in n-C_6 SAGD for the homogeneous case for the cumulative bitumen production of approximately 83932 m^3.

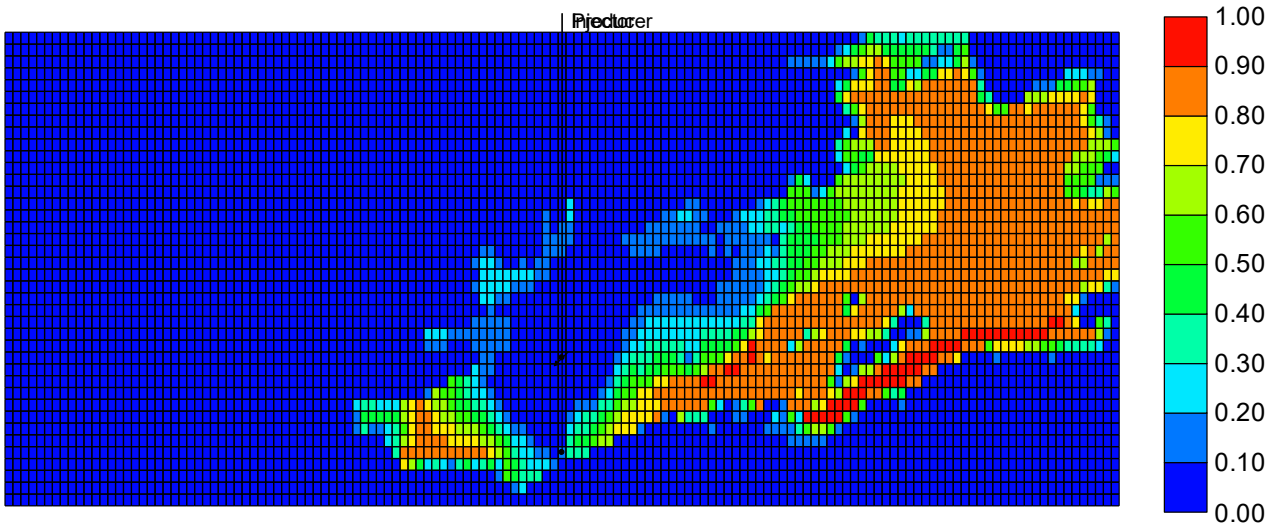

Figure H-10. Simulated x-z cross-sectional map for x_{sL} in n-C_6 SAGD for the 2-D heterogeneous case for the cumulative bitumen production of approximately 83932 m^3.

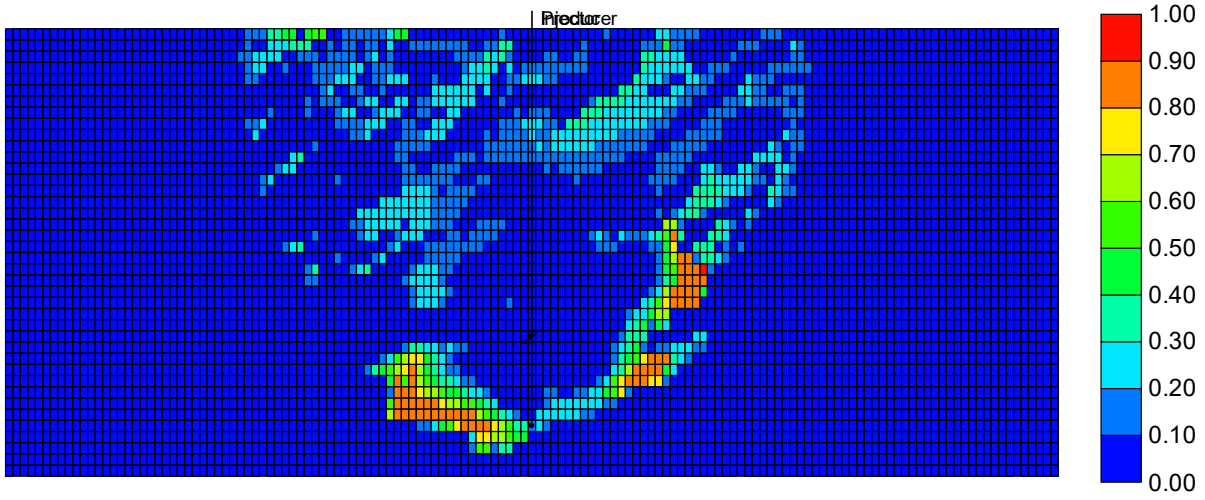

(a) x-z cross-sectional map for x_{sL} at y = 1

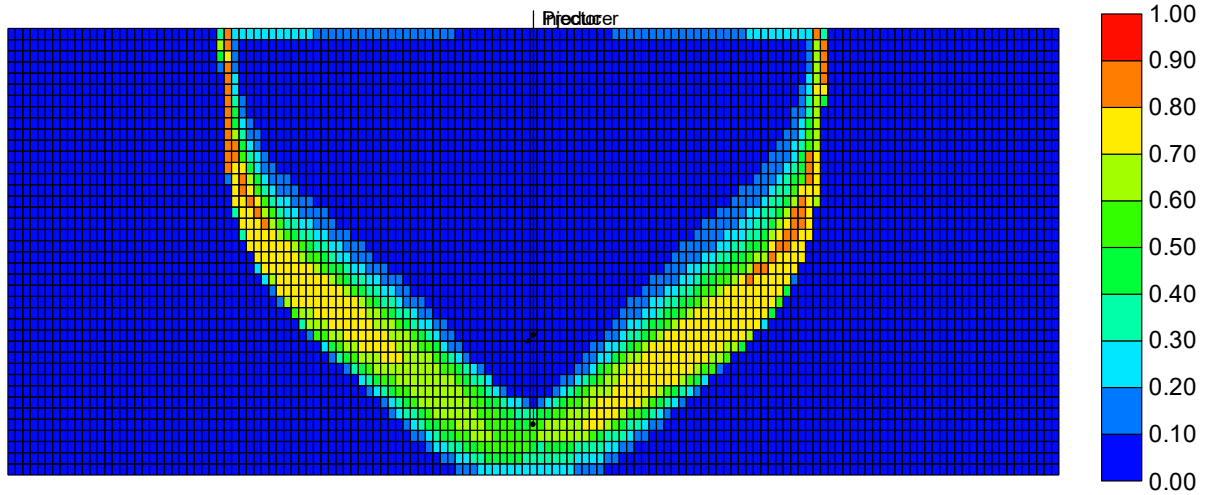

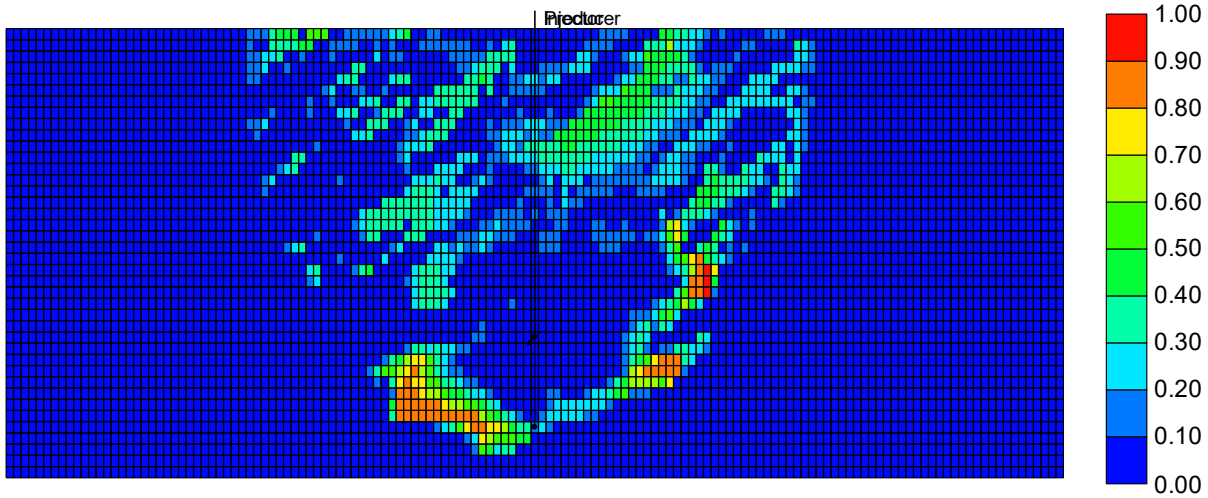

(c) x-z cross-sectional map for x_{sL} at y = 7

Figure H-11. Simulated x-z and y-z cross-sectional maps for x_{sL} in n-C_6 SAGD for the 3-D heterogeneous case for the cumulative bitumen production of approximately 83932 m^3. There are ten x-z cross-sections along the y-coordinate; y = j corresponds to the j^{th} cross-section.

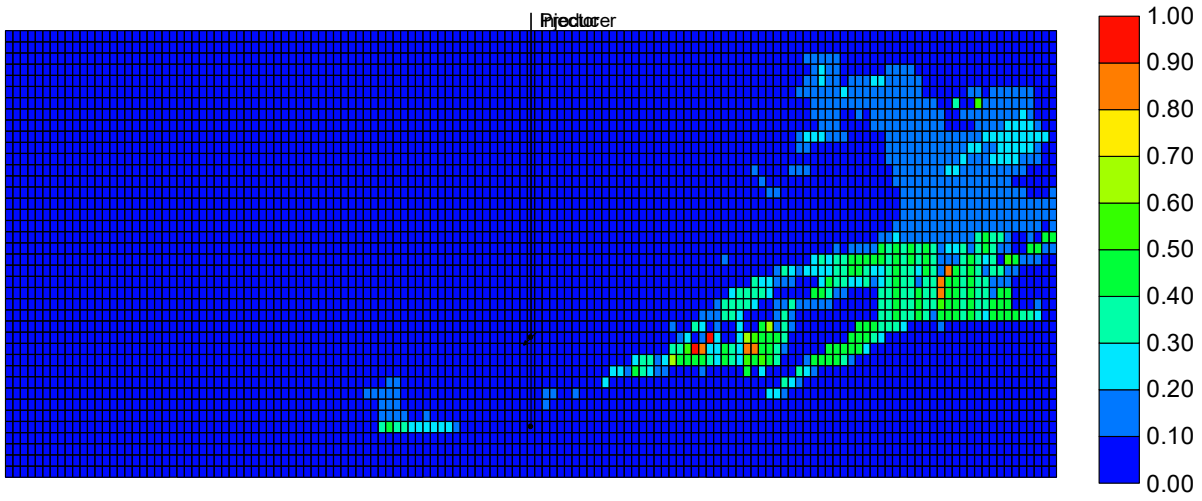

Figure H-12. Simulated x-z cross-sectional map for $\beta_L x_{sL}$ in n-C_6 SAGD for the 2-D heterogeneous case for the cumulative bitumen production of approximately 83932 m^3.

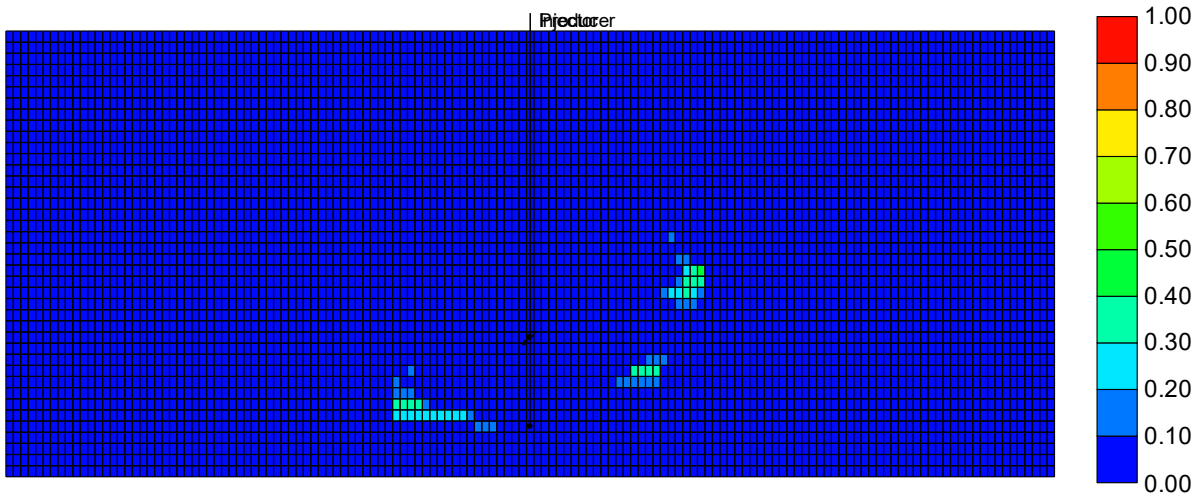

(a) x-z cross-sectional map for $\beta_{LX_{sL}}$ at y = 1

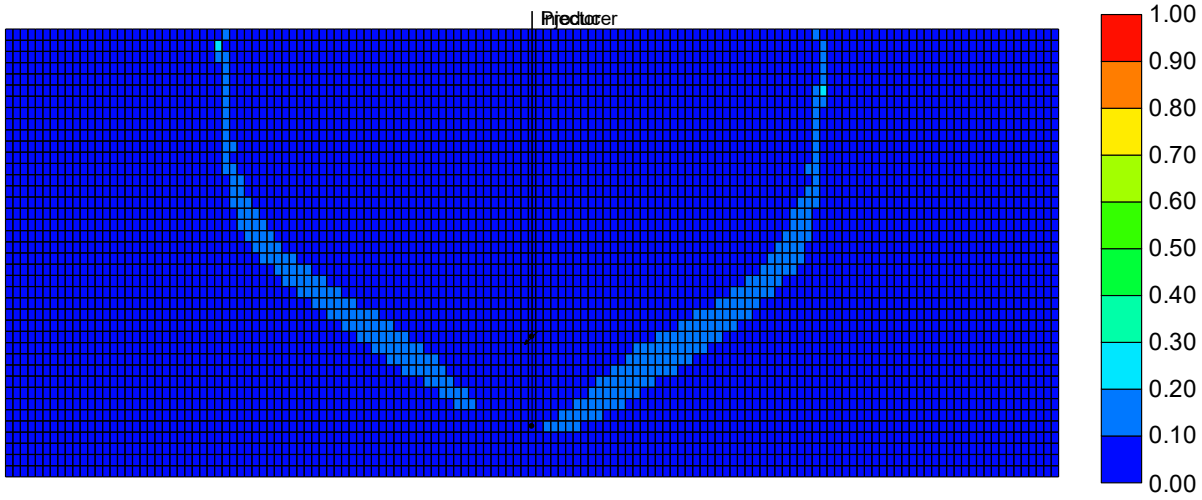

(b) x-z cross-sectional map for $\beta_{LX_{sL}}$ at y = 4

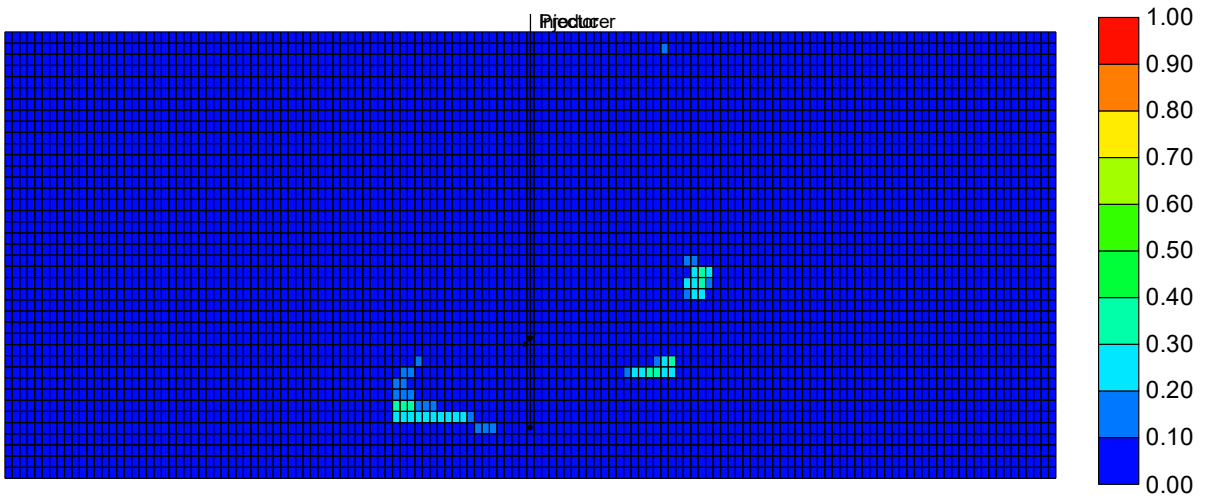

(c) x-z cross-sectional map for $\beta_{Lx_{sL}}$ at y = 7

Figure H-13. Simulated x-z and y-z cross-sectional maps for $\beta_{Lx_{sL}}$ in n-C_6 SAGD for the 3-D heterogeneous case for the cumulative bitumen production of approximately 83932 m^3. There are ten x-z cross-sections along the y-coordinate; y = j corresponds to the j^{th} cross-section.

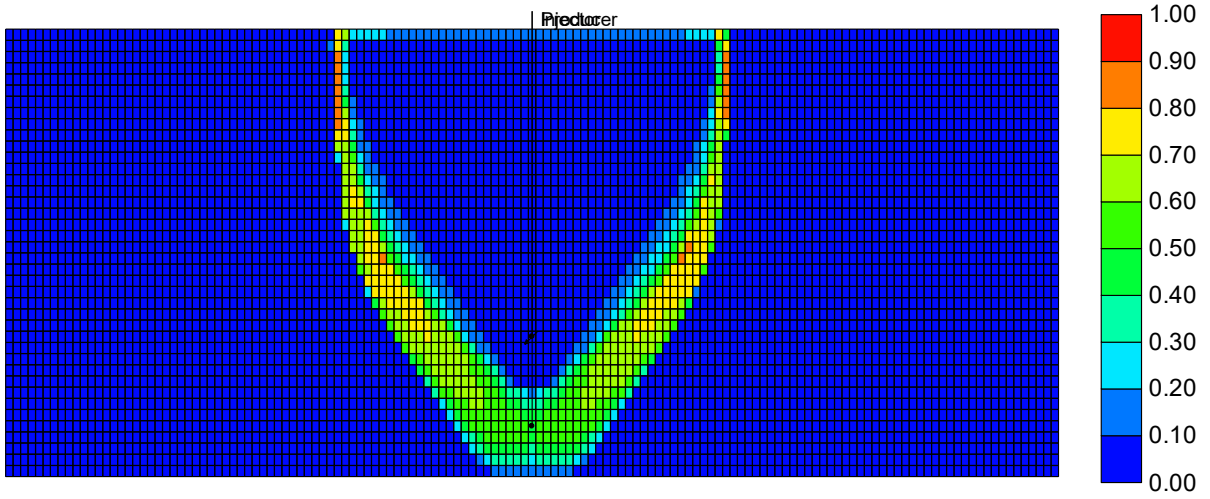

(a)

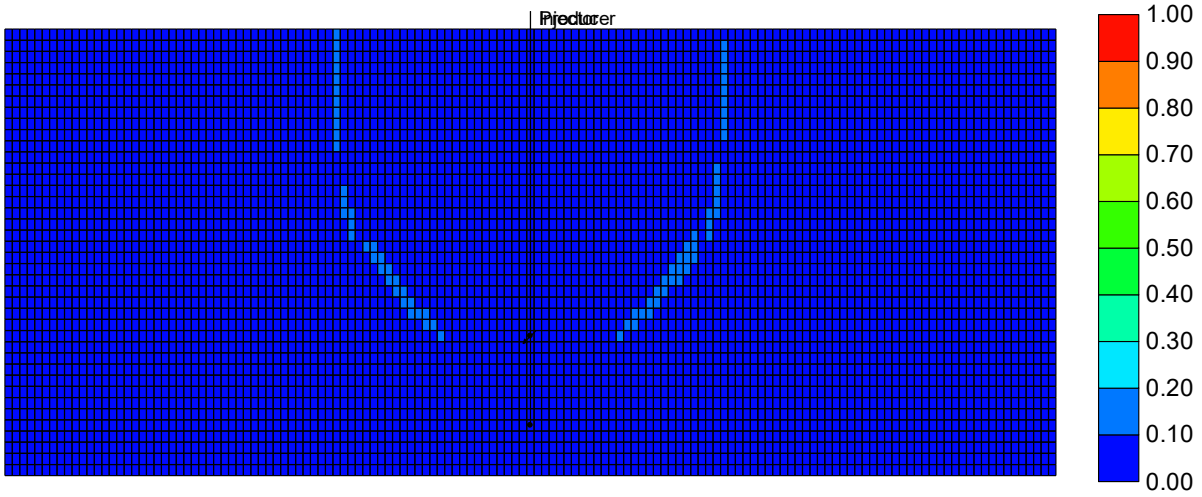

(b)

Figure H-14. Simulated x-z cross-sectional maps for x_{sL} and $\beta_L x_{sL}$ in n-C_6 SAGD for the homogeneous case (3-D discretized) for the cumulative bitumen production of approximately 83932 m^3; (a) x_{sL} map; (ii) $\beta_L x_{sL}$ map.

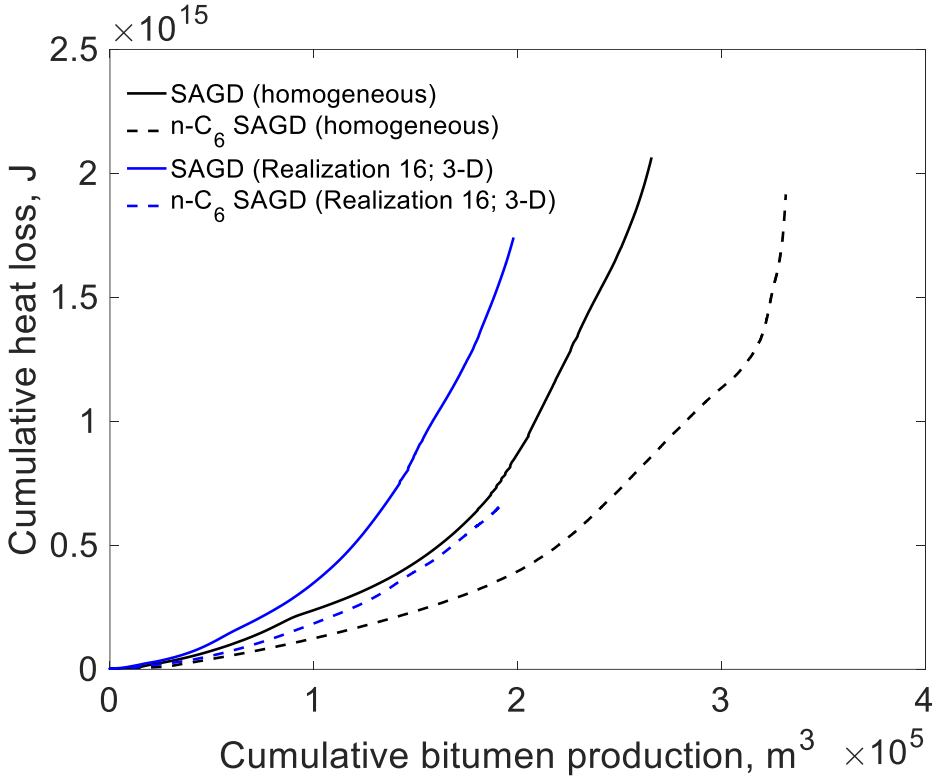

Figure H-15. Cumulative heat loss as a function of cumulative bitumen production for the homogeneous and 3-D heterogeneous cases.

Appendix I. Analytical Model for SAGD for a Homogeneous-Isotropic Reservoir by Shi and Okuno (2017)

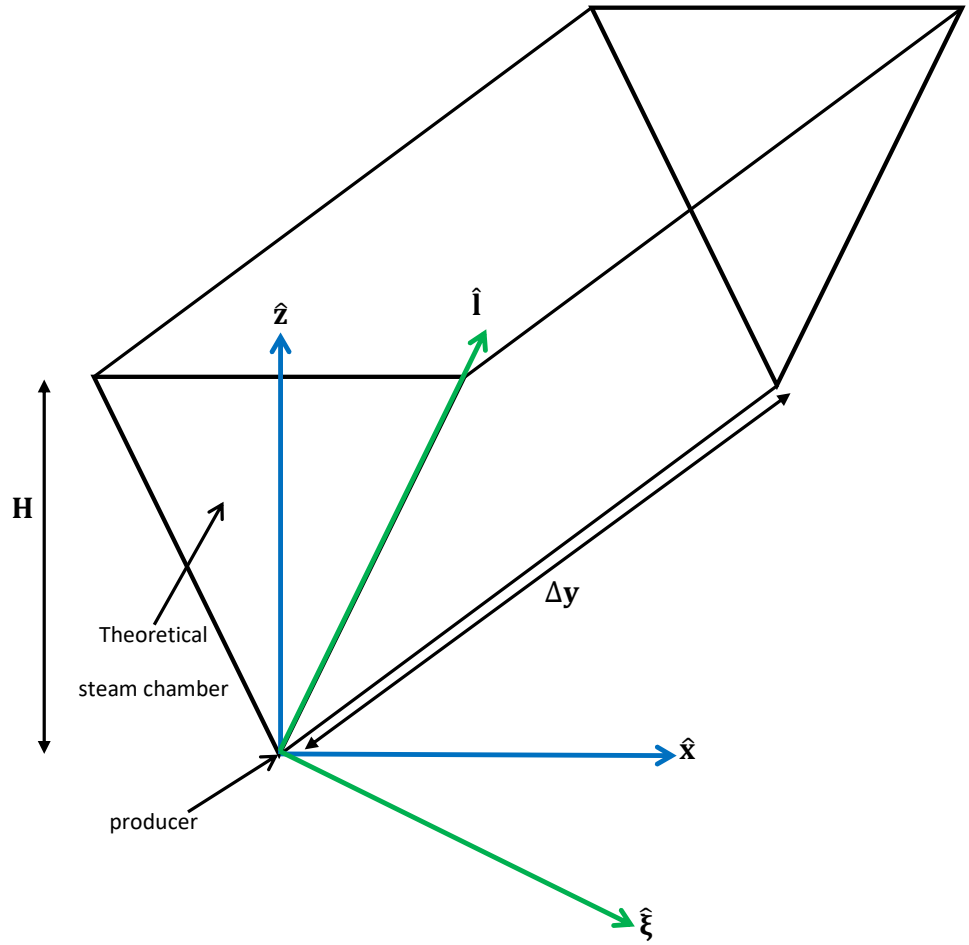

Figure I-1. Schematic of gravity drainage under steam-only injection for a linear interface

This appendix presents the derivation of an analytical expression for the global oil drainage rate in SAGD for a linear interface for one half of a steam chamber. The steam chamber is assumed to be an inverted triangle, with the producer located at the bottom vertex. The derivation is based on the following assumptions:

i. The production well is assumed to be a line-sink to which the chamber edge (interface) is anchored.

ii. The direction of drainage is assumed to be parallel to the chamber edge, which is reasonable away from the producer; this assumption is invalid at and near the producer where velocity field lines on each side of the steam chamber converge.

iii. The oleic phase is incompressible and entirely comprises of oil, and its relative permeability is unity (i.e., single-phase flow). The change in saturation across the interface is equivalent to the difference between the initial oil saturation and the residual oil saturation of the medium.

iv. The gradient of temperature is assumed to occur along a coordinate ($\hat{\xi}$) that is orthogonal to the chamber edge, while the direction of fluid flow is assumed to occur strictly in the direction of the chamber edge (-$\hat{l}$). Consequently, thermal conduction is the only mode by which heat is transferred beyond the chamber edge, as the convective heat flux is zero under this assumption.

v. The chamber edge is assumed to act as a non-accelerating source for thermal conduction, with heat transfer considered to be under steady state.

vi. Asphaltene precipitation is neglected.

There are two important aspects pertaining to the derivation of the production rate of oil in this model: (i) local and global material balance; and (ii) coupling of Darcy's law for flow with conductive heat transfer beyond the chamber edge.

The local material balance for oil for an element dl along the $\hat{l}$-coordinate and $d\xi$ along the $\hat{\xi}$-coordinate depicted in **Figure I-1** reads as

$$\frac{\partial q_o}{\partial l} = -\varphi \Delta S_o \Delta y U, \tag{I-1}$$

where $U = \frac{d\xi}{dt}$, is the local interface velocity along the $\hat{\xi}$-coordinate. The negative sign in the right-hand side of Equation I-1 reflects that the drainage of oil occurs along the $(-\hat{l})$-coordinate. Equation I-1 can be transformed from the $\hat{l}$-$\hat{\xi}$ basis to the $\hat{x}$-$\hat{z}$ basis using the transformations $\xi = x \sin\theta$ and $z = l \sin\theta$, where θ is the angle subtended by the chamber edge with respect to the horizontal as follows

$$\frac{\partial q_o}{\partial z_D} = -\varphi H \Delta S_o \Delta y v, \tag{I-2}$$

where v is the local interface velocity along the $\hat{x}$-coordinate, H is the vertical distance between the producer and reservoir ceiling, and z_D is the dimensionless distance defined as the vertical distance relative to the producer divided by H. If the interface is assumed to be linear, then the

local interface velocity in the horizontal direction reads as $v = v_{max} z_D$, where v_{max} is the interface velocity at the ceiling of the reservoir model. Using this in Equation I-2, we have

$$\frac{\partial q_o}{\partial z_D} = -\varphi H \Delta S_o \Delta y v_{max} z_D. \tag{I-3}$$

Assumption of the drainage to be strictly along $(-\hat{I})$-coordinate, single-phase flow and vapor-phase density to negligible to oil density results in the following expression for the local Darcy velocity $(\overrightarrow{U_o})$ at a location ξ relative to the chamber edge at z_D,

$$\overrightarrow{U_o}(\xi, z_D) = \left[\frac{kg \sin\theta \rho_o}{\mu_o}\right] = \left[\frac{kg \sin\theta}{\vartheta_o}\right], \tag{I-4}$$

where ρ_o, μ_o and ϑ_o respectively are the mass density, dynamic and kinematic viscosity of the oleic phase, while k and g represent the absolute permeability, and acceleration due to gravity, respectively. Note that ρ_o, μ_o and ϑ_o are functions of temperature, which in turn is location-dependent.

The average volumetric flow rate over a distance ξ_L from the chamber edge (at elevation z_D from the producer) can be calculated as

$$q_o(z_D) = \xi_L \Delta y \overline{U_o}(z_D) = \left\{\Delta y \int_0^{\xi_L} \left[\frac{kg \sin\theta}{\vartheta_o}\right] d\xi\right\}, \tag{I-5}$$

where $\overline{U_o}(z_D)$ is the average Darcy velocity corresponding to a distance ξ_L from the chamber edge, and is given by $\overline{U_o}(z_D) = \int_0^{\xi_L} U_o d\xi \Big/ \xi_L$. Since the reservoir is homogeneous-isotropic, Equation I-5 can be rewritten as

$$q_o(z_D) = \left[kg \sin\theta \, \Delta y \int_0^{\xi_L} \frac{1}{\vartheta_o} d\xi\right] = [kg \sin\theta \, I_o], \tag{I-6}$$

where $I_o = \int_0^{\xi_L} \frac{1}{\vartheta_o} d\xi$.

Calculation of the integral I_o in Equation I-6 requires knowledge of the temperature distribution beyond the chamber. The mechanism by which heat is transferred beyond the chamber edge is assumed to be due to steady-state 1-D heat conduction, with any given point along the chamber edge considered as a source that moves with a constant velocity. This results in the following equation for the temperature profile along the $\hat{\xi}$-coordinate,

$$T(\xi, z_D) = T_R + (T_{edge} - T_R) \exp\left\{-\xi \frac{U}{\alpha}\right\} = T_R + (T_{edge} - T_R) \exp\left\{-\xi \frac{v \sin\theta}{\alpha}\right\}, \tag{I-7}$$

where T_{edge} and T_R respectively are the chamber-edge and initial reservoir temperatures, while α is the effective thermal diffusivity. I_o can be rewritten using Equation I-7 as

$$I_o = \frac{1}{U}\int_{T_L}^{T_{edge}(z_D)} \frac{\alpha}{\vartheta_o}\frac{dT}{(T-T_R)}. \quad \text{(I-8)}$$

Multiplying Equation I-8 by U results in the dimensionless variable τ, which is a function of of elevation that reads as

$$\tau(z_D) = UI_o = \int_{T_L}^{T_{edge}(z_D)} \frac{\alpha}{\vartheta_o}\frac{dT}{(T-T_R)}. \quad \text{(I-9)}$$

Using Equation I-9 in Equation I-6,

$$q_o(z_D) = \frac{kg\sin\theta\tau\Delta y}{U} = \frac{kg\tau\Delta y}{v}. \quad \text{(I-10)}$$

Equation I-2 can be integrated as

$$\int_1^{z_D} dq_o = -\varphi H\Delta S_o \Delta y v_{max}\int_1^{z_D} z_D dz_D \quad \text{(I-11)}$$

which yields

$$q_o(z_D) = q_o(z_D = 1) + 0.5\varphi H\Delta S_o \Delta y v_{max}(1 - z_D^2). \quad \text{(I-12)}$$

The value of $q_o(z_D = 1)$ is zero as there is no oil draining into the reservoir ceiling. The term $[0.5\varphi H\Delta S_o\Delta y]v_{max}(\hat{x})$ is equivalent to the production rate ($q_{oil\text{-}prod}$) rate of oil for one-half of the steam chamber [based on Reis (1992)] for a linear interface; this is the global material balance. Hence, the local drainage rate at elevation z_D relative to the producer is related to the production rate as

$$q_o(z_D) = q_{oil-prod}(1 - z_D^2) \quad \text{(I-13)}$$

Equation I-13 is a key novelty in the analytical theory of Shi and Okuno (2017). Now, the right-hand side of Equation I-10 can be rewritten using the global material balance for a linear interface as follows

$$q_o(z_D) = \frac{kg\tau\Delta y}{v} = \frac{kg\tau\Delta y}{z_D}\left(\frac{1}{v_{max}}\right) = \frac{kg\tau\Delta y}{z_D}\left(\frac{0.5\varphi H\Delta S_o\Delta y}{q_{oil-prod}}\right) \quad \text{(I-14)}$$

Using Equation I-14 in Equation I-13, the production rate of bitumen can be expressed as follows

$$q_{oil-prod} = \sqrt{kg\varphi H\Delta S_o(\Delta y)^2}\sqrt{\frac{\tau}{2z_D(1-z_D^2)}}. \quad \text{(I-15)}$$

Internal consistency requires the fulfilment of the following criteria: (i) the velocity of the interface at the producer $\left(\text{i.e., } v|_{z_D=0}\right)$ should be zero; (ii) the chamber-edge temperature must vary with elevation relative to the producer (i.e., z_D). In this model, the first criterion is fulfilled

because $\left.\frac{\partial q_o}{\partial z_D}\right|_{z_D=0} = 0$. The second criterion is also fulfilled as the variability of temperature along the chamber edge is a starting premise of this analytical model.

Appendix J. Calculation of τ, U and I_o for Homogeneous-Anisotropic and Heterogeneous Realizations

This appendix presents a step-wise procedure for the calculation of τ, U and I_o for the homogeneous-isotropic analogs of homogeneous-anisotropic and heterogenous realizations on the basis of the simulated production histories for SAGD. We begin with the procedure for the homogeneous-anisotropic case.

Step-wise procedure for the homogeneous case

1. For a given cumulative bitumen production, estimate the corresponding instantaneous production rate of bitumen in SAGD $\left[q_{oil-prod}^{hom}(t_{hom})\right]$ from simulations. Here t_{hom} pertains to the time at which the cumulative bitumen production is met.
2. On the basis of the simulated vapor-phase saturation profile, obtain an estimate for the angle subtended by the chamber edge with respect to the horizontal (θ^{hom}).
3. Calculate the equivalent absolute permeability for gravity drainage using the following equation (Azom and Srinivasan, 2011)

   $$k^{hom} = k_h \cos^2\theta^{hom} + k_v \sin^2\theta^{hom}, \quad \text{(J-1)}$$

   where k_h and k_v respectively are the horizontal and vertical permeabilities of the clean sand facies.
4. Calculate τ^{hom} for $z_D = 0.5$ from the equation for bitumen production rate (for a full steam chamber),

   $$q_{oil-prod}^{hom}(t_{hom}) = 2\sqrt{\tau^{hom} H^{hom}}\left(\sqrt{k\varphi\Delta S_o}\right)^{hom}\sqrt{\frac{g}{[2z_D(1-z_D^2)]}}\Delta y, \quad \text{(J-2)}$$

   where φ^{hom} is the porosity of the clean sand facies, $\Delta S_o{}^{hom}$ is the difference between the initial oleic-phase saturation and residual oleic-phase saturation of the medium, Δy is the well-pair length .
5. Estimate the interface velocity U^{hom} from the global material balance equation,

   $$U^{hom}(z_D) = \sin\theta^{hom}\, z_D \left\{\frac{q_{oil-prod}^{hom}(t_{hom})}{H^{hom}(\varphi\Delta S_o)^{hom}\Delta y}\right\} \quad \text{(J-3)}$$

6. Calculate $I_o{}^{hom}$ using the equation

   $$I_o{}^{hom} = \frac{\tau^{hom}}{U^{hom}}. \quad \text{(J-4)}$$

Step-wise procedure for heterogeneous cases

1. As with the homogeneous case, estimate the instantaneous bitumen production rate for a given heterogeneous realization and cumulative bitumen production $q_{oil-prod}^{het}(t_{het})$ from simulations.
2. Obtain an estimate for the chamber-edge angle for the homogeneous-isotropic analog of the heterogeneous realization (θ^{het}) using the following method. Within the steam chamber, the concentration of methane in the vapor phase (x_{C1V}) is expected to be small (< 10 mol%). The area of the steam chamber for the heterogeneous case in the x-z plane (A) can be calculated on the basis of the simulated vapor-phase saturation and x_{C1V} concentration maps by setting an upper bound for x_{C1V} (e.g., 10 mol%), and then counting the grid blocks that satisfy this criterion. Subsequently, based on the schematic given in Figure I-1 (see Appendix I), the chamber-edge angle can be estimated using the following equations

   $$W = {}^{A}/_{H}, \tag{J-5}$$

   where A is the area of the steam chamber for the heterogeneous case in the x-z plane, W is the width of the steam chamber at the ceiling of the reservoir, and H is the vertical distance between the producer and the reservoir ceiling, and

   $$\theta^{het} = \cot^{-1}\left(\frac{W/2}{H}\right) \tag{J-6}$$

3. Obtain an estimate for the ratio $\frac{\tau^{het}}{\tau^{hom}}$ using the approximation,

   $$\frac{\tau^{het}}{\tau^{hom}} \cong \left[\frac{q_{oil-prod}^{het}(t_{het})}{q_{oil-prod}^{hom}(t_{hom})}\right]^2 \frac{H^{hom}(t_{hom})}{H^{het}(t_{het})}, \tag{J-7}$$

   and then calculate the value of τ^{het} using the pertinent value from τ^{hom} estimated using the procedure given above.

4. Calculate U^{het} from the global material balance equation.
5. Calculate ${I_o}^{het}$ using $${I_o}^{het} = \frac{\tau^{het}}{U^{het}} \tag{J-8}$$

Appendix K. Maps for Heterogeneous Realizations with Inclined Mudstone Barriers

This appendix presents simulated maps for several attributes pertaining to the performance of SAGD and n-C_6 SAGD in heterogeneous realizations considered in section 3.2.2 of Chapter 3 (and also Chapter 4). The operating pressure of 35 bars is used in the simulations; the injection concentration of solvent in n-C_6 SAGD is set to 2 mol%. The following maps are presented for each realization:

i. Cumulative bitumen production histories for SAGD and n-C_6 SAGD
ii. Cumulative SOR as a function of cumulative bitumen production in SAGD and n-C_6 SAGD
iii. 2-D maps for vapor-, oleic-, and aqueous-phase saturations, molar flow rate of bitumen, and temperature for SAGD for a pertinent cumulative bitumen production
iv. 2-D maps for vapor-, oleic-, and aqueous-phase saturations, molar flow rate of bitumen, temperature, and $\beta_L x_{sL}$ for n-C_6 SAGD at approximately the same cumulative bitumen production considered in (iii).
v. Maps for τ, U and I_o in SAGD as a function of cumulative bitumen production.

The choice of cumulative bitumen production for items (iii) and (iv) requires consideration of a few aspects. This research aims to examine if the significance of steam-solvent coinjection in terms of the reduction of the steam-oil ratio for a given cumulative bitumen production is pronounced for highly heterogeneous reservoirs compared to those that are relatively homogeneous. The analyses presented in Chapters 3 and 4 indicate this to be the case due to increased solvent-retention in-situ, which is accompanied by greater dissolution of solvent in the oleic phase over a larger reservoir volume near the chamber edge. The accumulation of solvent under a given injection strategy is also time-sensitive. So, to identify conditions of heterogeneous fluid flow conducive to significant improvement of local bitumen flow near the chamber edge under heterogeneity, the cumulative bitumen production chosen for the analysis of property distributions must be large enough so that the discrepancy between the homogeneous and heterogeneous cases in terms of the benefit of coinjection is apparent.

The cumulative bitumen production under consideration must also be small enough considering that coinjection will realistically be performed for a limited duration in the

production phase following the establishment of communication between the injection and production wells. This is because of challenges associated with the recovery of solvent under significantly large steam-chamber volumes.

Based on these, the 2-D maps presented in this appendix corresponding to the cumulative bitumen production of approximately 31218 m^3; this represents nearly 10% of the potentially recoverable live-bitumen volume at initial conditions. The porosity and initial oleic-phase saturation assigned to the clean sand facies of the simulated heterogeneous realizations in case study 3.2.2. of Chapter 3 at initial conditions are 0.36 and 0.85, respectively. The dimensions of the reservoir model are 141 m × 500 m × 20 m, with the global proportion of clean sand facies set to 75% for geostatistical modeling. Based on this, the approximate initial live-bitumen volume is 323595 m^3.

Table K-1 gives the range of SORs and times taken to meet the aforementioned cumulative bitumen production for each process across different realizations. There are 29 heterogeneous realizations that meet this cumulative bitumen production; these realizations are listed in Table K-1 in decreasing order of the simulated reduction in SOR due to coinjection of n-C_6. The pertinent values for the performance parameters for the cumulative bitumen production of 98458 m^3 can be found in Table 3.9 (Chapter 3). **Figures K-1 through K-29** present property maps for the realizations listed in Table K-1.

Table K-1. Summary of performance of parameters in SAGD and n-C_6 SAGD for the cumulative bitumen production (Q) of 31218 m^3. The homogeneous case is labelled realization 0. The mudstone barriers in the heterogeneous realizations are inclined (see Chapter 3). Δt_D is the normalized margin by which the time taken to meet a given cumulative bitumen production is reduced by steam-solvent coinjection for a specified reservoir, and is given by $\Delta t_D = \frac{t^{het}_{SAGD}(Q) - t^{het}_{ES-SAGD}(Q)}{t^{hom}_{SAGD}(Q) - t^{hom}_{ES-SAGD}(Q)}$.

Realization	Time, days (SAGD)	Time, days (n-C_6 SAGD)	SOR (SAGD)	SOR (n-C_6 SAGD)	$\Delta_{sol}SOR$	Δt_D
34	3040.25	1146.24	15.06	7.29	7.76	67.84
19	2095.43	904.06	14.98	8.02	6.97	42.67
16	1054.12	565.70	11.15	6.78	4.37	17.49
37	655.16	378.51	7.52	4.27	3.25	9.91
12	670.88	406.79	7.10	4.15	2.95	9.46
36	748.47	555.20	7.23	4.33	2.90	6.92
17	549.18	355.98	6.20	3.43	2.78	6.92
14	1182.07	1230.55	7.32	4.73	2.59	-1.74
33	648.39	414.31	6.58	4.10	2.48	8.38
7	507.57	347.59	6.07	3.60	2.47	5.73
48	799.37	501.52	7.25	4.86	2.39	10.67
4	683.56	426.81	6.41	4.14	2.27	9.20
13	591.15	382.82	6.04	3.78	2.26	7.46
23	480.49	340.93	5.46	3.32	2.15	5.00
26	508.85	349.72	5.88	3.77	2.11	5.70
30	596.51	420.78	6.21	4.18	2.03	6.29
24	867.77	602.88	7.77	5.77	2.00	9.49
49	454.41	316.85	4.88	2.88	2.00	4.93
50	678.60	478.78	6.86	4.88	1.98	7.16
18	518.66	359.37	5.66	3.71	1.95	5.71
31	511.23	346.02	5.32	3.55	1.76	5.92
6	470.51	340.49	4.96	3.48	1.48	4.66
32	426.25	315.92	4.74	3.28	1.46	3.95
44	396.30	297.83	4.32	2.92	1.40	3.53
20	528.30	384.23	5.29	3.91	1.38	5.16
28	413.49	317.93	4.11	2.76	1.35	3.42
35	393.46	312.63	4.28	3.17	1.11	2.90
21	364.57	290.00	3.85	2.76	1.09	2.67
15	347.22	280.62	3.84	2.87	0.96	2.39
0	274.00	246.08	2.99	2.13	0.86	1.00

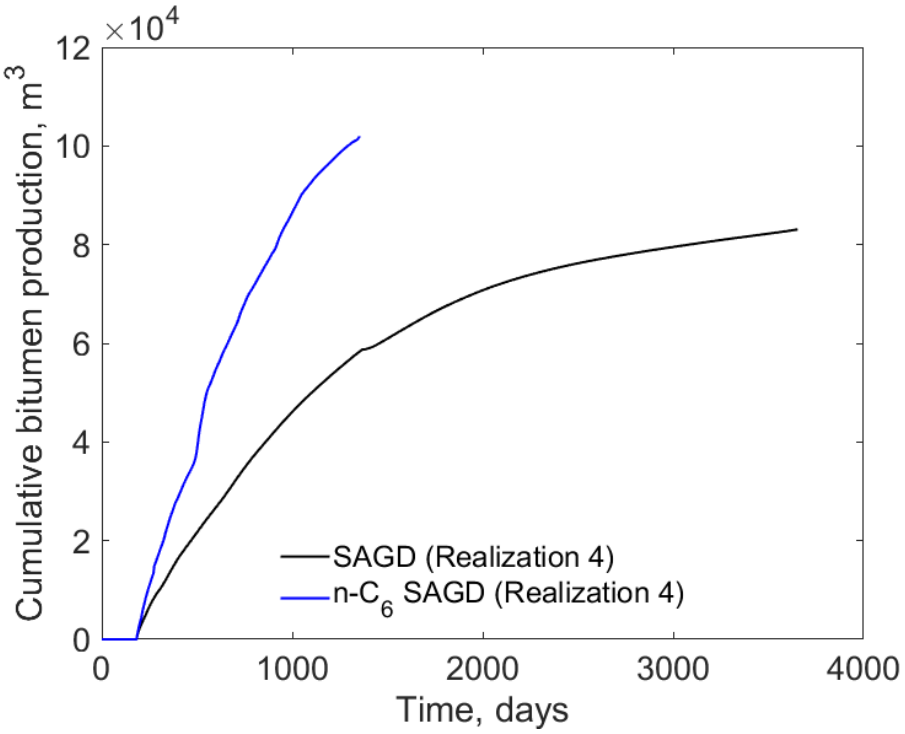

Figure K-1(a). Cumulative bitumen production histories for SAGD and n-C_6 SAGD for realization 4

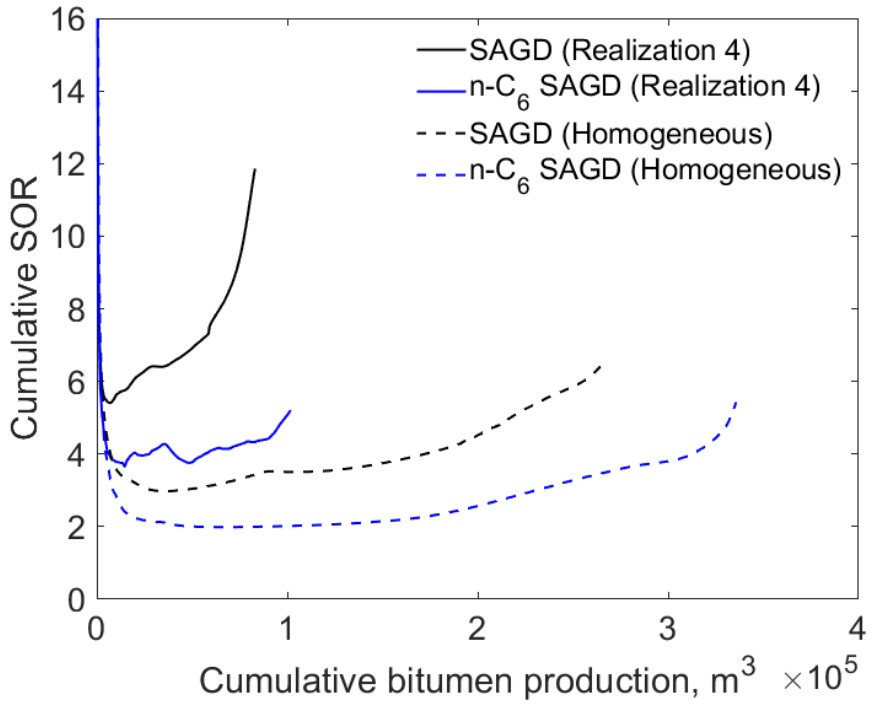

Figure K-1(b). Cumulative SOR for SAGD and n-C_6 SAGD for realization 4

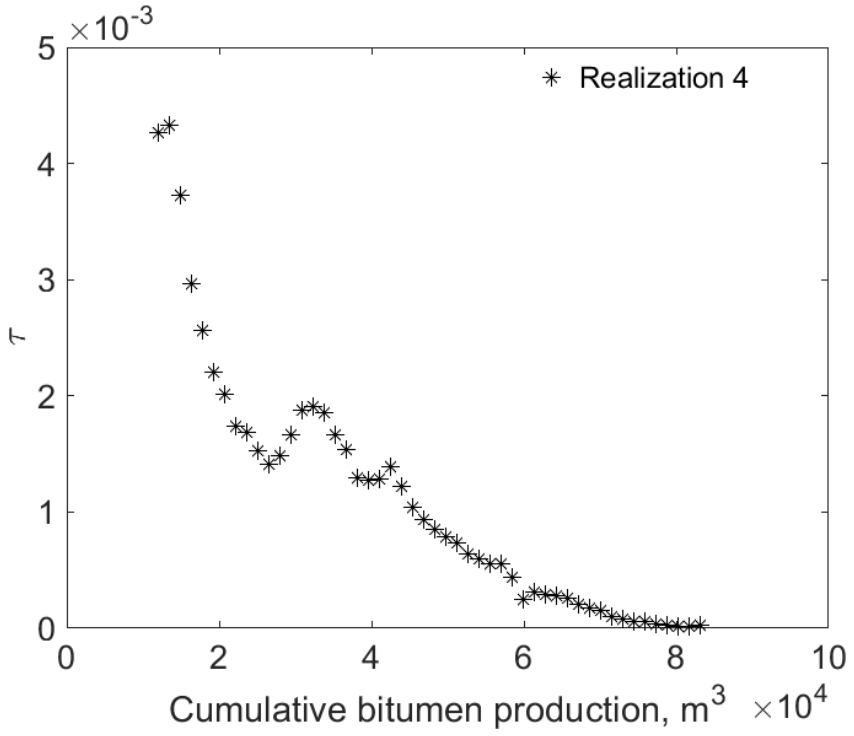

Figure K-1 (c). τ for SAGD as a function of cumulative bitumen production for realization 4

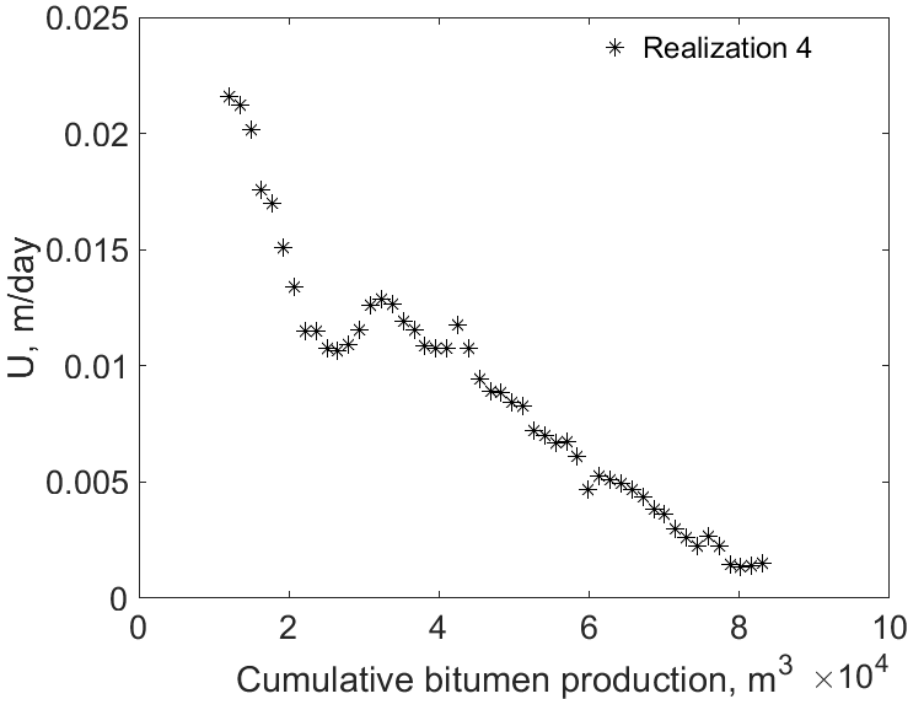

Figure K-1 (d). U for SAGD as a function of cumulative bitumen production for realization 4

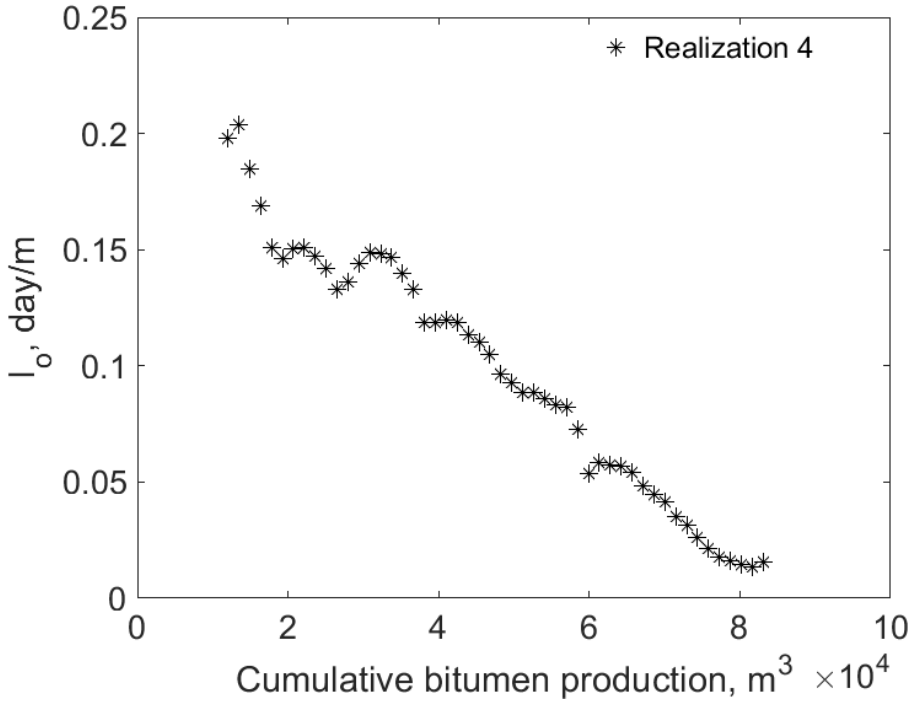

Figure K-1(e).I_o for SAGD as a function of cumulative bitumen production for realization 17

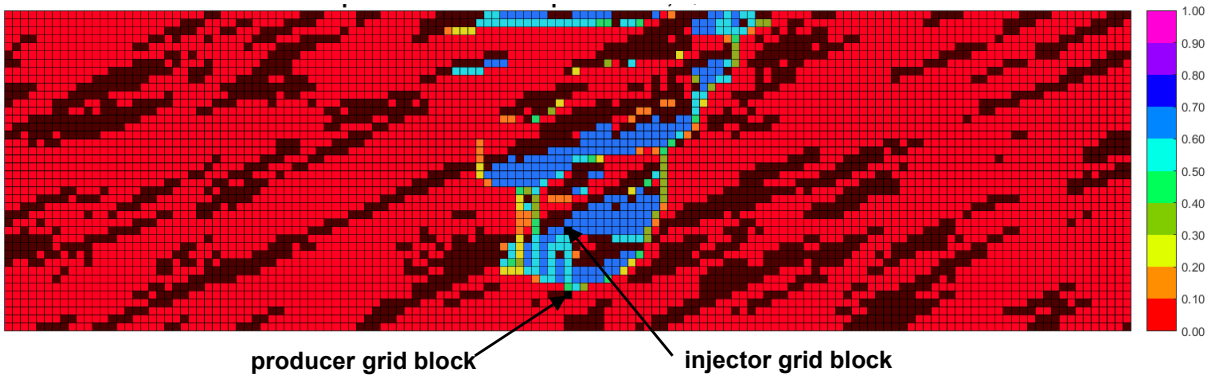

Figure K-1(f). Vapor-phase saturation map in SAGD for realization 4 for Q ≈ 31218 m^3

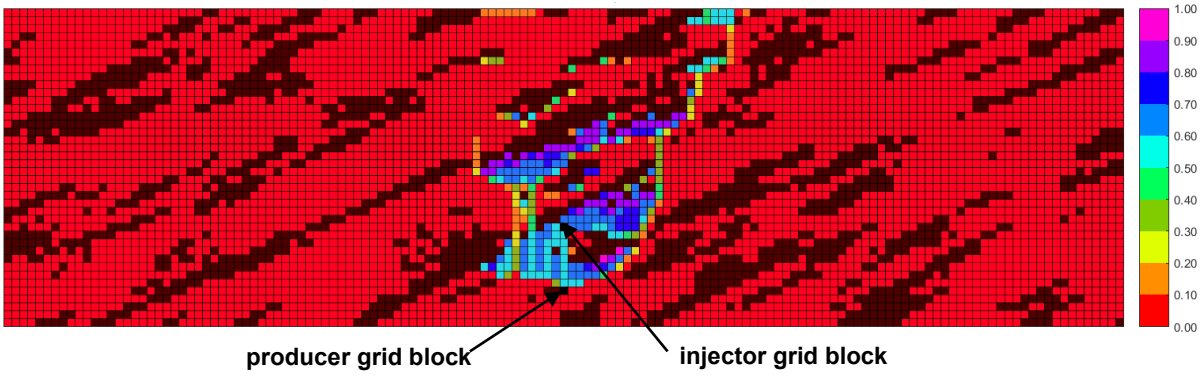

Figure K-1(g). Vapor-phase saturation map in n-C_6 SAGD for realization 4 for Q ≈ 31218 m^3

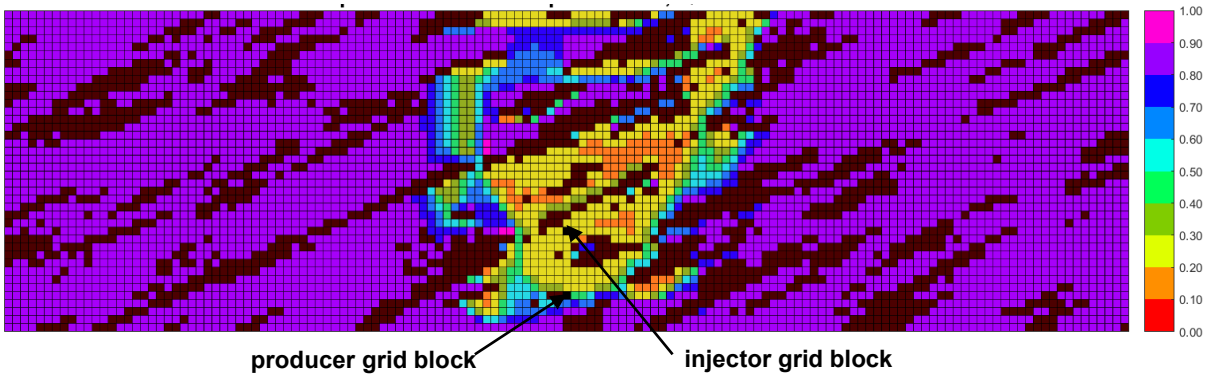

Figure K-1(h). Oleic-phase saturation map in SAGD for realization 4 for Q ≈ 31218 m^3

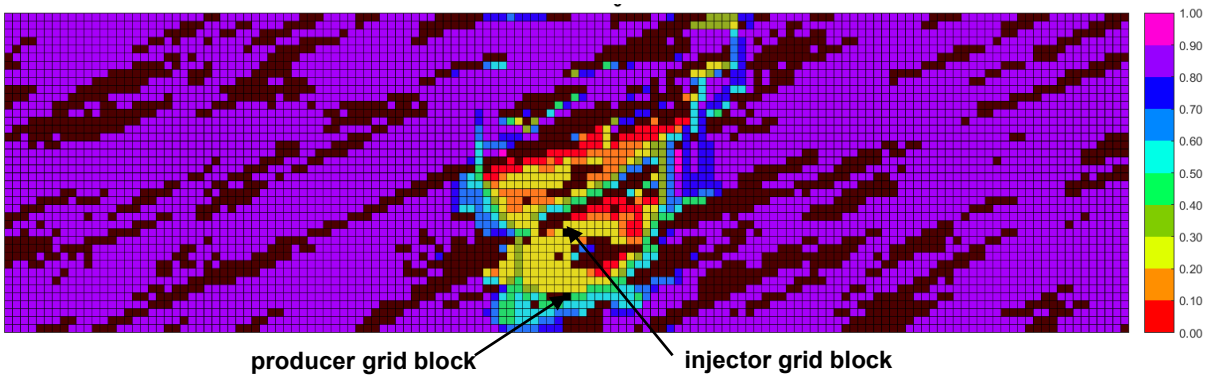

Figure K-1(i). Oleic-phase saturation map in n-C_6 SAGD for realization 4 for Q ≈ 31218 m^3

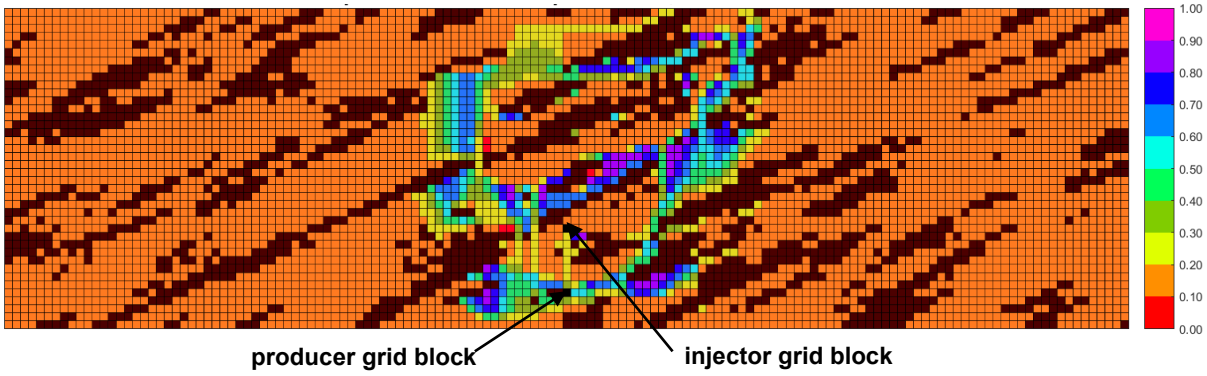

Figure K-1(j). Aqueous-phase saturation map in SAGD for realization 4 for Q ≈ 31218 m^3

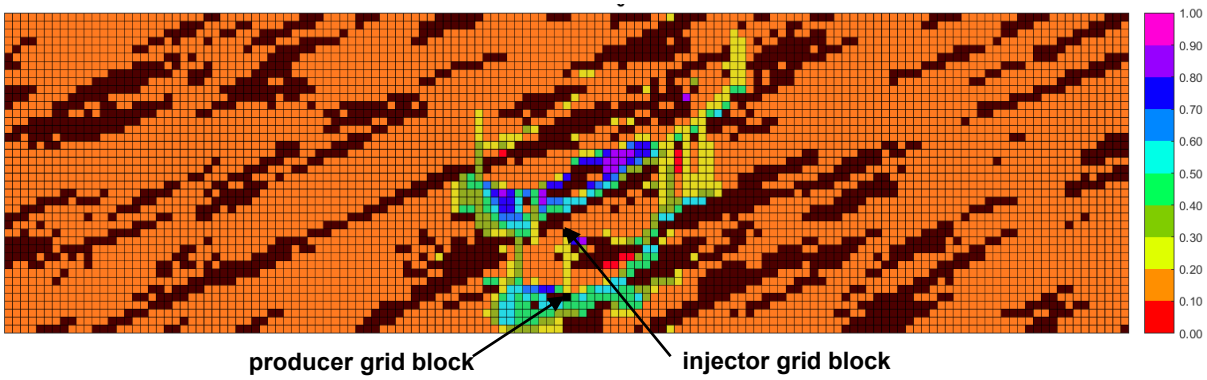

Figure K-1(k). Aqueous-phase saturation map in n-C_6 SAGD for realization 4 for Q ≈ 31218 m^3

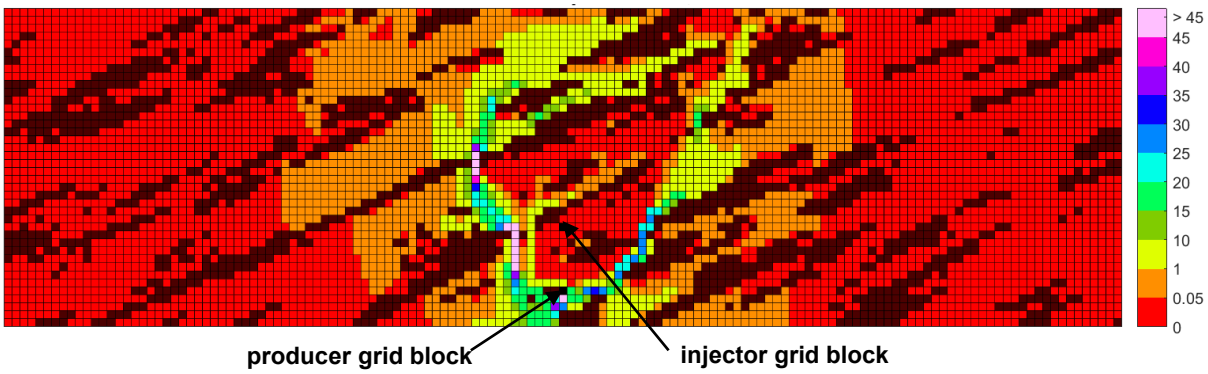

Figure K-1(l). Bitumen molar flow rate (kg-mole/day) map in SAGD for realization 4 for Q ≈ 31218 m^3

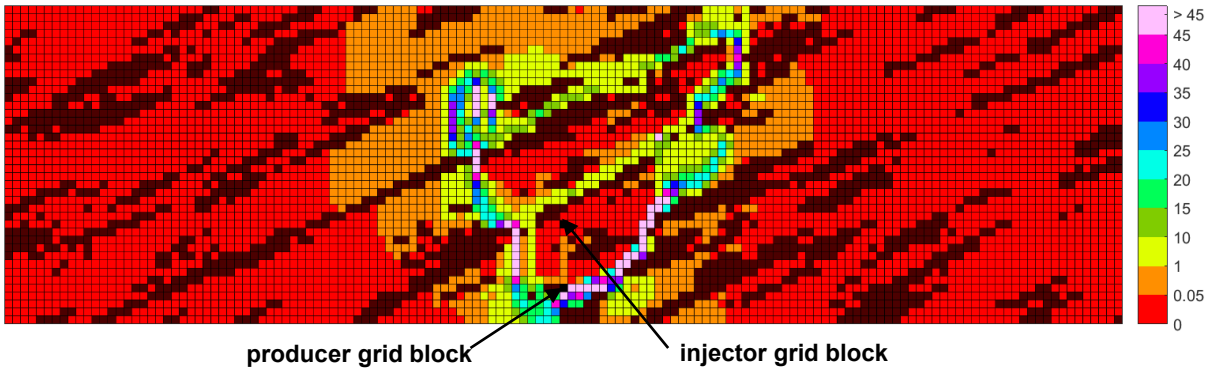

Figure K-1(m). Bitumen molar flow rate (kg-mole/day) map in n-C_6 SAGD for realization 4 for Q ≈ 31218 m^3

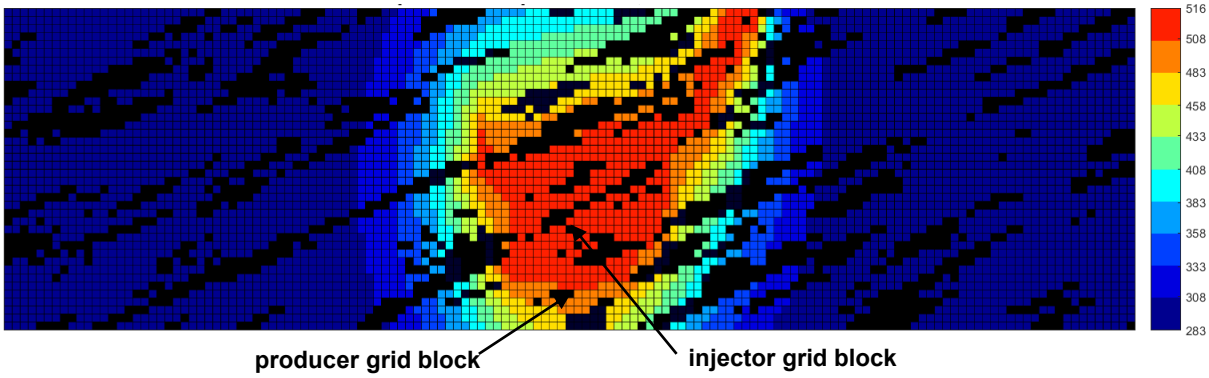

Figure K-1(n). Temperature (Kelvin) map in SAGD for realization 4 for Q ≈ 31218 m^3

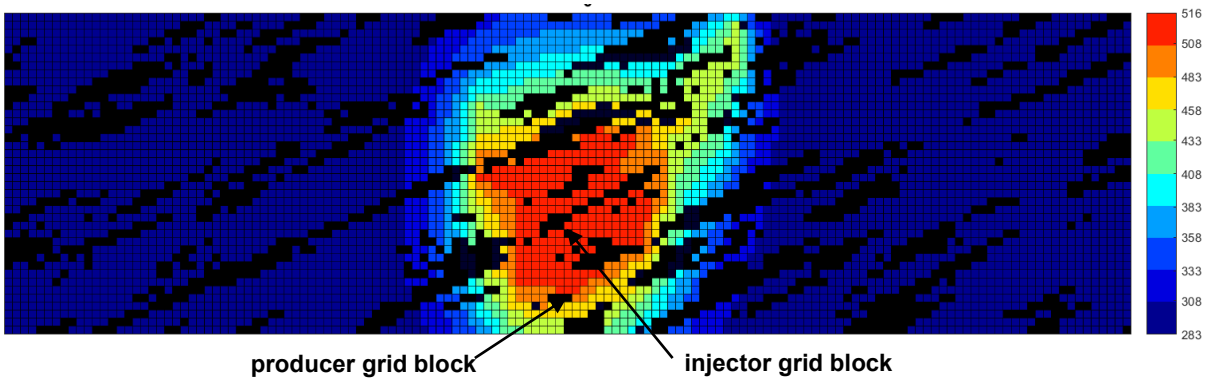

Figure K-1(o). Temperature (Kelvin) map in n-C_6 SAGD for realization 4 for Q ≈ 31218 m^3

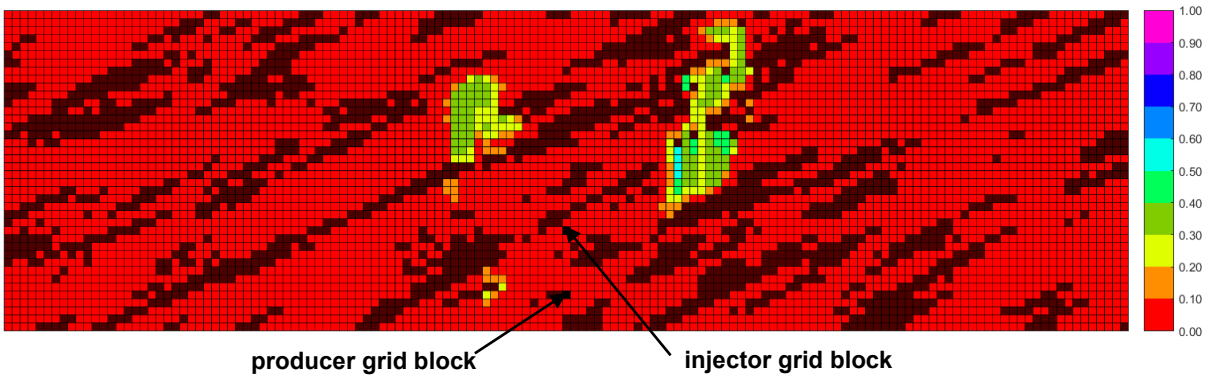

Figure K-1(p). $\beta_L x_{sL}$ map in n-C_6 SAGD for realization 4 for Q ≈ 31218 m^3

Figure K-1. Property maps for SAGD and n-C_6 SAGD for realization 4

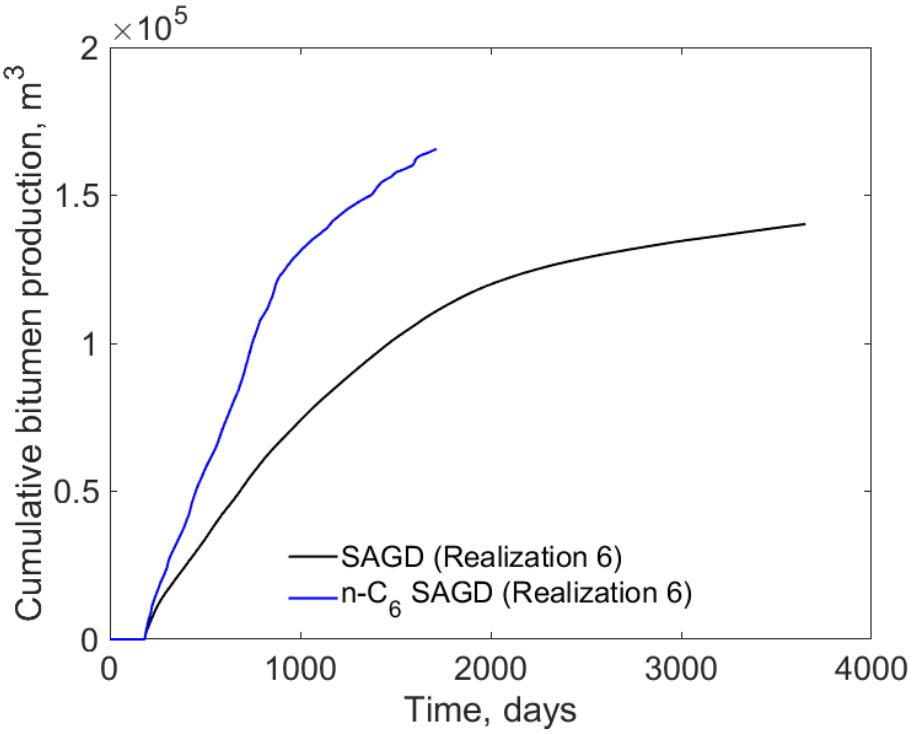

Figure K-2(a). Cumulative bitumen production histories for SAGD and n-C_6 SAGD for realization 6

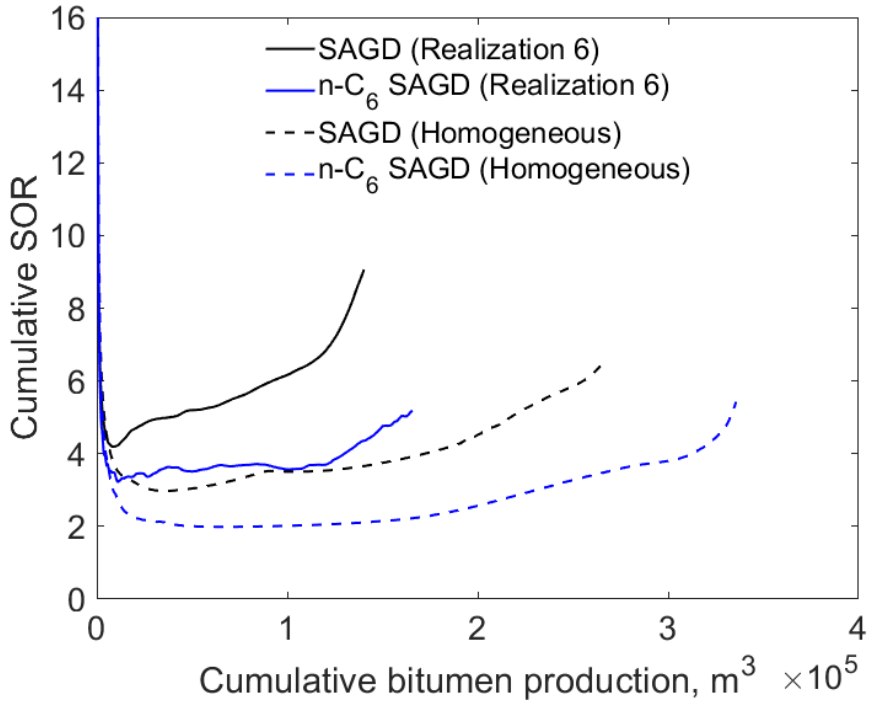

Figure K-2(b). Cumulative SOR for SAGD and n-C_6 SAGD for realization 6

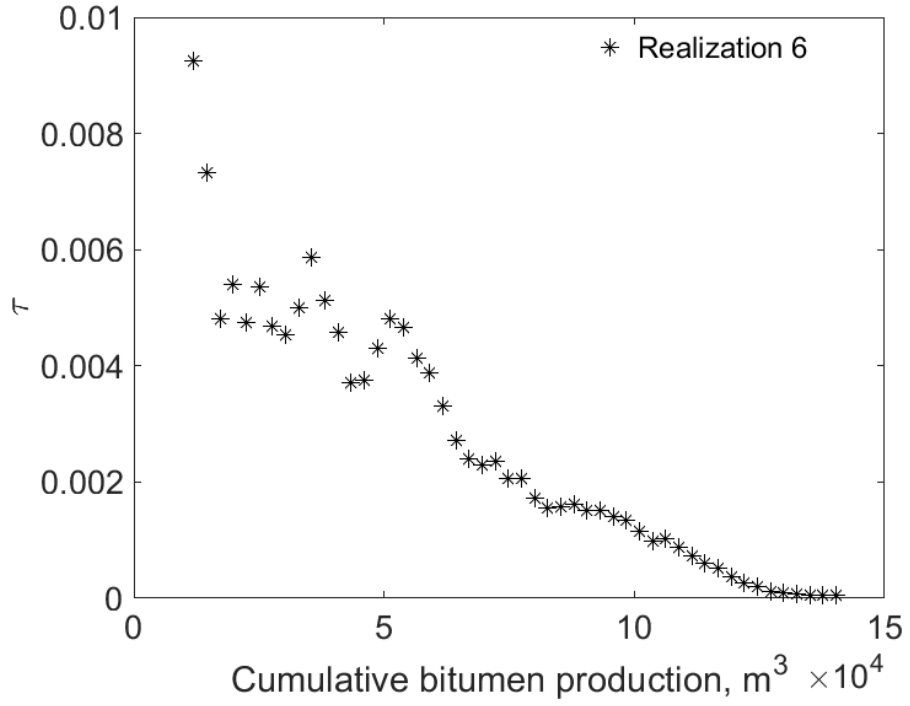

Figure K-2 (c). τ for SAGD as a function of cumulative bitumen production for realization 6

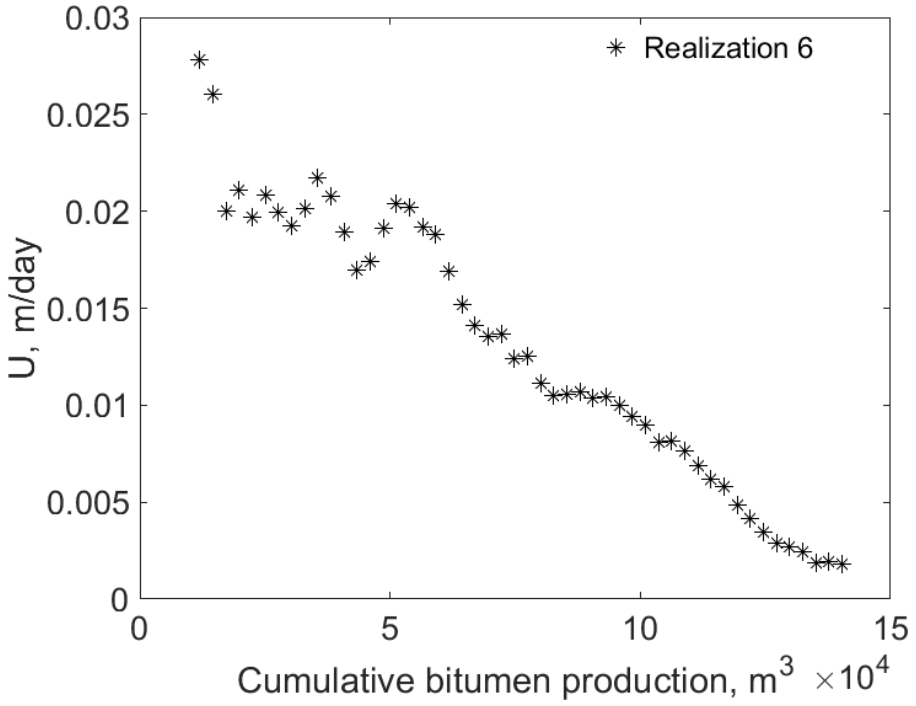

Figure K-2 (d). U for SAGD as a function of cumulative bitumen production for realization 6

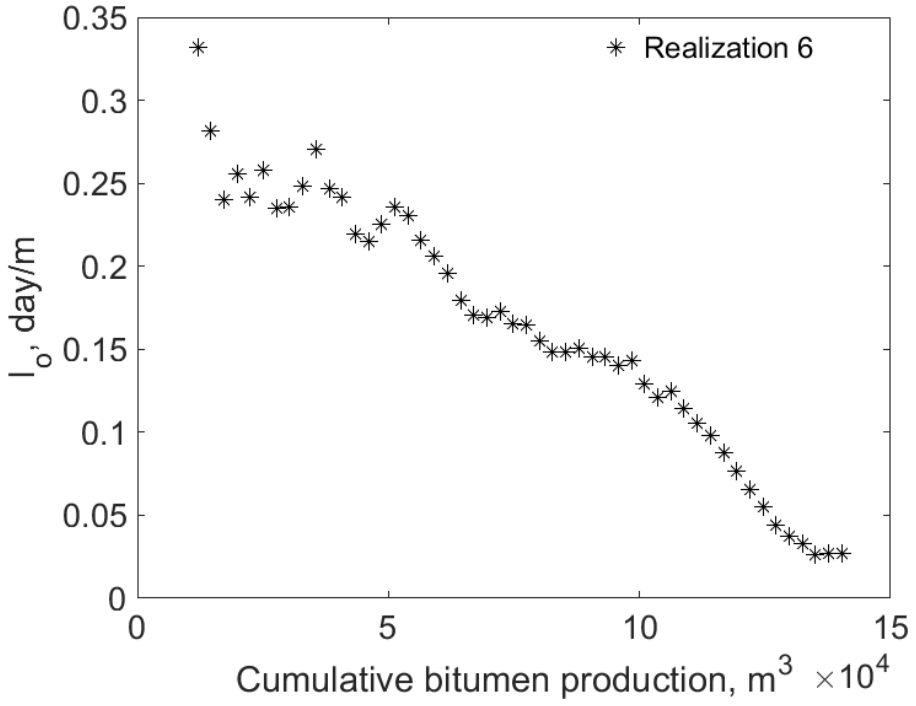

Figure K-2(e).I_o for SAGD as a function of cumulative bitumen production for realization 6

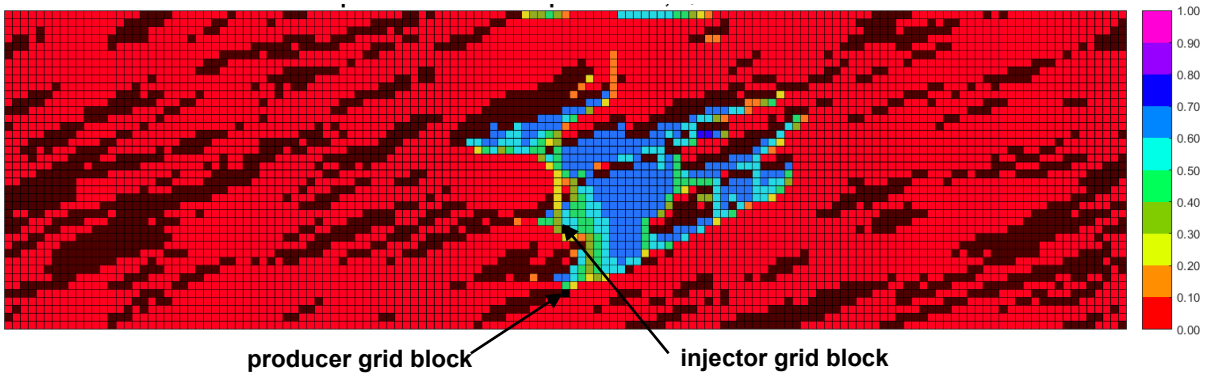

Figure K-2(f). Vapor-phase saturation map in SAGD for realization 6 for Q ≈ 31218 m^3

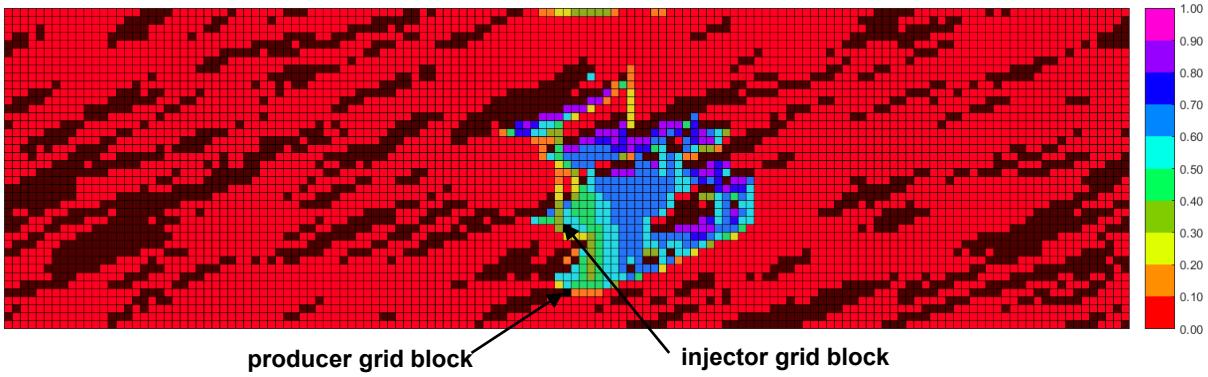

Figure K-2(g). Vapor-phase saturation map in n-C_6 SAGD for realization 6 for Q ≈ 31218 m^3

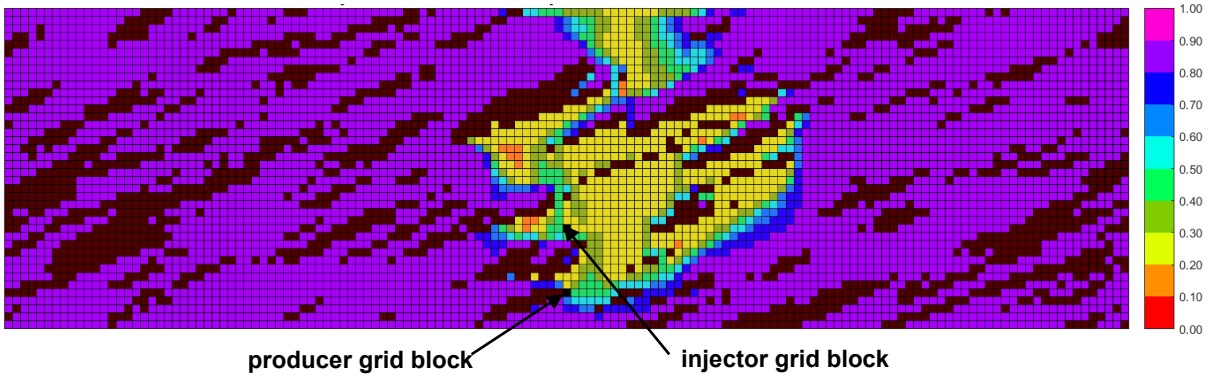

Figure K-2(h). Oleic-phase saturation map in SAGD for realization 6 for Q ≈ 31218 m^3

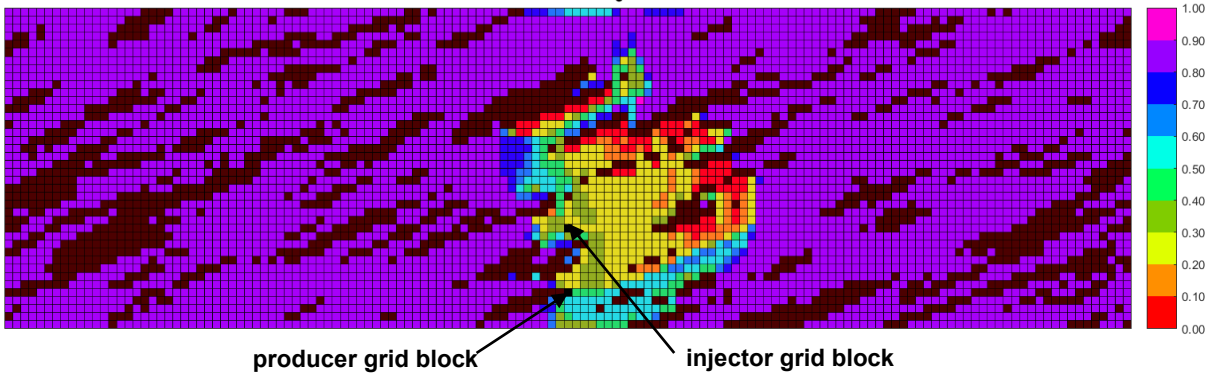

Figure K-2(i). Oleic-phase saturation map in n-C_6 SAGD for realization 6 for Q ≈ 31218 m^3

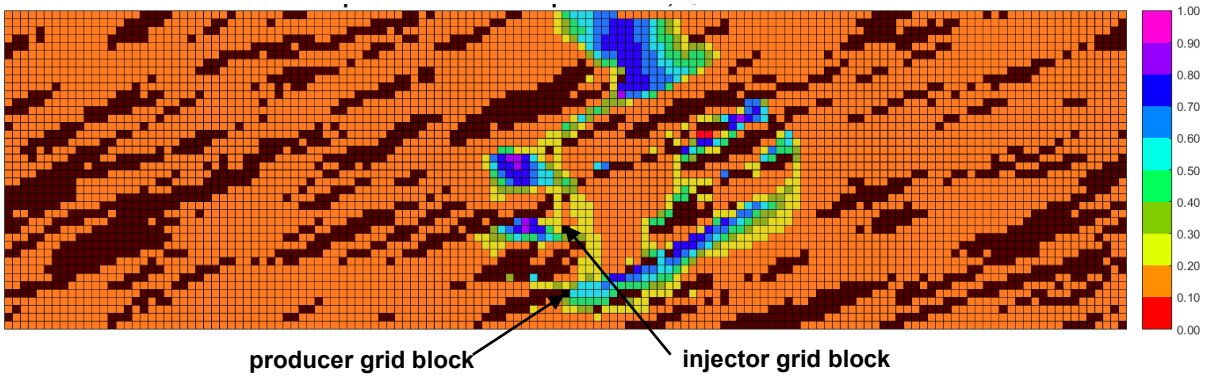

Figure K-2(j). Aqueous-phase saturation map in SAGD for realization 6 for Q ≈ 31218 m^3

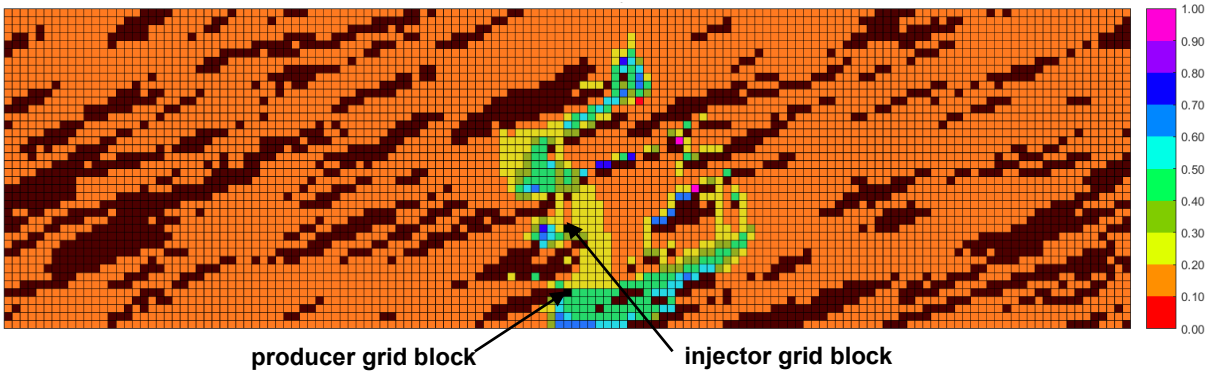

Figure K-2(k). Aqueous-phase saturation map in n-C_6 SAGD for realization 6 for Q ≈ 31218 m^3

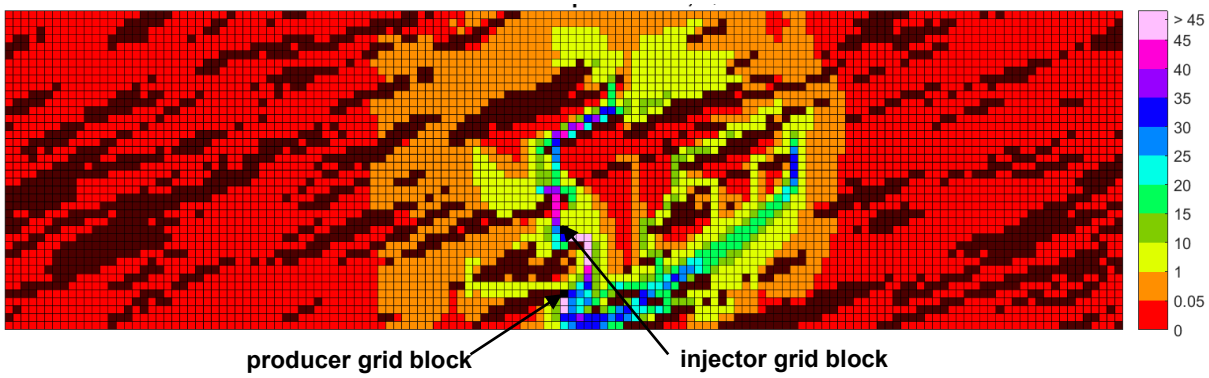

Figure K-2(l). Bitumen molar flow rate (kg-mole/day) map in SAGD for realization 6 for Q ≈ 31218 m^3

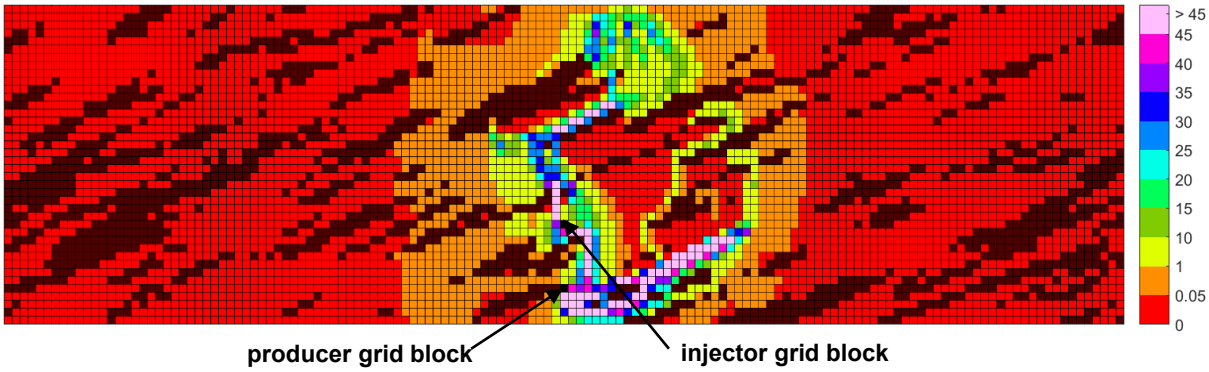

Figure K-2(m). Bitumen molar flow rate (kg-mole/day) map in n-C_6 SAGD for realization 6 for Q ≈ 31218 m^3

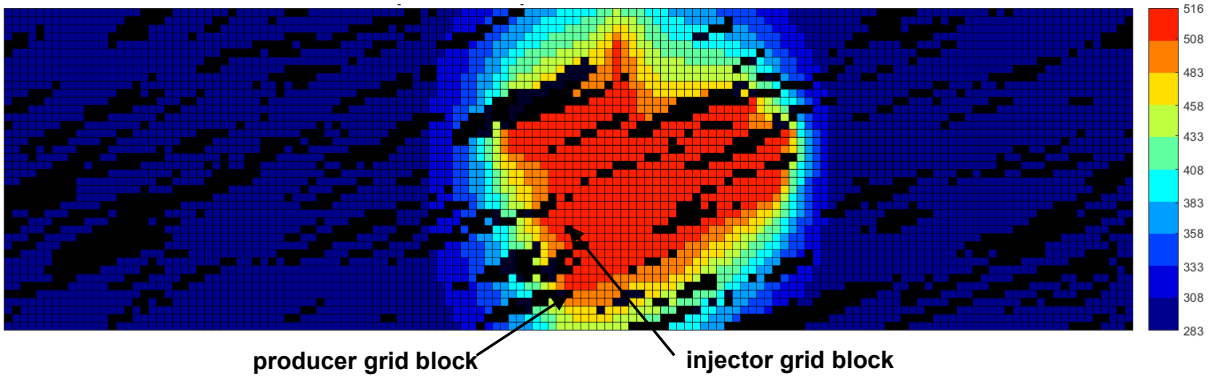

Figure K-2(n). Temperature (Kelvin) map in SAGD for realization 6 for Q ≈ 31218 m^3

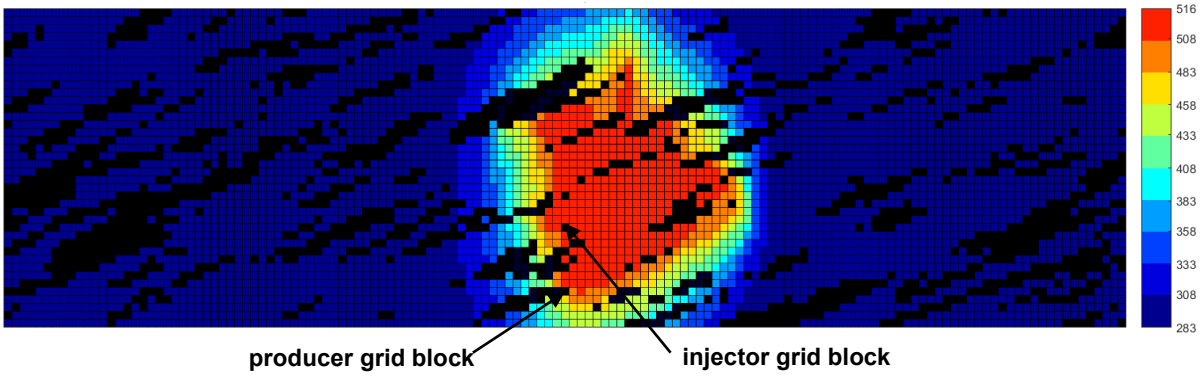

Figure K-2(o). Temperature (Kelvin) map in n-C_6 SAGD for realization 6 for Q ≈ 31218 m^3

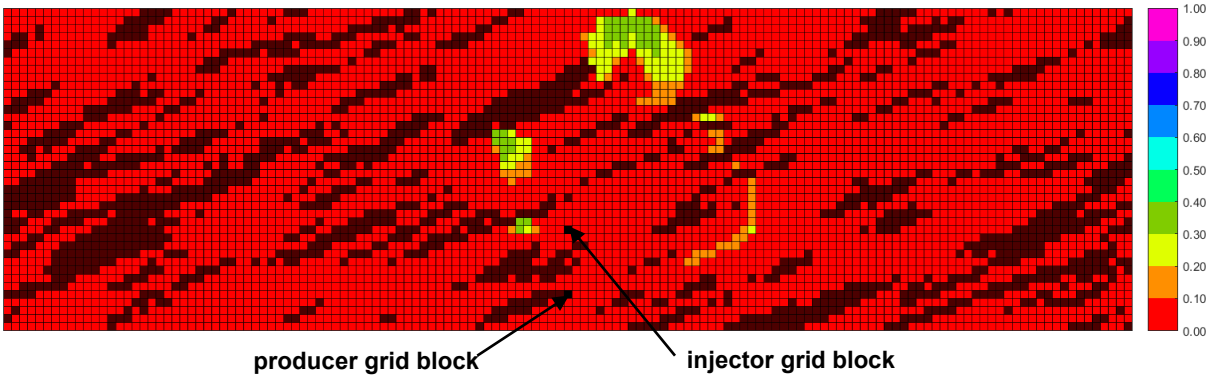

Figure K-2(p). $\beta_{LX_{sL}}$ map in n-C_6 SAGD for realization 6 for Q ≈ 31218 m^3

Figure K-2. Property maps for SAGD and n-C_6 SAGD for realization 6

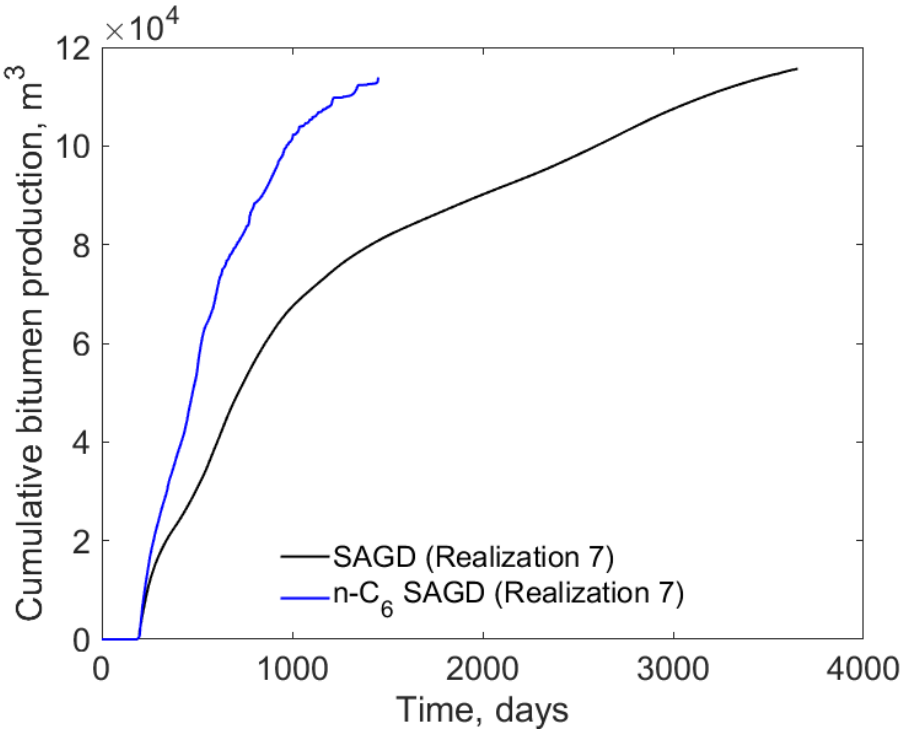

Figure K-3(a). Cumulative bitumen production histories for SAGD and n-C_6 SAGD for realization 7

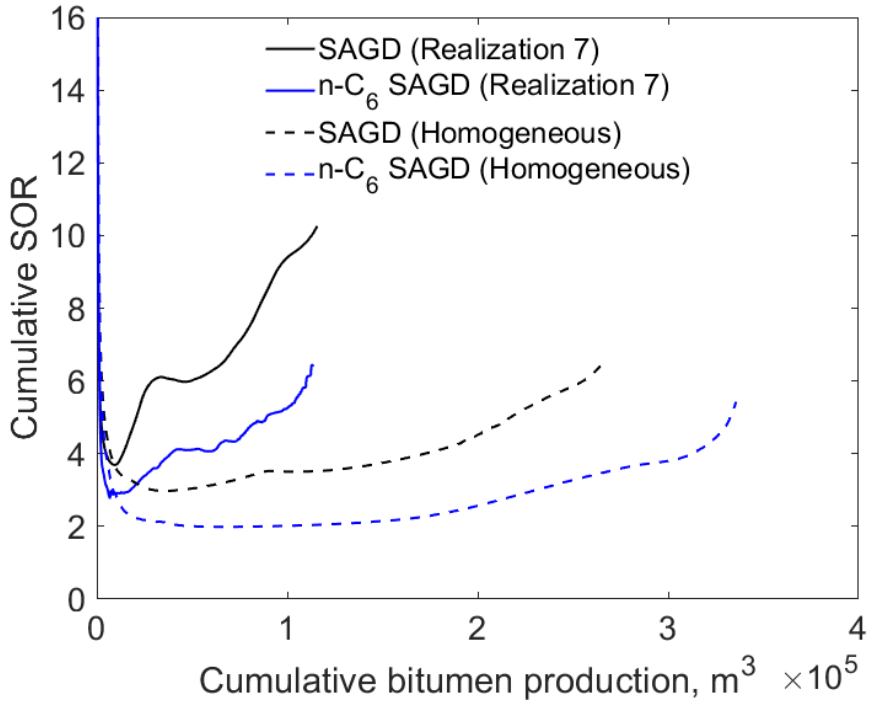

Figure K-3(b). Cumulative SOR for SAGD and n-C_6 SAGD for realization 7

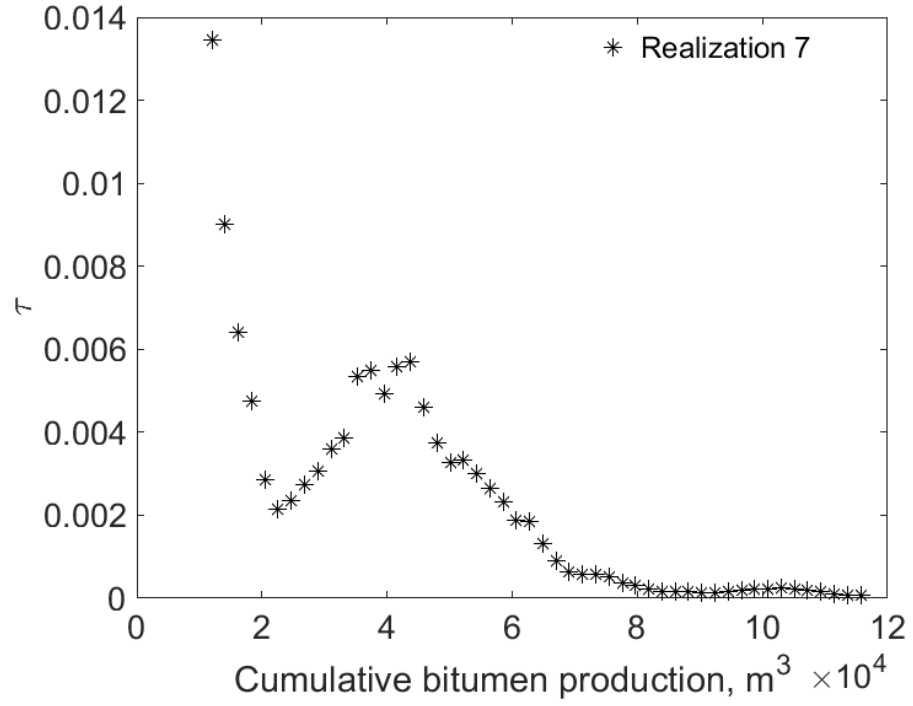

Figure K-3(c). τ for SAGD as a function of cumulative bitumen production for realization 7

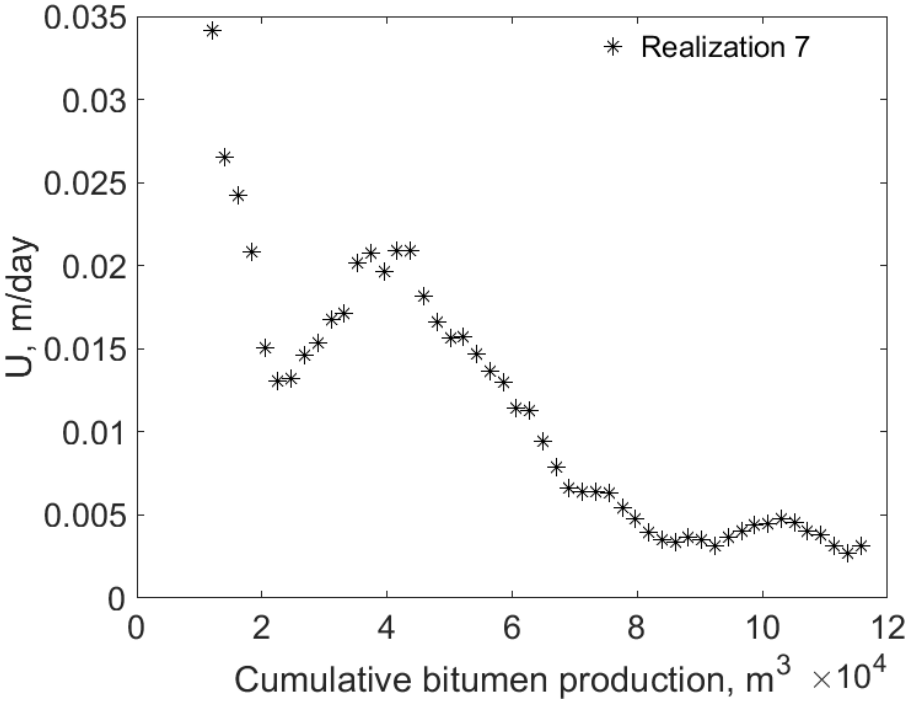

Figure K-3(d). U for SAGD as a function of cumulative bitumen production for realization 7

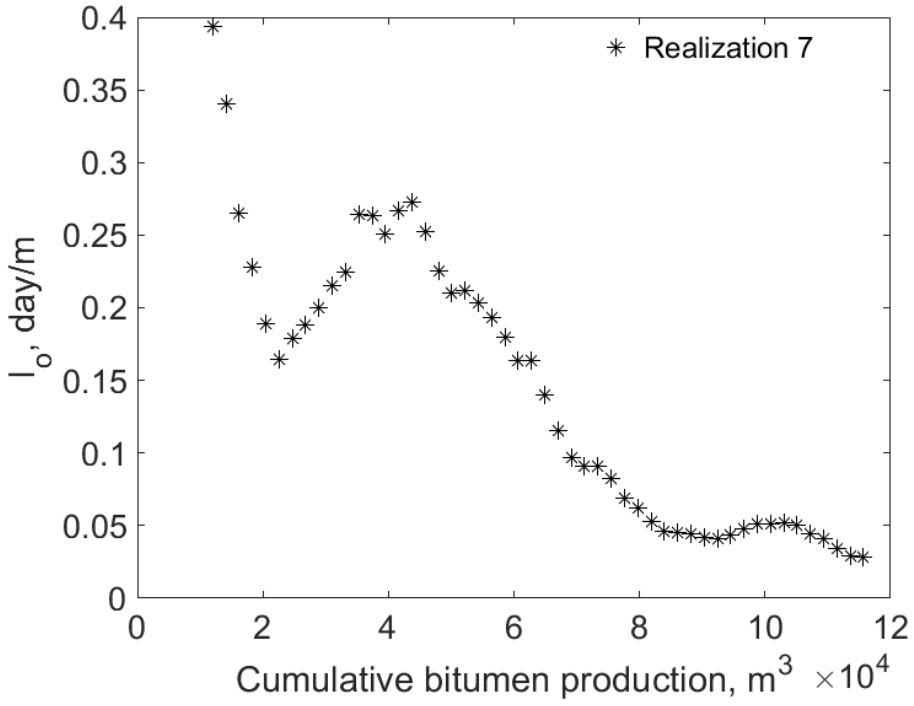

Figure K-3(e).I_o for SAGD as a function of cumulative bitumen production for realization 7

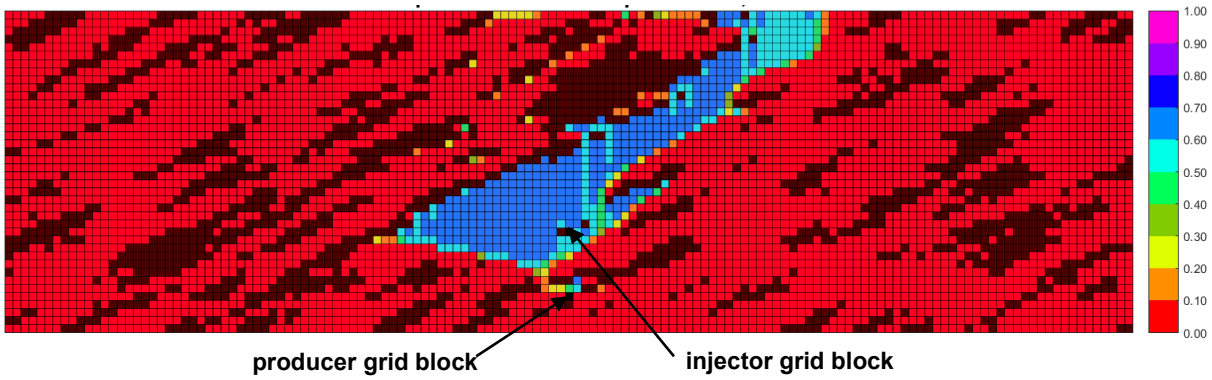

Figure K-3(f). Vapor-phase saturation map in SAGD for realization 7 for Q ≈ 31218 m^3

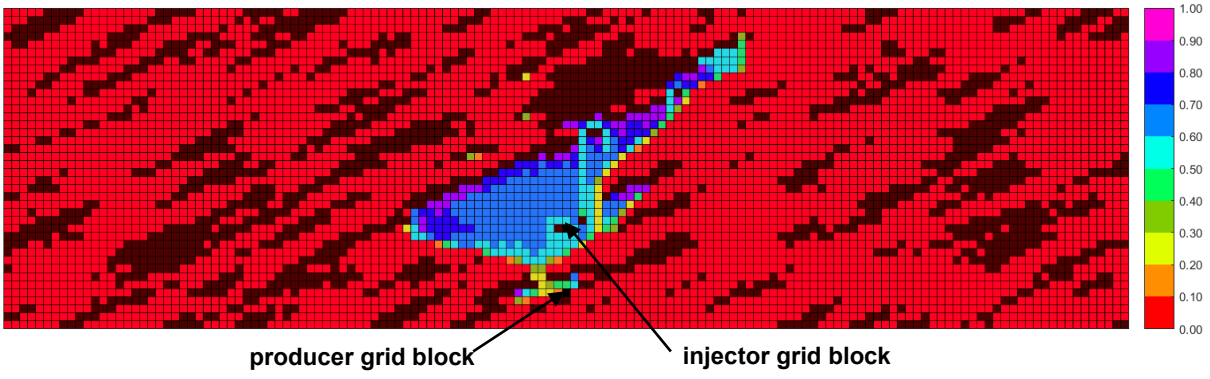

Figure K-3(g). Vapor-phase saturation map in n-C_6 SAGD for realization 7 for Q ≈ 31218 m^3

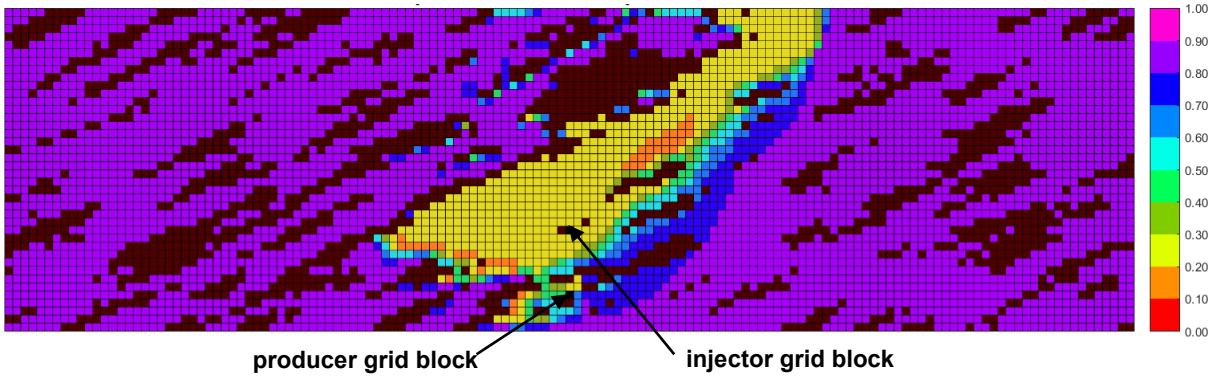

Figure K-3(h). Oleic-phase saturation map in SAGD for realization 7 for Q ≈ 31218 m^3

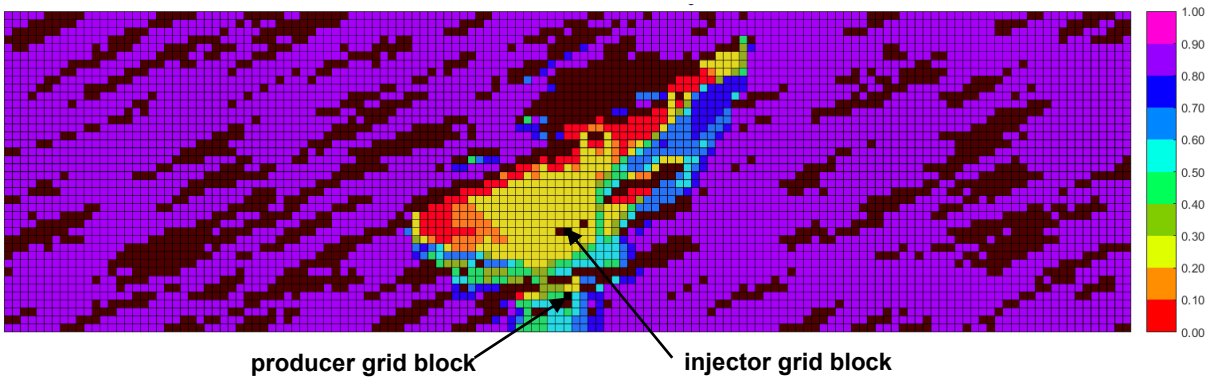

Figure K-3(i). Oleic-phase saturation map in n-C_6 SAGD for realization 7 for Q ≈ 31218 m^3

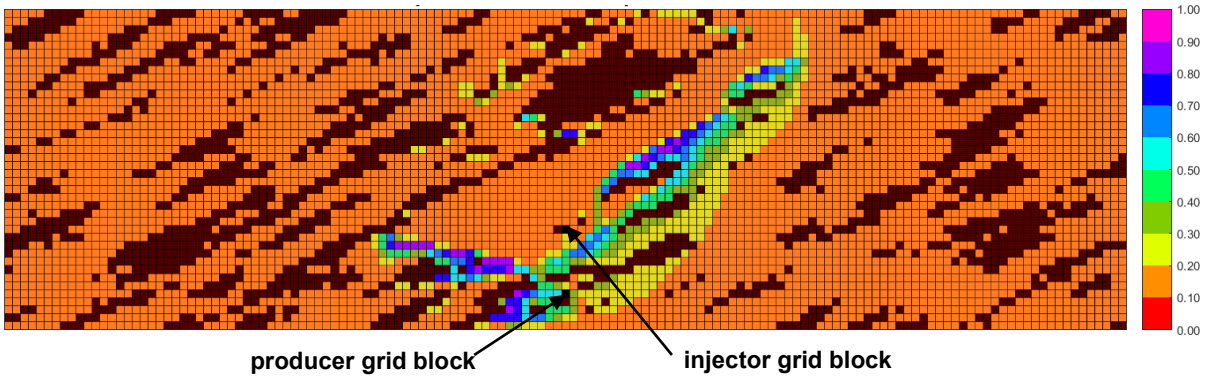

Figure K-3(j). Aqueous-phase saturation map in SAGD for realization 7 for Q ≈ 31218 m^3

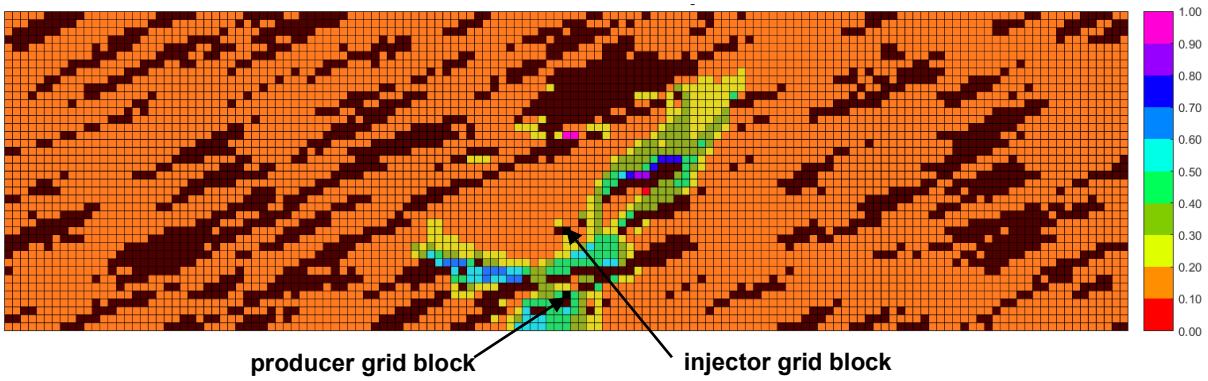

Figure K-3(k). Aqueous-phase saturation map in n-C_6 SAGD for realization 7 for Q ≈ 31218 m^3

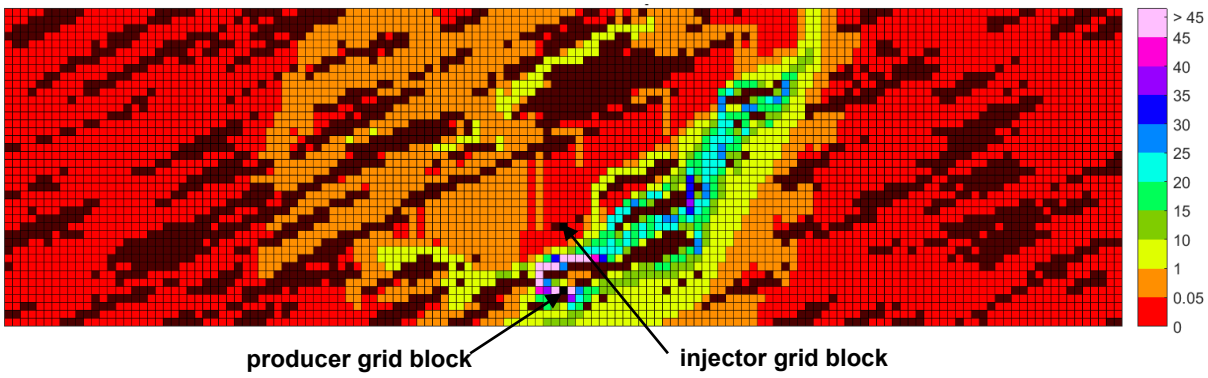

Figure K-3(l). Bitumen molar flow rate (kg-mole/day) map in SAGD for realization 7 for Q ≈ 31218 m^3

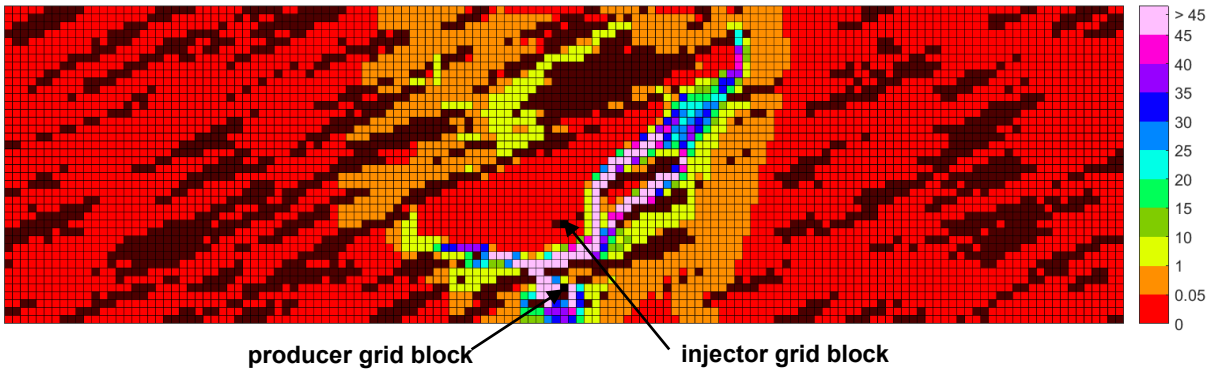

Figure K-3(m). Bitumen molar flow rate (kg-mole/day) map in n-C_6 SAGD for realization 7 for Q ≈ 31218 m^3

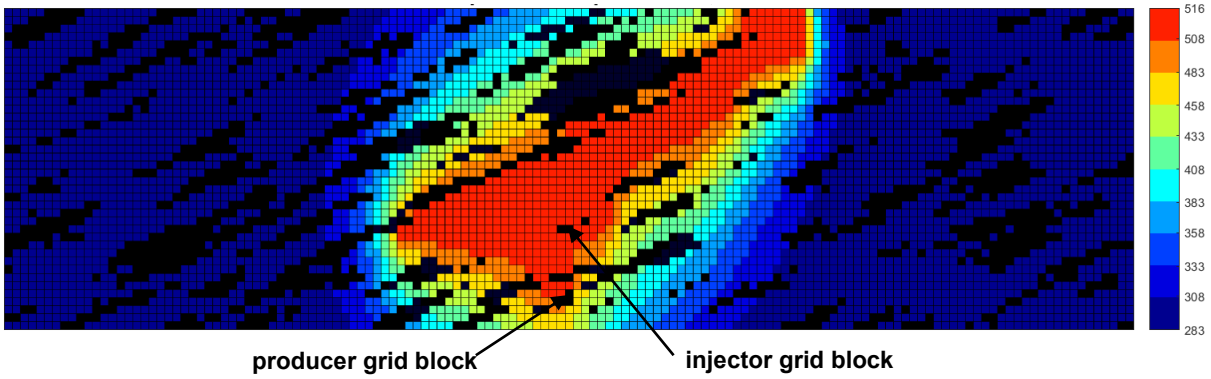

Figure K-3(n). Temperature (Kelvin) map in SAGD for realization 7 for Q ≈ 31218 m^3

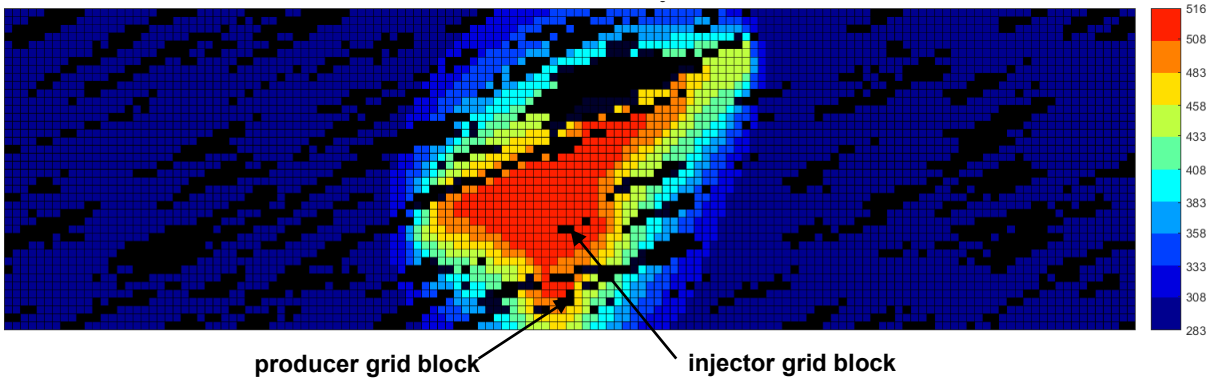

Figure K-3(o). Temperature (Kelvin) map in n-C_6 SAGD for realization 7 for Q ≈ 31218 m^3

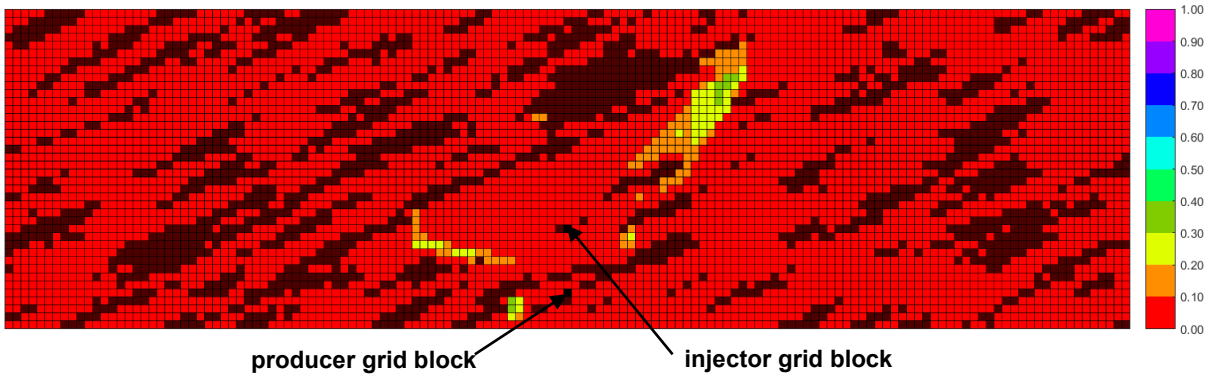

Figure K-3(p). $\beta_{LX_{sL}}$ map in n-C_6 SAGD for realization 7 for Q ≈ 31218 m^3

Figure K-3. Property maps for SAGD and n-C_6 SAGD for realization 7

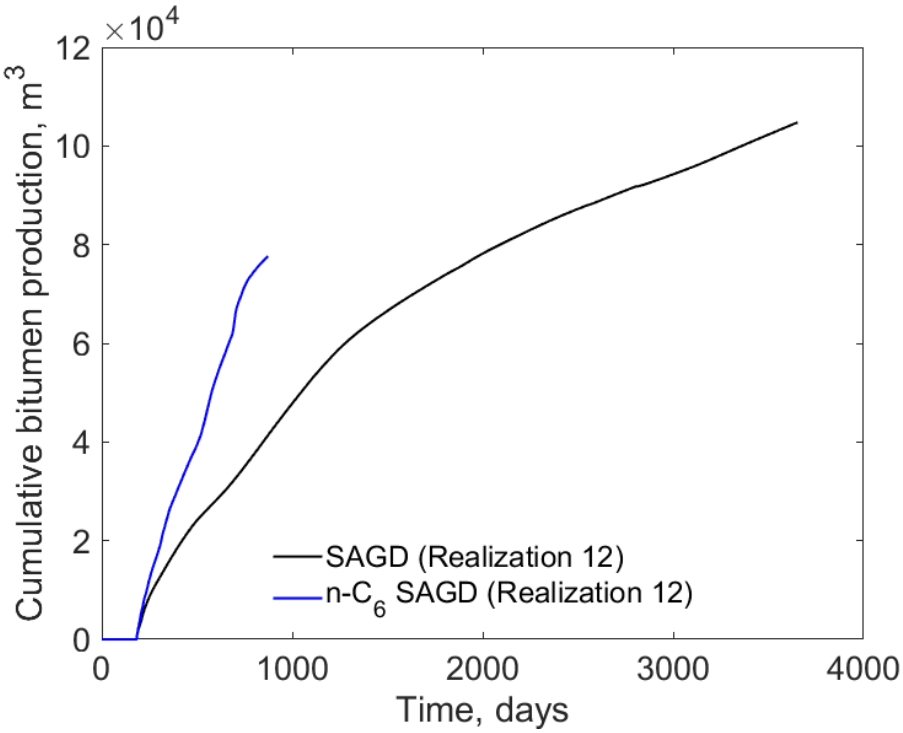

Figure K-4(a). Cumulative bitumen production histories for SAGD and n-C_6 SAGD for realization 12

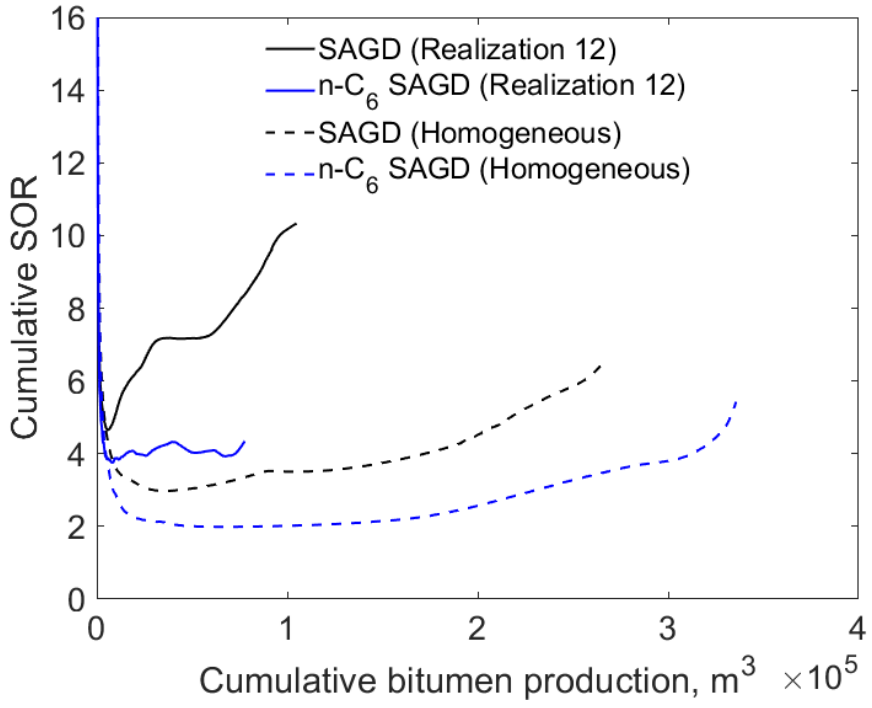

Figure K-4(b). Cumulative SOR for SAGD and n-C_6 SAGD for realization 12

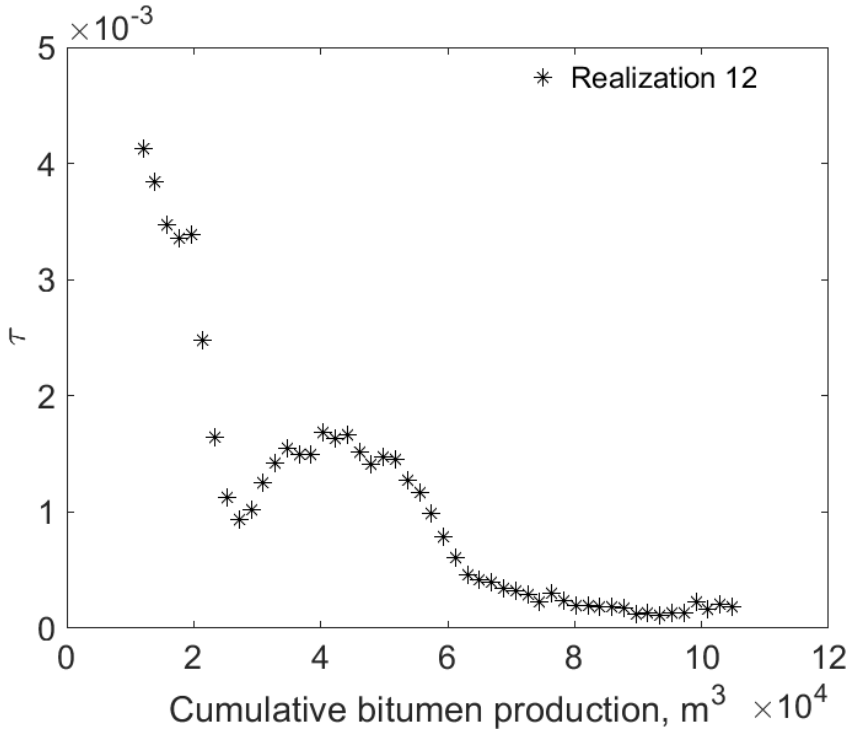

Figure K-4(c). τ for SAGD as a function of cumulative bitumen production for realization 12

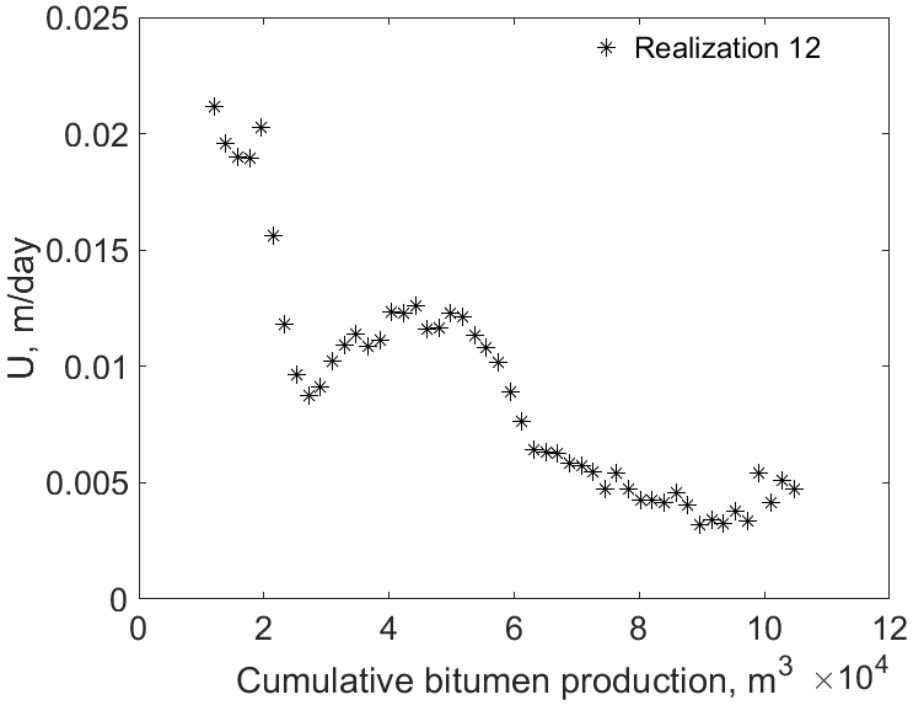

Figure K-4(d). U for SAGD as a function of cumulative bitumen production for realization 12

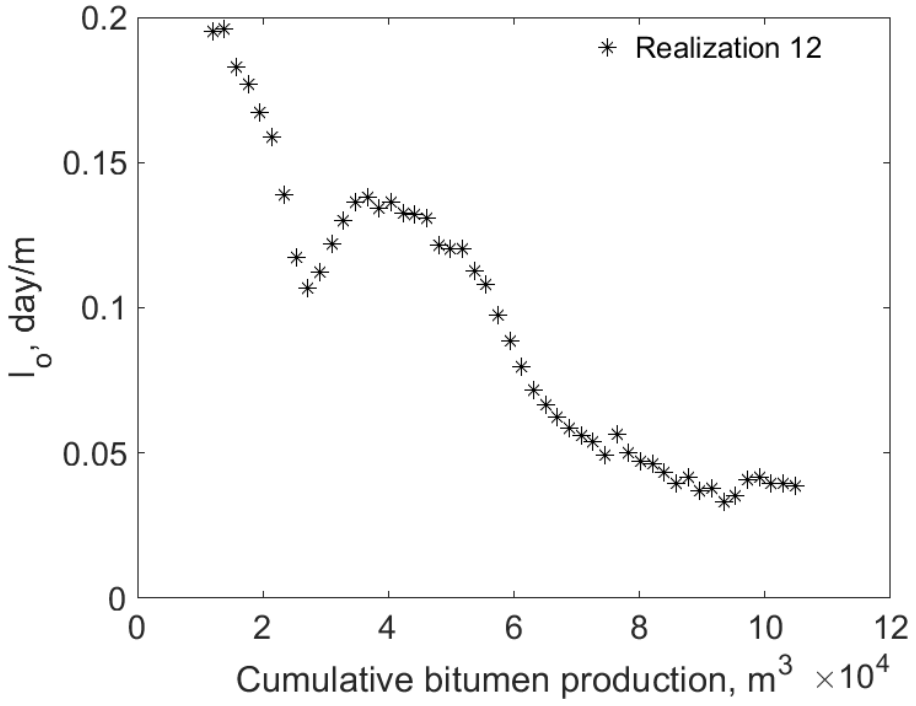

Figure K-4(e).I_o for SAGD as a function of cumulative bitumen production for realization 12

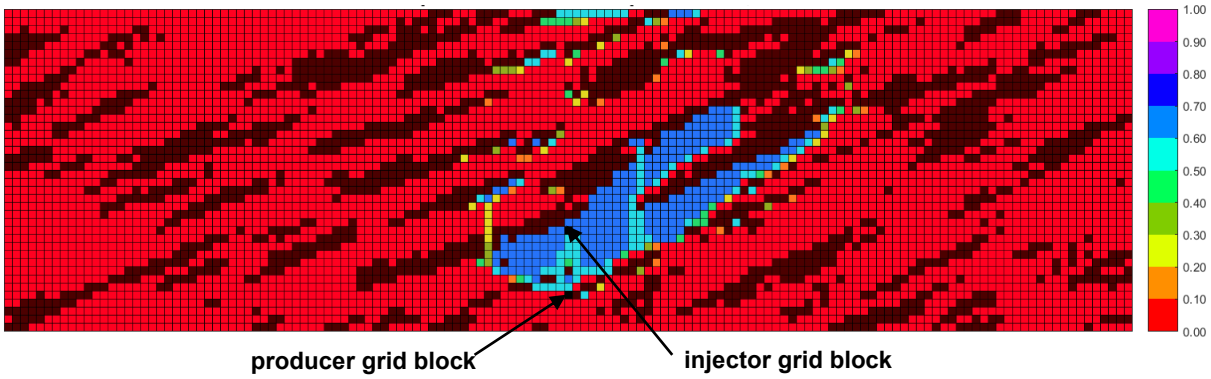

Figure K-4(f). Vapor-phase saturation map in SAGD for realization 12 for Q ≈ 31218 m^3

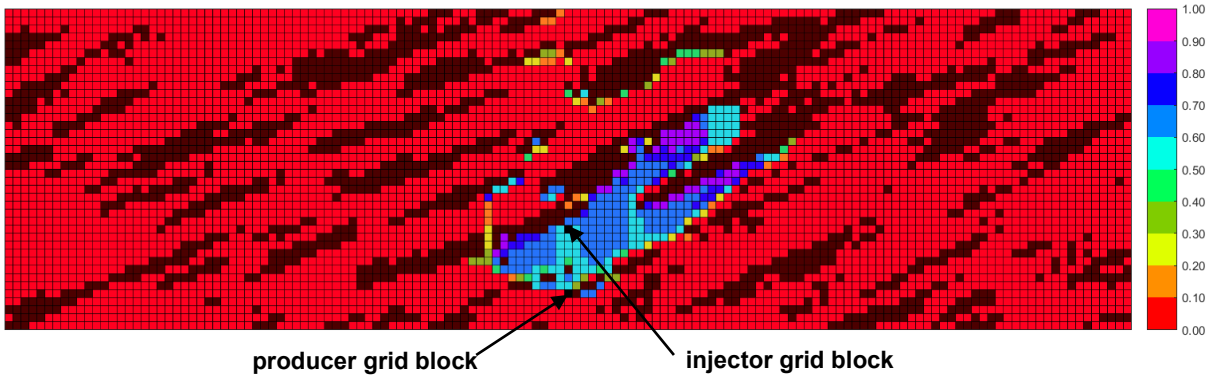

Figure K-4(g). Vapor-phase saturation map in n-C_6 SAGD for realization 12 for Q ≈ 31218 m^3

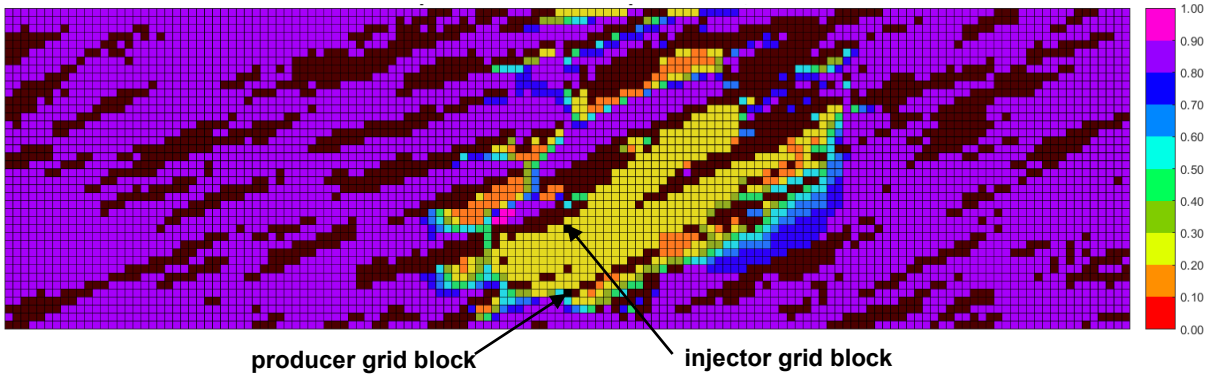

Figure K-4(h). Oleic-phase saturation map in SAGD for realization 12 for Q ≈ 31218 m^3

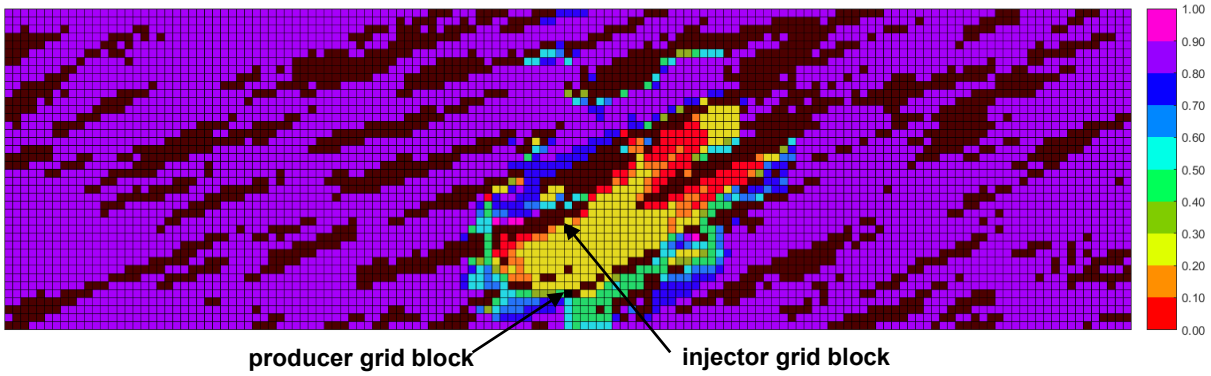

Figure K-4(i). Oleic-phase saturation map in n-C_6 SAGD for realization 12 for Q ≈ 31218 m^3

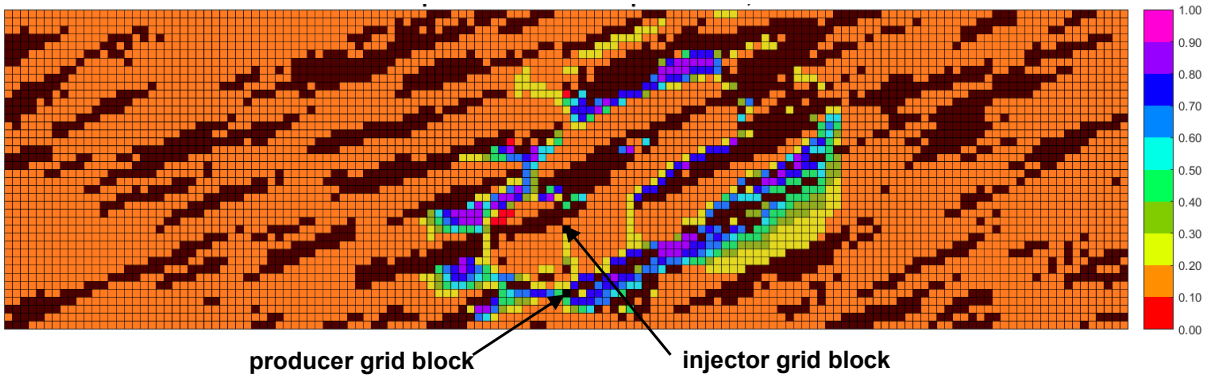

Figure K-4(j). Aqueous-phase saturation map in SAGD for realization 12 for Q ≈ 31218 m^3

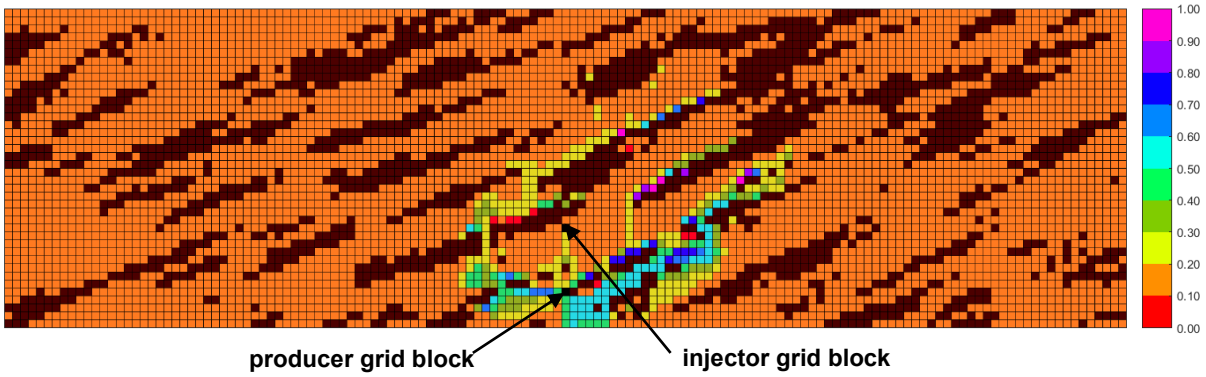

Figure K-4(k). Aqueous-phase saturation map in n-C_6 SAGD for realization 12 for Q ≈ 31218 m^3

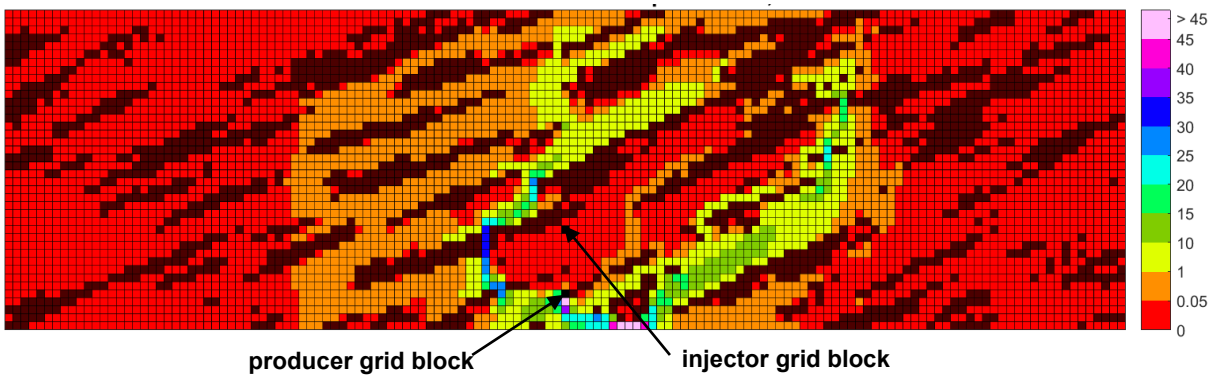

Figure K-4(l). Bitumen molar flow rate (kg-mole/day) map in SAGD for realization 12 for Q ≈ 31218 m^3

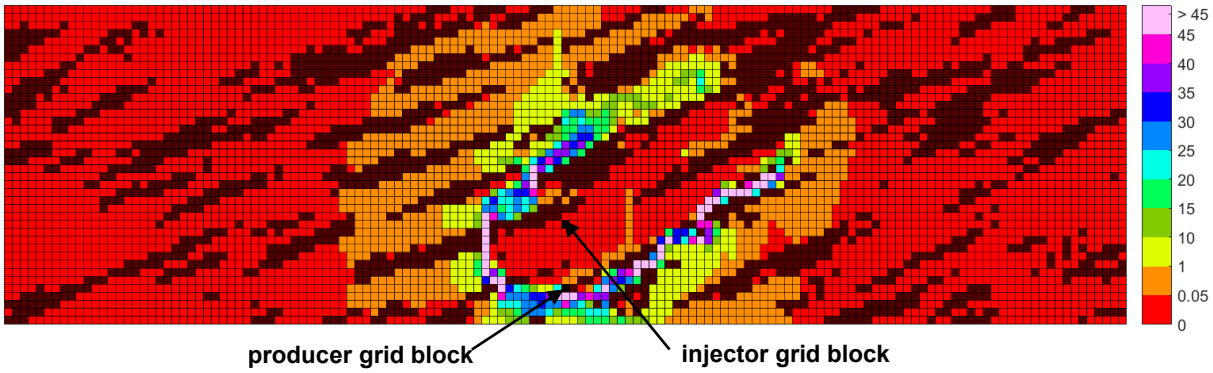

Figure K-4(m). Bitumen molar flow rate (kg-mole/day) map in n-C_6 SAGD for realization 12 for Q ≈ 31218 m^3

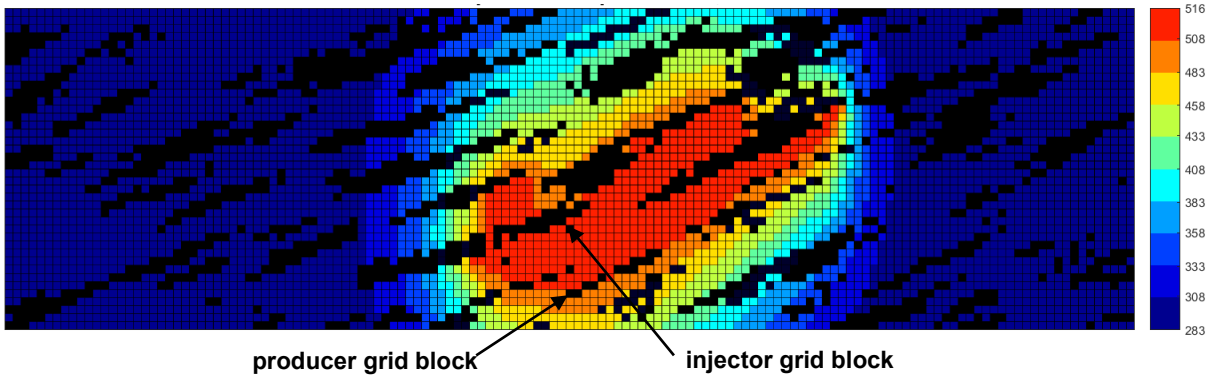

Figure K-4(n). Temperature (Kelvin) map in SAGD for realization 12 for Q ≈ 31218 m^3

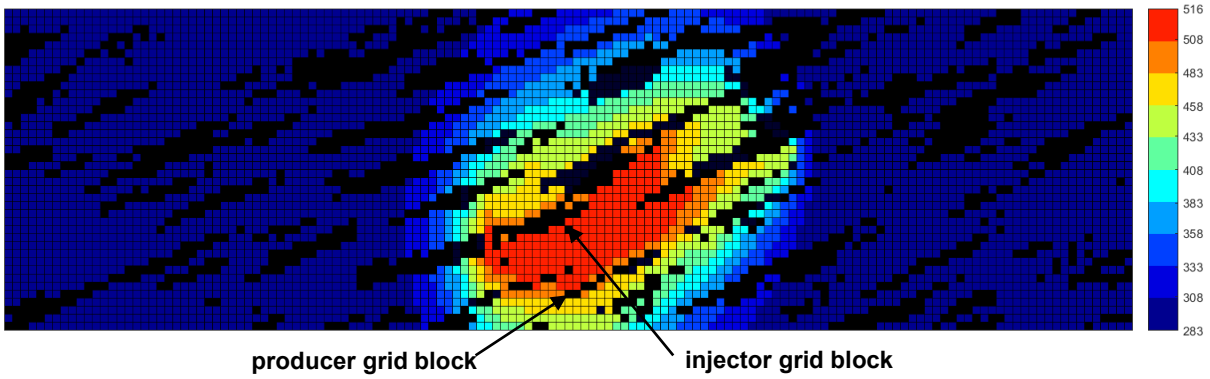

Figure K-4(o). Temperature (Kelvin) map in n-C_6 SAGD for realization 12 for Q ≈ 31218 m^3

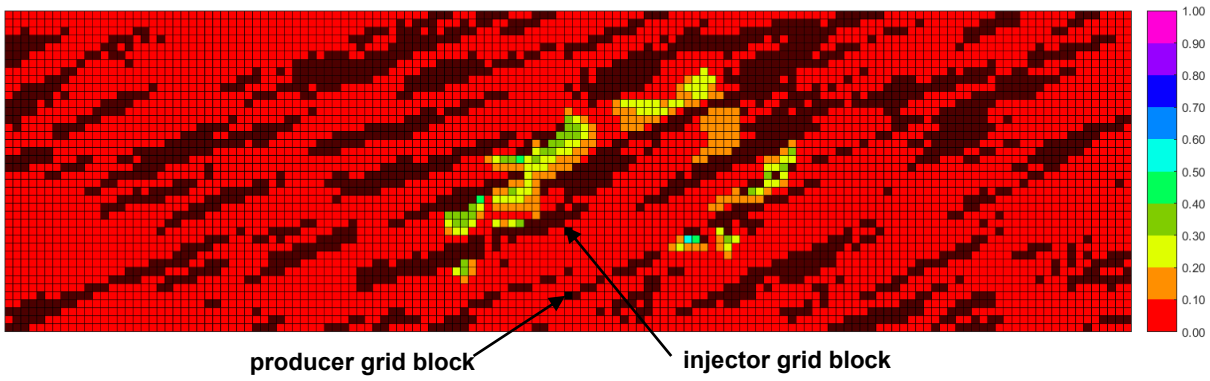

Figure K-4(p). $\beta_L x_{sL}$ map in n-C_6 SAGD for realization 12 for Q ≈ 31218 m^3

Figure K-4. Property maps for SAGD and n-C_6 SAGD for realization 12

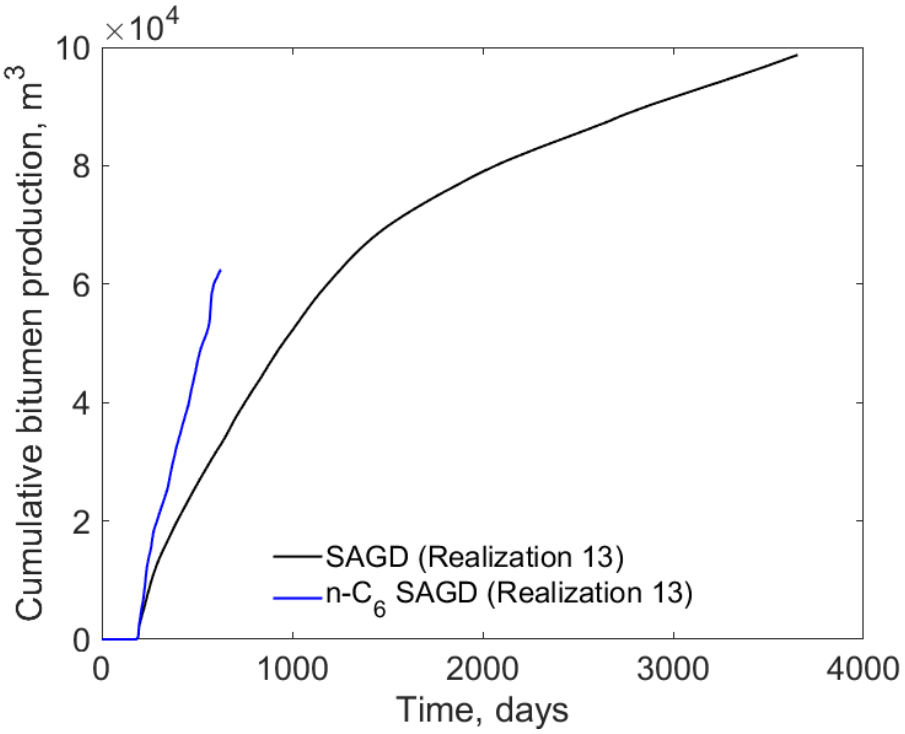

Figure K-5(a). Cumulative bitumen production histories for SAGD and n-C_6 SAGD for realization 13

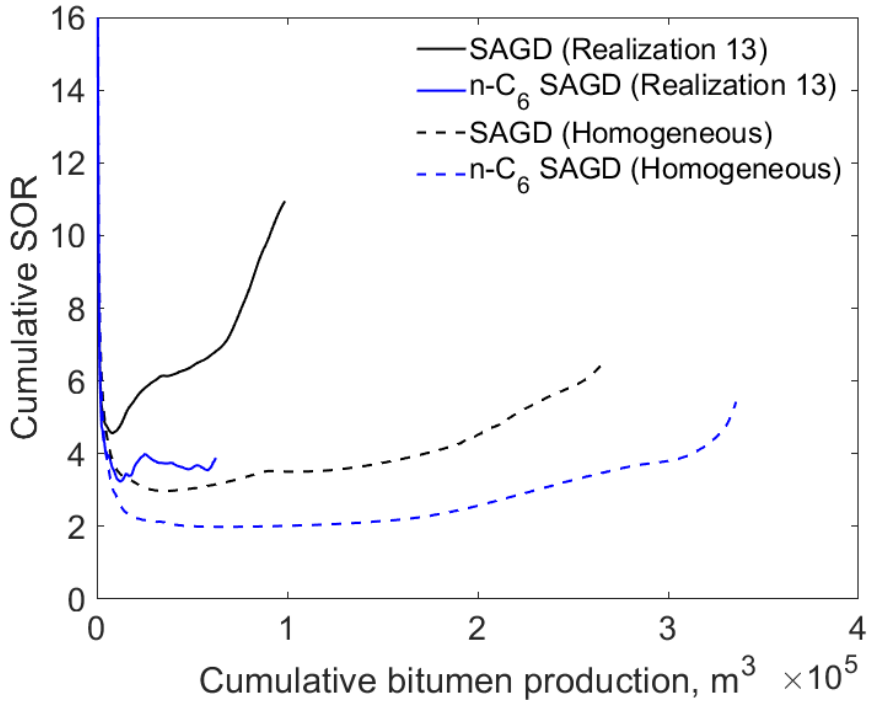

Figure K-5(b). Cumulative SOR for SAGD and n-C_6 SAGD for realization 13

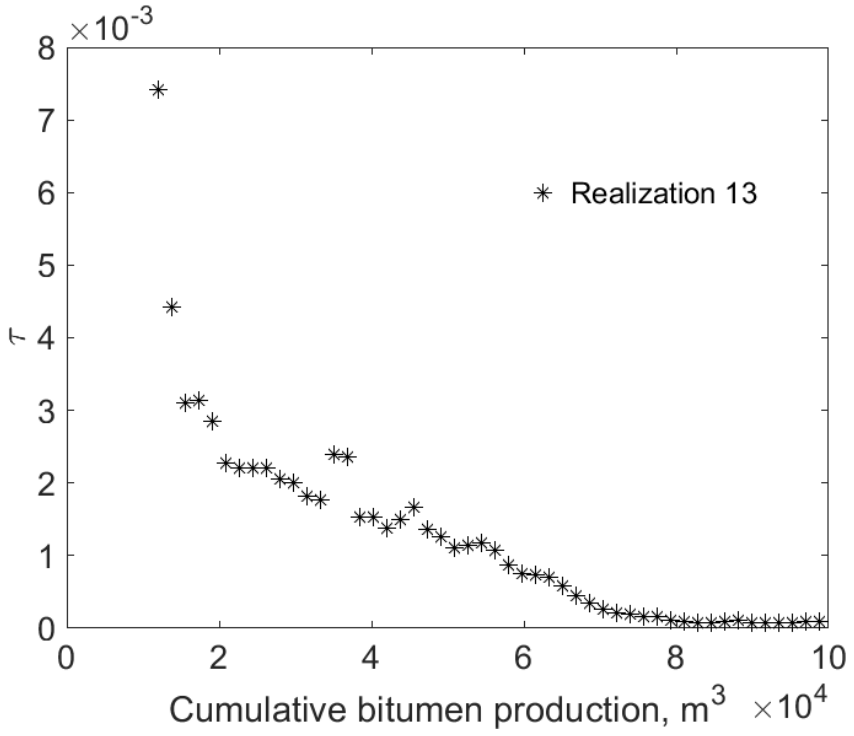

Figure K-5(c). τ for SAGD as a function of cumulative bitumen production for realization 13

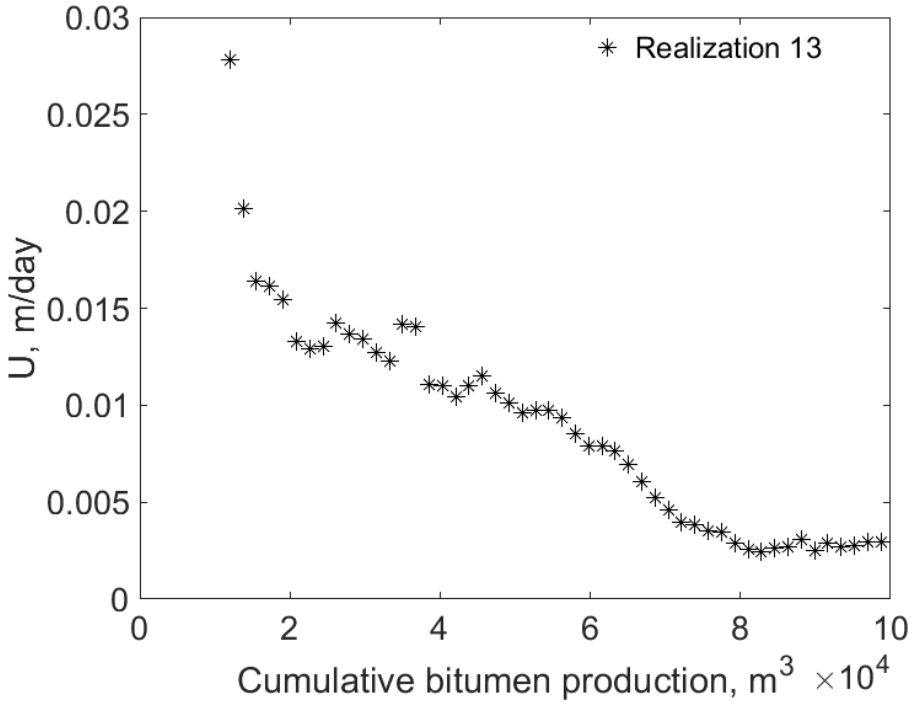

Figure K-5(d). U for SAGD as a function of cumulative bitumen production for realization 13

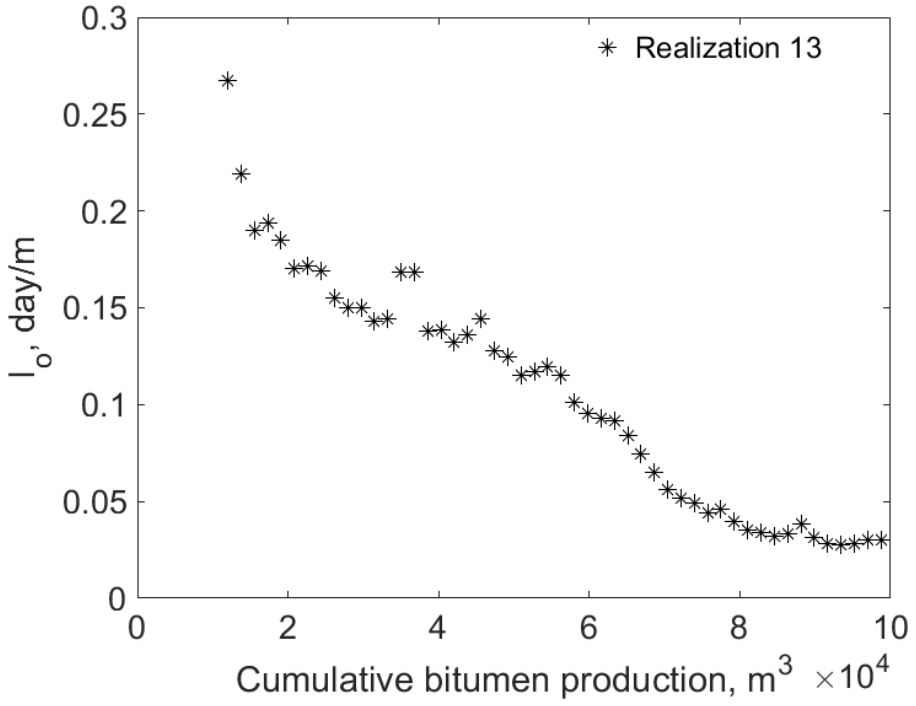

Figure K-5(e).I_o for SAGD as a function of cumulative bitumen production for realization 13

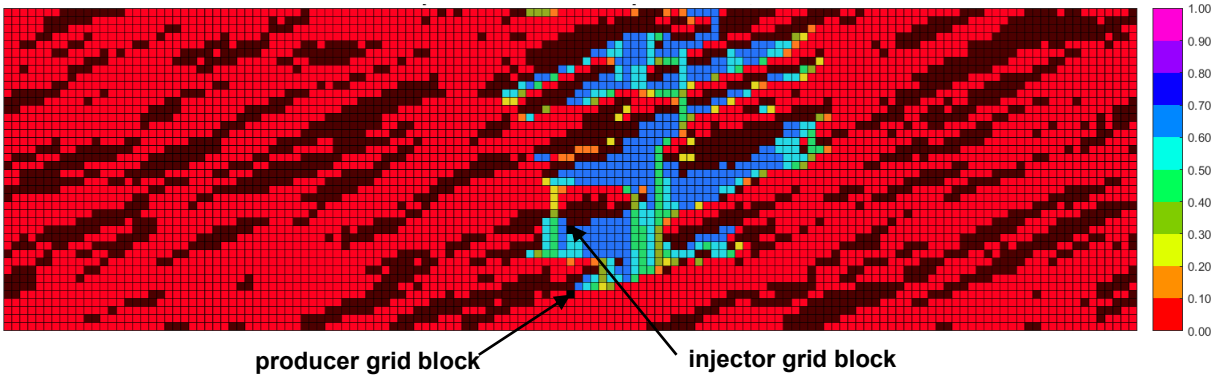

Figure K-5(f). Vapor-phase saturation map in SAGD for realization 13 for Q ≈ 31218 m^3

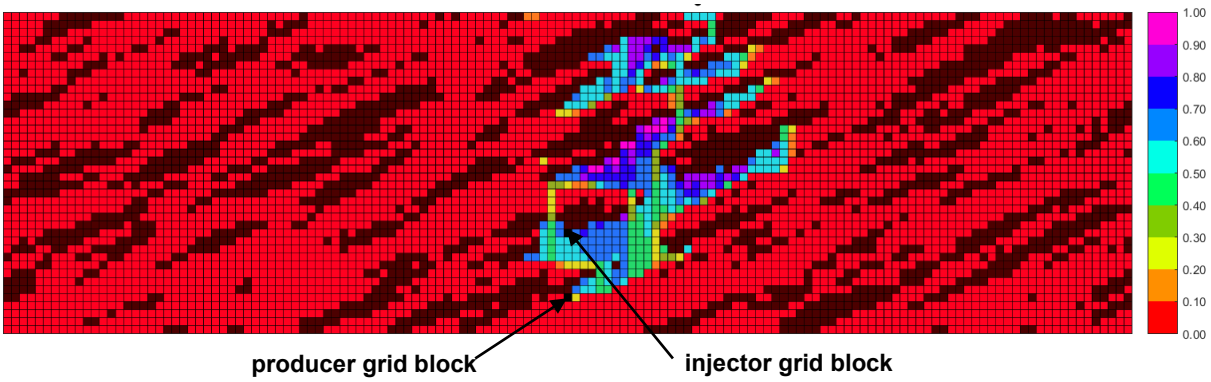

Figure K-5(g). Vapor-phase saturation map in n-C_6 SAGD for realization 13 for Q ≈ 31218 m^3

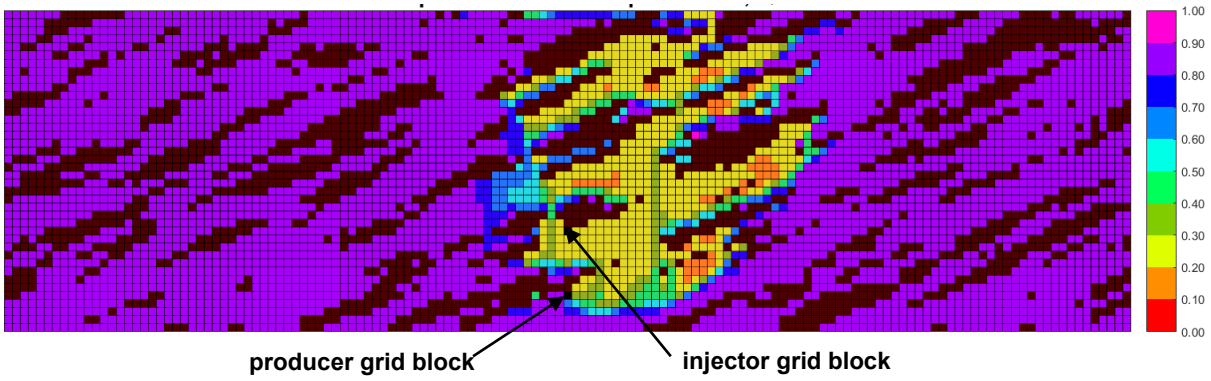

Figure K-5(h). Oleic-phase saturation map in SAGD for realization 13 for Q ≈ 31218 m^3

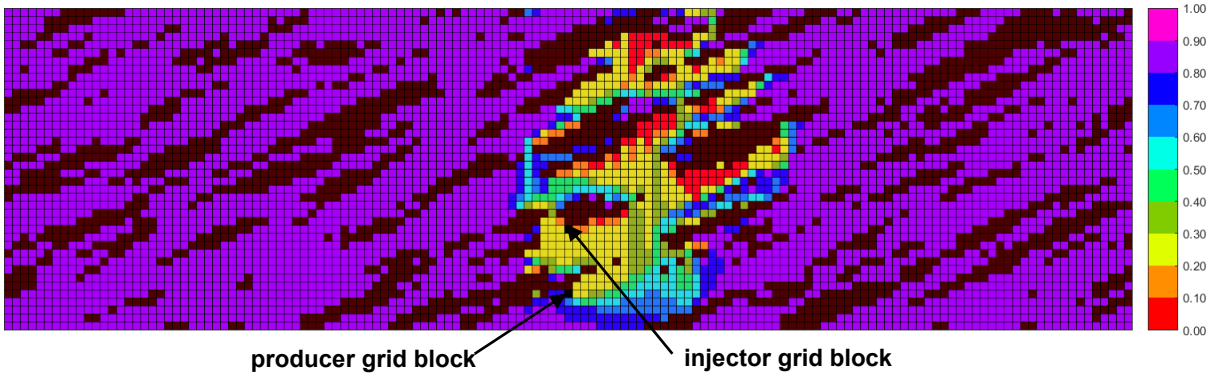

Figure K-5(i). Oleic-phase saturation map in n-C_6 SAGD for realization 13 for Q ≈ 31218 m^3

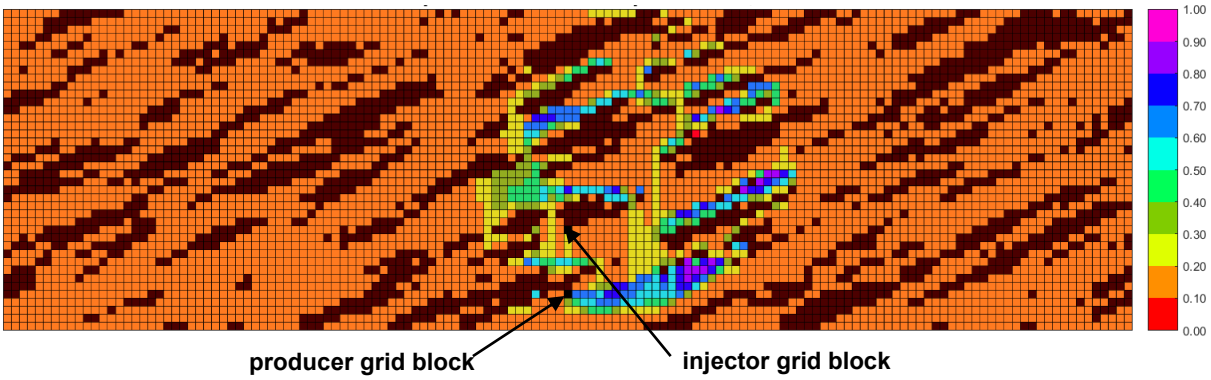

Figure K-5(j). Aqueous-phase saturation map in SAGD for realization 13 for Q ≈ 31218 m^3

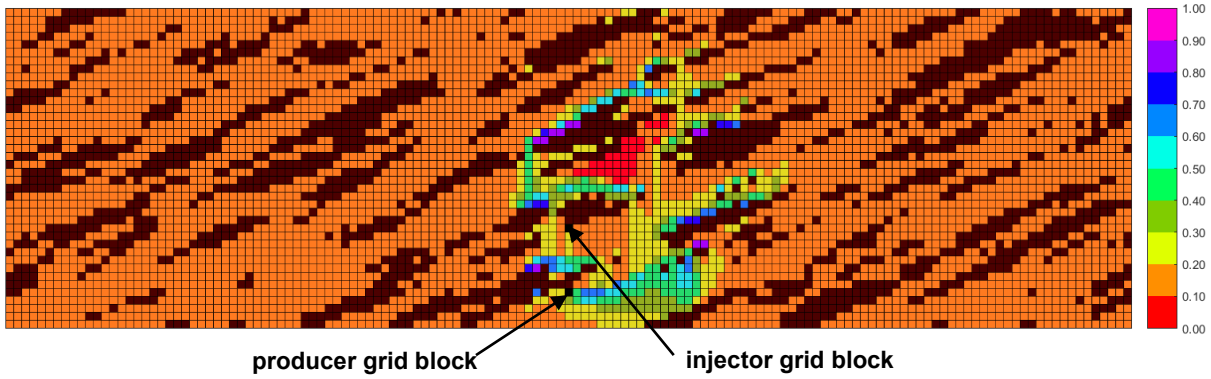

Figure K-5(k). Aqueous-phase saturation map in n-C_6 SAGD for realization 13 for Q ≈ 31218 m^3

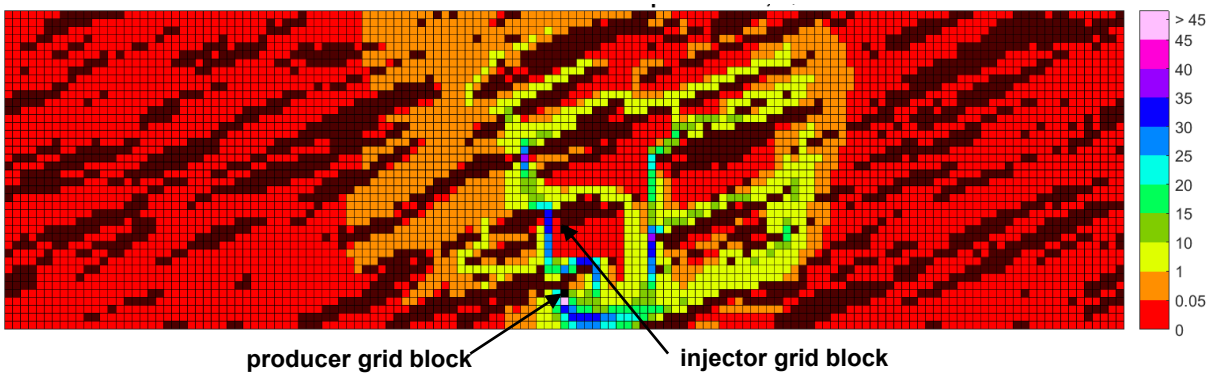

Figure K-5(l). Bitumen molar flow rate (kg-mole/day) map in SAGD for realization 13 for Q ≈ 31218 m^3

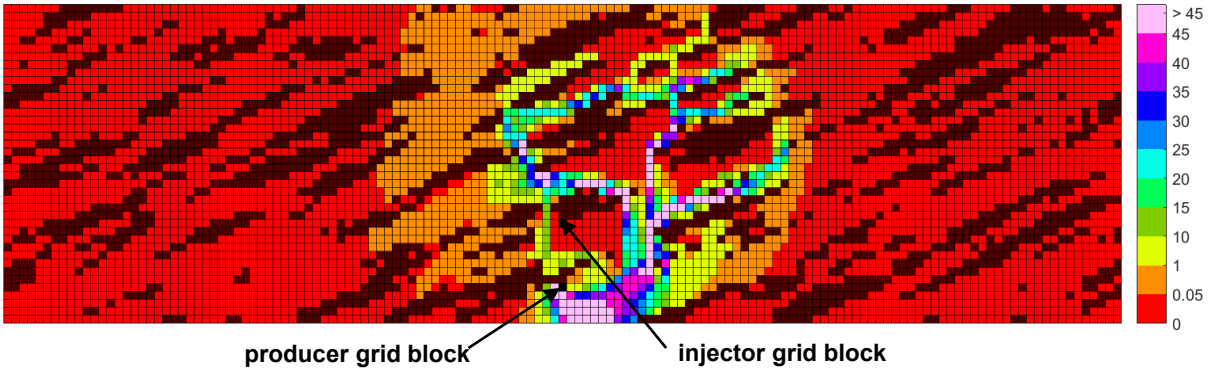

Figure K-5(m). Bitumen molar flow rate (kg-mole/day) map in n-C_6 SAGD for realization 13 for Q ≈ 31218 m^3

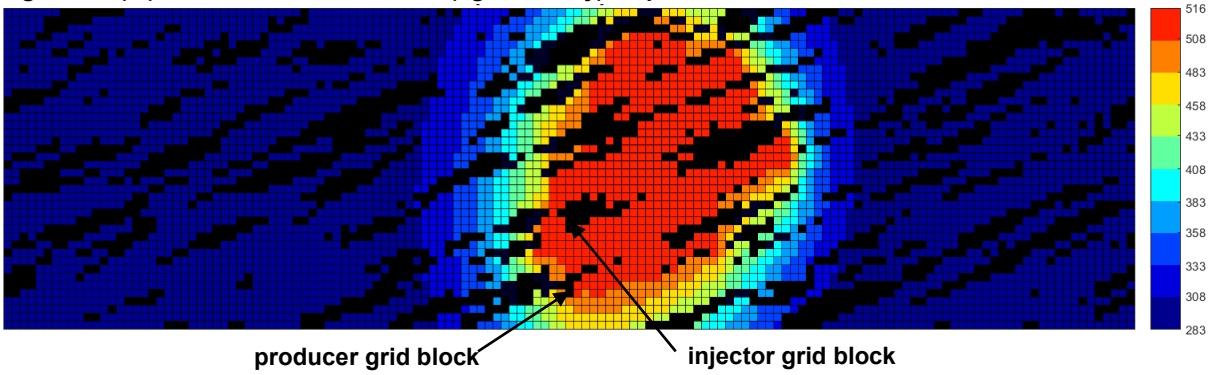

Figure K-5(n). Temperature (Kelvin) map in SAGD for realization 13 for Q ≈ 31218 m^3

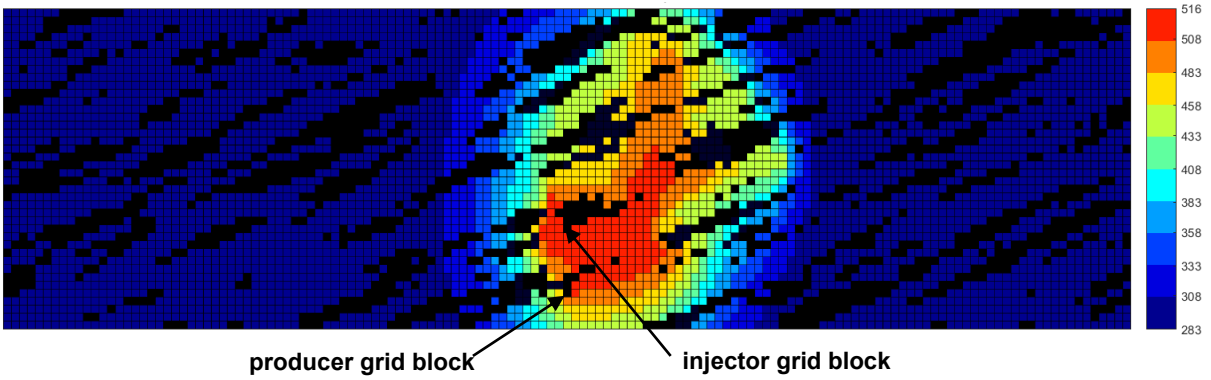

Figure K-5(o). Temperature (Kelvin) map in n-C_6 SAGD for realization 13 for Q ≈ 31218 m^3

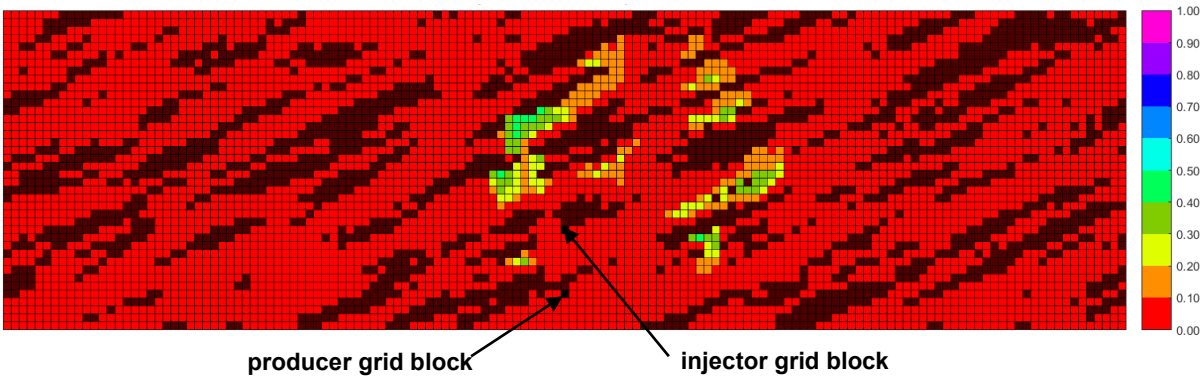

Figure K-5(p). $\beta_L x_{sL}$ map in n-C_6 SAGD for realization 13 for Q ≈ 31218 m^3

Figure K-5. Property maps for SAGD and n-C_6 SAGD for realization 13

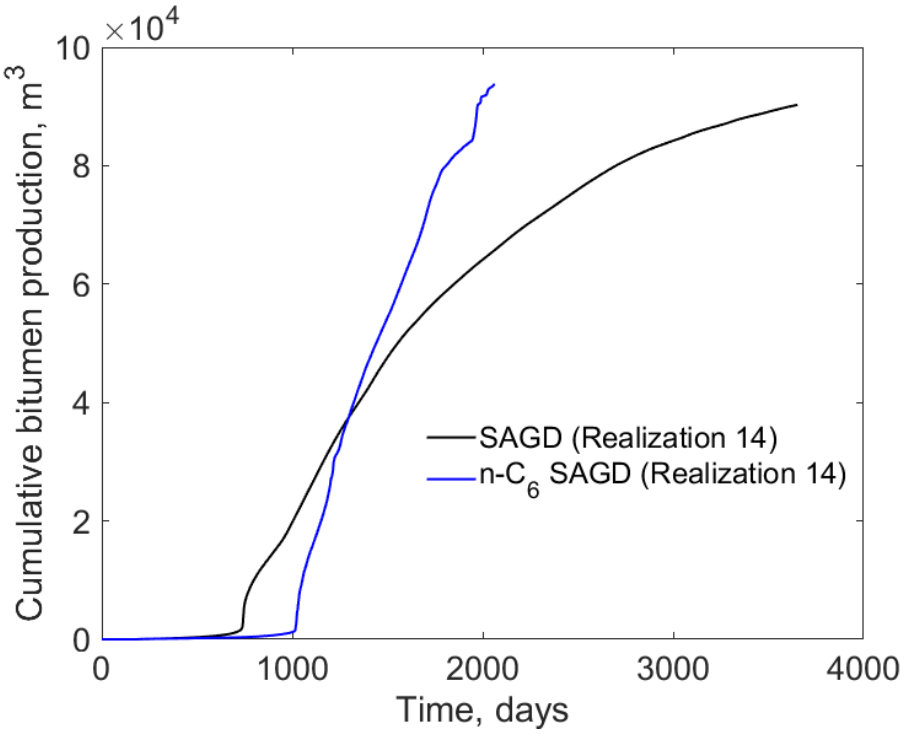

Figure K-6(a). Cumulative bitumen production histories for SAGD and n-C_6 SAGD for realization 14

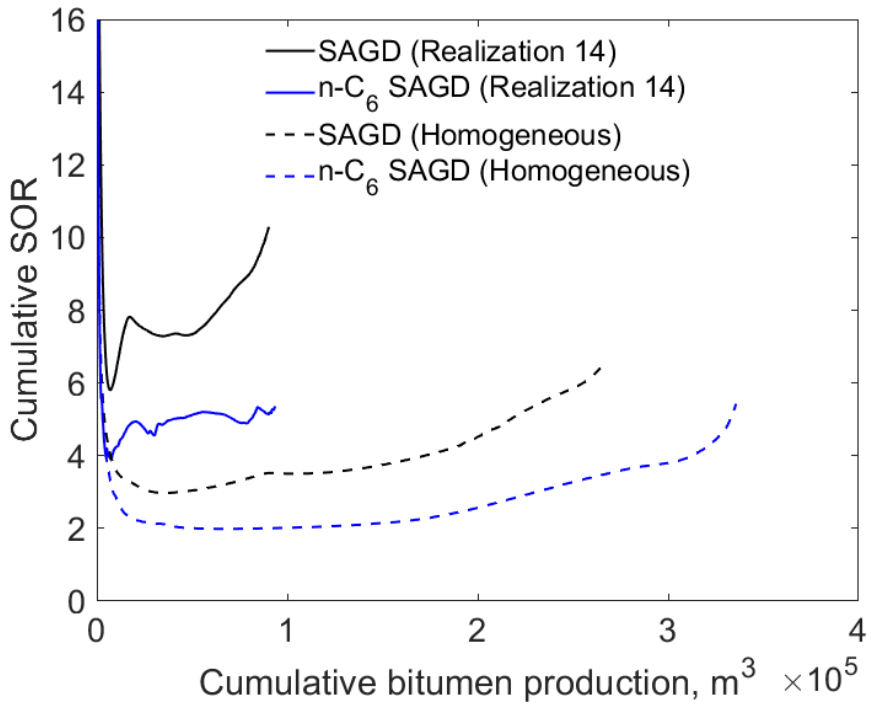

Figure K-6(b). Cumulative SOR for SAGD and n-C_6 SAGD for realization 14

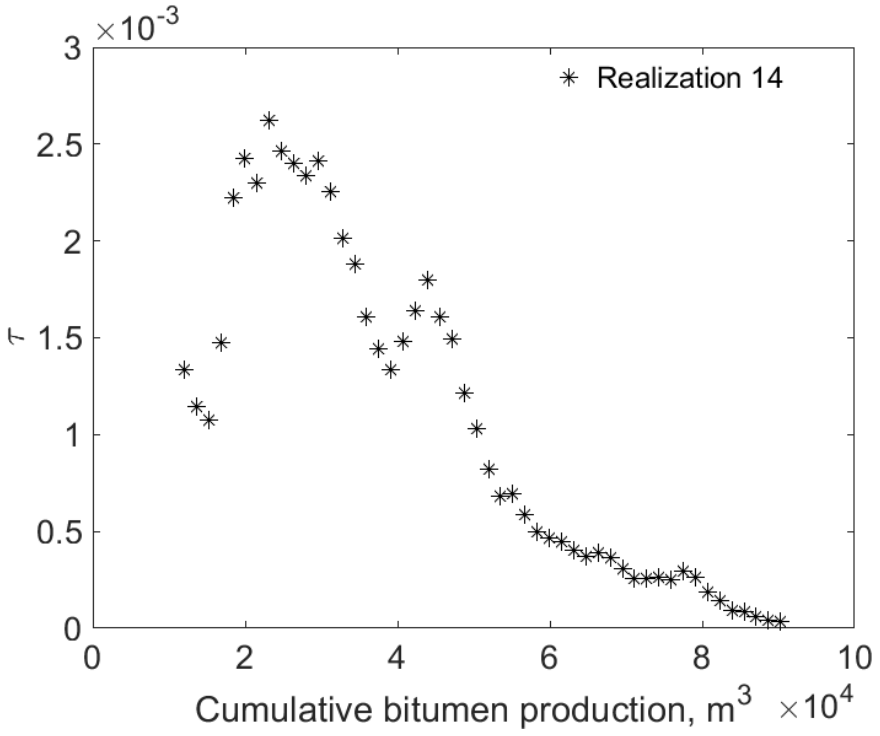

Figure K-6(c). τ for SAGD as a function of cumulative bitumen production for realization 14

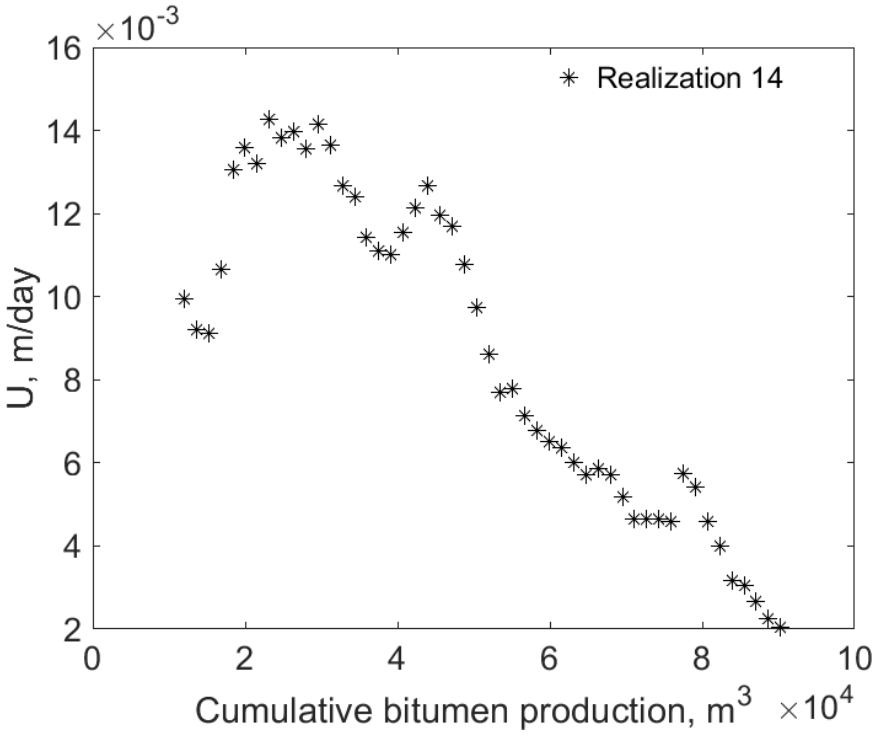

Figure K-6(d). U for SAGD as a function of cumulative bitumen production for realization 14

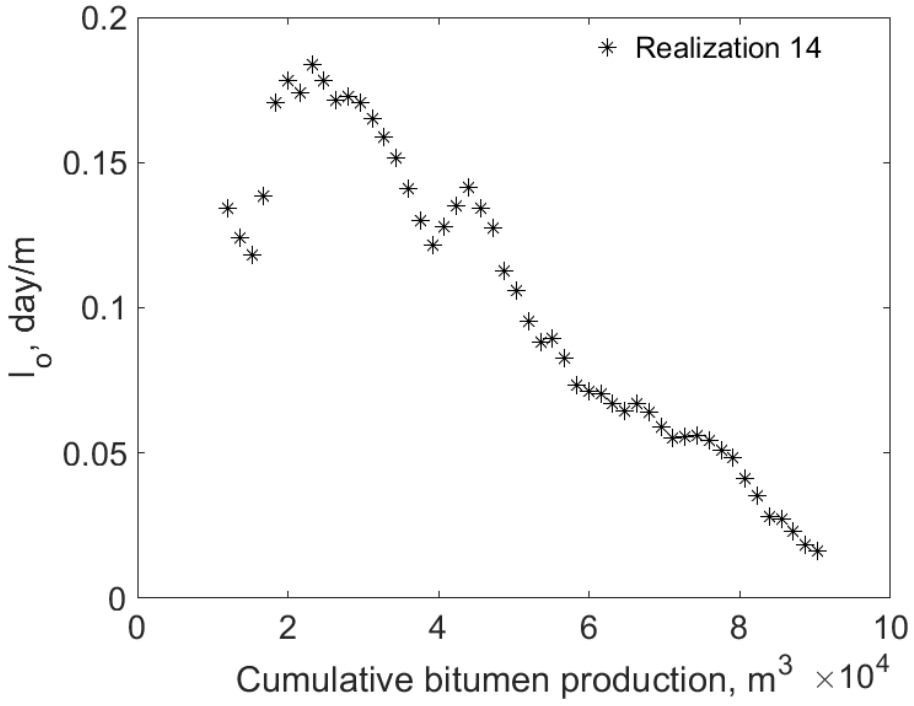

Figure K-6(e).I_o for SAGD as a function of cumulative bitumen production for realization 14

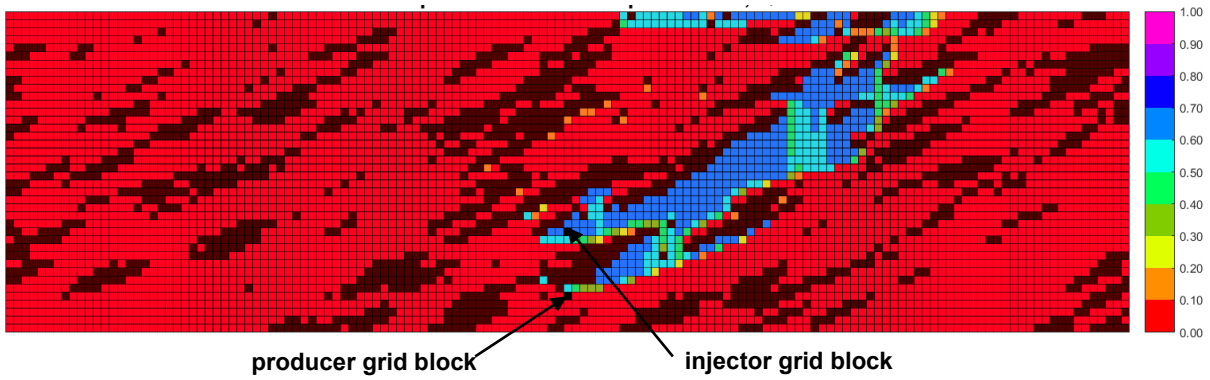

Figure K-6(f). Vapor-phase saturation map in SAGD for realization 14 for Q ≈ 31218 m^3

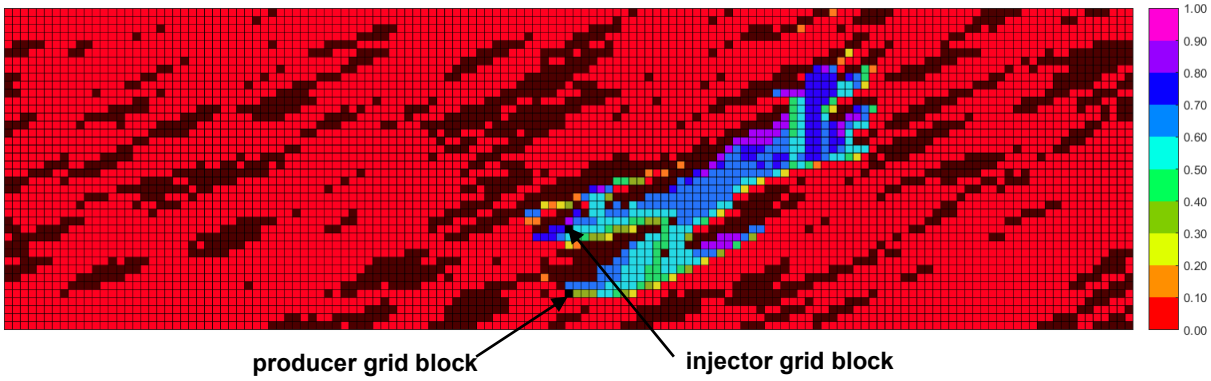

Figure K-6(g). Vapor-phase saturation map in n-C_6 SAGD for realization 14 for Q ≈ 31218 m^3

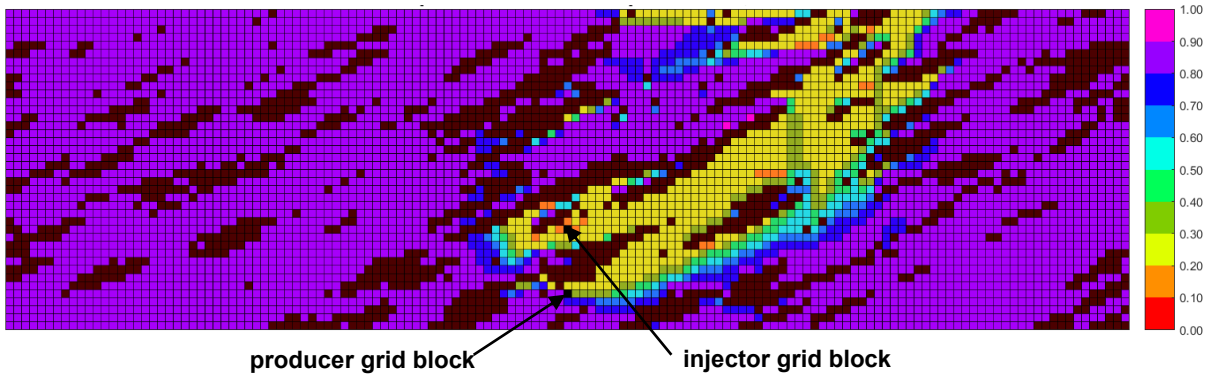

Figure K-6(h). Oleic-phase saturation map in SAGD for realization 14 for Q ≈ 31218 m^3

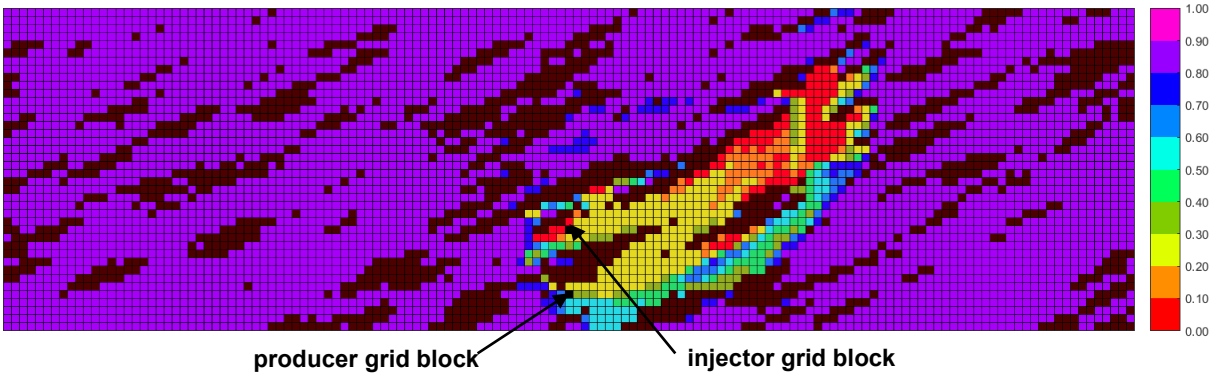

Figure K-6(i). Oleic-phase saturation map in n-C_6 SAGD for realization 14 for Q ≈ 31218 m^3

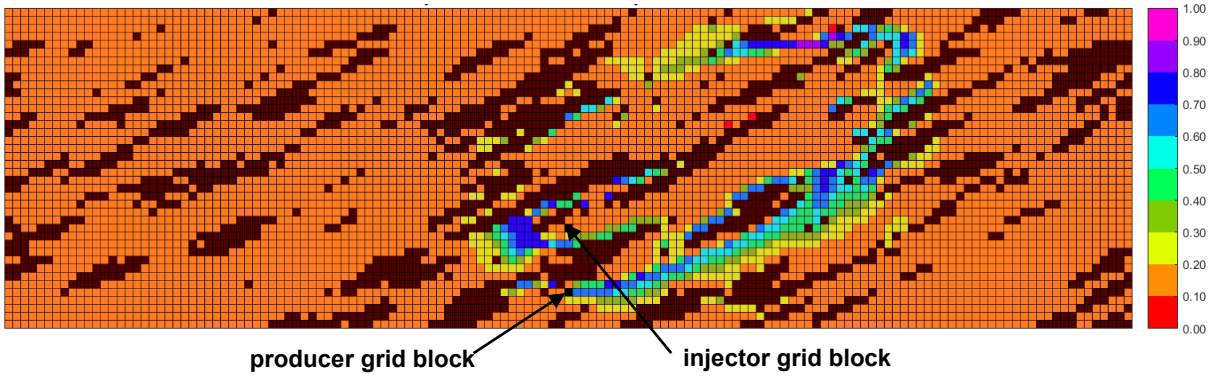

Figure K-6(j). Aqueous-phase saturation map in SAGD for realization 14 for Q ≈ 31218 m^3

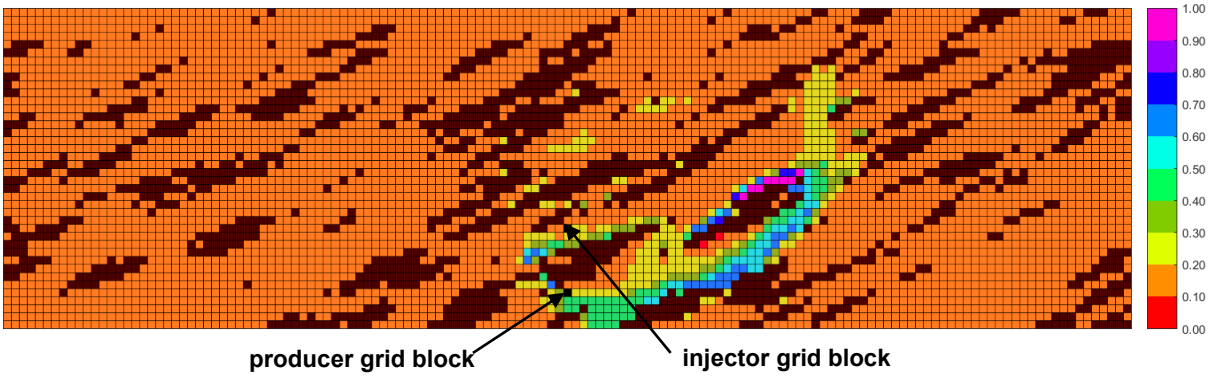

Figure K-6(k). Aqueous-phase saturation map in n-C_6 SAGD for realization 14 for Q ≈ 31218 m^3

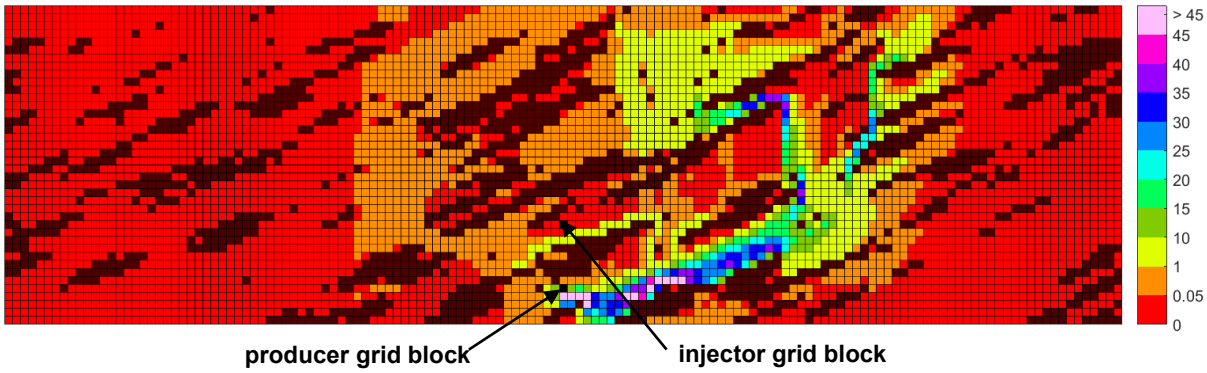

Figure K-6(l). Bitumen molar flow rate (kg-mole/day) map in SAGD for realization 14 for Q ≈ 31218 m^3

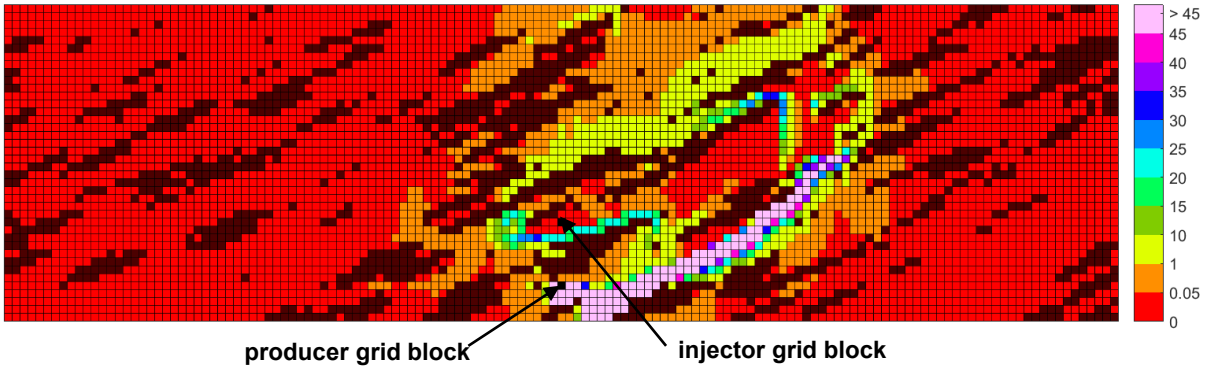

Figure K-6(m). Bitumen molar flow rate (kg-mole/day) map in n-C_6 SAGD for realization 14 for Q ≈ 31218 m^3

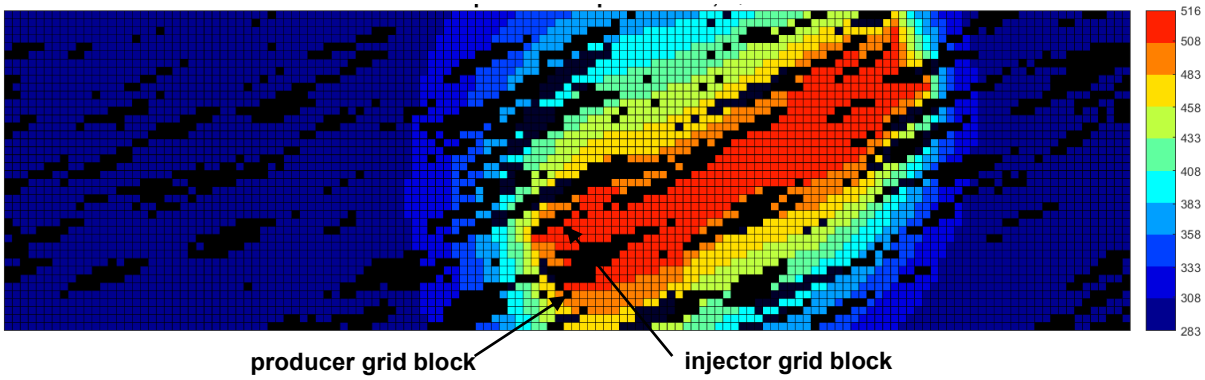

Figure K-6(n). Temperature (Kelvin) map in SAGD for realization 14 for Q ≈ 31218 m^3

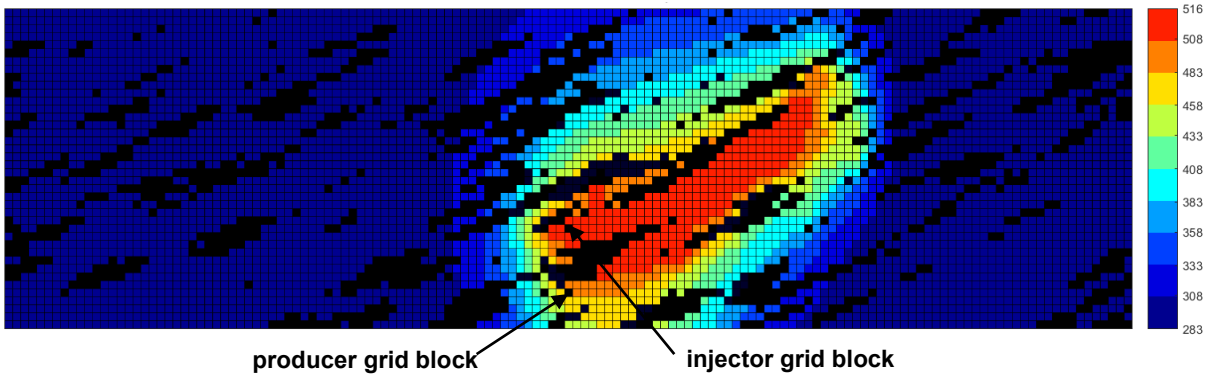

Figure K-6(o). Temperature (Kelvin) map in n-C_6 SAGD for realization 14 for Q ≈ 31218 m^3

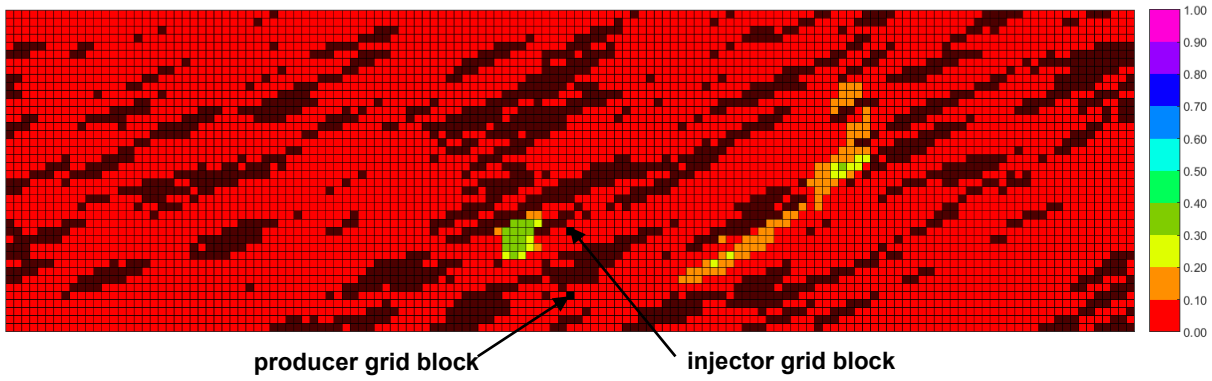

Figure K-6(p). $\beta_L x_{sL}$ map in n-C_6 SAGD for realization 14 for Q ≈ 31218 m^3

Figure K-6. Property maps for SAGD and n-C_6 SAGD for realization 14

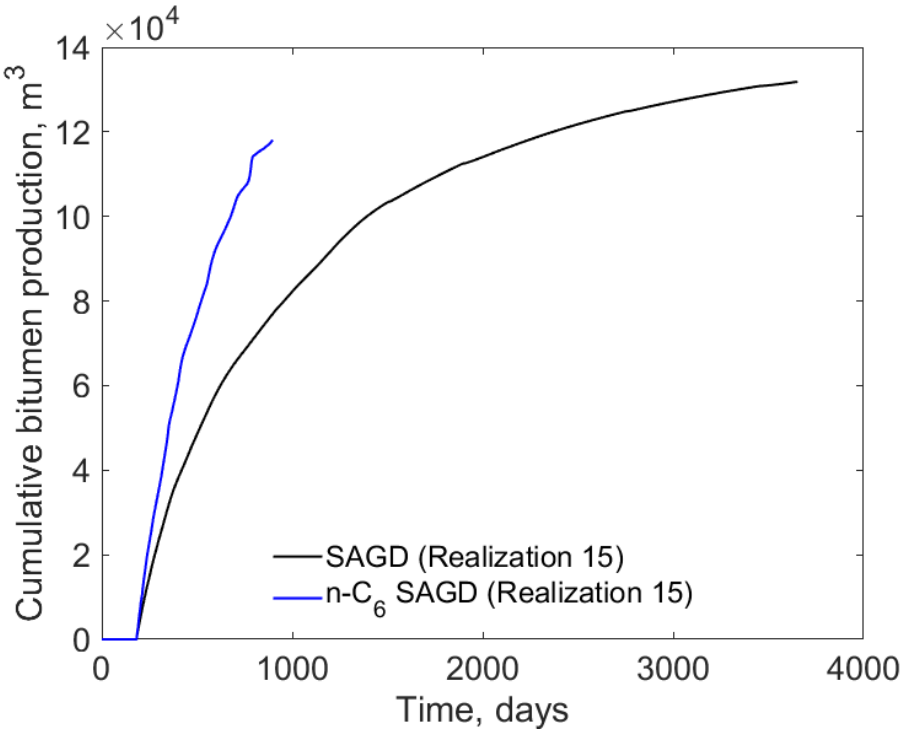

Figure K-7(a). Cumulative bitumen production histories for SAGD and n-C_6 SAGD for realization 15

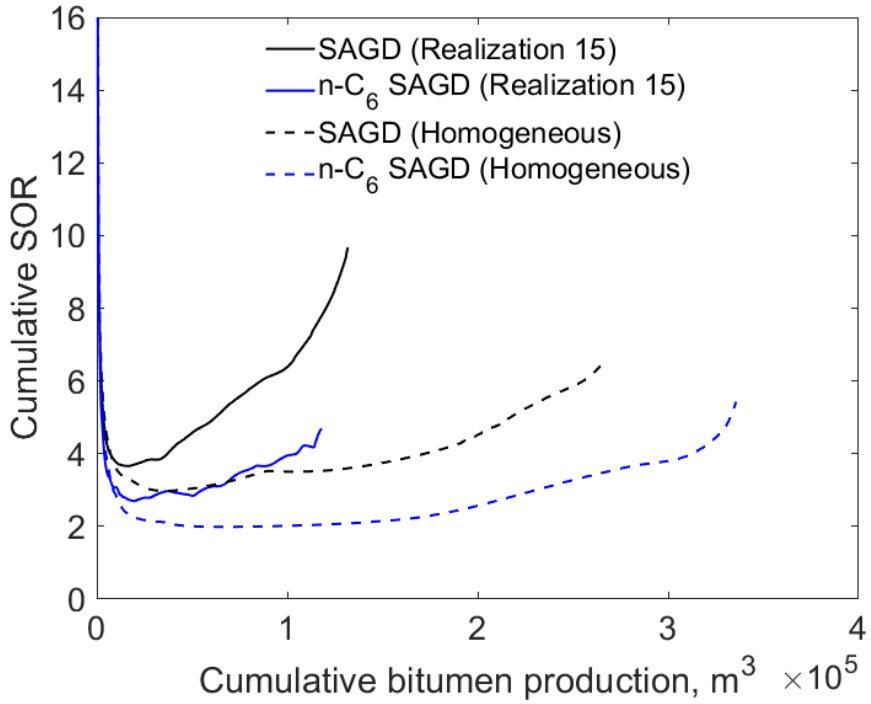

Figure K-7(b). Cumulative SOR for SAGD and n-C_6 SAGD for realization 15

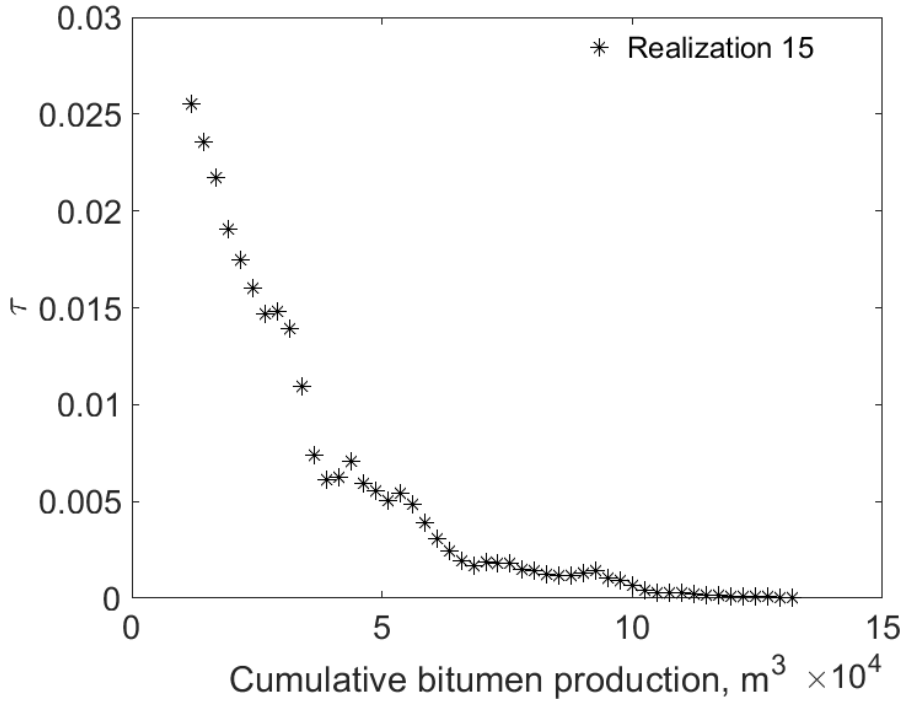

Figure K-7(c). τ for SAGD as a function of cumulative bitumen production for realization 15

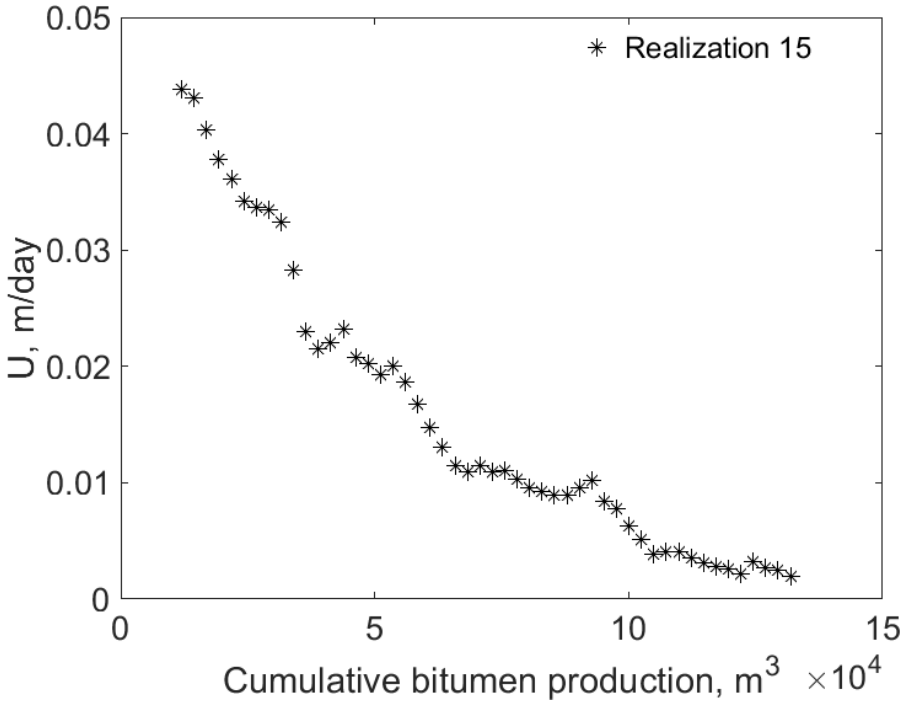

Figure K-7(d). U for SAGD as a function of cumulative bitumen production for realization 15

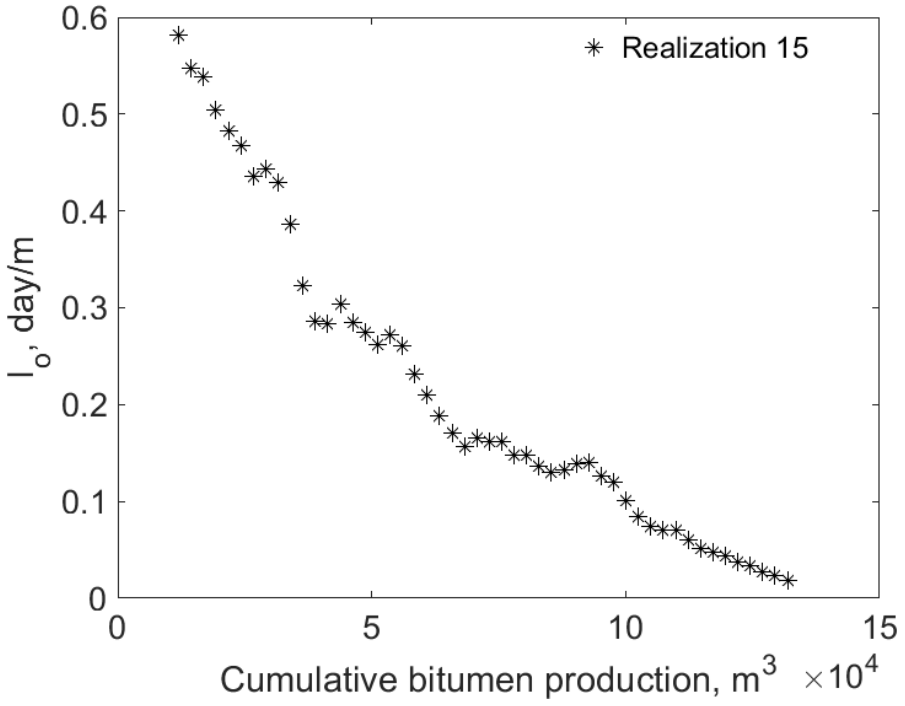

Figure K-7(e).I_o for SAGD as a function of cumulative bitumen production for realization 15

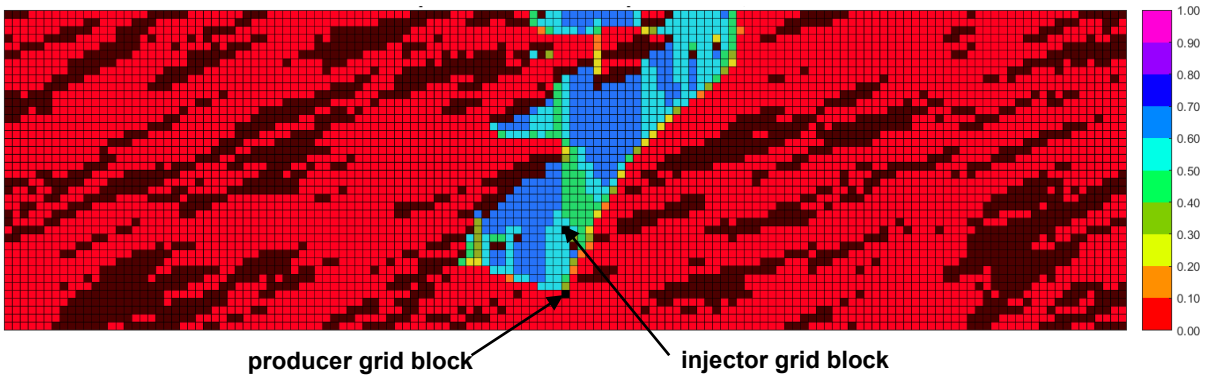

Figure K-7(f). Vapor-phase saturation map in SAGD for realization 15 for Q ≈ 31218 m^3

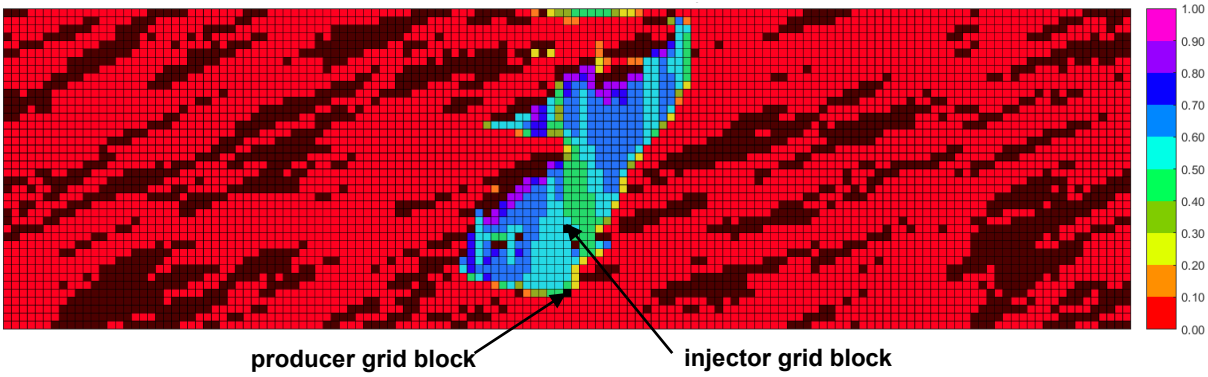

Figure K-7(g). Vapor-phase saturation map in n-C_6 SAGD for realization 15 for Q ≈ 31218 m^3

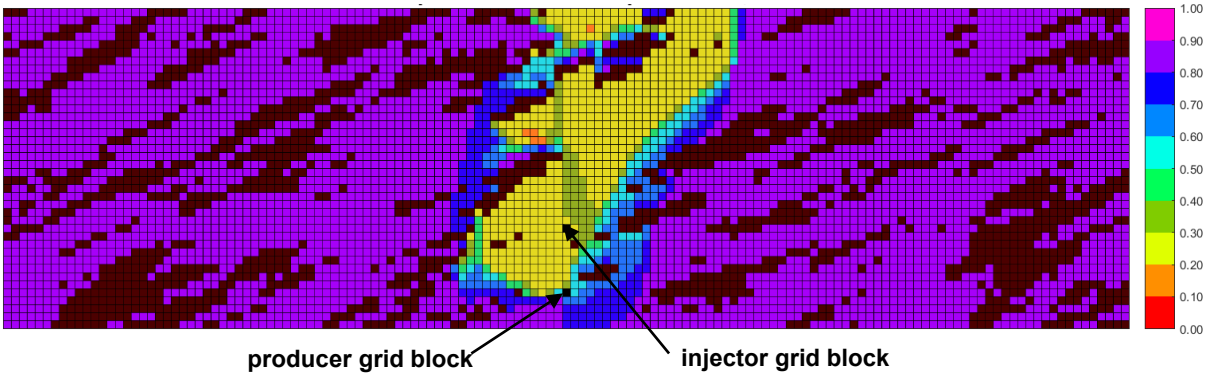

Figure K-7(h). Oleic-phase saturation map in SAGD for realization 15 for Q ≈ 31218 m^3

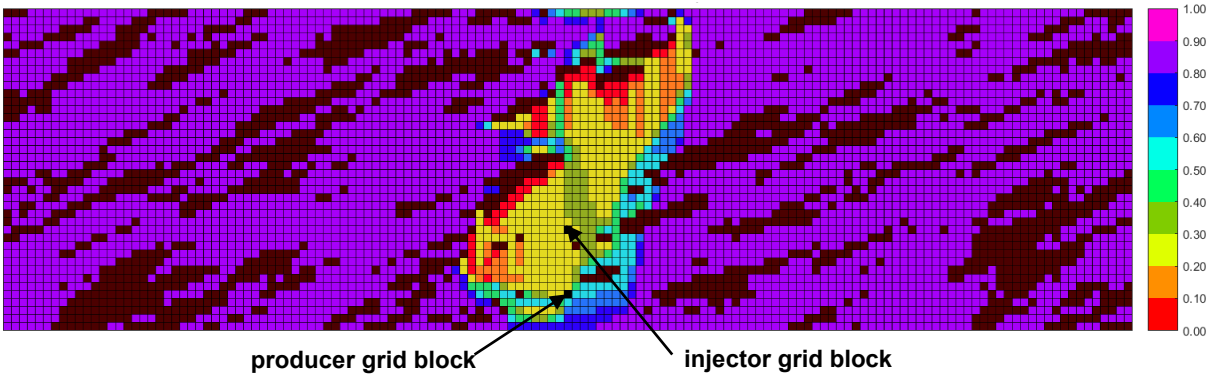

Figure K-7(i). Oleic-phase saturation map in n-C_6 SAGD for realization 15 for Q ≈ 31218 m^3

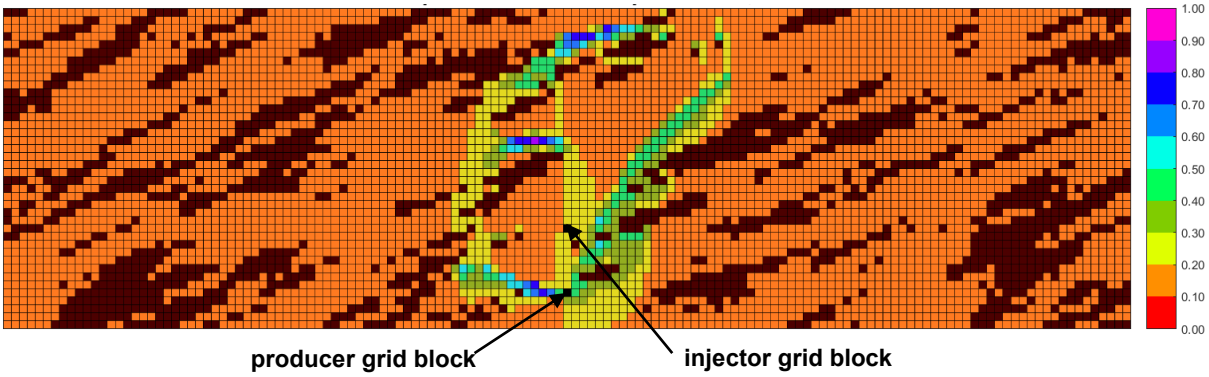

Figure K-7(j). Aqueous-phase saturation map in SAGD for realization 15 for Q ≈ 31218 m^3

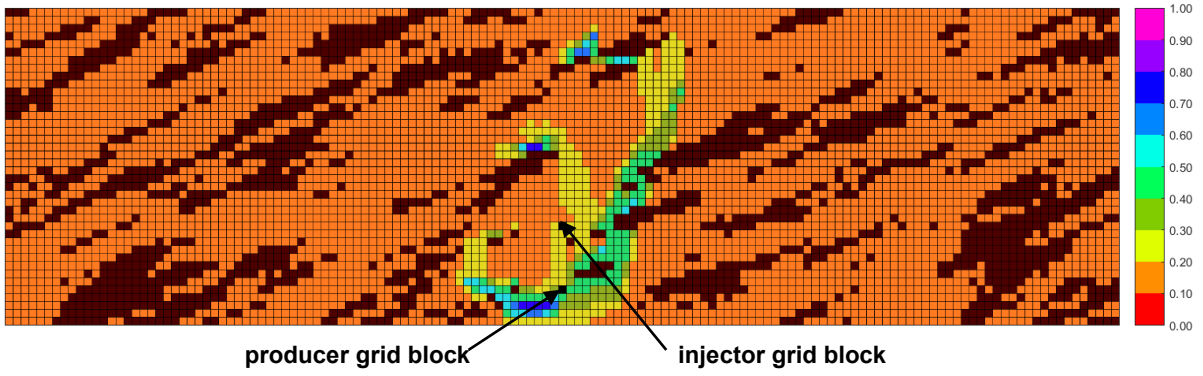

Figure K-7(k). Aqueous-phase saturation map in n-C_6 SAGD for realization 15 for Q ≈ 31218 m^3

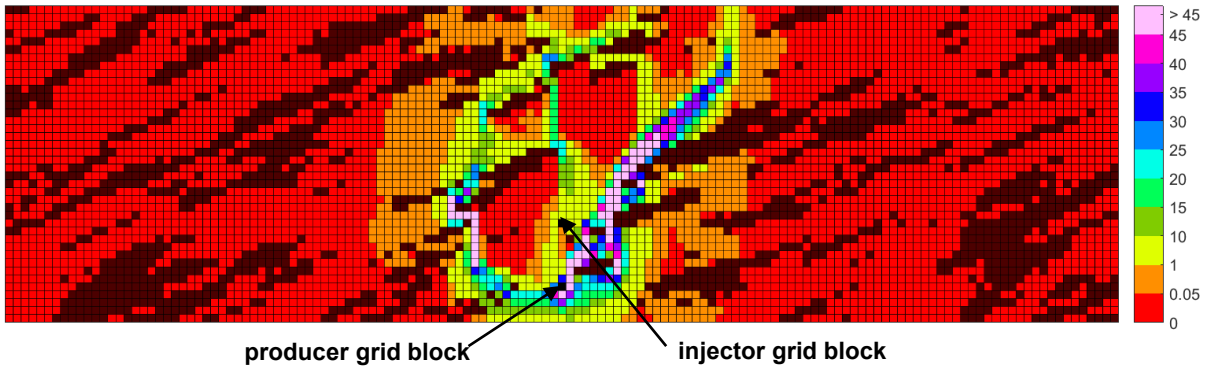

Figure K-7(l). Bitumen molar flow rate (kg-mole/day) map in SAGD for realization 15 for Q ≈ 31218 m^3

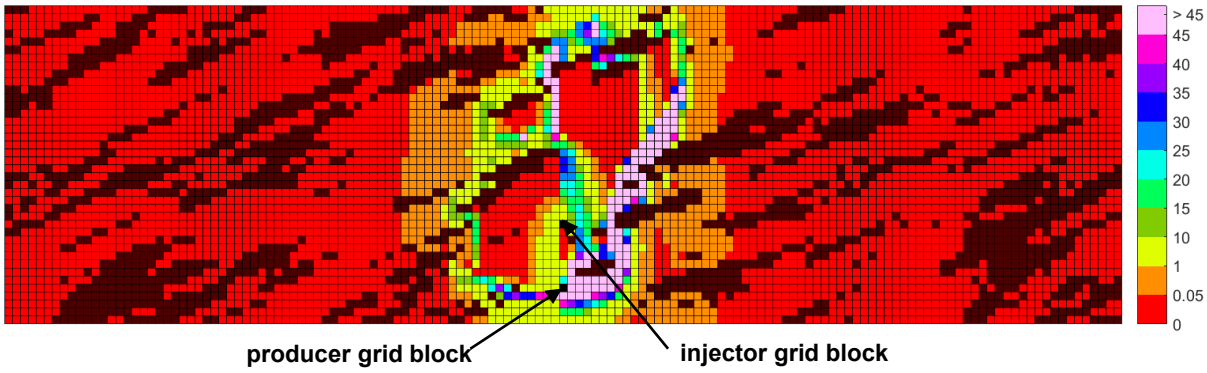

Figure K-7(m). Bitumen molar flow rate (kg-mole/day) map in n-C_6 SAGD for realization 15 for Q ≈ 31218 m^3

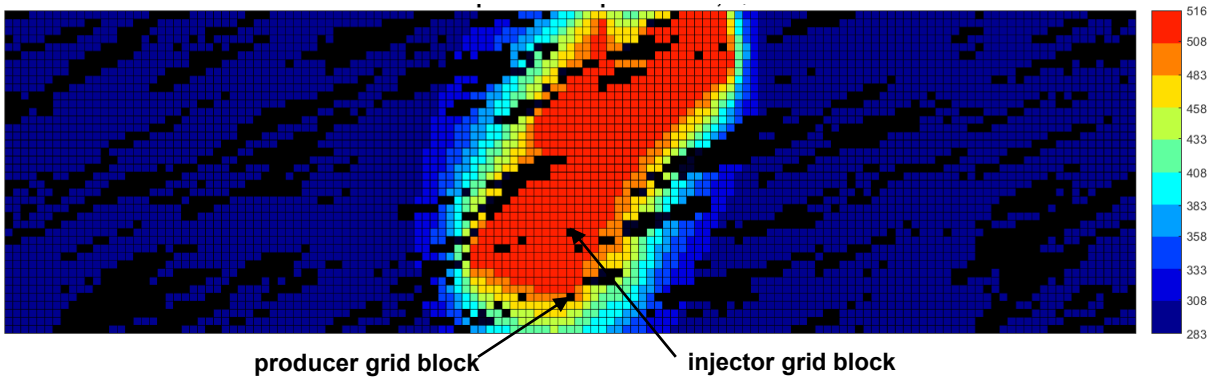

Figure K-7(n). Temperature (Kelvin) map in SAGD for realization 15 for Q ≈ 31218 m^3

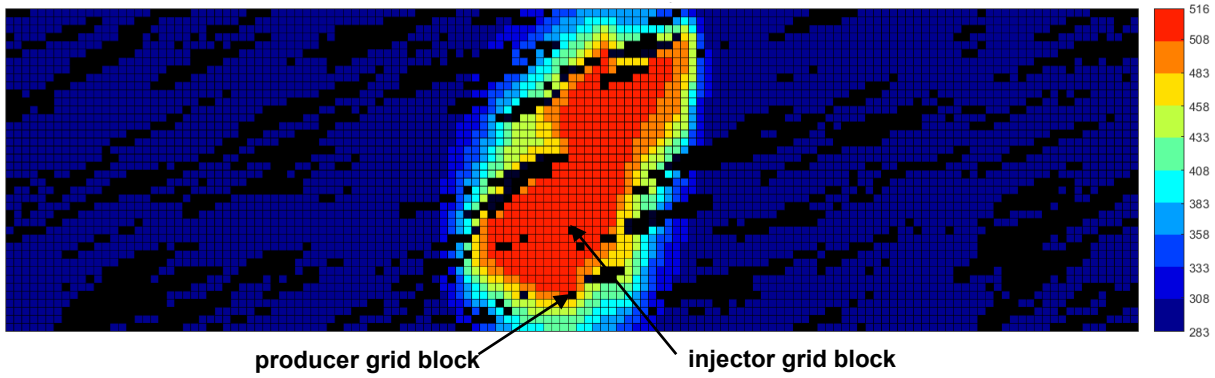

Figure K-7(o). Temperature (Kelvin) map in n-C_6 SAGD for realization 15 for Q ≈ 31218 m^3

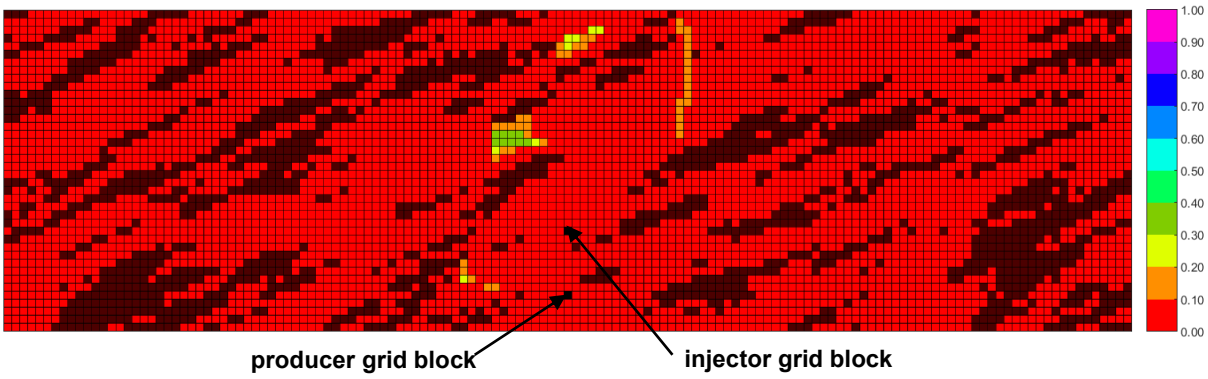

Figure K-7(p). $\beta_L x_{sL}$ map in n-C_6 SAGD for realization 15 for Q ≈ 31218 m^3

Figure K-7. Property maps for SAGD and n-C_6 SAGD for realization 15

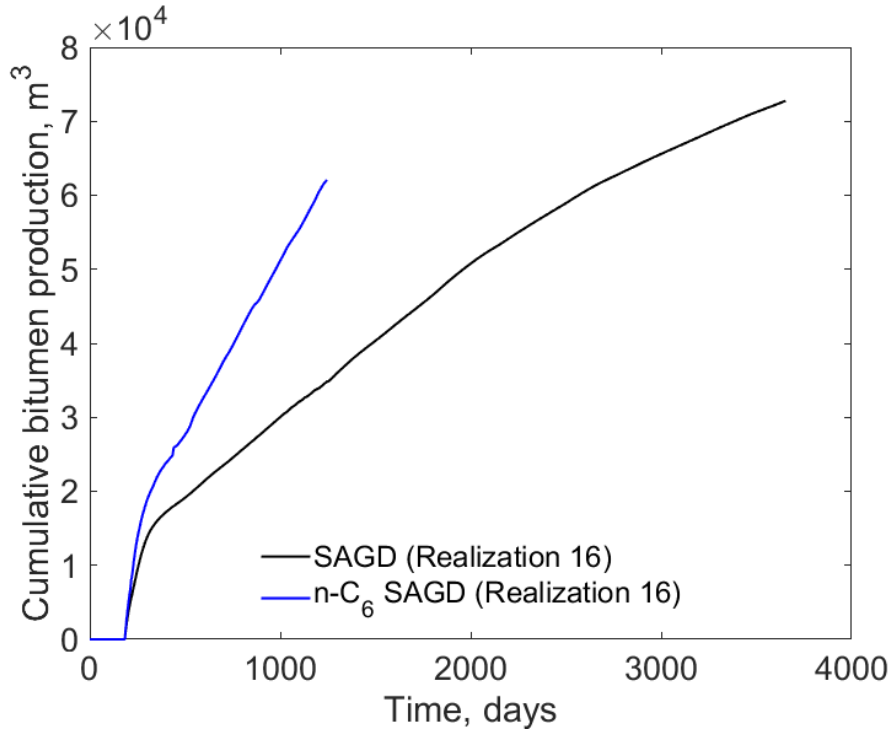

Figure K-8(a). Cumulative bitumen production histories for SAGD and n-C_6 SAGD for realization 16

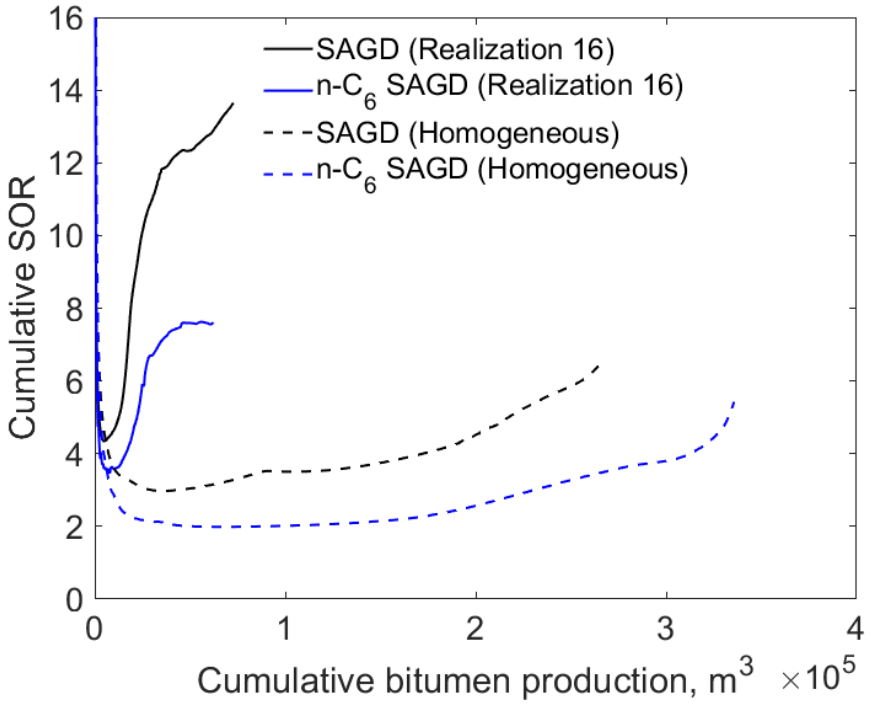

Figure K-8(b). Cumulative SOR for SAGD and n-C_6 SAGD for realization 16

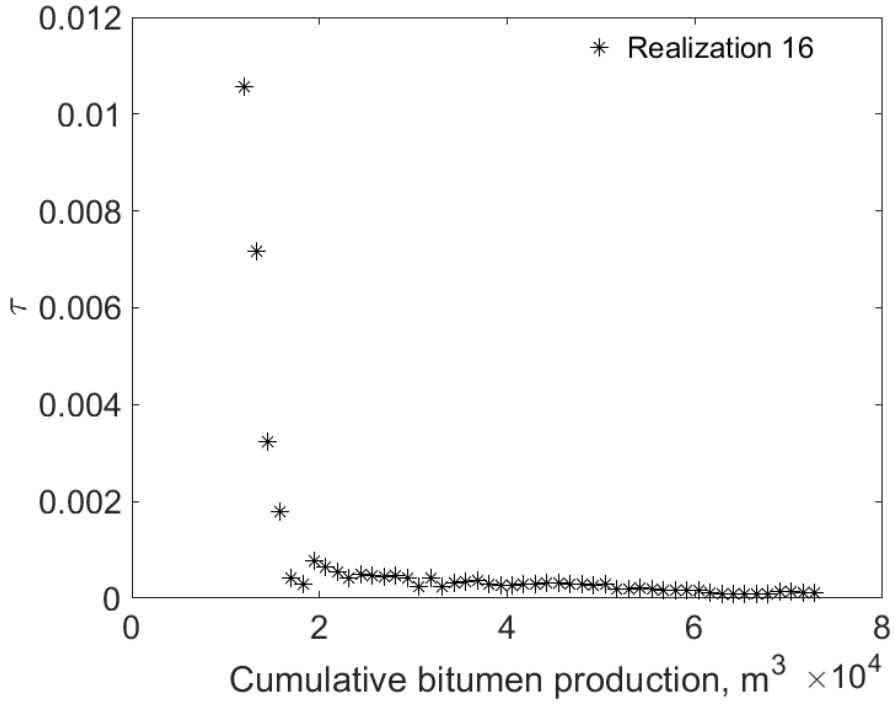

Figure K-8(c). τ for SAGD as a function of cumulative bitumen production for realization 16

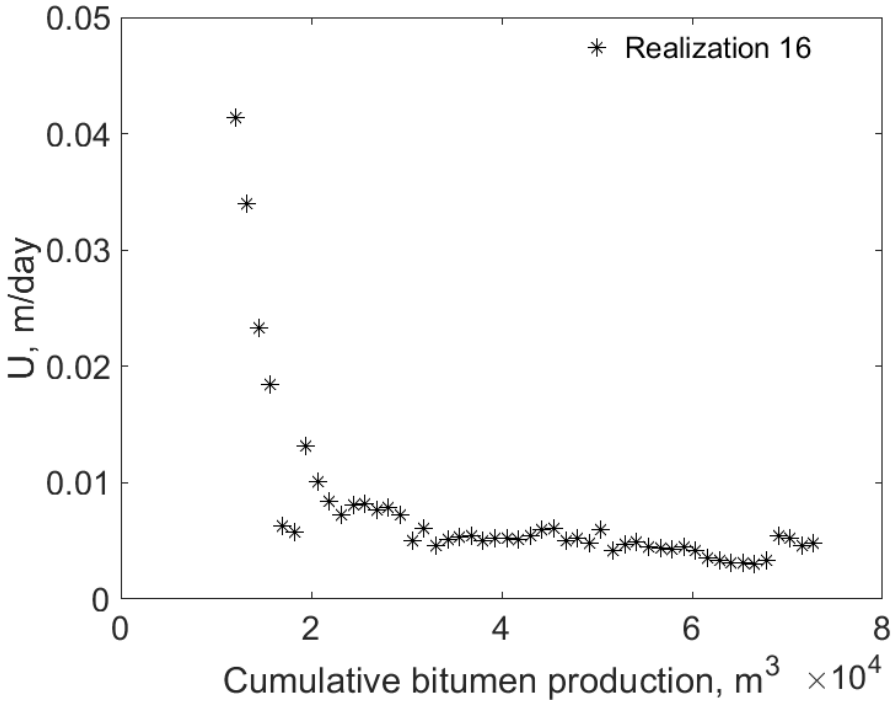

Figure K-8(d). U for SAGD as a function of cumulative bitumen production for realization 16

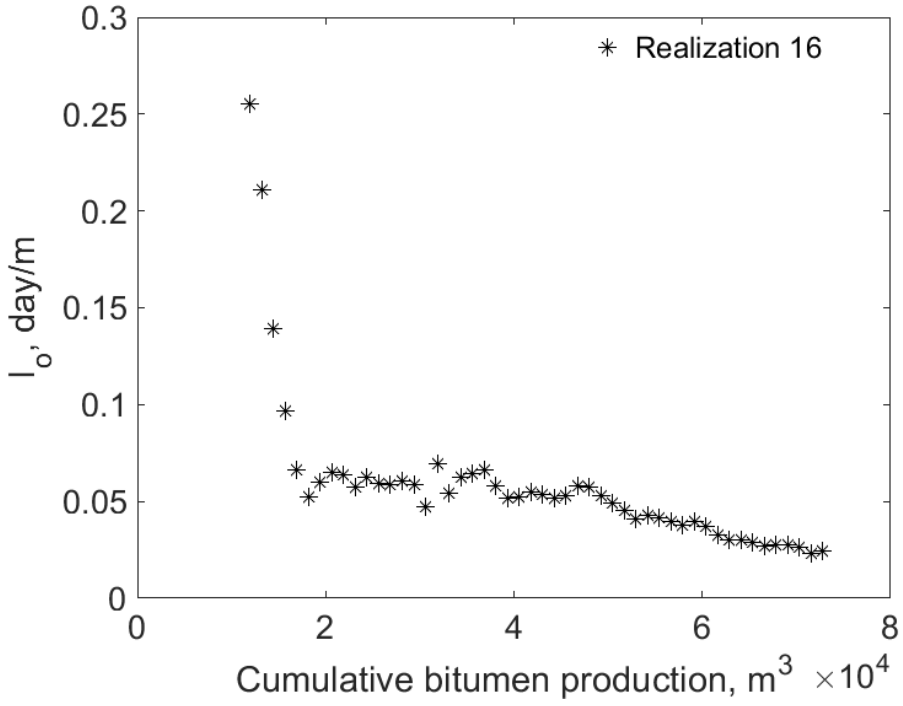

Figure K-8(e).I_o for SAGD as a function of cumulative bitumen production for realization 16

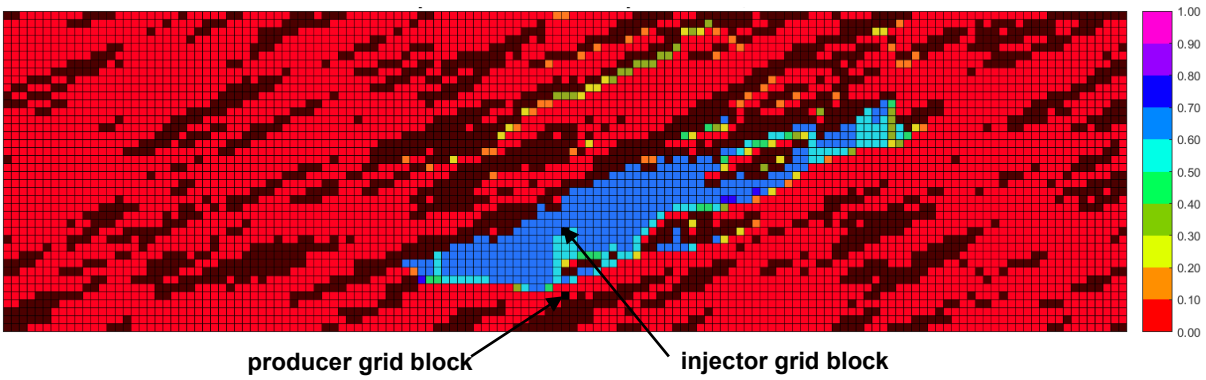

Figure K-8(f). Vapor-phase saturation map in SAGD for realization 16 for Q ≈ 31218 m^3

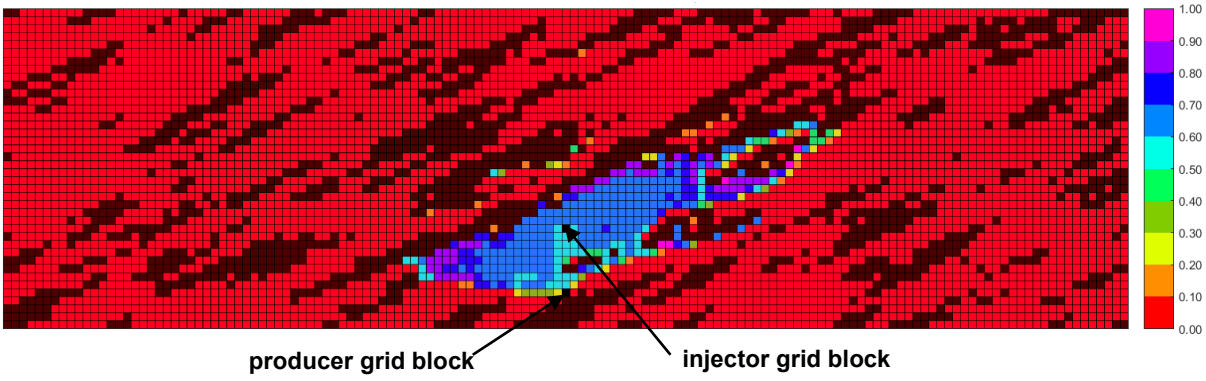

Figure K-8(g). Vapor-phase saturation map in n-C_6 SAGD for realization 16 for Q ≈ 31218 m^3

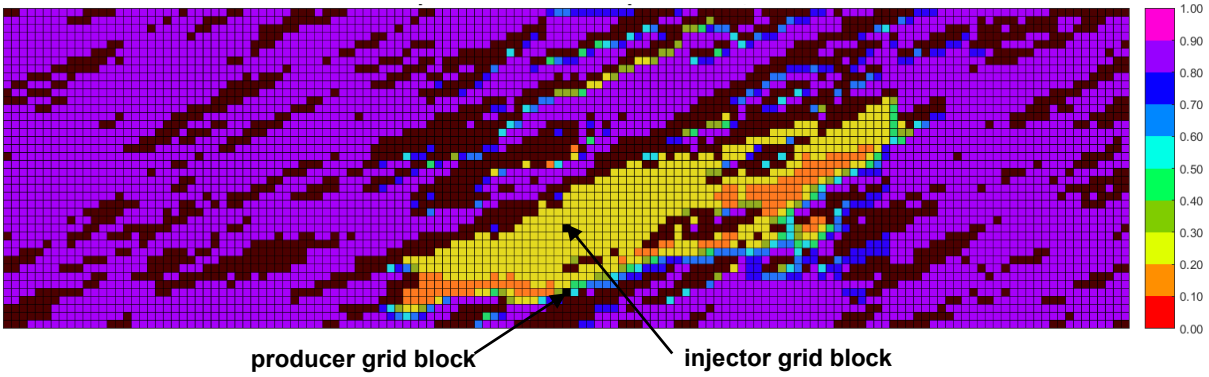

Figure K-8(h). Oleic-phase saturation map in SAGD for realization 16 for Q ≈ 31218 m^3

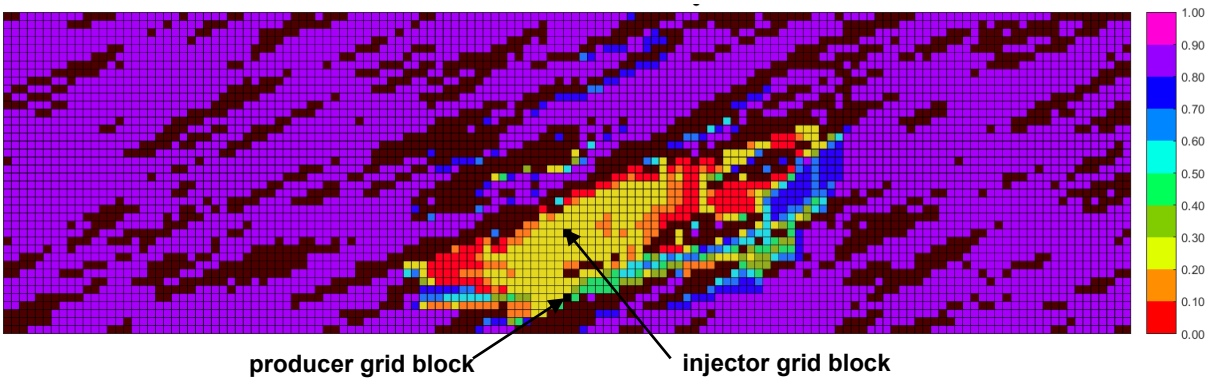

Figure K-8(i). Oleic-phase saturation map in n-C_6 SAGD for realization 16 for Q ≈ 31218 m^3

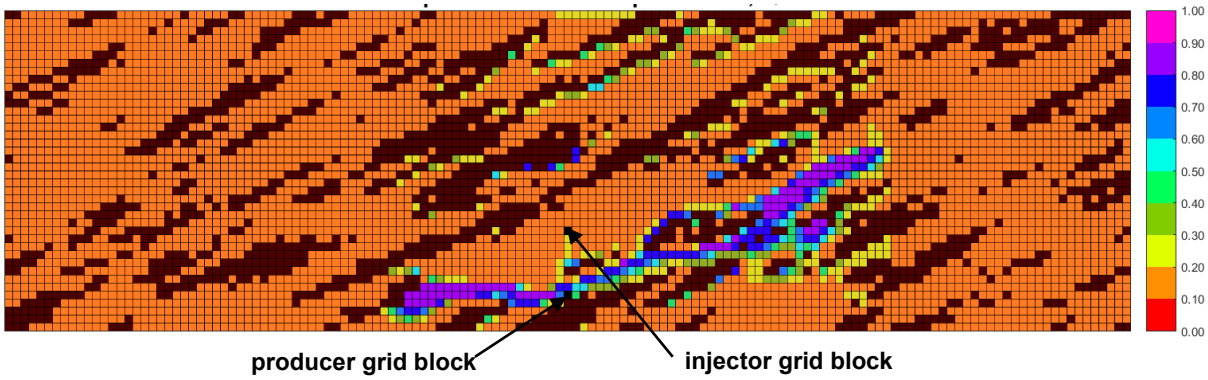

Figure K-8(j). Aqueous-phase saturation map in SAGD for realization 16 for Q ≈ 31218 m^3

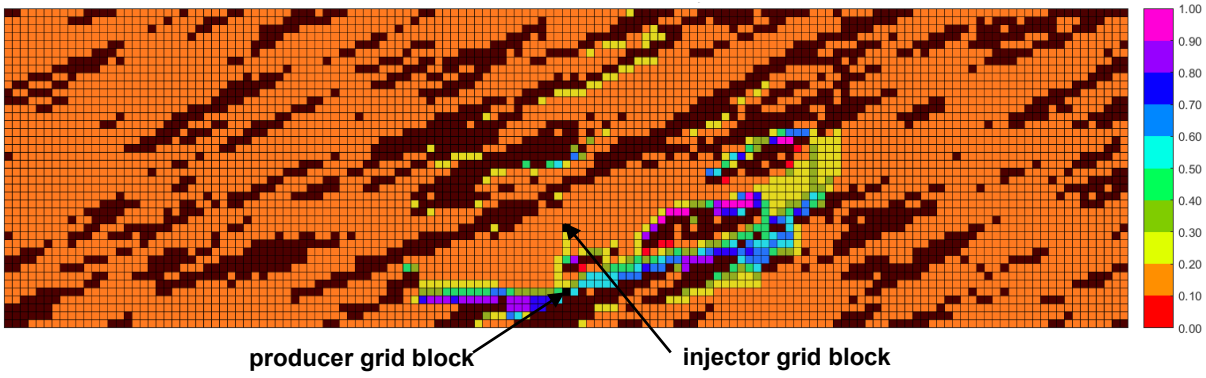

Figure K-8(k). Aqueous-phase saturation map in n-C_6 SAGD for realization 16 for Q ≈ 31218 m^3

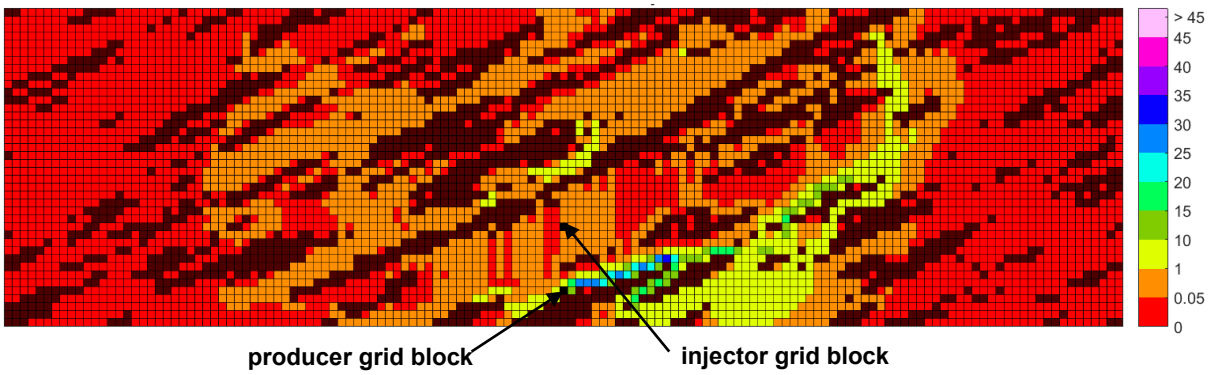

Figure K-8(l). Bitumen molar flow rate (kg-mole/day) map in SAGD for realization 16 for Q ≈ 31218 m^3

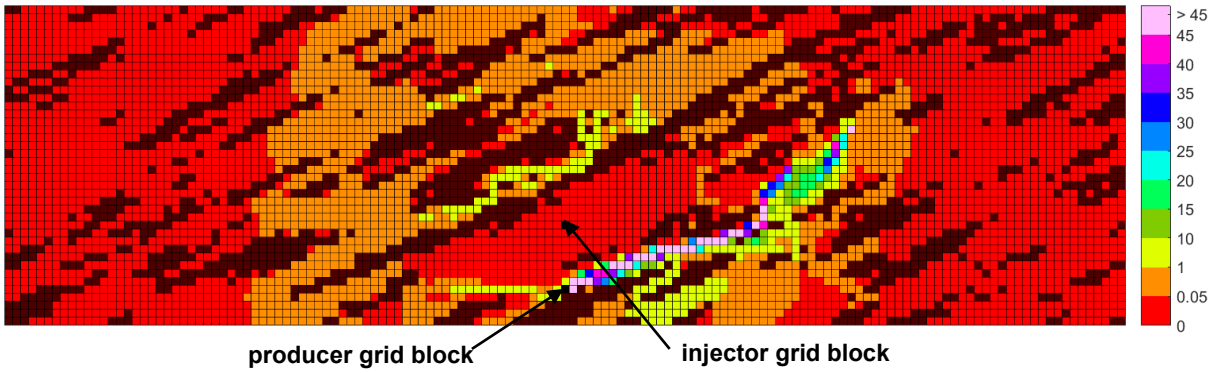

Figure K-8(m). Bitumen molar flow rate (kg-mole/day) map in n-C_6 SAGD for realization 16 for Q ≈ 31218 m^3

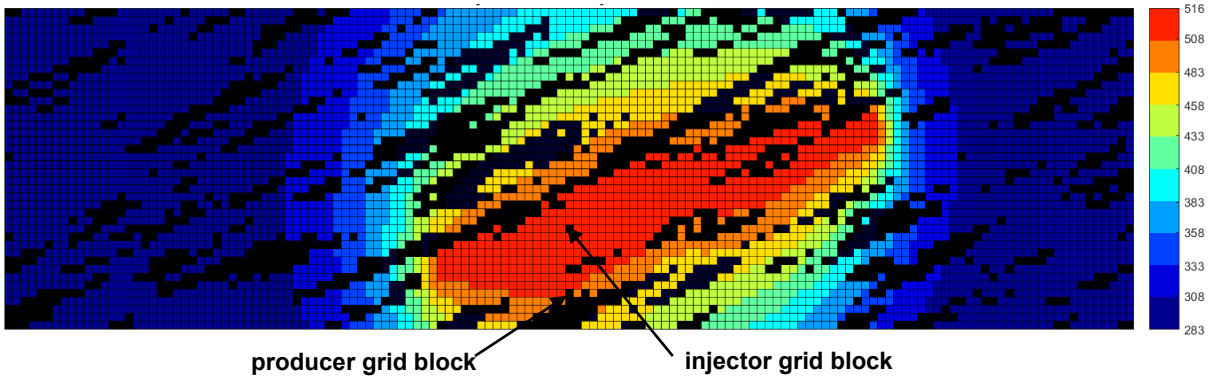

Figure K-8(n). Temperature (Kelvin) map in SAGD for realization 16 for Q ≈ 31218 m^3

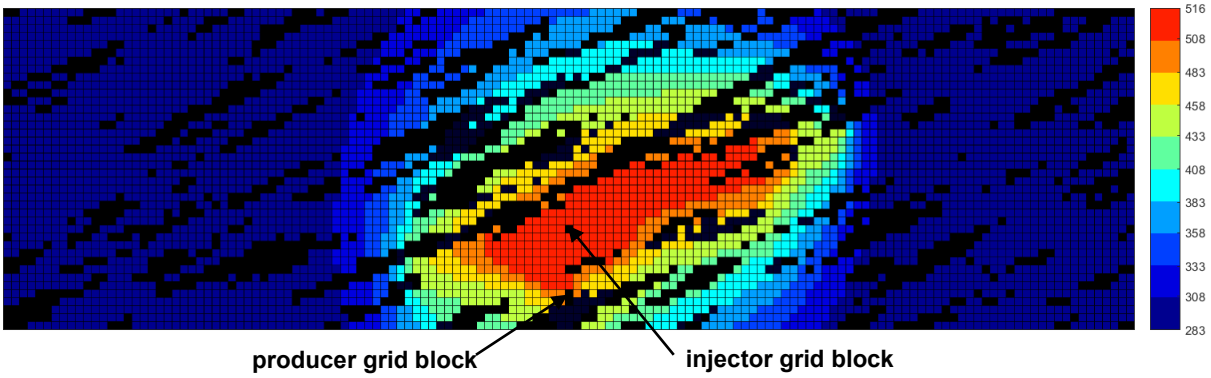

Figure K-8(o). Temperature (Kelvin) map in n-C_6 SAGD for realization 16 for Q ≈ 31218 m^3

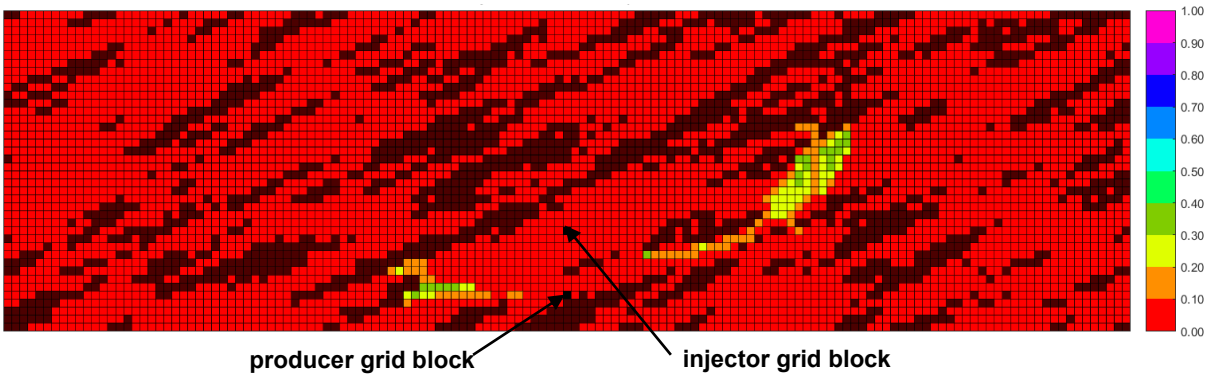

Figure K-8(p). $\beta_L x_{sL}$ map in n-C_6 SAGD for realization 16 for Q ≈ 31218 m^3

Figure K-8. Property maps for SAGD and n-C_6 SAGD for realization 16

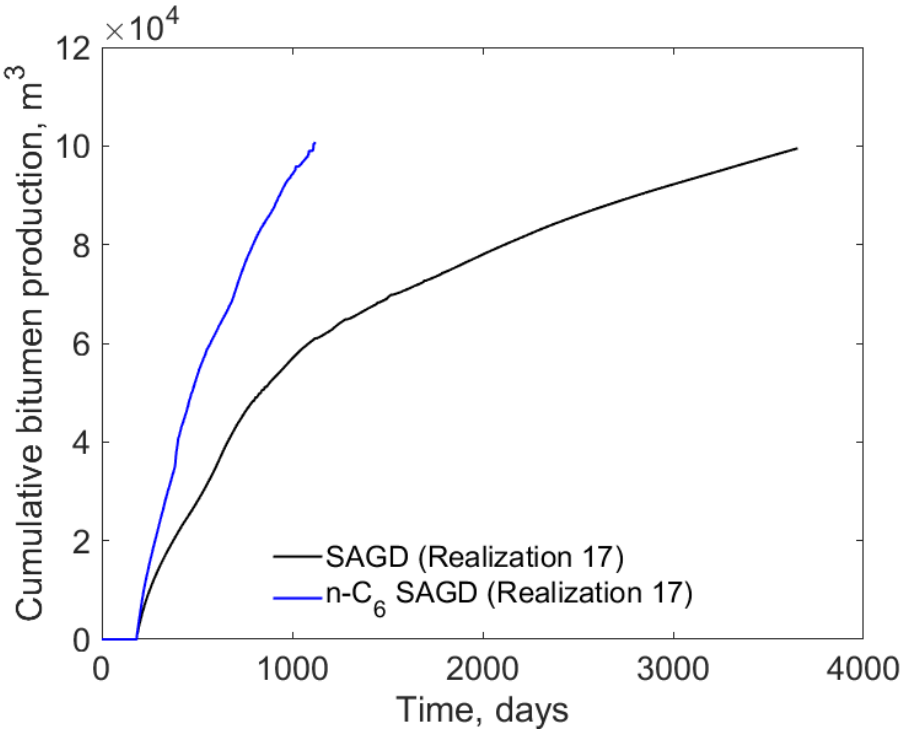

Figure K-9(a). Cumulative bitumen production histories for SAGD and n-C_6 SAGD for realization 17

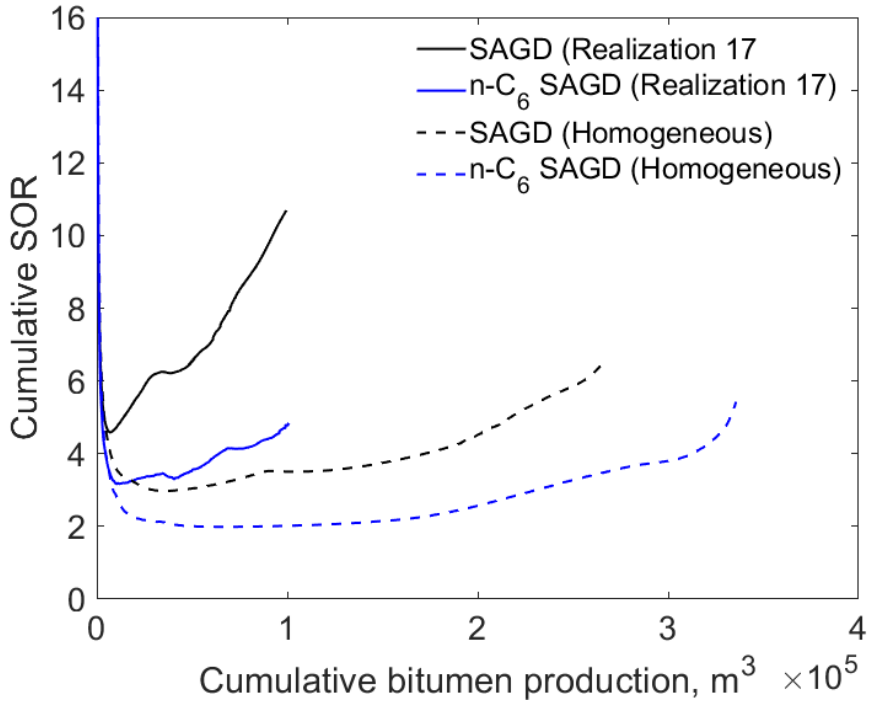

Figure K-9(b). Cumulative SOR for SAGD and n-C_6 SAGD for realization 17

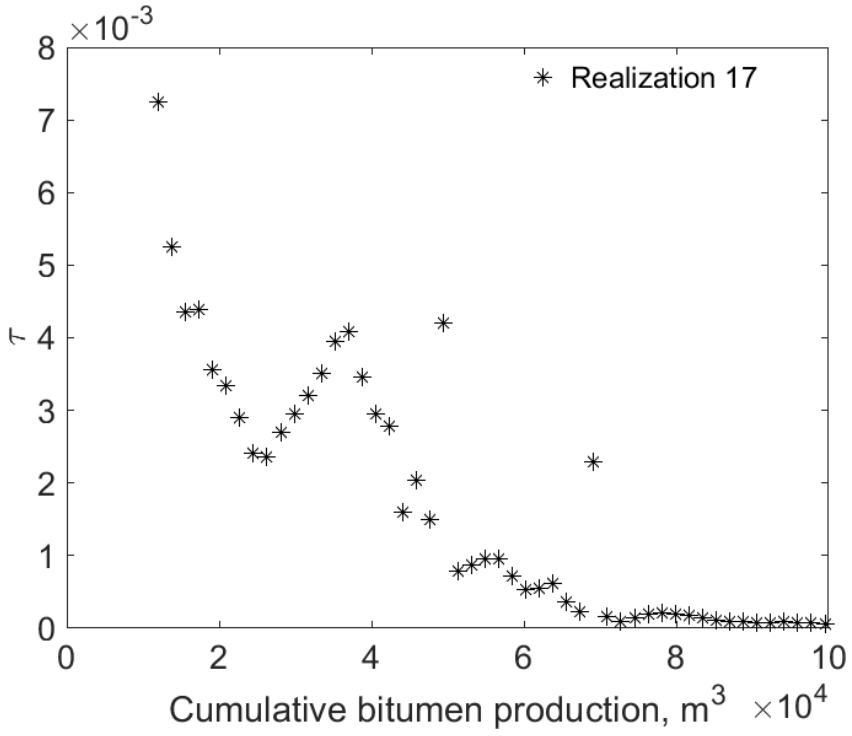

Figure K-9(c). τ for SAGD as a function of cumulative bitumen production for realization 17

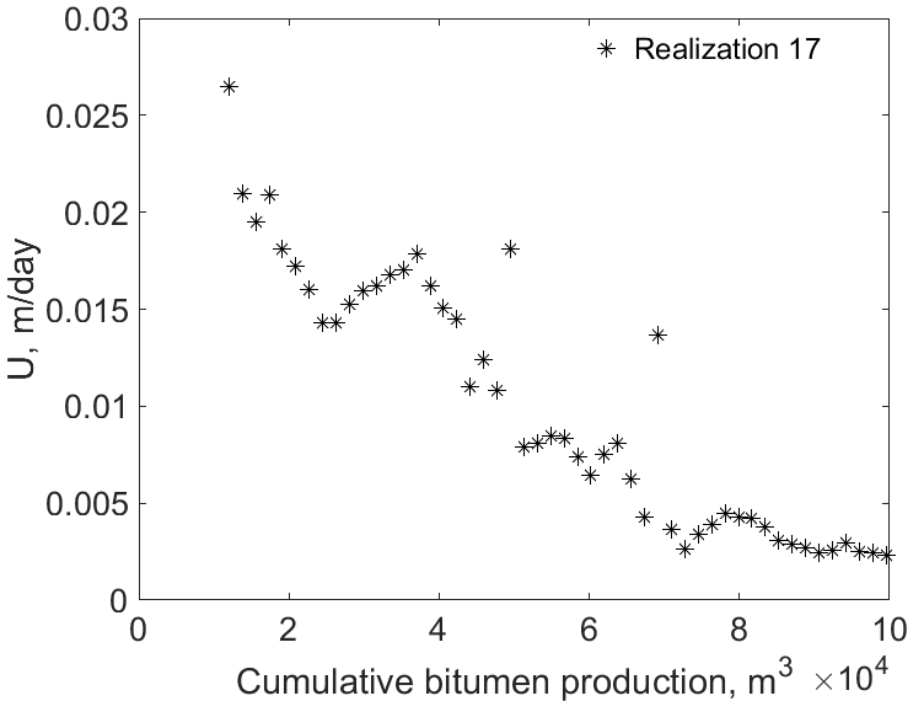

Figure K-9(d). U for SAGD as a function of cumulative bitumen production for realization 17

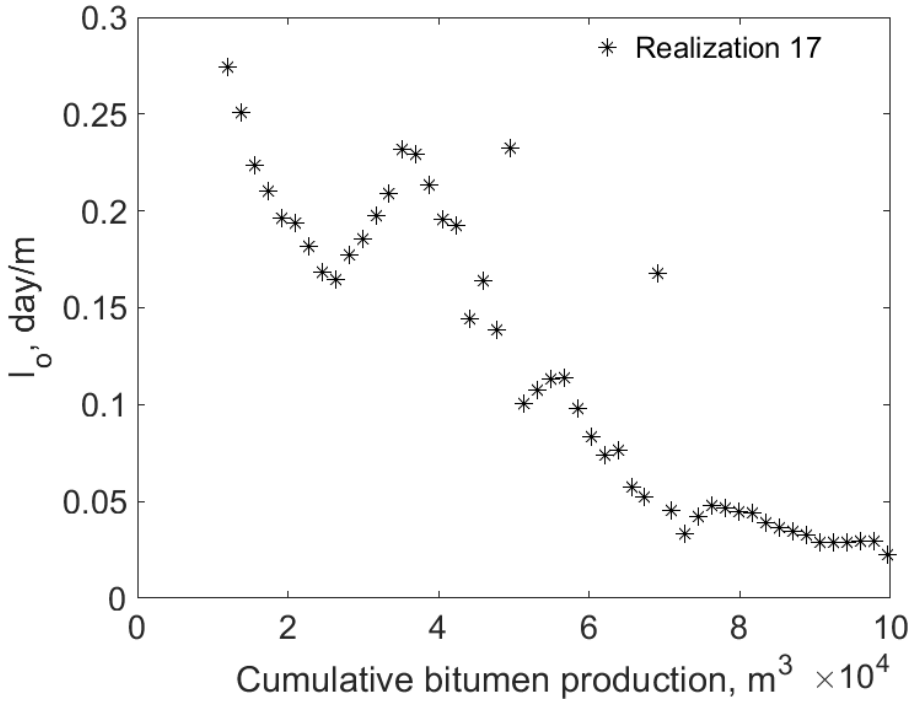

Figure K-9(e).I_o for SAGD as a function of cumulative bitumen production for realization 17

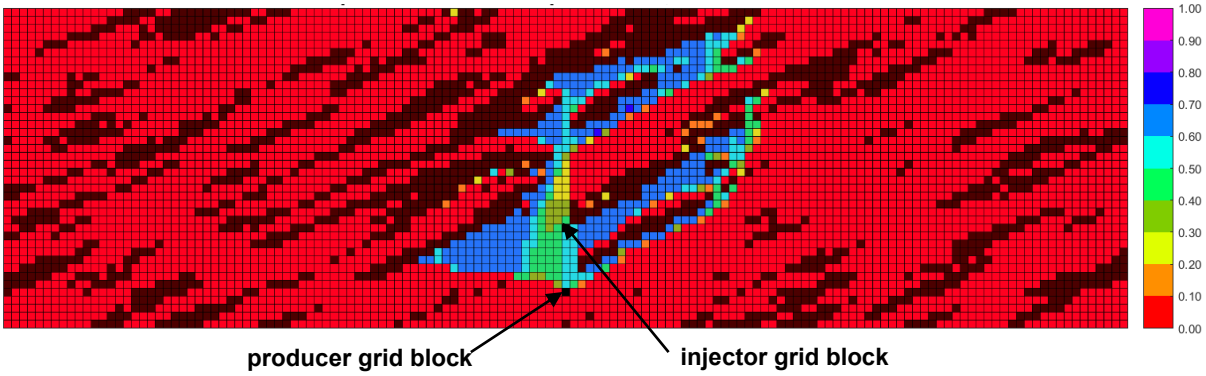

Figure K-9(f). Vapor-phase saturation map in SAGD for realization 17 for Q ≈ 31218 m^3

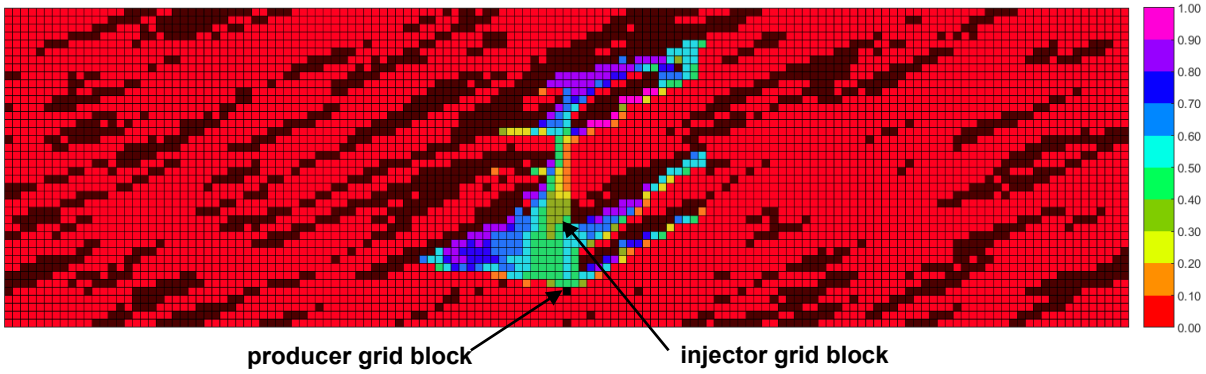

Figure K-9(g). Vapor-phase saturation map in n-C_6 SAGD for realization 17 for Q ≈ 31218 m^3

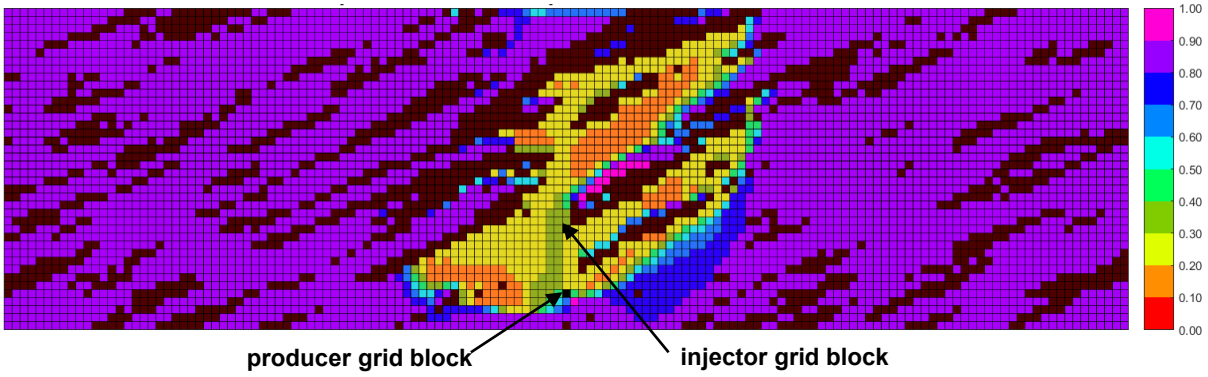

Figure K-9(h). Oleic-phase saturation map in SAGD for realization 17 for Q ≈ 31218 m^3

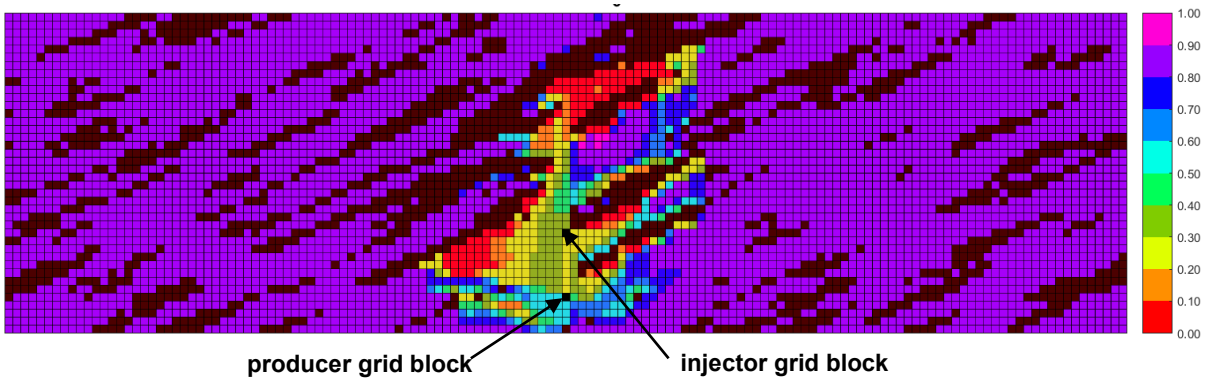

Figure K-9(i). Oleic-phase saturation map in n-C_6 SAGD for realization 17 for Q ≈ 31218 m^3

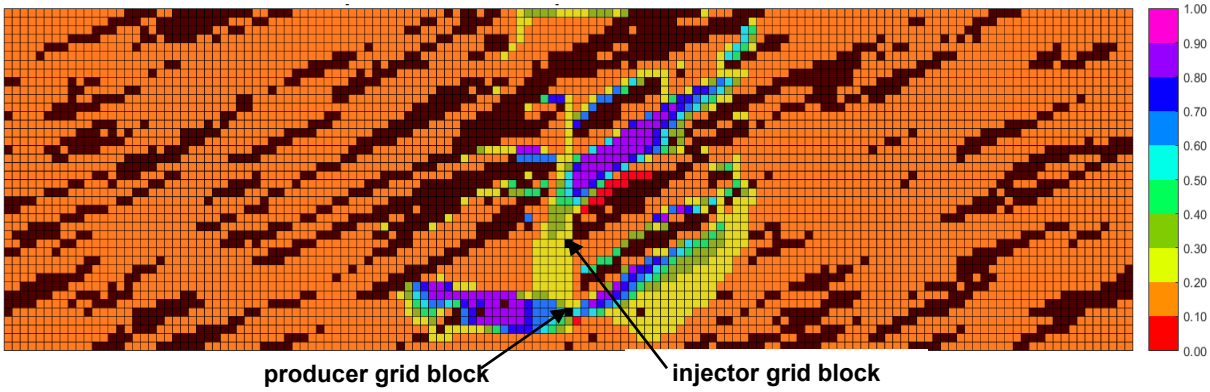

Figure K-9(j). Aqueous-phase saturation map in SAGD for realization 17 for Q ≈ 31218 m^3

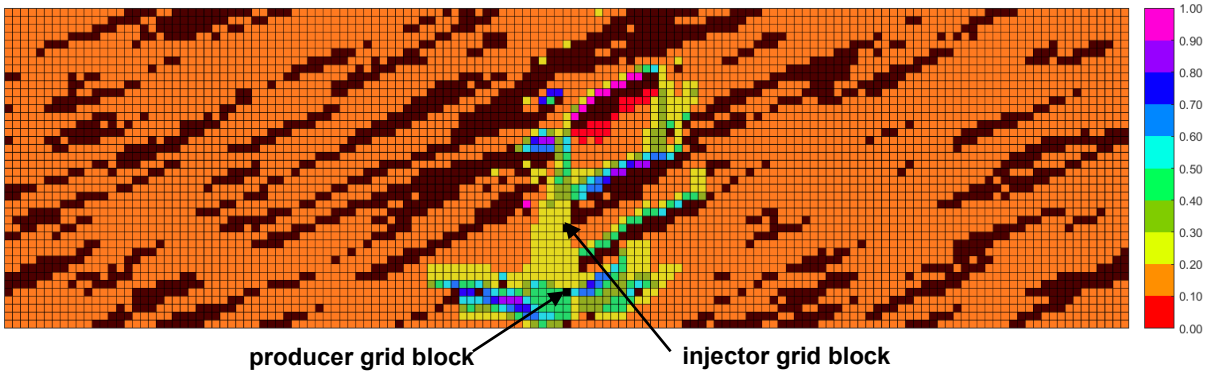

Figure K-9(k). Aqueous-phase saturation map in n-C_6 SAGD for realization 17 for Q ≈ 31218 m^3

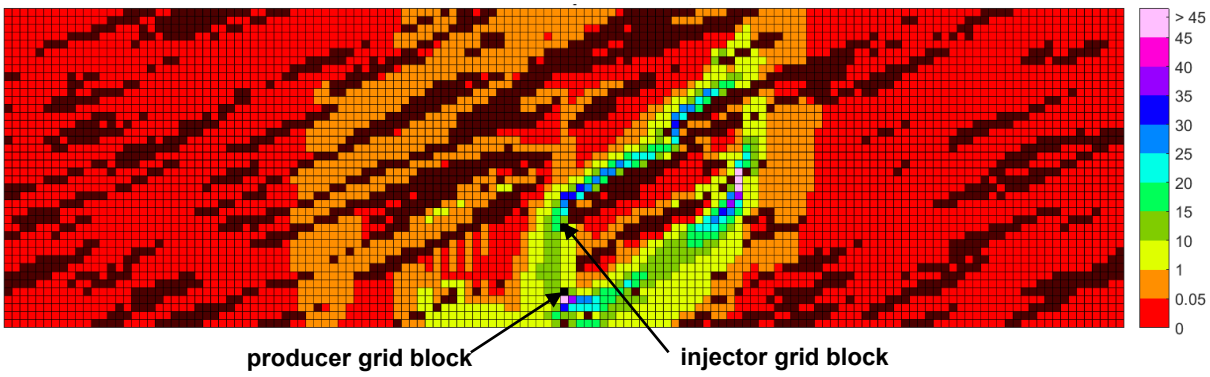

Figure K-9(l). Bitumen molar flow rate (kg-mole/day) map in SAGD for realization 17 for Q ≈ 31218 m^3

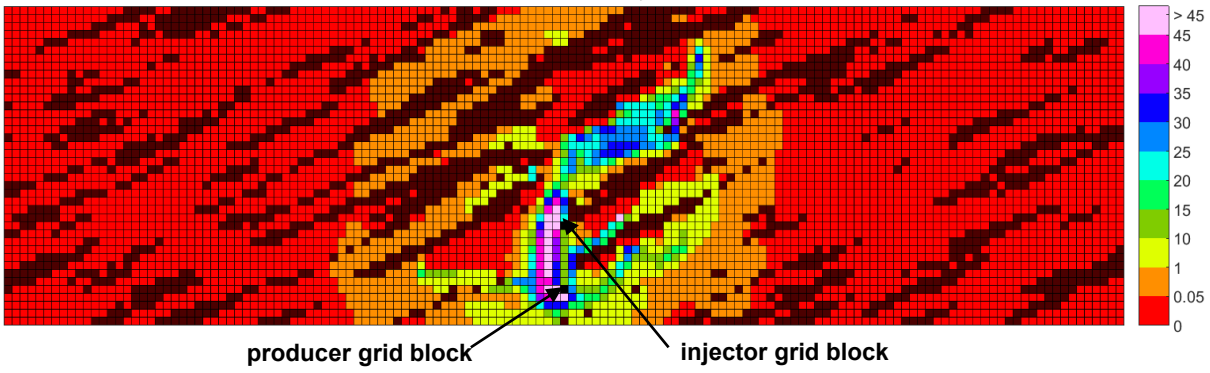

Figure K-9(m). Bitumen molar flow rate (kg-mole/day) map in n-C_6 SAGD for realization 17 for Q ≈ 31218 m^3

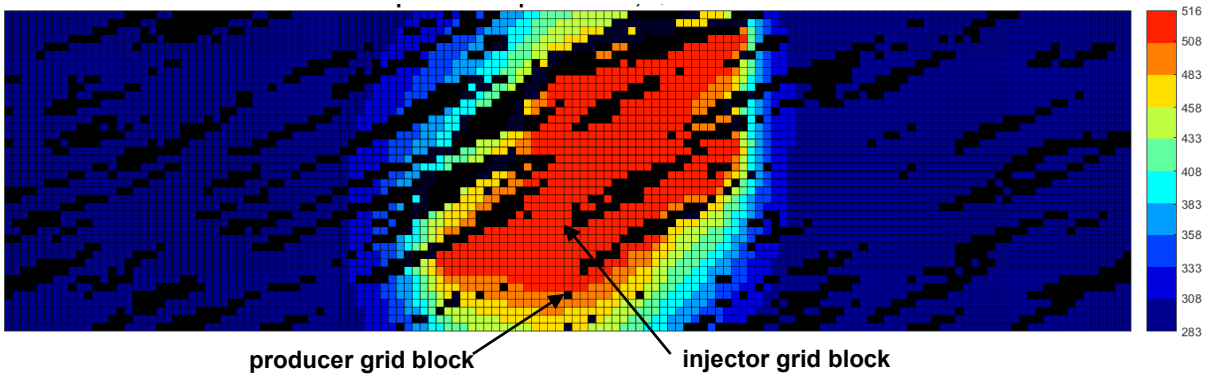

Figure K-9(n). Temperature (Kelvin) map in SAGD for realization 17 for Q ≈ 31218 m^3

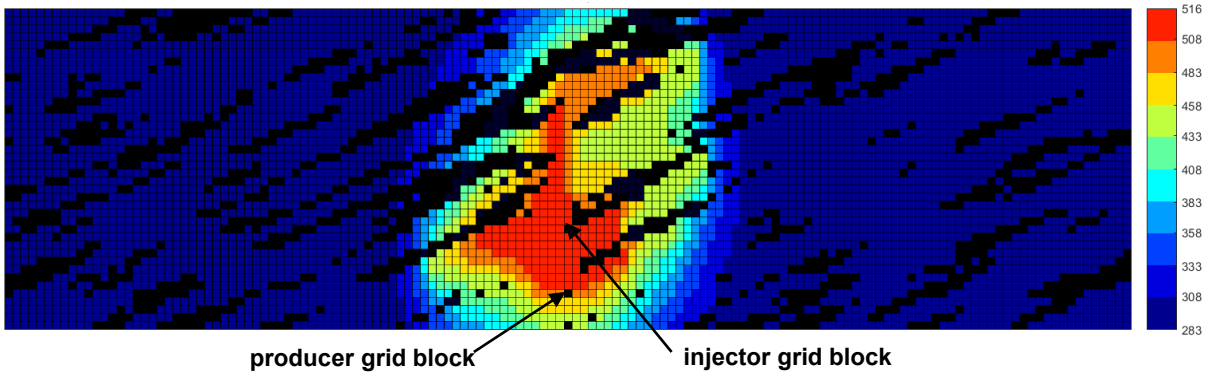

Figure K-9(o). Temperature (Kelvin) map in n-C_6 SAGD for realization 17 for Q ≈ 31218 m^3

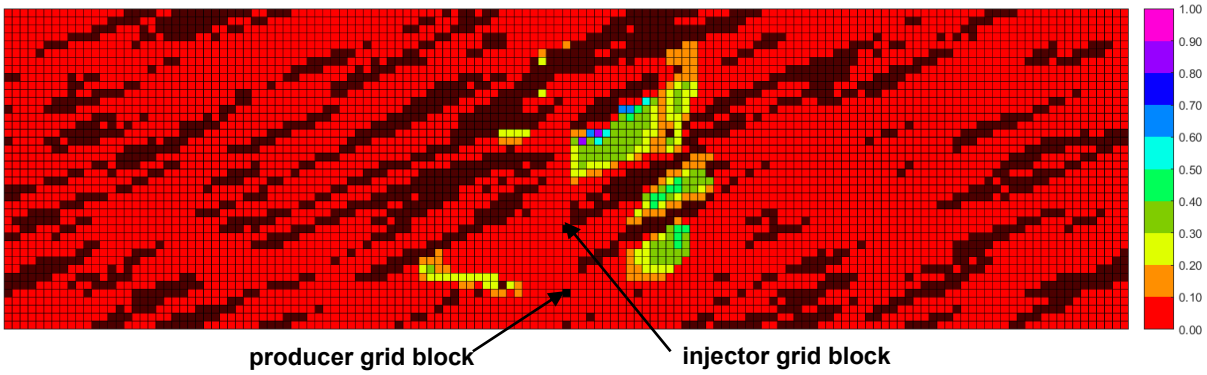

Figure K-9(p). $\beta_{LX_{sL}}$ map in n-C_6 SAGD for realization 17 for Q ≈ 31218 m^3

Figure K-9. Property maps for SAGD and n-C_6 SAGD for realization 17

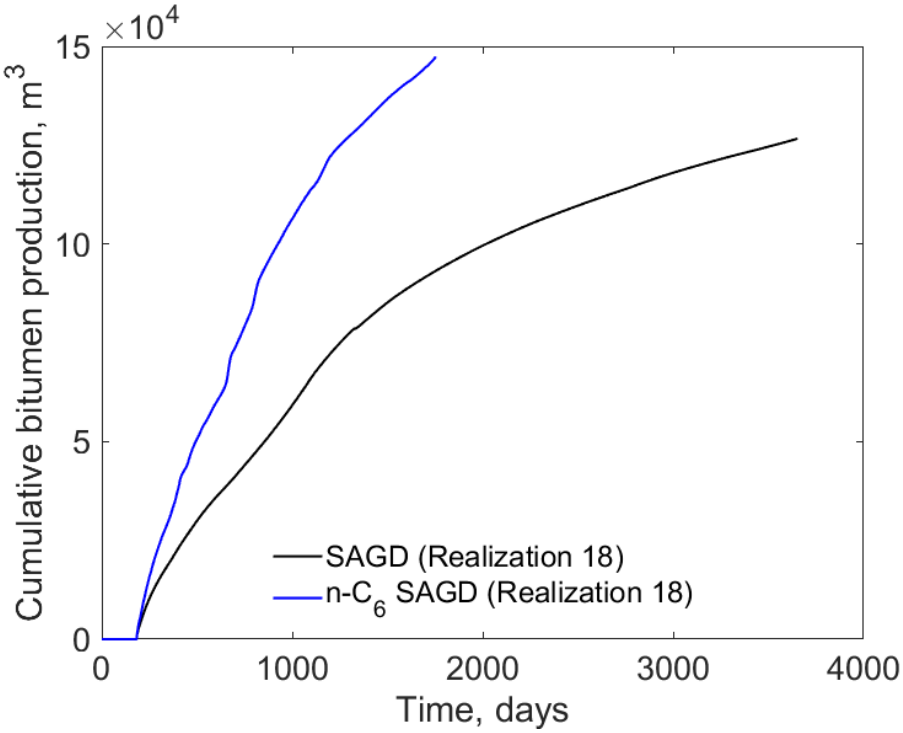

Figure K-10(a). Cumulative bitumen production histories for SAGD and n-C_6 SAGD for realization 18

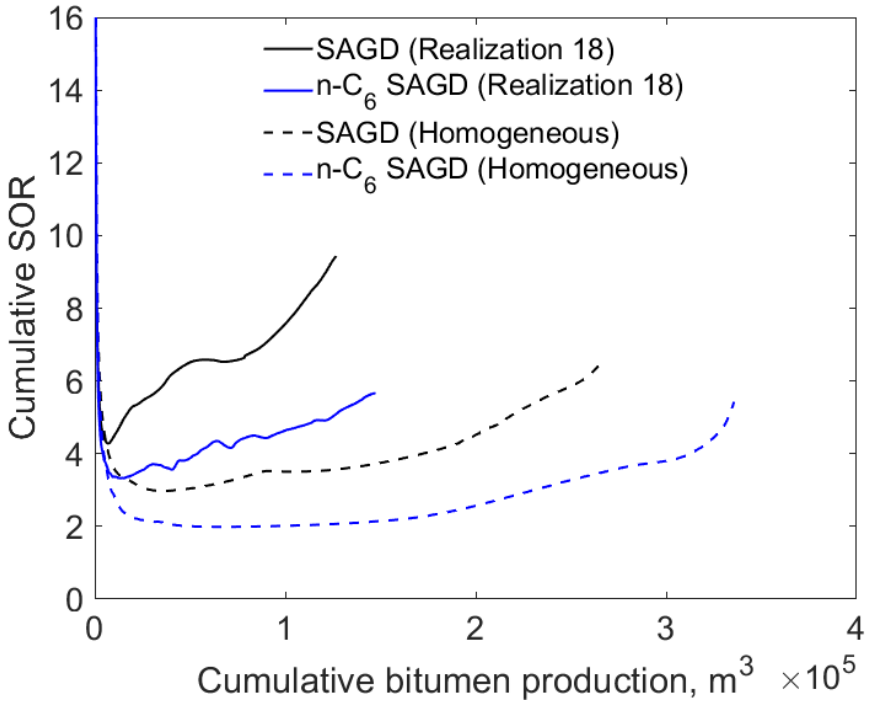

Figure K-10(b). Cumulative SOR for SAGD and n-C_6 SAGD for realization 18

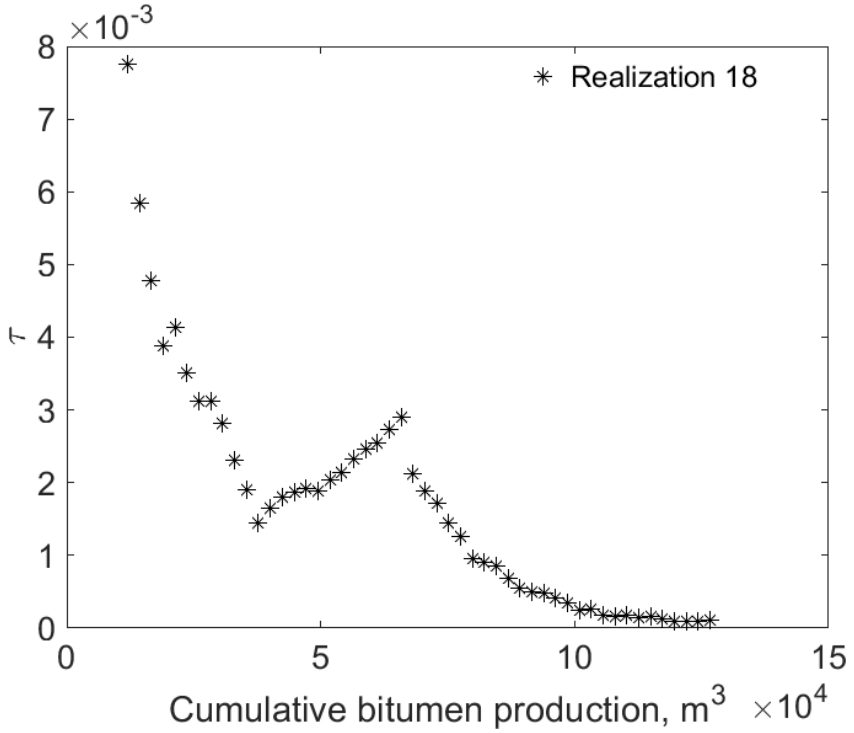

Figure K-10(c). τ for SAGD as a function of cumulative bitumen production for realization 18

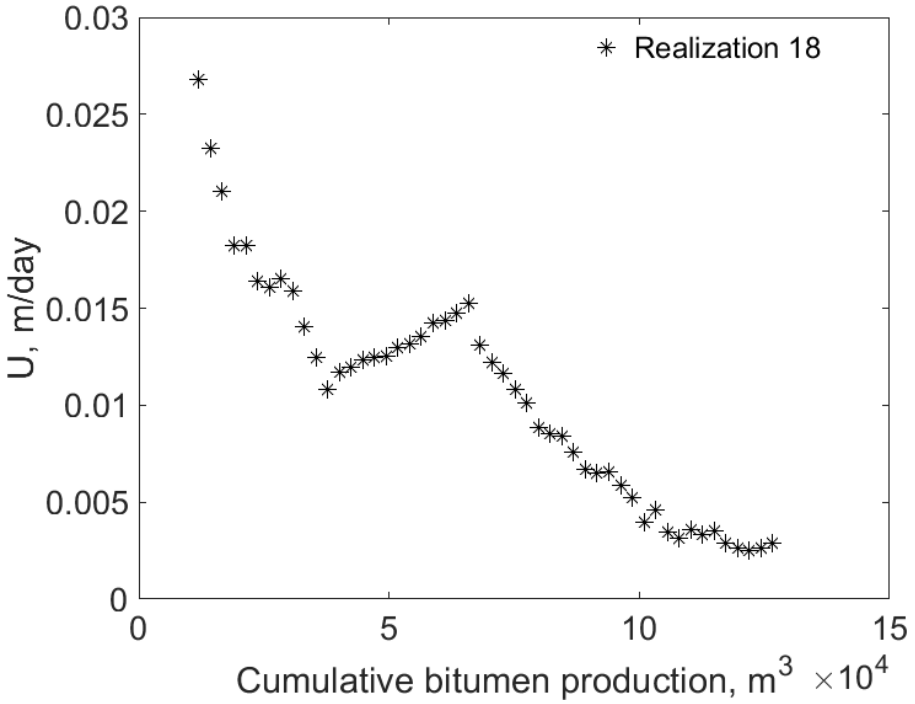

Figure K-10(d). U for SAGD as a function of cumulative bitumen production for realization 18

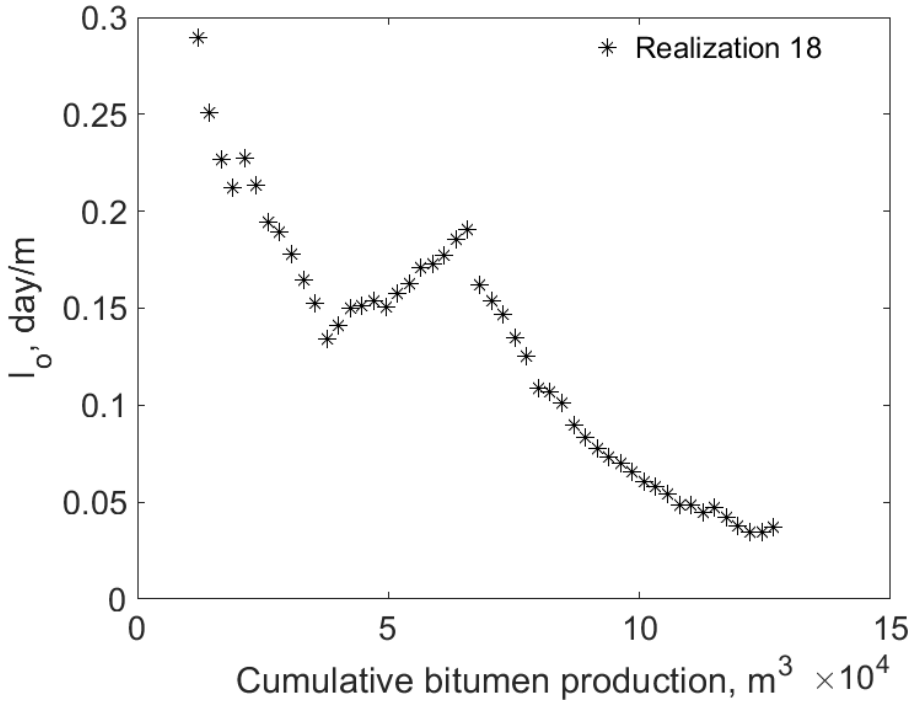

Figure K-10(e).I_o for SAGD as a function of cumulative bitumen production for realization 18

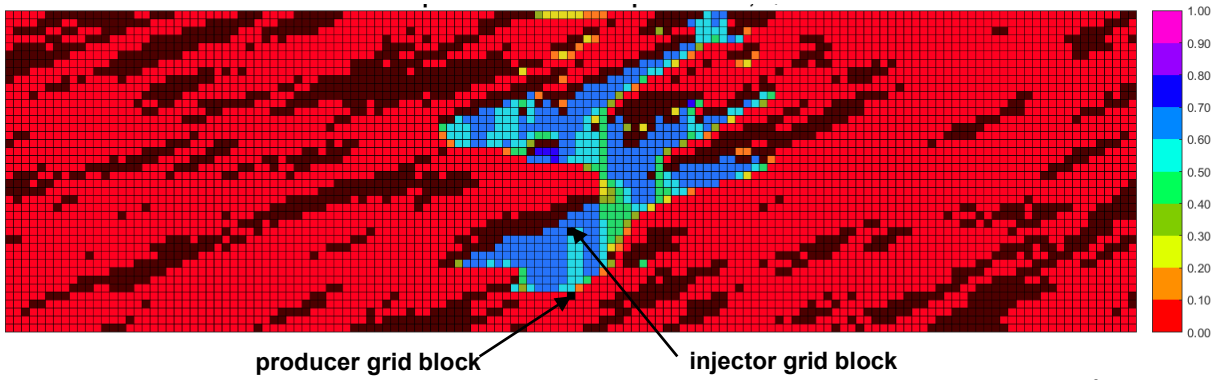

Figure K-10(f). Vapor-phase saturation map in SAGD for realization 18 for Q ≈ 31218 m^3

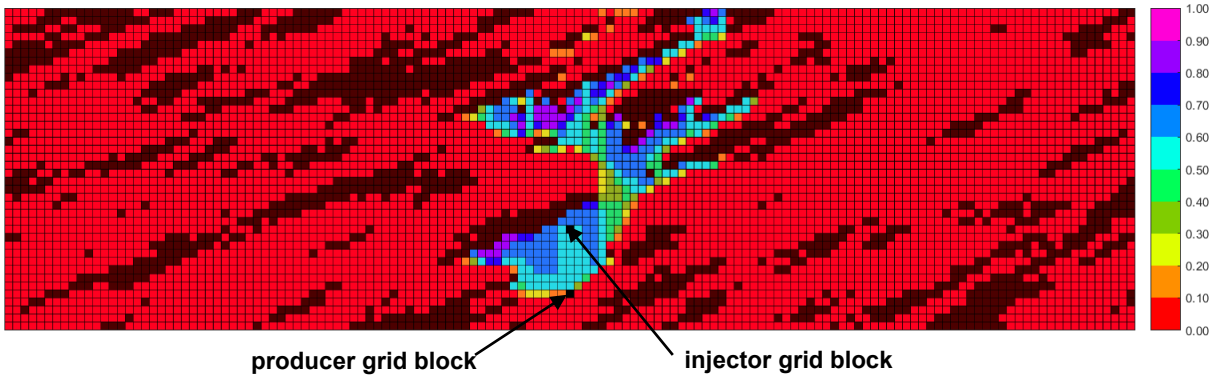

Figure K-10(g). Vapor-phase saturation map in n-C_6 SAGD for realization 18 for Q ≈ 31218 m^3

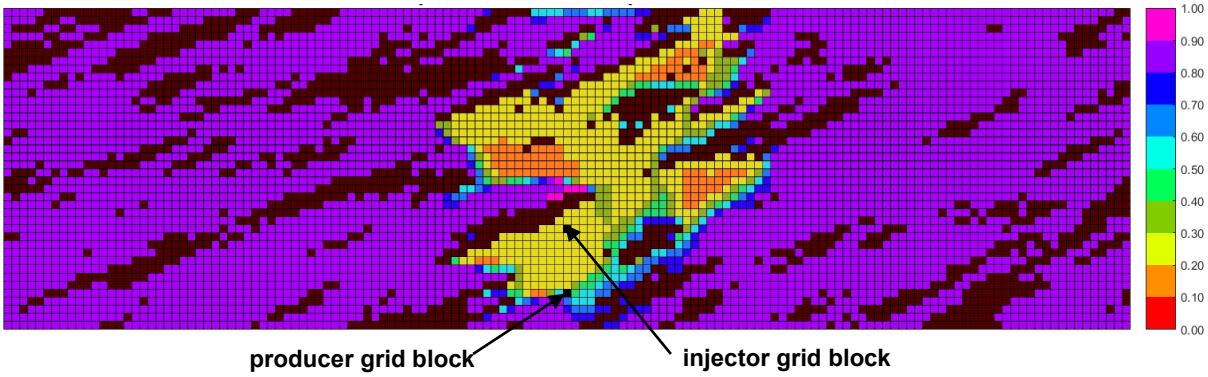

Figure K-10(h). Oleic-phase saturation map in SAGD for realization 18 for Q ≈ 31218 m^3

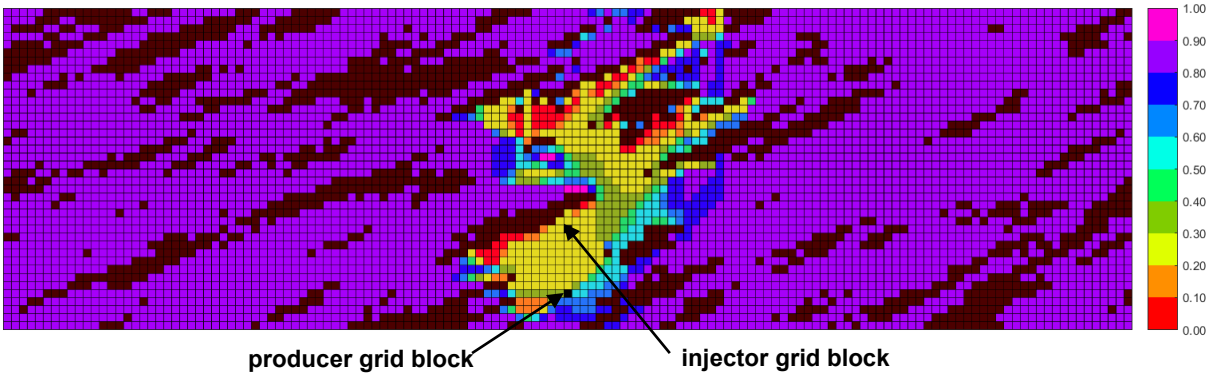

Figure K-10(i). Oleic-phase saturation map in n-C_6 SAGD for realization 18 for Q ≈ 31218 m^3

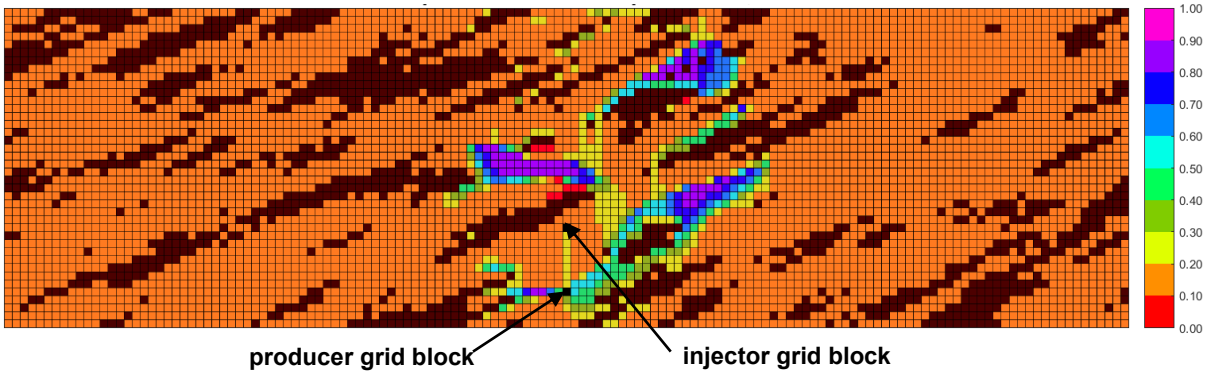

Figure K-10(j). Aqueous-phase saturation map in SAGD for realization 18 for Q ≈ 31218 m^3

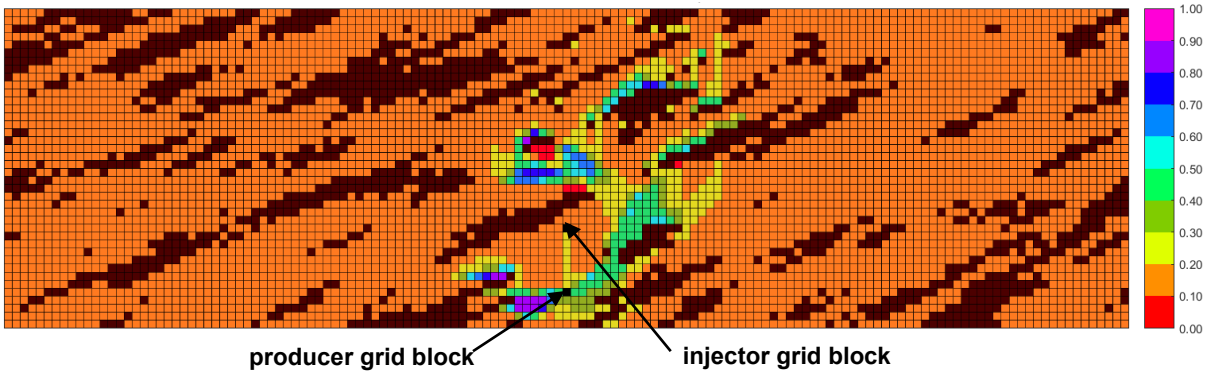

Figure K-10(k). Aqueous-phase saturation map in n-C_6 SAGD for realization 18 for Q ≈ 31218 m^3

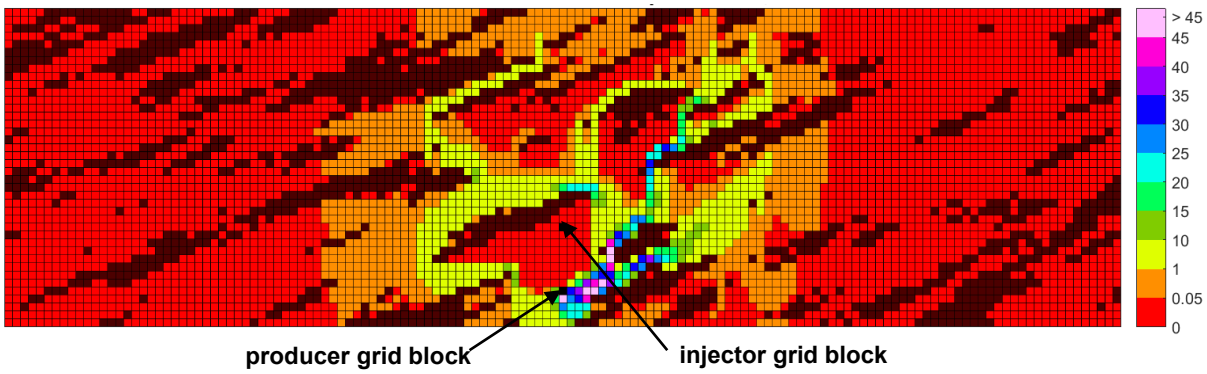

Figure K-10(l). Bitumen molar flow rate (kg-mole/day) map in SAGD for realization 18 for Q ≈ 31218 m^3

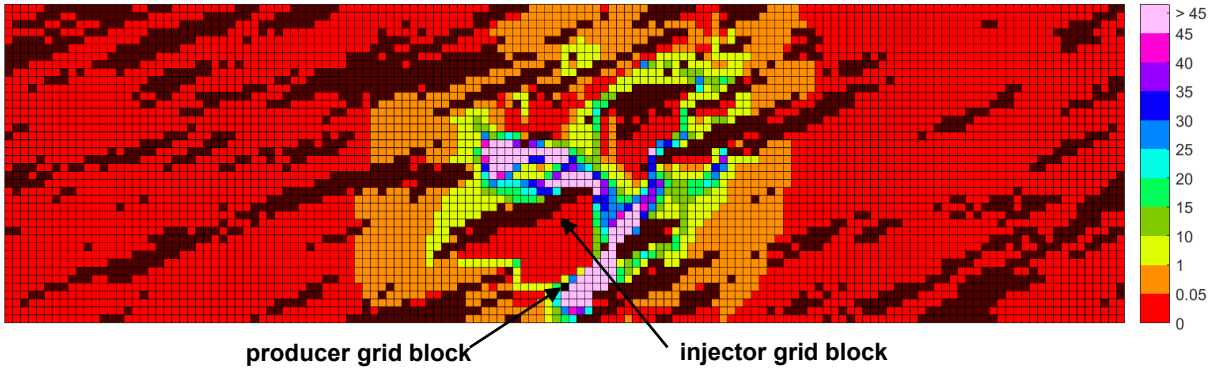

Figure K-10(m). Bitumen molar flow rate (kg-mole/day) map in n-C_6 SAGD for realization 18 for Q ≈ 31218 m^3

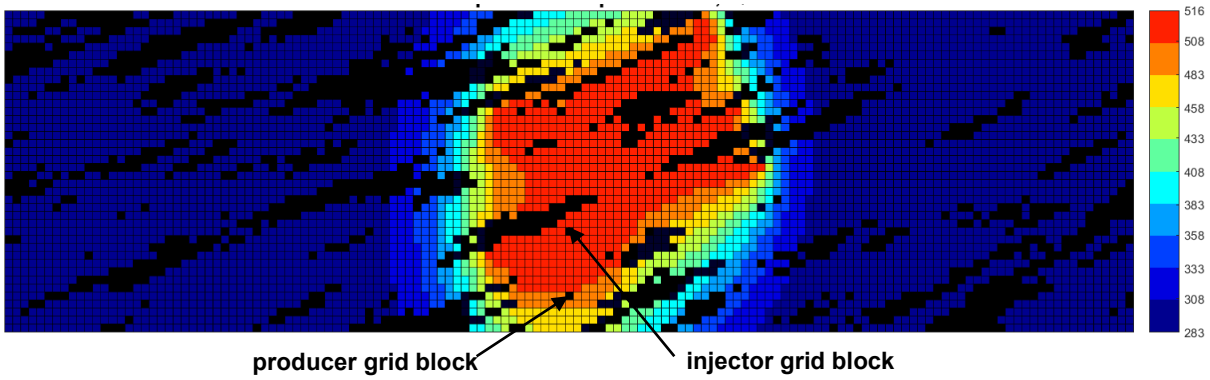

Figure K-10(n). Temperature (Kelvin) map in SAGD for realization 18 for Q ≈ 31218 m^3

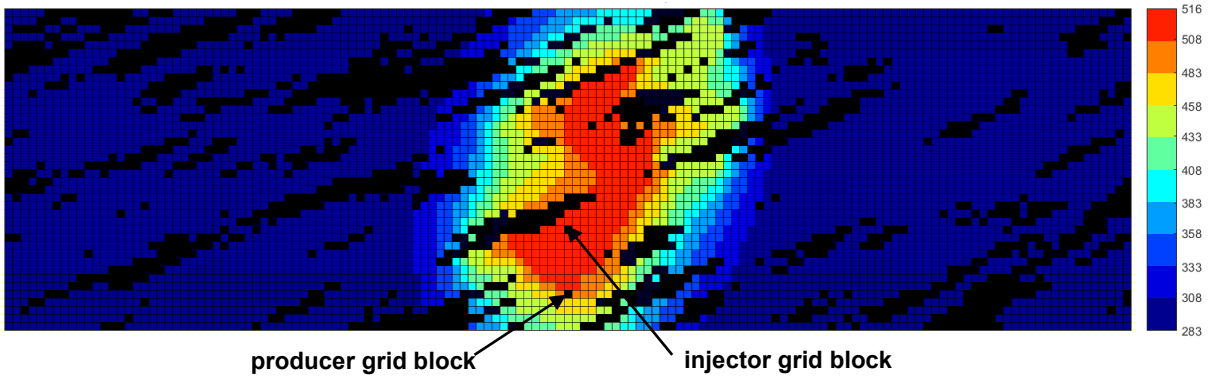

Figure K-10(o). Temperature (Kelvin) map in n-C_6 SAGD for realization 18 for Q ≈ 31218 m^3

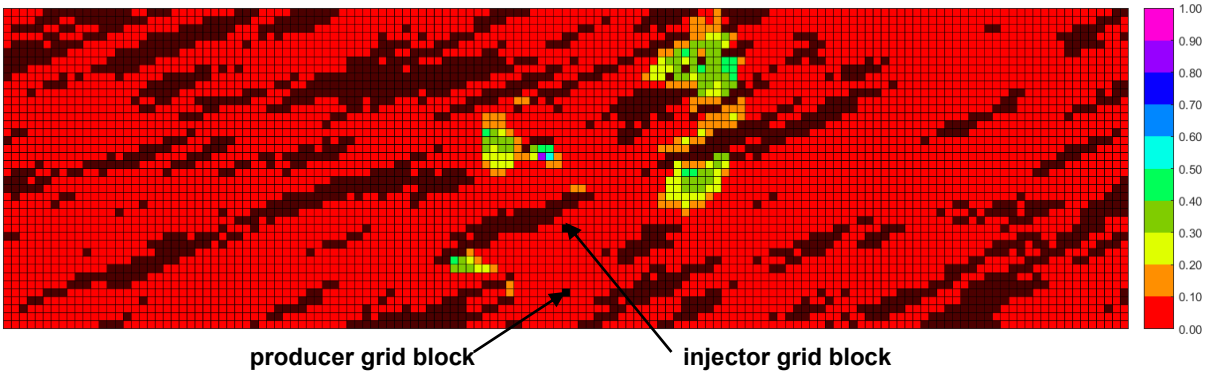

Figure K-10(p). $\beta_{LX}x_{sL}$ map in n-C_6 SAGD for realization 18 for Q ≈ 31218 m^3

Figure K-10. Property maps for SAGD and n-C_6 SAGD for realization 18

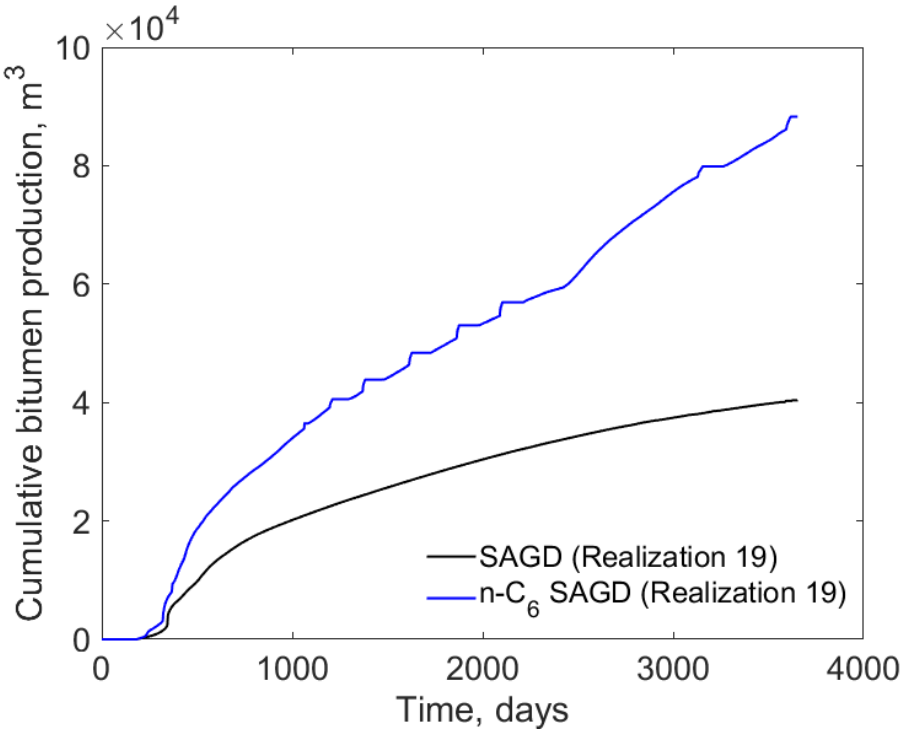

Figure K-11(a). Cumulative bitumen production histories for SAGD and n-C_6 SAGD for realization 19

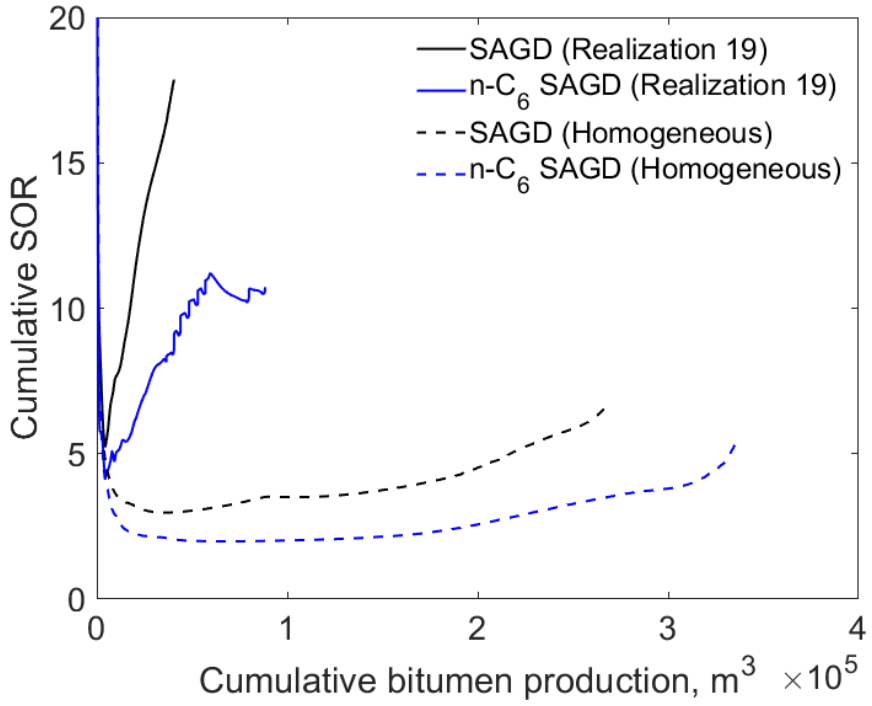

Figure K-11(b). Cumulative SOR for SAGD and n-C_6 SAGD for realization 19

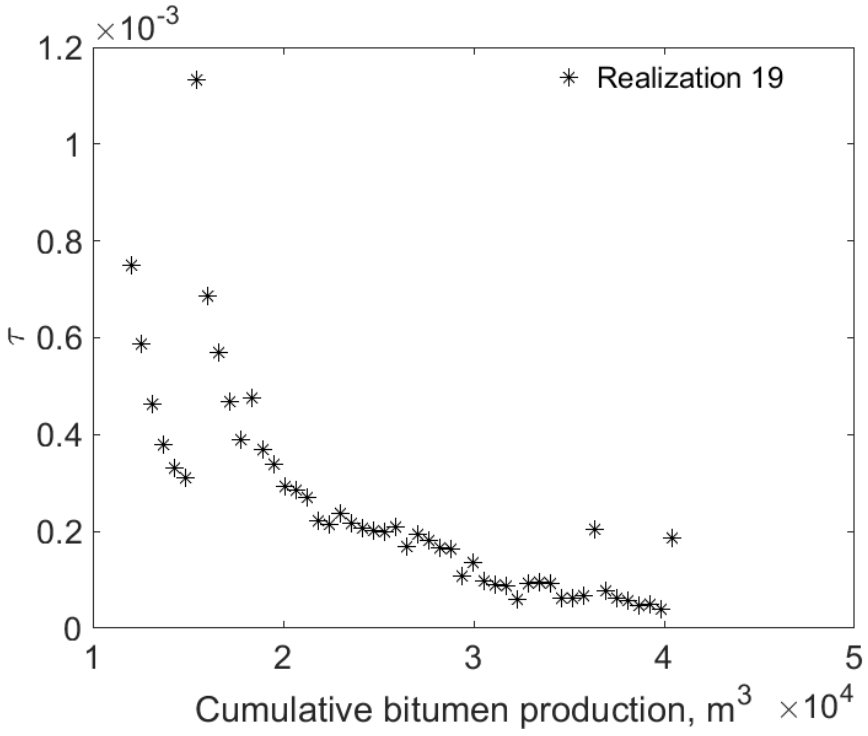

Figure K-11(c). τ for SAGD as a function of cumulative bitumen production for realization 19

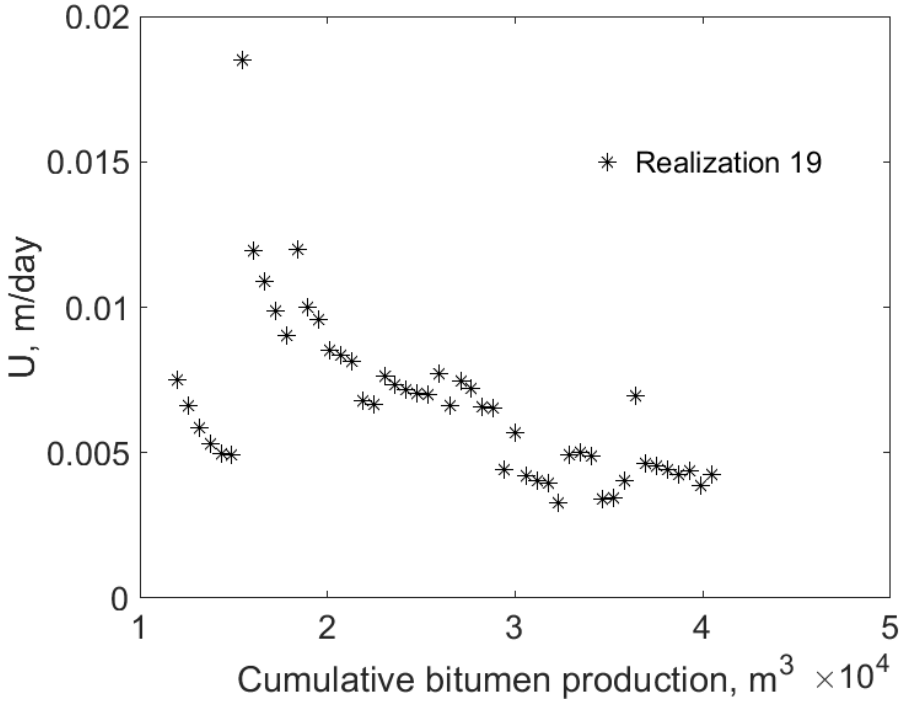

Figure K-11(d). U for SAGD as a function of cumulative bitumen production for realization 19

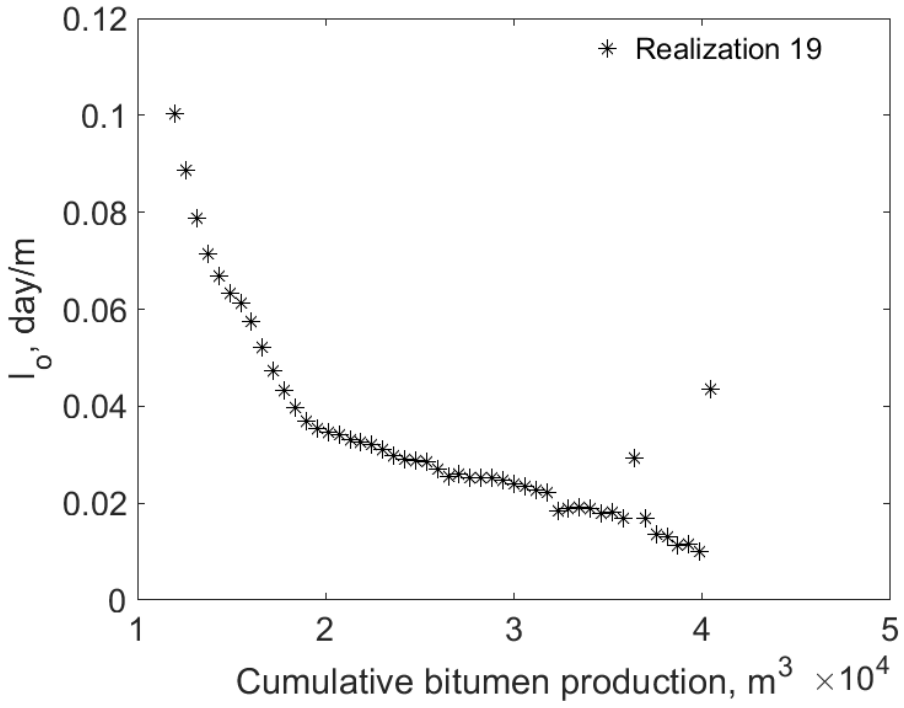

Figure K-11(e).I_o for SAGD as a function of cumulative bitumen production for realization 19

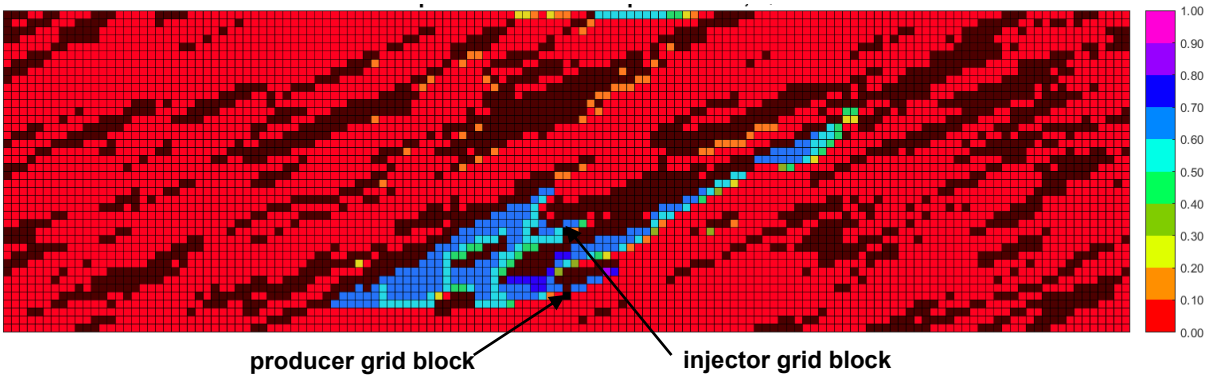

Figure K-11(f). Vapor-phase saturation map in SAGD for realization 19 for Q ≈ 31218 m^3

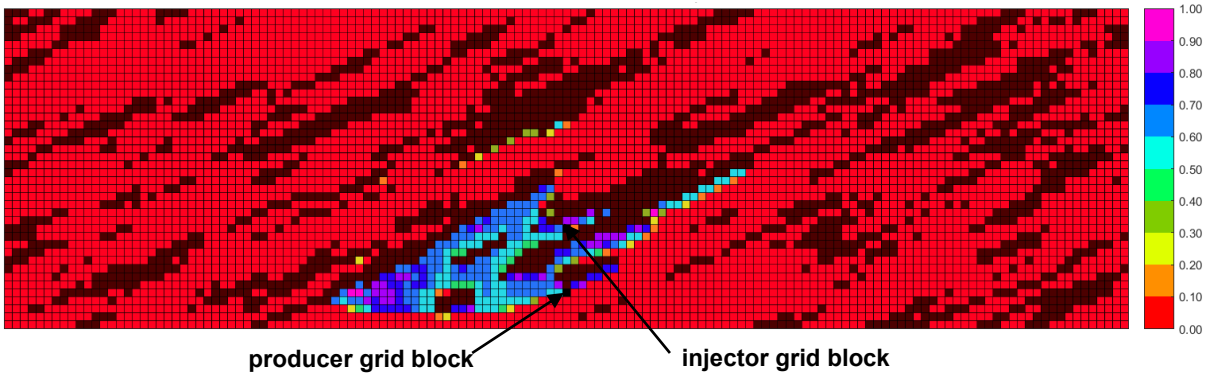

Figure K-11(g). Vapor-phase saturation map in n-C_6 SAGD for realization 19 for Q ≈ 31218 m^3

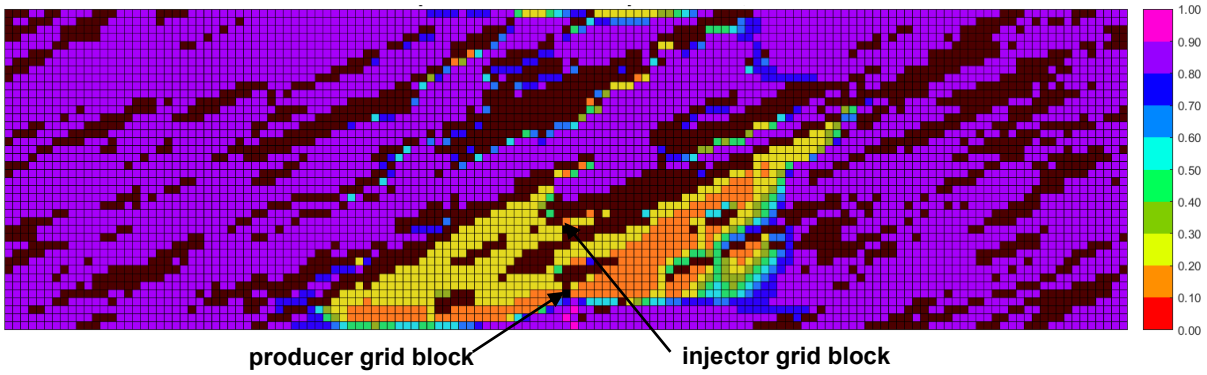

Figure K-11(h). Oleic-phase saturation map in SAGD for realization 19 for Q ≈ 31218 m^3

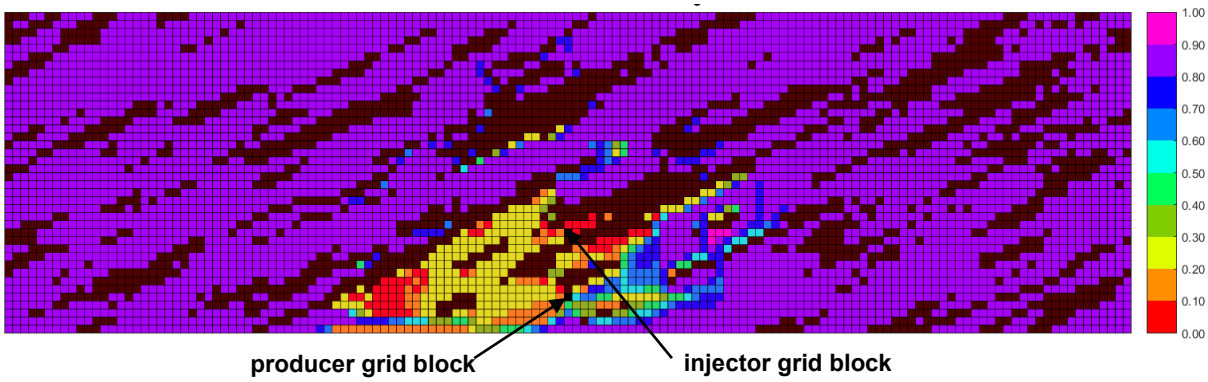

Figure K-1(i). Oleic-phase saturation map in n-C_6 SAGD for realization 19 for Q ≈ 31218 m^3

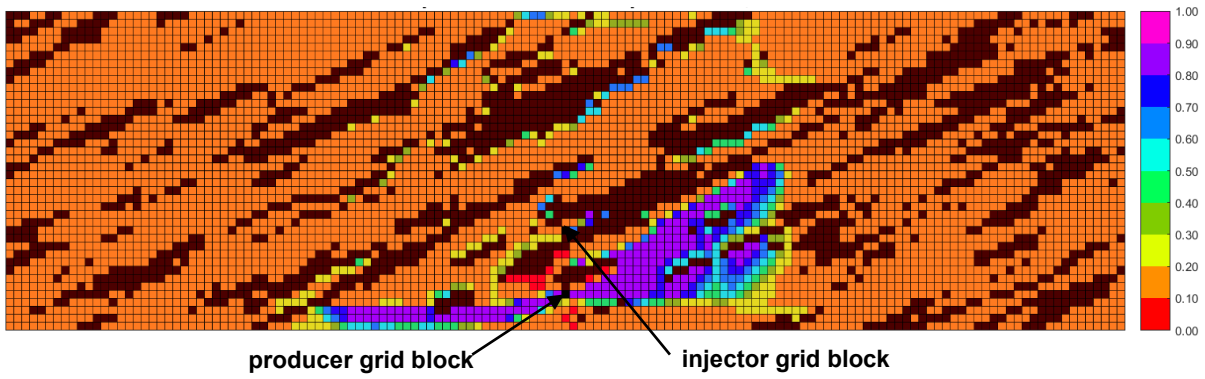

Figure K-11(j). Aqueous-phase saturation map in SAGD for realization 19 for Q ≈ 31218 m^3

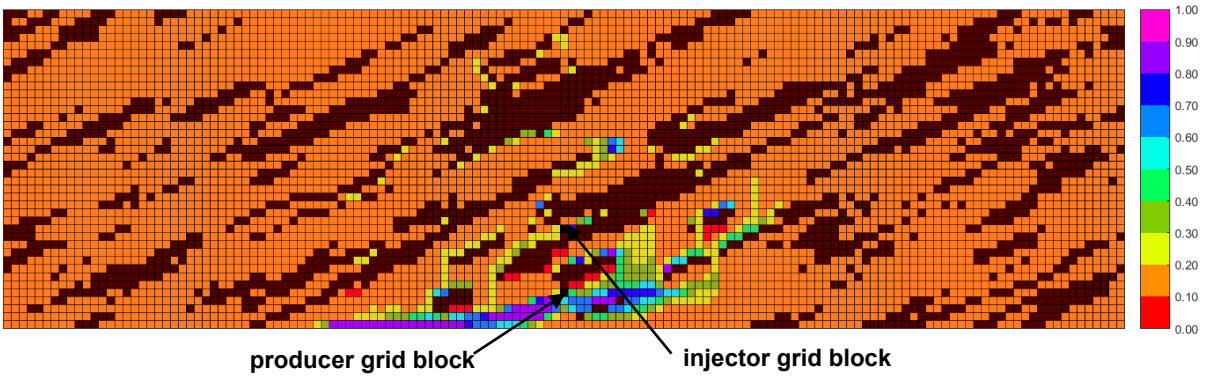

Figure K-11(k). Aqueous-phase saturation map in n-C_6 SAGD for realization 19 for Q ≈ 31218 m^3

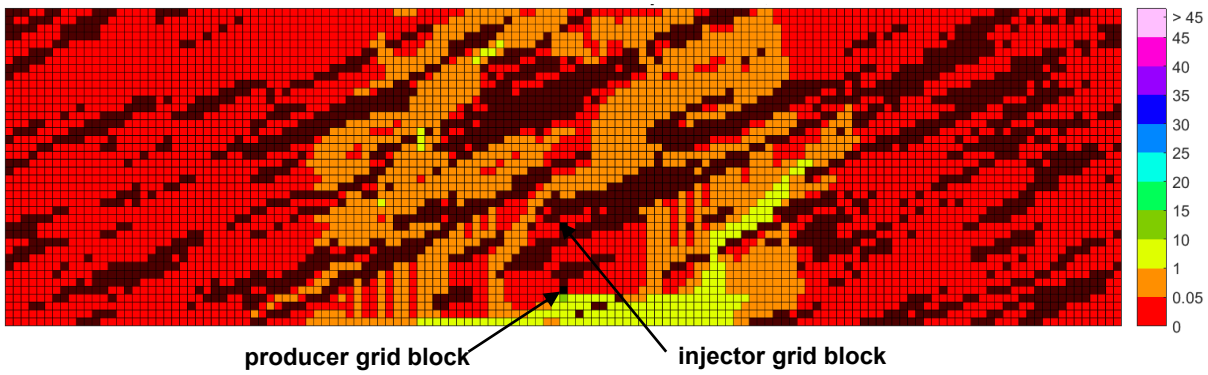

Figure K-11(l). Bitumen molar flow rate (kg-mole/day) map in SAGD for realization 19 for Q ≈ 31218 m^3

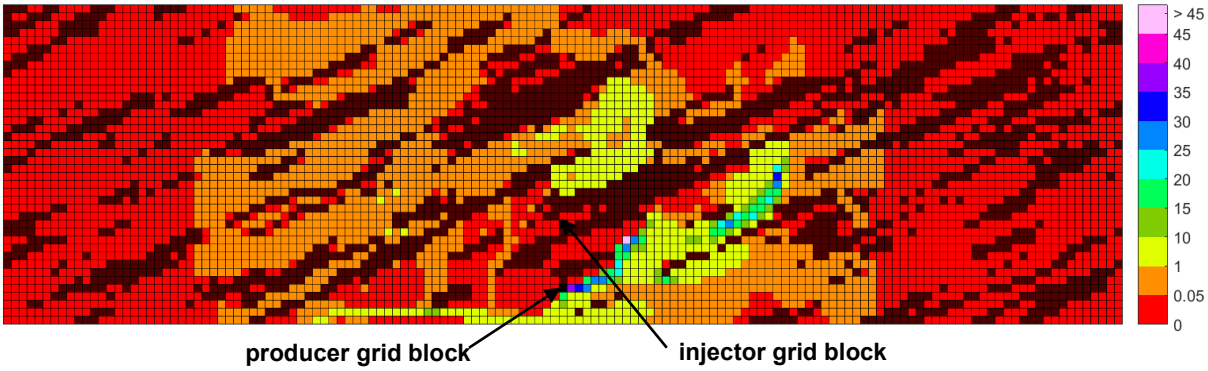

Figure K-11(m). Bitumen molar flow rate (kg-mole/day) map in n-C_6 SAGD for realization 19 for Q ≈ 31218 m^3

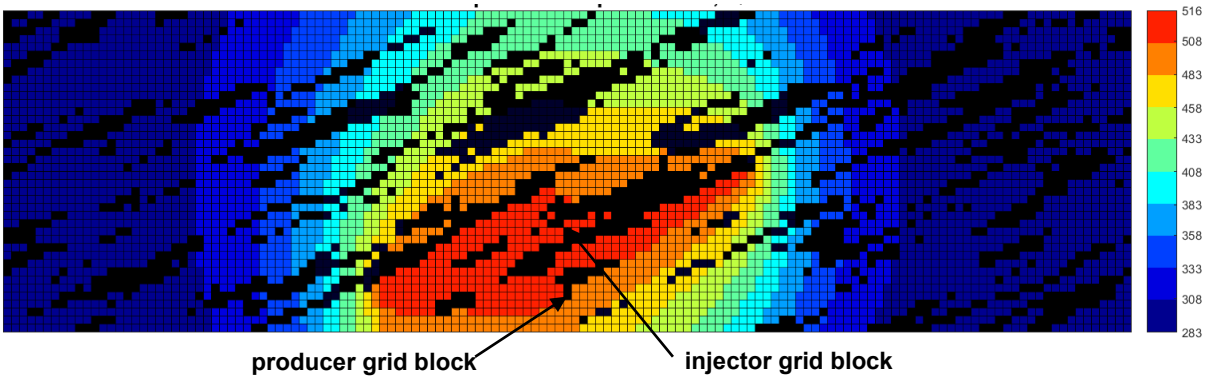

Figure K-11(n). Temperature (Kelvin) map in SAGD for realization 19 for Q ≈ 31218 m^3

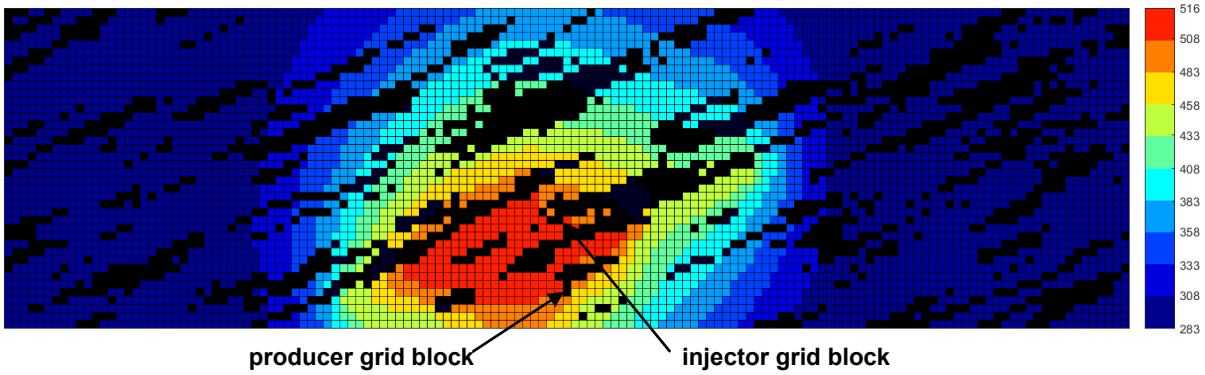

Figure K-11(o). Temperature (Kelvin) map in n-C_6 SAGD for realization 19 for Q ≈ 31218 m^3

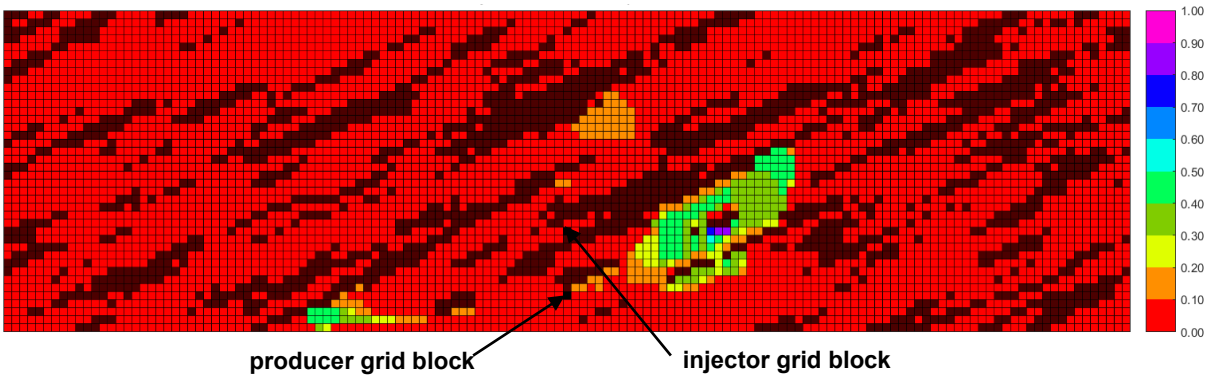

Figure K-11(p). $\beta_{Lx_{sL}}$ map in n-C_6 SAGD for realization 19 for Q ≈ 31218 m^3

Figure K-11. Property maps for SAGD and n-C_6 SAGD for realization 19

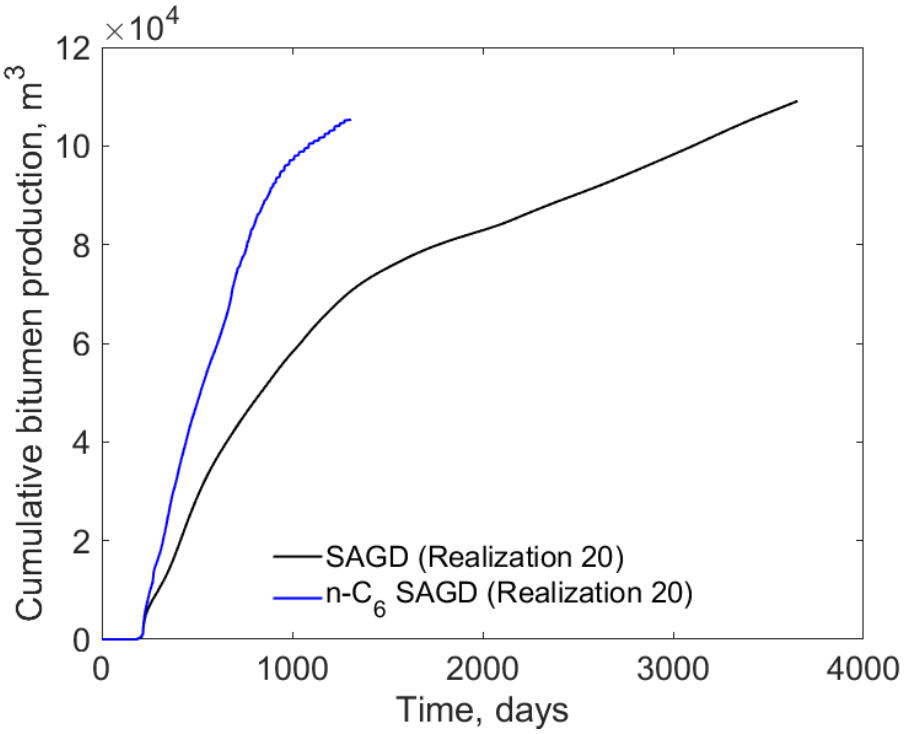

Figure K-12(a). Cumulative bitumen production histories for SAGD and n-C_6 SAGD for realization 10

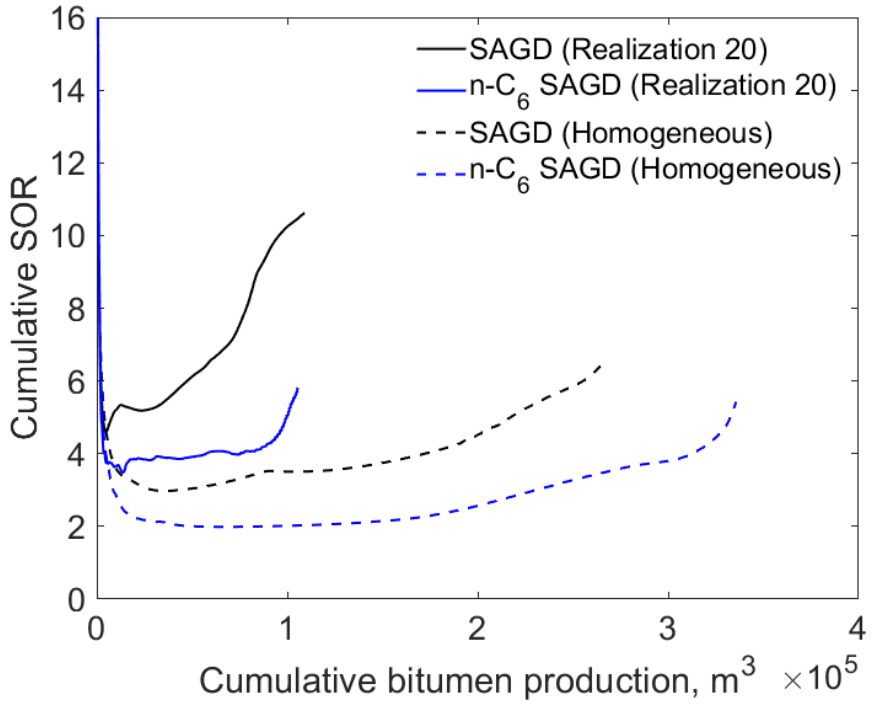

Figure K-12(a). Cumulative SOR for SAGD and n-C_6 SAGD for realization 20

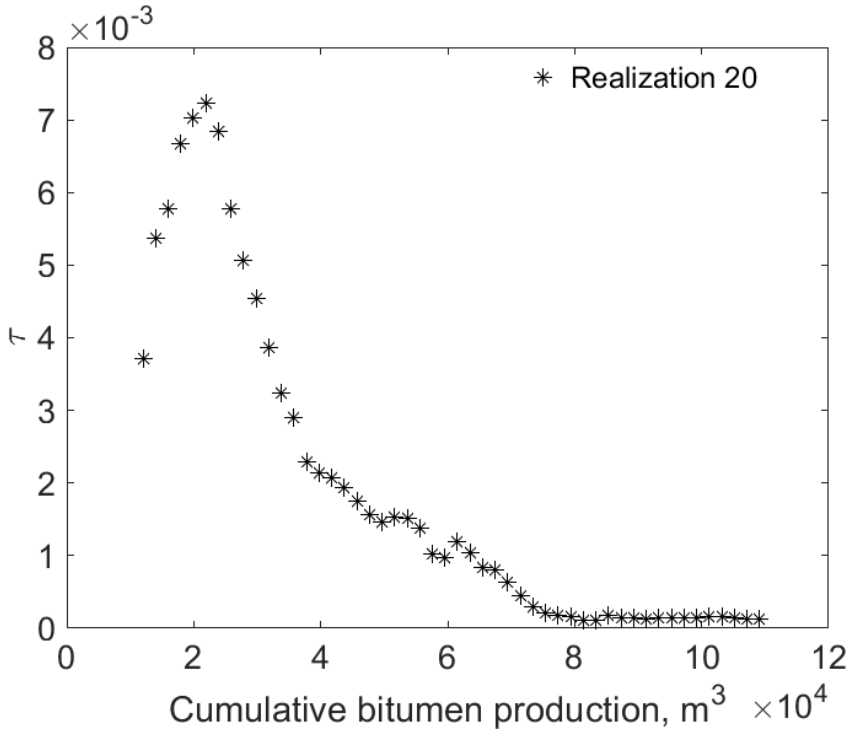

Figure K-12(c). τ for SAGD as a function of cumulative bitumen production for realization 20

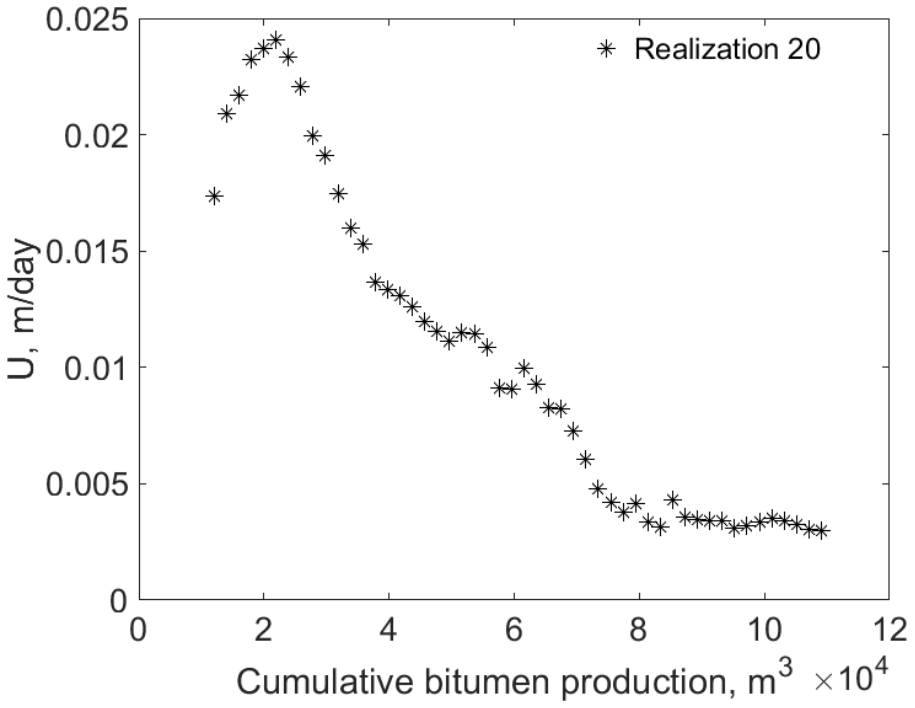

Figure K-12(d). U for SAGD as a function of cumulative bitumen production for realization 20

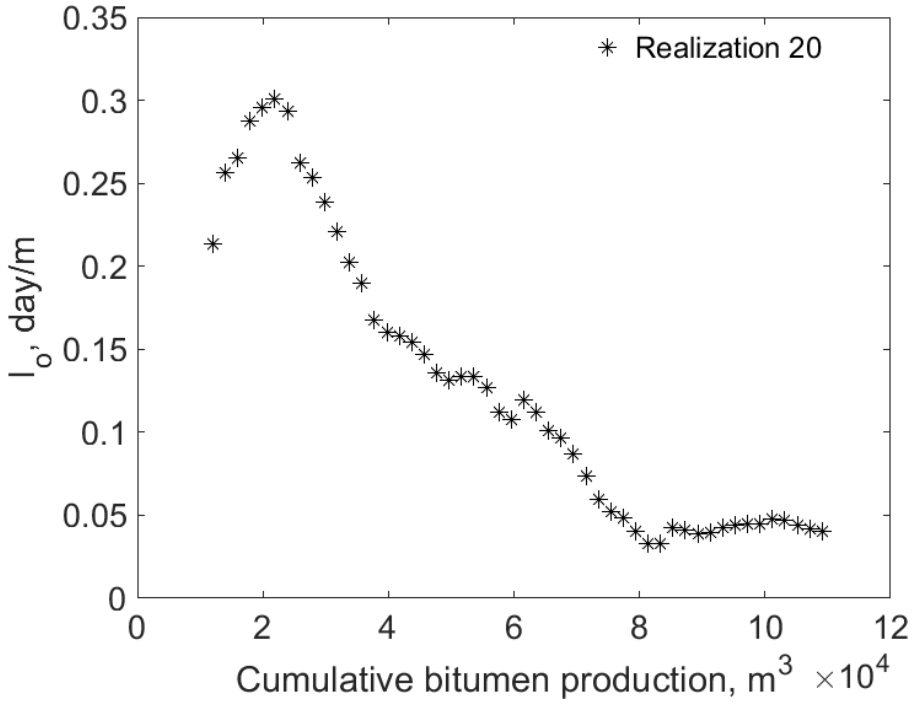

Figure K-12(e).I_o for SAGD as a function of cumulative bitumen production for realization 20

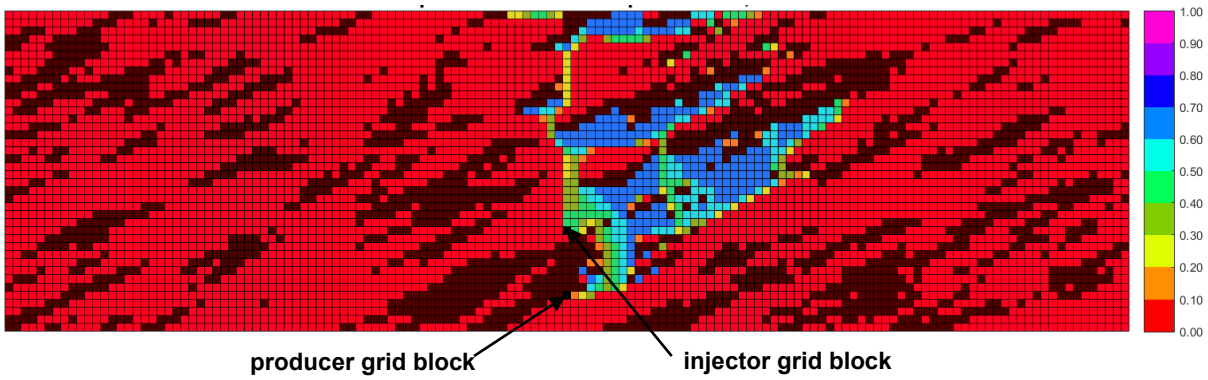

Figure K-12(f). Vapor-phase saturation map in SAGD for realization 20 for Q ≈ 31218 m^3

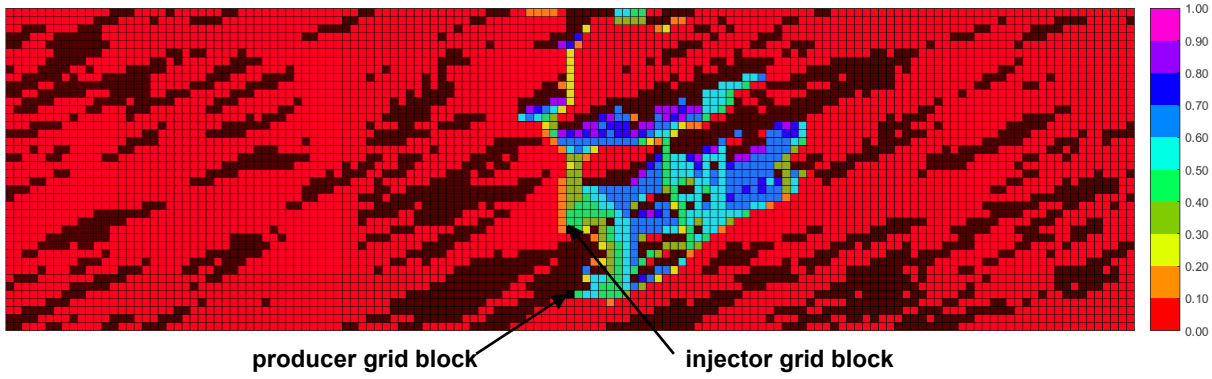

Figure K-12(g). Vapor-phase saturation map in n-C_6 SAGD for realization 20 for Q ≈ 31218 m^3

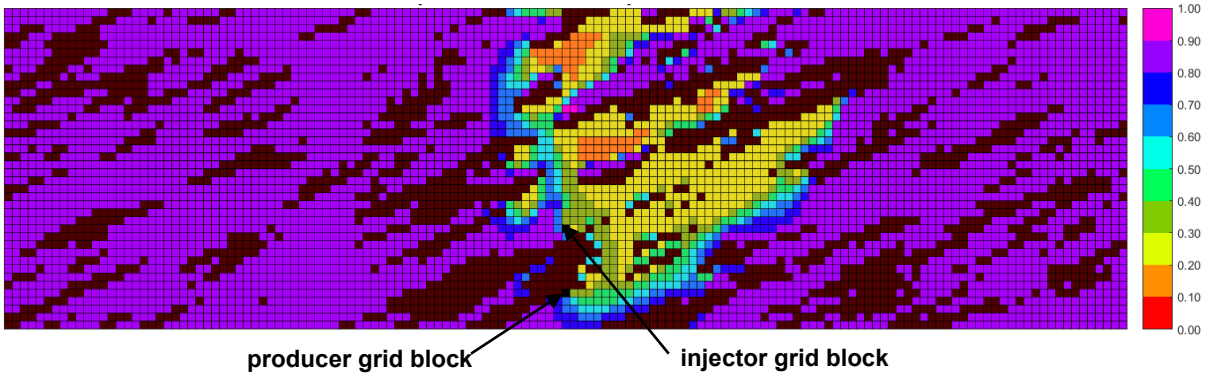

Figure K-12(h). Oleic-phase saturation map in SAGD for realization 20 for Q ≈ 31218 m^3

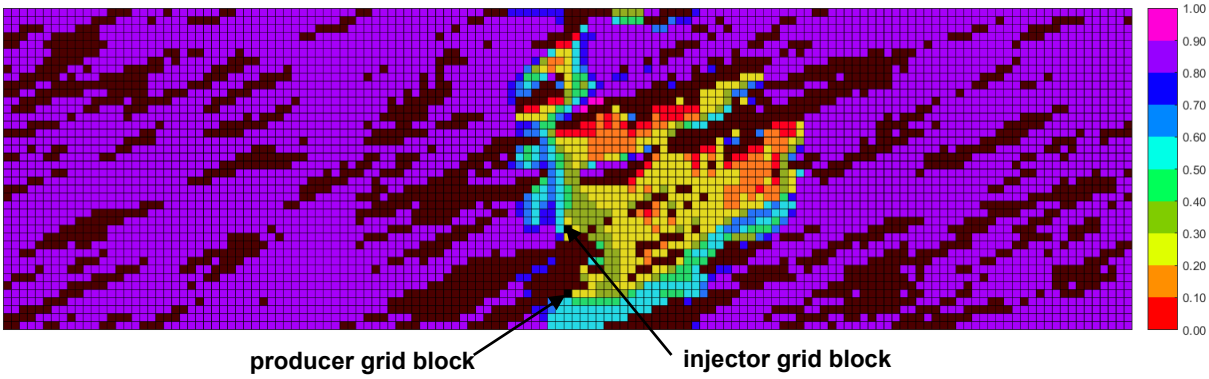

Figure K-12(i). Oleic-phase saturation map in n-C_6 SAGD for realization 20 for Q ≈ 31218 m^3

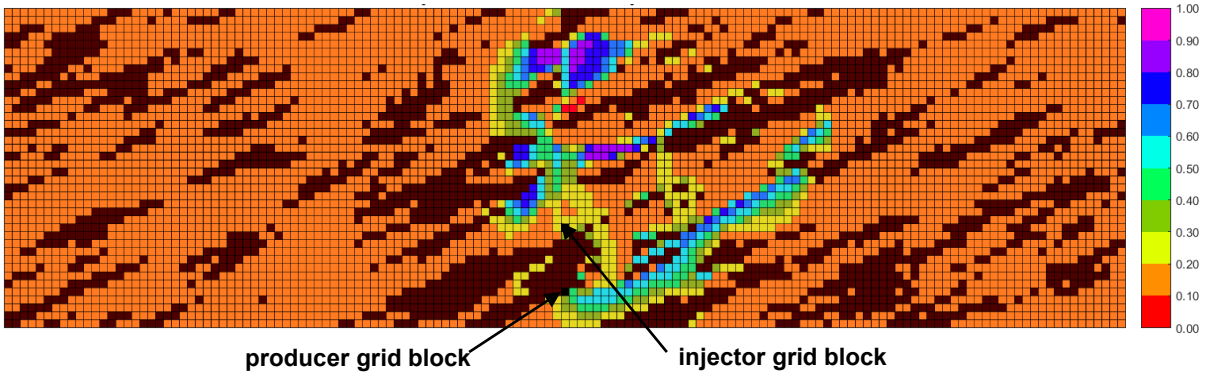

Figure K-12(j). Aqueous-phase saturation map in SAGD for realization 20 for Q ≈ 31218 m^3

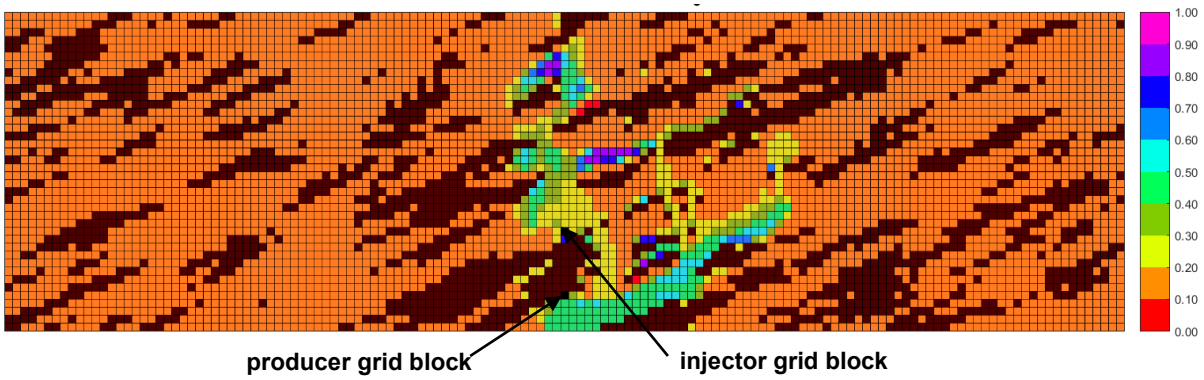

Figure K-12(k). Aqueous-phase saturation map in n-C_6 SAGD for realization 20 for Q ≈ 31218 m^3

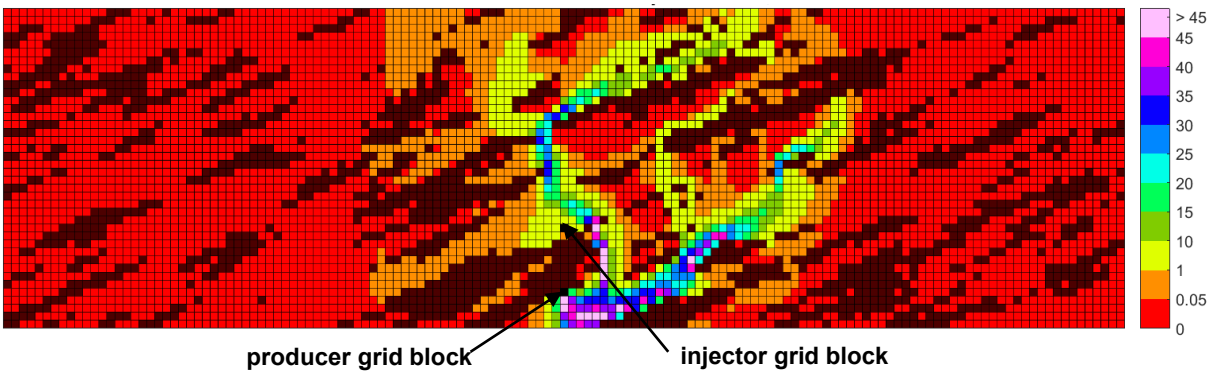

Figure K-12(l). Bitumen molar flow rate (kg-mole/day) map in SAGD for realization 20 for Q ≈ 31218 m^3

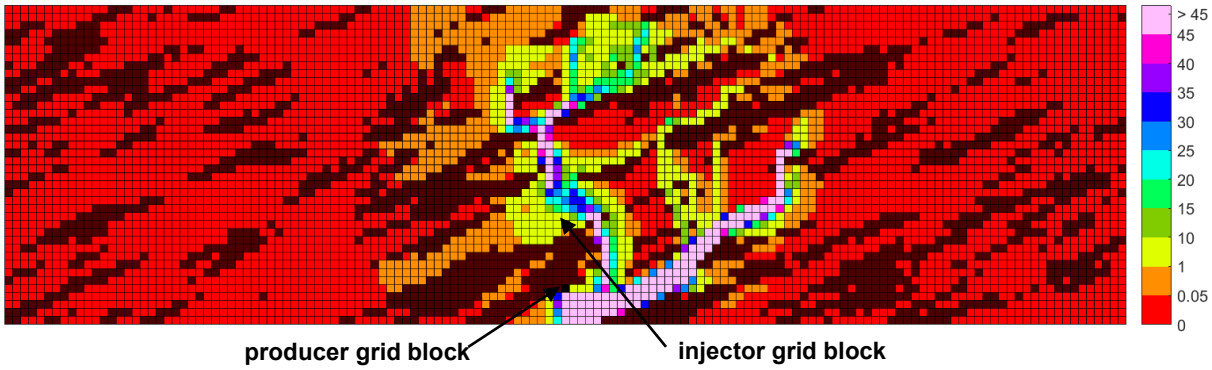

Figure K-12(m). Bitumen molar flow rate (kg-mole/day) map in n-C_6 SAGD for realization 20 for Q ≈ 31218 m^3

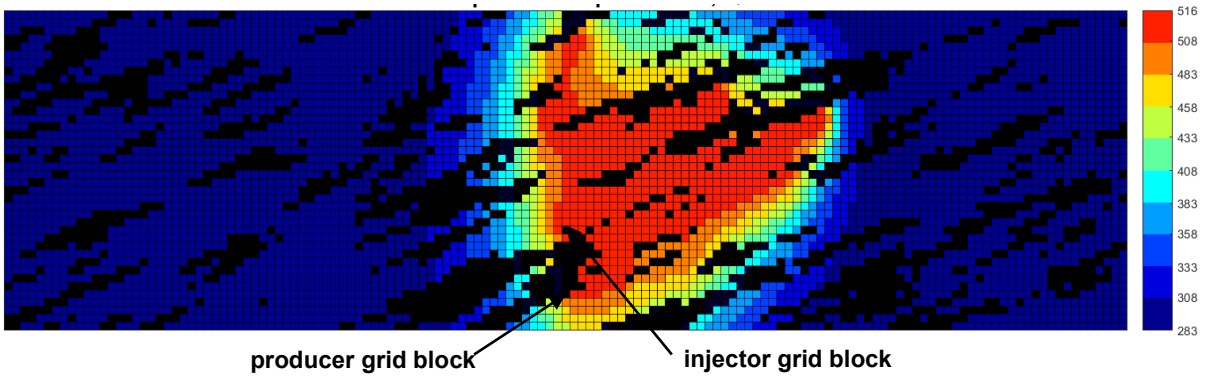

Figure K-12(n). Temperature (Kelvin) map in SAGD for realization 20 for Q ≈ 31218 m^3

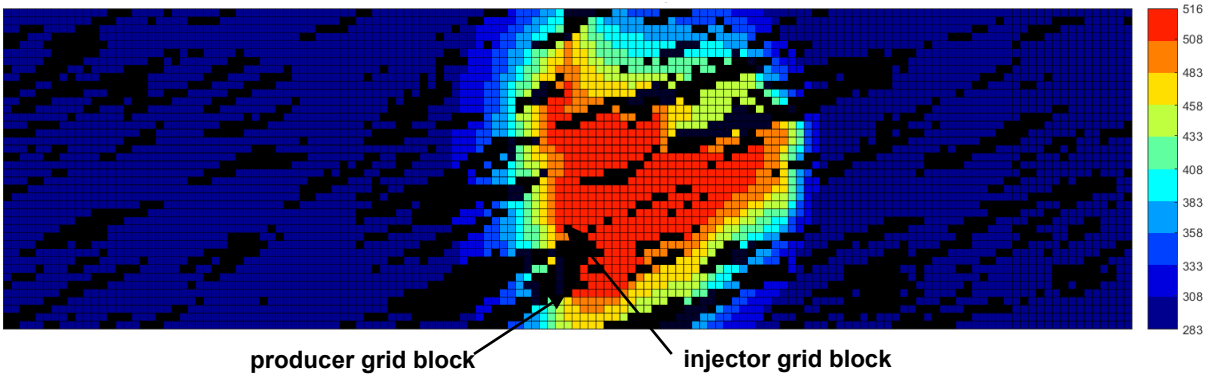

Figure K-12(o). Temperature (Kelvin) map in n-C_6 SAGD for realization 20 for Q ≈ 31218 m^3

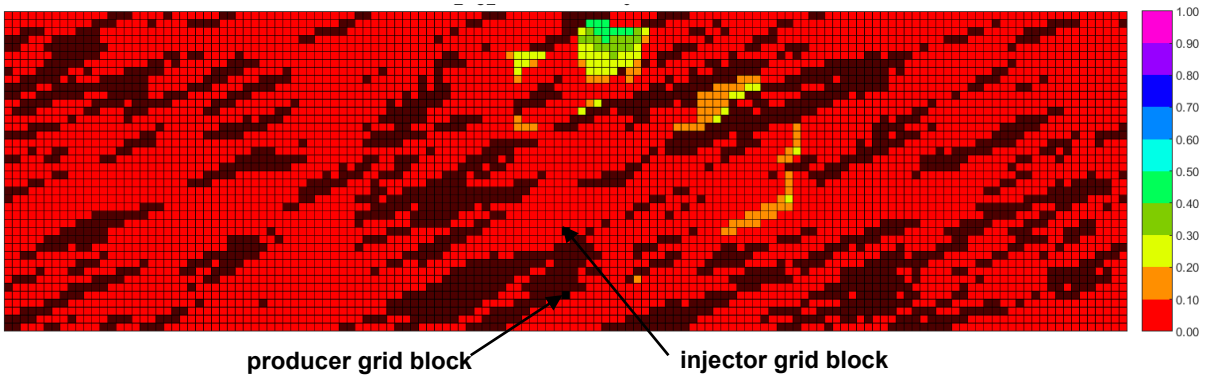

Figure K-12(p). $\beta_{LX_{sL}}$ map in n-C_6 SAGD for realization 20 for Q ≈ 31218 m^3

Figure K-12. Property maps for SAGD and n-C_6 SAGD for realization 20

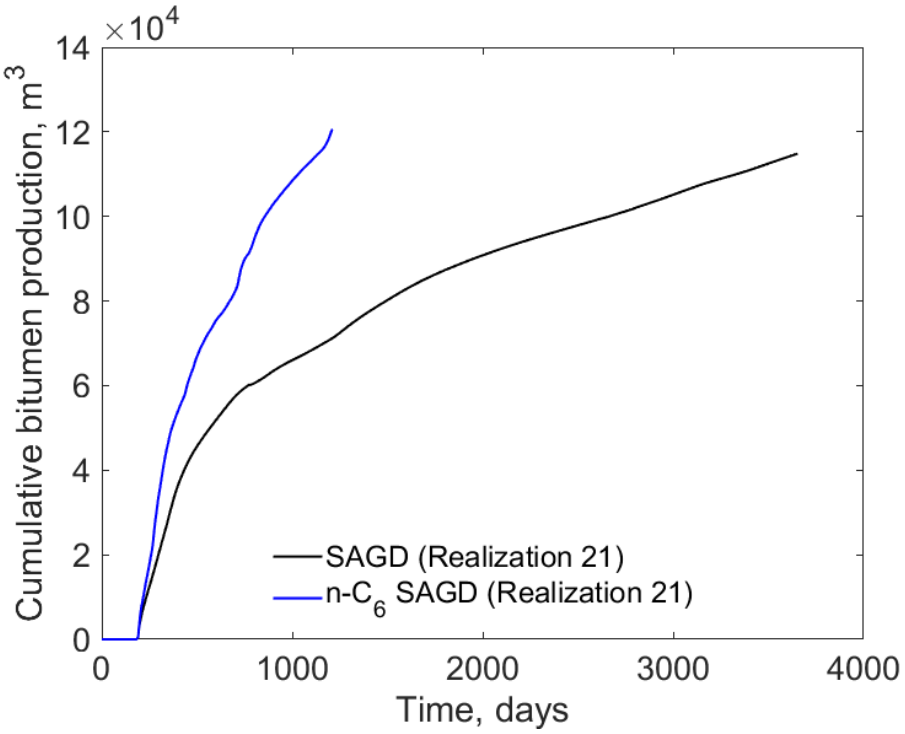

Figure K-13(a). Cumulative bitumen production histories for SAGD and n-C_6 SAGD for realization 21

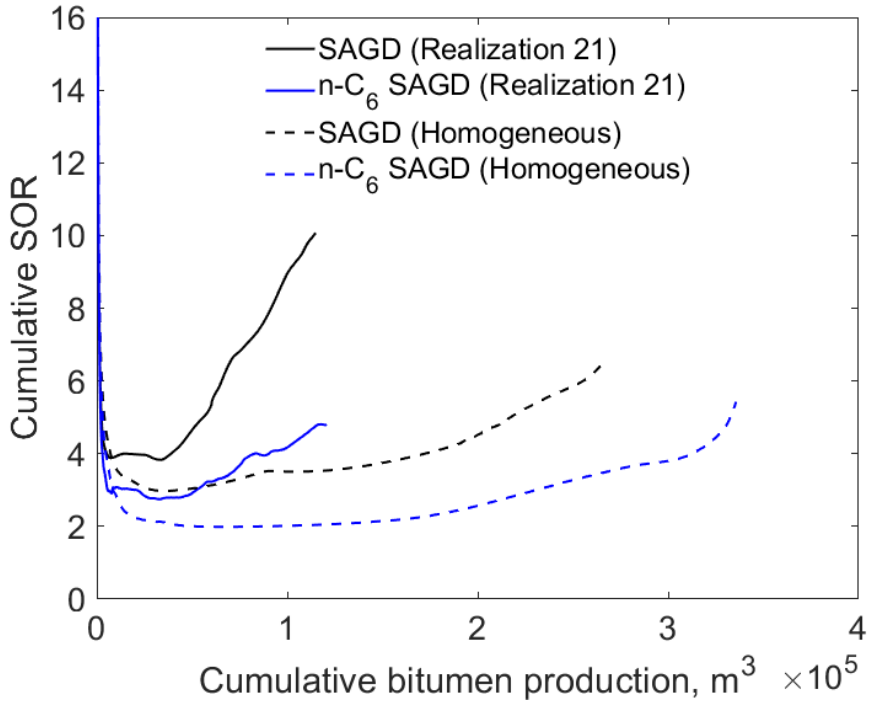

Figure K-13(a). Cumulative SOR for SAGD and n-C_6 SAGD for realization 21

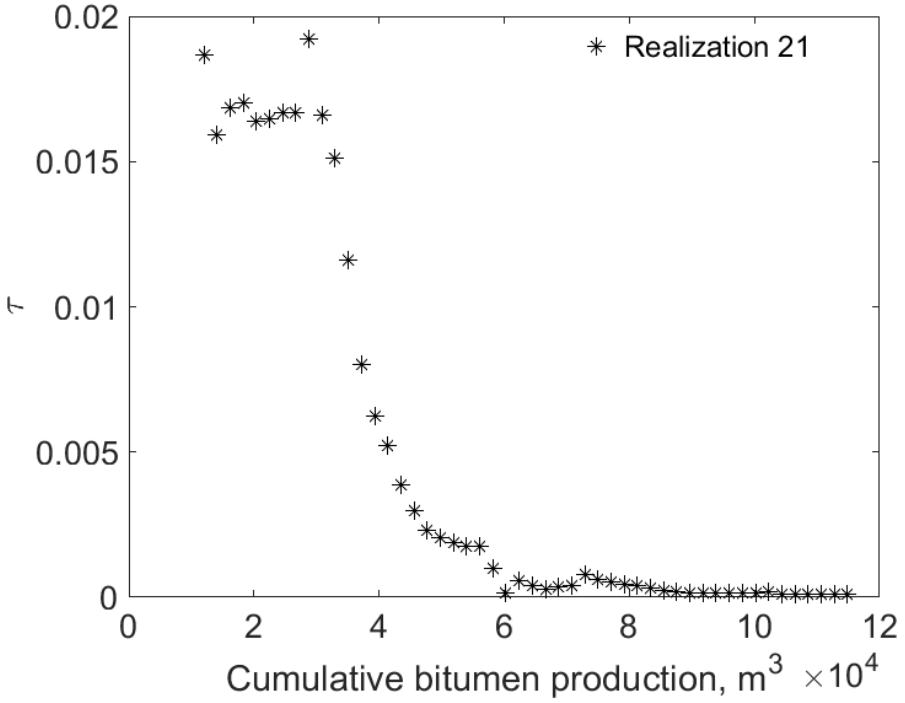

Figure K-13(a). τ for SAGD as a function of cumulative bitumen production for realization 21

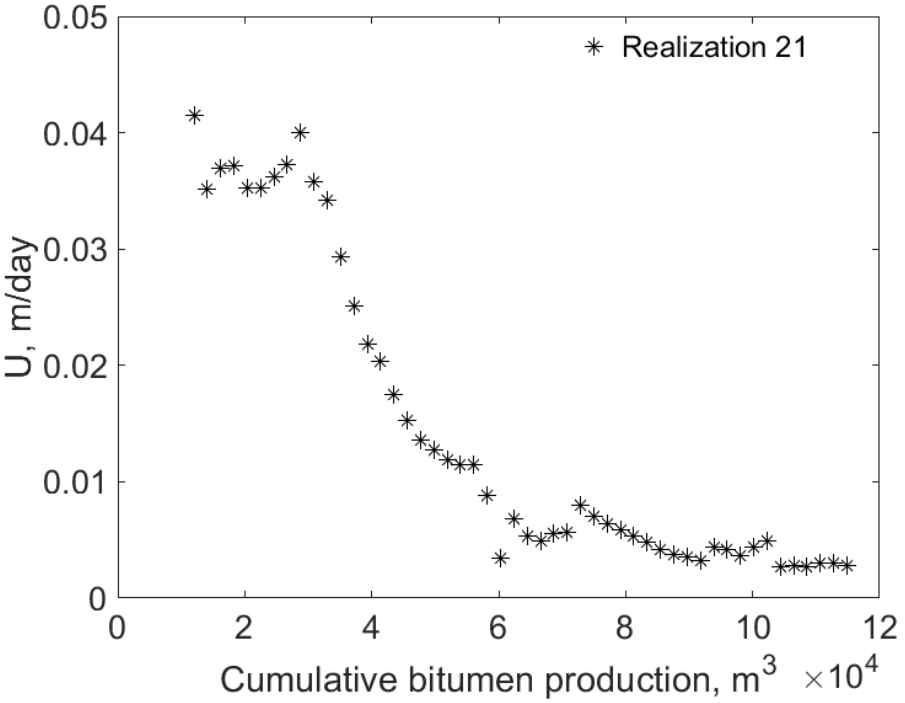

Figure K-13(b). U for SAGD as a function of cumulative bitumen production for realization 21

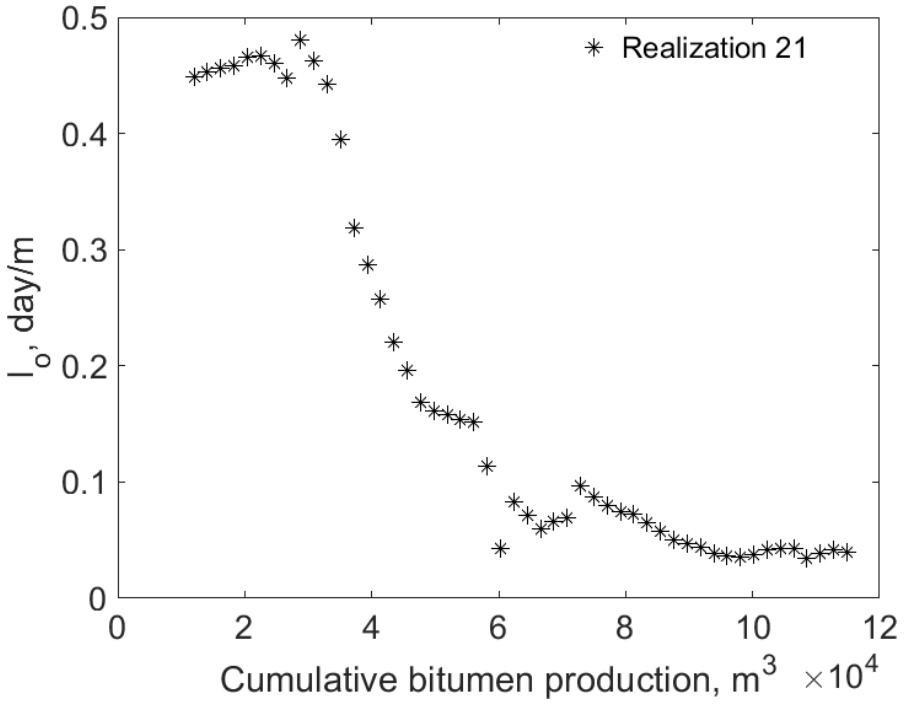

Figure K-13(e).I_o for SAGD as a function of cumulative bitumen production for realization 21

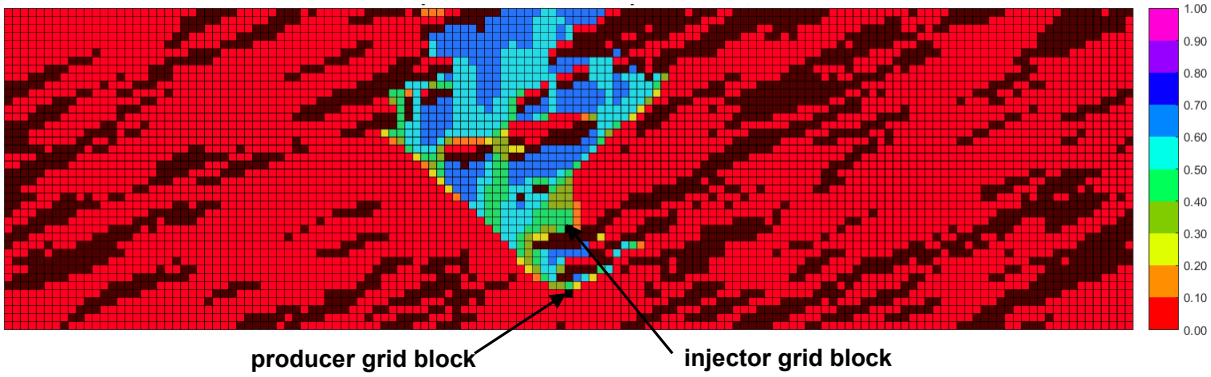

Figure K-13(f). Vapor-phase saturation map in SAGD for realization 21 for Q ≈ 31218 m^3

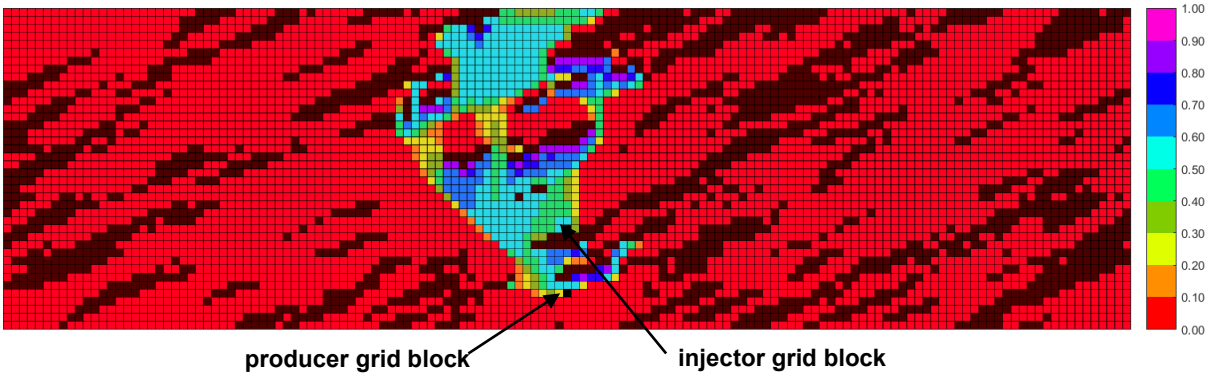

Figure K-13(g). Vapor-phase saturation map in n-C_6 SAGD for realization 21 for Q ≈ 31218 m^3

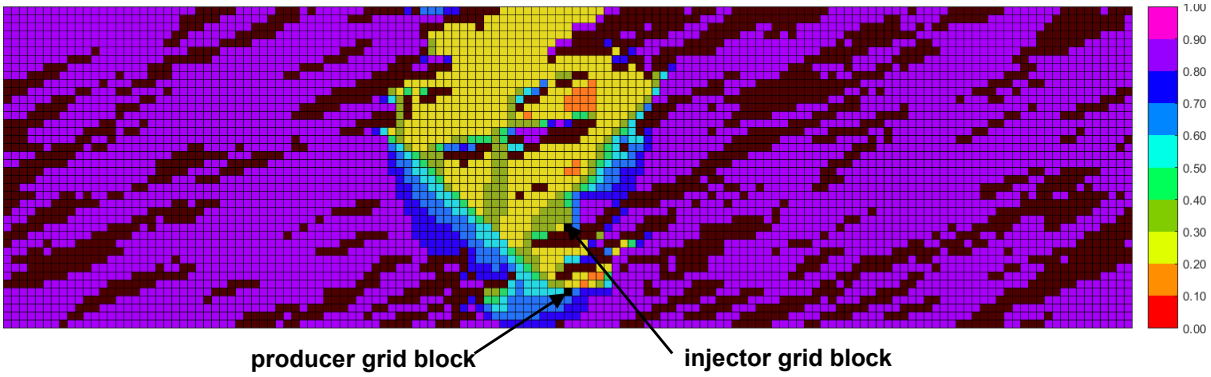

Figure K-13(h). Oleic-phase saturation map in SAGD for realization 21 for Q ≈ 31218 m^3

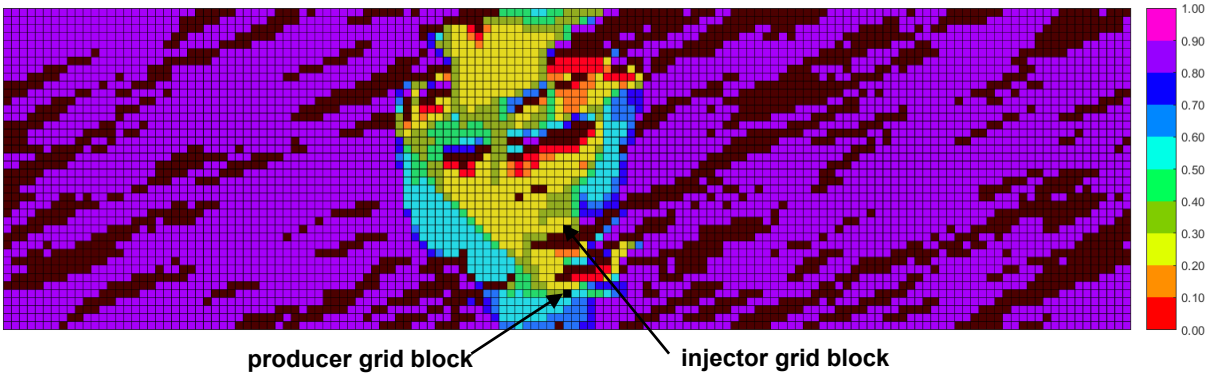

Figure K-13(i). Oleic-phase saturation map in n-C_6 SAGD for realization 21 for Q ≈ 31218 m^3

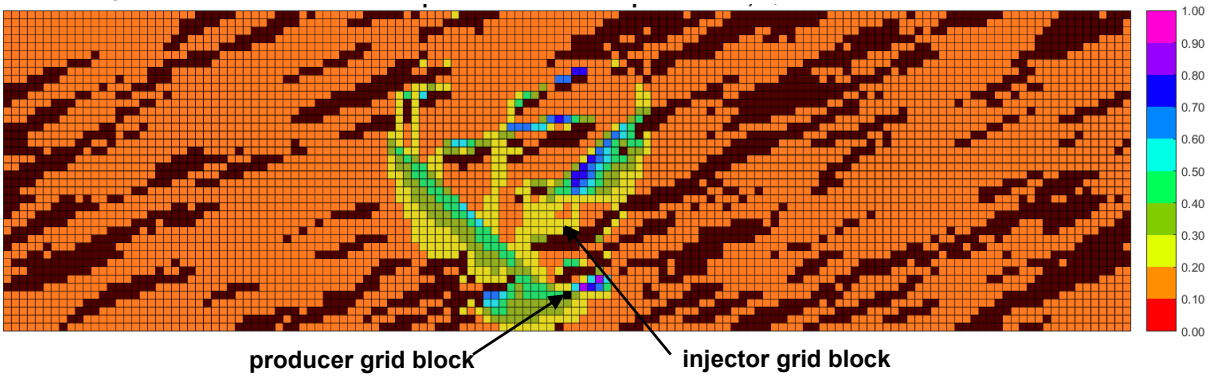

Figure K-13(j). Aqueous-phase saturation map in SAGD for realization 21 for Q ≈ 31218 m^3

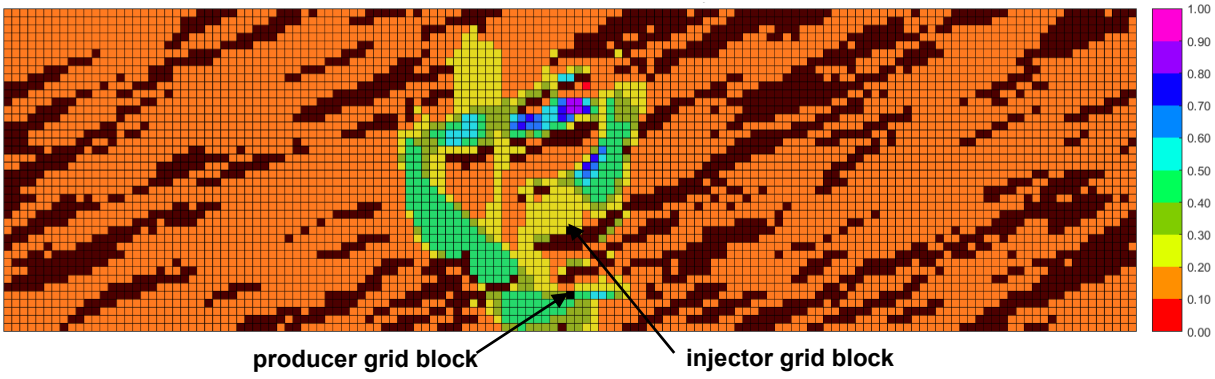

Figure K-13(k). Aqueous-phase saturation map in n-C_6 SAGD for realization 21 for Q ≈ 31218 m^3

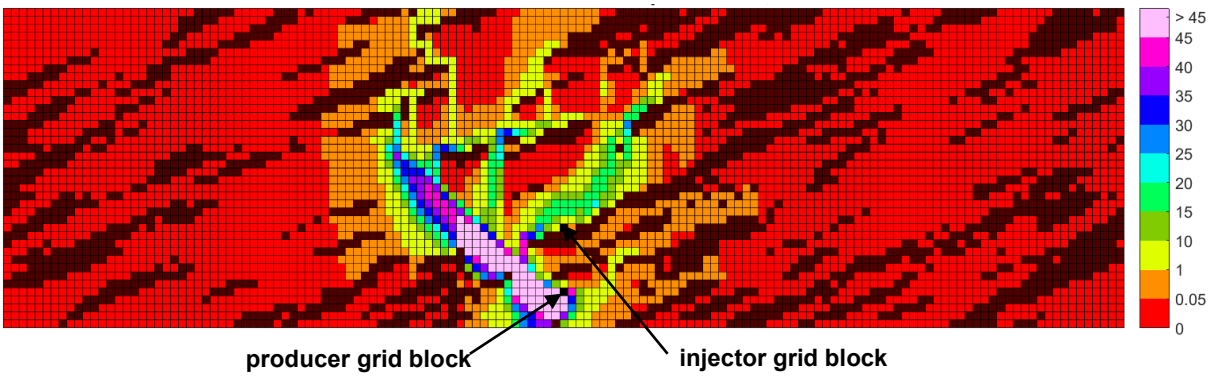

Figure K-13(l). Bitumen molar flow rate (kg-mole/day) map in SAGD for realization 21 for Q ≈ 31218 m^3

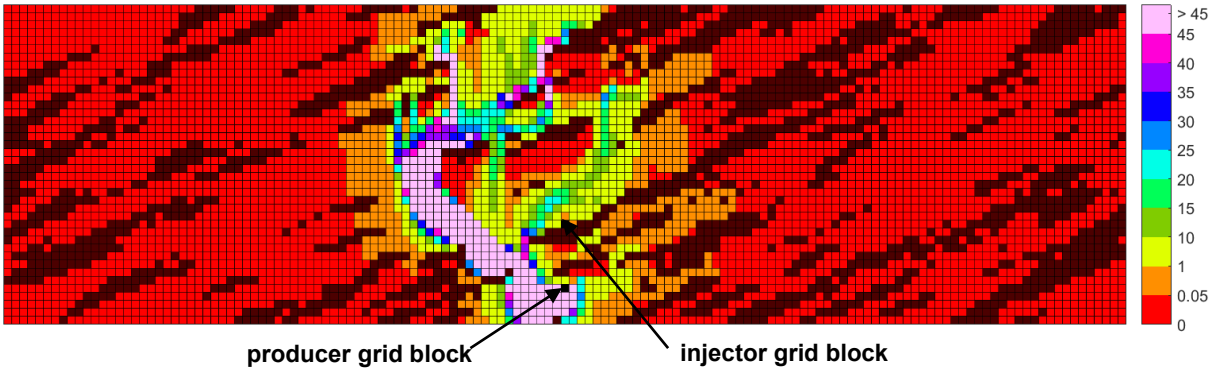

Figure K-13(m). Bitumen molar flow rate (kg-mole/day) map in n-C_6 SAGD for realization 21 for Q ≈ 31218 m^3

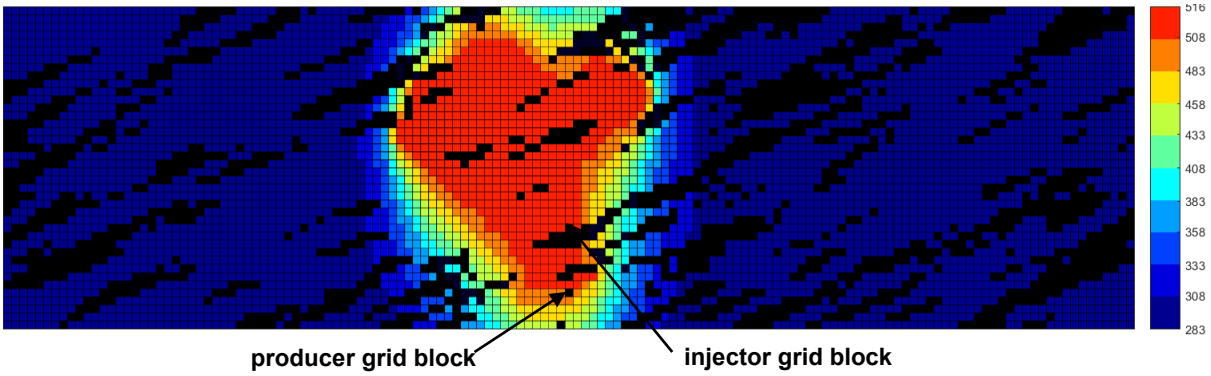

Figure K-13(n). Temperature (Kelvin) map in SAGD for realization 21 for Q ≈ 31218 m^3

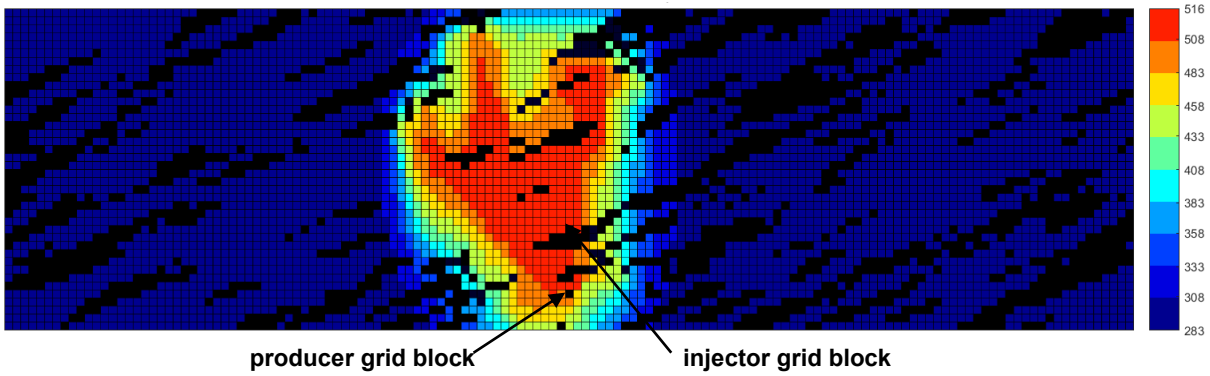

Figure K-13(o). Temperature (Kelvin) map in n-C_6 SAGD for realization 21 for Q ≈ 31218 m^3

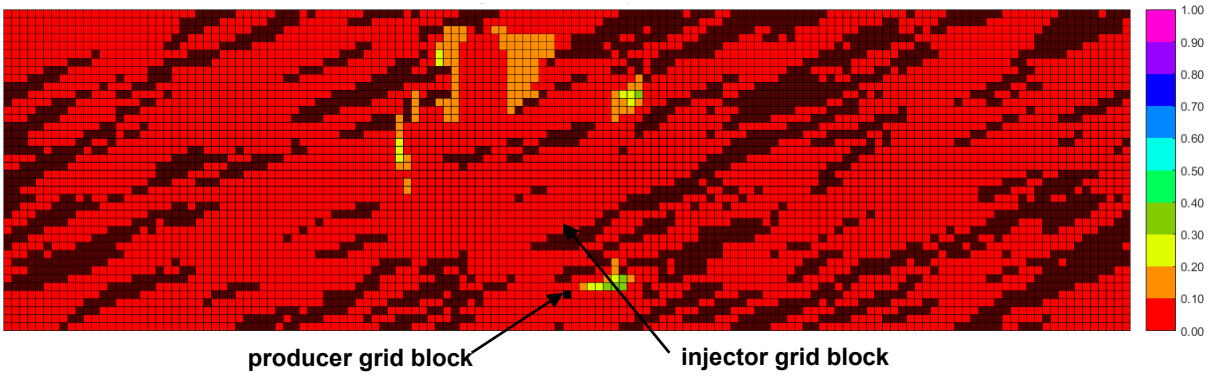

Figure K-13(p). $\beta_L x_{sL}$ map in n-C_6 SAGD for realization 21 for Q ≈ 31218 m^3

Figure K-13. Property maps for SAGD and n-C_6 SAGD for realization 21

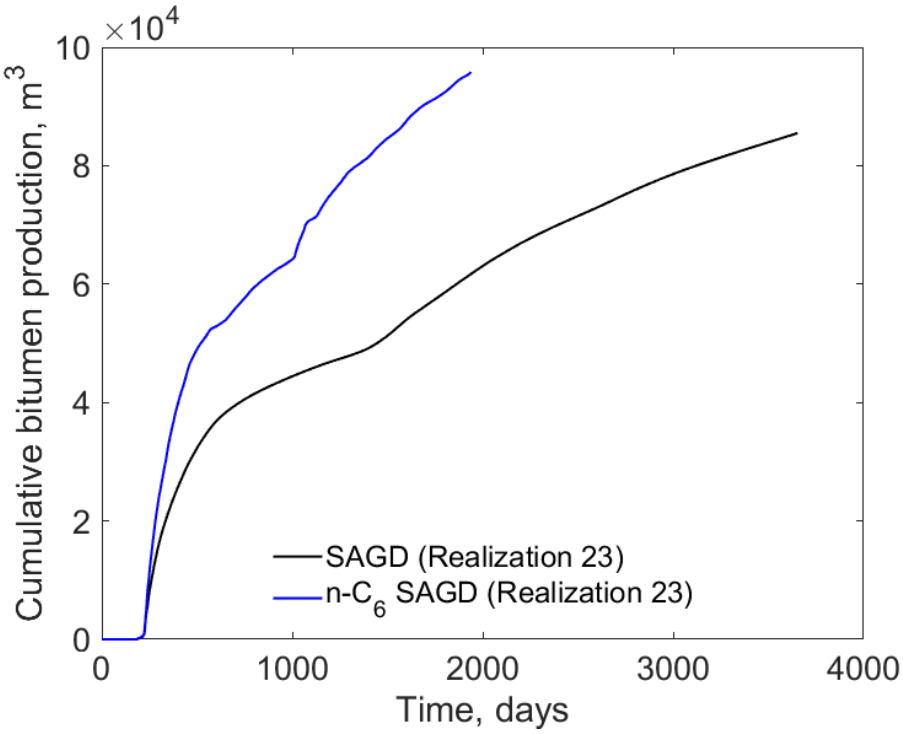

Figure K-14(a). Cumulative bitumen production histories for SAGD and n-C_6 SAGD for realization 23

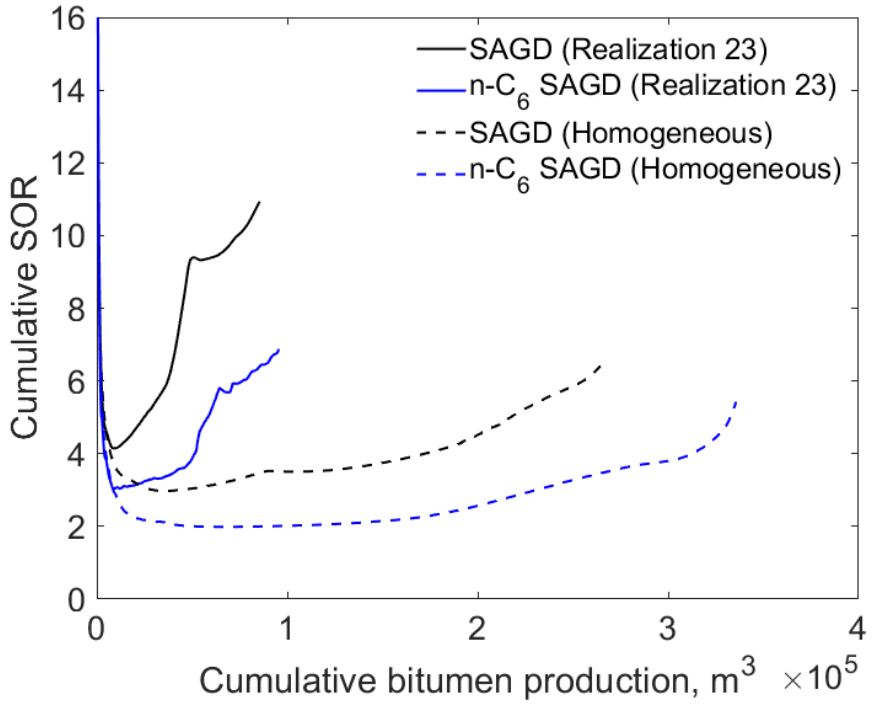

Figure K-14(b). Cumulative SOR for SAGD and n-C_6 SAGD for realization 23

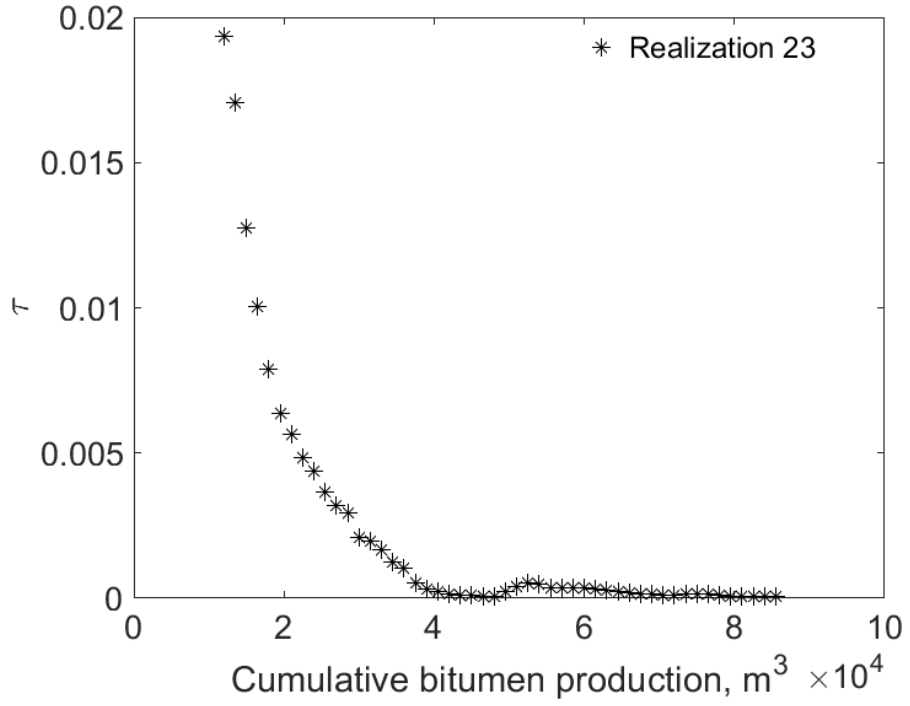

Figure K-14(c). τ for SAGD as a function of cumulative bitumen production for realization 23

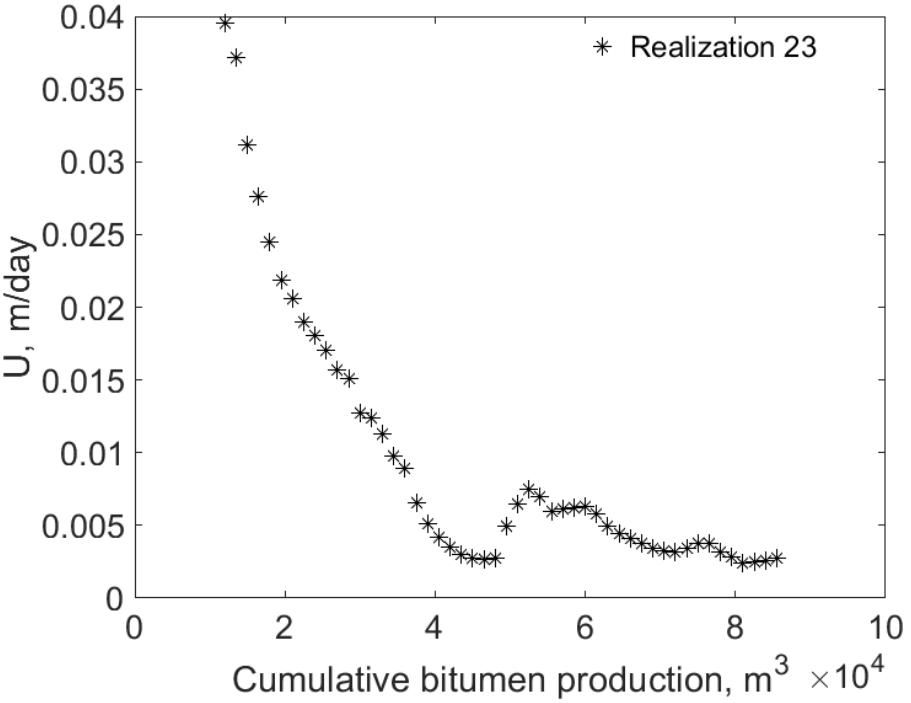

Figure K-14(d). U for SAGD as a function of cumulative bitumen production for realization 23

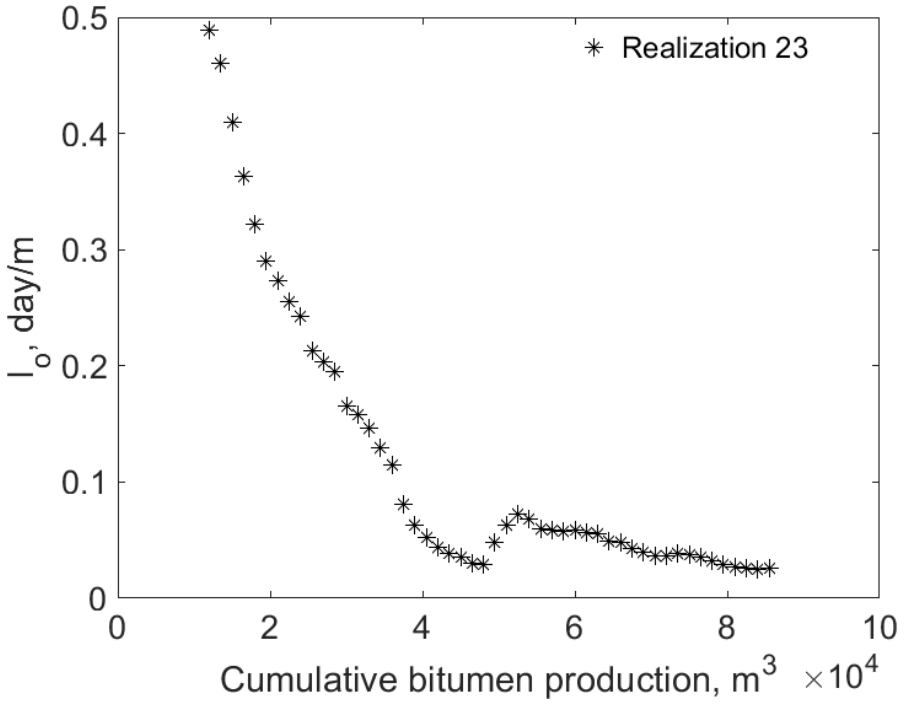

Figure K-14(e).I_o for SAGD as a function of cumulative bitumen production for realization 23

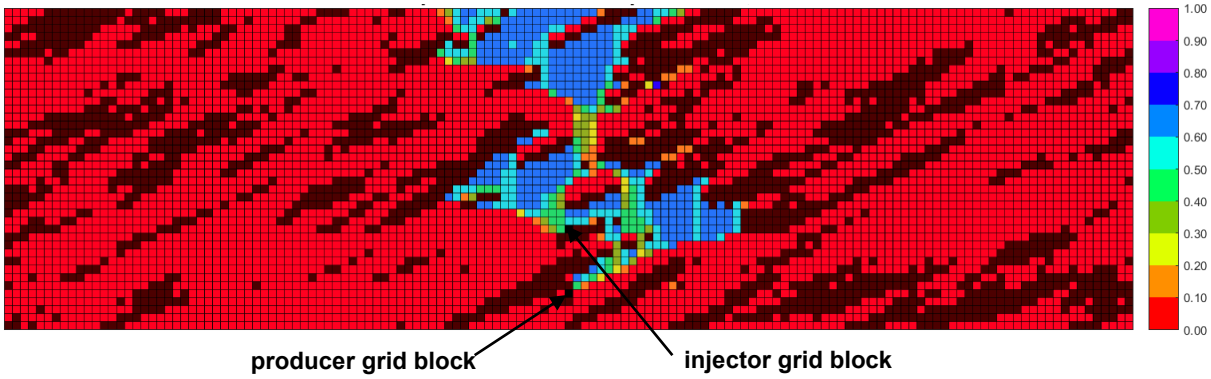

Figure K-14(f). Vapor-phase saturation map in SAGD for realization 23 for Q ≈ 31218 m^3

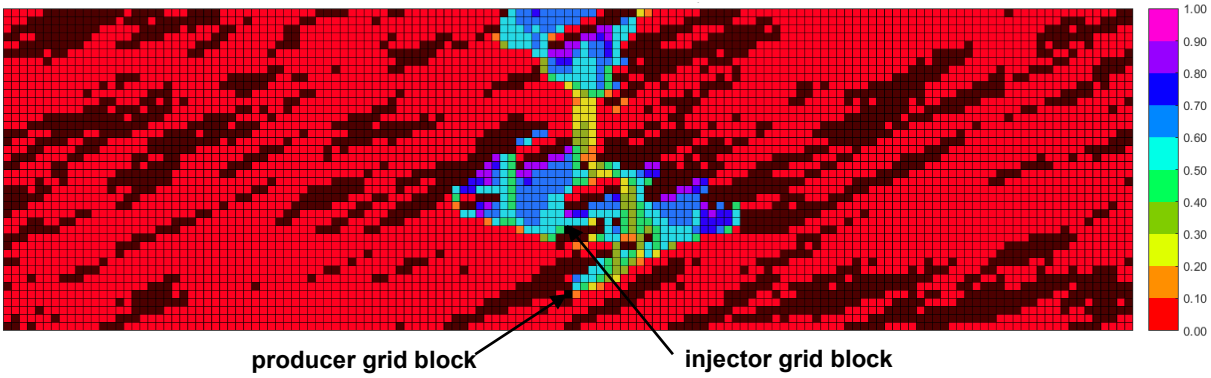

Figure K-14(g). Vapor-phase saturation map in n-C_6 SAGD for realization 23 for Q ≈ 31218 m^3

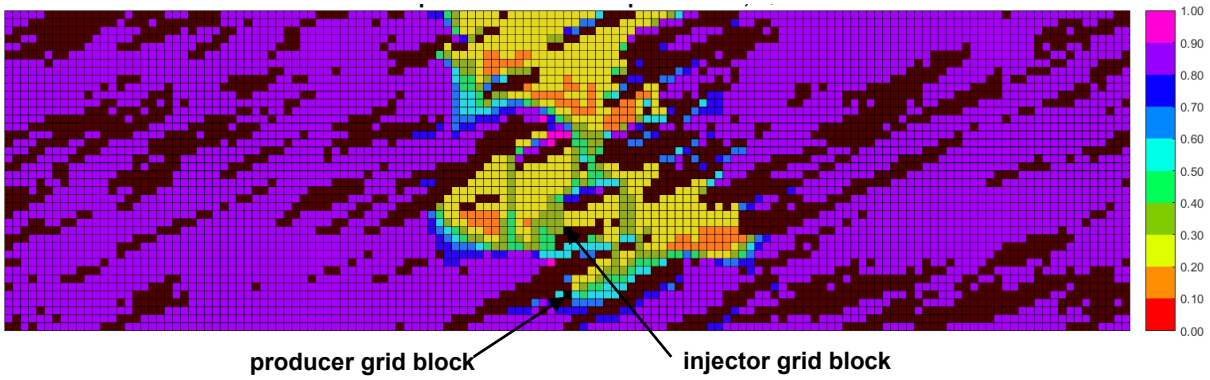

Figure K-14(h). Oleic-phase saturation map in SAGD for realization 23 for Q ≈ 31218 m^3

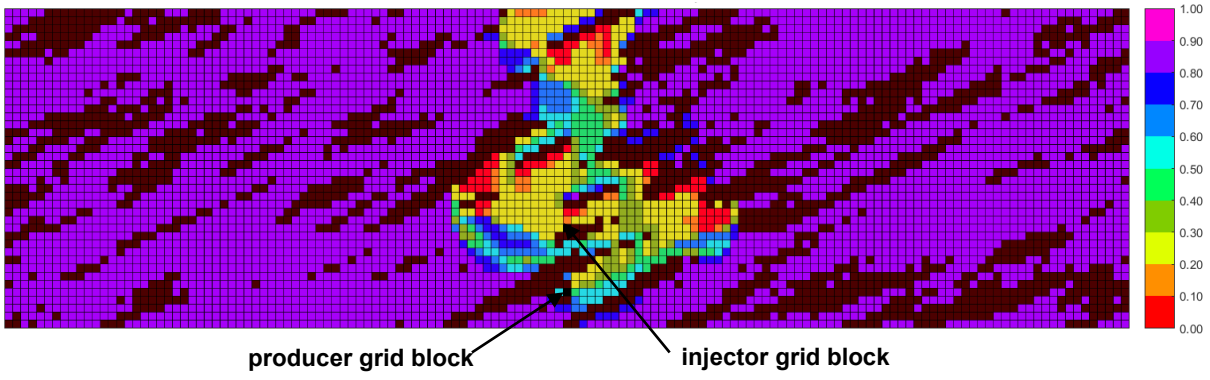

Figure K-14(i). Oleic-phase saturation map in n-C_6 SAGD for realization 23 for Q ≈ 31218 m^3

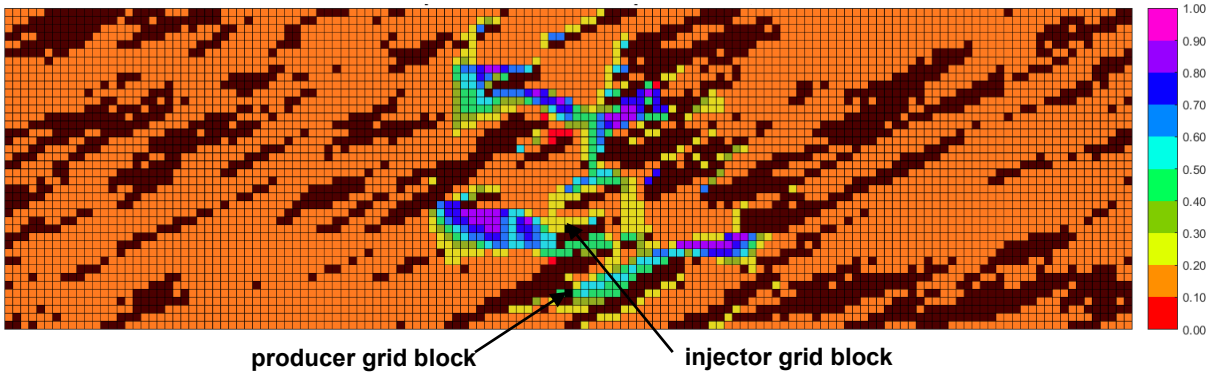

Figure K-14(j). Aqueous-phase saturation map in SAGD for realization 23 for Q ≈ 31218 m^3

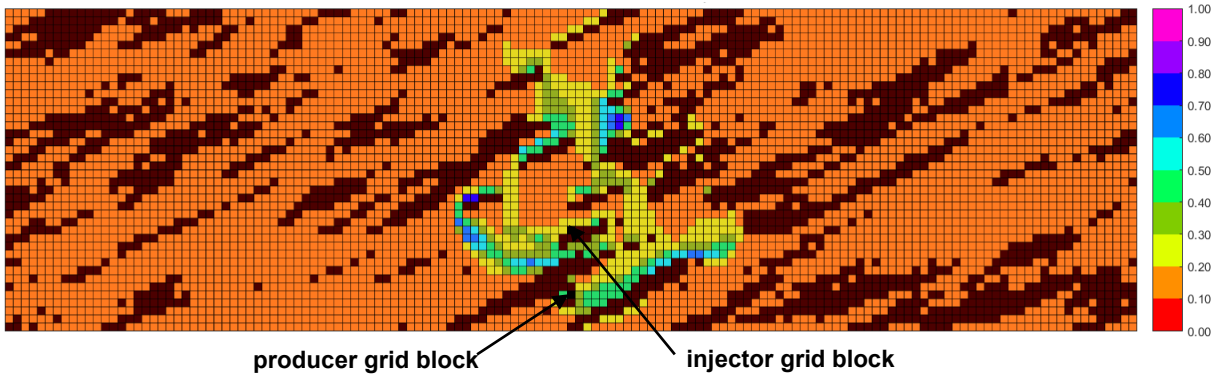

Figure K-14(k). Aqueous-phase saturation map in n-C_6 SAGD for realization 23 for Q ≈ 31218 m^3

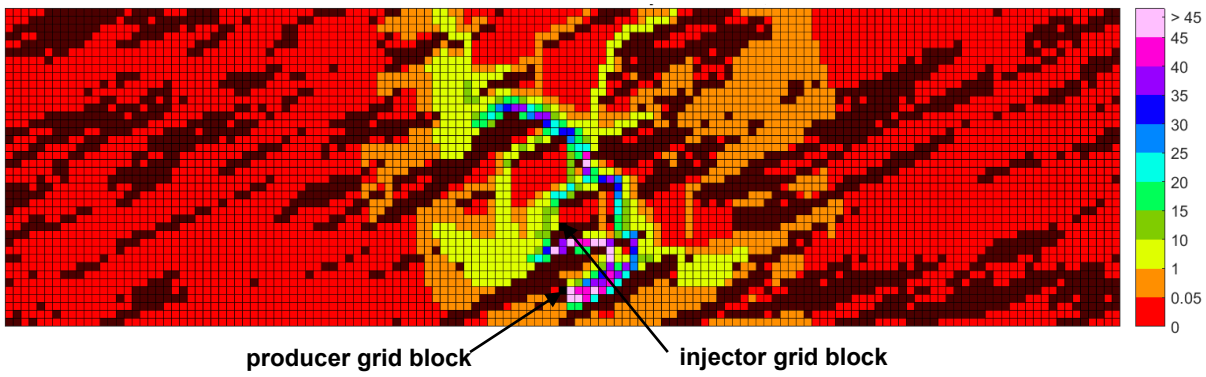

Figure K-14(l). Bitumen molar flow rate (kg-mole/day) map in SAGD for realization 23 for Q ≈ 31218 m^3

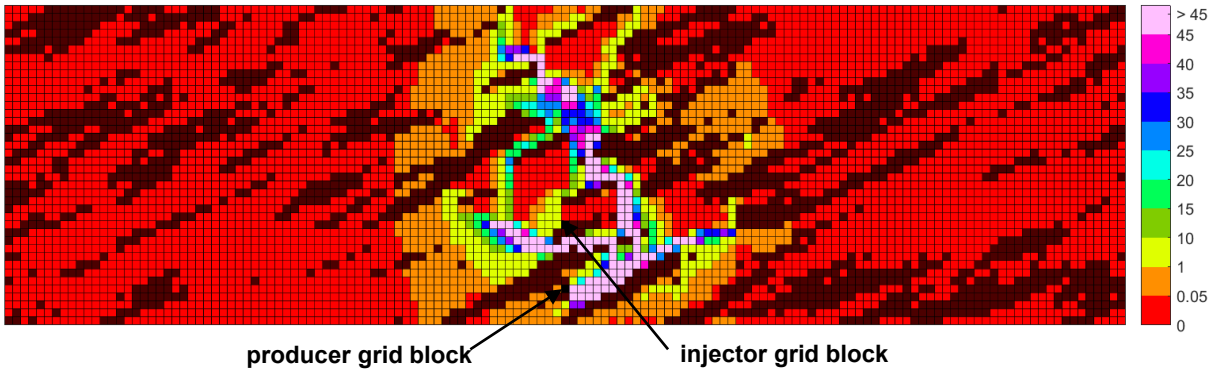

Figure K-14(m). Bitumen molar flow rate (kg-mole/day) map in n-C_6 SAGD for realization 23 for Q ≈ 31218 m^3

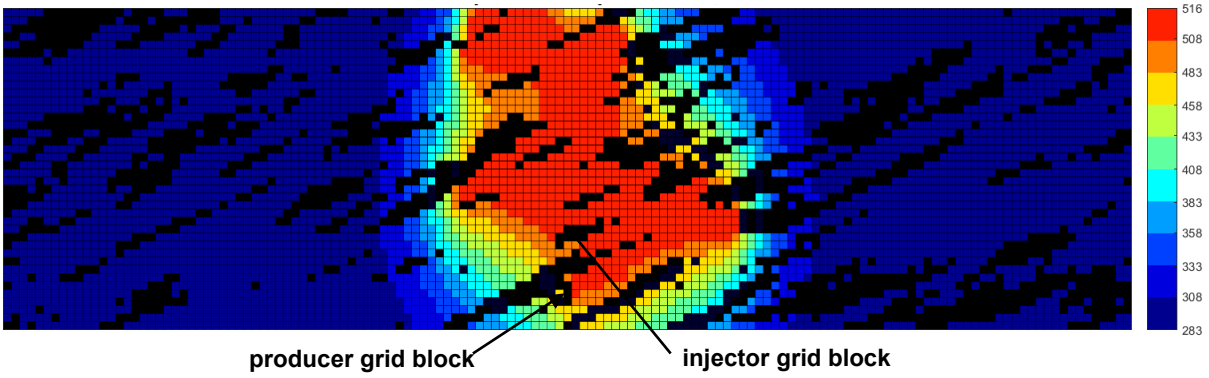

Figure K-14(n). Temperature (Kelvin) map in SAGD for realization 23 for Q ≈ 31218 m^3

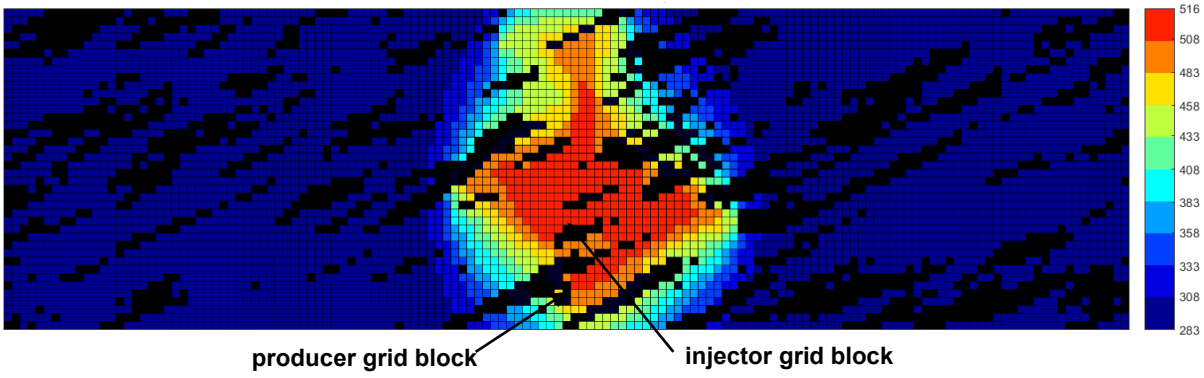

Figure K-14(o). Temperature (Kelvin) map in n-C_6 SAGD for realization 23 for Q ≈ 31218 m^3

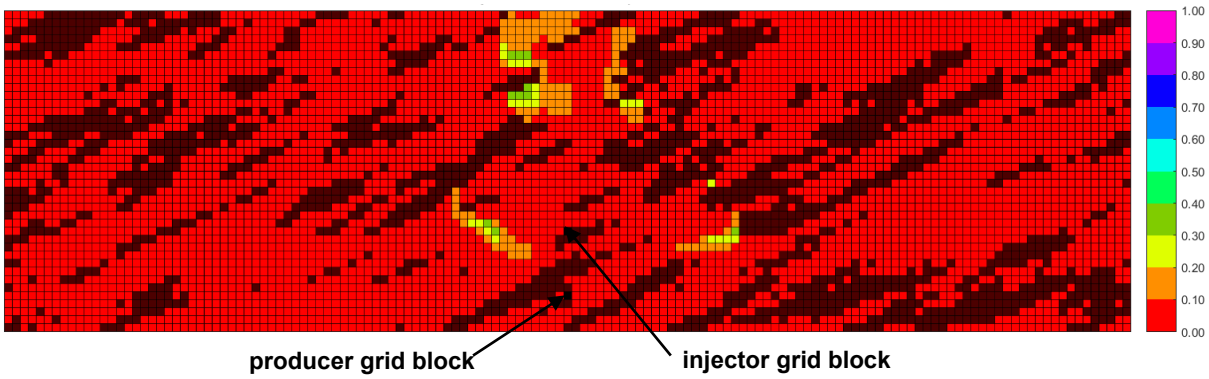

Figure K-14(p). $\beta_{Lx_{sL}}$ map in n-C_6 SAGD for realization 23 for Q ≈ 31218 m^3

Figure K-14. Property maps for SAGD and n-C_6 SAGD for realization 23

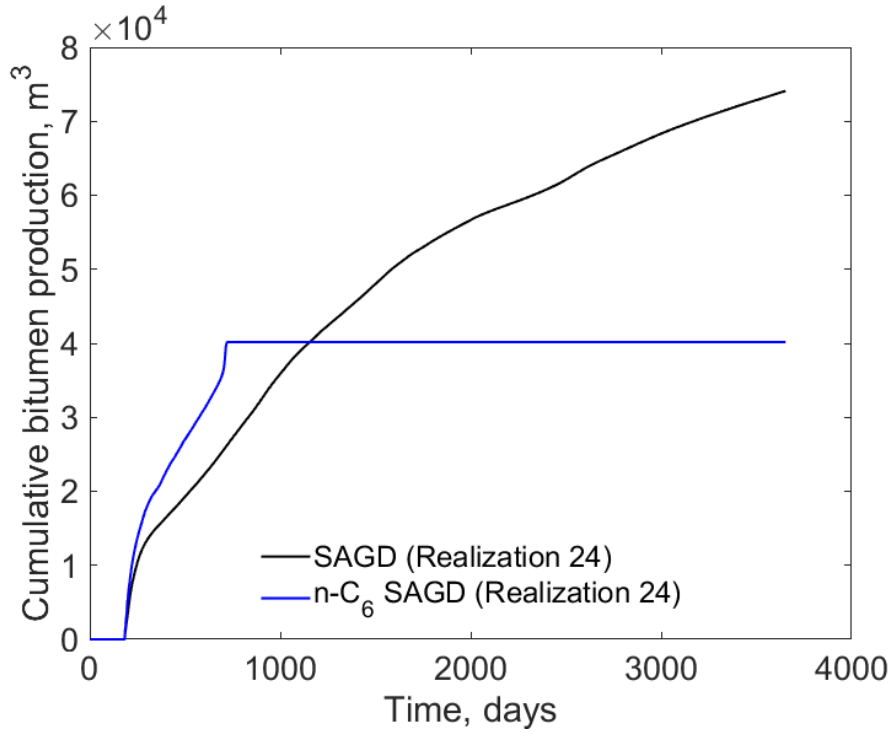

Figure K-15(a). Cumulative bitumen production histories for SAGD and n-C_6 SAGD for realization 24

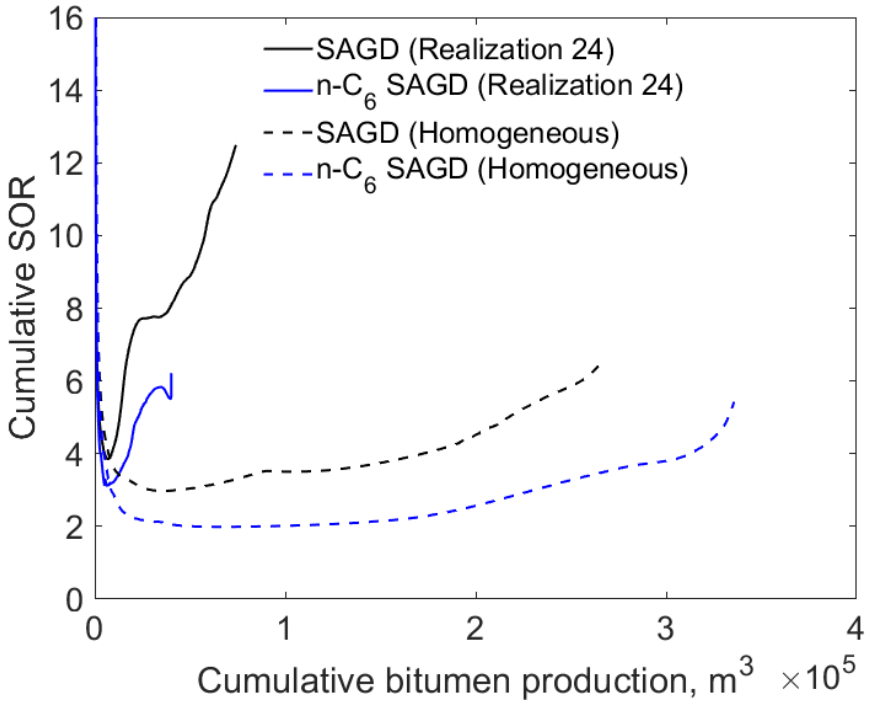

Figure K-15(b). Cumulative SOR for SAGD and n-C_6 SAGD for realization 24

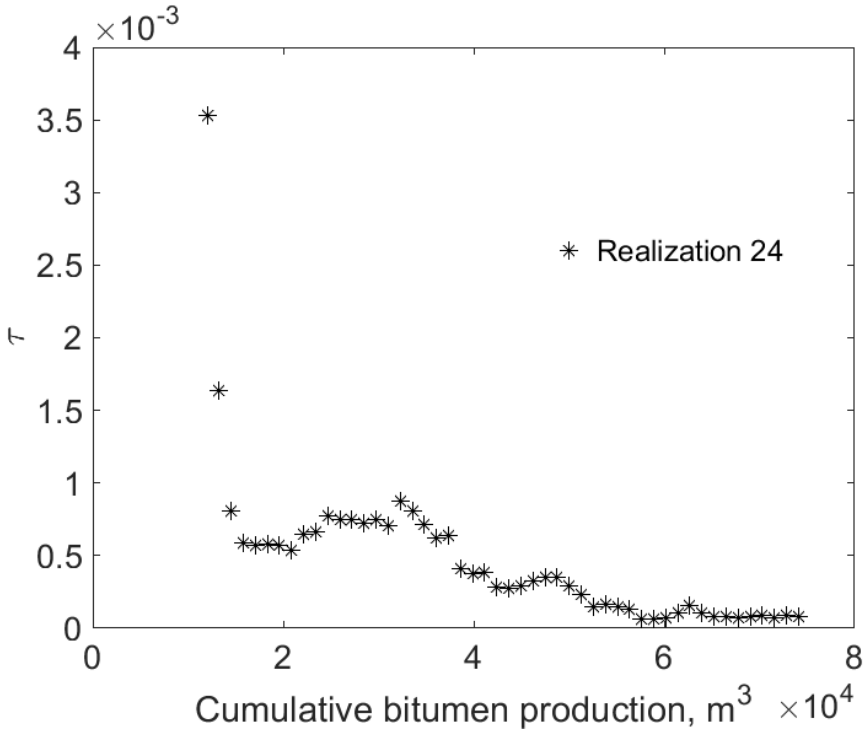

Figure K-15(c). τ for SAGD as a function of cumulative bitumen production for realization 24

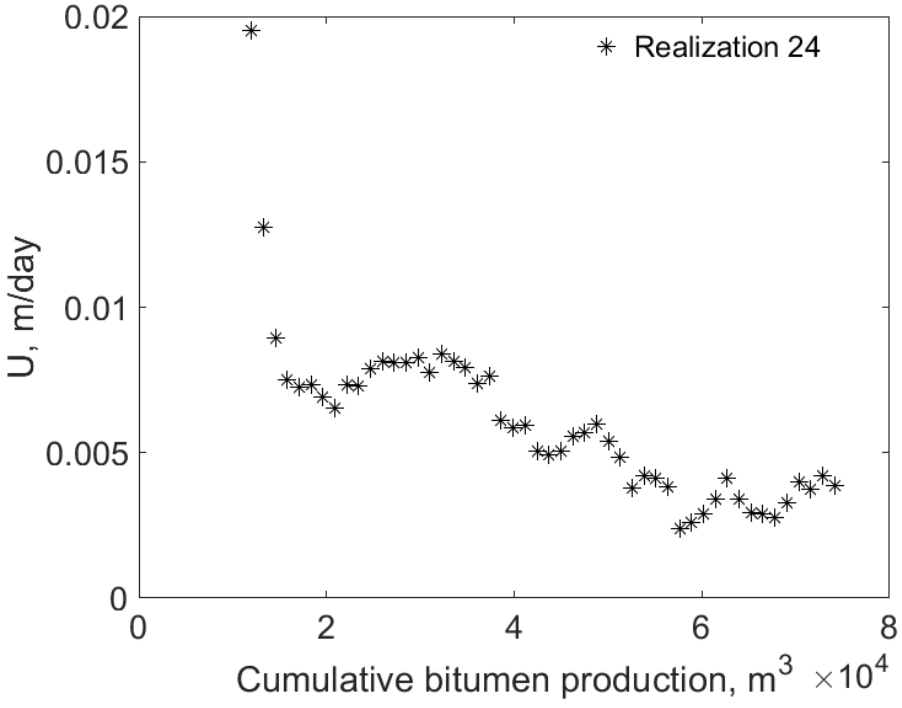

Figure K-15(d). U for SAGD as a function of cumulative bitumen production for realization 24

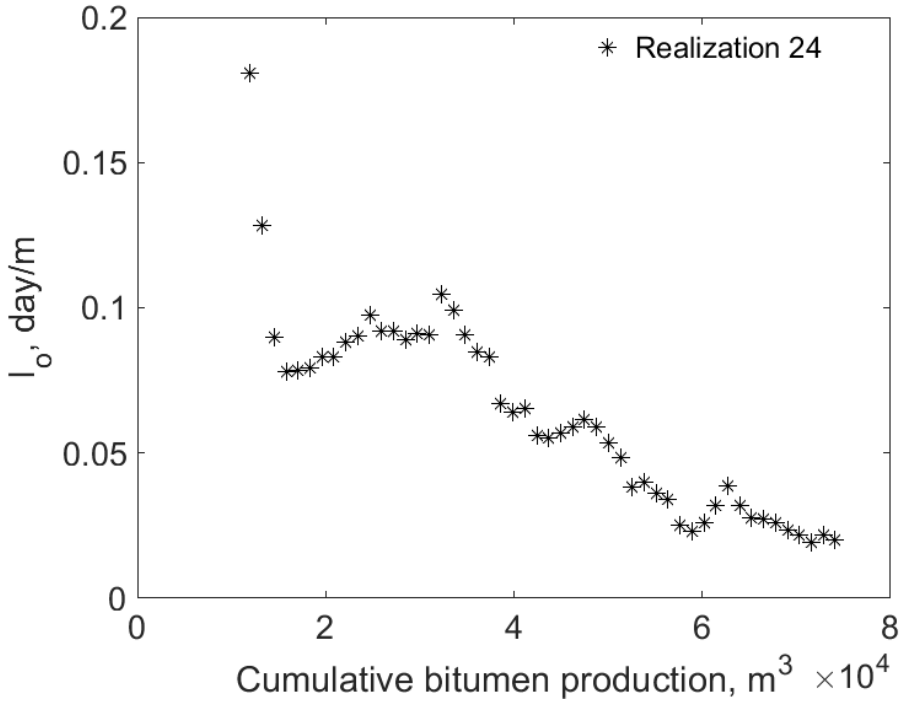

Figure K-15(e).I_o for SAGD as a function of cumulative bitumen production for realization 24

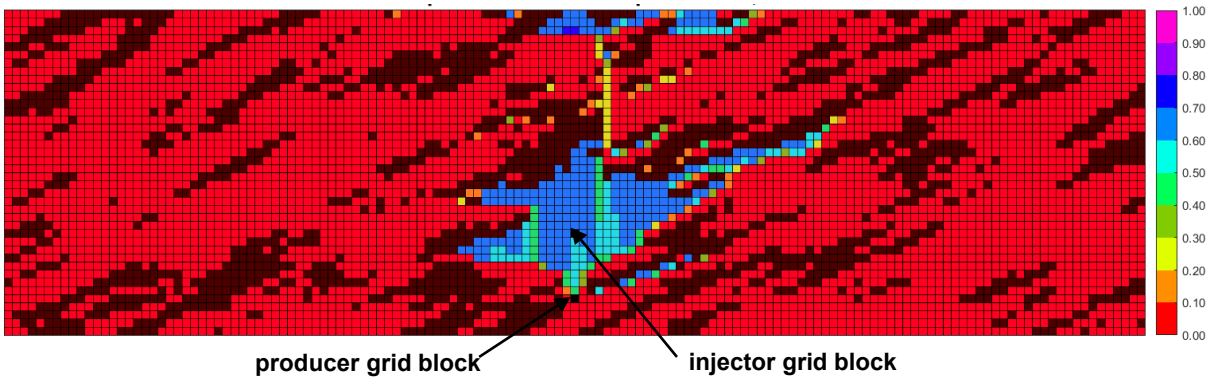

Figure K-15(f). Vapor-phase saturation map in SAGD for realization 24 for Q ≈ 31218 m^3

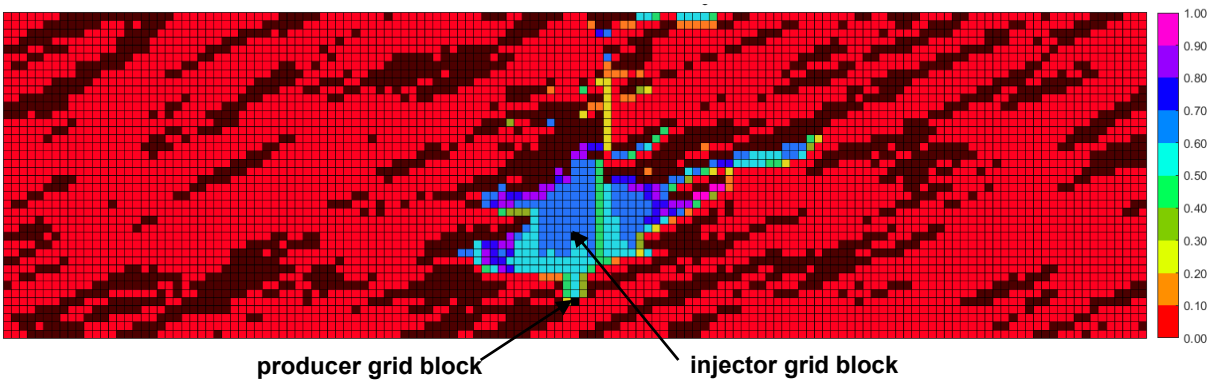

Figure K-15(g). Vapor-phase saturation map in n-C_6 SAGD for realization 24 for Q ≈ 31218 m^3

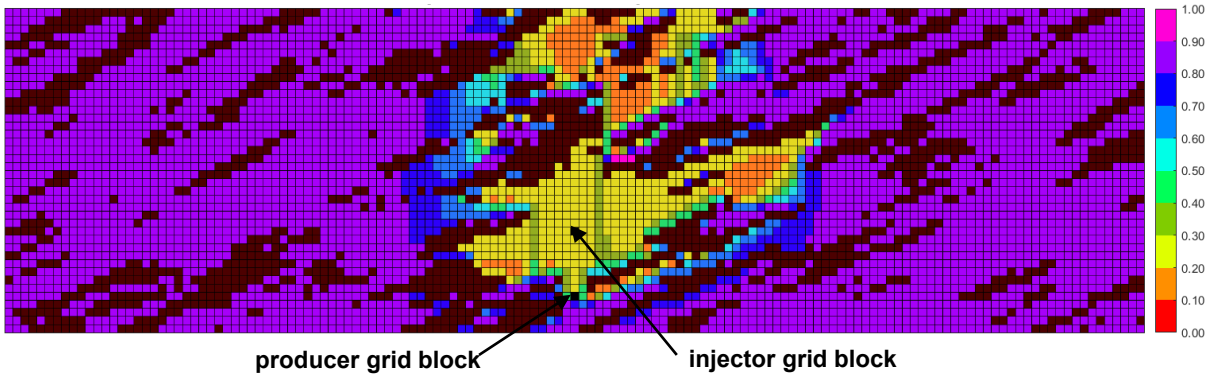

Figure K-15(h). Oleic-phase saturation map in SAGD for realization 24 for Q ≈ 31218 m^3

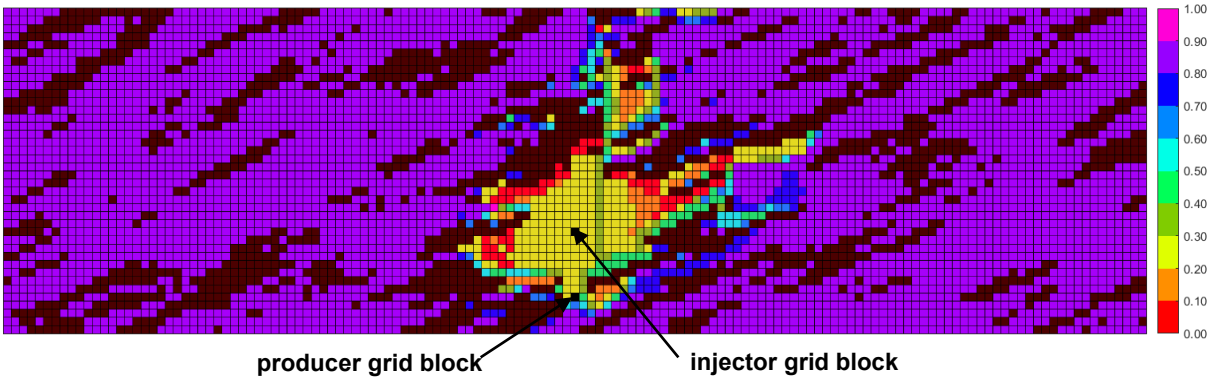

Figure K-15(i). Oleic-phase saturation map in n-C_6 SAGD for realization 24 for Q ≈ 31218 m^3

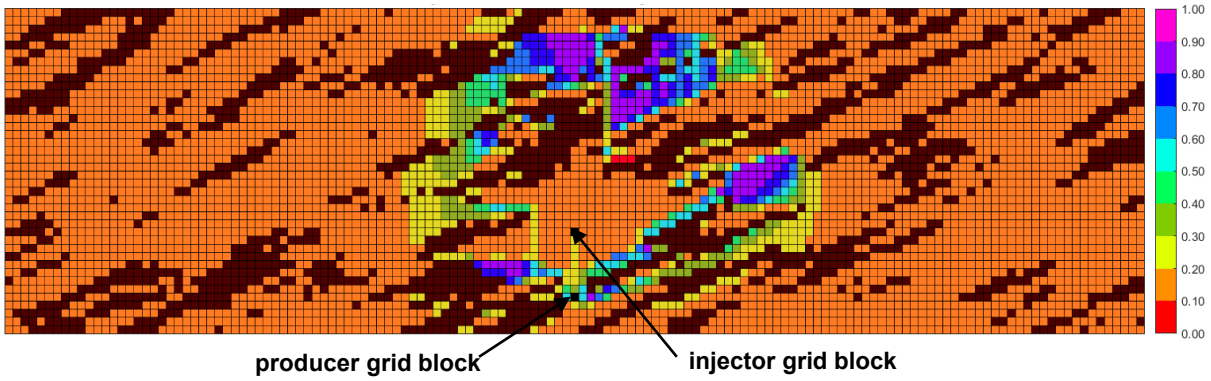

Figure K-15(j). Aqueous-phase saturation map in SAGD for realization 24 for Q ≈ 31218 m^3

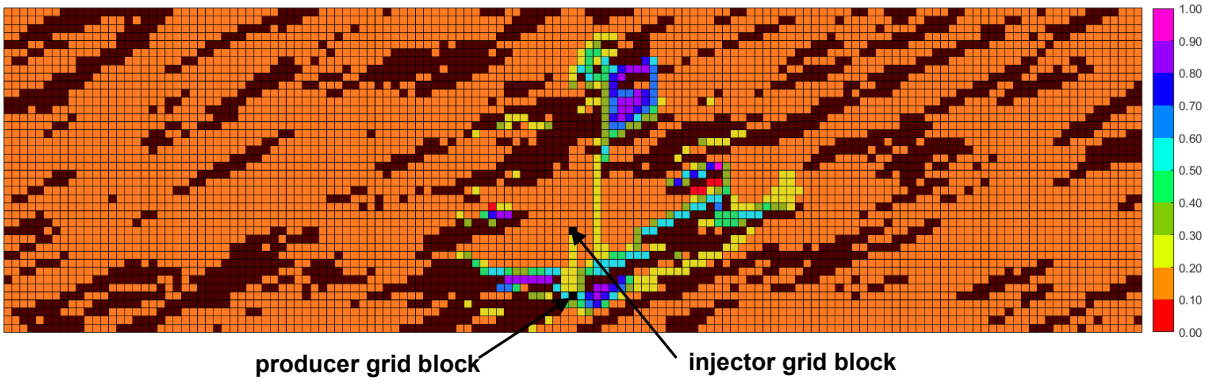

Figure K-15(k). Aqueous-phase saturation map in n-C_6 SAGD for realization 24 for Q ≈ 31218 m^3

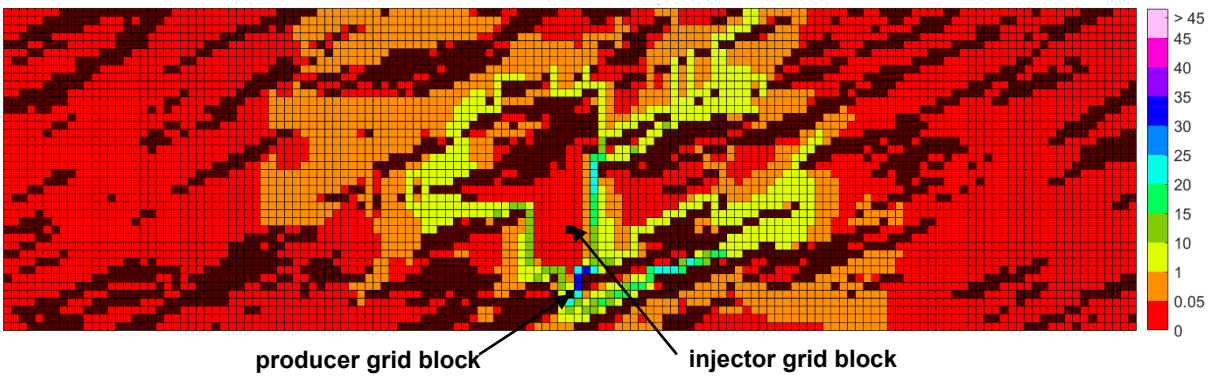

Figure K-15(l). Bitumen molar flow rate (kg-mole/day) map in SAGD for realization 24 for Q ≈ 31218 m^3

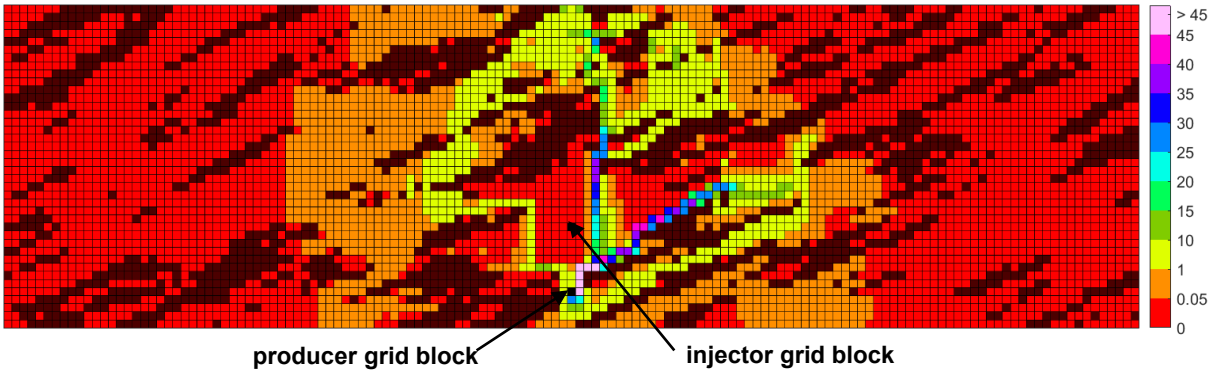

Figure K-15(m). Bitumen molar flow rate (kg-mole/day) map in n-C_6 SAGD for realization 24 for Q ≈ 31218 m^3

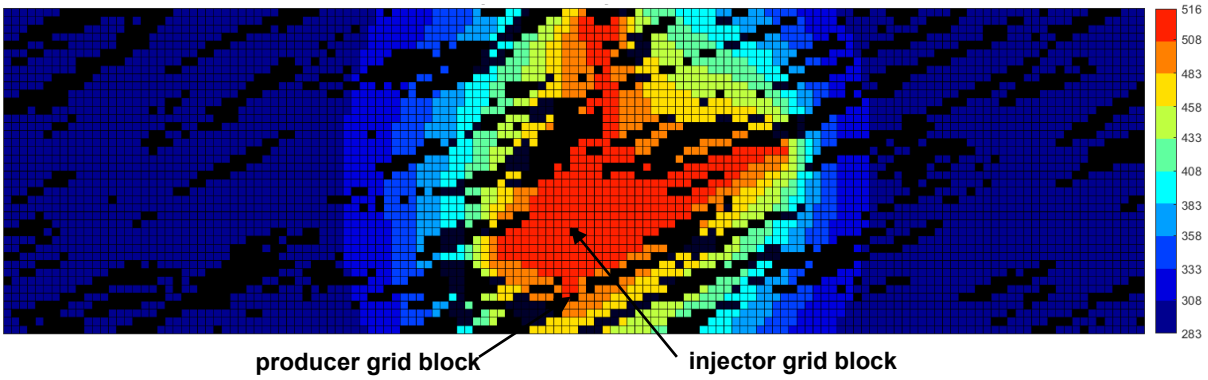

Figure K-15(n). Temperature (Kelvin) map in SAGD for realization 24 for Q ≈ 31218 m^3

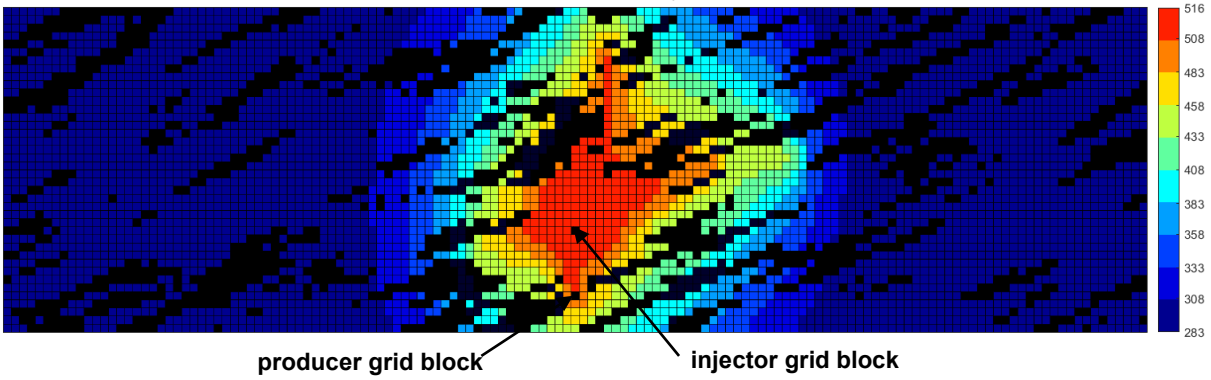

Figure K-15(o). Temperature (Kelvin) map in n-C_6 SAGD for realization 24 for Q ≈ 31218 m^3

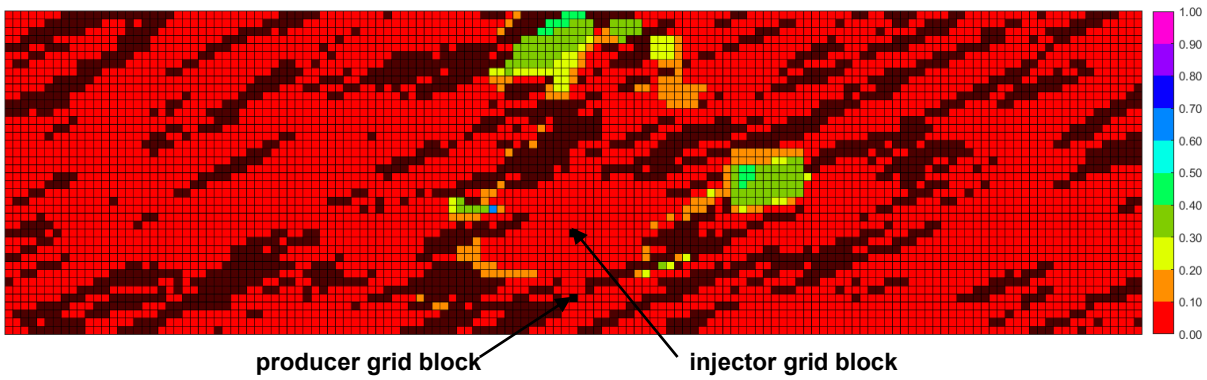

Figure K-15(p). $\beta_{Lx_{sL}}$ map in n-C_6 SAGD for realization 24 for Q ≈ 31218 m^3

Figure K-15. Property maps for SAGD and n-C_6 SAGD for realization 24

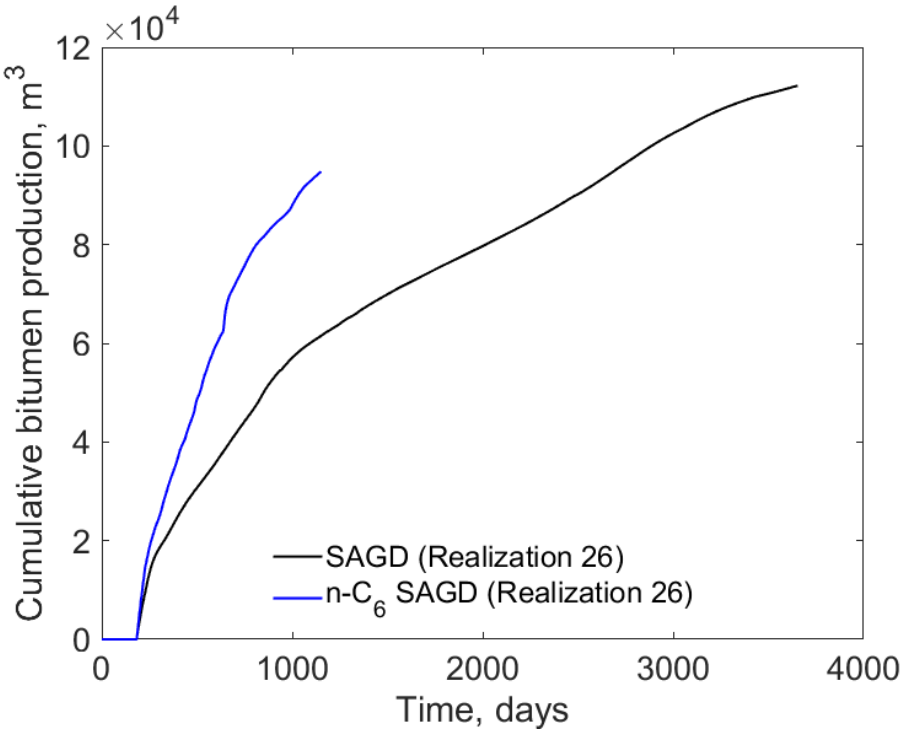

Figure K-16(a). Cumulative bitumen production histories for SAGD and n-C_6 SAGD for realization 26

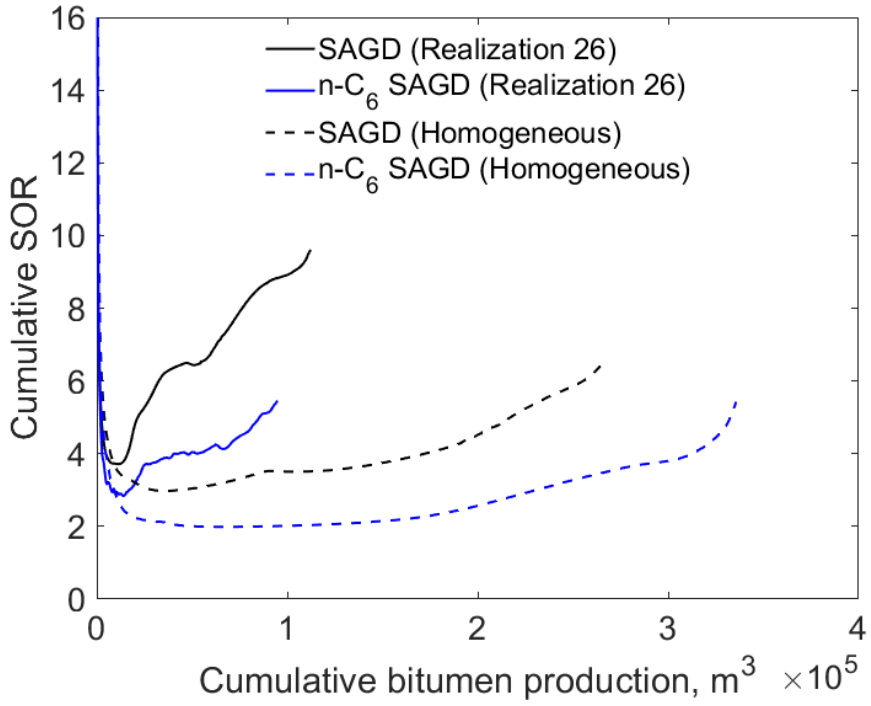

Figure K-16(b). Cumulative SOR for SAGD and n-C_6 SAGD for realization 26

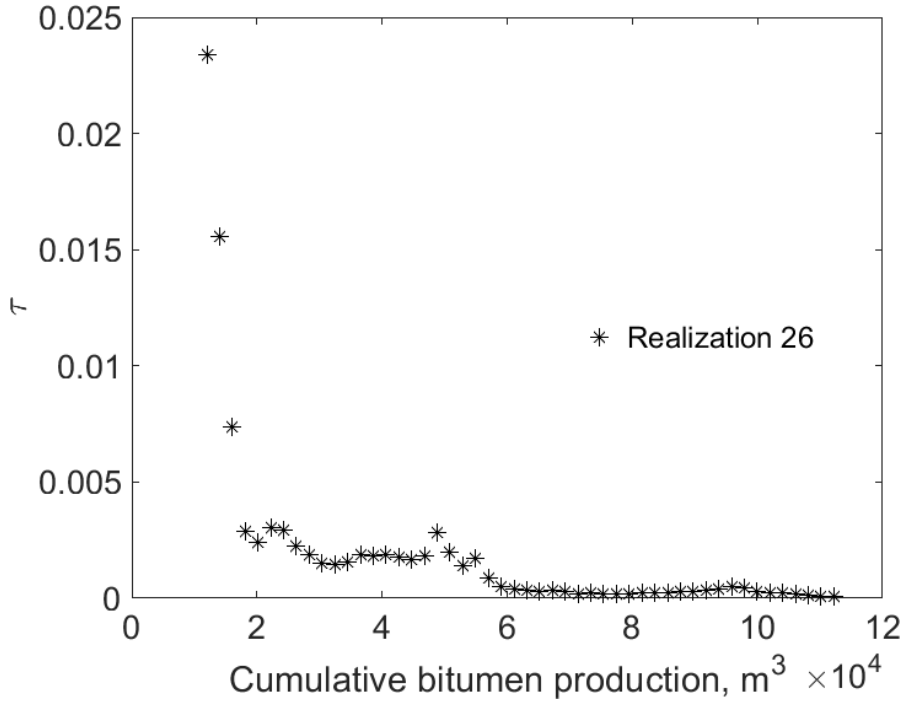

Figure K-16(c). τ for SAGD as a function of cumulative bitumen production for realization 26

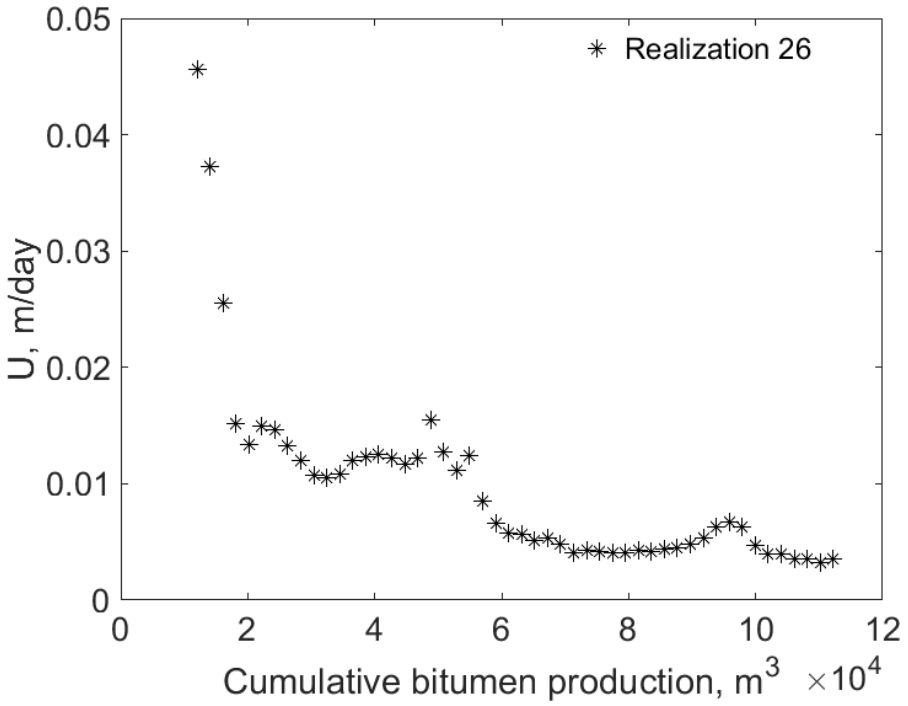

Figure K-16(d). U for SAGD as a function of cumulative bitumen production for realization 26

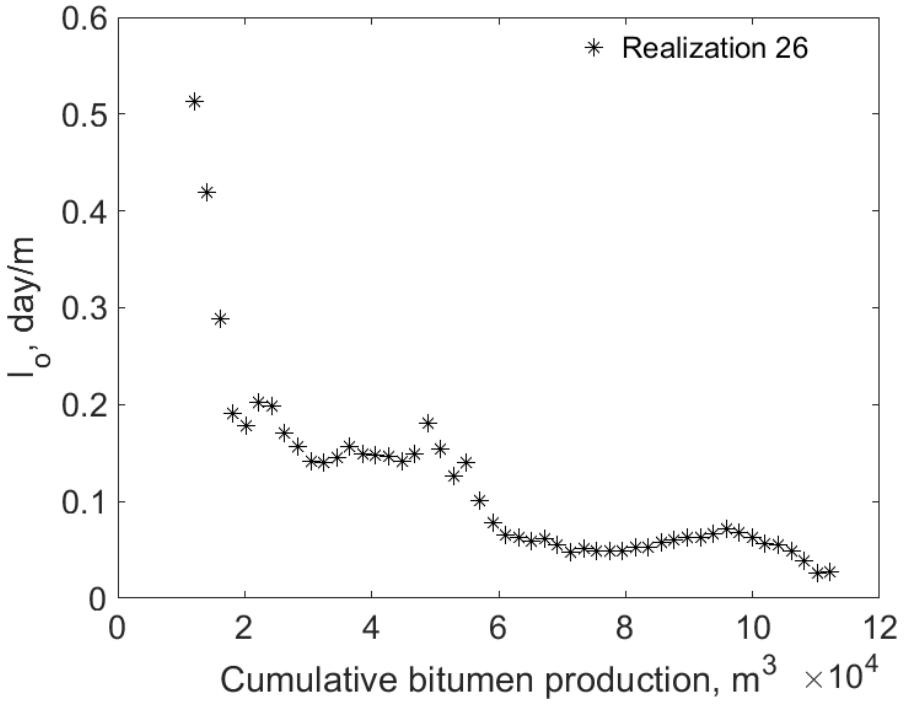

Figure K-16(e).I_o for SAGD as a function of cumulative bitumen production for realization 26

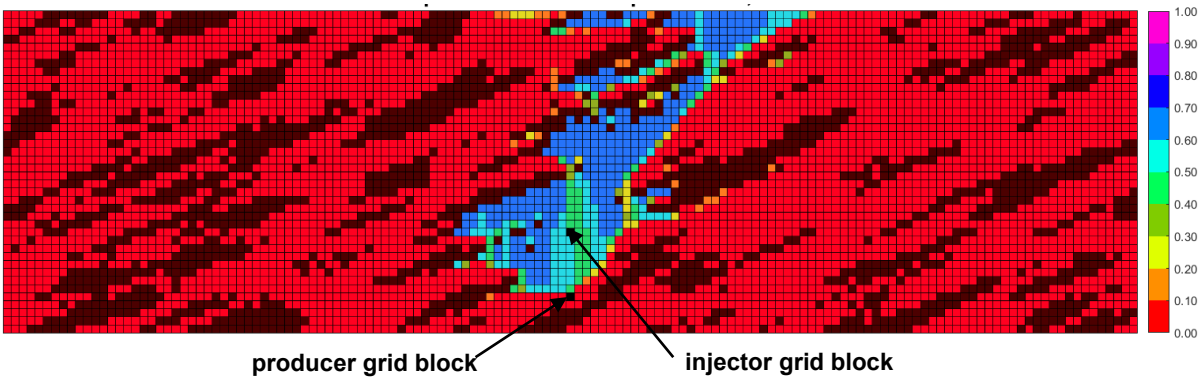

Figure K-16(f). Vapor-phase saturation map in SAGD for realization 26 for Q ≈ 31218 m^3

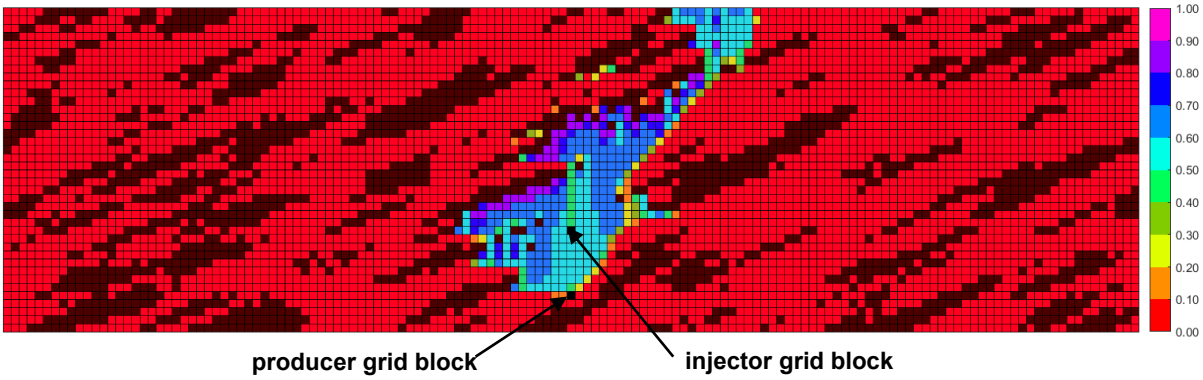

Figure K-16(g). Vapor-phase saturation map in n-C_6 SAGD for realization 26 for Q ≈ 31218 m^3

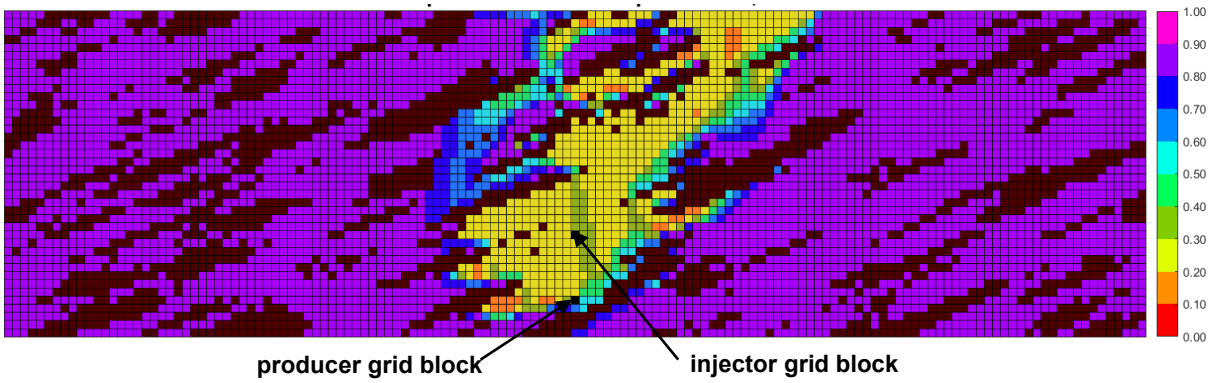

Figure K-16(h). Oleic-phase saturation map in SAGD for realization 26 for Q ≈ 31218 m^3

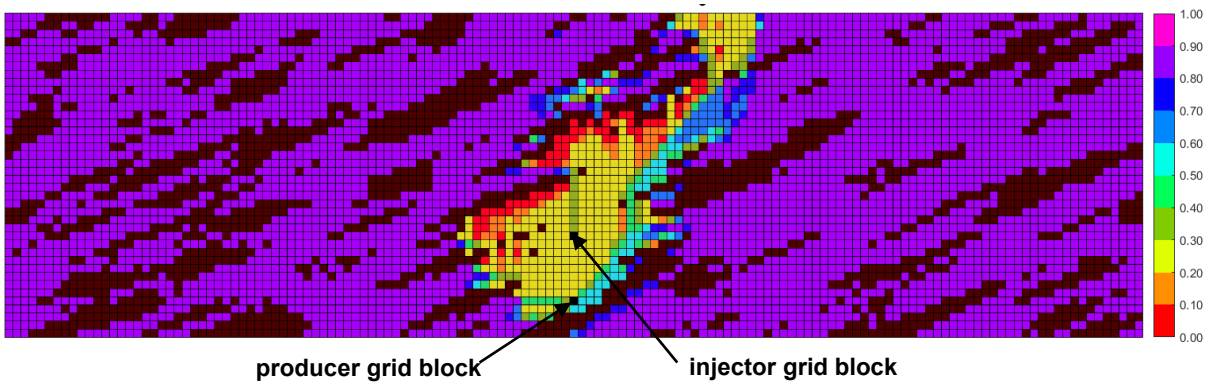

Figure K-16(i). Oleic-phase saturation map in n-C_6 SAGD for realization 26 for Q ≈ 31218 m^3

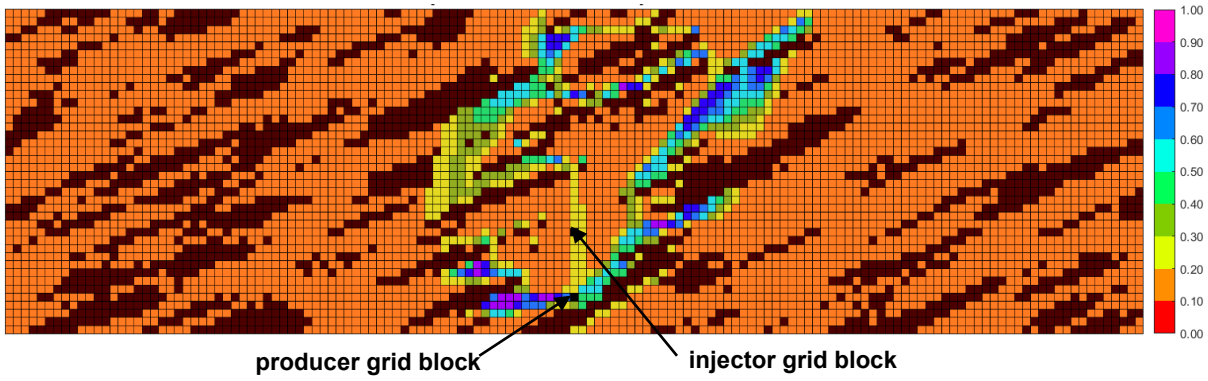

Figure K-16(j). Aqueous-phase saturation map in SAGD for realization 26 for Q ≈ 31218 m^3

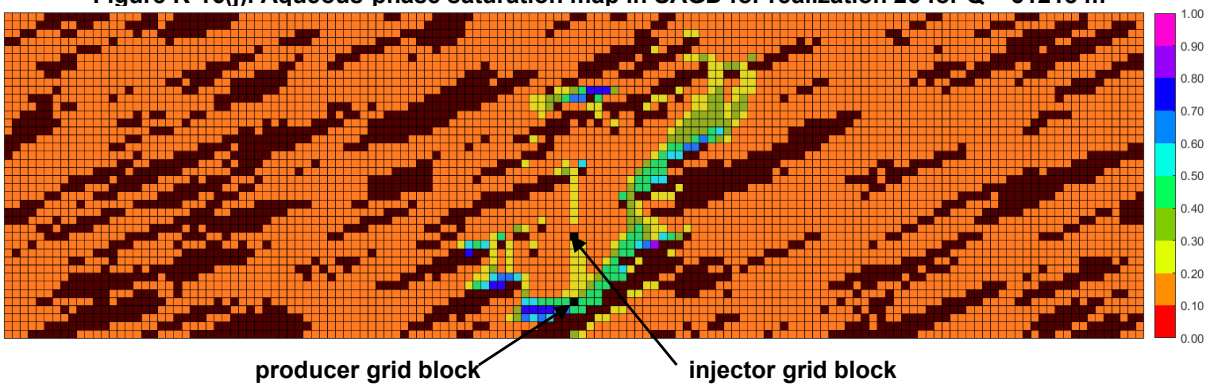

Figure K-16(k). Aqueous-phase saturation map in n-C_6 SAGD for realization 26 for Q ≈ 31218 m^3

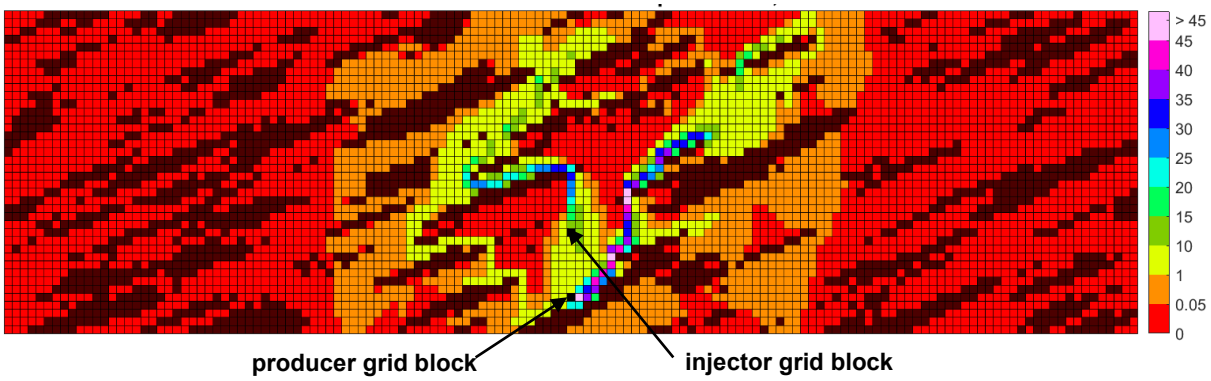

Figure K-16(l). Bitumen molar flow rate (kg-mole/day) map in SAGD for realization 26 for Q ≈ 31218 m^3

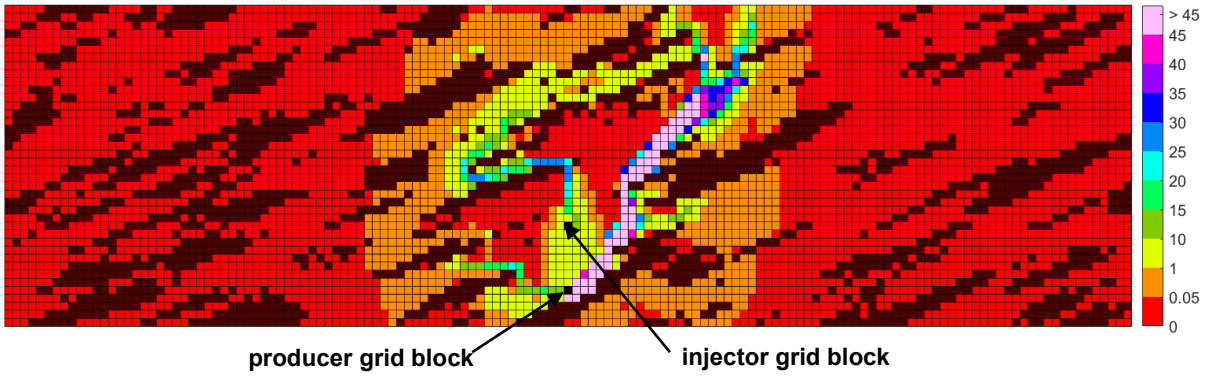

Figure K-16(m). Bitumen molar flow rate (kg-mole/day) map in n-C_6 SAGD for realization 26 for Q ≈ 31218 m^3

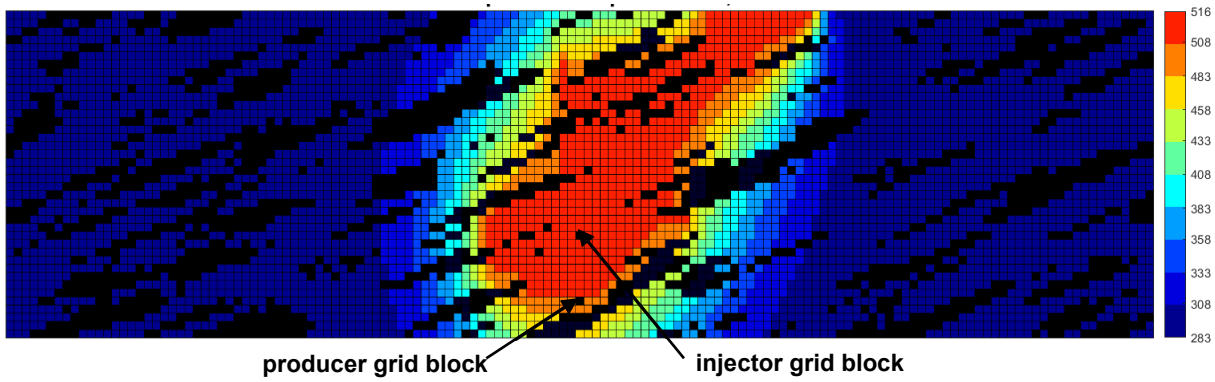

Figure K-16(n). Temperature (Kelvin) map in SAGD for realization 26 for Q ≈ 31218 m^3

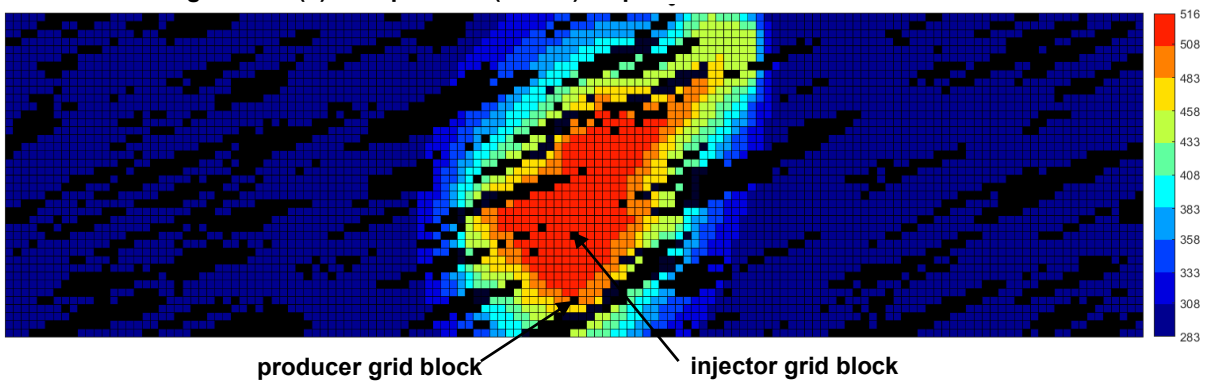

Figure K-16(o). Temperature (Kelvin) map in n-C_6 SAGD for realization 26 for Q ≈ 31218 m^3

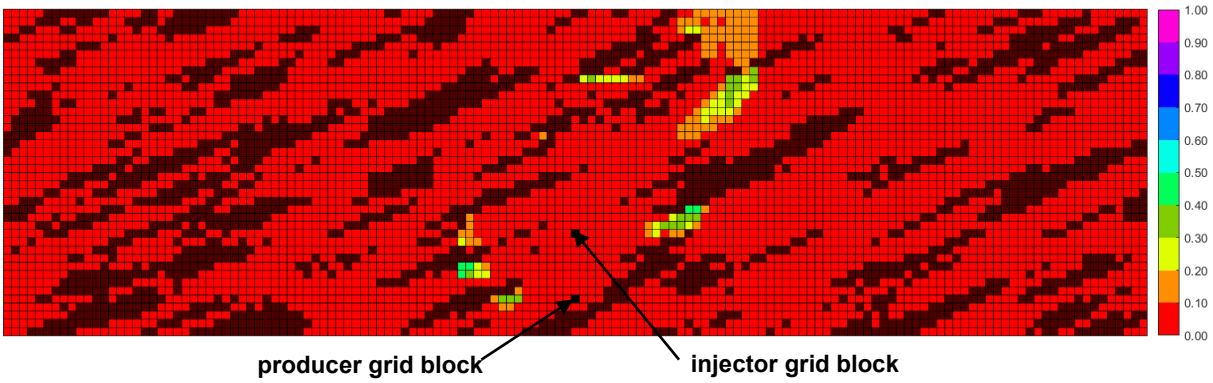

Figure K-16(p). $\beta_{L}x_{sL}$ map in n-C_6 SAGD for realization 26 for Q ≈ 31218 m^3

Figure K-16. Property maps for SAGD and n-C_6 SAGD for realization 26

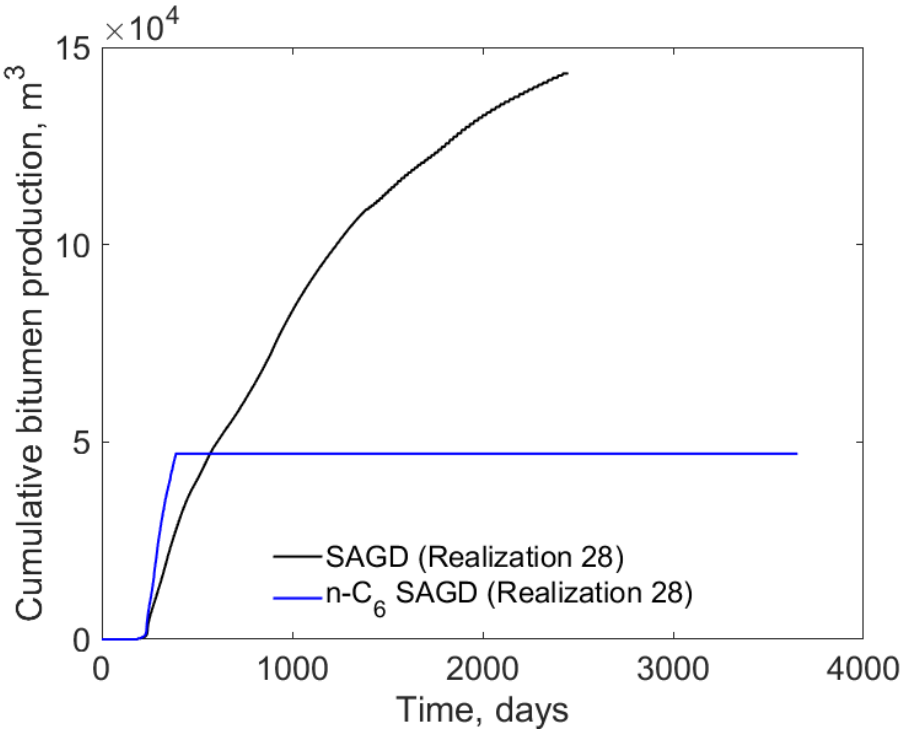

Figure K-17(a). Cumulative bitumen production histories for SAGD and n-C_6 SAGD for realization 28

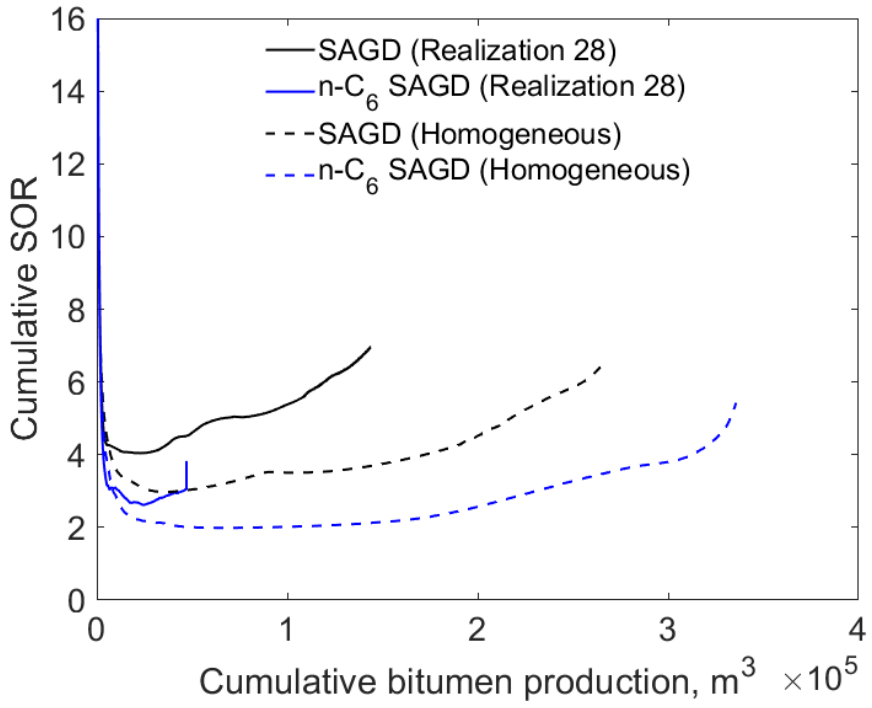

Figure K-17(b). Cumulative SOR for SAGD and n-C_6 SAGD for realization 28

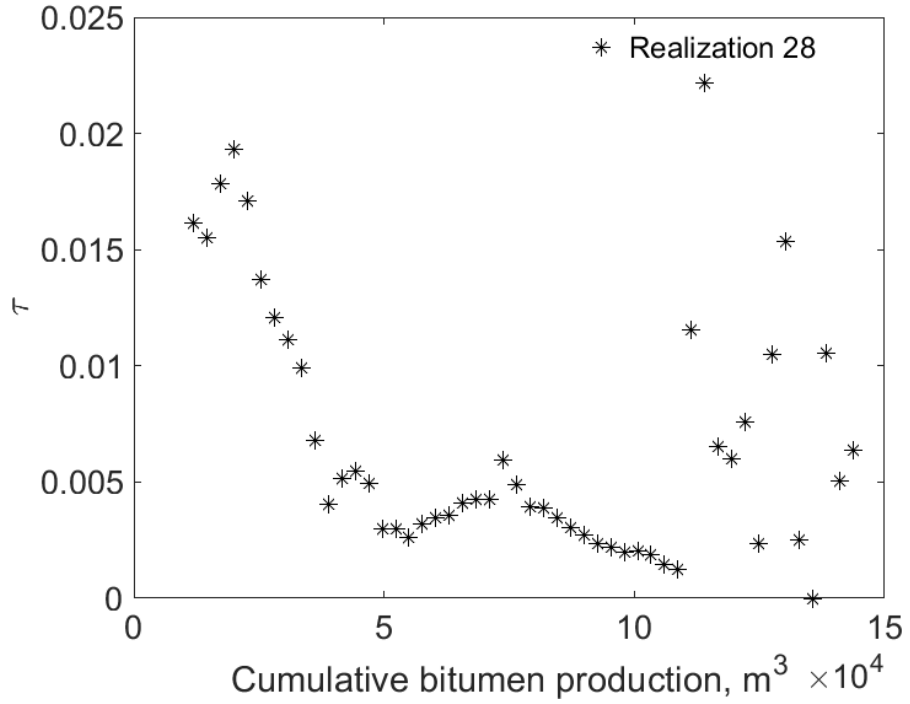

Figure K-17(c). τ for SAGD as a function of cumulative bitumen production for realization 28

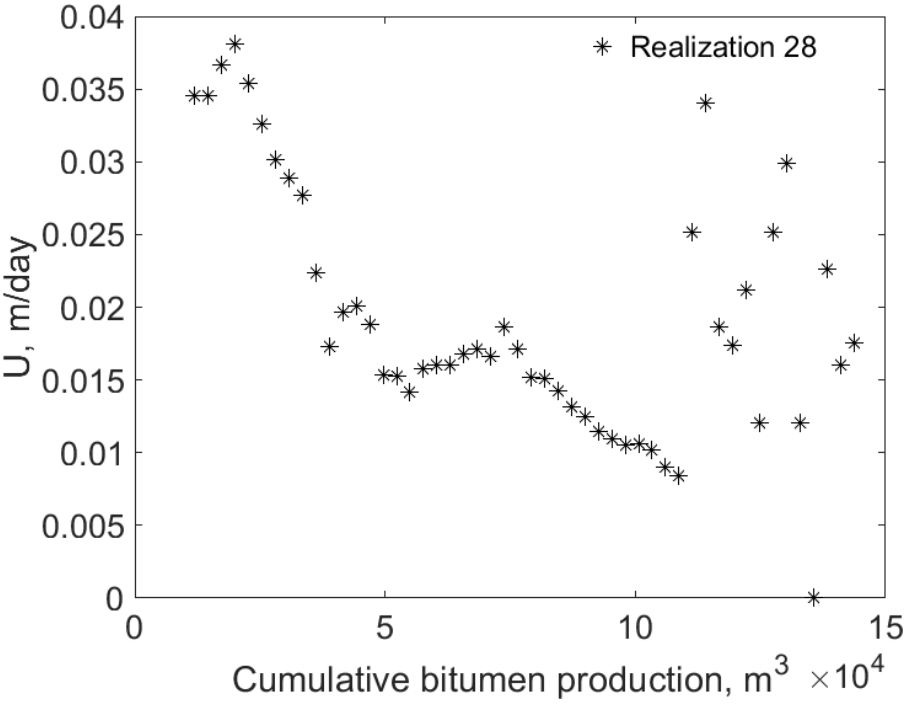

Figure K-17(d). U for SAGD as a function of cumulative bitumen production for realization 28

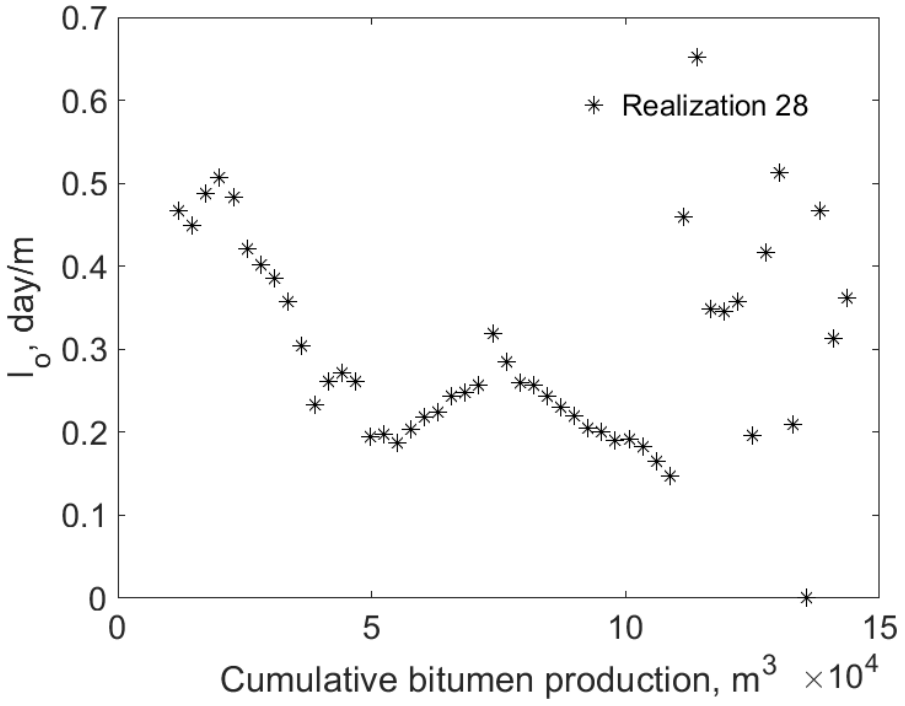

Figure K-17(e).I_o for SAGD as a function of cumulative bitumen production for realization 28

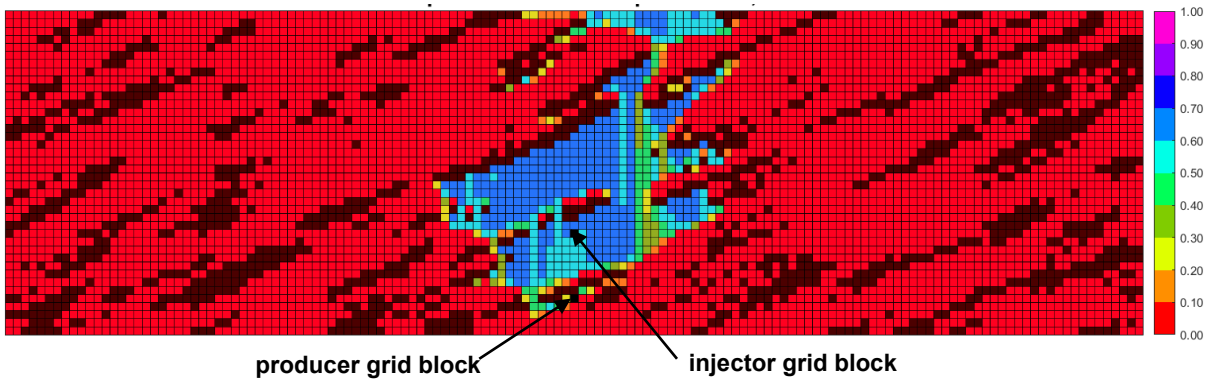

Figure K-17(f). Vapor-phase saturation map in SAGD for realization 28 for Q ≈ 31218 m^3

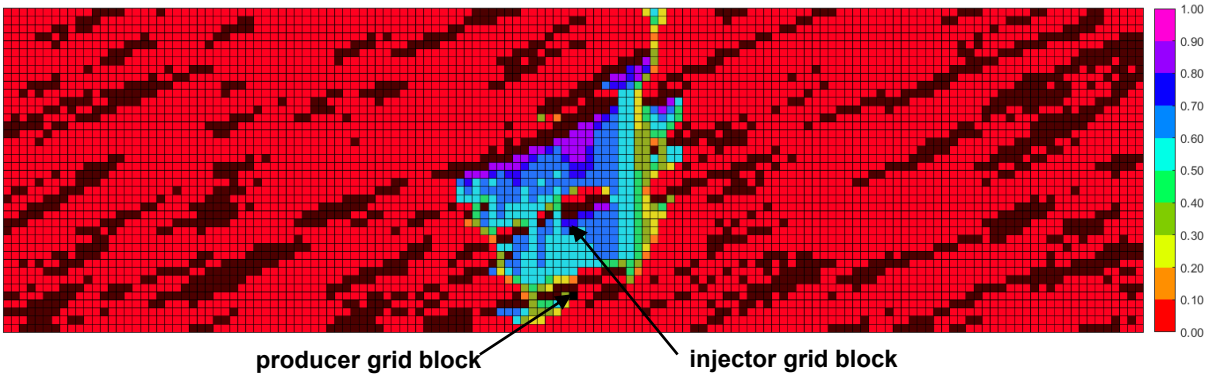

Figure K-17(g). Vapor-phase saturation map in n-C_6 SAGD for realization 28 for Q ≈ 31218 m^3

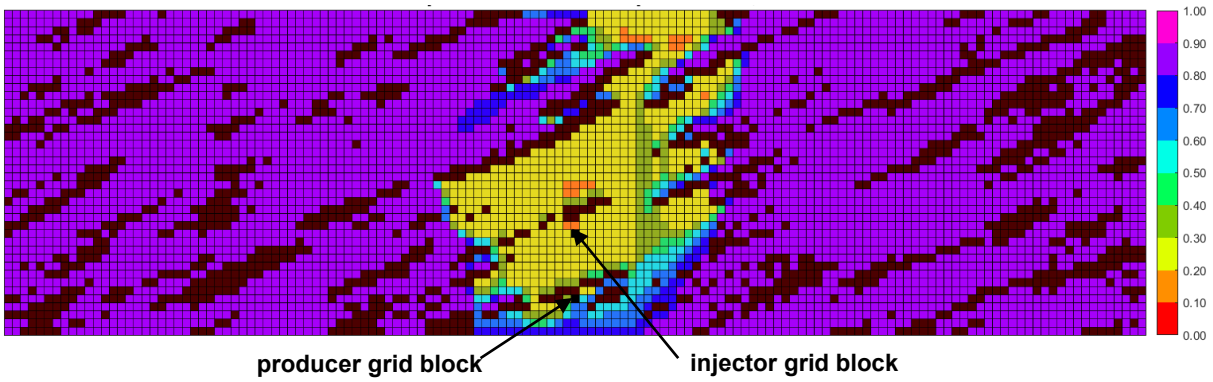

Figure K-17(h). Oleic-phase saturation map in SAGD for realization 28 for Q ≈ 31218 m^3

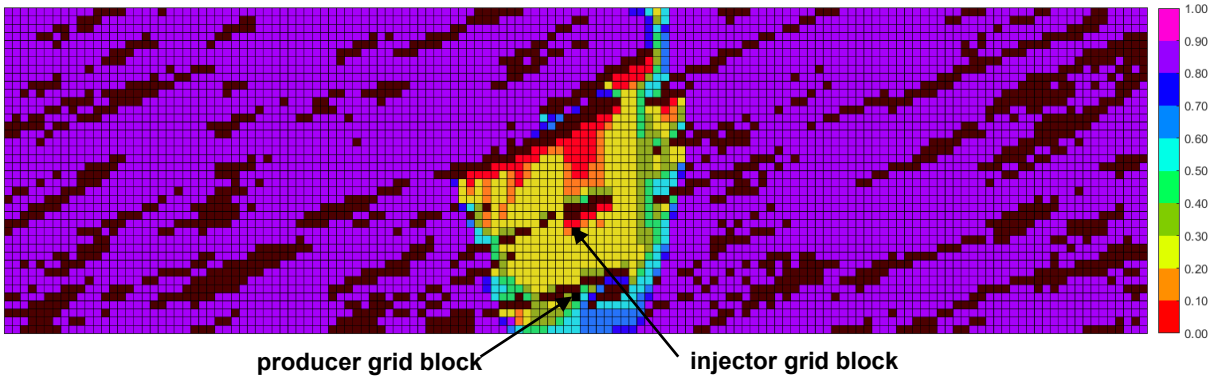

Figure K-17(i). Oleic-phase saturation map in n-C_6 SAGD for realization 28 for Q ≈ 31218 m^3

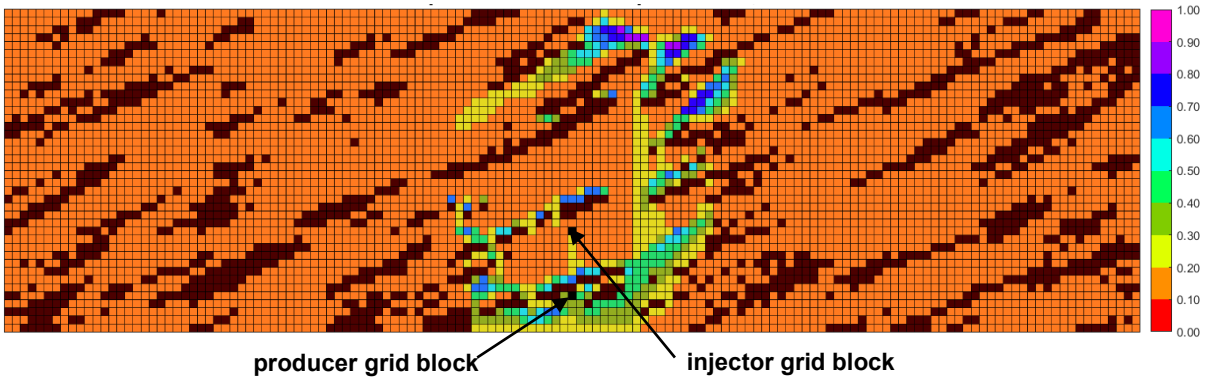

Figure K-17(j). Aqueous-phase saturation map in SAGD for realization 28 for Q ≈ 31218 m^3

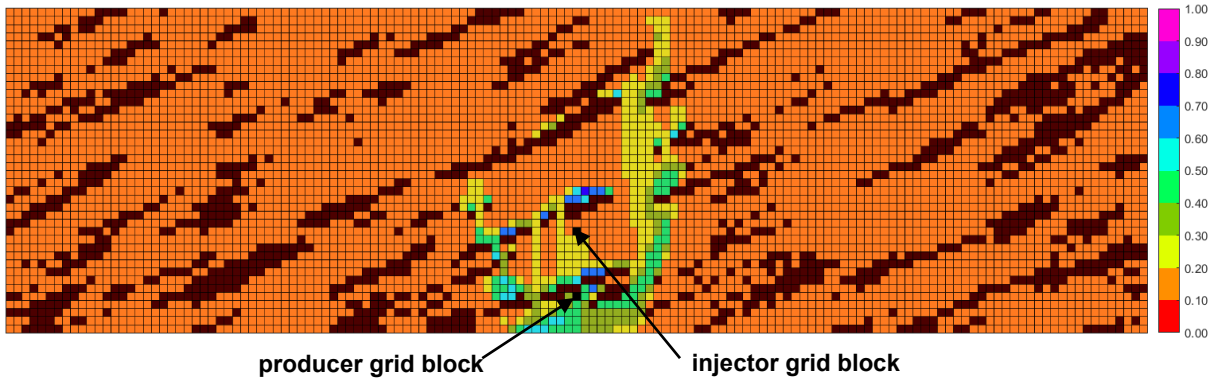

Figure K-17(k). Aqueous-phase saturation map in n-C_6 SAGD for realization 28 for Q ≈ 31218 m^3

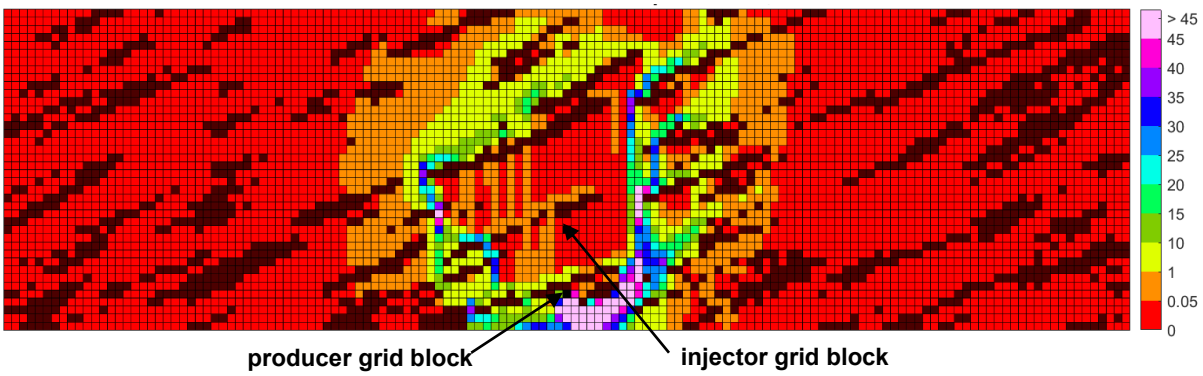

Figure K-17(l). Bitumen molar flow rate (kg-mole/day) map in SAGD for realization 28 for Q ≈ 31218 m^3

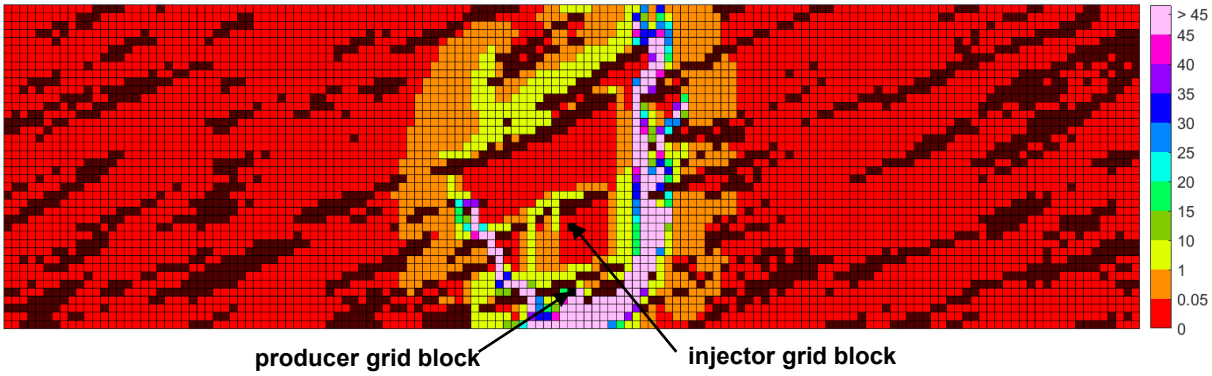

Figure K-17(m). Bitumen molar flow rate (kg-mole/day) map in n-C_6 SAGD for realization 28 for Q ≈ 31218 m^3

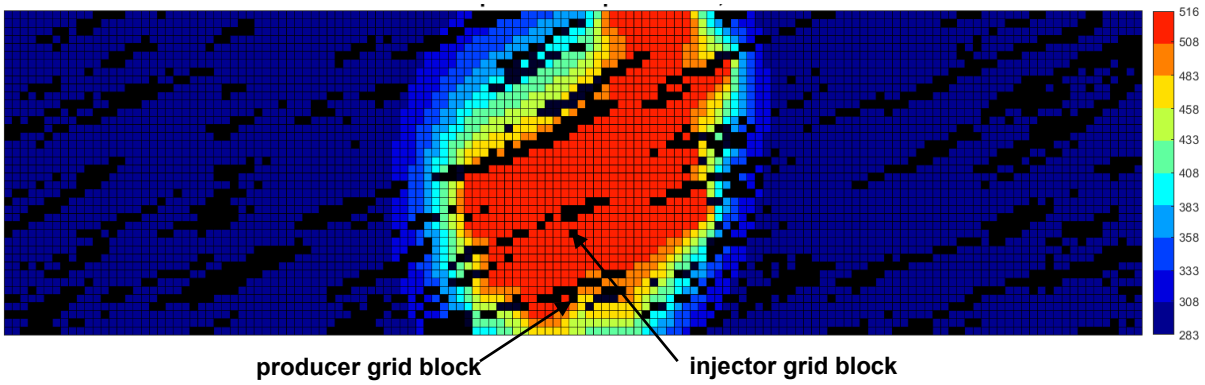

Figure K-17(n). Temperature (Kelvin) map in SAGD for realization 28 for Q ≈ 31218 m^3

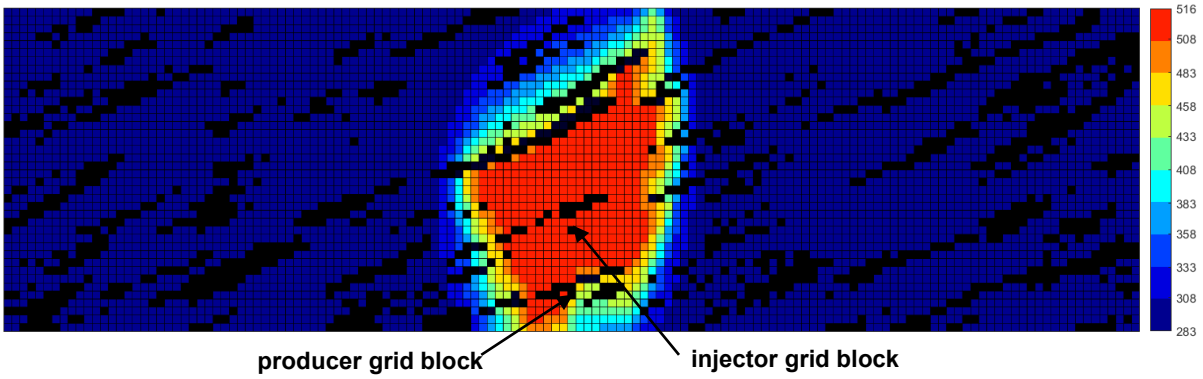

Figure K-17(o). Temperature (Kelvin) map in n-C_6 SAGD for realization 28 for Q ≈ 31218 m^3

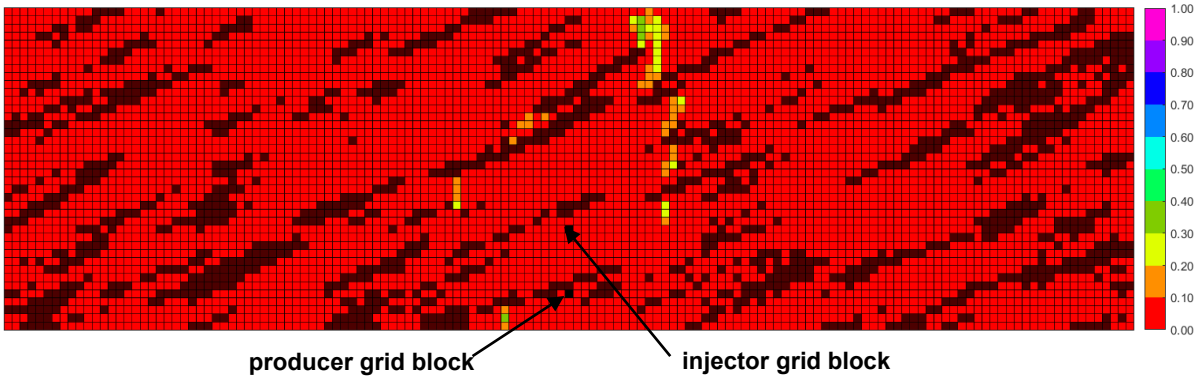

Figure K-17(p). $\beta_L x_{sL}$ map in n-C_6 SAGD for realization 28 for Q ≈ 31218 m^3

Figure K-17. Property maps for SAGD and n-C_6 SAGD for realization 28

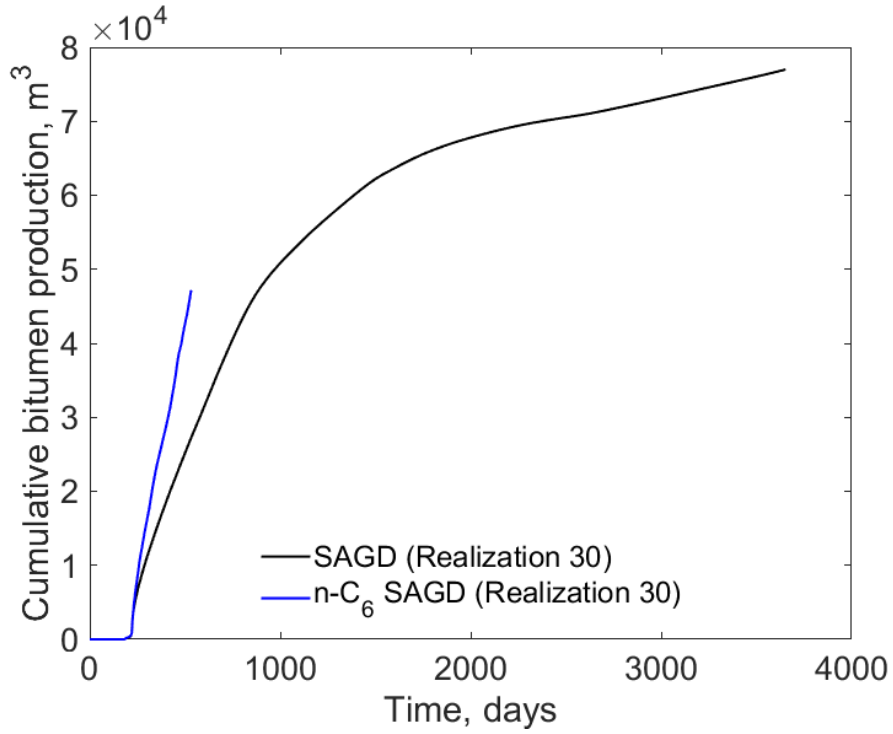

Figure K-18(a). Cumulative bitumen production histories for SAGD and n-C_6 SAGD for realization 30

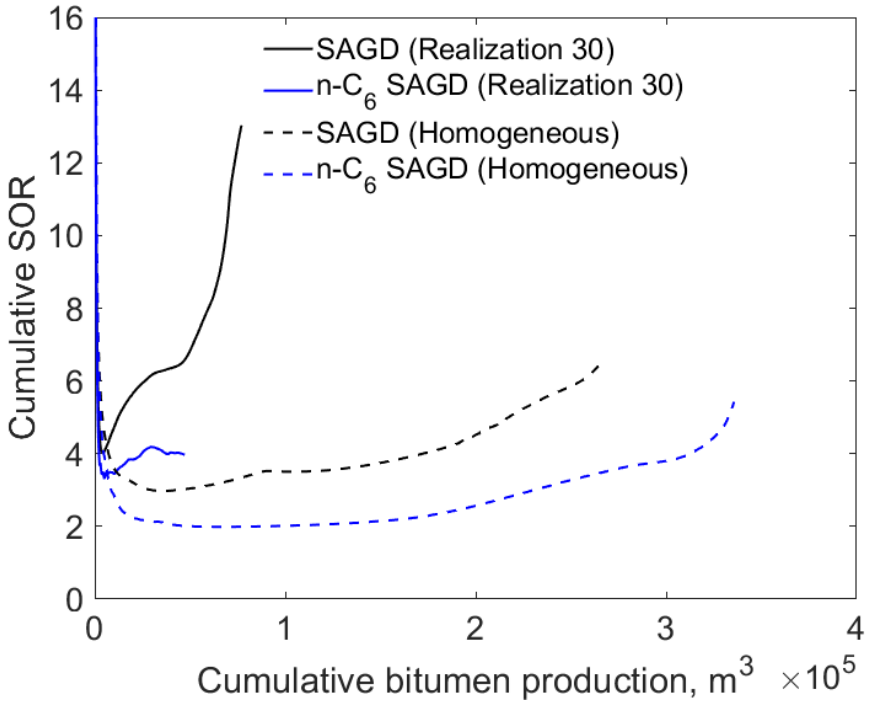

Figure K-18(b). Cumulative SOR for SAGD and n-C_6 SAGD for realization 30

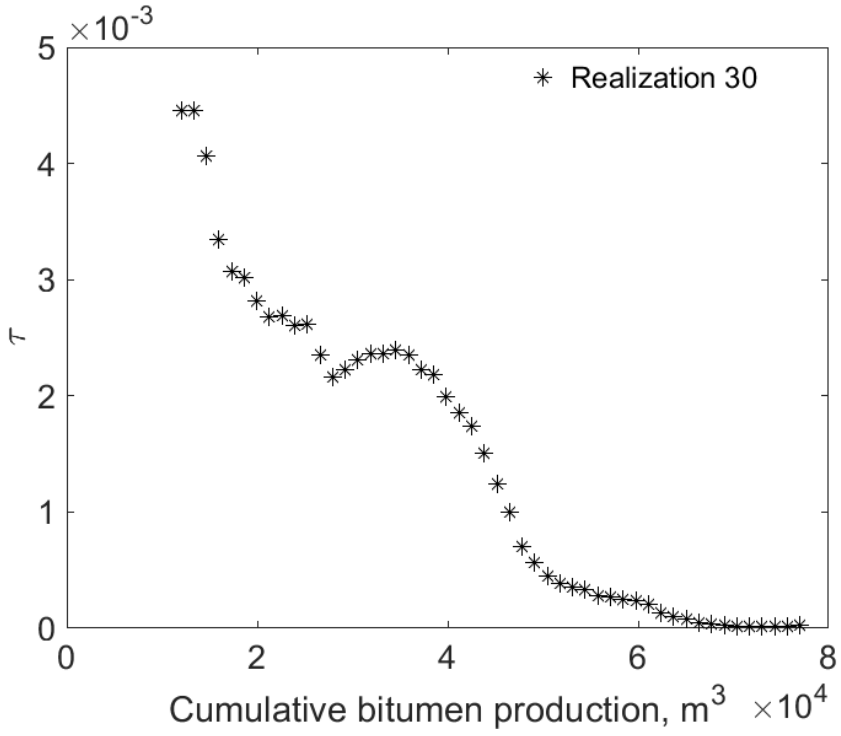

Figure K-18(c). τ for SAGD as a function of cumulative bitumen production for realization 30

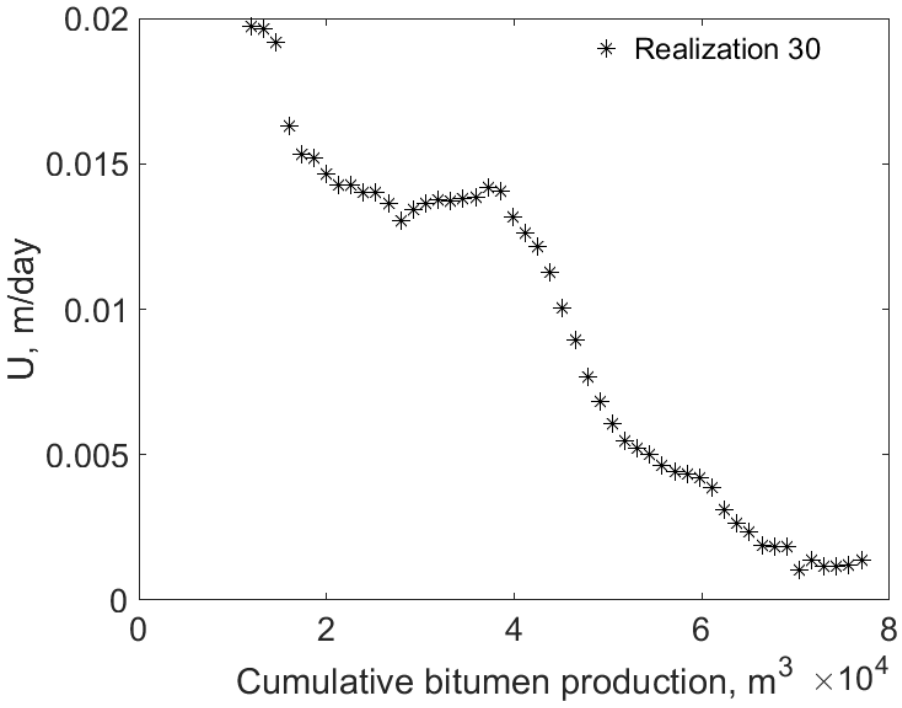

Figure K-18(d). U for SAGD as a function of cumulative bitumen production for realization 30

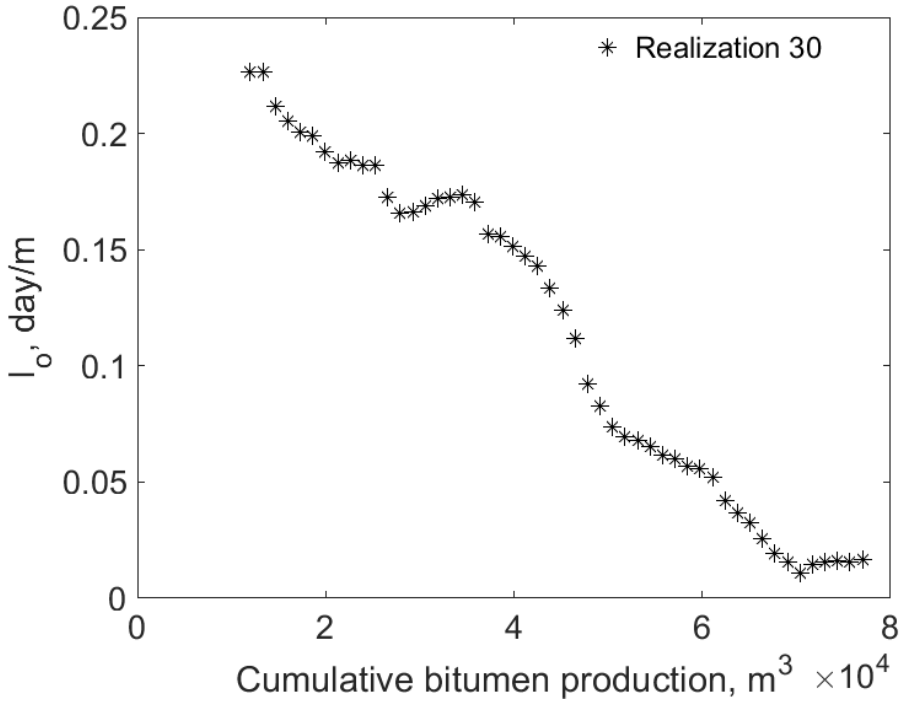

Figure K-18(e).I_o for SAGD as a function of cumulative bitumen production for realization 30

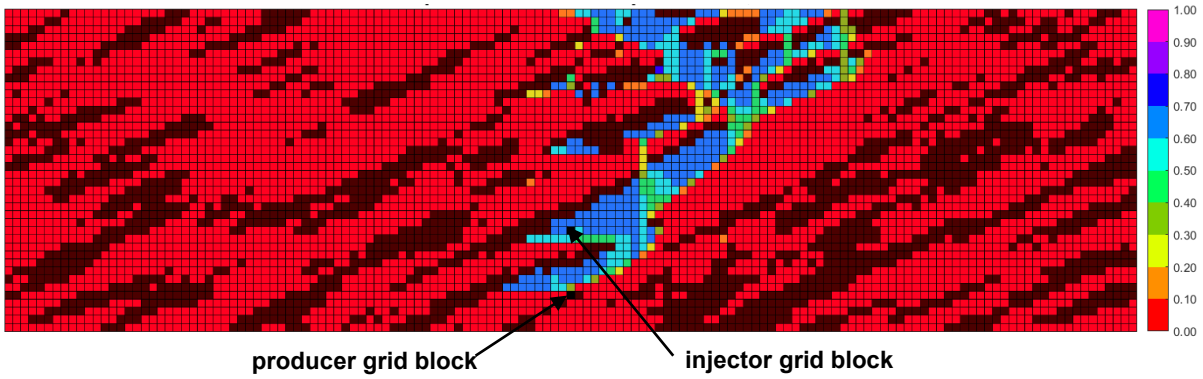

Figure K-18(f). Vapor-phase saturation map in SAGD for realization 30 for Q ≈ 31218 m^3

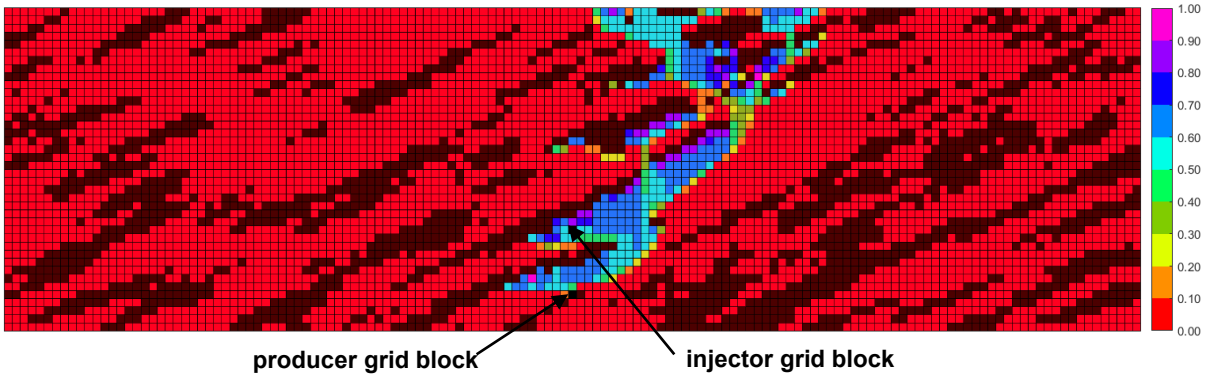

Figure K-18(g). Vapor-phase saturation map in n-C_6 SAGD for realization 30 for Q ≈ 31218 m^3

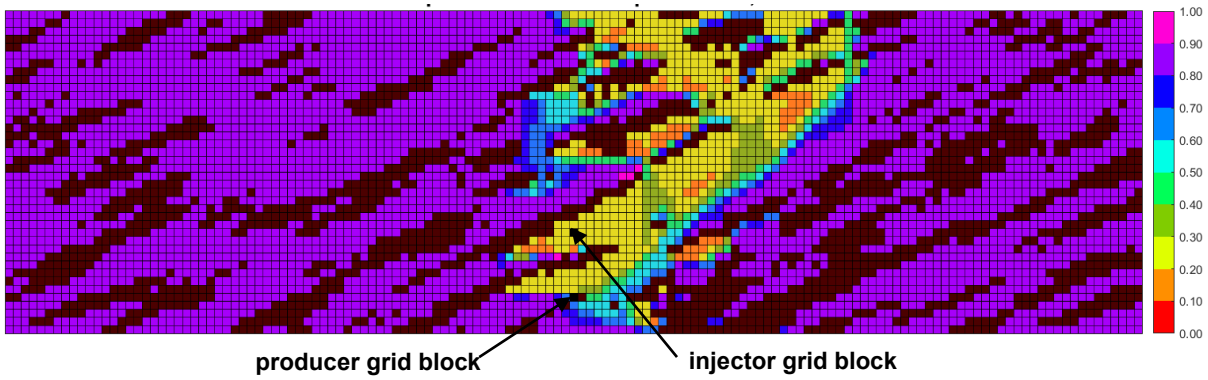

Figure K-18(h). Oleic-phase saturation map in SAGD for realization 30 for Q ≈ 31218 m^3

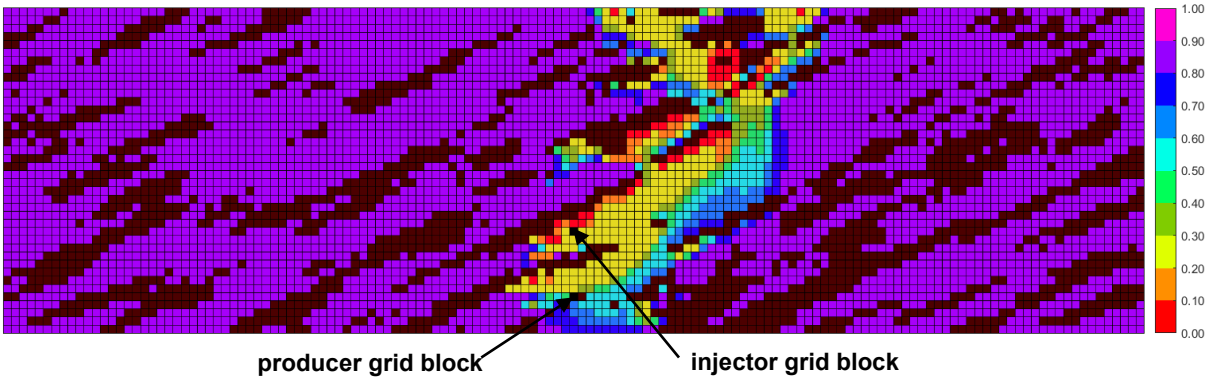

Figure K-18(i). Oleic-phase saturation map in n-C_6 SAGD for realization 30 for Q ≈ 31218 m^3

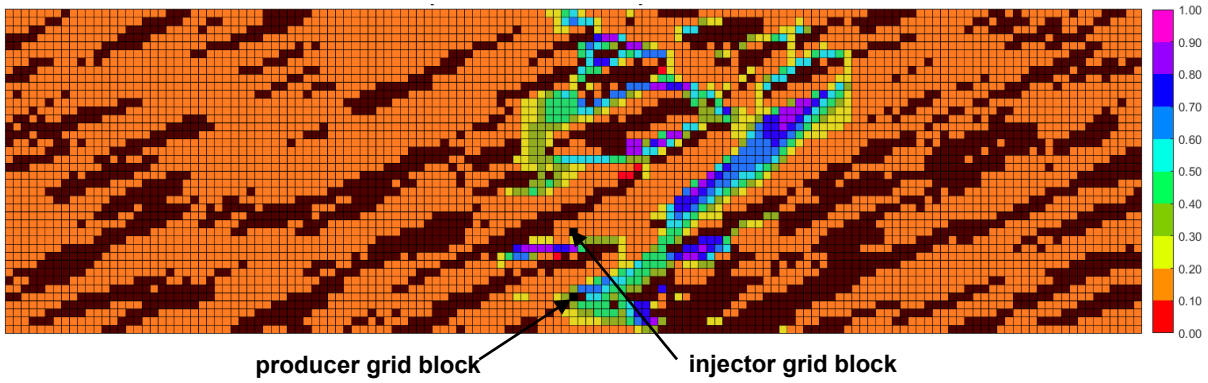

Figure K-18(j). Aqueous-phase saturation map in SAGD for realization 30 for Q ≈ 31218 m^3

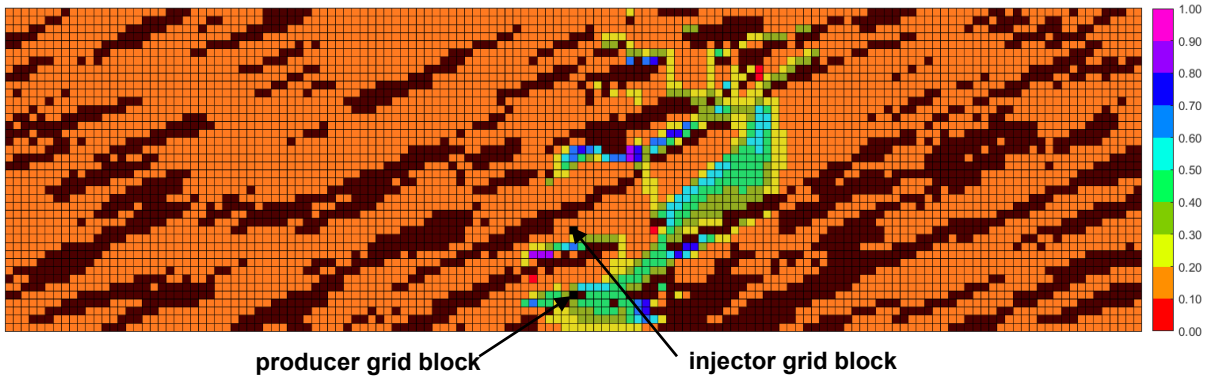

Figure K-18(k). Aqueous-phase saturation map in n-C_6 SAGD for realization 30 for Q ≈ 31218 m^3

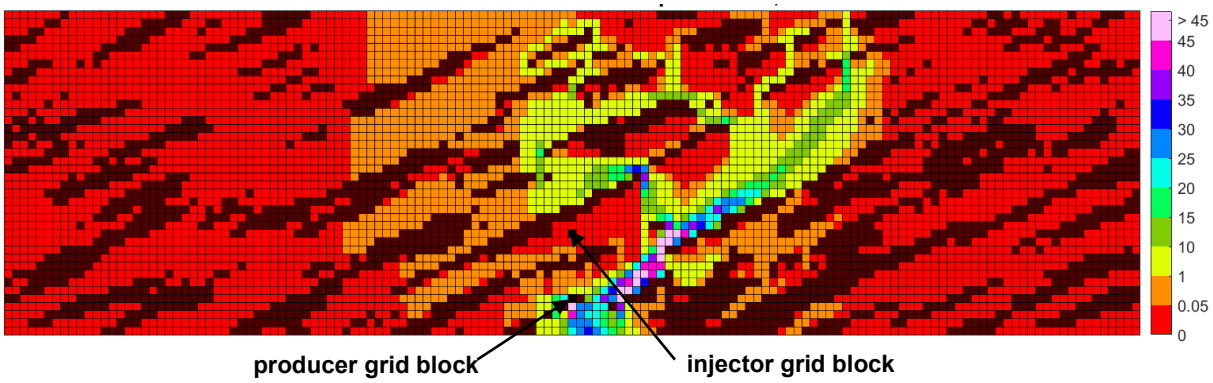

Figure K-18(l). Bitumen molar flow rate (kg-mole/day) map in SAGD for realization 30 for Q ≈ 31218 m^3

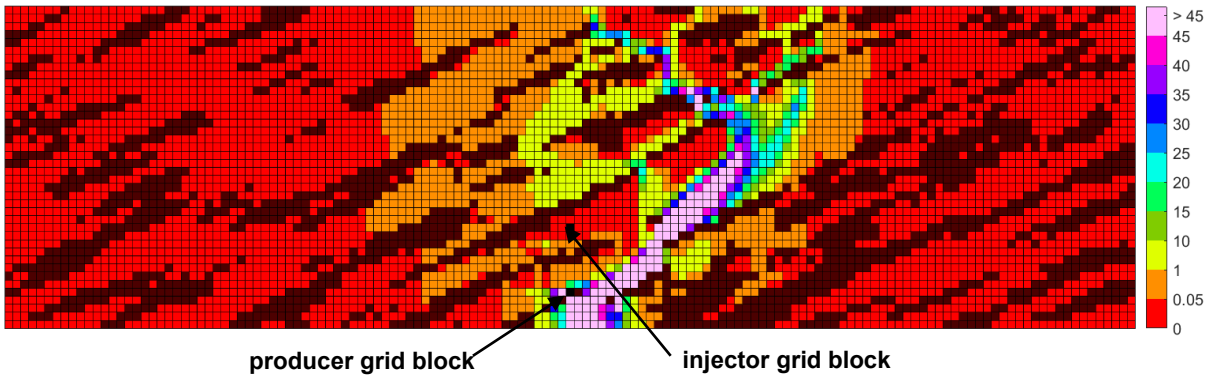

Figure K-18(m). Bitumen molar flow rate (kg-mole/day) map in n-C_6 SAGD for realization 30 for Q ≈ 31218 m^3

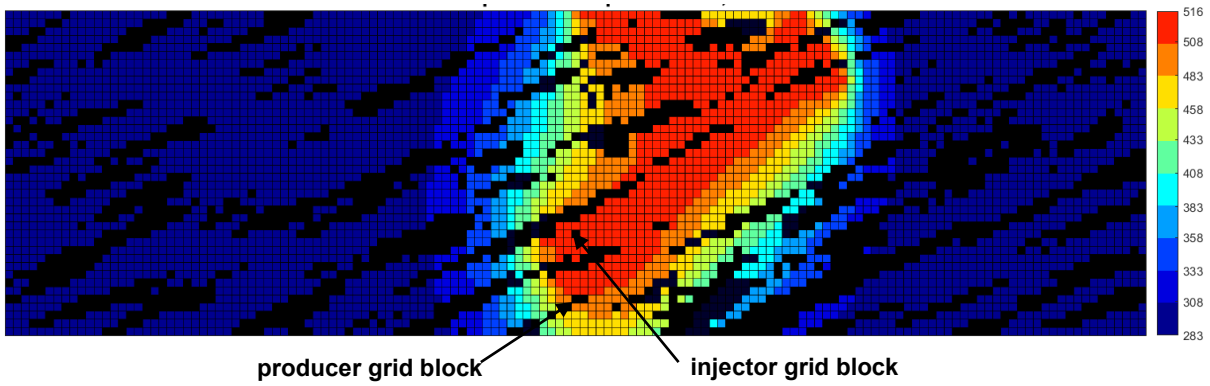

Figure K-18(n). Temperature (Kelvin) map in SAGD for realization 30 for Q ≈ 31218 m^3

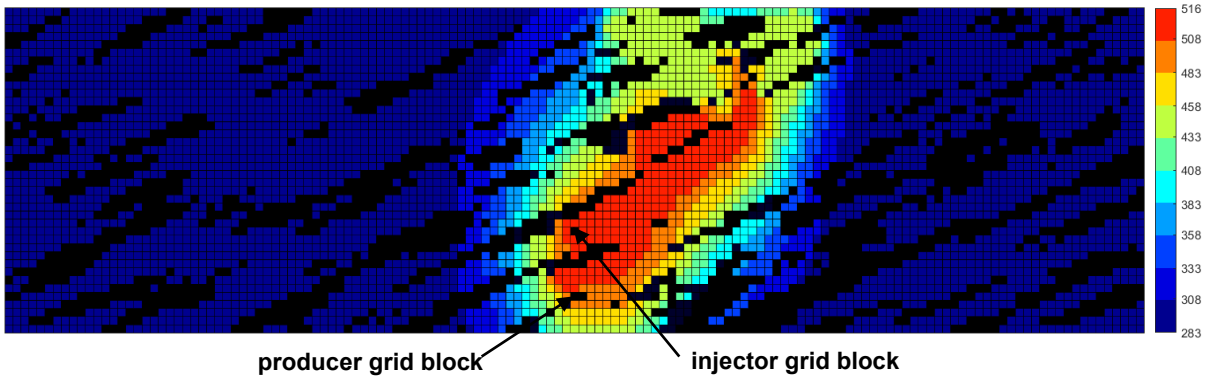

Figure K-18(o). Temperature (Kelvin) map in n-C_6 SAGD for realization 30 for Q ≈ 31218 m^3

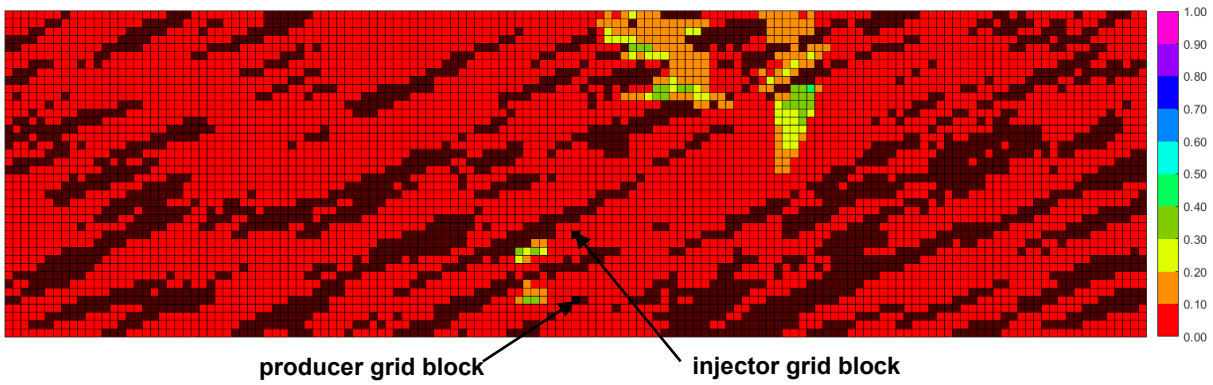

Figure K-18(p). $\beta_L x_{sL}$ map in n-C_6 SAGD for realization 30 for Q ≈ 31218 m^3

Figure K-18. Property maps for SAGD and n-C_6 SAGD for realization 30

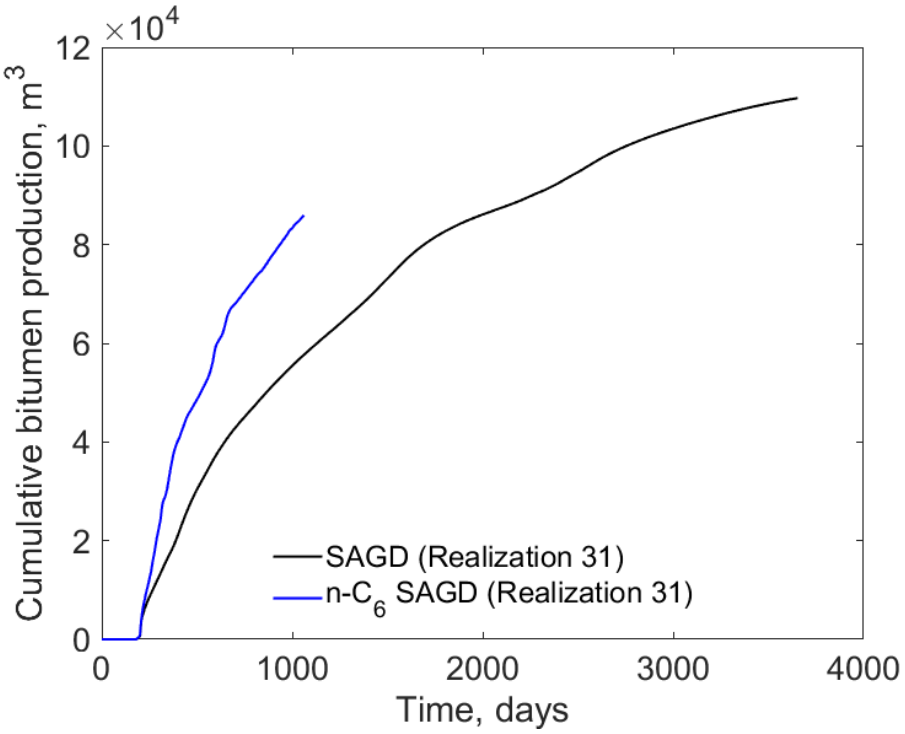

Figure K-19(a). Cumulative bitumen production histories for SAGD and n-C_6 SAGD for realization 31

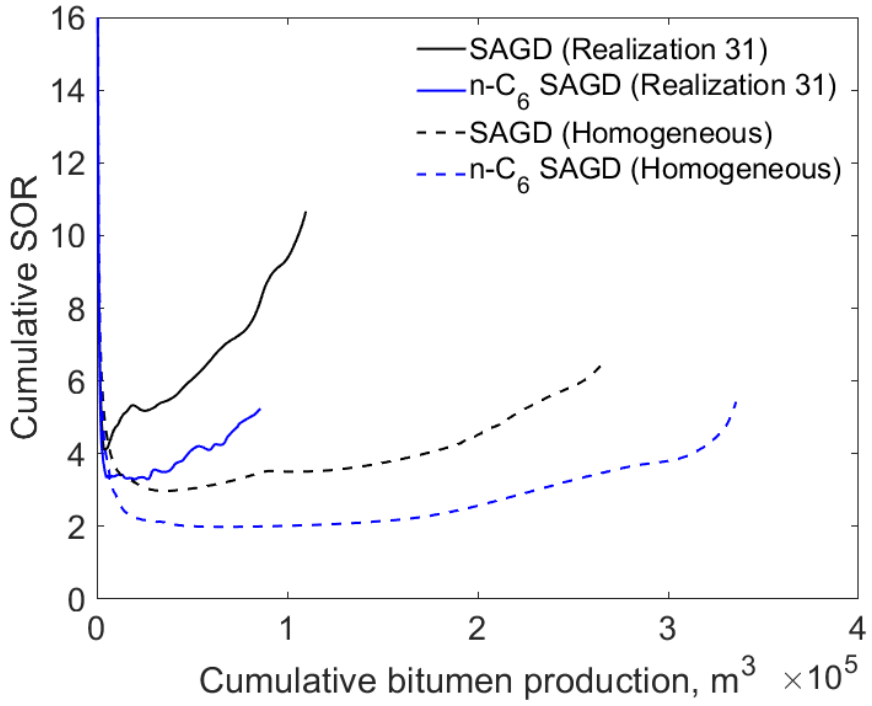

Figure K-19(b). Cumulative SOR for SAGD and n-C_6 SAGD for realization 31

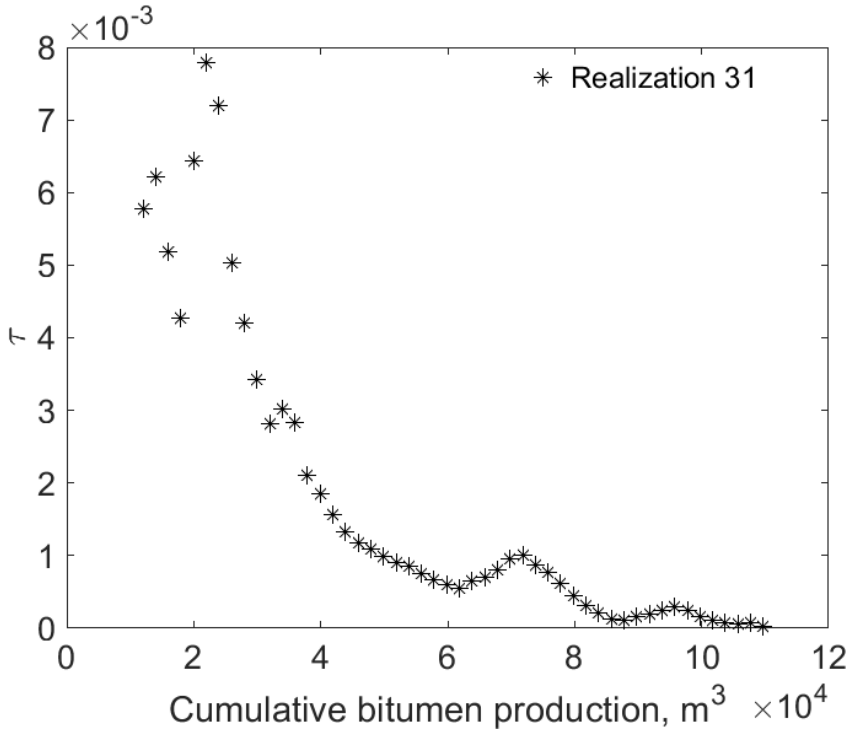

Figure K-19(c). τ for SAGD as a function of cumulative bitumen production for realization 31

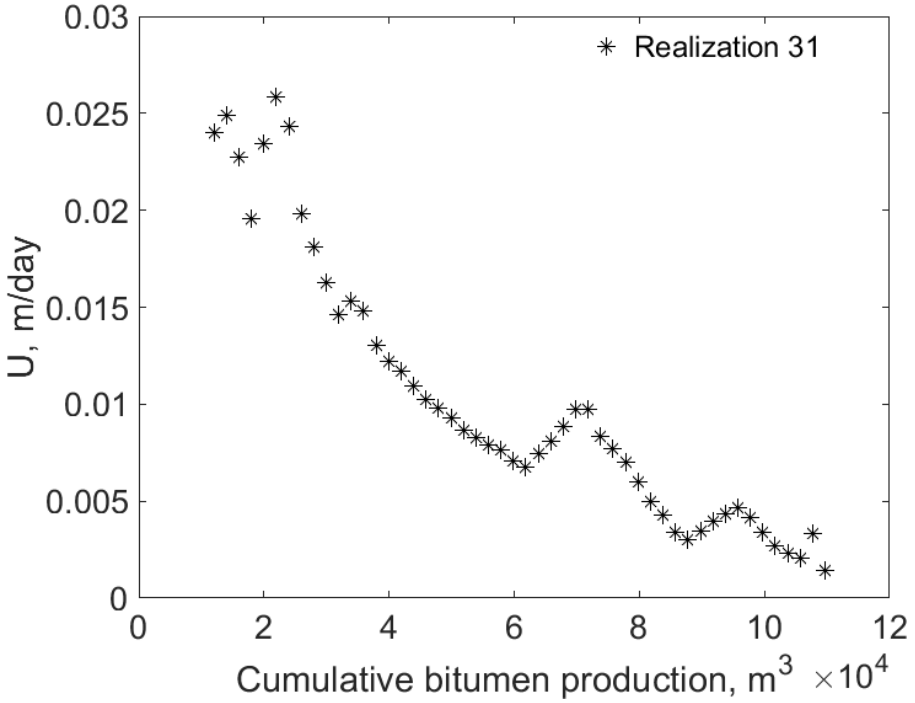

Figure K-19(d). U for SAGD as a function of cumulative bitumen production for realization 31

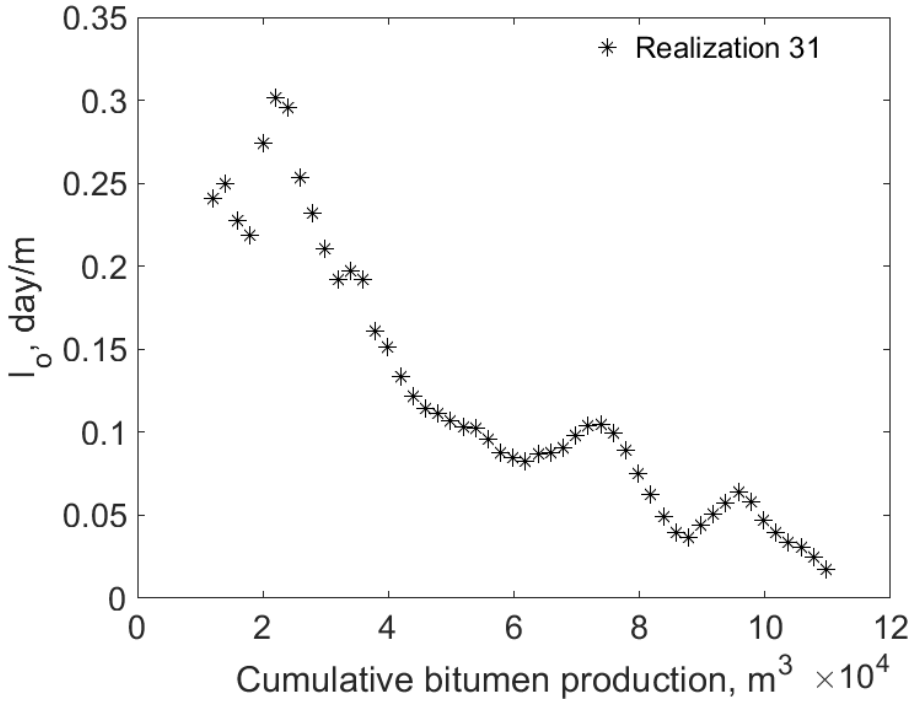

Figure K-19(e).I_o for SAGD as a function of cumulative bitumen production for realization 31

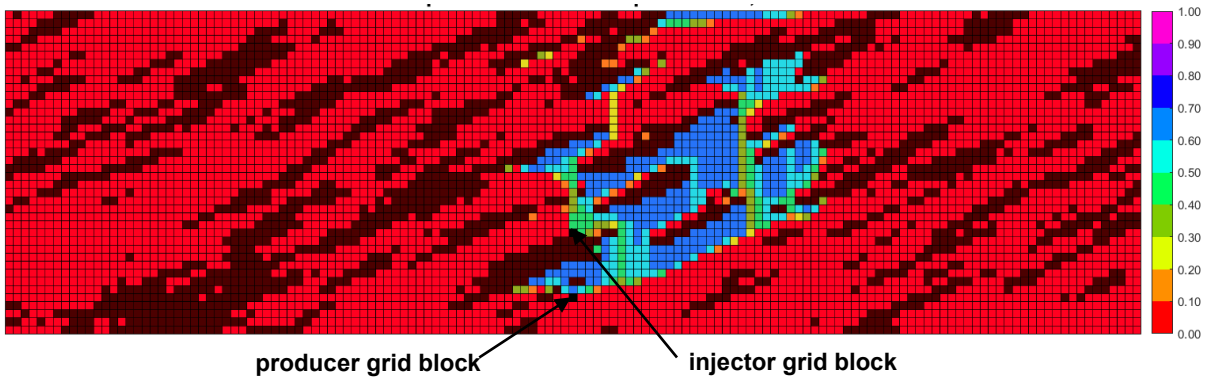

Figure K-19(f). Vapor-phase saturation map in SAGD for realization 31 for Q ≈ 31218 m^3

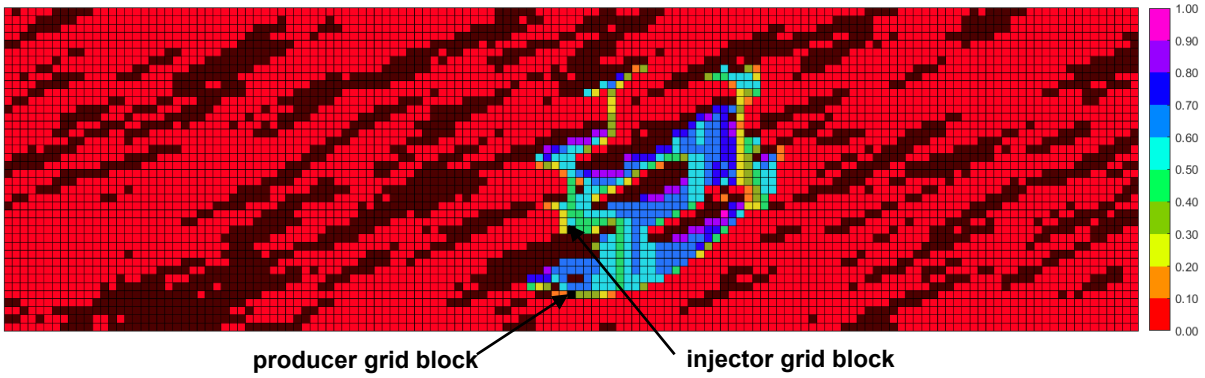

Figure K-19(g). Vapor-phase saturation map in n-C_6 SAGD for realization 31 for Q ≈ 31218 m^3

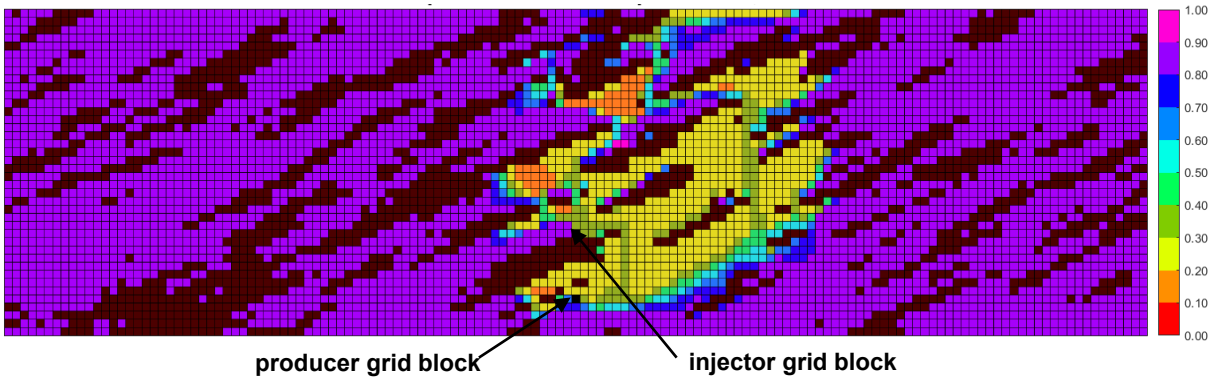

Figure K-19(h). Oleic-phase saturation map in SAGD for realization 31 for Q ≈ 31218 m^3

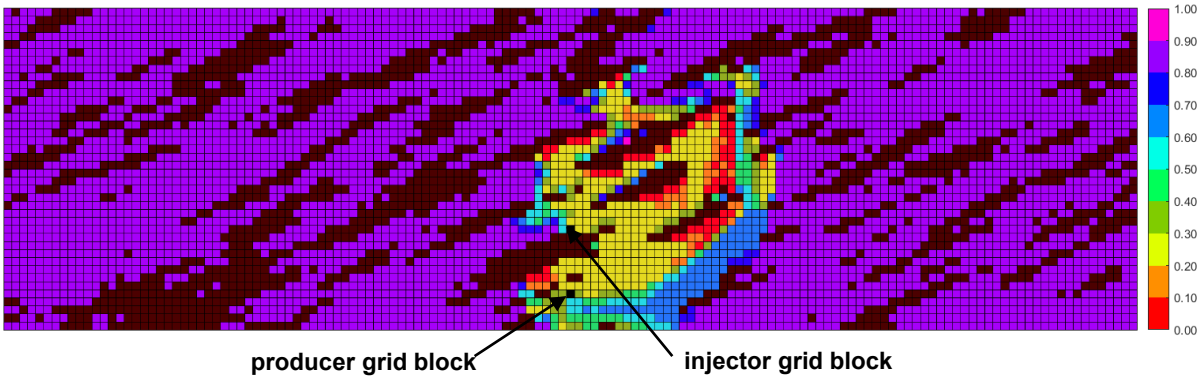

Figure K-19(i). Oleic-phase saturation map in n-C_6 SAGD for realization 31 for Q ≈ 31218 m^3

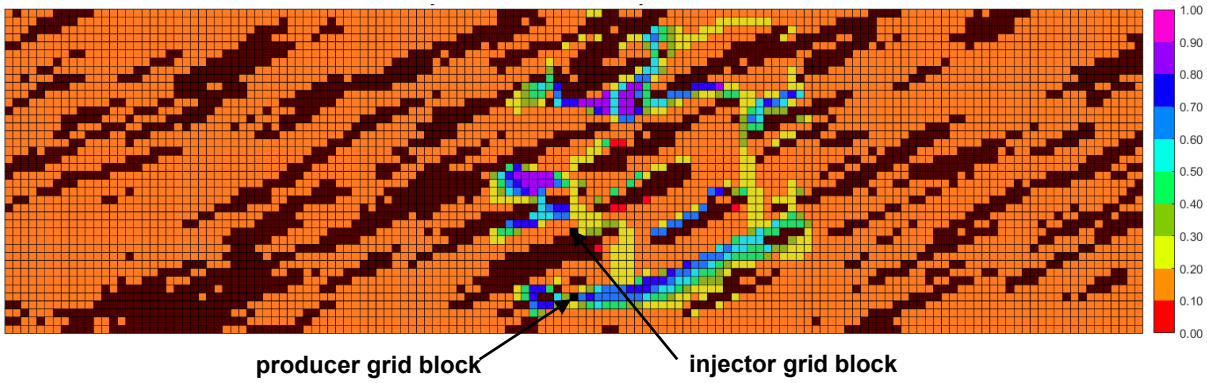

Figure K-19(j). Aqueous-phase saturation map in SAGD for realization 31 for Q ≈ 31218 m^3

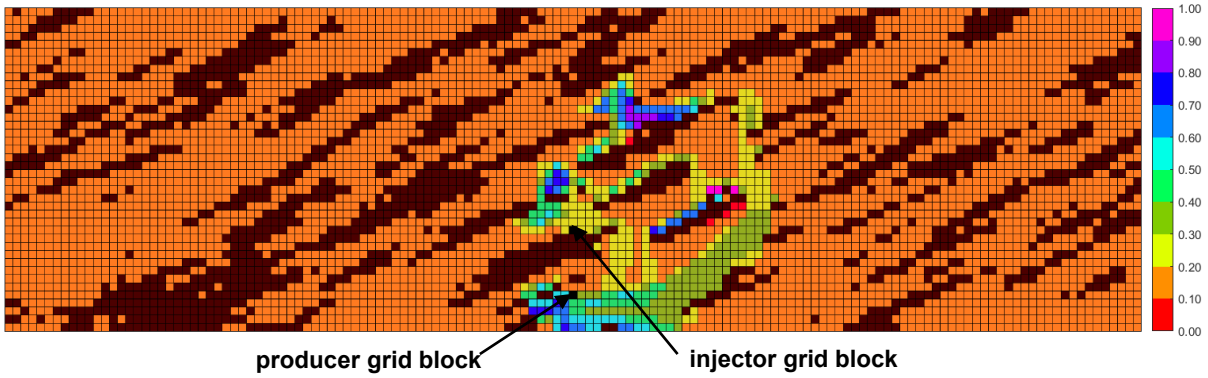

Figure K-19(k). Aqueous-phase saturation map in n-C_6 SAGD for realization 31 for Q ≈ 31218 m^3

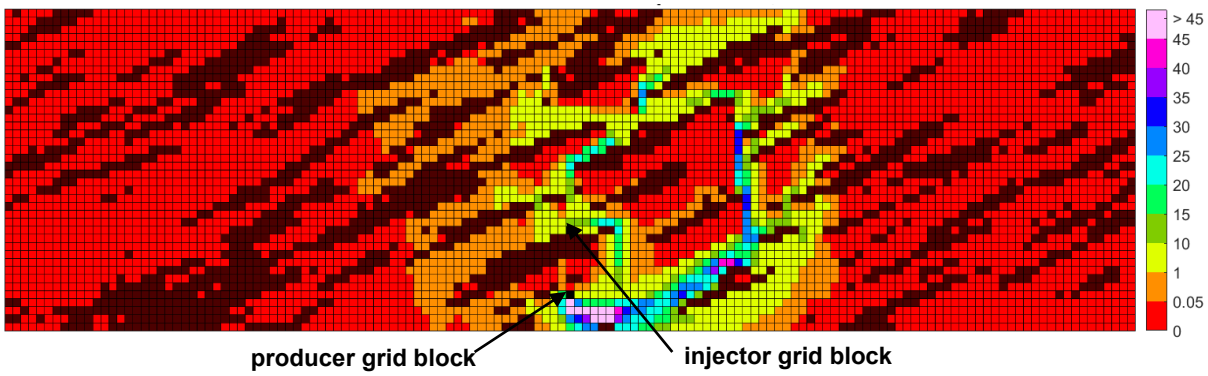

Figure K-19(l). Bitumen molar flow rate (kg-mole/day) map in SAGD for realization 31 for Q ≈ 31218 m^3

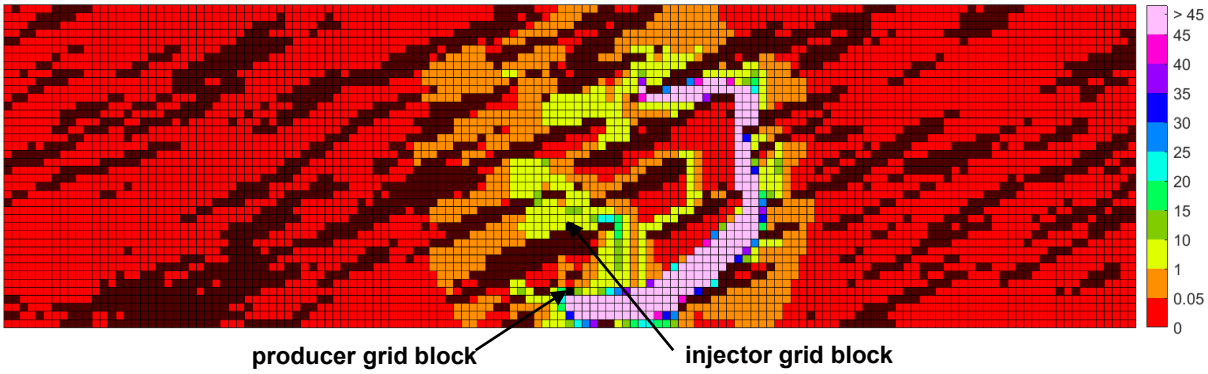

Figure K-19(m). Bitumen molar flow rate (kg-mole/day) map in n-C_6 SAGD for realization 31 for Q ≈ 31218 m^3

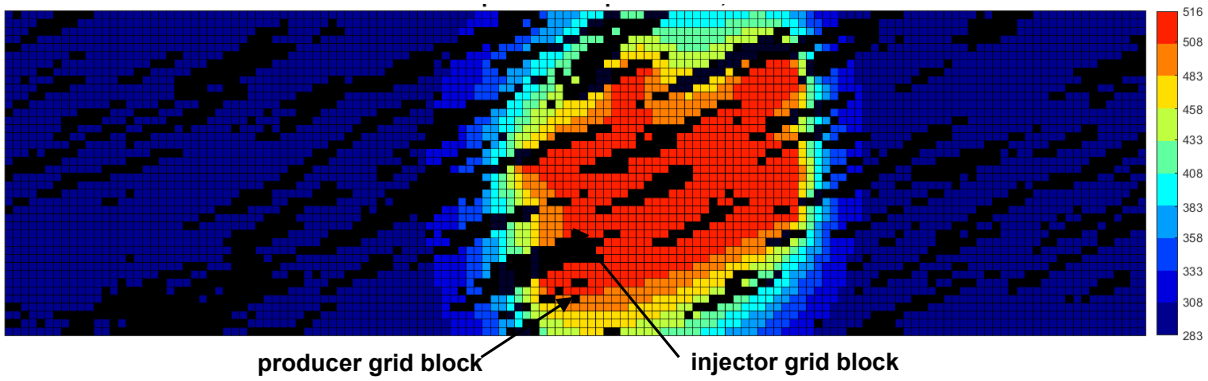

Figure K-19(n). Temperature (Kelvin) map in SAGD for realization 31 for Q ≈ 31218 m^3

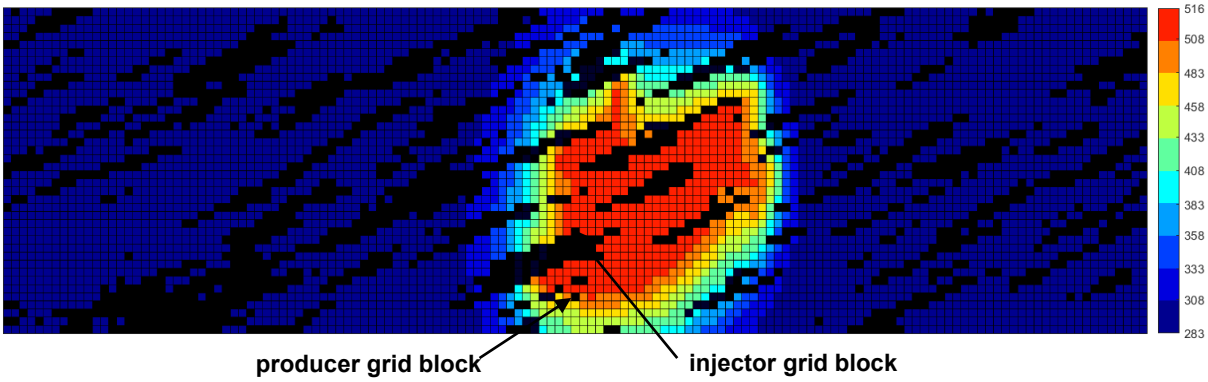

Figure K-19(o). Temperature (Kelvin) map in n-C_6 SAGD for realization 31 for Q ≈ 31218 m^3

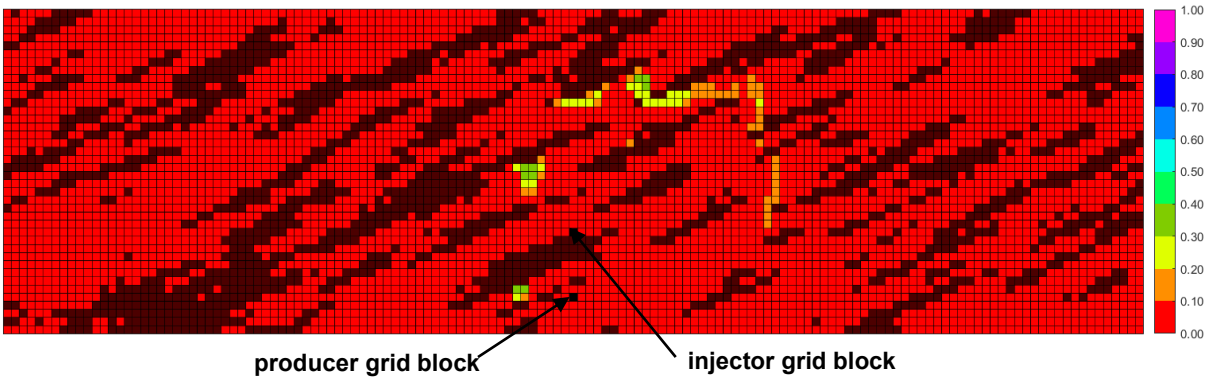

Figure K-19(p). $\beta_L x_{sL}$ map in n-C_6 SAGD for realization 31 for Q ≈ 31218 m^3

Figure K-19. Property maps for SAGD and n-C_6 SAGD for realization 31

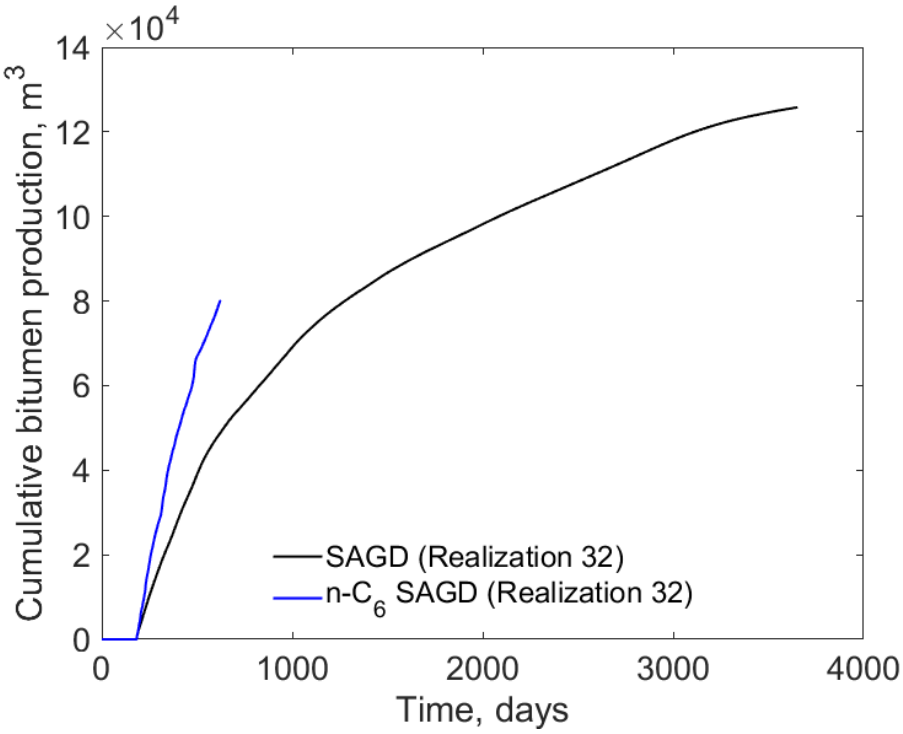

Figure K-20(a). Cumulative bitumen production histories for SAGD and n-C_6 SAGD for realization 32

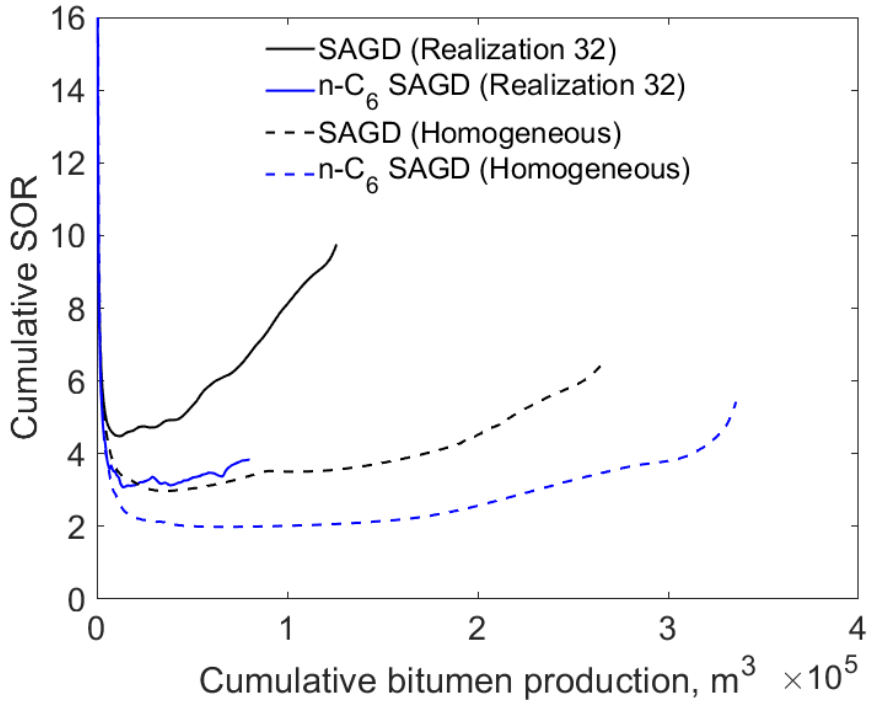

Figure K-20(b). Cumulative SOR for SAGD and n-C_6 SAGD for realization 32

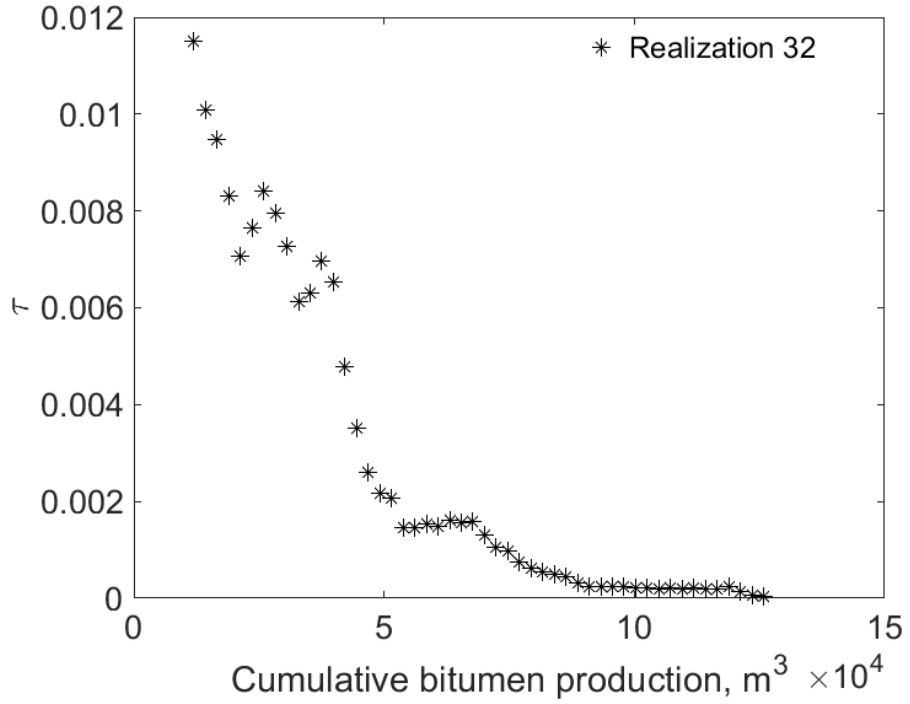

Figure K-20(c). τ for SAGD as a function of cumulative bitumen production for realization 32

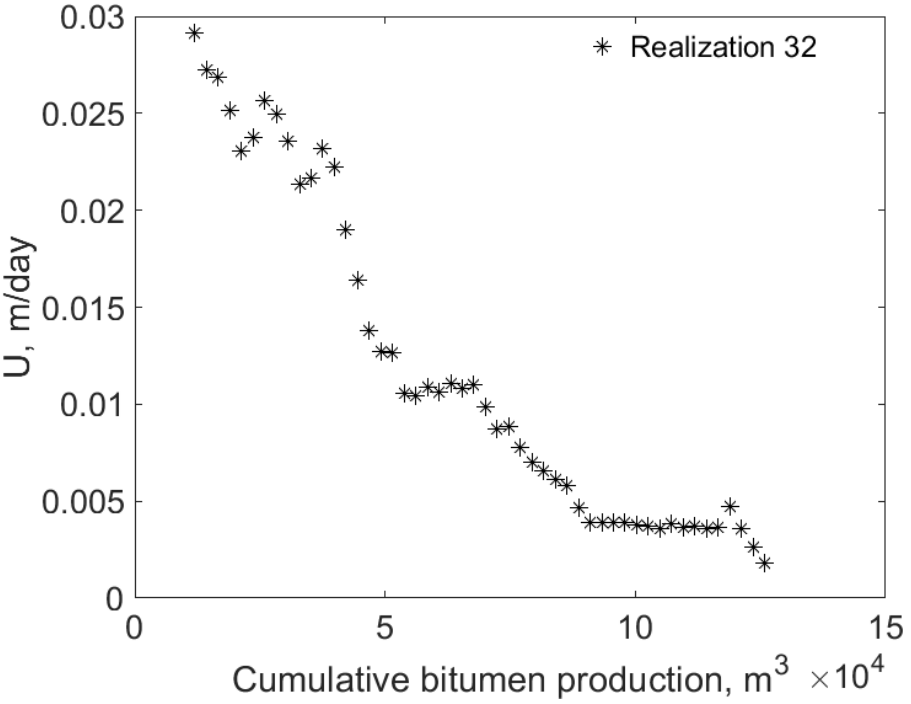

Figure K-20(d). U for SAGD as a function of cumulative bitumen production for realization 32

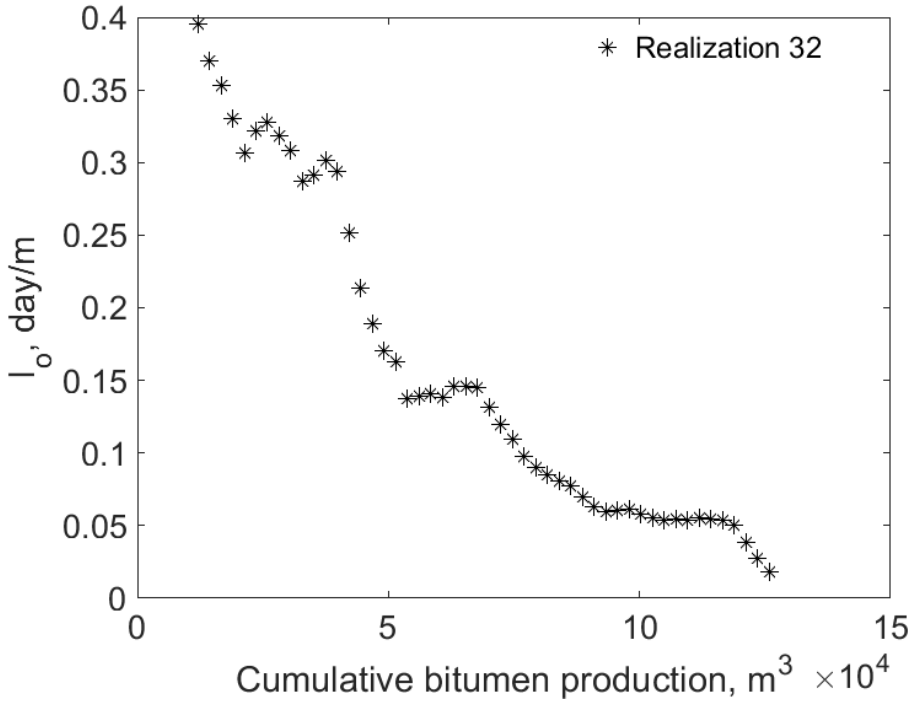

Figure K-20(e).I_o for SAGD as a function of cumulative bitumen production for realization 32

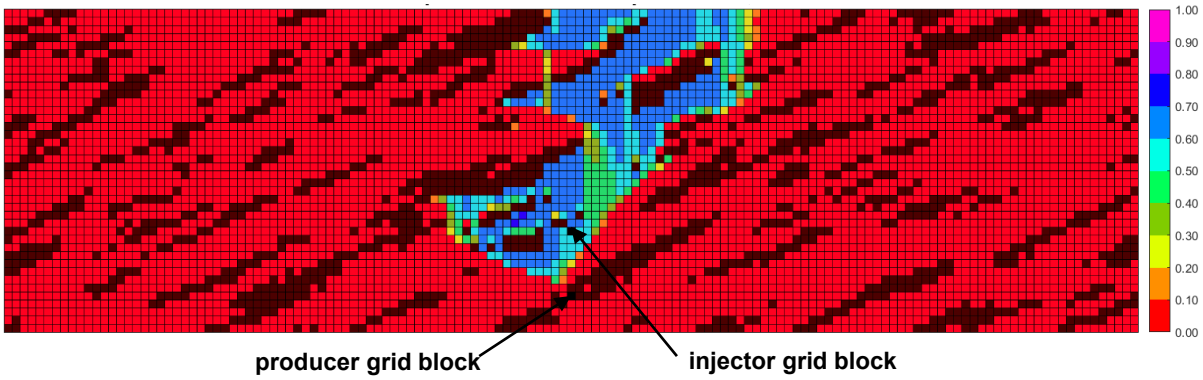

Figure K-20(f). Vapor-phase saturation map in SAGD for realization 32 for Q ≈ 31218 m^3

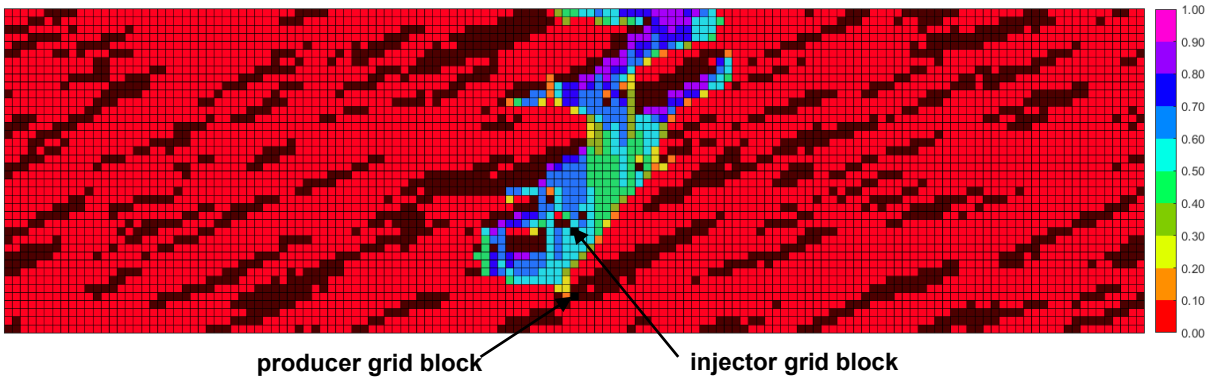

Figure K-20(g). Vapor-phase saturation map in n-C_6 SAGD for realization 32 for Q ≈ 31218 m^3

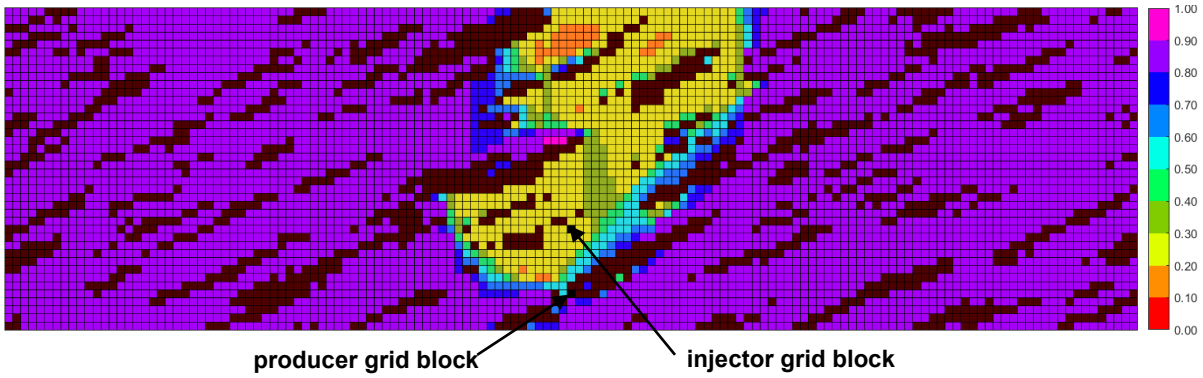

Figure K-20(h). Oleic-phase saturation map in SAGD for realization 32 for Q ≈ 31218 m^3

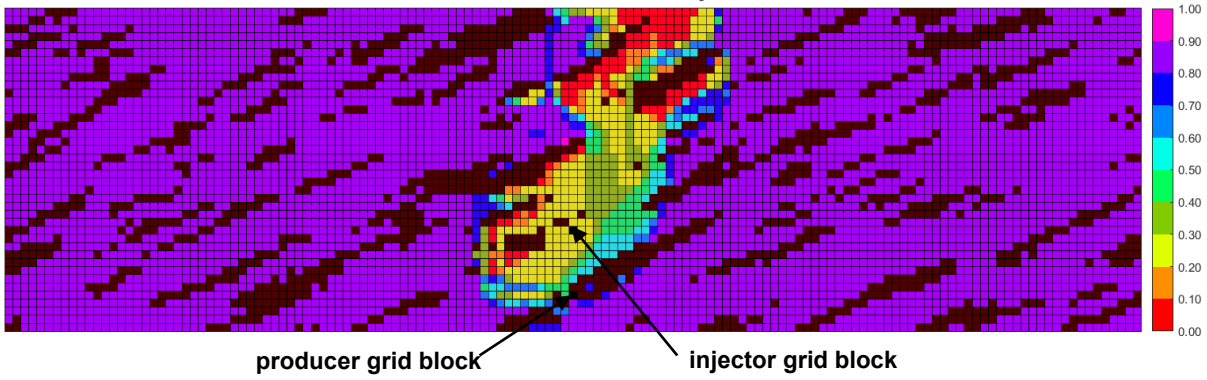

Figure K-20(i). Oleic-phase saturation map in n-C_6 SAGD for realization 32 for Q ≈ 31218 m^3

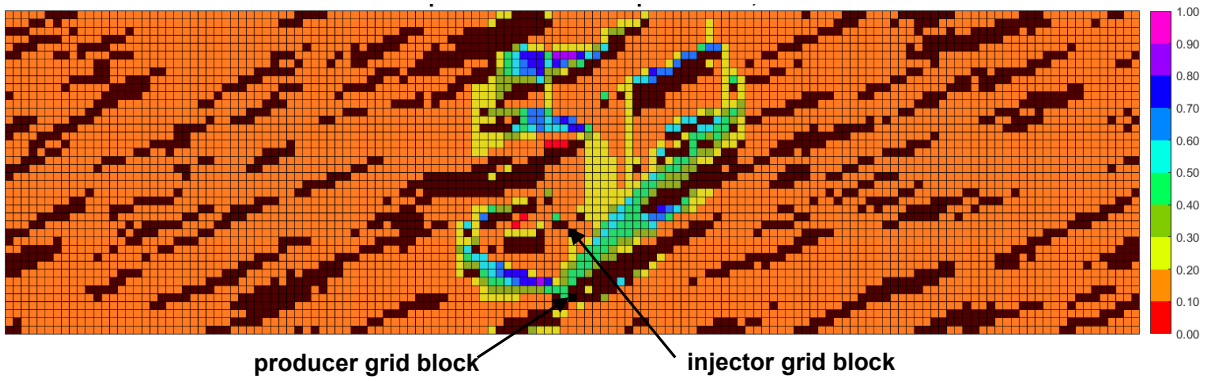

Figure K-20(j). Aqueous-phase saturation map in SAGD for realization 32 for Q ≈ 31218 m^3

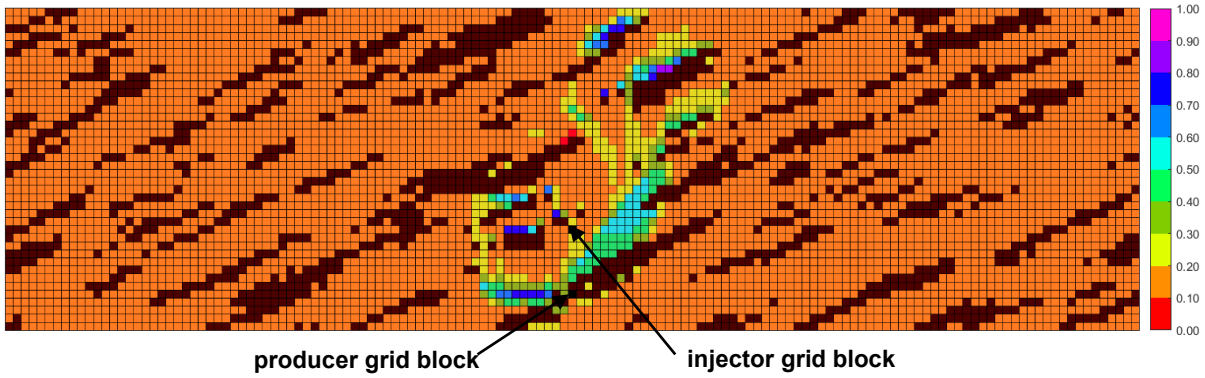

Figure K-20(k). Aqueous-phase saturation map in n-C_6 SAGD for realization 32 for Q ≈ 31218 m^3

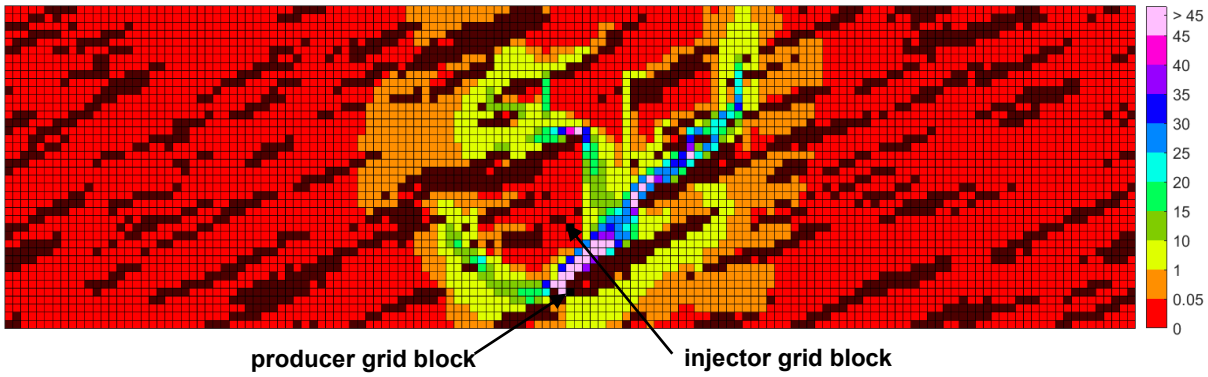

Figure K-20(l). Bitumen molar flow rate (kg-mole/day) map in SAGD for realization 32 for Q ≈ 31218 m^3

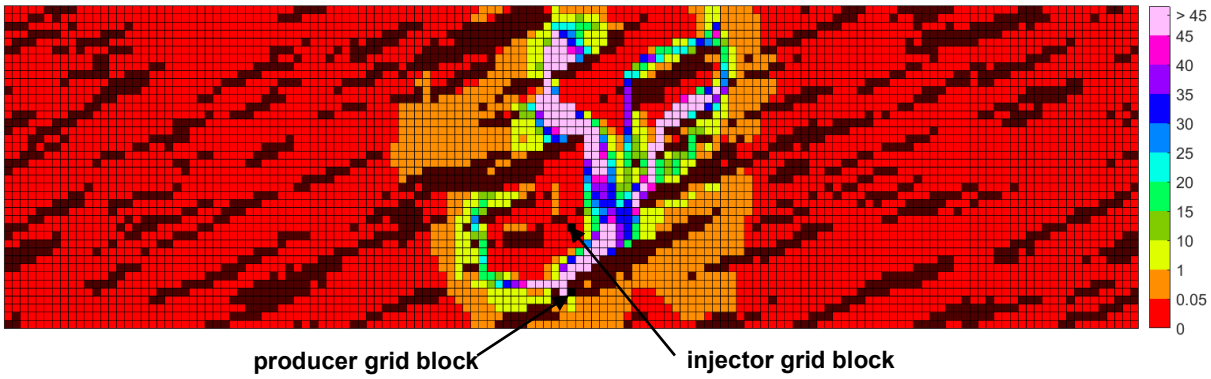

Figure K-20(m). Bitumen molar flow rate (kg-mole/day) map in n-C_6 SAGD for realization 32 for Q ≈ 31218 m^3

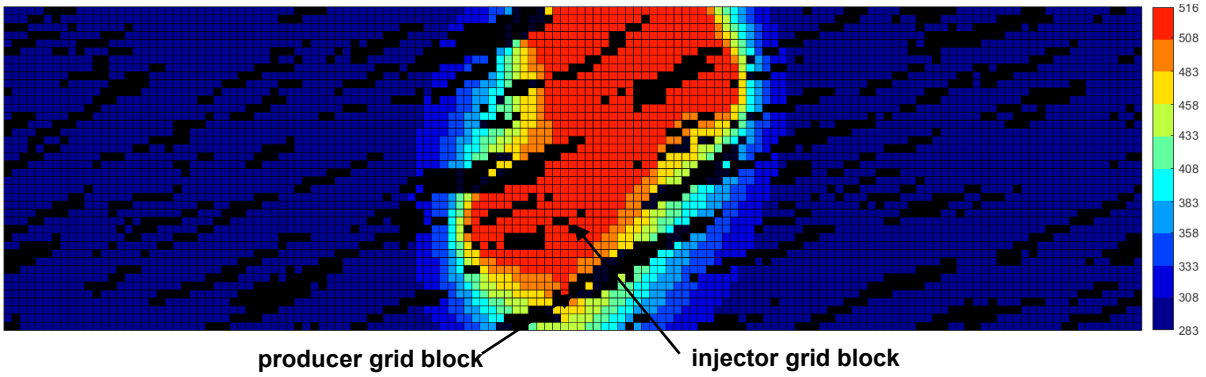

Figure K-20(n). Temperature (Kelvin) map in SAGD for realization 32 for Q ≈ 31218 m^3

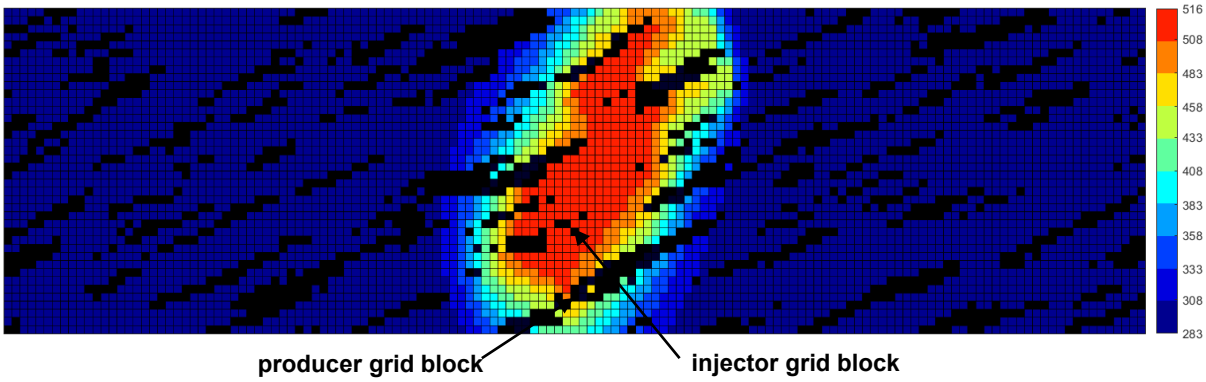

Figure K-20(o). Temperature (Kelvin) map in n-C_6 SAGD for realization 32 for Q ≈ 31218 m^3

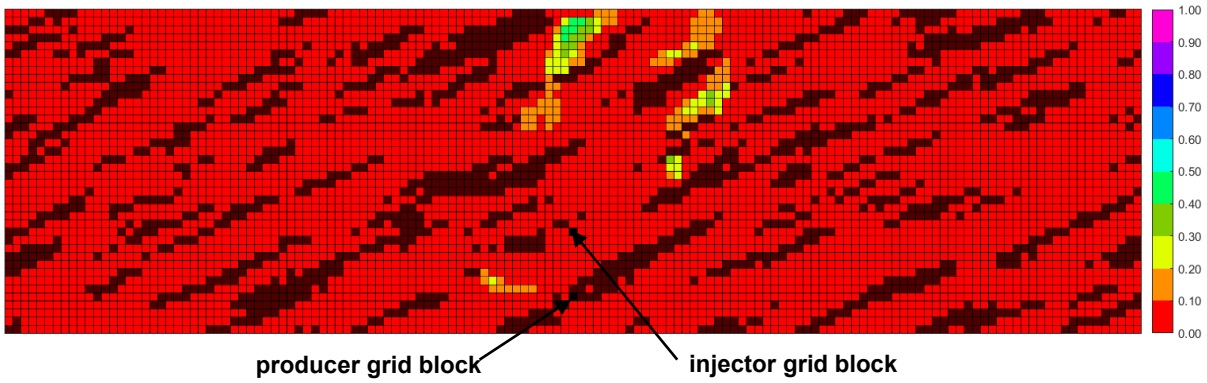

Figure K-20(p). $\beta_L x_{sL}$ map in n-C_6 SAGD for realization 32 for Q ≈ 31218 m^3

Figure K-20. Property maps for SAGD and n-C_6 SAGD for realization 32

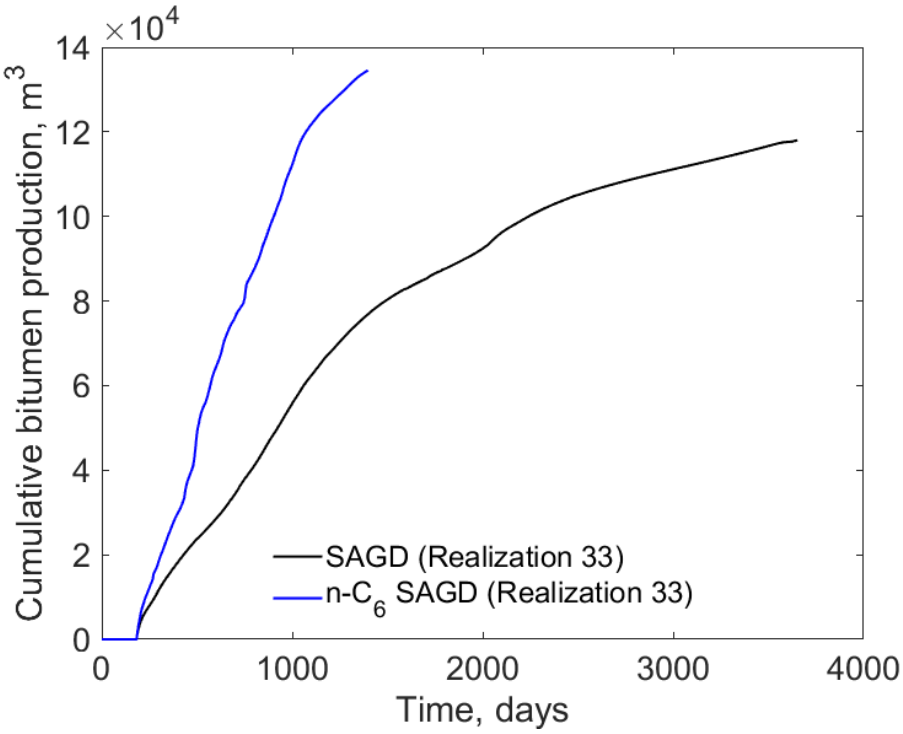

Figure K-21(a). Cumulative bitumen production histories for SAGD and n-C_6 SAGD for realization 33

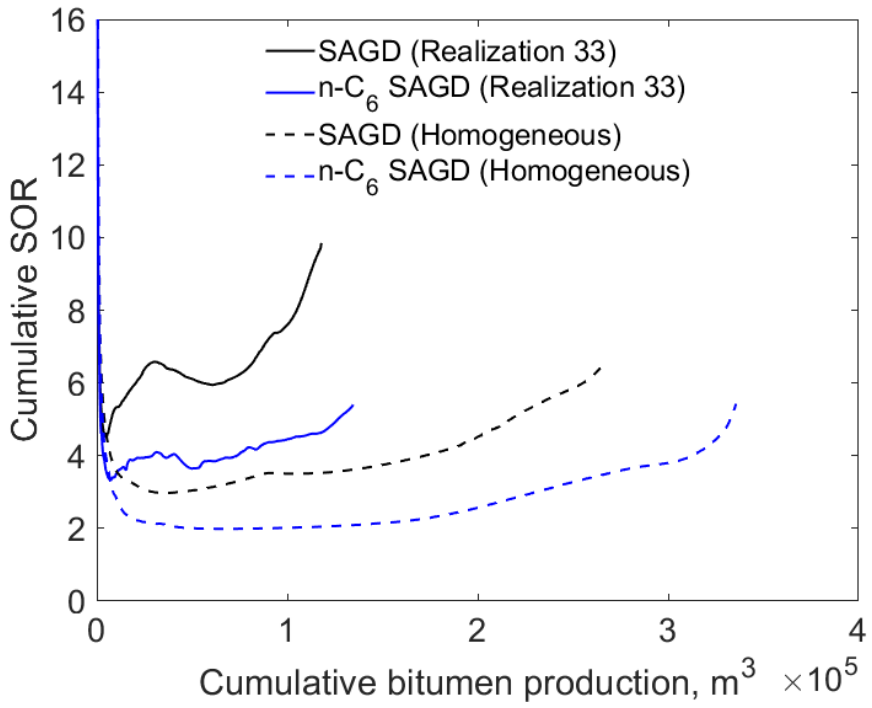

Figure K-21(b). Cumulative SOR for SAGD and n-C_6 SAGD for realization 33

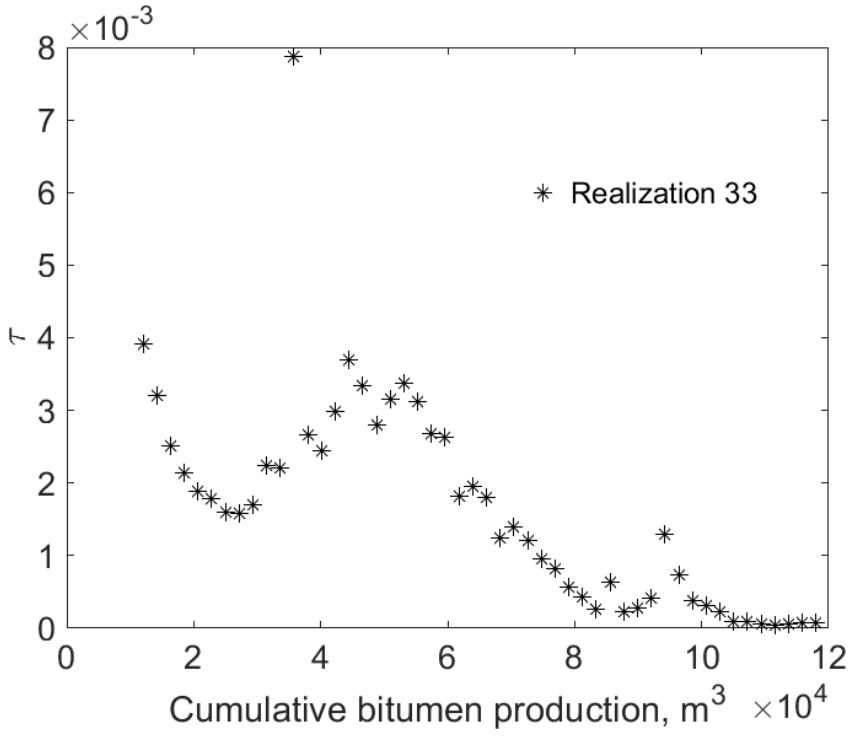

Figure K-21(c). τ for SAGD as a function of cumulative bitumen production for realization 33

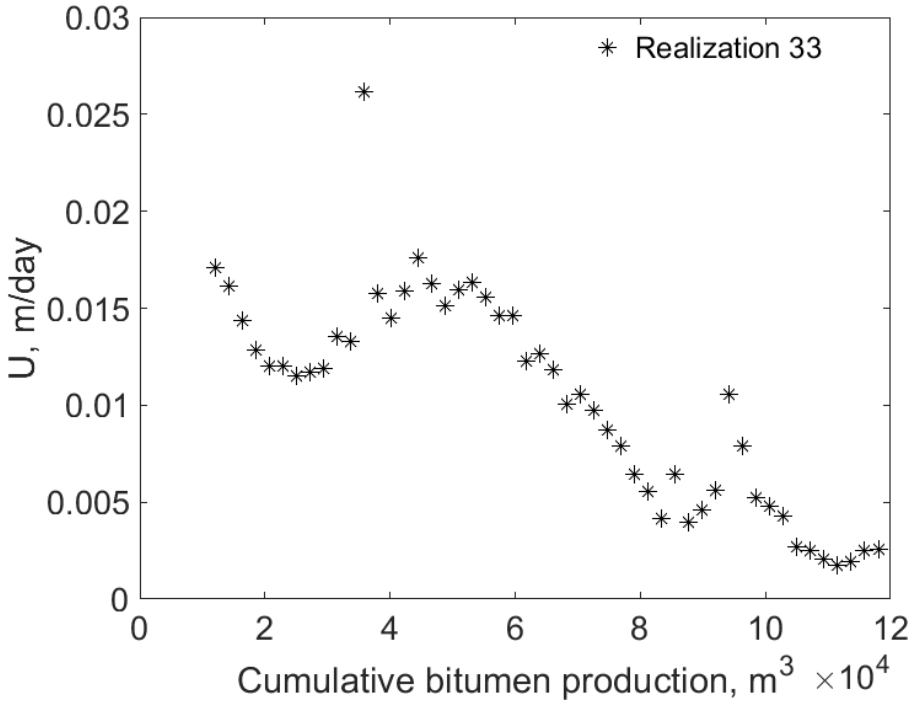

Figure K-21(d). U for SAGD as a function of cumulative bitumen production for realization 33

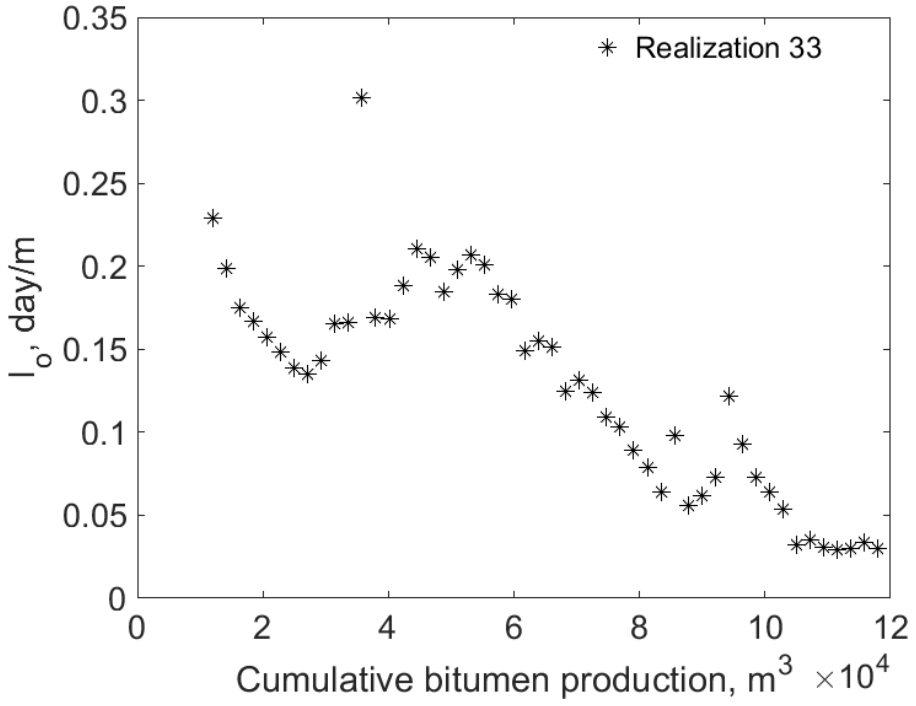

Figure K-21(e).I_o for SAGD as a function of cumulative bitumen production for realization 33

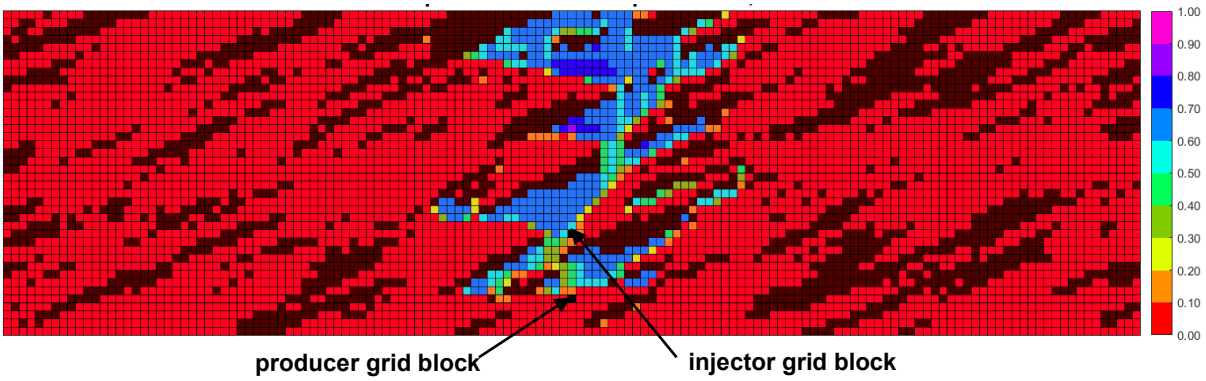

Figure K-21(f). Vapor-phase saturation map in SAGD for realization 33 for Q ≈ 31218 m^3

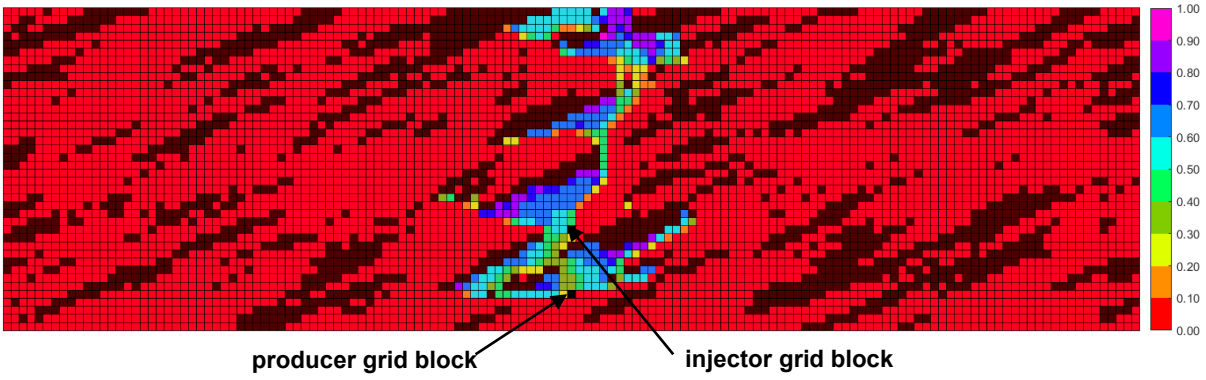

Figure K-21(g). Vapor-phase saturation map in n-C_6 SAGD for realization 33 for Q ≈ 31218 m^3

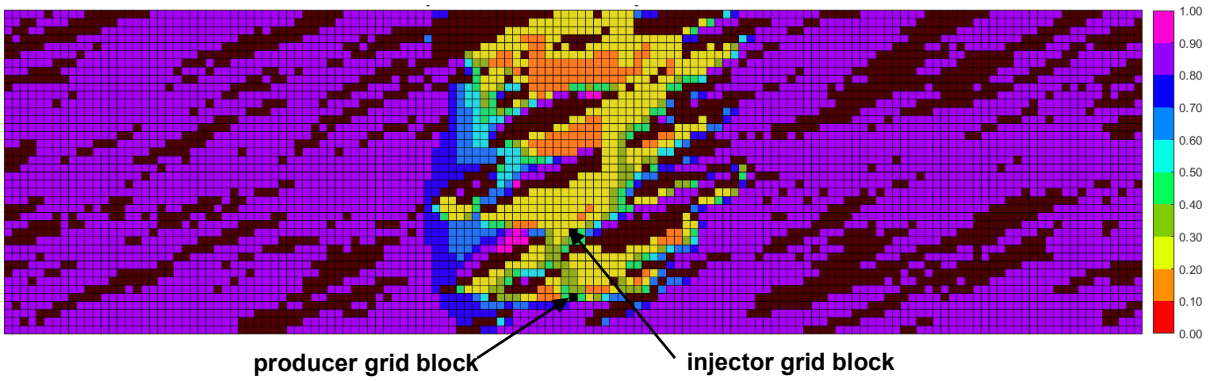

Figure K-21(h). Oleic-phase saturation map in SAGD for realization 33 for Q ≈ 31218 m^3

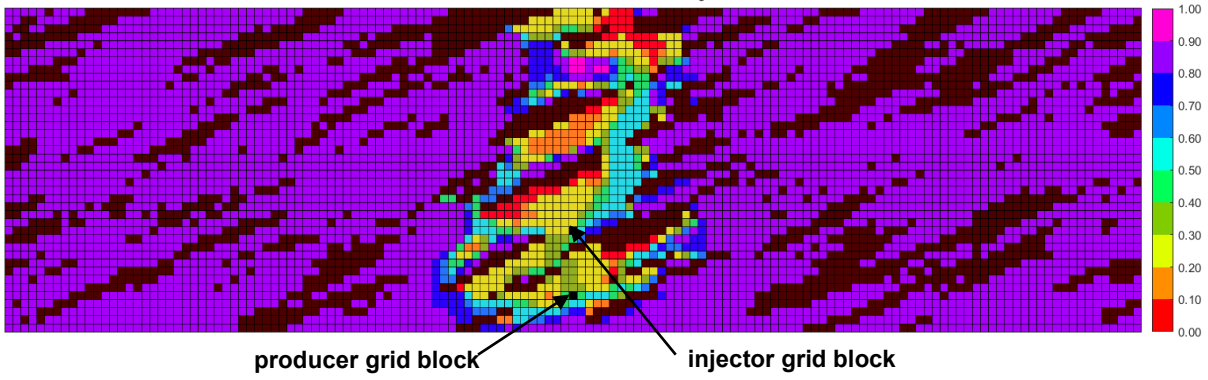

Figure K-21(i). Oleic-phase saturation map in n-C_6 SAGD for realization 33 for Q ≈ 31218 m^3

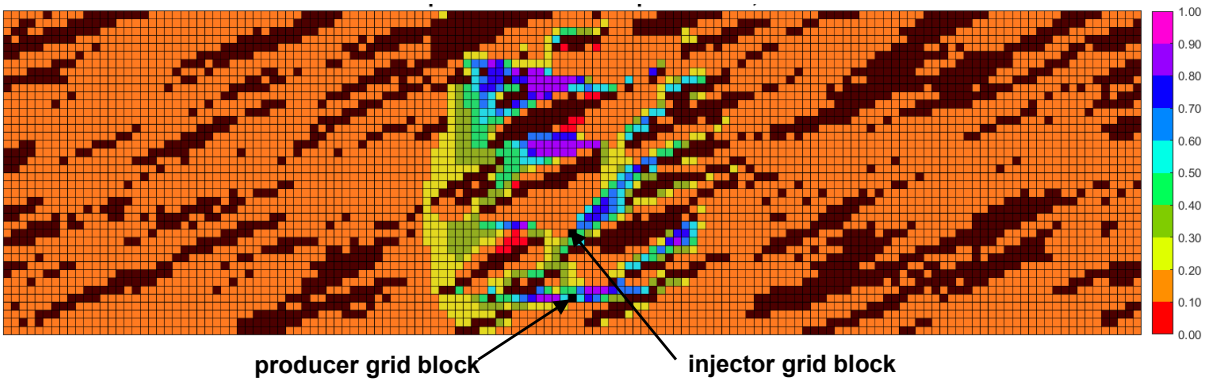

Figure K-21(j). Aqueous-phase saturation map in SAGD for realization 33 for Q ≈ 31218 m^3

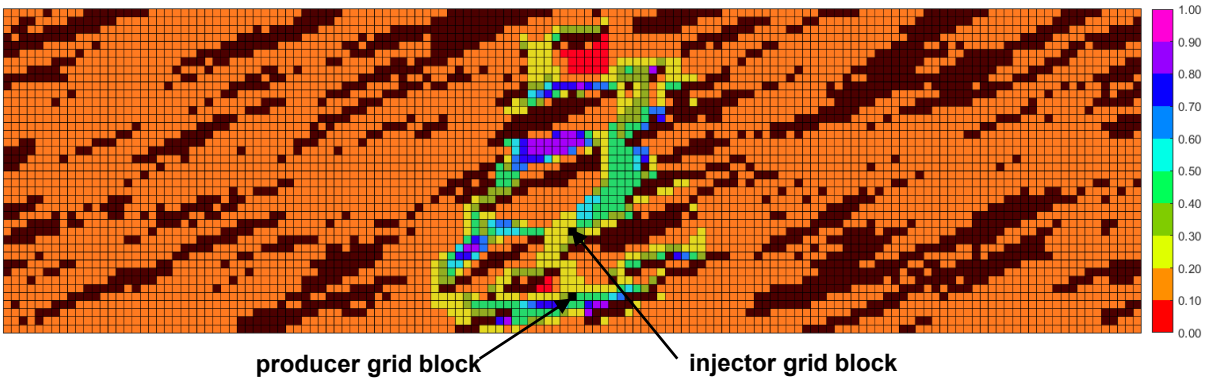

Figure K-21(k). Aqueous-phase saturation map in n-C_6 SAGD for realization 33 for Q ≈ 31218 m^3

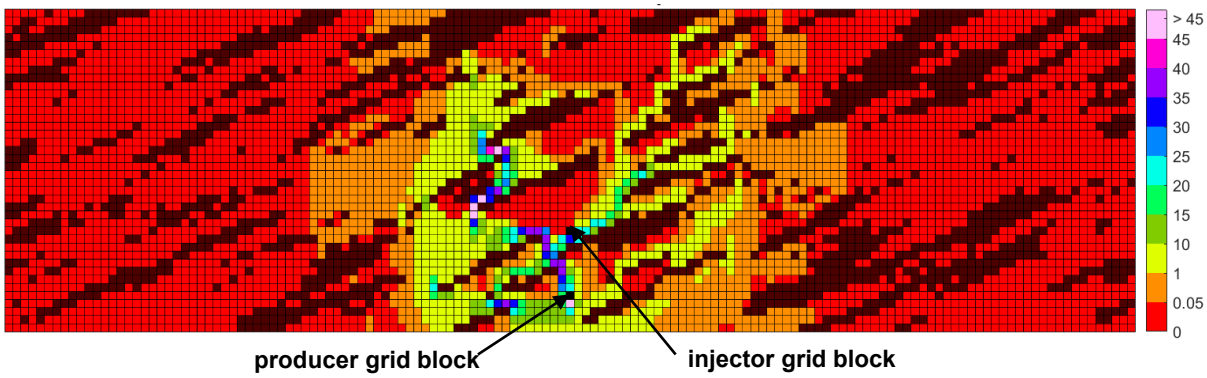

Figure K-21(l). Bitumen molar flow rate (kg-mole/day) map in SAGD for realization 33 for Q ≈ 31218 m^3

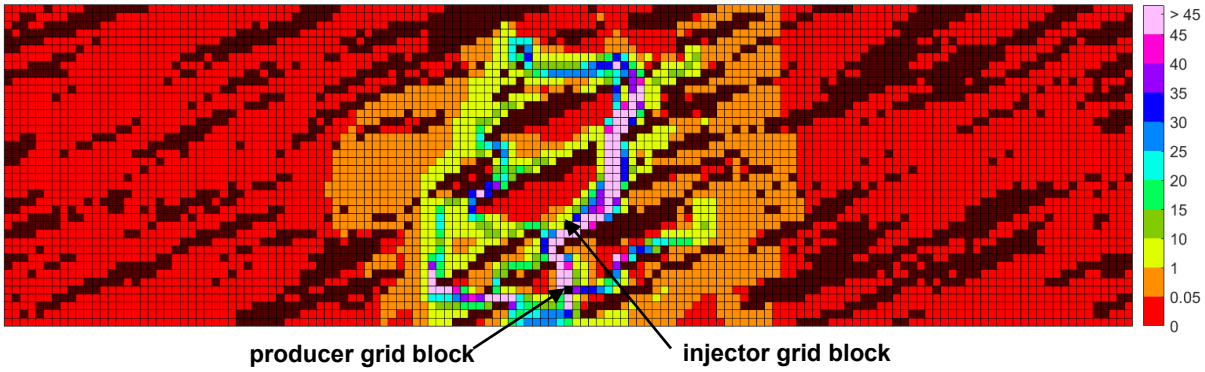

Figure K-21(m). Bitumen molar flow rate (kg-mole/day) map in n-C_6 SAGD for realization 33 for Q ≈ 31218 m^3

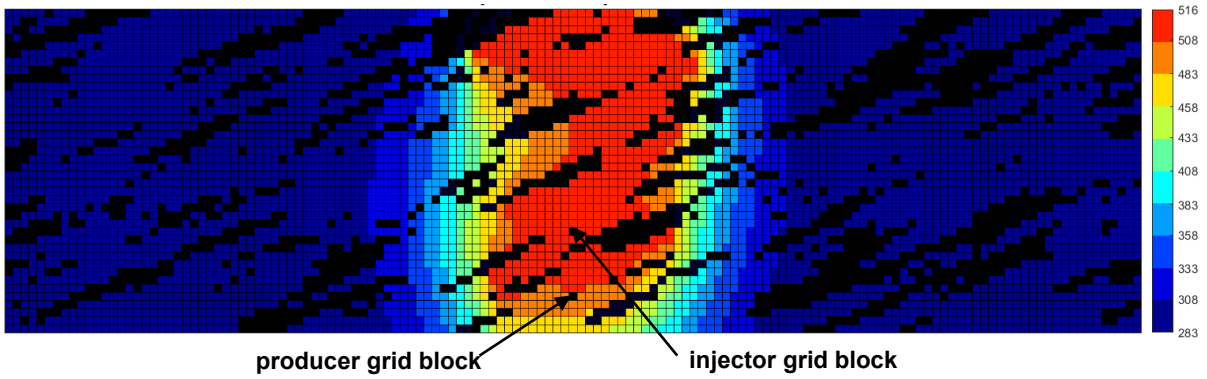

Figure K-21(n). Temperature (Kelvin) map in SAGD for realization 33 for Q ≈ 31218 m^3

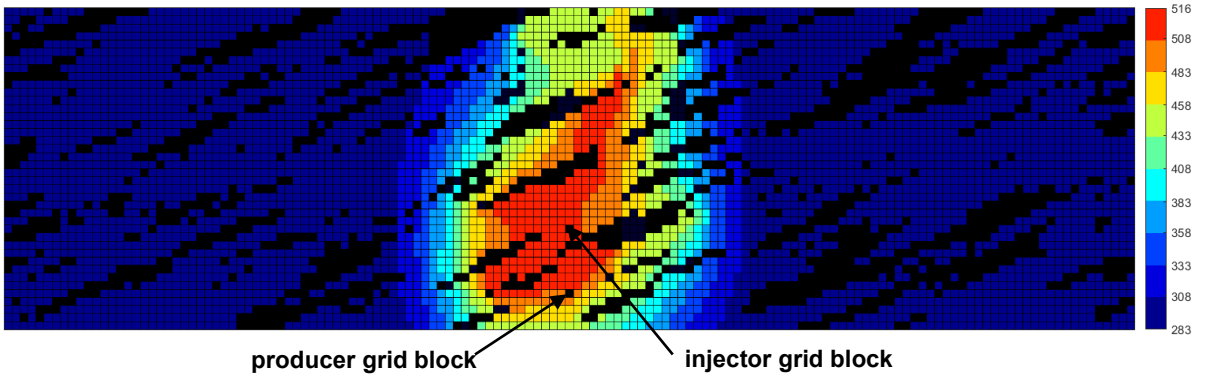

Figure K-21(o). Temperature (Kelvin) map in n-C_6 SAGD for realization 33 for Q ≈ 31218 m^3

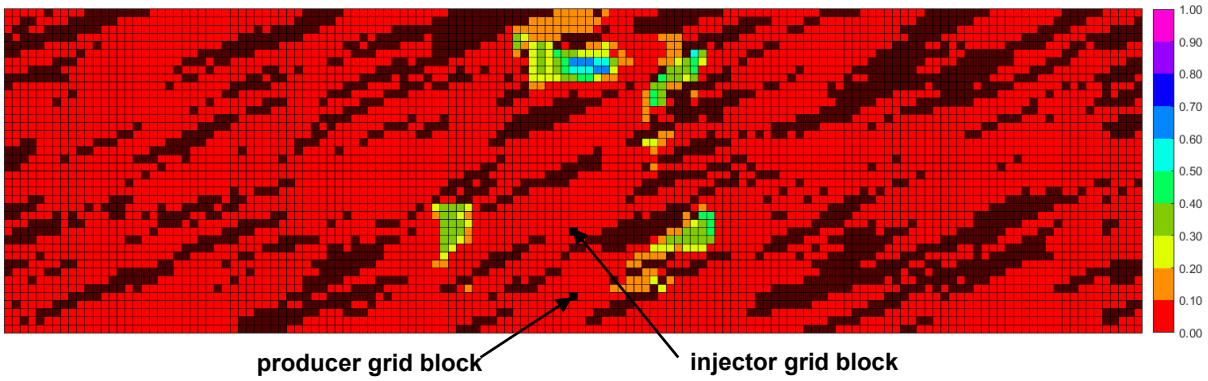

Figure K-21(p). $\beta_L x_{sL}$ map in n-C_6 SAGD for realization 33 for Q ≈ 31218 m^3

Figure K-21. Property maps for SAGD and n-C_6 SAGD for realization 33

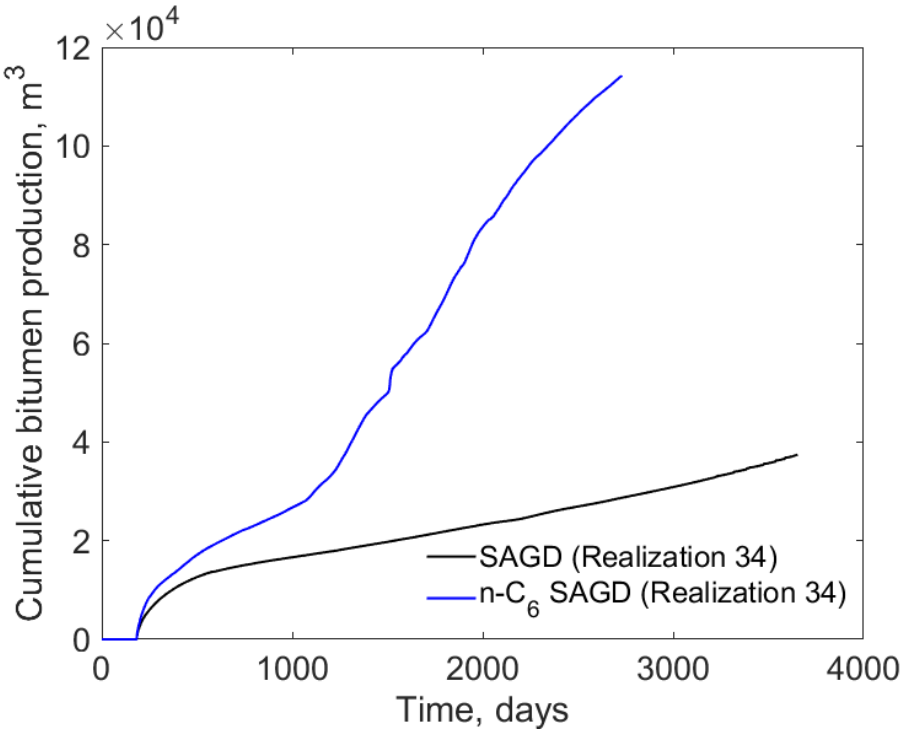

Figure K-22(a). Cumulative bitumen production histories for SAGD and n-C_6 SAGD for realization 34

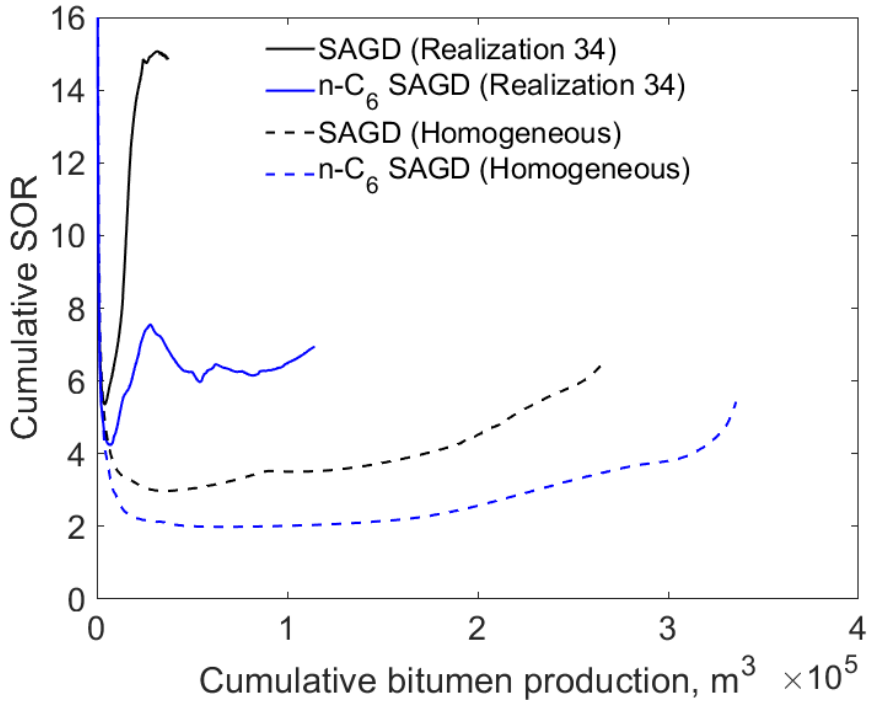

Figure K-22(b). Cumulative SOR for SAGD and n-C_6 SAGD for realization 34

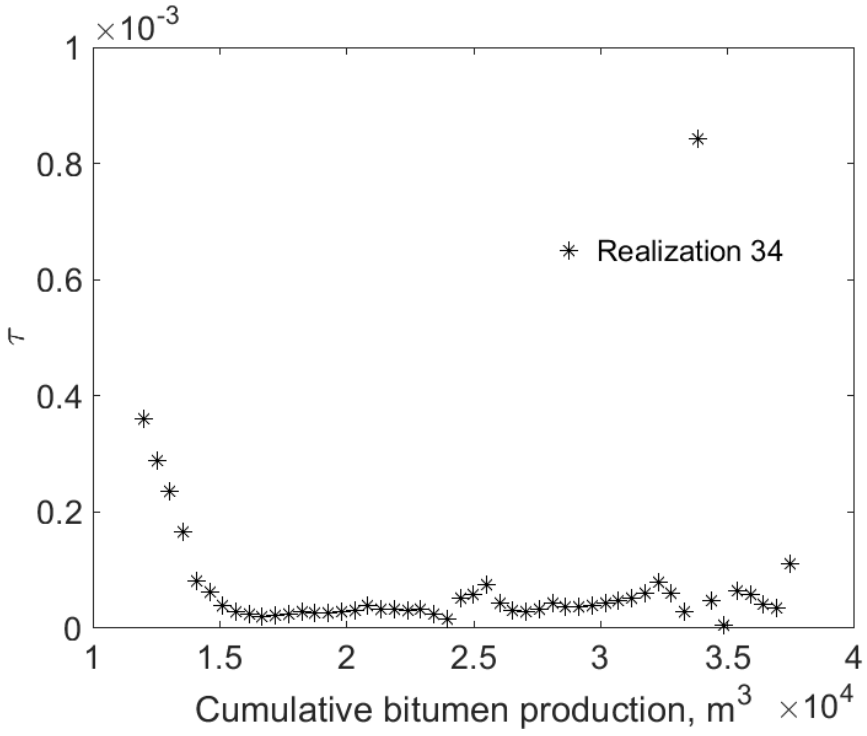

Figure K-22(c). τ for SAGD as a function of cumulative bitumen production for realization 34

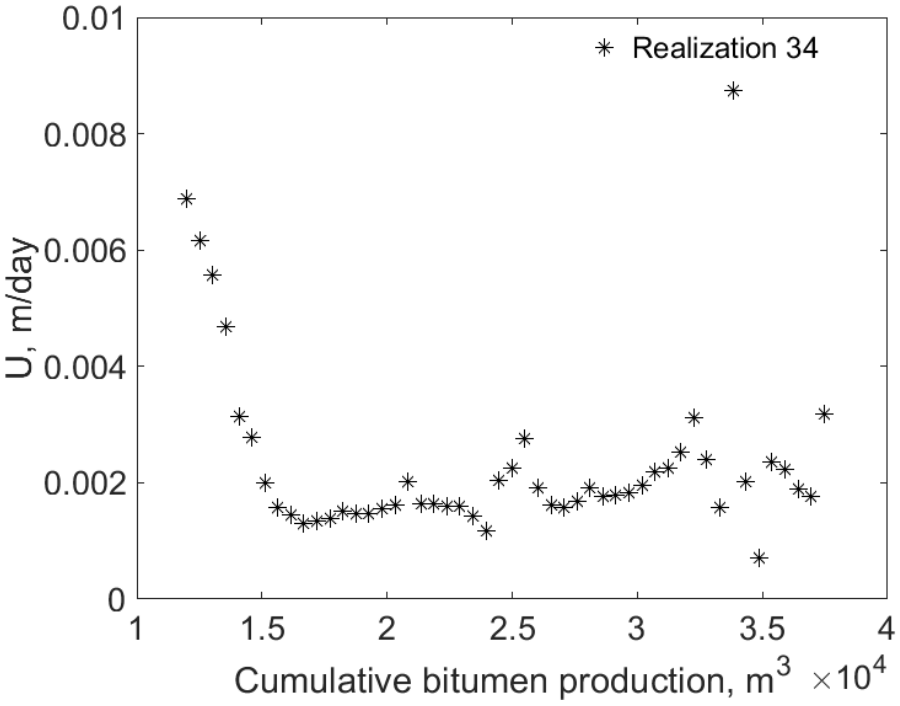

Figure K-22(d). U for SAGD as a function of cumulative bitumen production for realization 34

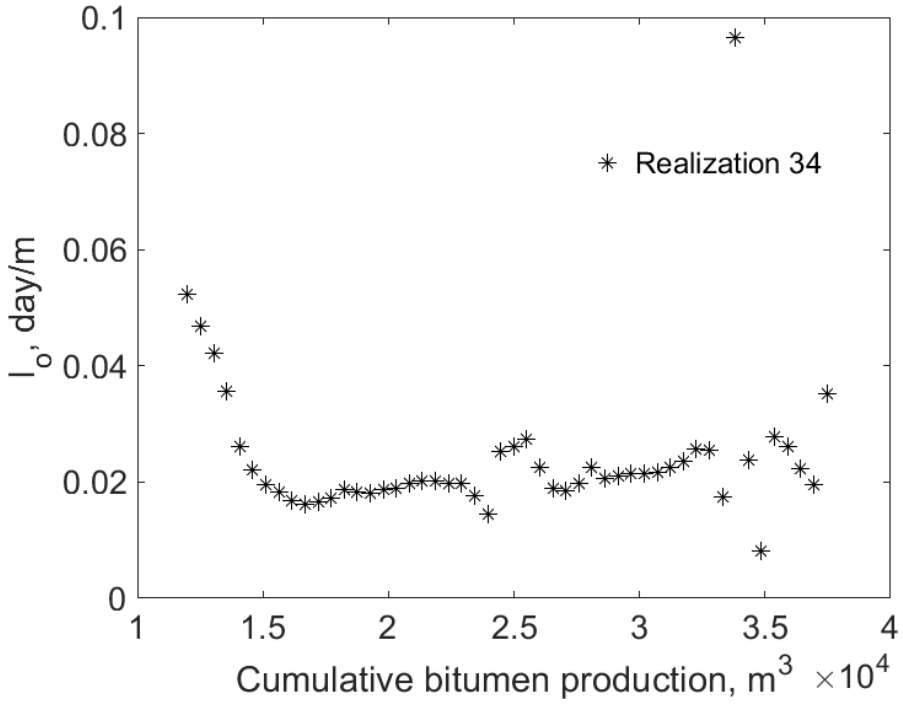

Figure K-22(e).I_o for SAGD as a function of cumulative bitumen production for realization 34

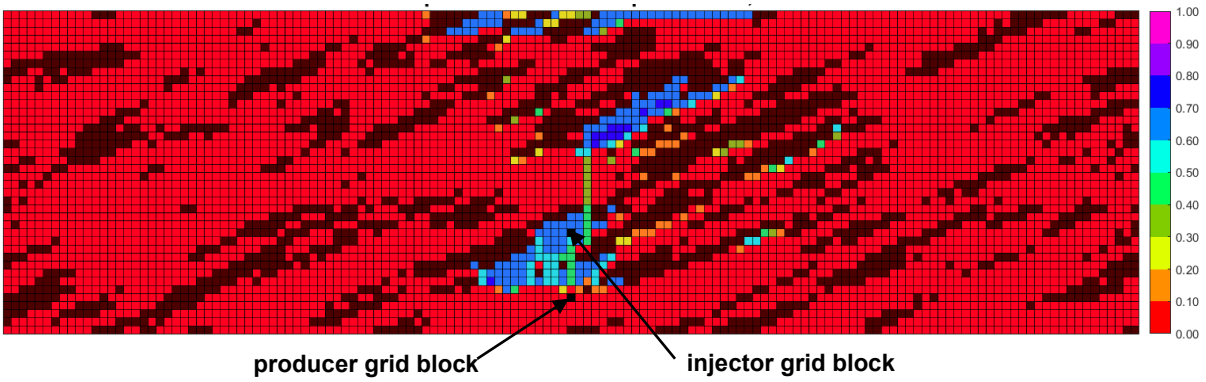

Figure K-22(f). Vapor-phase saturation map in SAGD for realization 34 for Q ≈ 31218 m^3

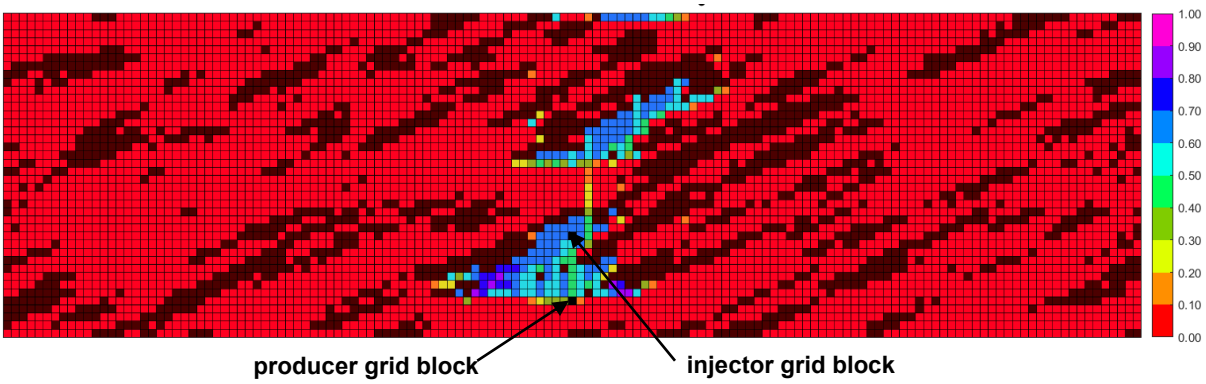

Figure K-22(g). Vapor-phase saturation map in n-C_6 SAGD for realization 34 for Q ≈ 31218 m^3

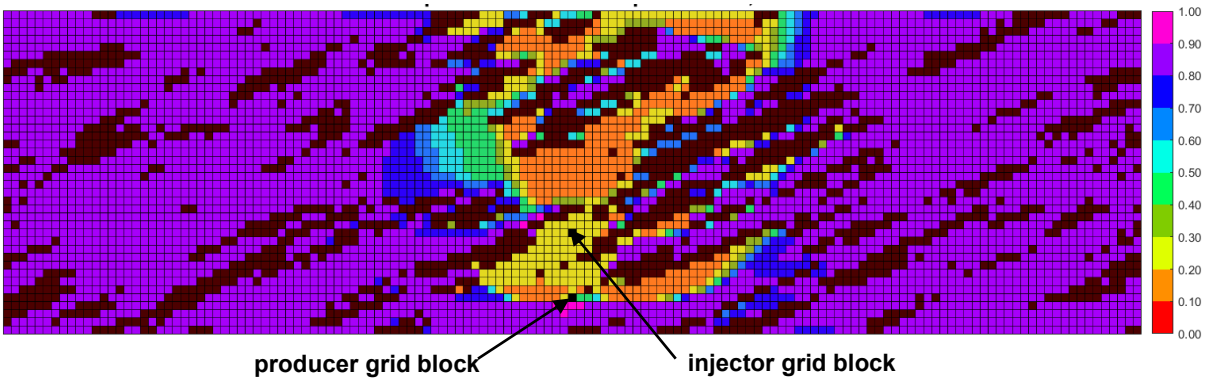

Figure K-22(h). Oleic-phase saturation map in SAGD for realization 34 for Q ≈ 31218 m^3

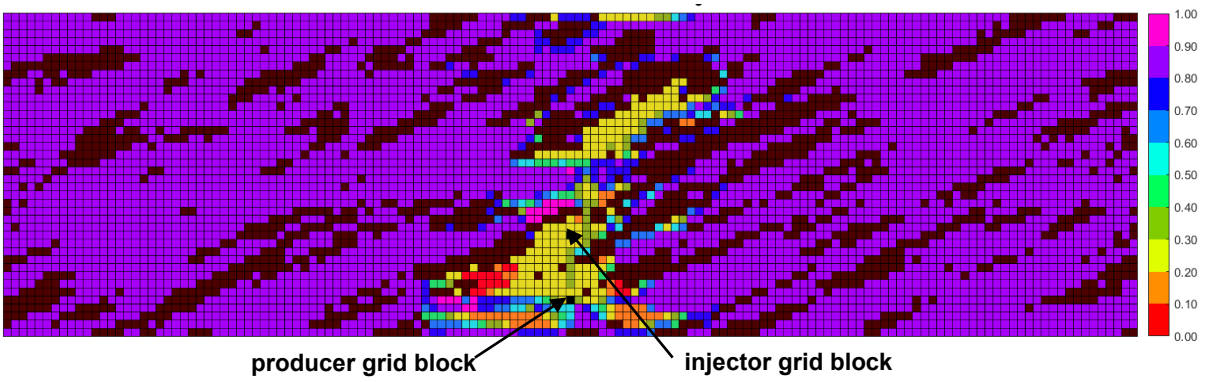

Figure K-22(i). Oleic-phase saturation map in n-C_6 SAGD for realization 34 for Q ≈ 31218 m^3

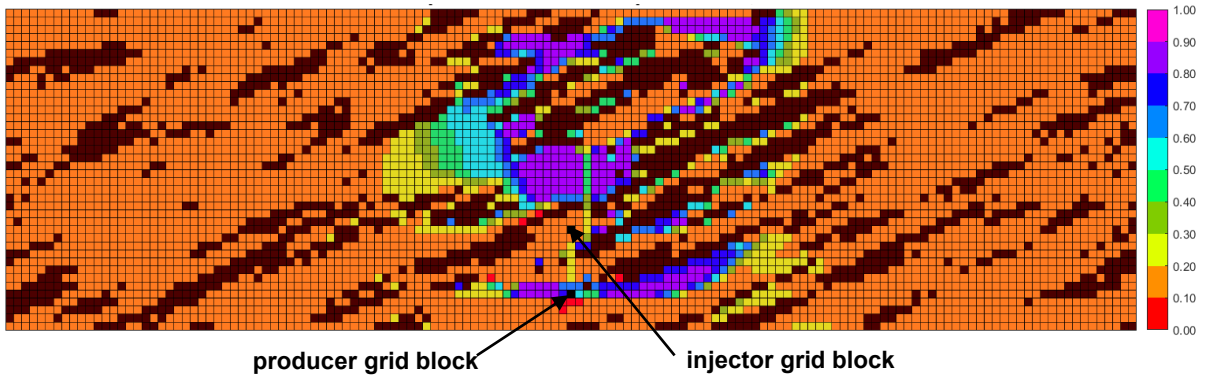

Figure K-22(j). Aqueous-phase saturation map in SAGD for realization 34 for Q ≈ 31218 m^3

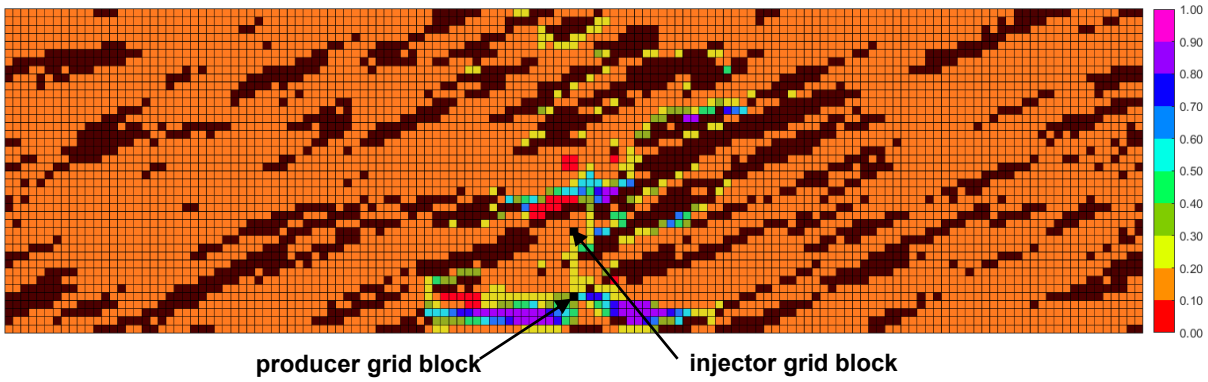

Figure K-22(k). Aqueous-phase saturation map in n-C_6 SAGD for realization 34 for Q ≈ 31218 m^3

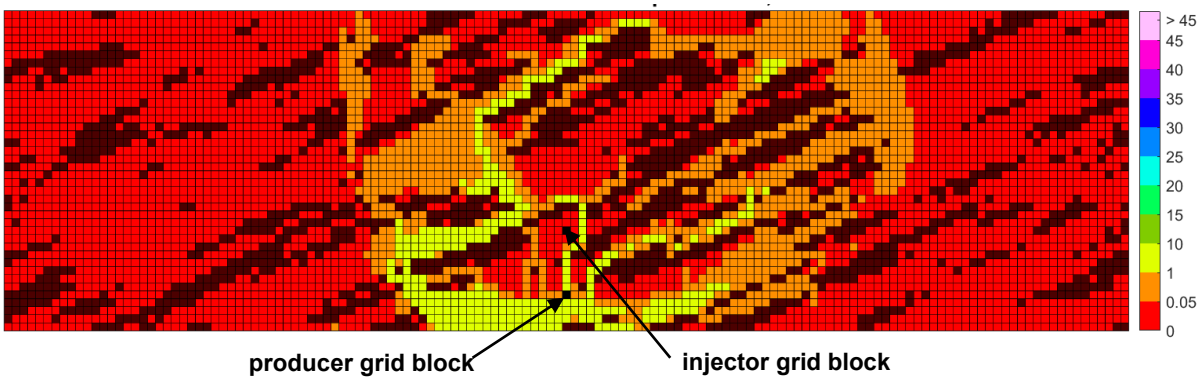

Figure K-22(l). Bitumen molar flow rate (kg-mole/day) map in SAGD for realization 34 for Q ≈ 31218 m^3

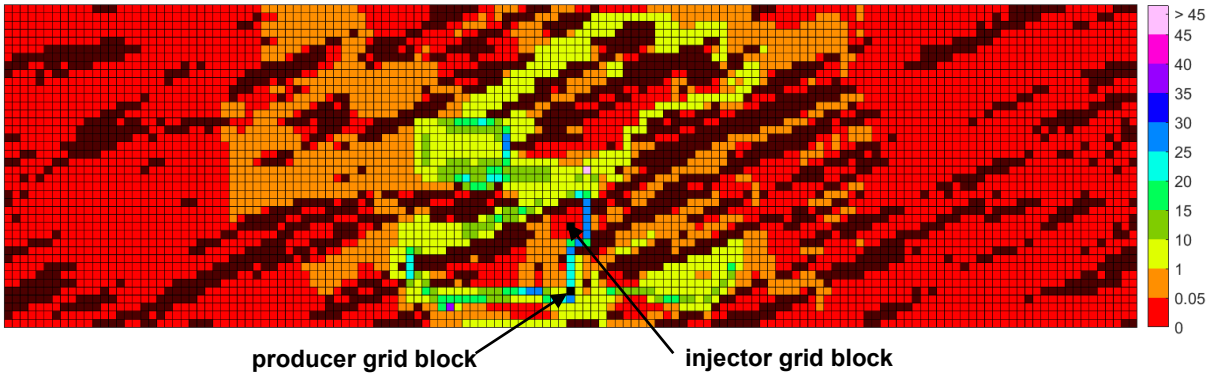

Figure K-22(m). Bitumen molar flow rate (kg-mole/day) map in n-C_6 SAGD for realization 34 for Q ≈ 31218 m^3

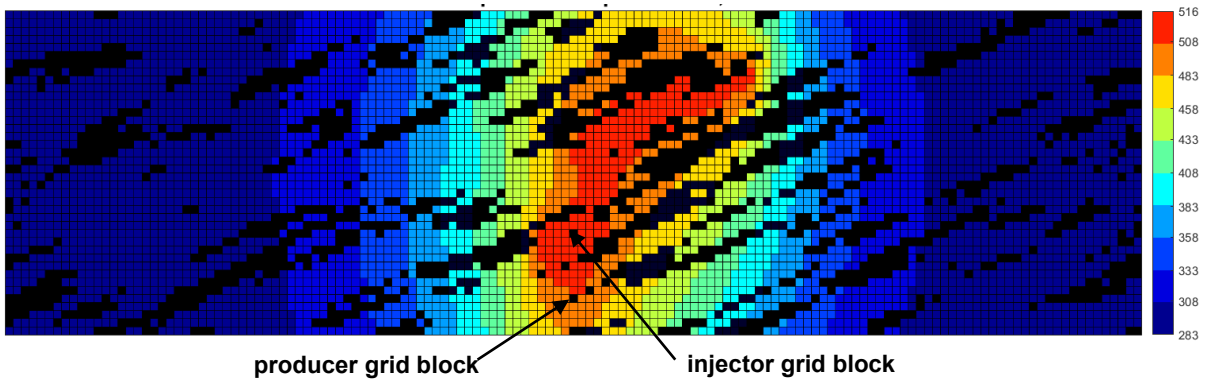

Figure K-22(n). Temperature (Kelvin) map in SAGD for realization 34 for Q ≈ 31218 m^3

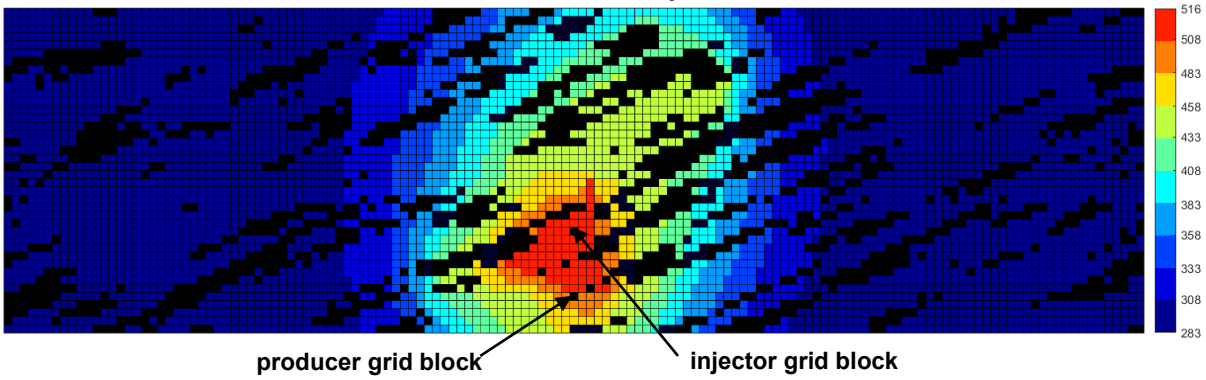

Figure K-22(o). Temperature (Kelvin) map in n-C_6 SAGD for realization 34 for Q ≈ 31218 m^3

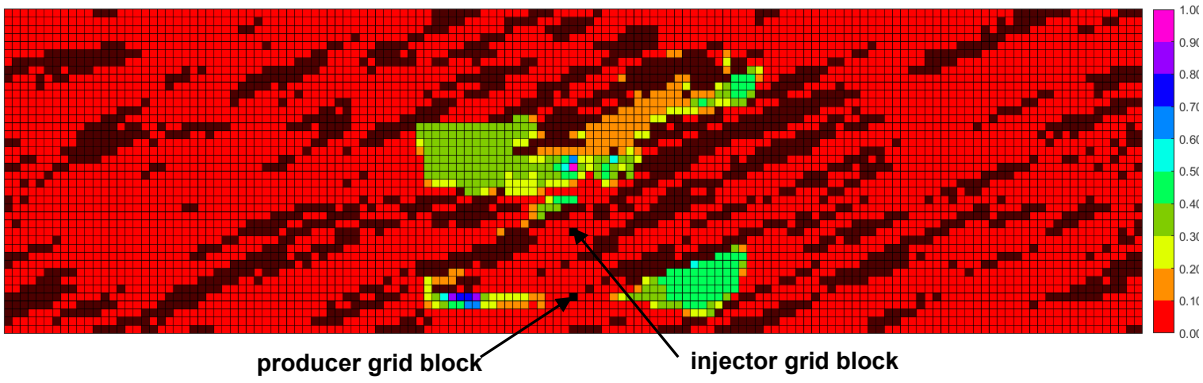

Figure K-22(p). $\beta_L x_{sL}$ map in n-C_6 SAGD for realization 34 for Q ≈ 31218 m^3

Figure K-22. Property maps for SAGD and n-C_6 SAGD for realization 34

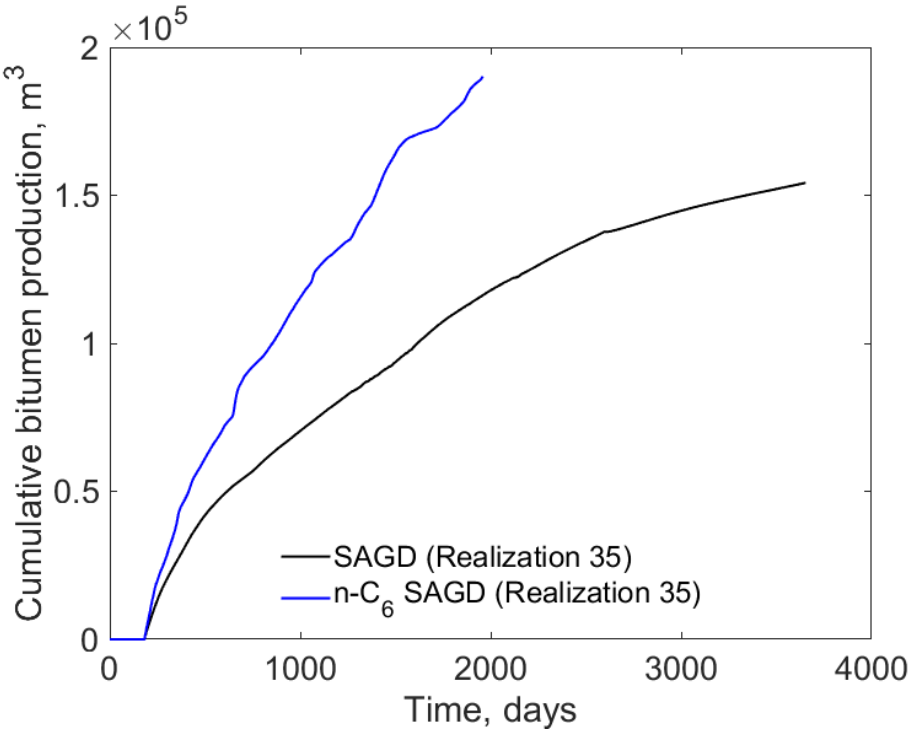

Figure K-23(a). Cumulative bitumen production histories for SAGD and n-C_6 SAGD for realization 35

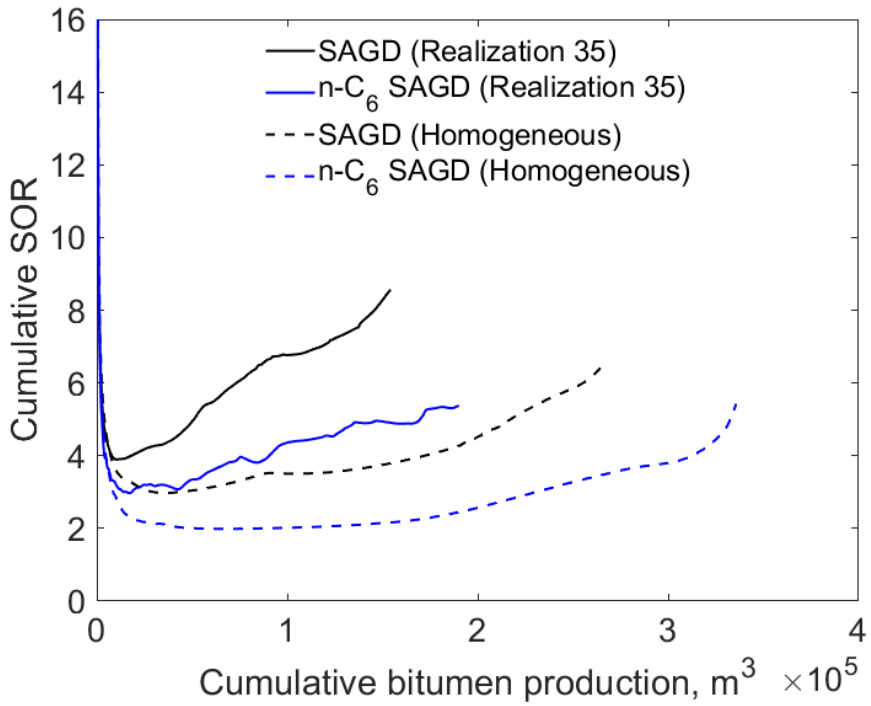

Figure K-23(b). Cumulative SOR for SAGD and n-C_6 SAGD for realization 35

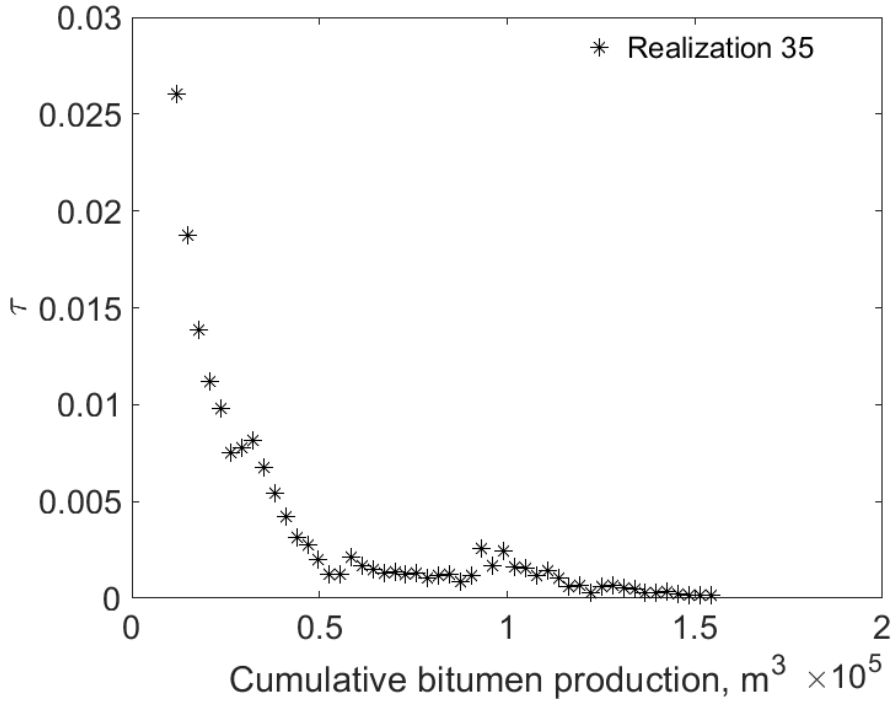

Figure K-23(c). τ for SAGD as a function of cumulative bitumen production for realization 35

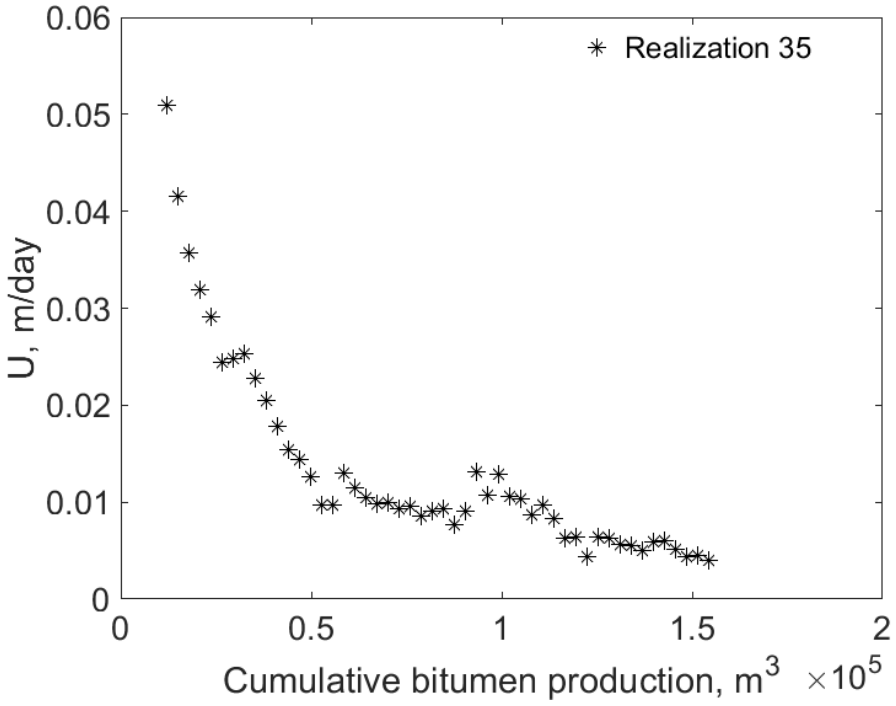

Figure K-23(d). U for SAGD as a function of cumulative bitumen production for realization 35

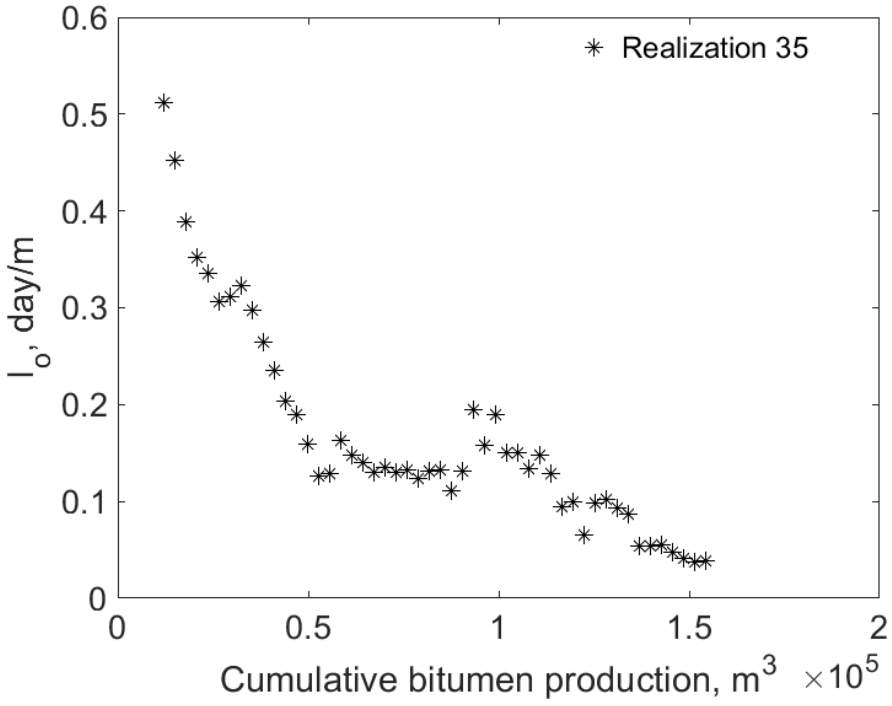

Figure K-23(e).I_o for SAGD as a function of cumulative bitumen production for realization 35

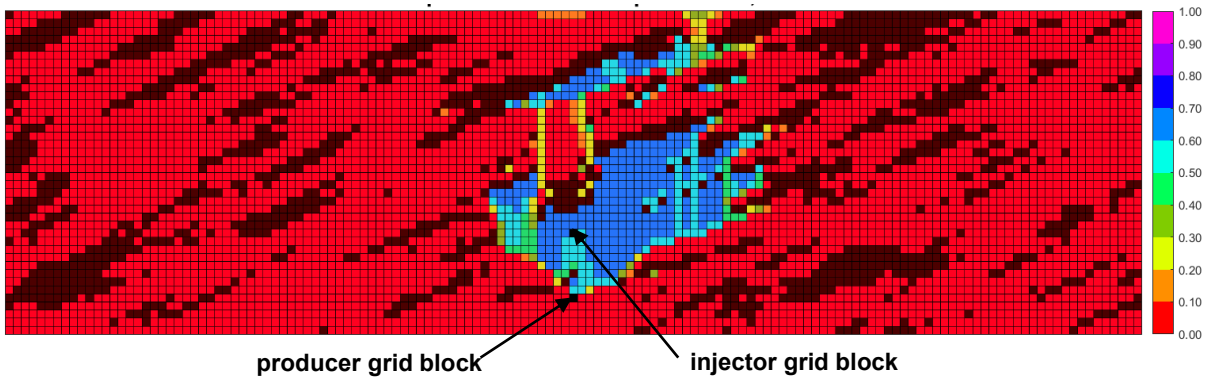

Figure K-23(f). Vapor-phase saturation map in SAGD for realization 35 for Q ≈ 31218 m^3

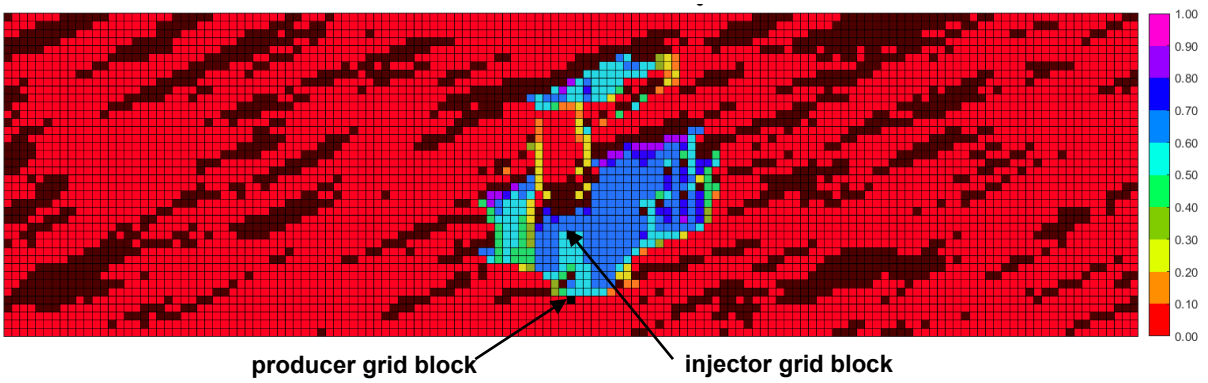

Figure K-23(g). Vapor-phase saturation map in n-C_6 SAGD for realization 35 for Q ≈ 31218 m^3

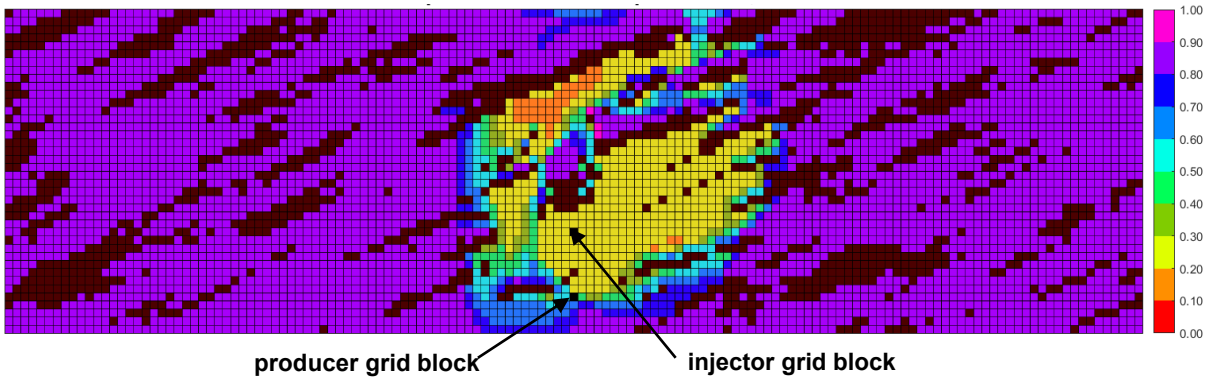

Figure K-23(h). Oleic-phase saturation map in SAGD for realization 35 for Q ≈ 31218 m^3

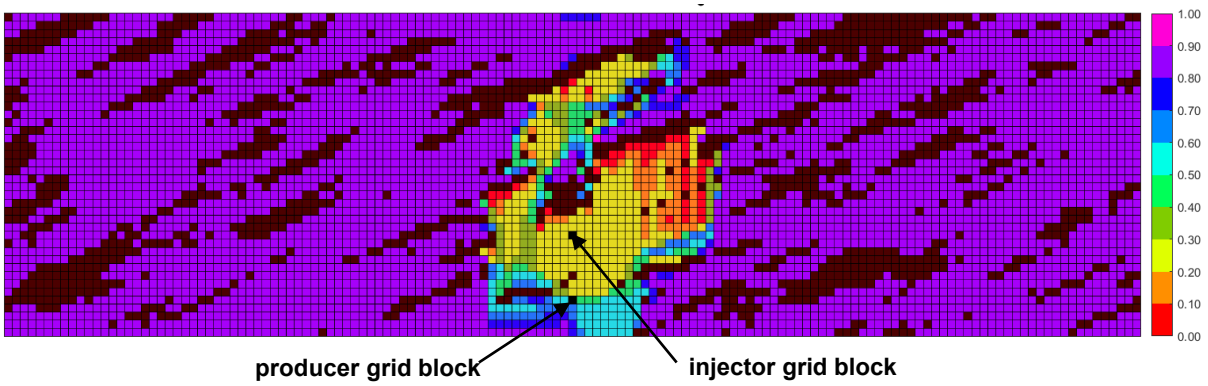

Figure K-23(i). Oleic-phase saturation map in n-C_6 SAGD for realization 35 for Q ≈ 31218 m^3

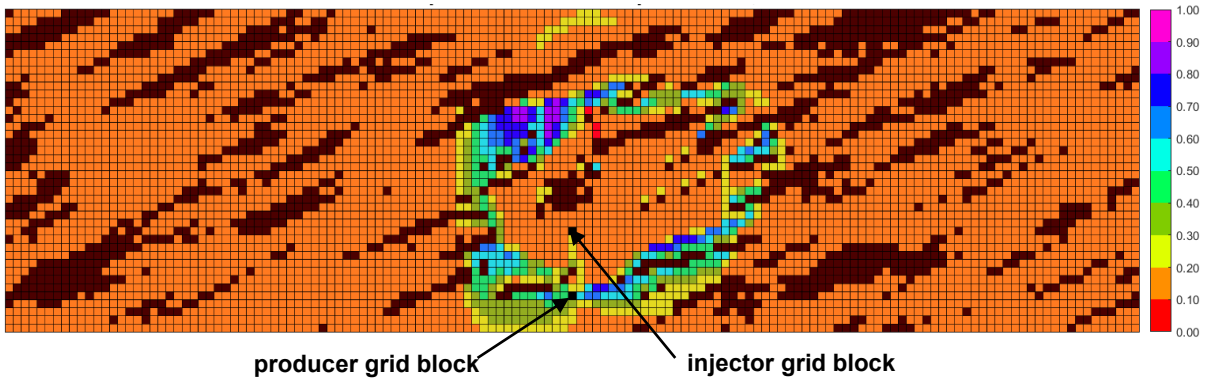

Figure K-23(j). Aqueous-phase saturation map in SAGD for realization 35 for Q ≈ 31218 m^3

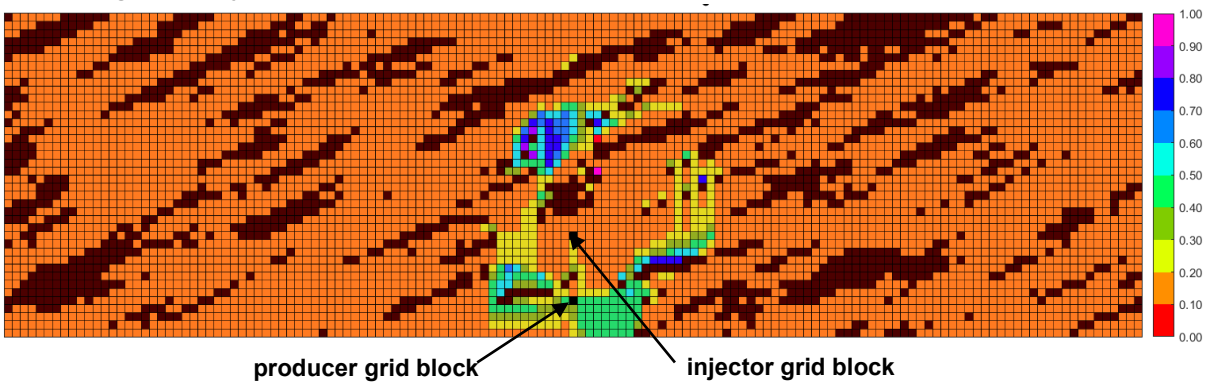

Figure K-23(k). Aqueous-phase saturation map in n-C_6 SAGD for realization 35 for Q ≈ 31218 m^3

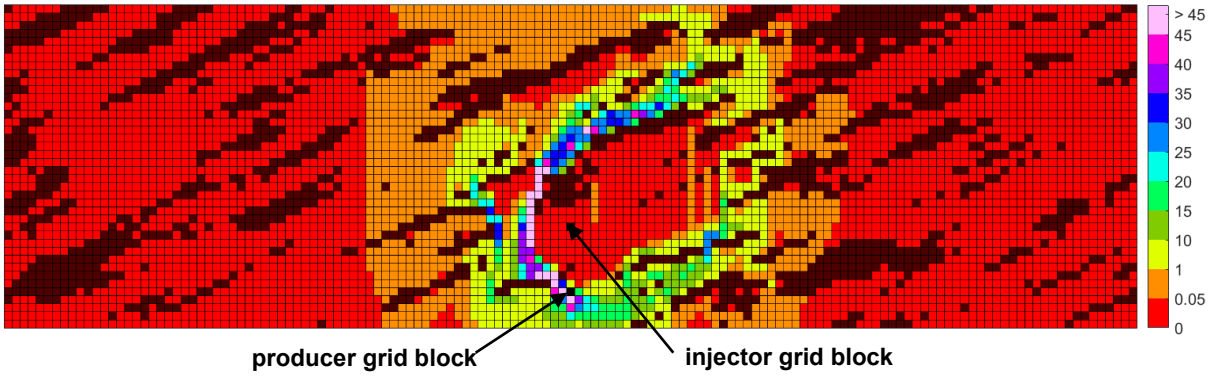

Figure K-23(l). Bitumen molar flow rate (kg-mole/day) map in SAGD for realization 35 for Q ≈ 31218 m^3

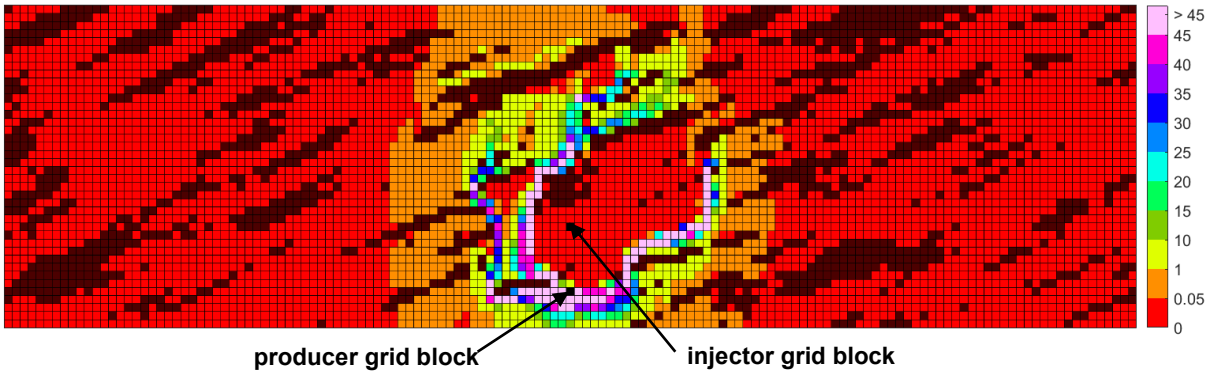

Figure K-23(m). Bitumen molar flow rate (kg-mole/day) map in n-C_6 SAGD for realization 35 for Q ≈ 31218 m^3

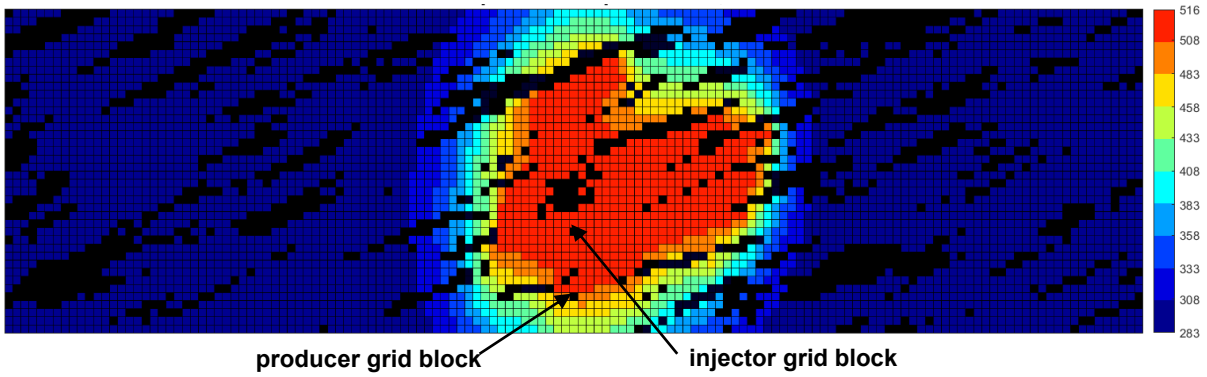

Figure K-23(n). Temperature (Kelvin) map in SAGD for realization 35 for Q ≈ 31218 m^3

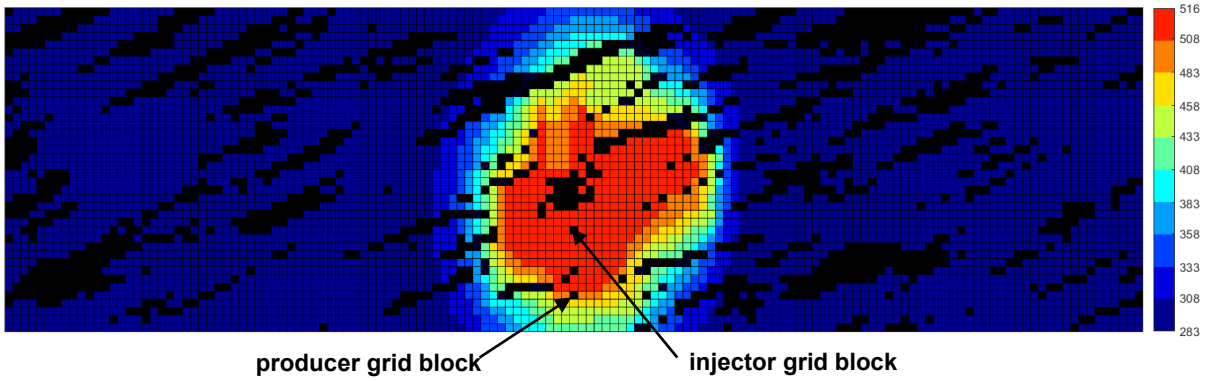

Figure K-23(o). Temperature (Kelvin) map in n-C_6 SAGD for realization 35 for Q ≈ 31218 m^3

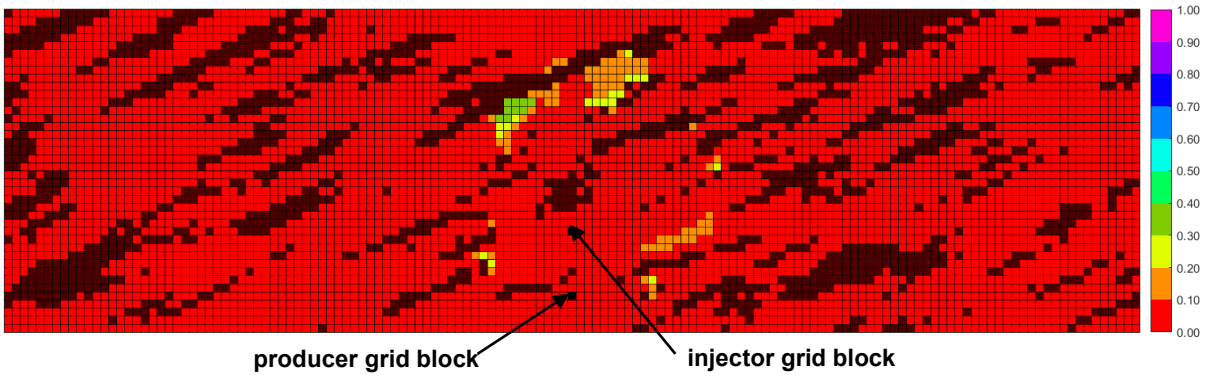

Figure K-23(p). $\beta_{LX_{sL}}$ map in n-C_6 SAGD for realization 35 for Q ≈ 31218 m^3

Figure K-23. Property maps for SAGD and n-C_6 SAGD for realization 35

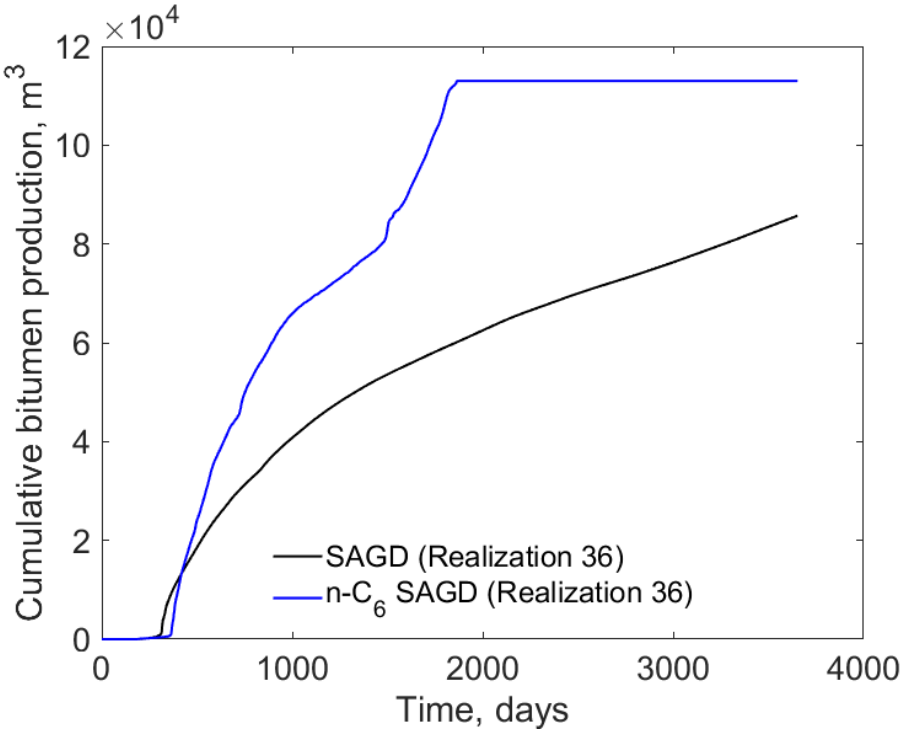

Figure K-24(a). Cumulative bitumen production histories for SAGD and n-C_6 SAGD for realization 36

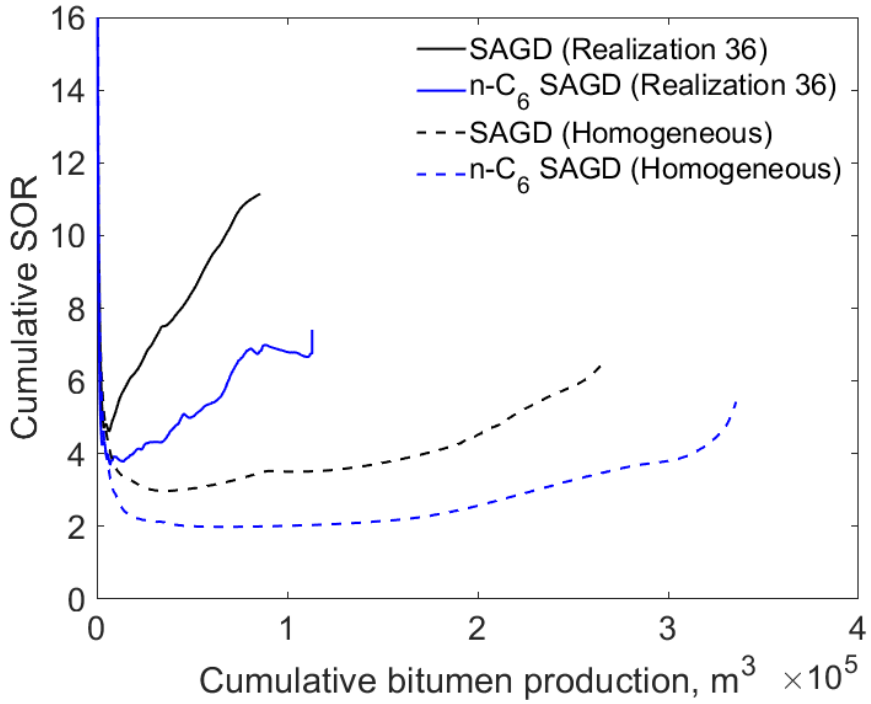

Figure K-24(b). Cumulative SOR for SAGD and n-C_6 SAGD for realization 36

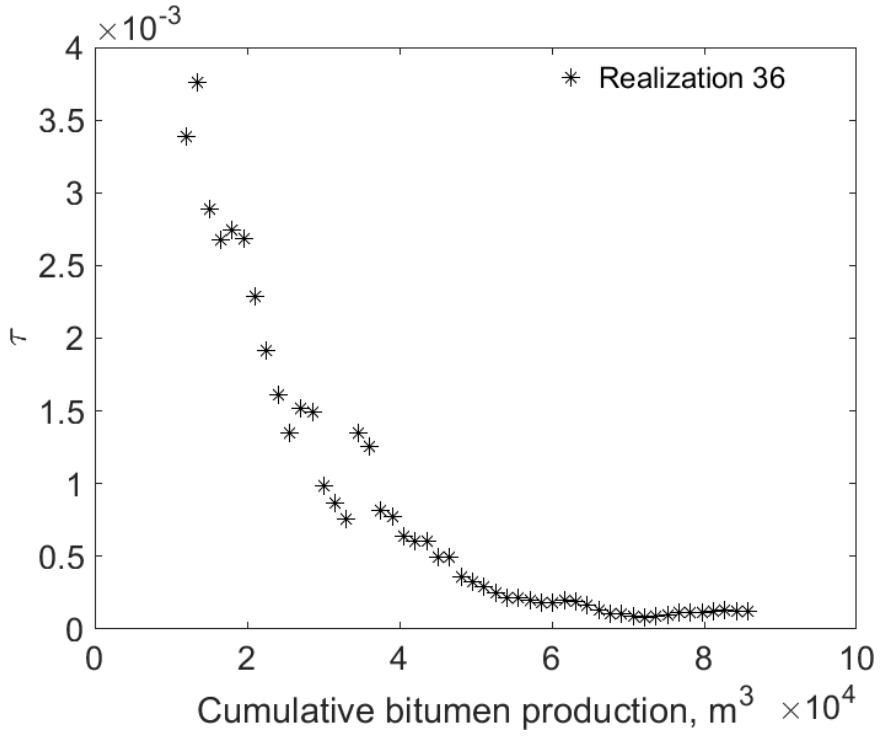

Figure K-24(c). τ for SAGD as a function of cumulative bitumen production for realization 36

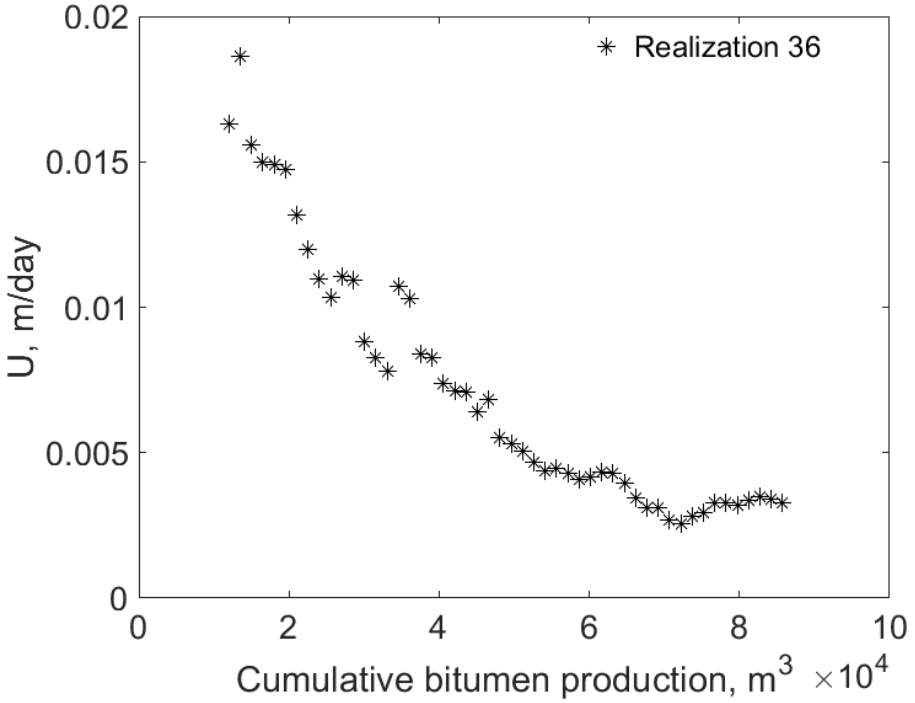

Figure K-24(d). U for SAGD as a function of cumulative bitumen production for realization 36

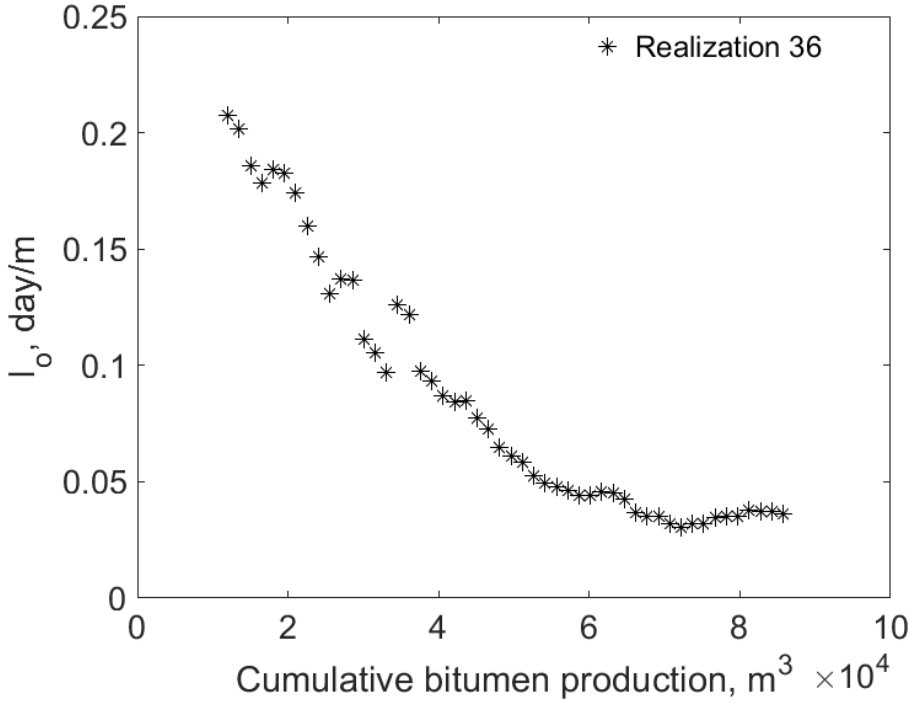

Figure K-24(e).I_o for SAGD as a function of cumulative bitumen production for realization 36

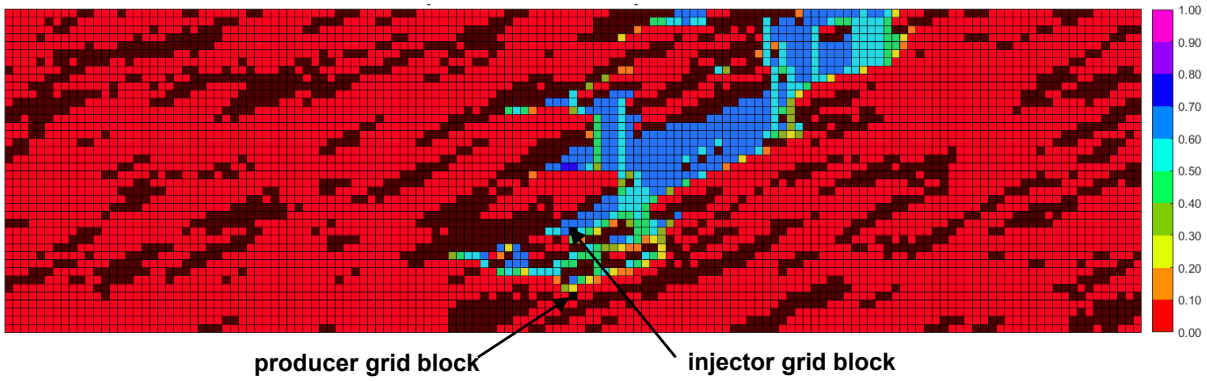

Figure K-24(f). Vapor-phase saturation map in SAGD for realization 36 for Q ≈ 31218 m^3

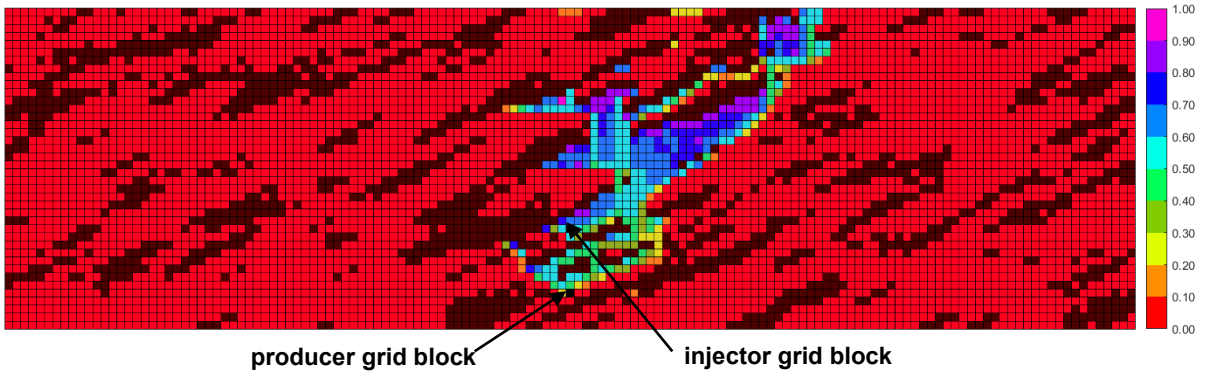

Figure K-24(g). Vapor-phase saturation map in n-C_6 SAGD for realization 36 for Q ≈ 31218 m^3

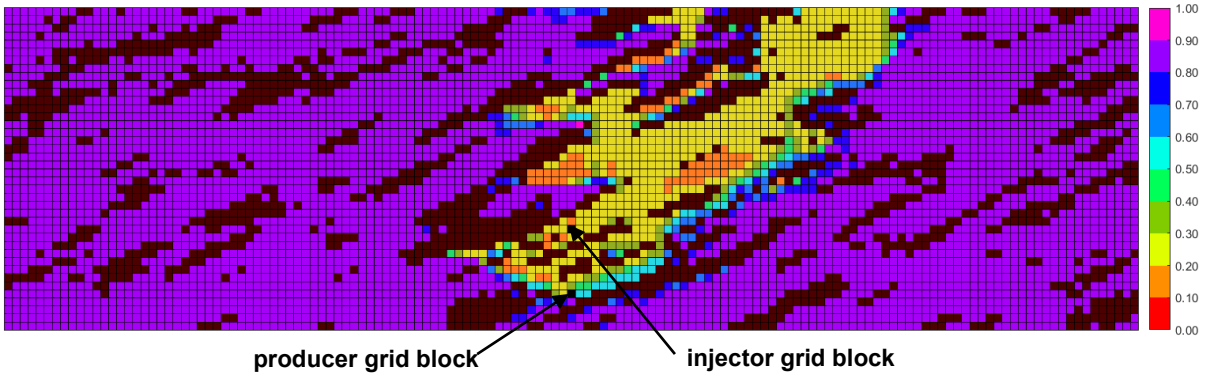

Figure K-24(h). Oleic-phase saturation map in SAGD for realization 36 for Q ≈ 31218 m^3

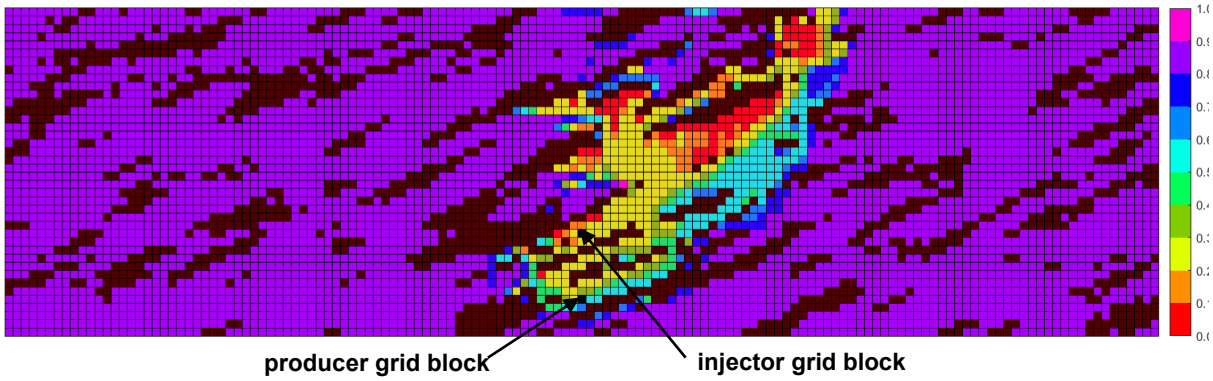

Figure K-24(i). Oleic-phase saturation map in n-C_6 SAGD for realization 36 for Q ≈ 31218 m^3

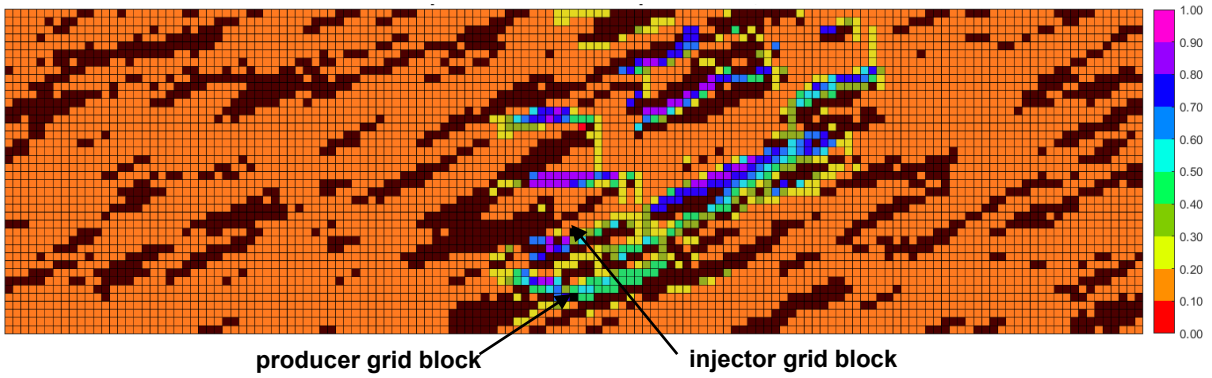

Figure K-24(j). Aqueous-phase saturation map in SAGD for realization 36 for Q ≈ 31218 m^3

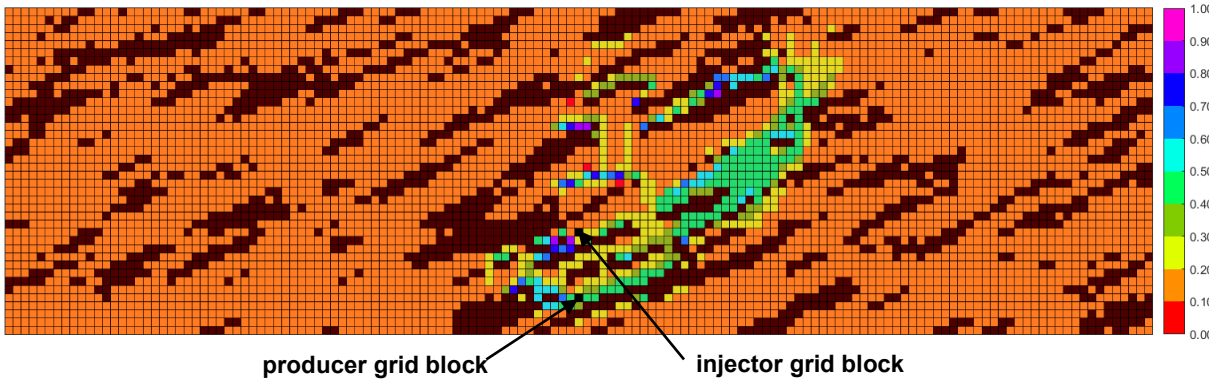

Figure K-24(k). Aqueous-phase saturation map in n-C_6 SAGD for realization 36 for Q ≈ 31218 m^3

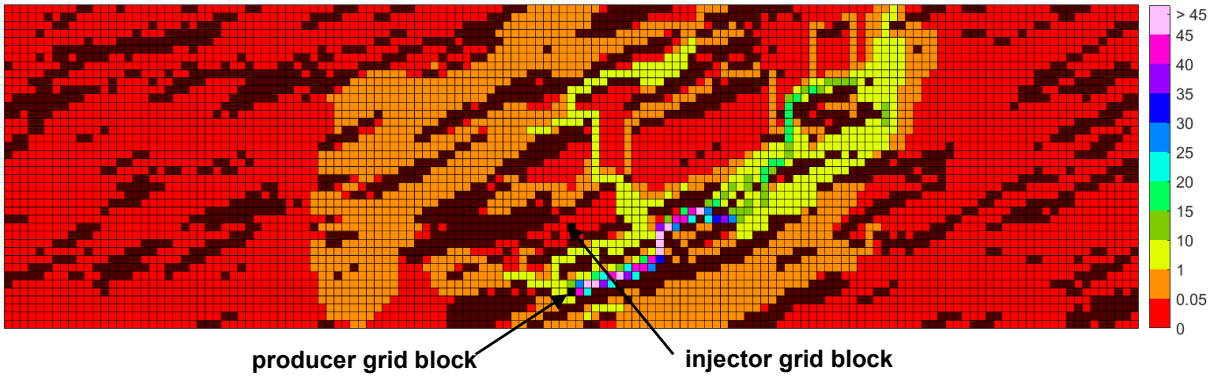

Figure K-24(l). Bitumen molar flow rate (kg-mole/day) map in SAGD for realization 36 for Q ≈ 31218 m³

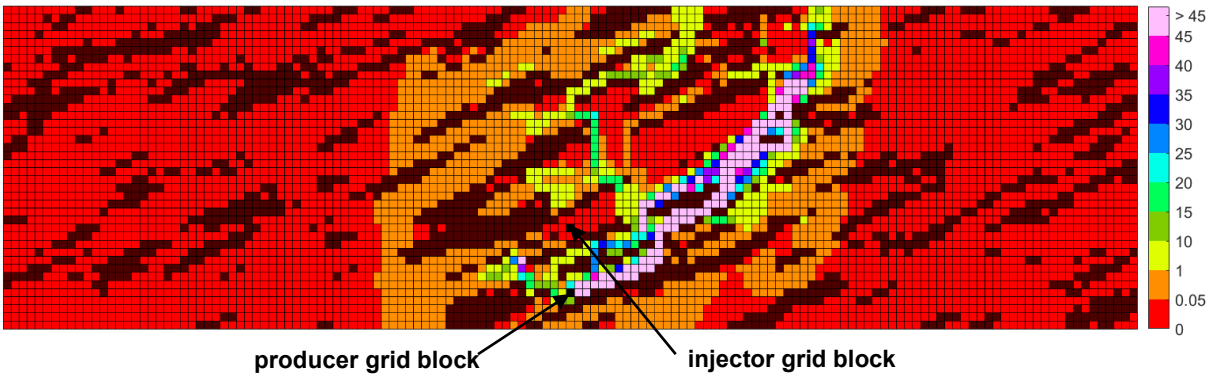

Figure K-24(m). Bitumen molar flow rate (kg-mole/day) map in n-C_6 SAGD for realization 36 for Q ≈ 31218 m³

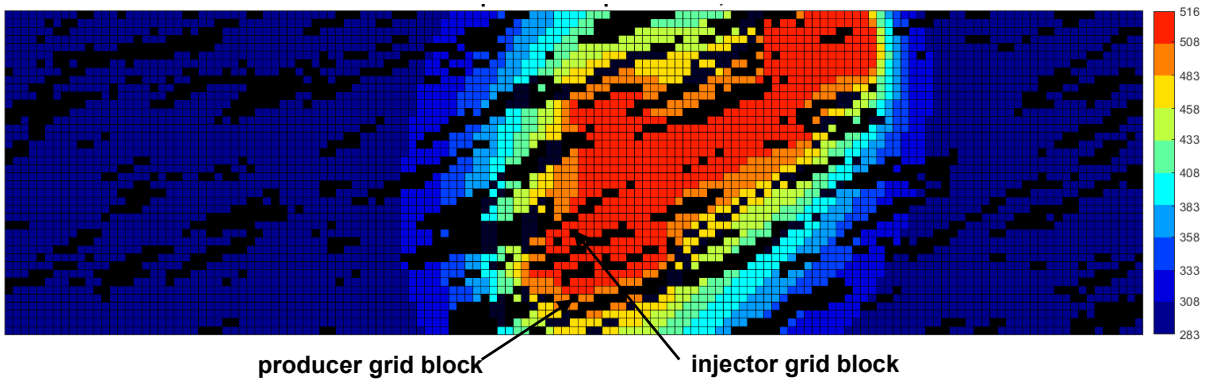

Figure K-24(n). Temperature (Kelvin) map in SAGD for realization 36 for Q ≈ 31218 m³

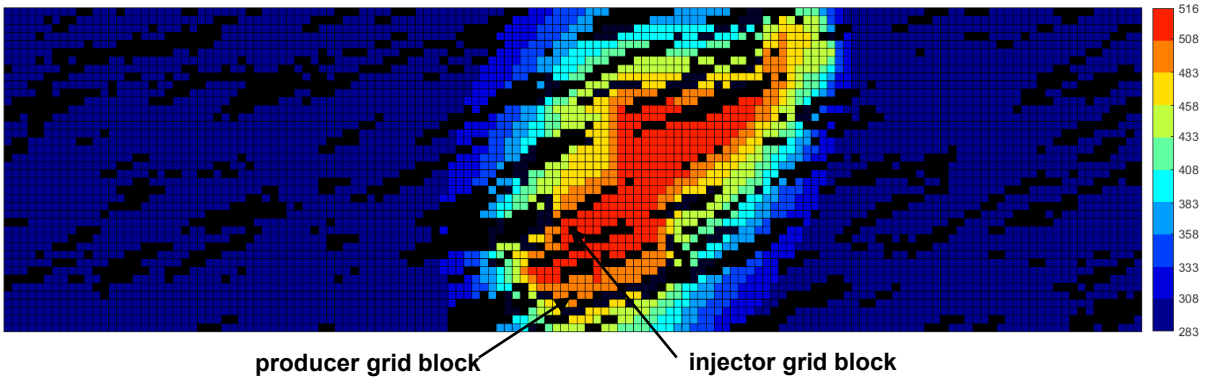

Figure K-24(o). Temperature (Kelvin) map in n-C_6 SAGD for realization 36 for Q ≈ 31218 m³

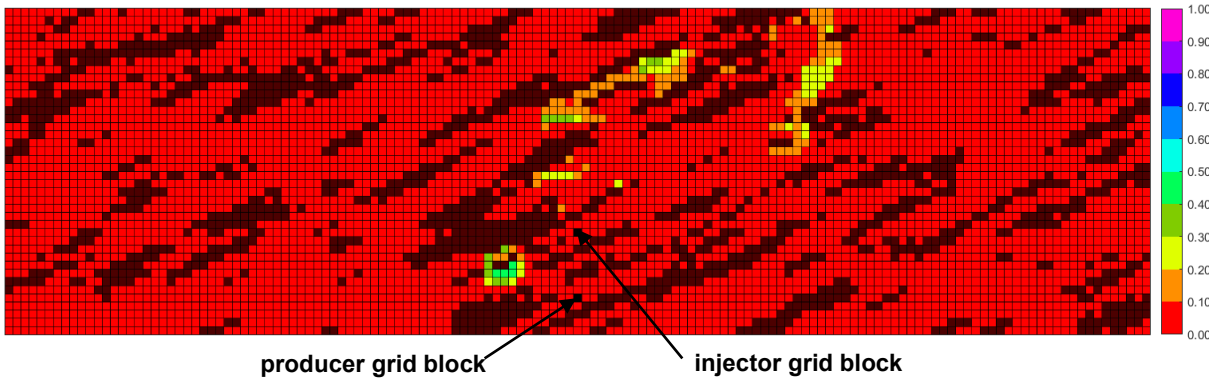

Figure K-24(p). $\beta_{Lx_{sL}}$ map in n-C_6 SAGD for realization 36 for Q ≈ 31218 m^3

Figure K-24. Property maps for SAGD and n-C_6 SAGD for realization 36

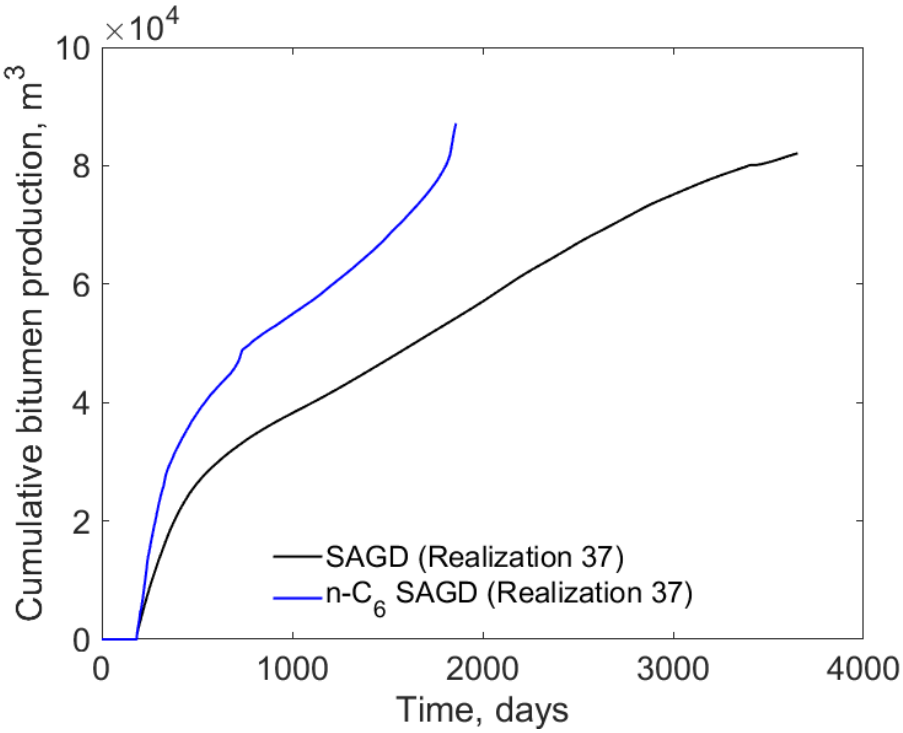

Figure K-25(a). Cumulative bitumen production histories for SAGD and n-C_6 SAGD for realization 37

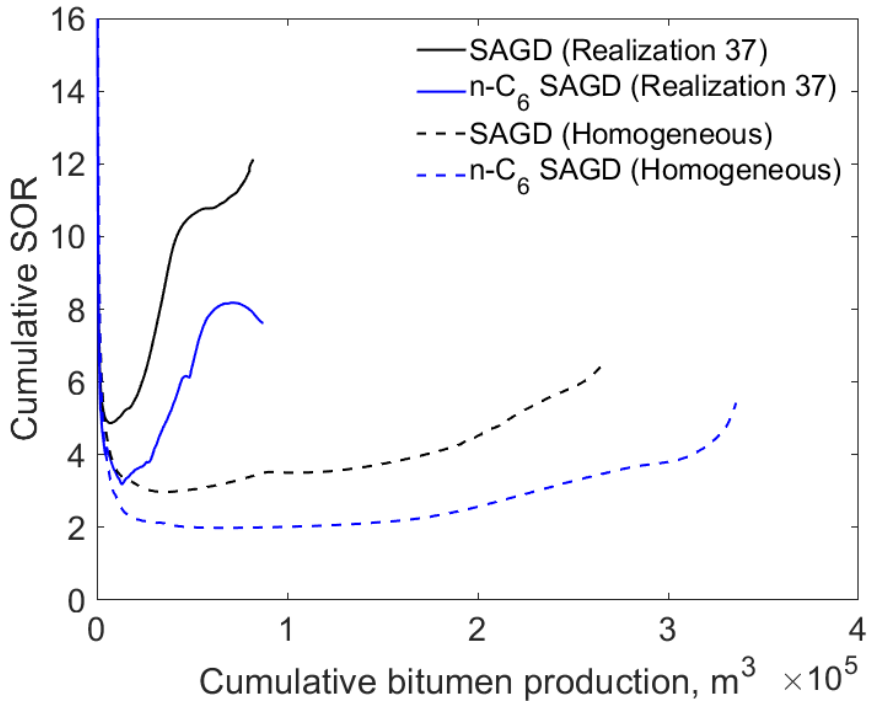

Figure K-25(b). Cumulative SOR for SAGD and n-C_6 SAGD for realization 37

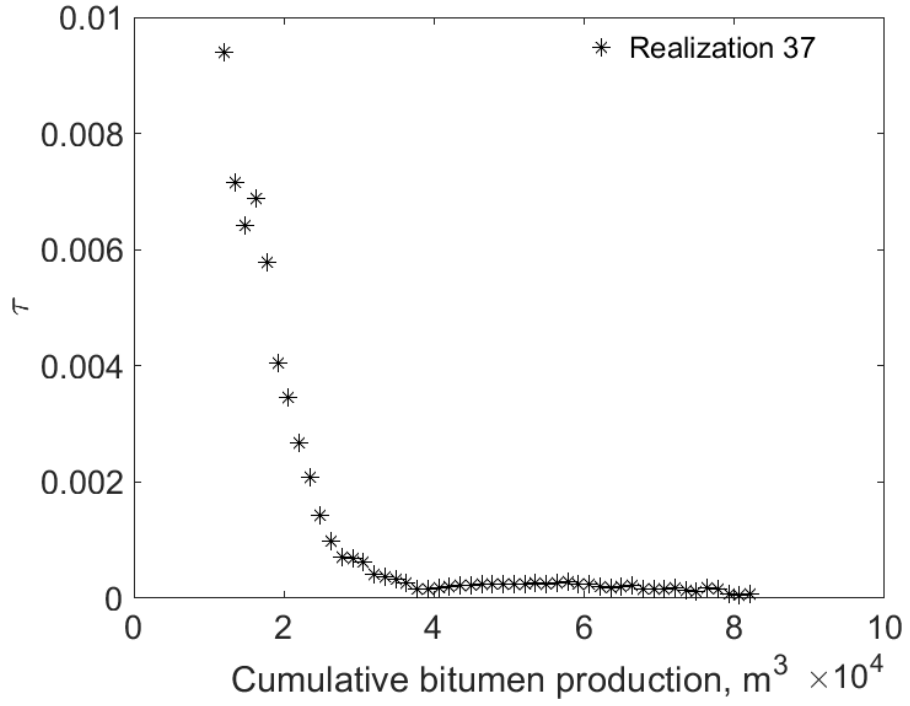

Figure K-25(c). τ for SAGD as a function of cumulative bitumen production for realization 37

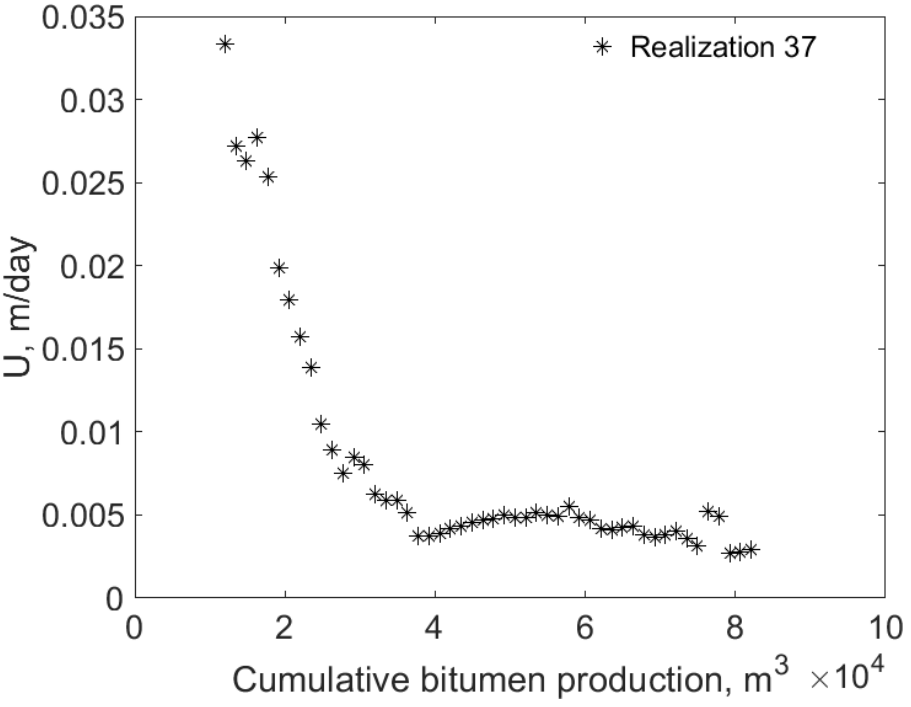

Figure K-25(d). U for SAGD as a function of cumulative bitumen production for realization 37

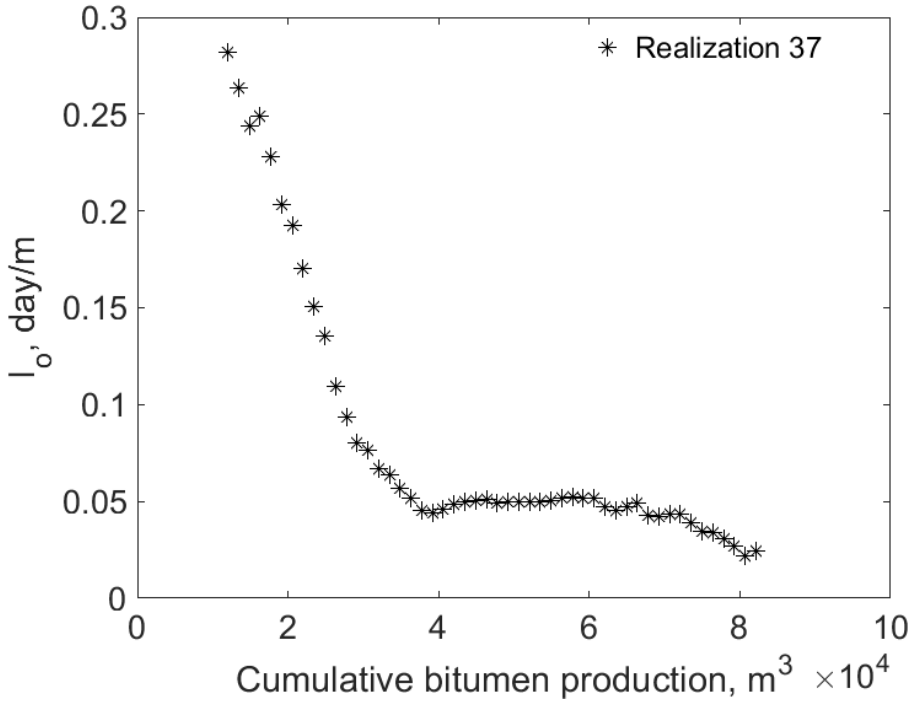

Figure K-25(e).I_o for SAGD as a function of cumulative bitumen production for realization 37

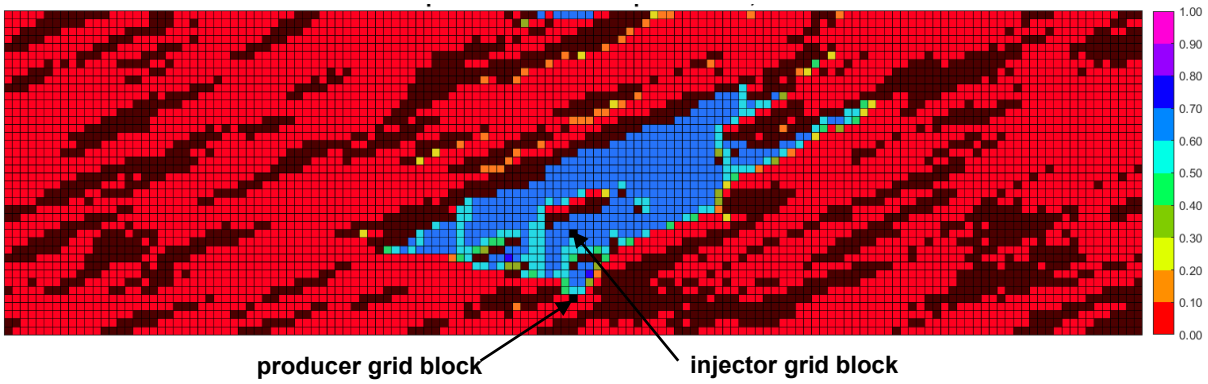

Figure K-25(f). Vapor-phase saturation map in SAGD for realization 37 for Q ≈ 31218 m^3

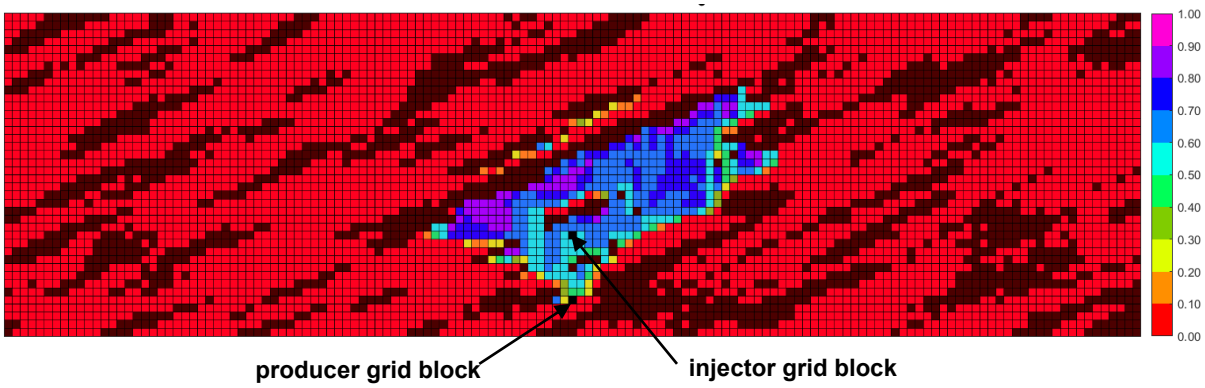

Figure K-25(g). Vapor-phase saturation map in n-C_6 SAGD for realization 37 for Q ≈ 31218 m^3

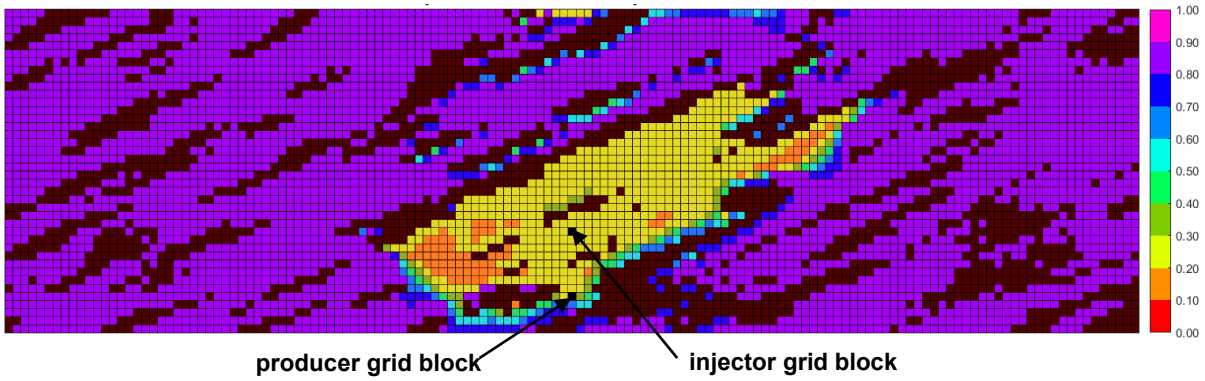

Figure K-25(h). Oleic-phase saturation map in SAGD for realization 37 for Q ≈ 31218 m^3

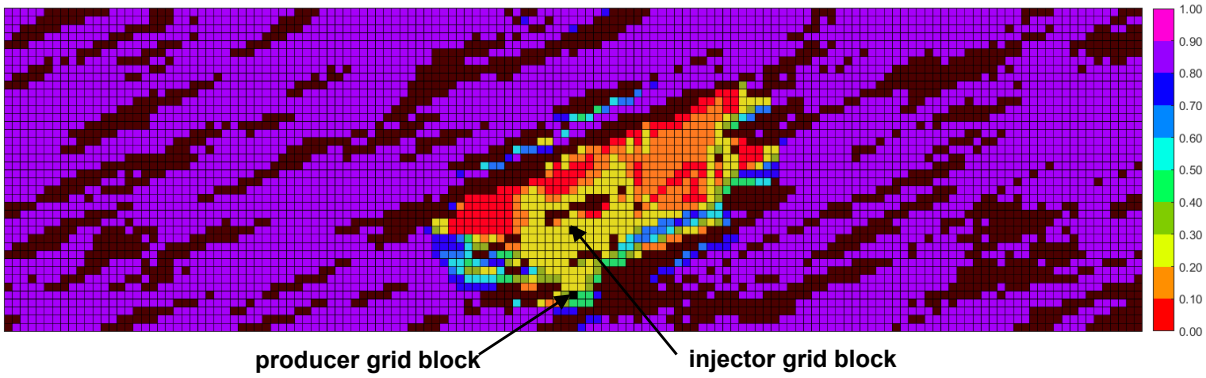

Figure K-25(i). Oleic-phase saturation map in n-C_6 SAGD for realization 37 for Q ≈ 31218 m^3

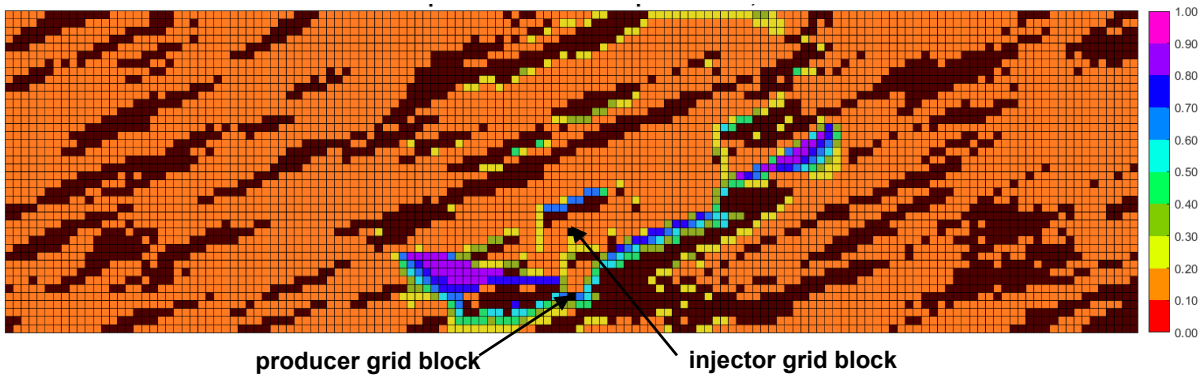

Figure K-25(j). Aqueous-phase saturation map in SAGD for realization 37 for Q ≈ 31218 m^3

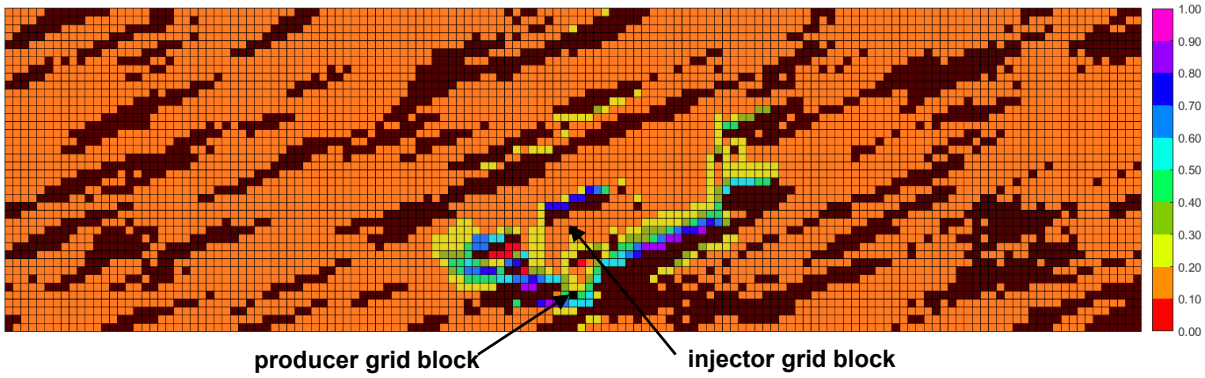

Figure K-25(k). Aqueous-phase saturation map in n-C_6 SAGD for realization 37 for Q ≈ 31218 m^3

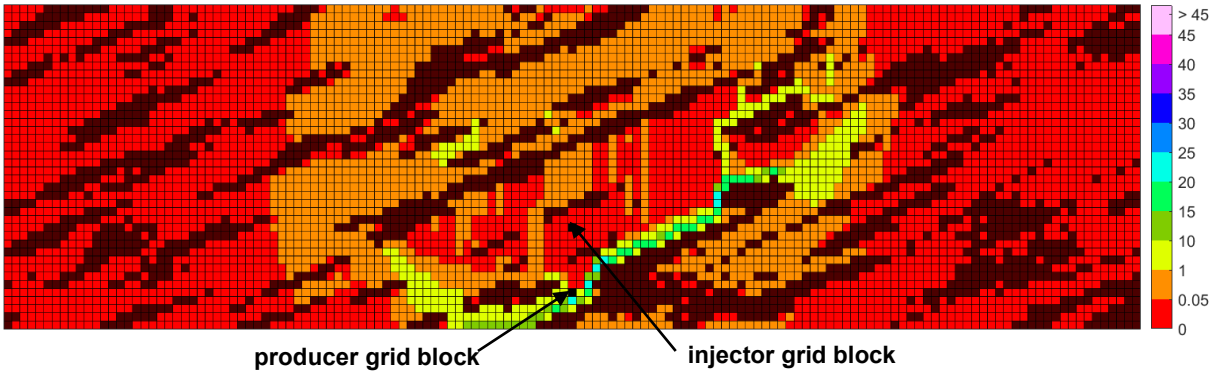

Figure K-25(l). Bitumen molar flow rate (kg-mole/day) map in SAGD for realization 37 for Q ≈ 31218 m^3

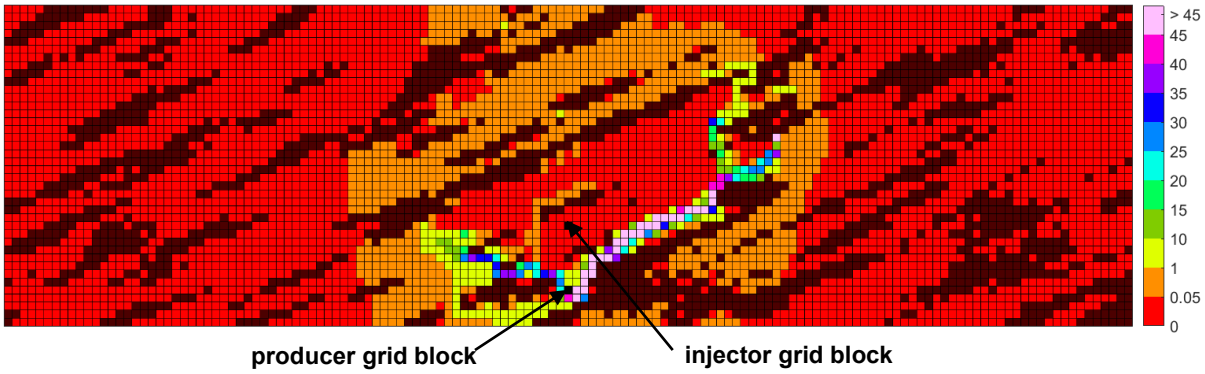

Figure K-25(m). Bitumen molar flow rate (kg-mole/day) map in n-C_6 SAGD for realization 37 for Q ≈ 31218 m^3

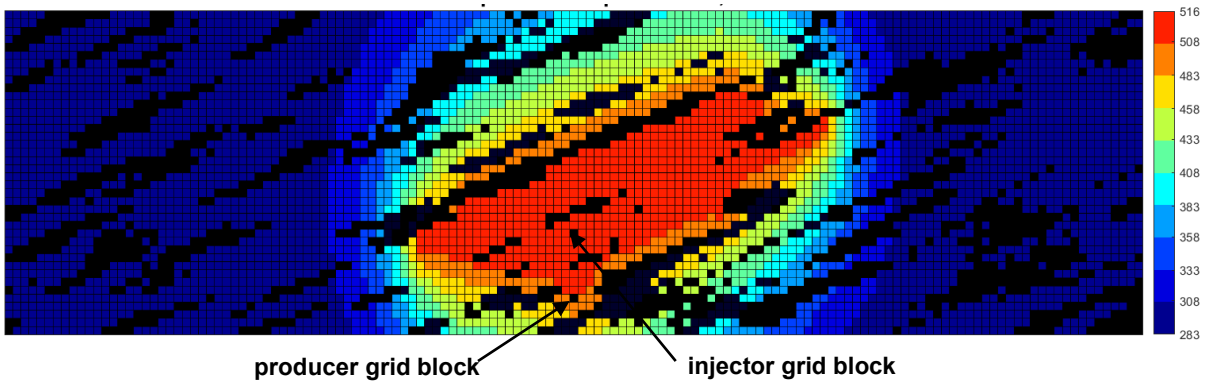

Figure K-25(n). Temperature (Kelvin) map in SAGD for realization 37 for Q ≈ 31218 m^3

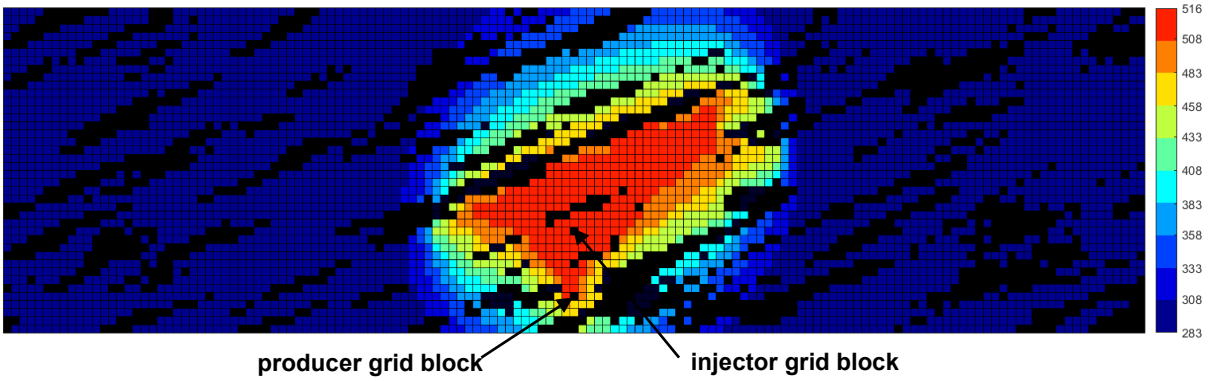

Figure K-25(o). Temperature (Kelvin) map in n-C_6 SAGD for realization 37 for Q ≈ 31218 m^3

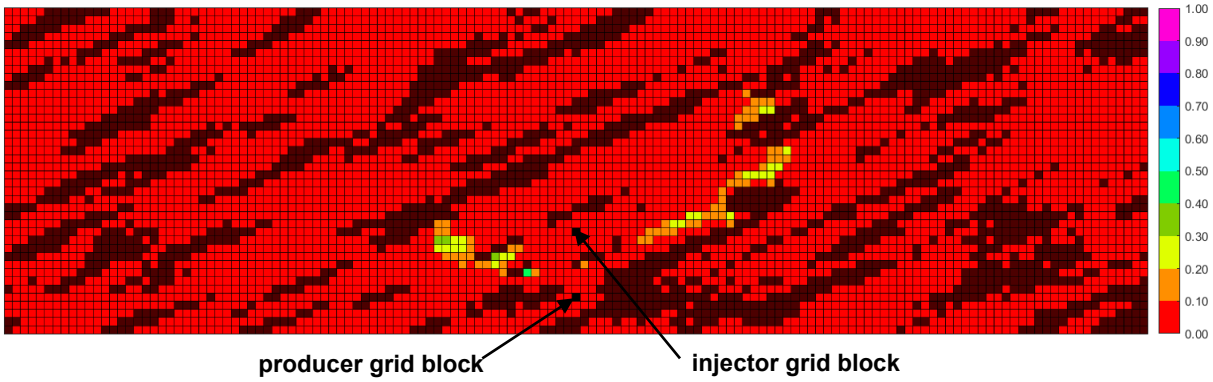

Figure K-25(p). $\beta_L x_{sL}$ map in n-C_6 SAGD for realization 37 for Q ≈ 31218 m^3

Figure K-25. Property maps for SAGD and n-C_6 SAGD for realization 37

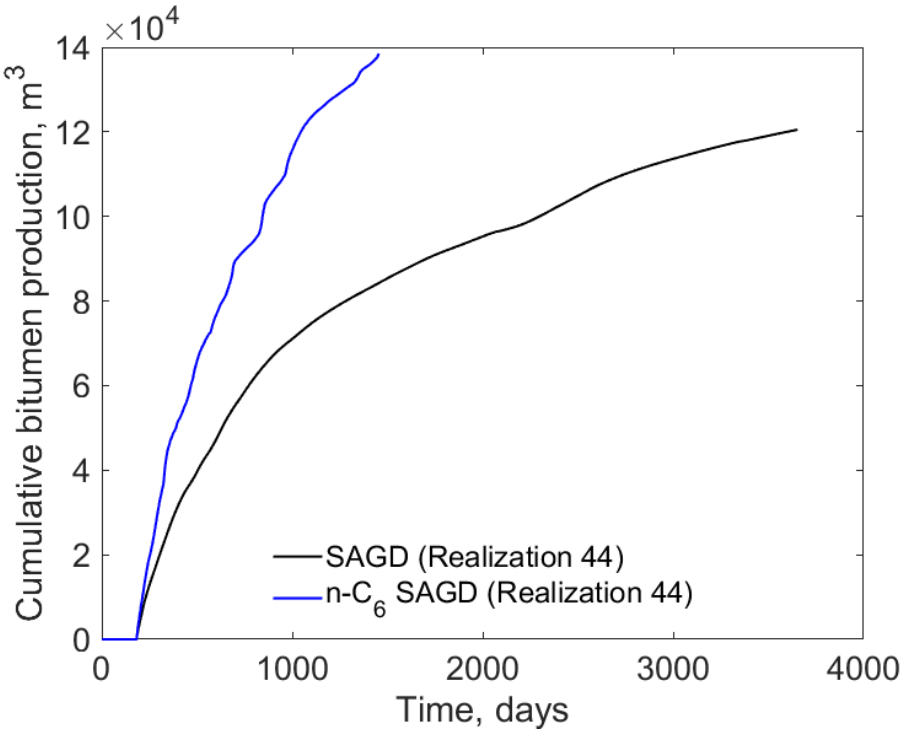

Figure K-26(a). Cumulative bitumen production histories for SAGD and n-C_6 SAGD for realization 44

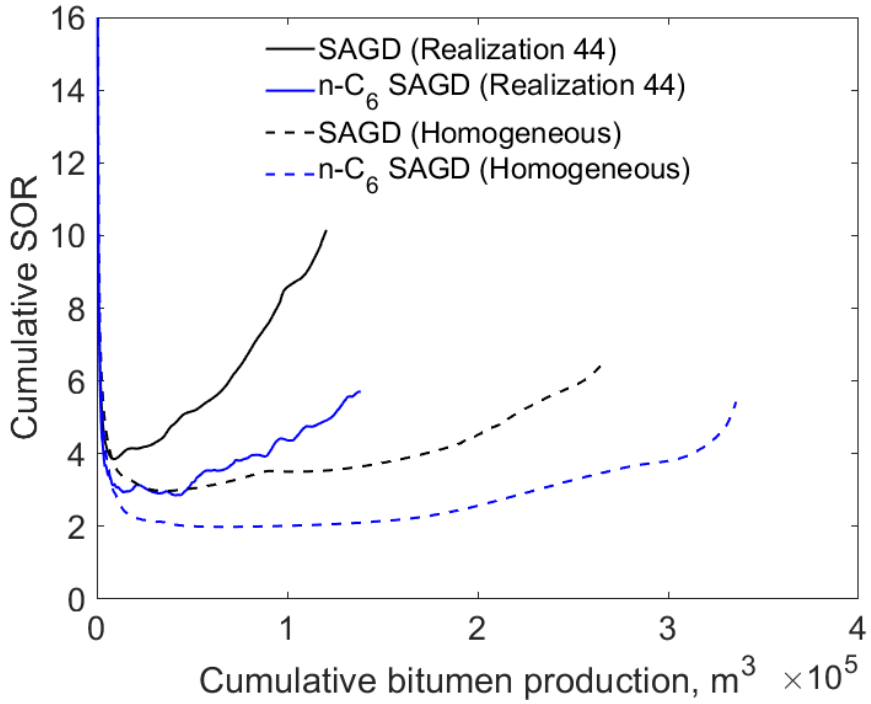

Figure K-26(b). Cumulative SOR for SAGD and n-C_6 SAGD for realization 44

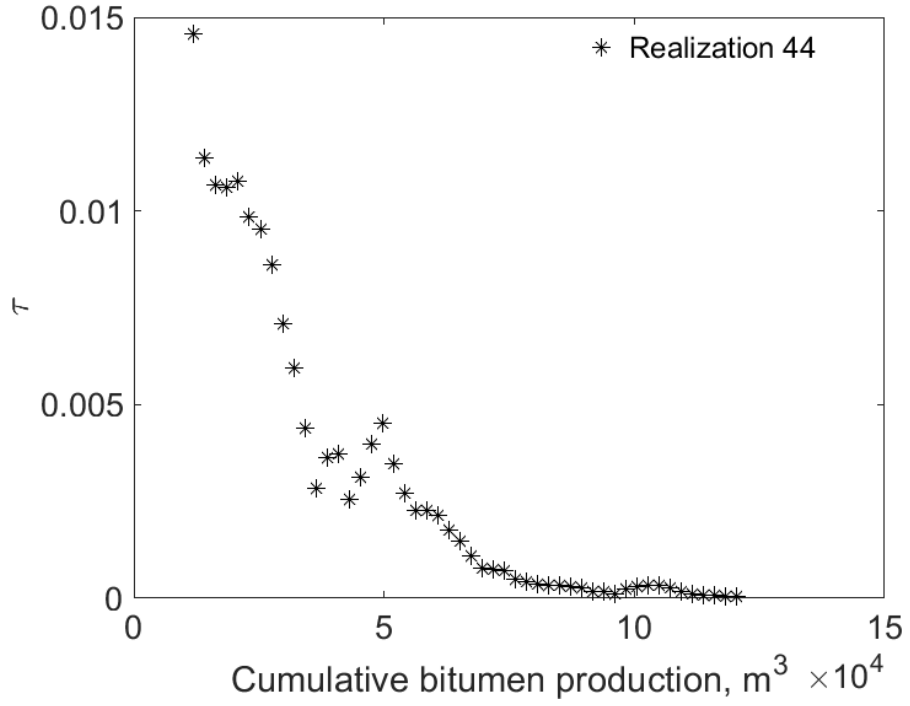

Figure K-26(c). τ for SAGD as a function of cumulative bitumen production for realization 44

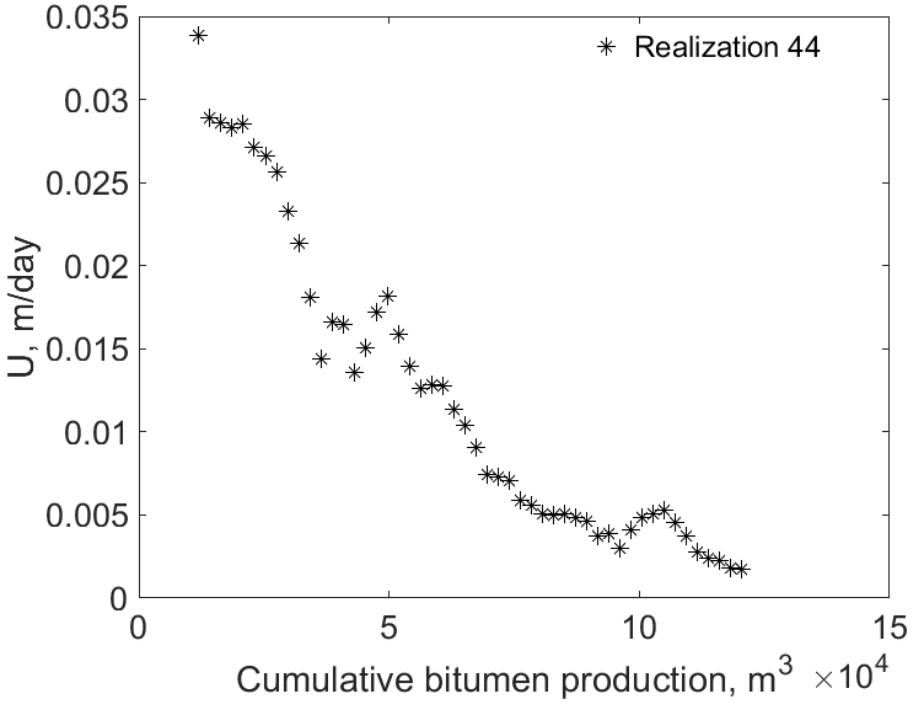

Figure K-26(d). U for SAGD as a function of cumulative bitumen production for realization 44

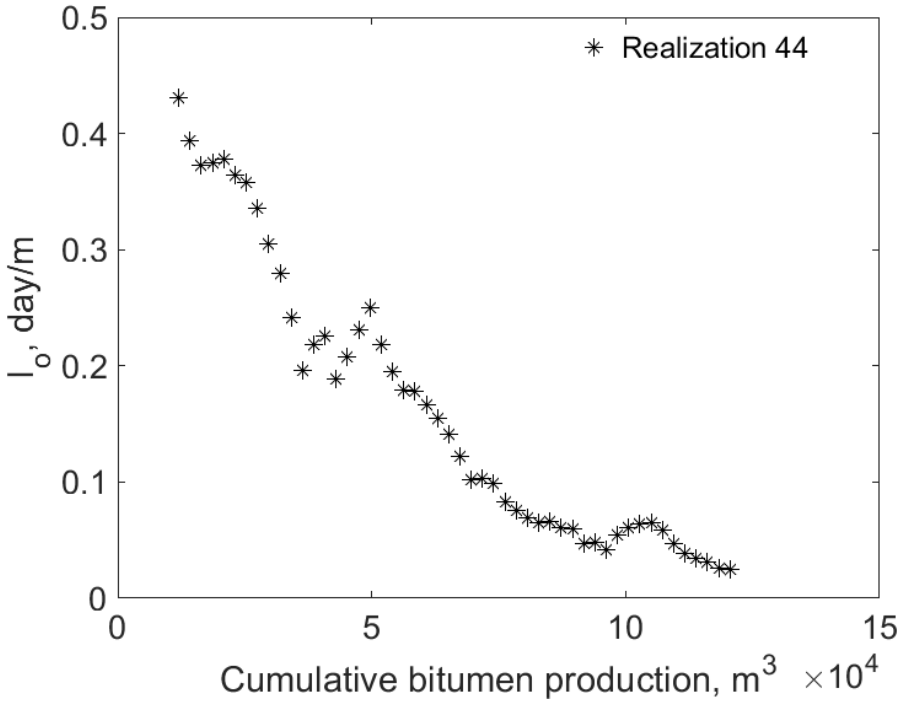

Figure K-26(e).I_o for SAGD as a function of cumulative bitumen production for realization 44

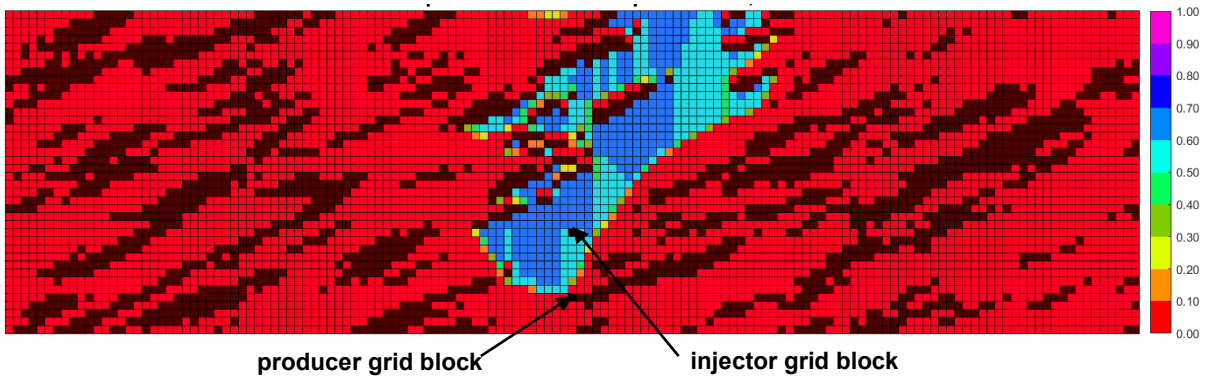

Figure K-26(f). Vapor-phase saturation map in SAGD for realization 44 for Q ≈ 31218 m^3

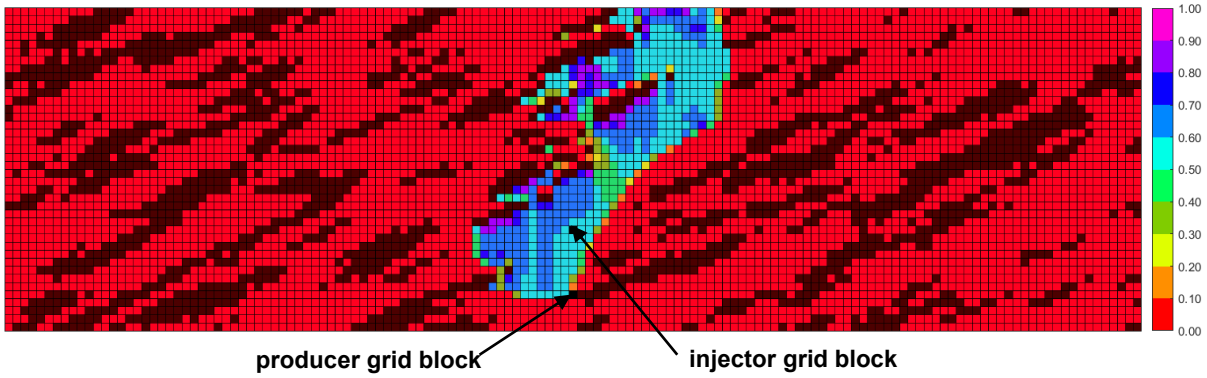

Figure K-26(g). Vapor-phase saturation map in n-C_6 SAGD for realization 44 for Q ≈ 31218 m^3

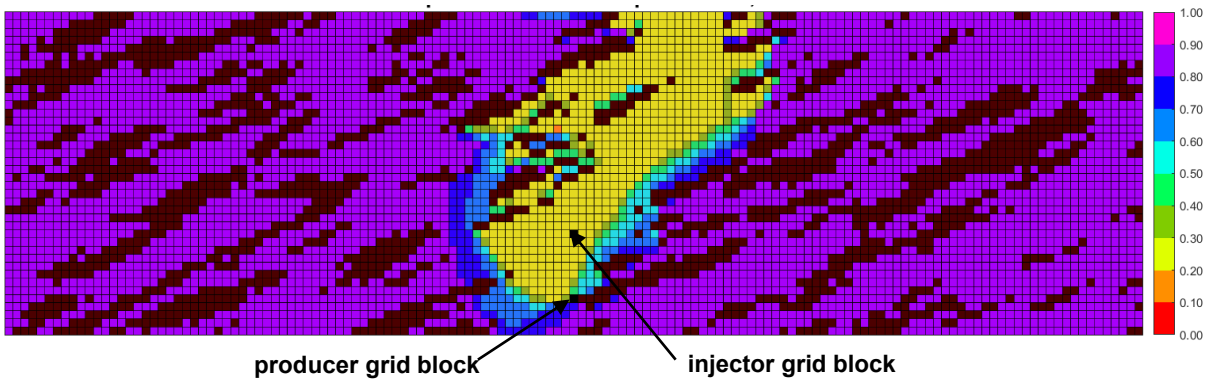

Figure K-26(h). Oleic-phase saturation map in SAGD for realization 44 for Q ≈ 31218 m^3

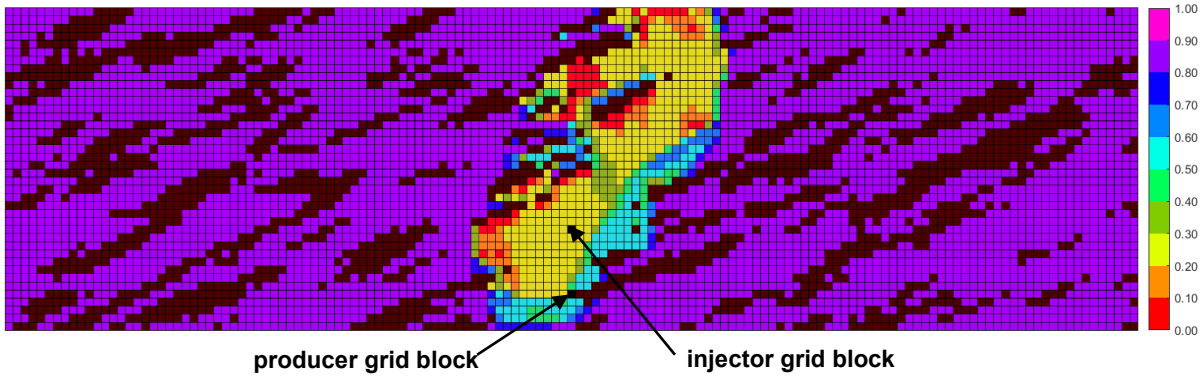

Figure K-26(i). Oleic-phase saturation map in n-C_6 SAGD for realization 44 for Q ≈ 31218 m^3

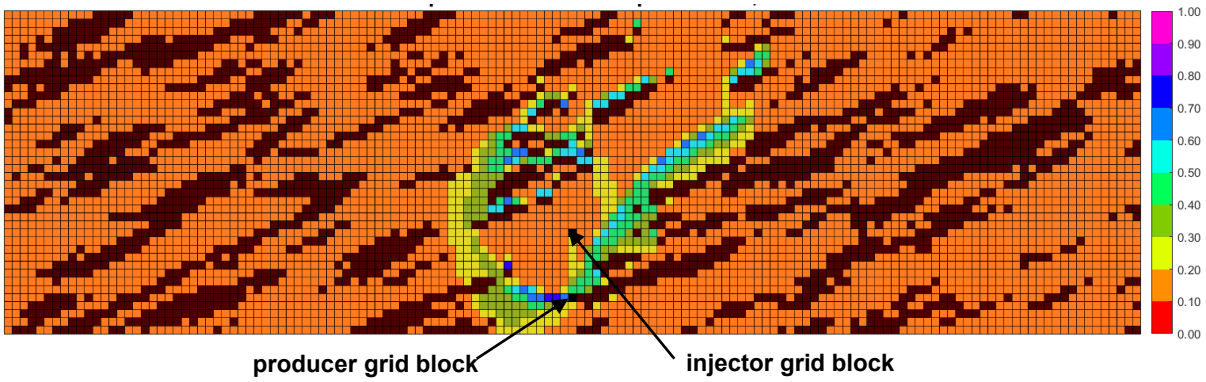

Figure K-26(j). Aqueous-phase saturation map in SAGD for realization 44 for Q ≈ 31218 m^3

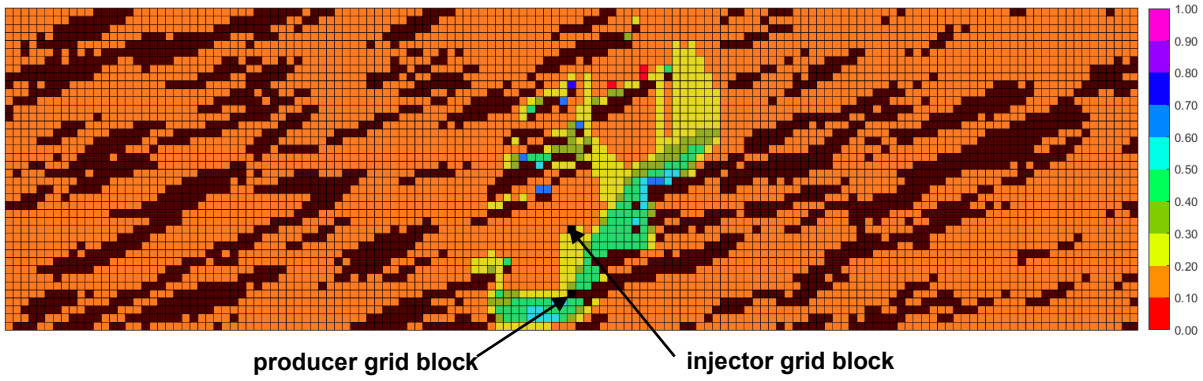

Figure K-26(k). Aqueous-phase saturation map in n-C_6 SAGD for realization 44 for Q ≈ 31218 m^3

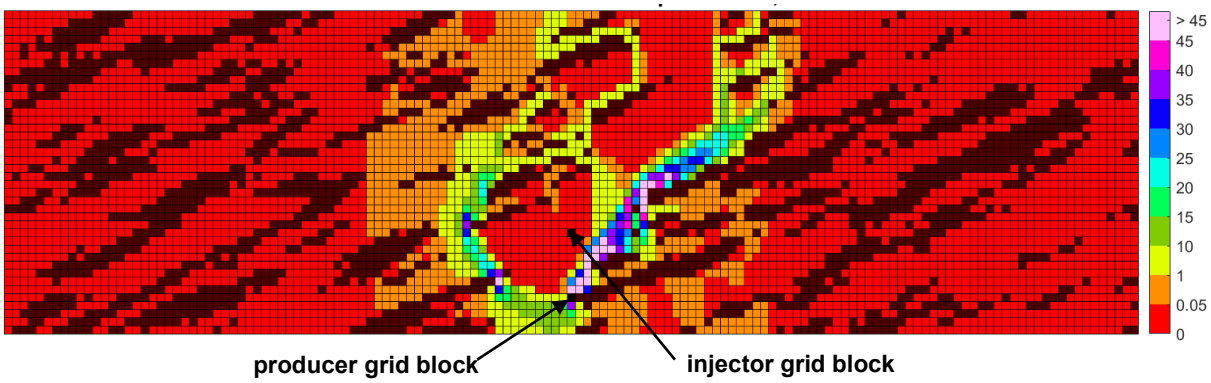

Figure K-26(l). Bitumen molar flow rate (kg-mole/day) map in SAGD for realization 44 for Q ≈ 31218 m^3

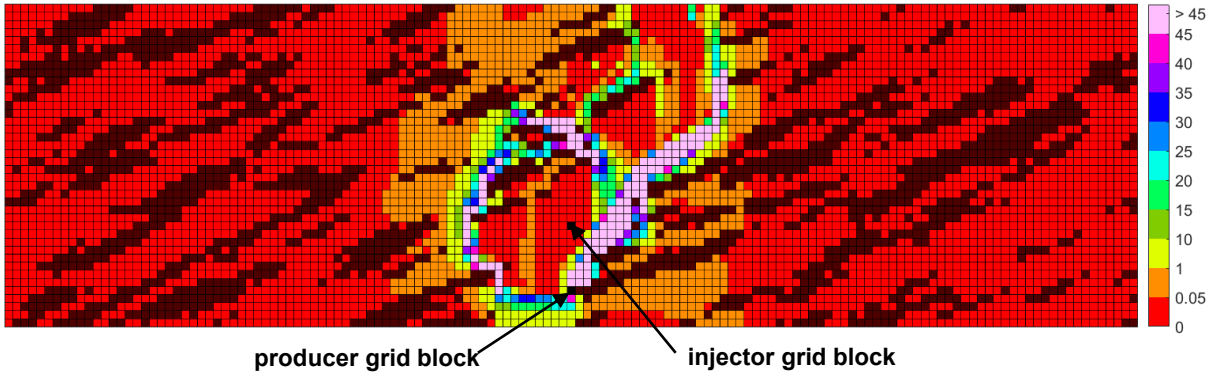

Figure K-26(m). Bitumen molar flow rate (kg-mole/day) map in n-C_6 SAGD for realization 44 for Q ≈ 31218 m^3

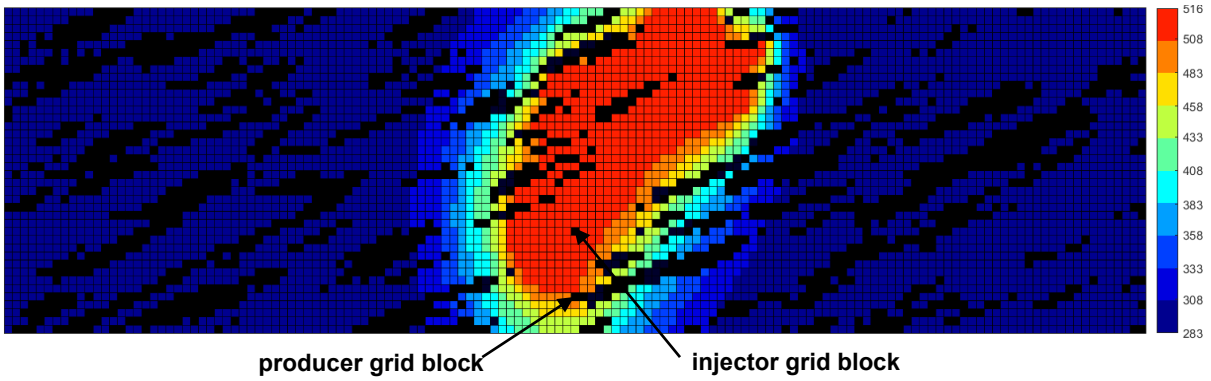

Figure K-26(n). Temperature (Kelvin) map in SAGD for realization 44 for Q ≈ 31218 m^3

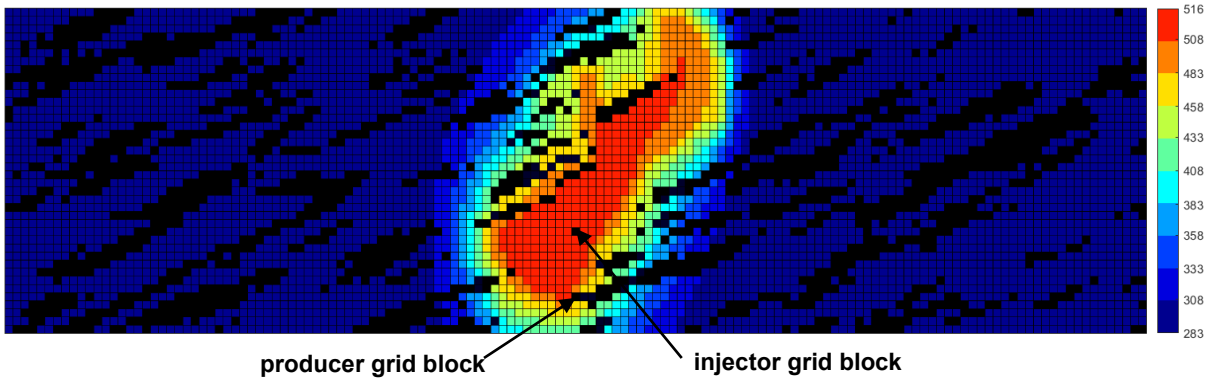

Figure K-26(o). Temperature (Kelvin) map in n-C_6 SAGD for realization 44 for Q ≈ 31218 m^3

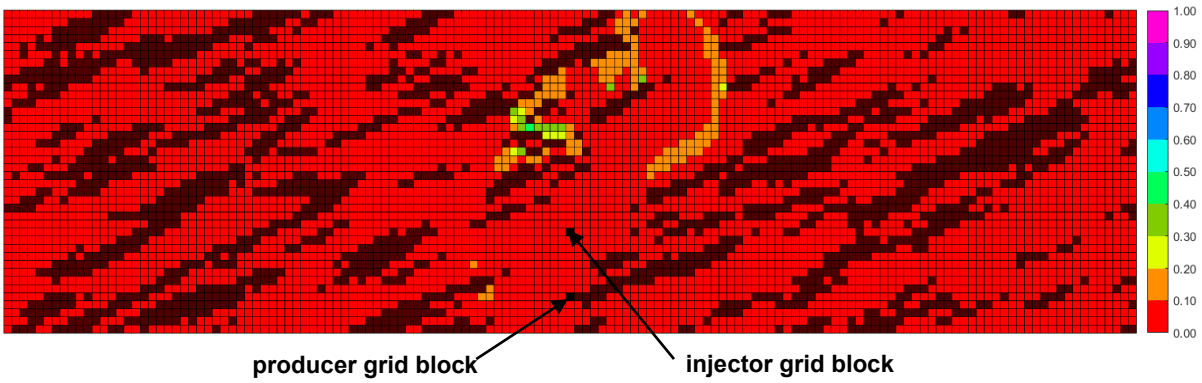

Figure K-26(p). $\beta_L x_{sL}$ map in n-C_6 SAGD for realization 44 for Q ≈ 31218 m^3

Figure K-26. Property maps for SAGD and n-C_6 SAGD for realization 44

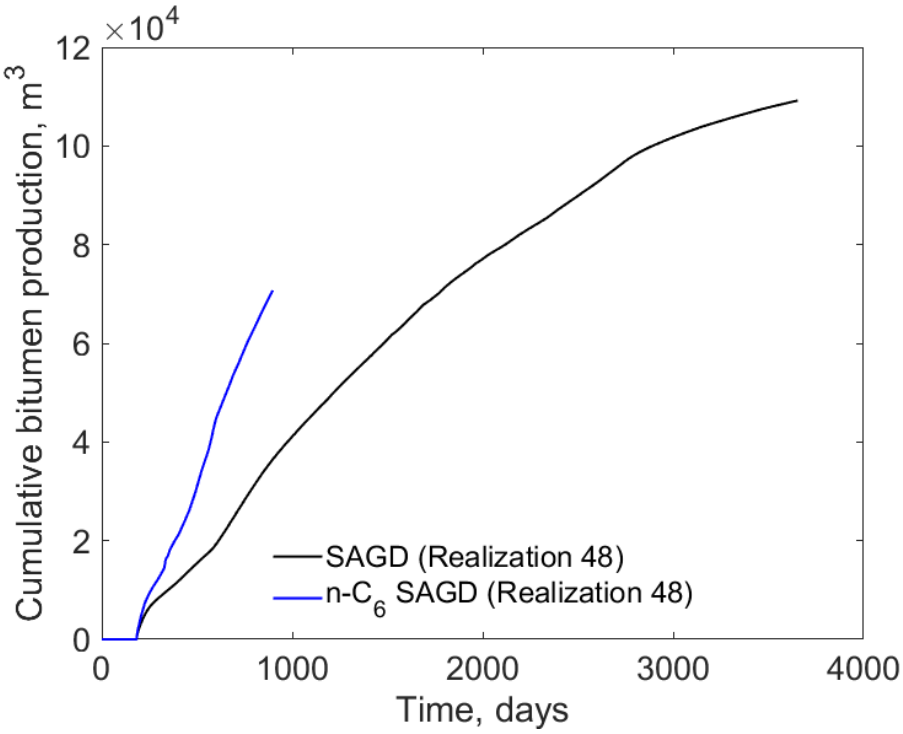

Figure K-27(a). Cumulative bitumen production histories for SAGD and n-C_6 SAGD for realization 48

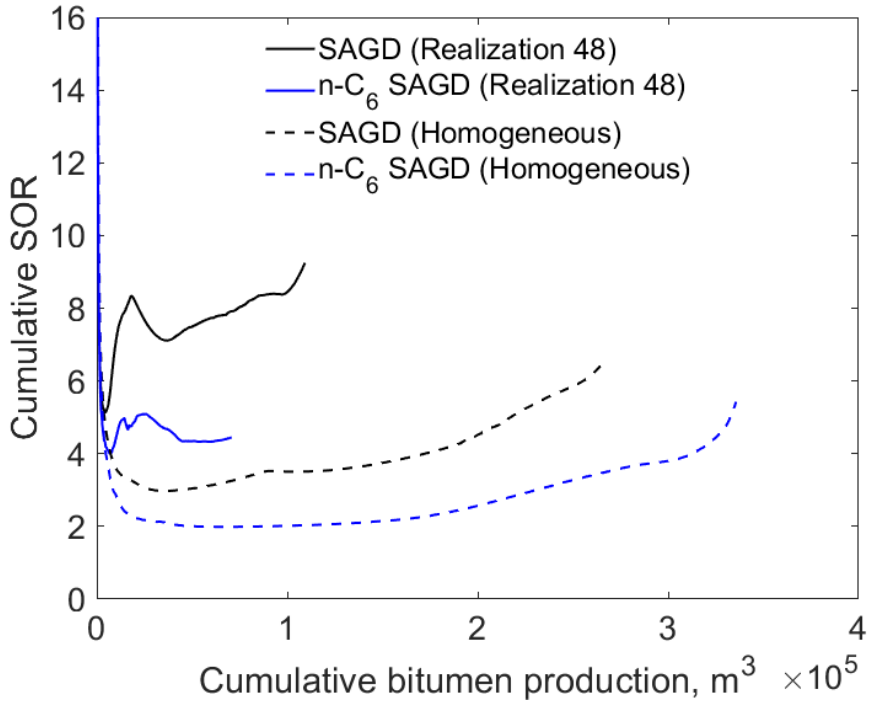

Figure K-27(b). Cumulative SOR for SAGD and n-C_6 SAGD for realization 48

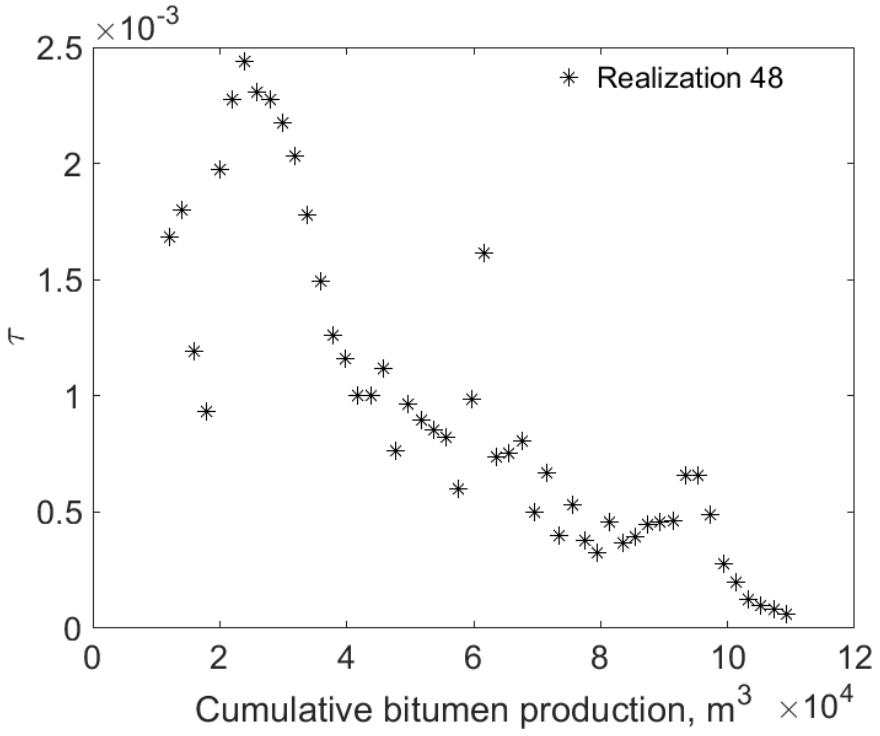

Figure K-27(c). τ for SAGD as a function of cumulative bitumen production for realization 48

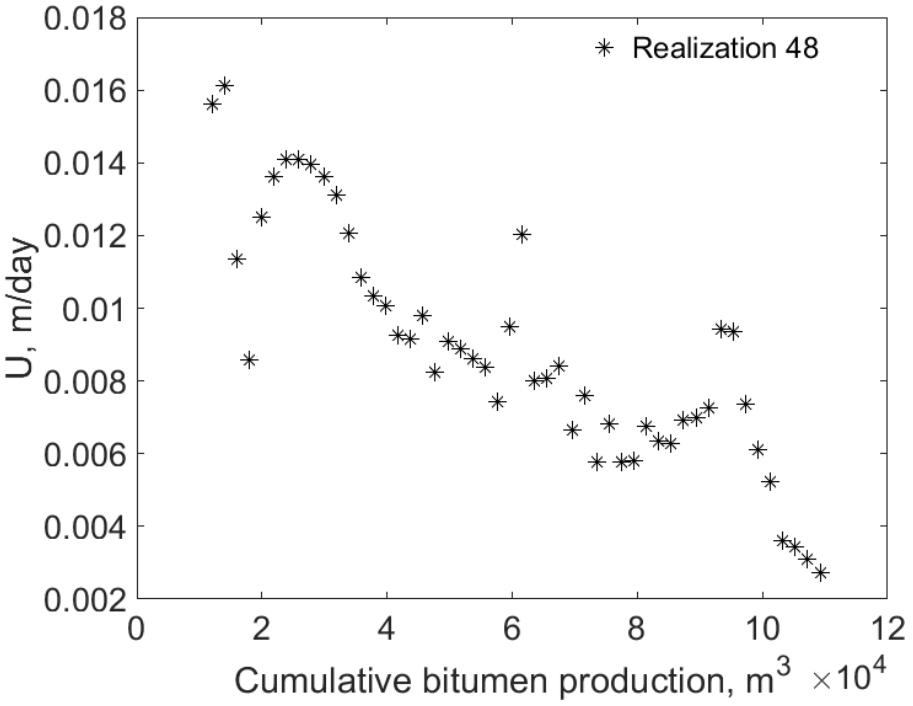

Figure K-27(d). U for SAGD as a function of cumulative bitumen production for realization 48

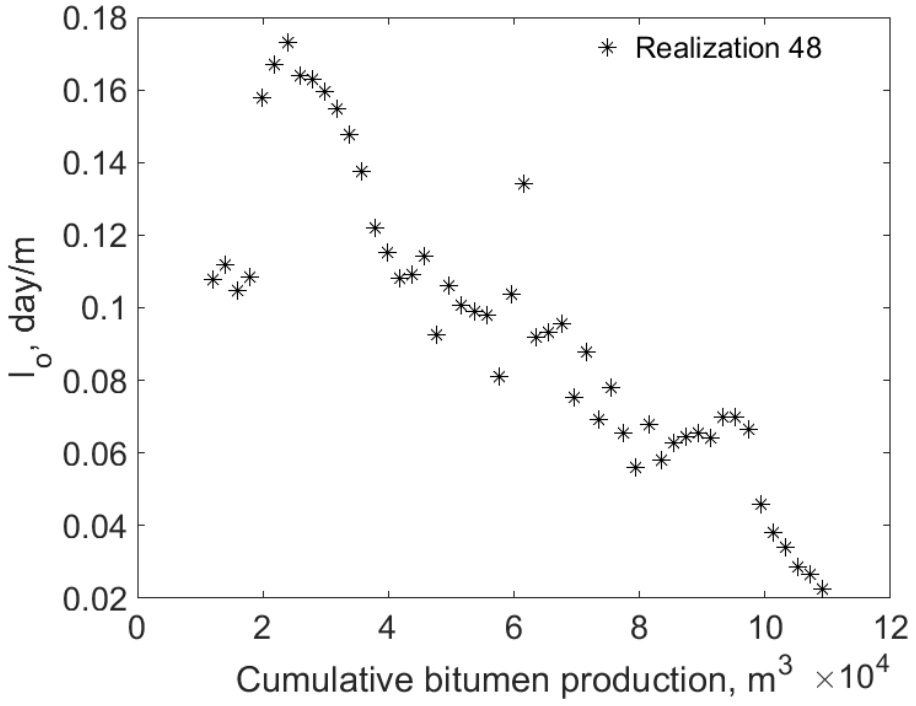

Figure K-27(e).I_o for SAGD as a function of cumulative bitumen production for realization 48

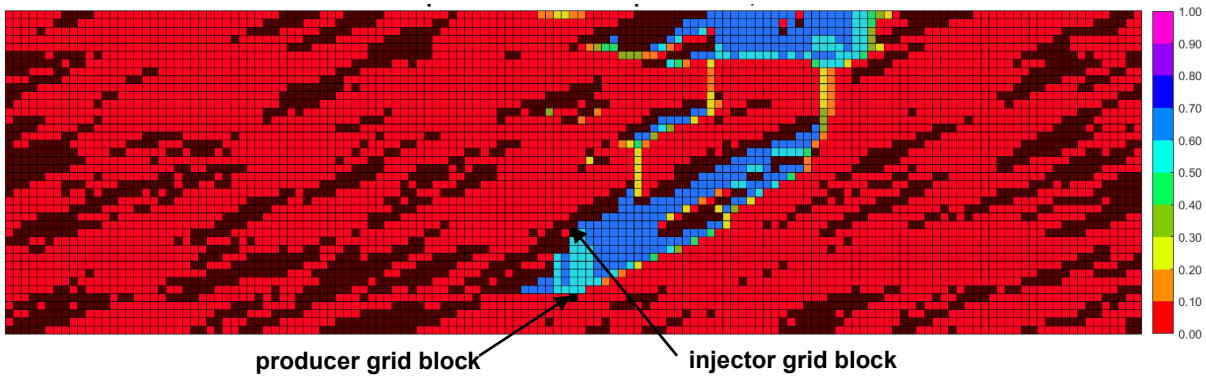

Figure K-27(f). Vapor-phase saturation map in SAGD for realization 48 for Q ≈ 31218 m^3

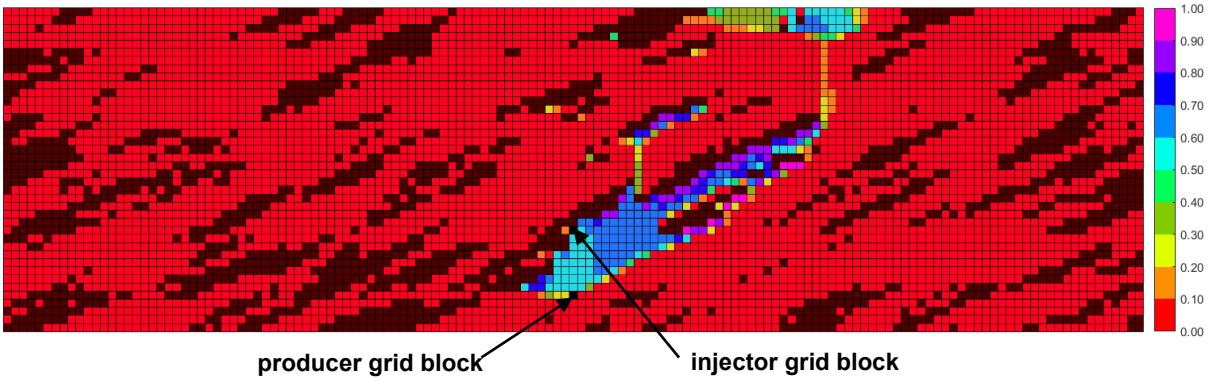

Figure K-27(g). Vapor-phase saturation map in n-C_6 SAGD for realization 48 for Q ≈ 31218 m^3

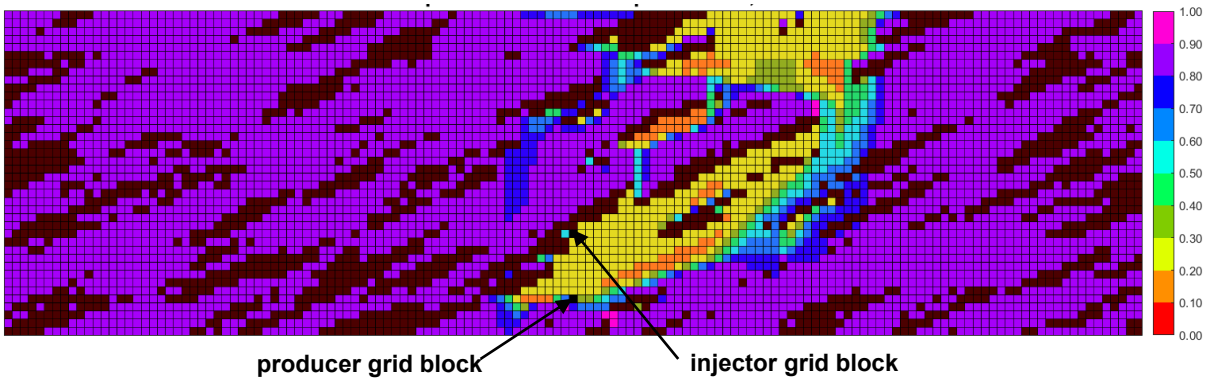

Figure K-27(h). Oleic-phase saturation map in SAGD for realization 48 for Q ≈ 31218 m^3

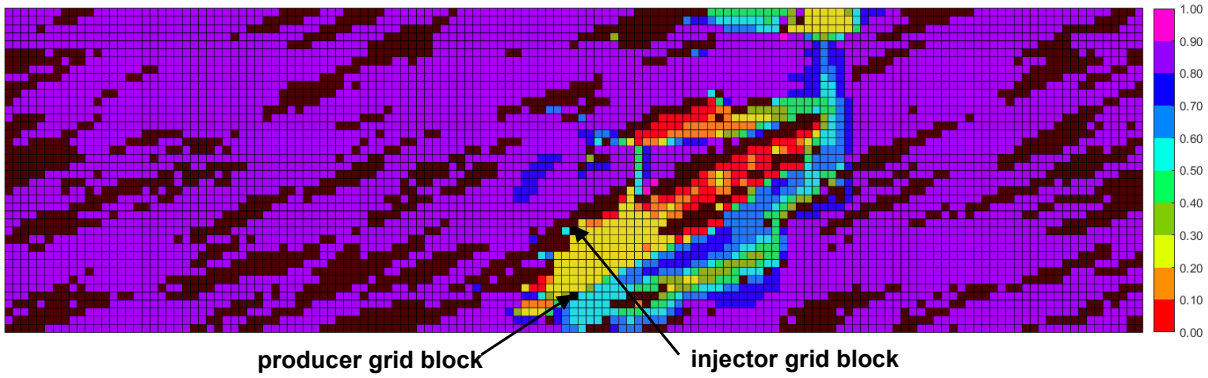

Figure K-27(i). Oleic-phase saturation map in n-C_6 SAGD for realization 48 for Q ≈ 31218 m^3

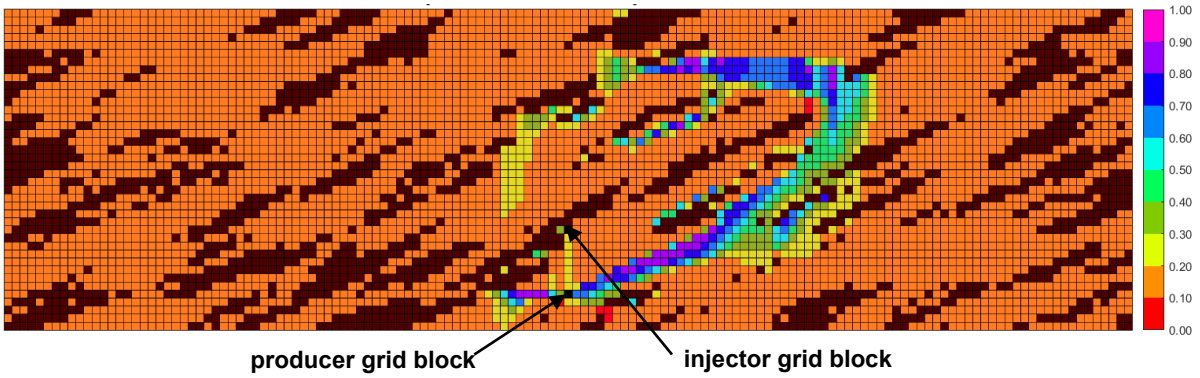

Figure K-27(j). Aqueous-phase saturation map in SAGD for realization 48 for Q ≈ 31218 m^3

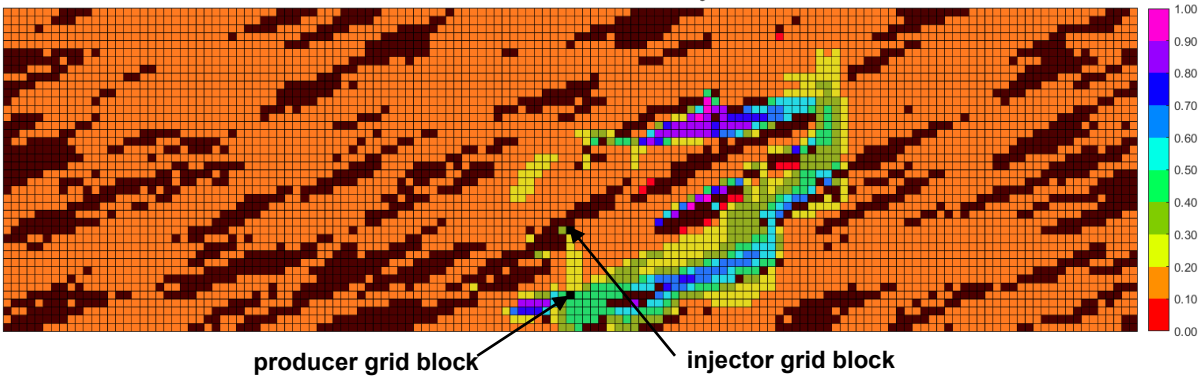

Figure K-27(k). Aqueous-phase saturation map in n-C_6 SAGD for realization 48 for Q ≈ 31218 m^3

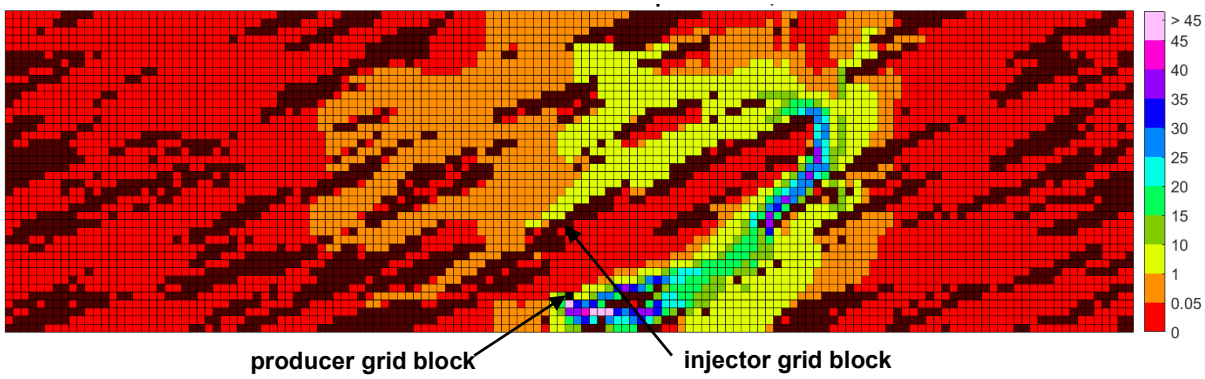

Figure K-27(l). Bitumen molar flow rate (kg-mole/day) map in SAGD for realization 48 for Q ≈ 31218 m^3

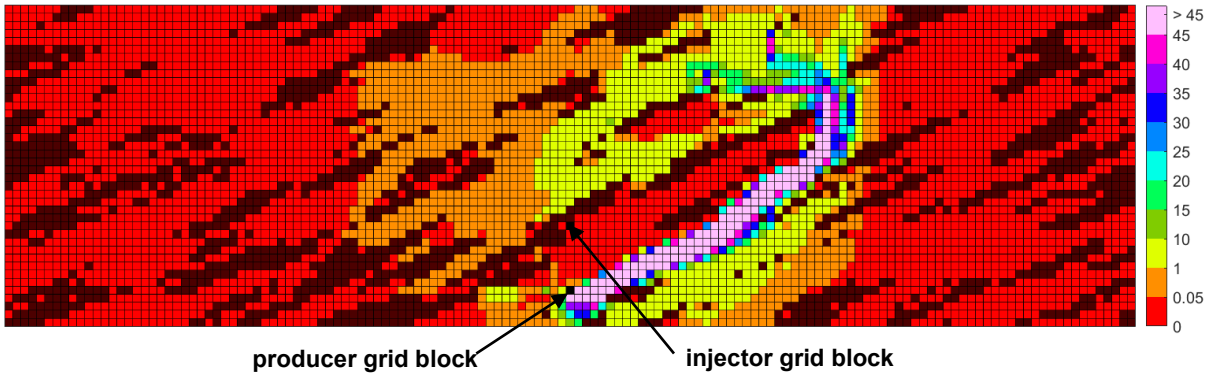

Figure K-27(m). Bitumen molar flow rate (kg-mole/day) map in n-C_6 SAGD for realization 48 for Q ≈ 31218 m^3

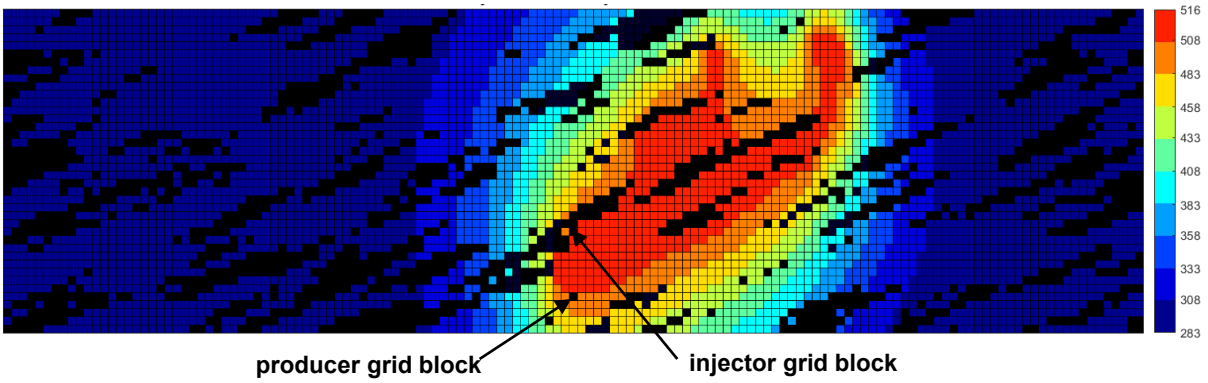

Figure K-27(n). Temperature (Kelvin) map in SAGD for realization 48 for Q ≈ 31218 m^3

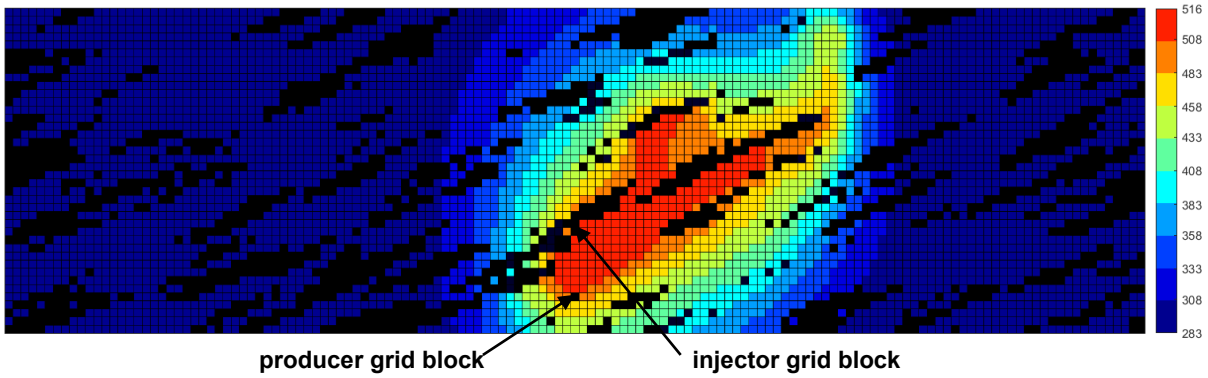

Figure K-27(o). Temperature (Kelvin) map in n-C_6 SAGD for realization 48 for Q ≈ 31218 m^3

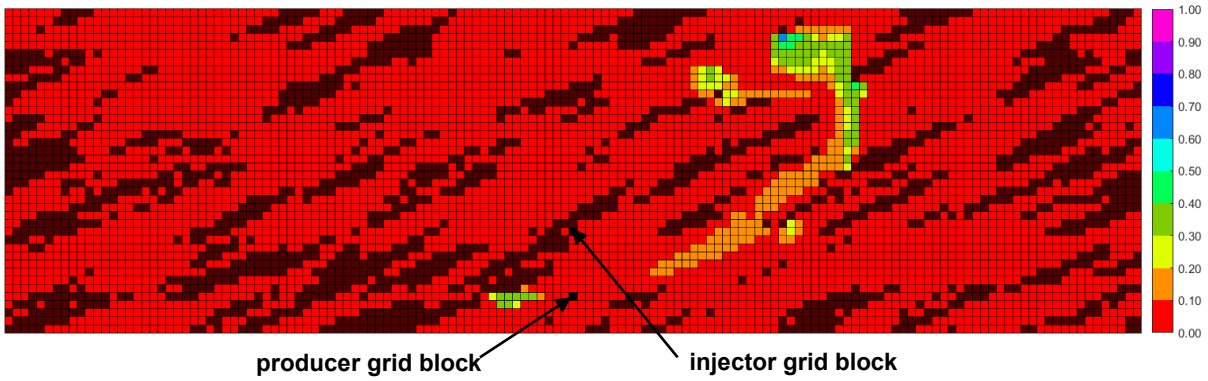

Figure K-27(p). $\beta_L x_{sL}$ map in n-C_6 SAGD for realization 48 for Q ≈ 31218 m^3

Figure K-27. Property maps for SAGD and n-C_6 SAGD for realization 48

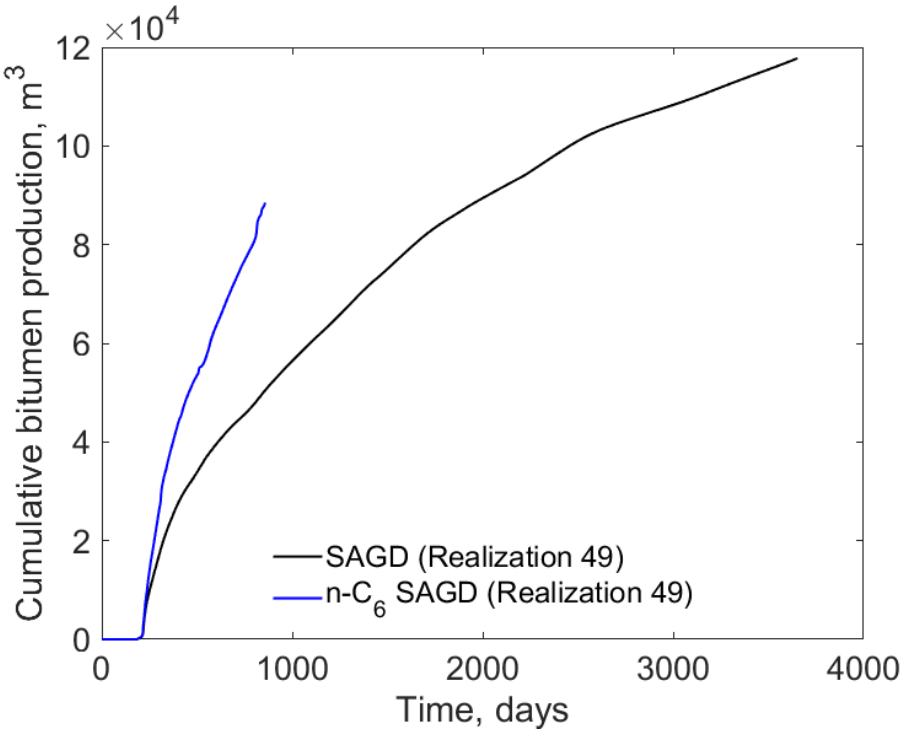

Figure K-28(a). Cumulative bitumen production histories for SAGD and n-C_6 SAGD for realization 49

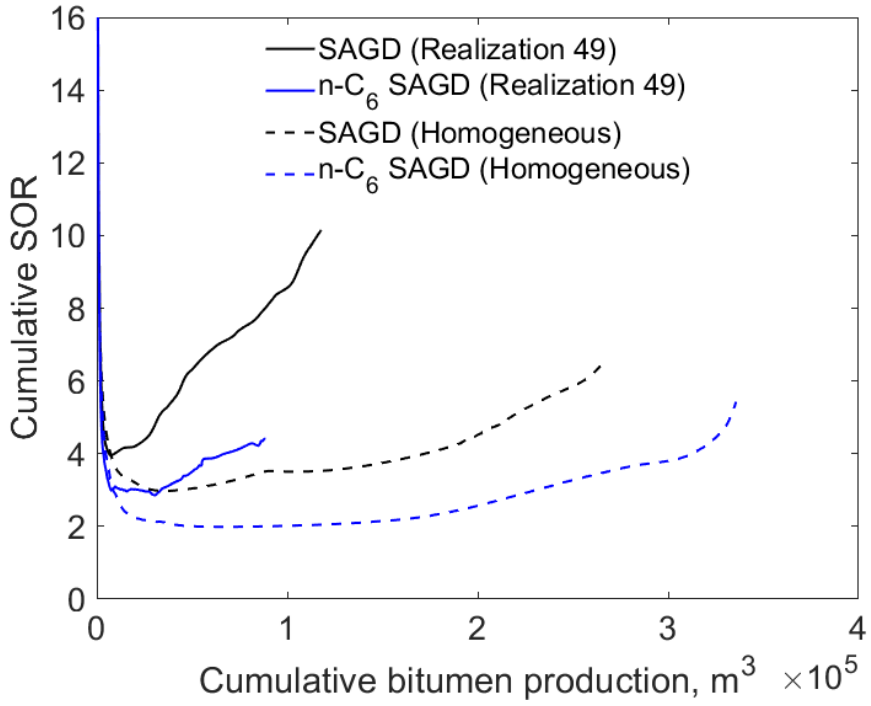

Figure K-28(b). Cumulative SOR for SAGD and n-C_6 SAGD for realization 49

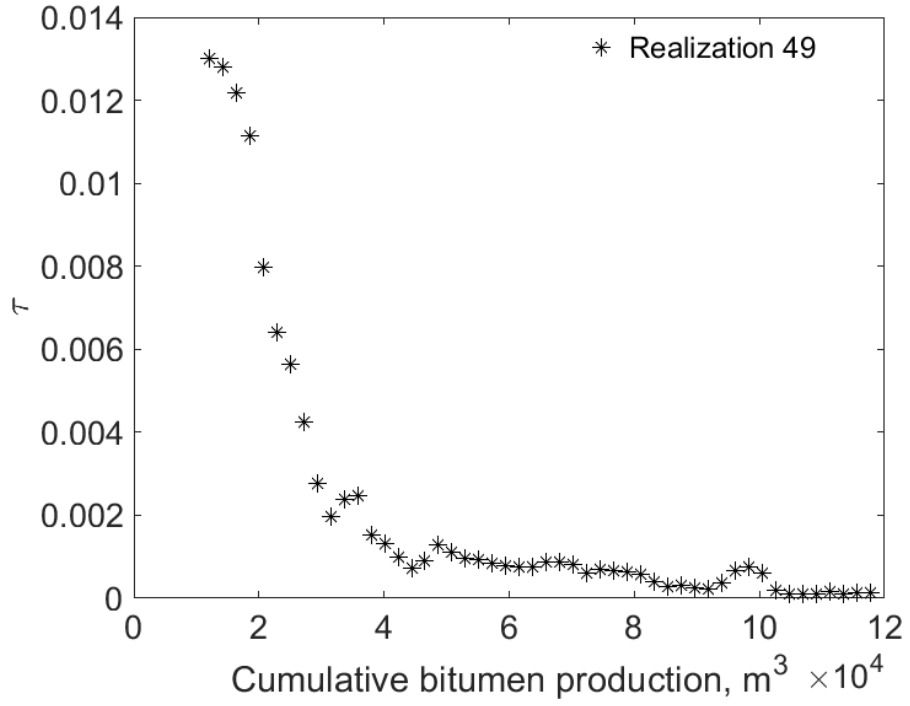

Figure K-28(c). τ for SAGD as a function of cumulative bitumen production for realization 49

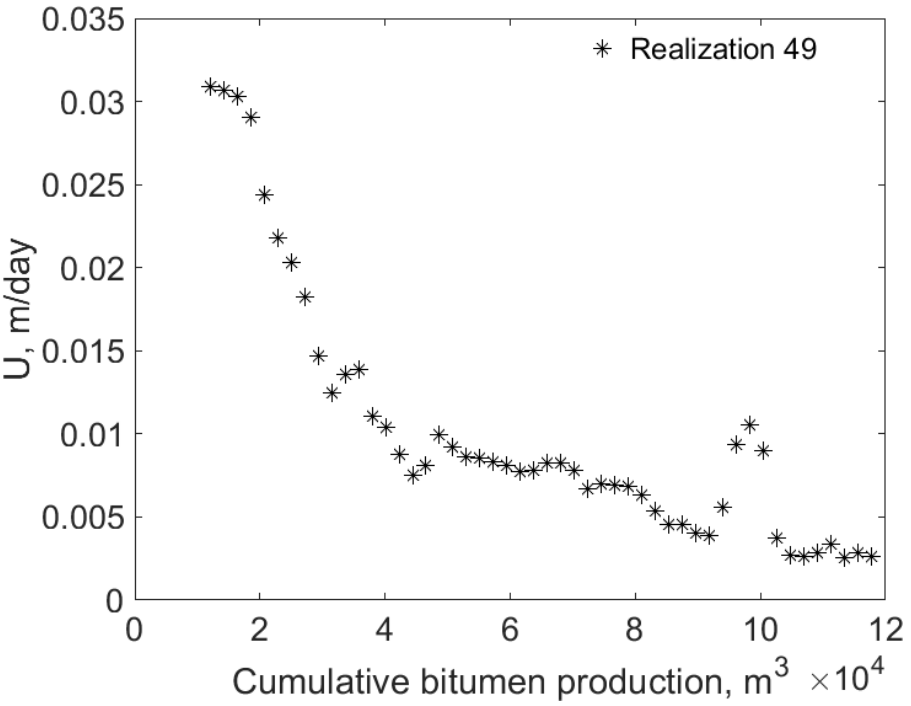

Figure K-28(d). U for SAGD as a function of cumulative bitumen production for realization 49

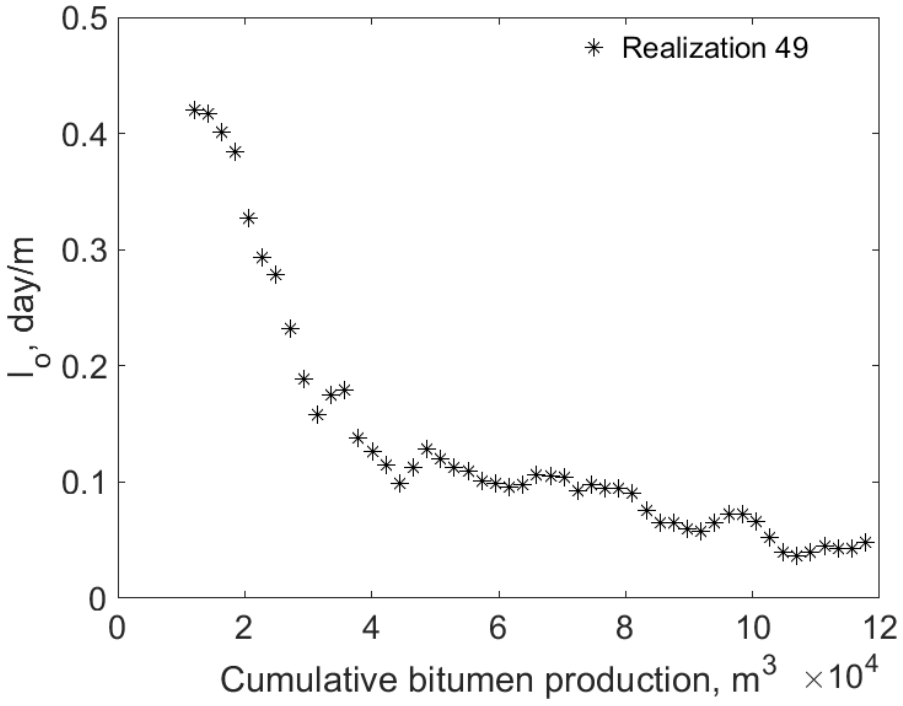

Figure K-28(e).I_o for SAGD as a function of cumulative bitumen production for realization 49

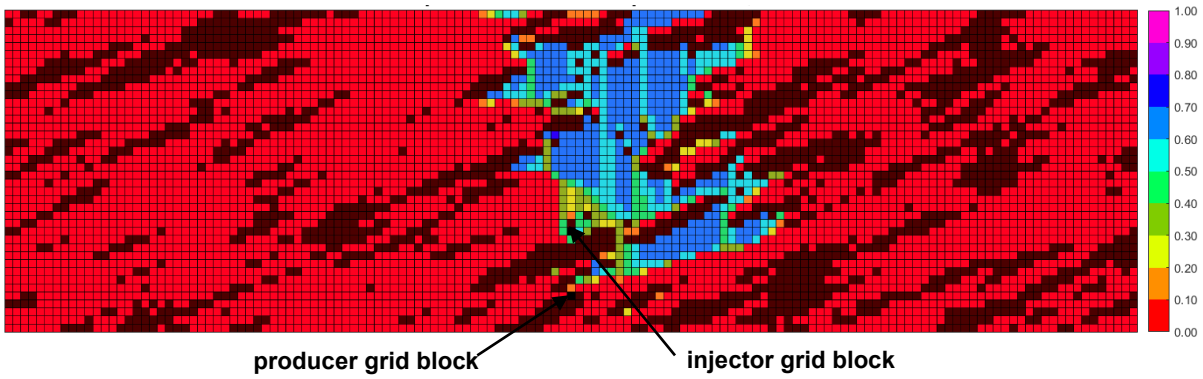

Figure K-28(f). Vapor-phase saturation map in SAGD for realization 49 for Q ≈ 31218 m^3

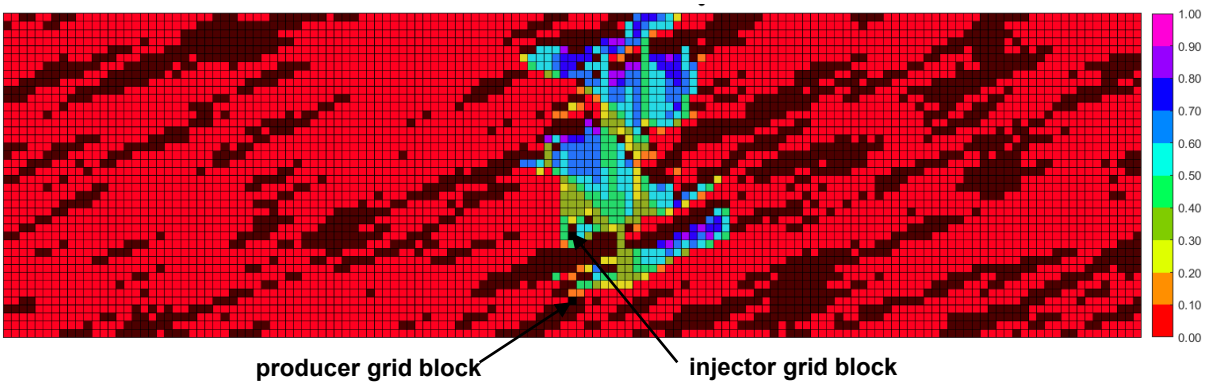

Figure K-28(g). Vapor-phase saturation map in n-C_6 SAGD for realization 49 for Q ≈ 31218 m^3

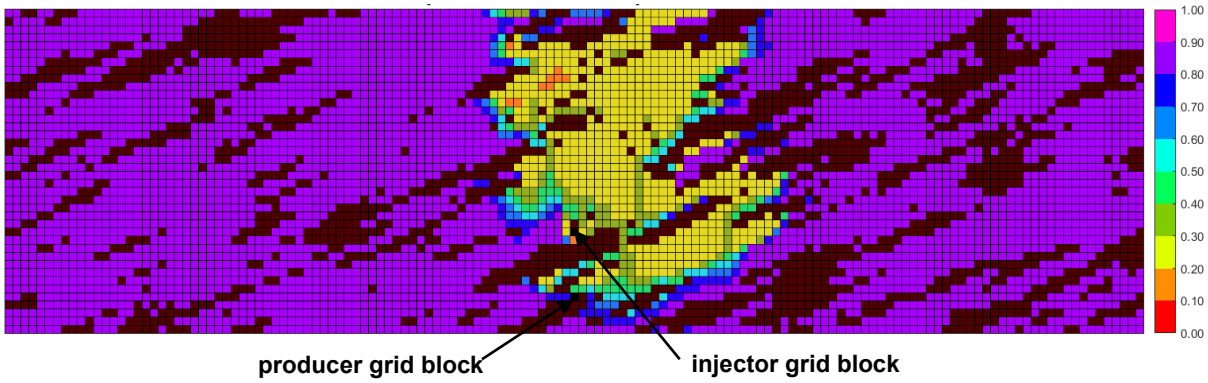

Figure K-28(h). Oleic-phase saturation map in SAGD for realization 49 for Q ≈ 31218 m^3

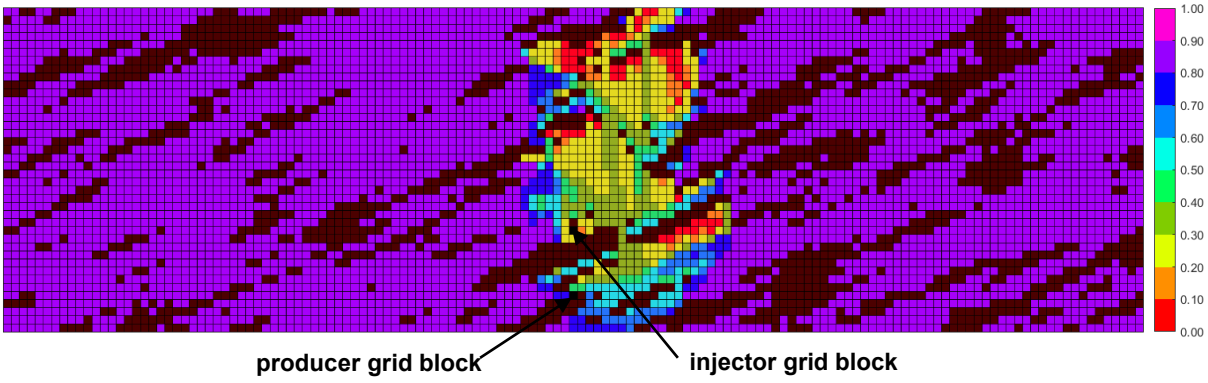

Figure K-28(i). Oleic-phase saturation map in n-C$_6$ SAGD for realization 49 for Q ≈ 31218 m^3

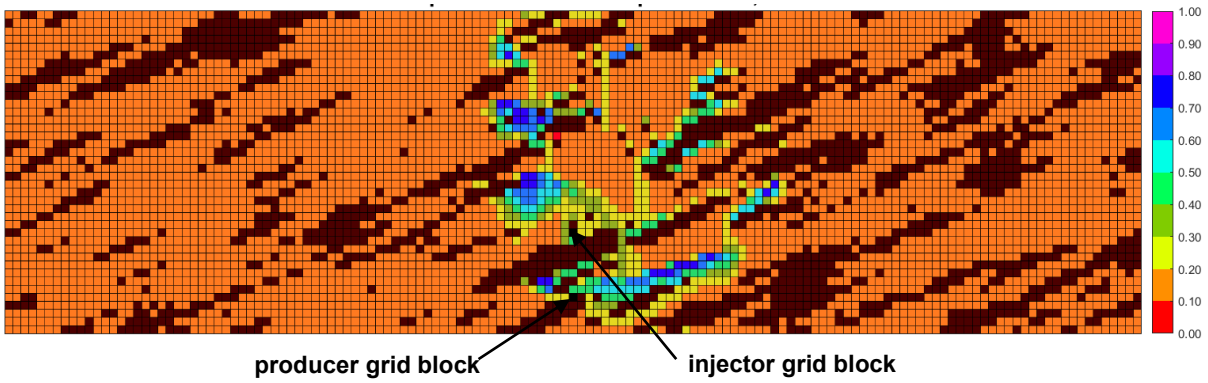

Figure K-28(j). Aqueous-phase saturation map in SAGD for realization 48 for Q ≈ 31218 m^3

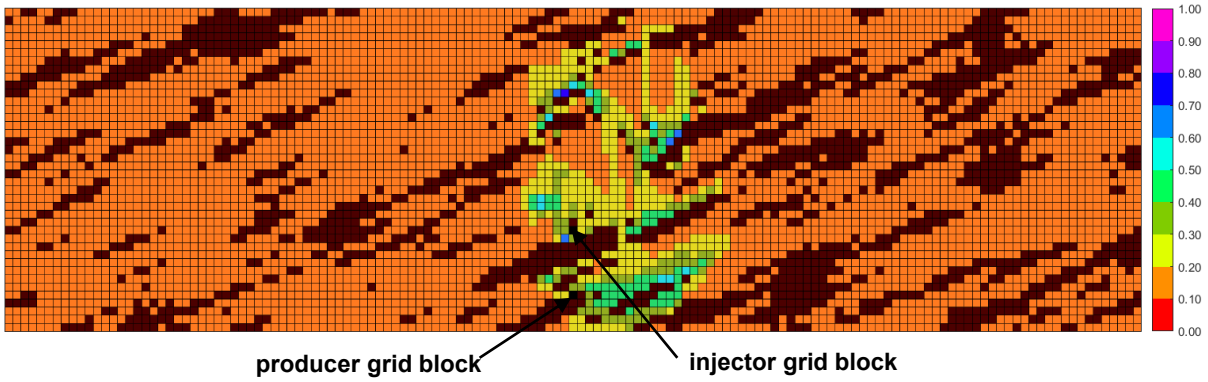

Figure K-28(k). Aqueous-phase saturation map in n-C$_6$ SAGD for realization 49 for Q ≈ 31218 m^3

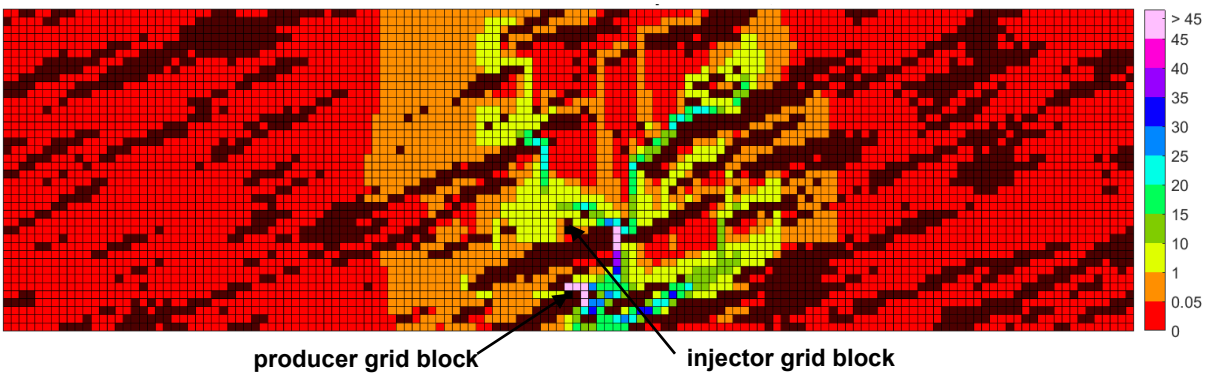

Figure K-28(l). Bitumen molar flow rate (kg-mole/day) map in SAGD for realization 49 for Q ≈ 31218 m^3

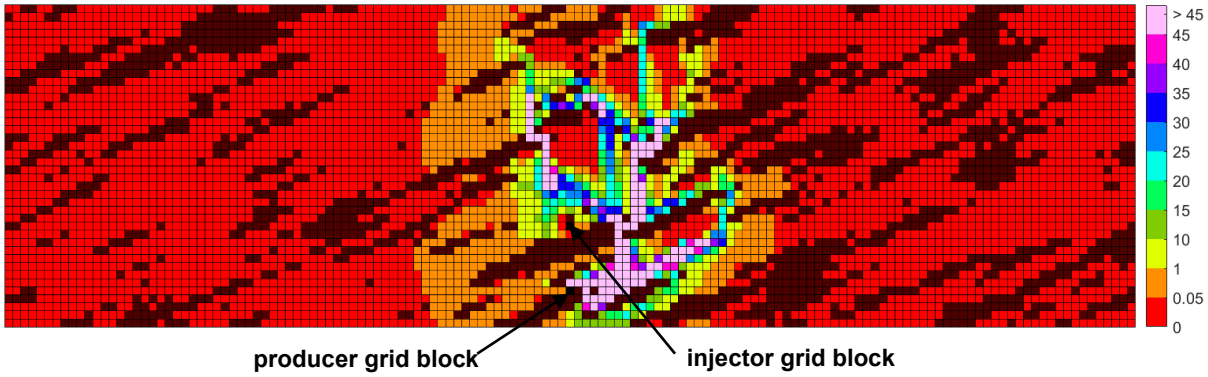

Figure K-28(m). Bitumen molar flow rate (kg-mole/day) map in n-C_6 SAGD for realization 49 for Q ≈ 31218 m^3

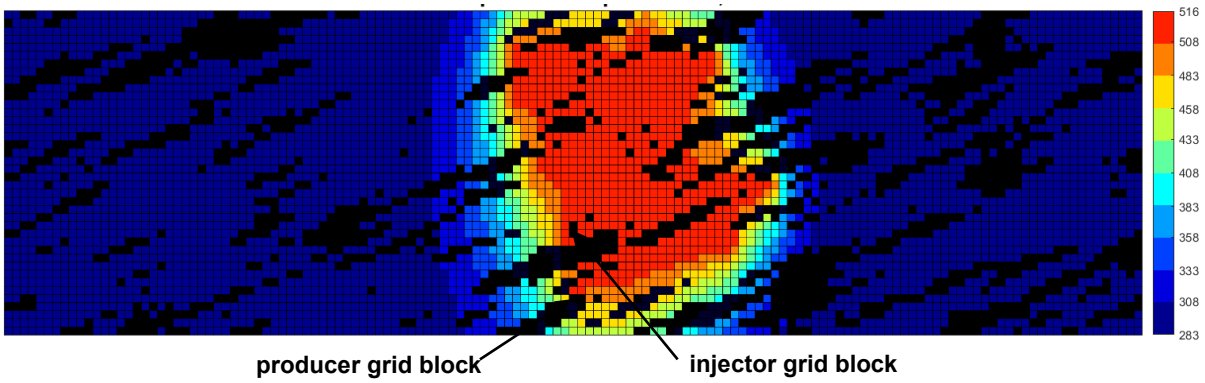

Figure K-28(n). Temperature (Kelvin) map in SAGD for realization 49 for Q ≈ 31218 m^3

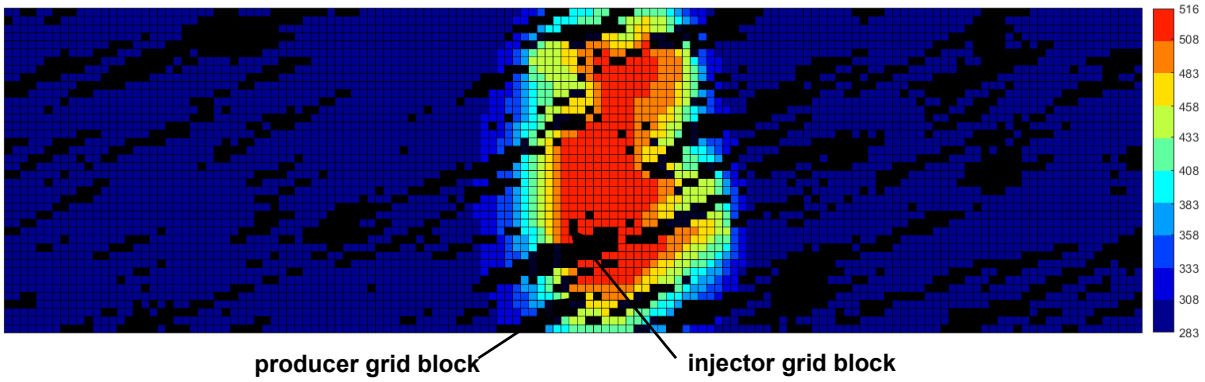

Figure K-28(o). Temperature (Kelvin) map in n-C_6 SAGD for realization 49 for Q ≈ 31218 m^3

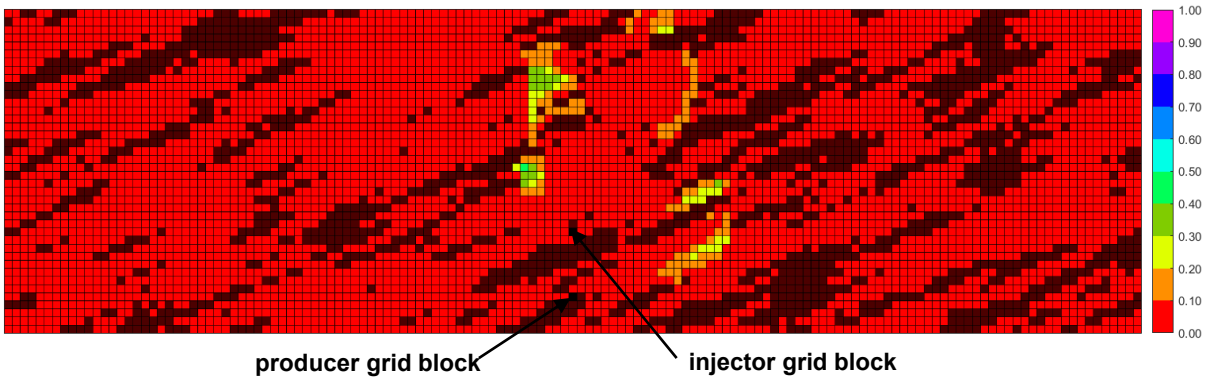

Figure K-28(p). $\beta_L x_{sL}$ map in n-C_6 SAGD for realization 49 for Q ≈ 31218 m^3

Figure K-28. Property maps for SAGD and n-C_6 SAGD for realization 49

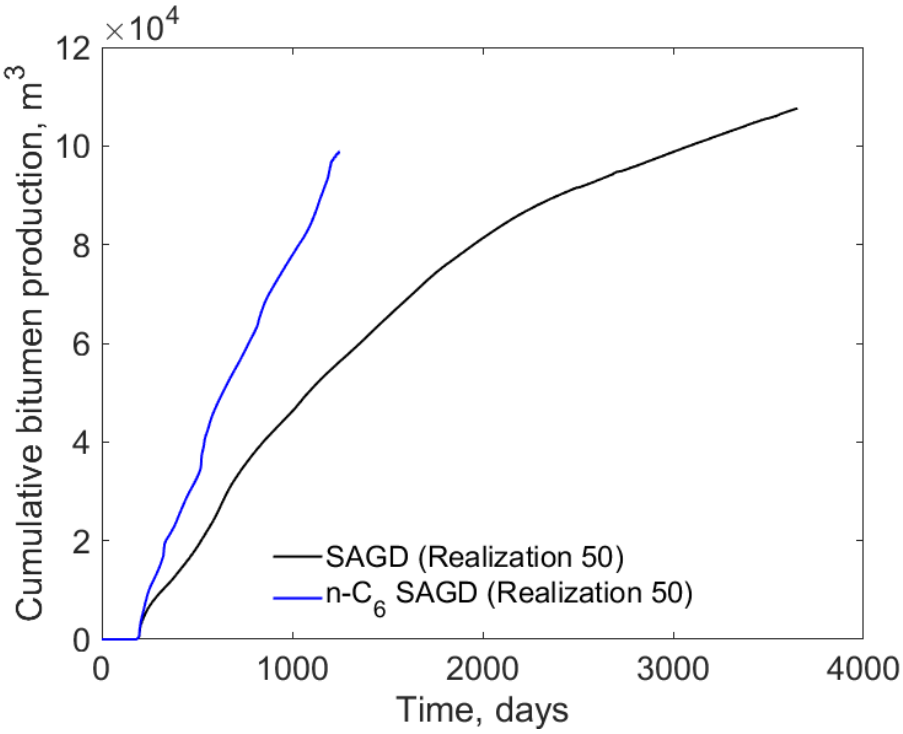

Figure K-29(a). Cumulative bitumen production histories for SAGD and n-C_6 SAGD for realization 50

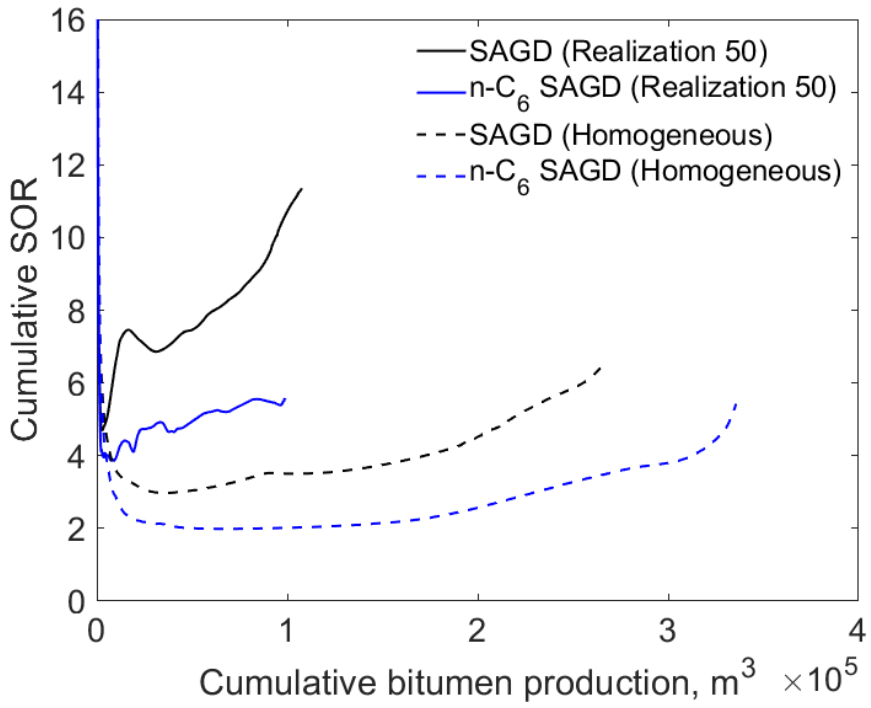

Figure K-29(b). Cumulative SOR for SAGD and n-C_6 SAGD for realization 50

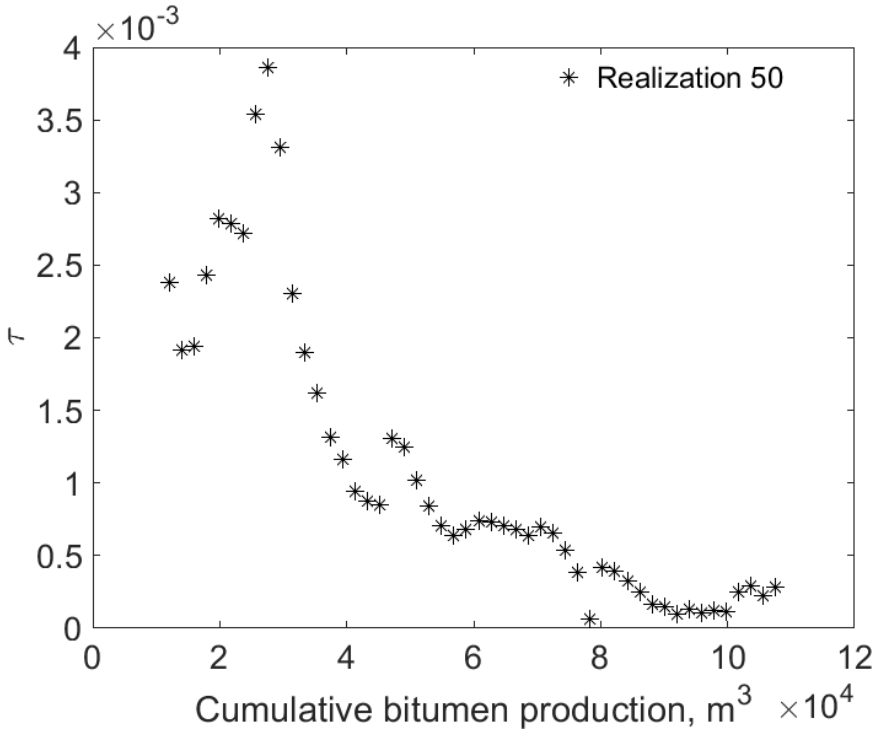

Figure K-29(c). τ for SAGD as a function of cumulative bitumen production for realization 50

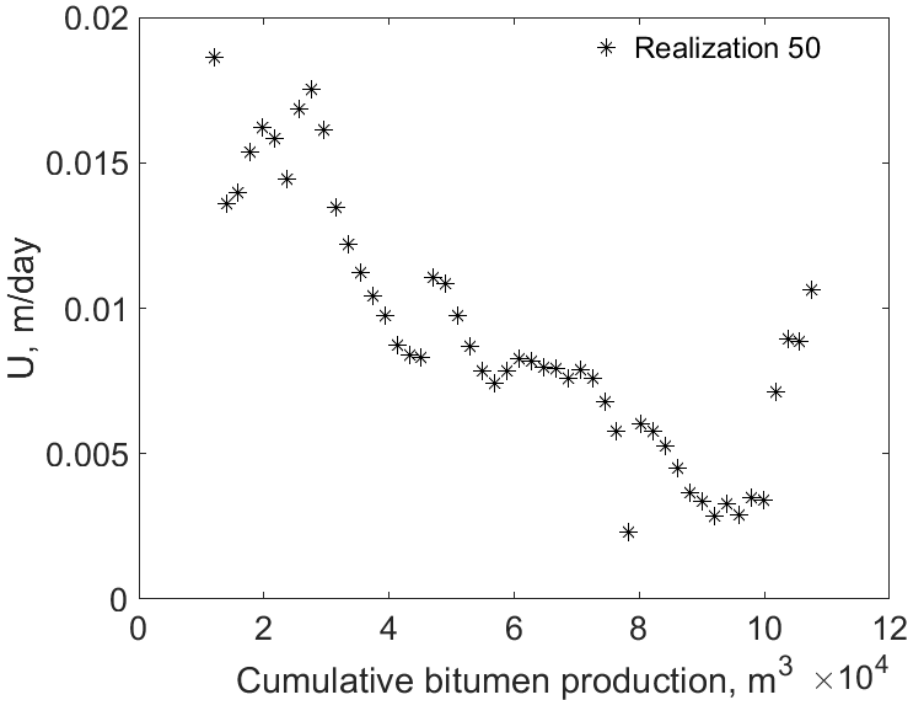

Figure K-29(d). U for SAGD as a function of cumulative bitumen production for realization 50

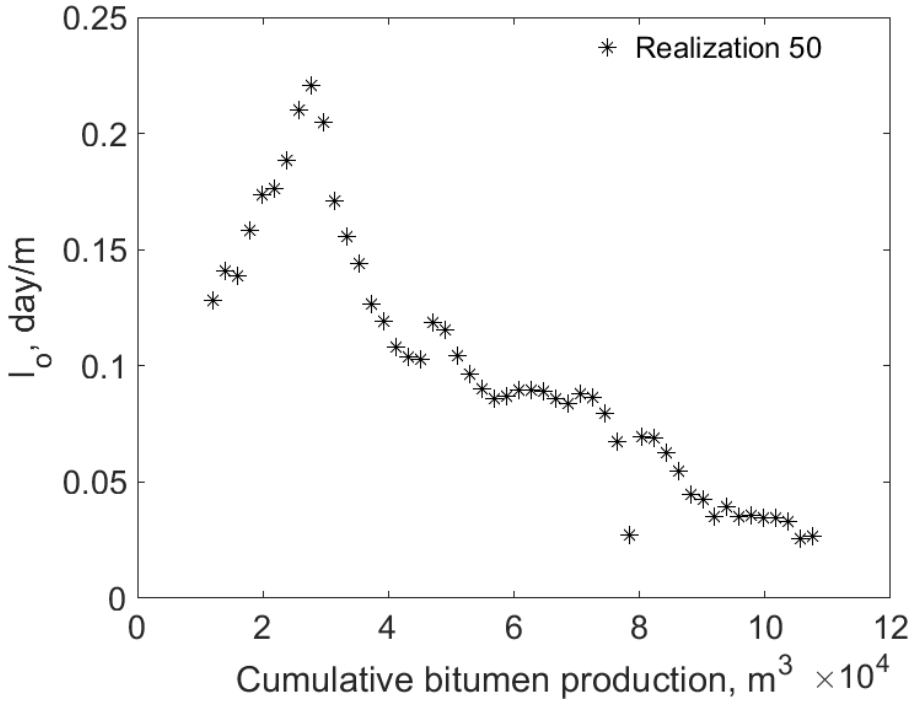

Figure K-29(e).I_o for SAGD as a function of cumulative bitumen production for realization 50

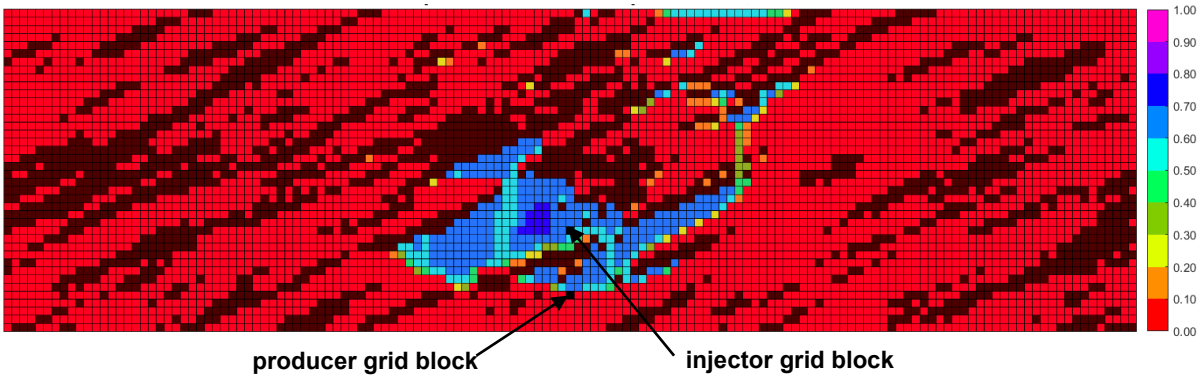

Figure K-29(f). Vapor-phase saturation map in SAGD for realization 50 for Q ≈ 31218 m^3

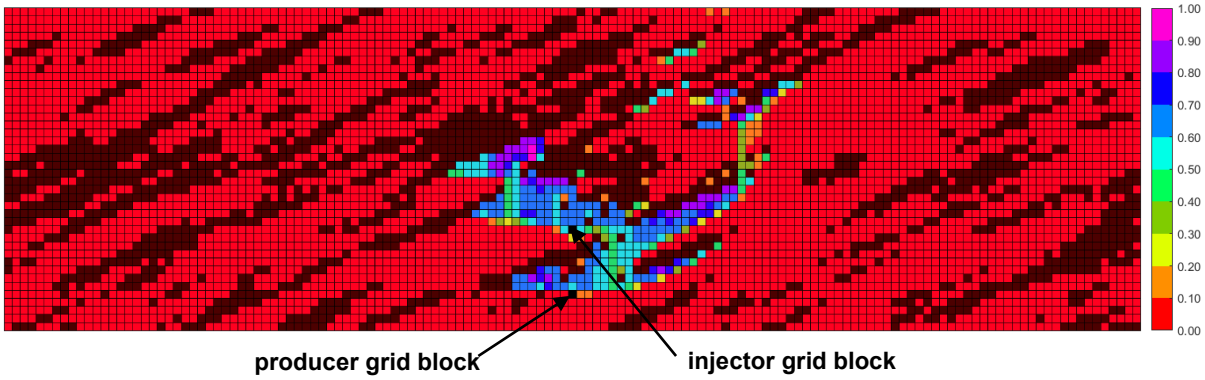

Figure K-29(g). Vapor-phase saturation map in n-C_6 SAGD for realization 50 for Q ≈ 31218 m^3

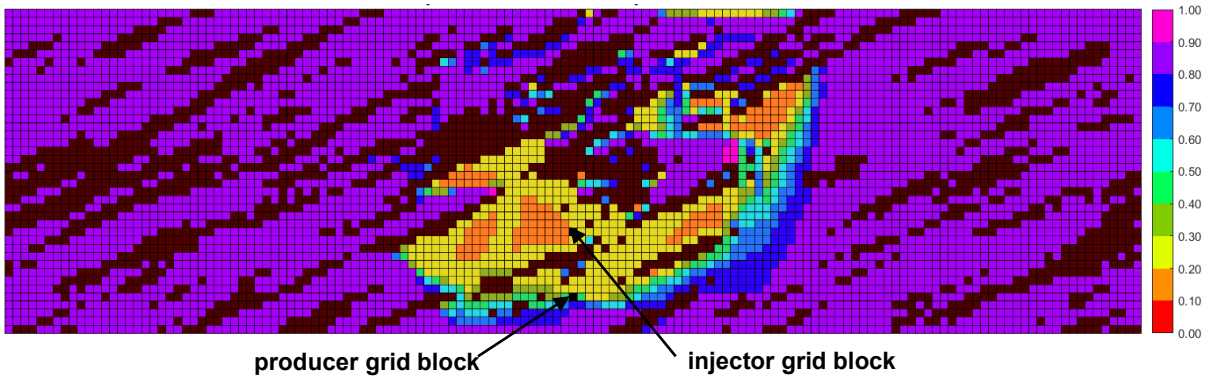

Figure K-29(h). Oleic-phase saturation map in SAGD for realization 50 for Q ≈ 31218 m^3

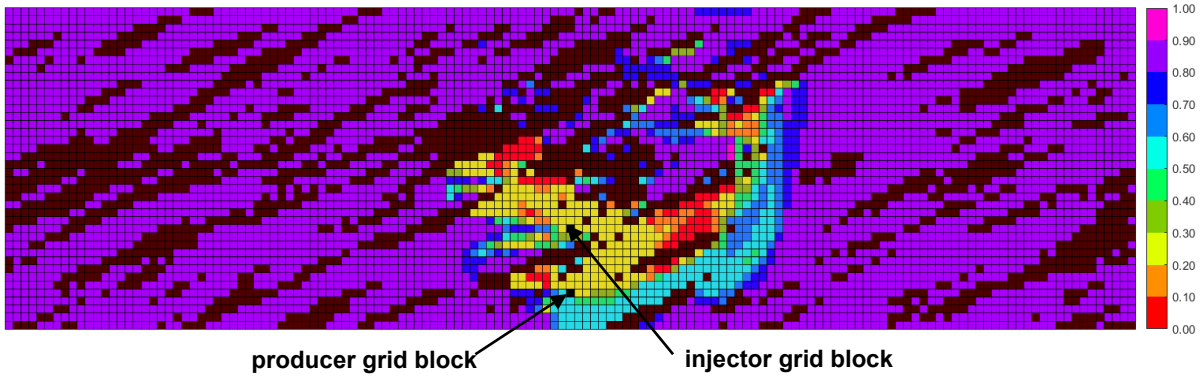

Figure K-29(i). Oleic-phase saturation map in n-C_6 SAGD for realization 50 for Q ≈ 31218 m^3

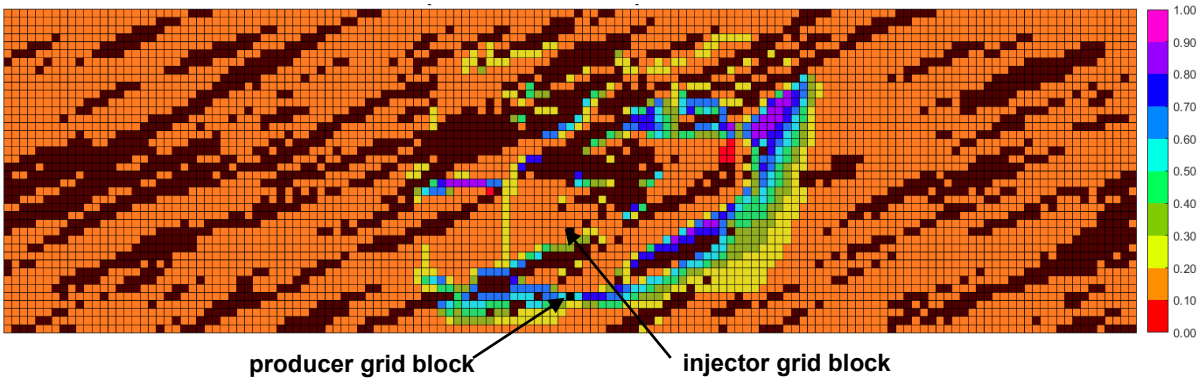

Figure K-29(j). Aqueous-phase saturation map in SAGD for realization 50 for Q ≈ 31218 m^3

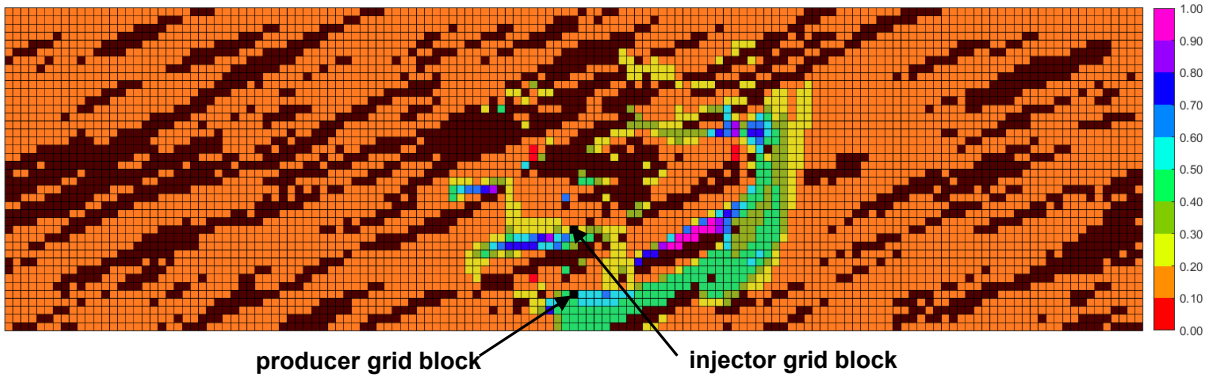

Figure K-29(k). Aqueous-phase saturation map in n-C_6 SAGD for realization 50 for Q ≈ 31218 m^3

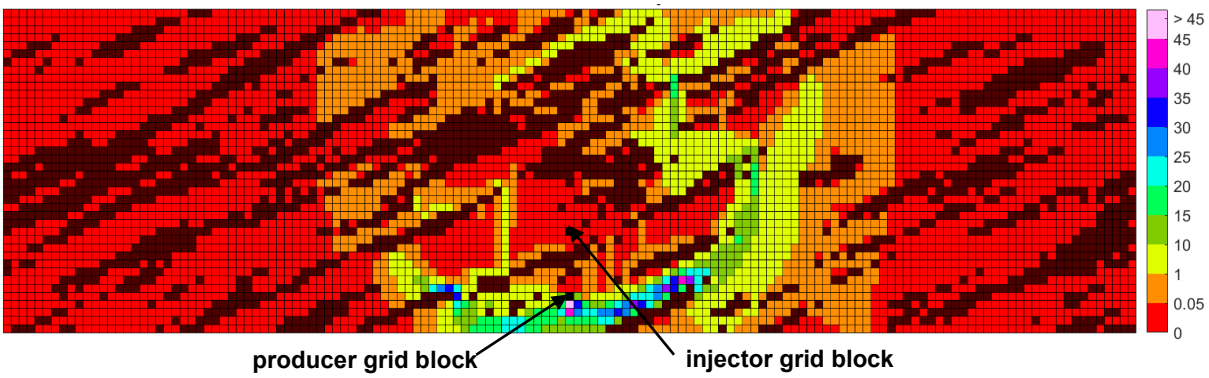

Figure K-29(l). Bitumen molar flow rate (kg-mole/day) map in SAGD for realization 50 for Q ≈ 31218 m^3

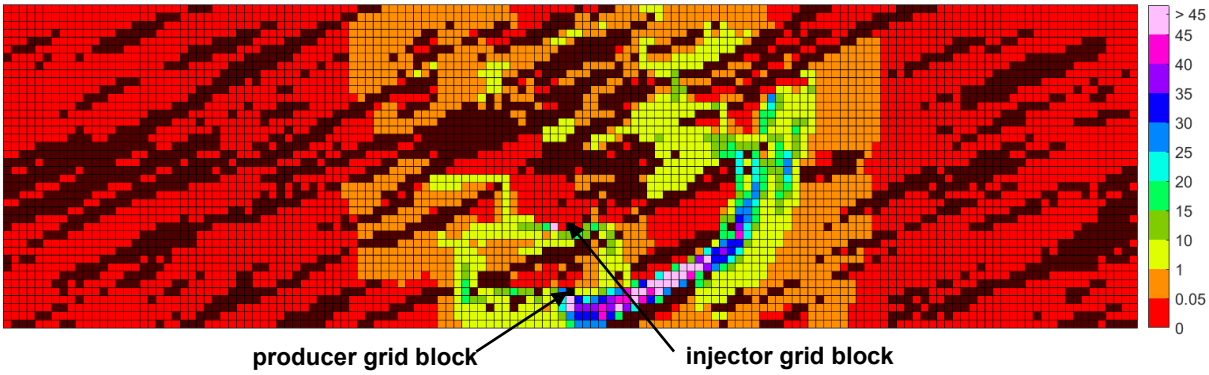

Figure K-29(m). Bitumen molar flow rate (kg-mole/day) map in n-C_6 SAGD for realization 50 for Q ≈ 31218 m^3

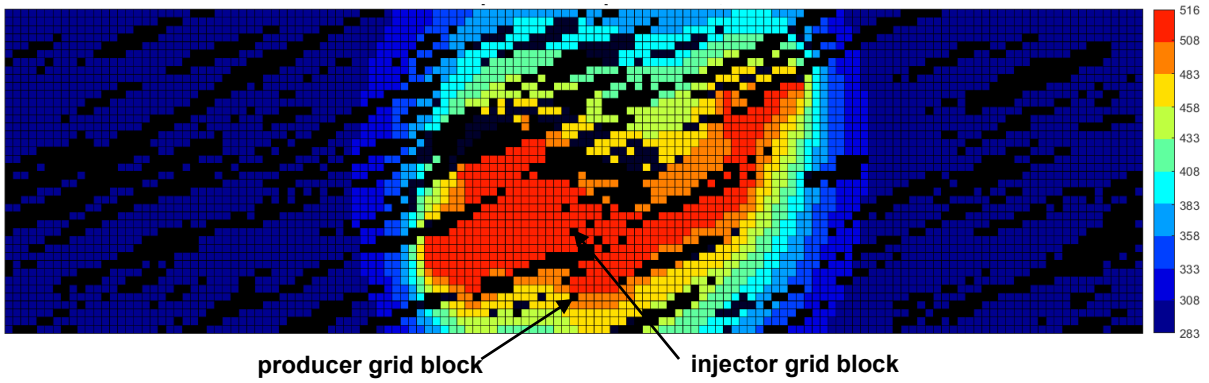

Figure K-29(n). Temperature (Kelvin) map in SAGD for realization 50 for Q ≈ 31218 m^3

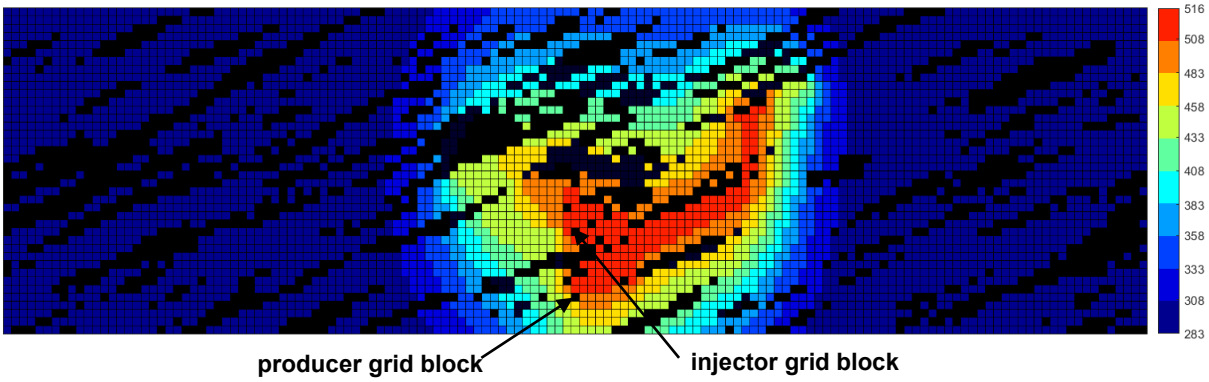

Figure K-29(o). Temperature (Kelvin) map in n-C_6 SAGD for realization 50 for Q ≈ 31218 m^3

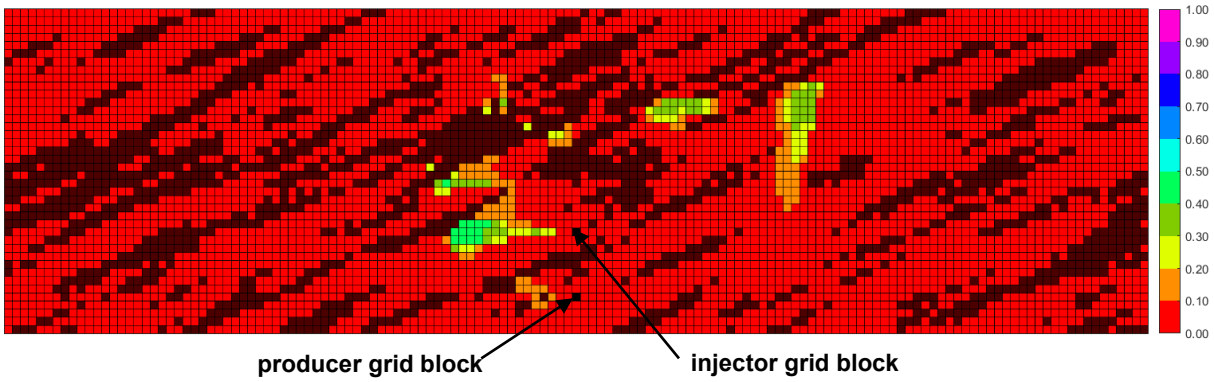

Figure K-29(p). $\beta_L x_{sL}$ map in n-C_6 SAGD for realization 50 for Q ≈ 31218 m^3

Figure K-29. Property maps for SAGD and n-C_6 SAGD for realization 50